

AI Agents Can Already Autonomously Perform Experimental High Energy Physics

Eric A. Moreno^{*†1,2}, Samuel Bright-Thonney^{*‡1,2}, Andrzej Novak^{*§1,2}, Dolores Garcia^{¶3},
and Philip Harris^{||1,2}

¹Department of Physics, Massachusetts Institute of Technology

²NSF AI Institute for Artificial Intelligence and Fundamental Interactions

³CERN

March 23, 2026

Abstract

Large language model-based AI agents are now able to autonomously execute substantial portions of a high energy physics (HEP) analysis pipeline with minimal expert-curated input. Given access to a HEP dataset, an execution framework, and a corpus of prior experimental literature, we find that Claude Code succeeds in automating all stages of a typical analysis: event selection, background estimation, uncertainty quantification, statistical inference, and paper drafting. We argue that the experimental HEP community is underestimating the current capabilities of these systems, and that most proposed agentic workflows are too narrowly scoped or scaffolded to specific analysis structures. We present a proof-of-concept framework, *Just Furnish Context* (JFC), that integrates autonomous analysis agents with literature-based knowledge retrieval and multi-agent review, and show that this is sufficient to plan, execute, and document a credible high energy physics analysis. We demonstrate this by conducting analyses on open data from ALEPH, DELPHI, and CMS to perform electroweak, QCD, and Higgs boson measurements. Rather than replacing physicists, these tools promise to offload the repetitive technical burden of analysis code development, freeing researchers to focus on physics insight, truly novel method development, and rigorous validation. Given these developments, we advocate for new strategies for how the community trains students, organizes analysis efforts, and allocates human expertise.

1 Introduction

A typical experimental high energy physics analysis is a years-long endeavor, often spanning the majority of a graduate student or postdoc’s time at an academic institution. For large collider experiments the process is algorithmic: a physicist (a) identifies an interesting measurement channel or new physics signature, (b) studies existing literature to understand how similar measurements have been done, (c) designs and validates an event selection procedure using Monte Carlo (MC) simulation, quantifies all relevant sources of systematic uncertainty, and finally (d) “unblinds” on real experimental data and performs statistical hypothesis tests to extract measurements or limits.

This process invariably involves writing thousands of lines of code to process data and apply standard, though not off-the-shelf, analysis techniques, most of which is structurally similar to code written in dozens of other analyses within the same collaboration. While this can be a useful exercise for developing programming

*These authors contributed equally.

†emoreno@mit.edu

‡sambt@mit.edu

§novaka@mit.edu

¶dolores.garcia@cern.ch

||pcharris@mit.edu

skills, it often consumes a substantial fraction of a physicist’s working time and demands little physics reasoning or insight. This is frequently exacerbated by the absence of high-quality, centralized, or up-to-date documentation for much of the core software infrastructure within experimental collaborations. The result is a slow, error-prone, and tedious process that, beyond a brief initial learning phase, adds little to a student’s education and robs all practitioners of valuable time that could be better spent on higher-level questions.

In this paper, we argue that the majority of this process can be delegated to AI agents. Modern coding assistants can autonomously write and execute code, access documentation (both local and online), iteratively critique and debug their own output, and document their progress for human overseers [14, 2]. As large language models (LLMs) and commercial agentic frameworks continue to improve, these tools will only become more reliable.

This is not a speculative claim about future capabilities. In this paper we show that, given a general framework distilling the processes used in practice at large HEP collaborations and an initial high-level physics prompt, Claude Code¹ is able to produce a complete analysis: event selection, background estimation, systematic uncertainty evaluation, statistical inference, and a written report with publication-grade figures. The report quality is typically, at a cursory expert review, indistinguishable from a report produced by a junior graduate student (or an expert under time constraints). Recent work by Badea et al. [4] demonstrated that an AI agent, with iterative physicist supervision at each step, can contribute to a measurement using LEP open data. We build on this direction but take a fundamentally different approach: rather than requiring continuous human feedback, JFC delegates review to specialized AI agents, concentrating human oversight at a single unblinding gate, yielding a nearly fully autonomous framework.

The framework specification splits roughly into three independent components:

- **Methodology.** We encode what a typical particle physics analysis workflow looks like, from planning and data exploration to statistical analysis. This structure, while not usually explicitly spelled out, generally lives as institutional knowledge in scientific collaborations and research groups. Roughly, this corresponds to the guidance a graduate student would receive as they progress through their thesis research.
 - **Review.** A separate aspect of the research methodology is how a scientific collaboration ensures that its published results are accurate. There is typically an official review process that progresses in tiers from junior postdocs within a group to senior postdocs leading analysis groups within collaborations, to senior academics who effectively function as internal journal reviewers. To simulate this, we encode tiers of review subagents at every step of the analysis.
- **General agent behavior.** In order to manage context windows, the analysis steps outlined in the methodology are sent to separate subagents. However, these agents still need to know the overall analysis context and plan. We therefore encode a strict specification of what each agent receives and outputs (operationally, no physics information), as well as a log that allows the process to be explored and verified by humans and that also facilitates agent-level debugging of complex failures.
- **Domain-specific conventions.** Finally, we specify a well-isolated set of desired conventions, such as tool use, visualizations, or more obscure or recent analysis techniques. Encoding this baseline level seems unavoidable, as general models are unable to correctly guess the specific conventions that vary greatly by field.

The analyses presented in the appendices of this paper were produced entirely by AI agents operating on archived open ALEPH and DELPHI data and Monte Carlo simulation from the Large Electron-Positron (LEP) collider and CMS Open Data from the Large Hadron Collider (LHC)[7], with the agents optionally accessing domain knowledge from published LEP papers through a structured retrieval system.

Importantly, **we do not present these analyses as legitimate scientific results, but rather to showcase the level of HEP analysis that current agentic systems can produce entirely autonomously**, based only on a short physics prompt and the framework we present as scaffolding for how a physics analysis is done. **We believe this warrants rethinking how mainstream analysis work is done in HEP collaborations and how student labor is utilized.** These developments also have

¹We see no barriers for this to generalize to other state-of-the-art coding assistants.

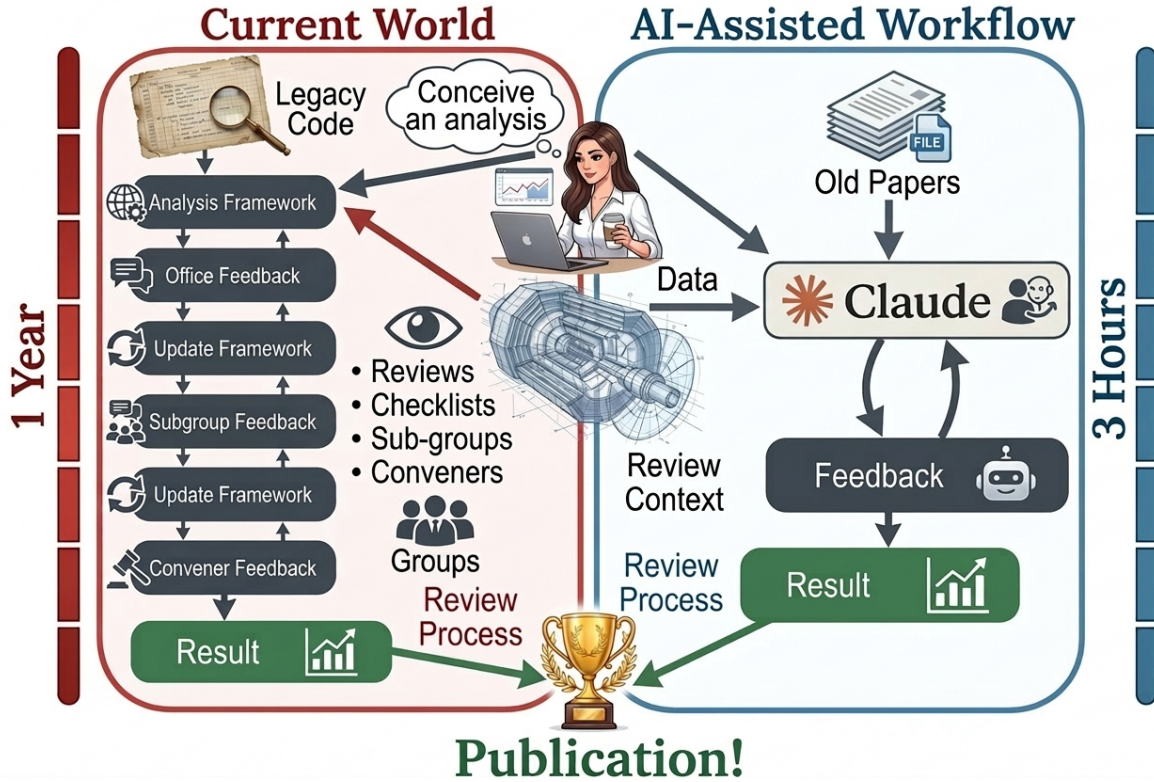


Figure 1: Diagram of how an AI-agent workflow can be used to mirror the typical high-energy physics analysis workflow. On the left, we show the typical analysis pipeline, which usually starts with legacy code that is then modified to perform the analysis. Analyses typically involve 3 or more levels of review, starting with feedback from other postdocs, students, and faculty collaborating on the analysis (office feedback). The next tier is typically done in an analysis subgroup (colloquially referred to as a level 3 group). The second tier of review involves a pre-approval phase, in which physics group conveners review an analysis, followed by a formal collaboration review leading to a result and a submission for publication. On the right side, an equivalent interactive workflow can be entirely handled by AI agents, from the conception of an idea through a result that would then undergo a similar collaboration review, followed by publication.

implications beyond routine analysis: they enable systematic reproducibility studies, lower the barrier to reanalyzing archived datasets, and facilitate rigorous documentation of analysis workflows—all longstanding challenges in the field, historically hindered by the significant human effort and expertise required to carry them out at scale.

We emphasize that we are not calling for AI agents to supplant humans in producing scientific results. The final output of any AI-assisted analysis must be thoroughly checked, understood, and validated by domain experts before it can be considered a scientific result, and must undergo the same internal scrutiny as any other collaboration paper. We also do not claim that current agents can handle every aspect of every analysis; complex analyses involving novel techniques, bespoke reconstruction algorithms, or subtle interplay between multiple systematic uncertainties will continue to require substantial hands-on human involvement. Agents make mistakes, sometimes subtle ones, and humans must remain responsible for judging their outputs and be held publicly accountable for their mistakes. Most importantly, it is our creativity, expertise, and judgment that defines the research agenda these tools will help us pursue.

The remainder of this paper describes our proof-of-concept framework, the lessons learned from applying it to ALEPH, DELPHI, and CMS open data, and its current limitations. Section 2 reviews the rapidly growing landscape of agentic AI for science and for HEP specifically. Section 3 describes the JFC framework, including its agent architecture, knowledge retrieval system, and multi-agent review process. Section 4 surveys the

analyses “we” have reproduced using JFC, discusses their quality, and examines the broader implications for analysis workflows, graduate training, legacy data reanalysis, and the limitations and risks of current systems. Section 5 concludes with a call to action.

2 Related Work

The application of AI agents to scientific research is a rapidly growing field spanning many domains, from chemistry and drug discovery to materials science and mathematics. In chemistry, ChemCrow [6] augments large language models with expert-designed chemistry tools to autonomously plan and execute synthesis tasks, while Coscientist [5] integrates LLMs with internet search, code execution, and robotic lab equipment to design and carry out chemical experiments end-to-end. The AI Scientist [16] demonstrated a fully autonomous pipeline, from idea generation through experiment execution to paper writing. Multi-agent architectures have also been explored for scientific discovery: SciAgents [11] combines LLMs with knowledge graphs in a multi-agent framework for materials science, while PaperQA2 [19] achieves superhuman performance on scientific literature synthesis through an agentic retrieval-augmented generation pipeline. These efforts illustrate a broad trend toward autonomous AI-driven research, but each domain brings its own unique challenges in terms of data complexity, validation requirements, and the need for domain-specific reasoning.

Within high energy physics (HEP), interest in applying LLM-based agents to analysis workflows has grown significantly in the past year, with several concurrent and complementary efforts emerging. A community vision paper [1] recently outlined grand challenges for building an AI-native research ecosystem for experimental particle physics, providing a high-level roadmap for how current and future facilities can benefit from AI integration. We review the existing landscape of HEP-focused agentic AI efforts below, organized by the type of task they address.

2.1 Agents for data analysis

The most directly relevant prior work is that of Gendreau-Distler et al. [10], who present an LLM-agent-driven data analysis framework. Their system pairs an LLM-based supervisor-coder agent with the Snakemake workflow manager to automate a Higgs boson diphoton cross-section measurement using ATLAS Open Data. The workflow manager enforces reproducibility and determinism, while the agent generates, executes, and iteratively corrects analysis code. The authors benchmark several state-of-the-art LLMs spanning the Gemini, GPT, and Claude families, as well as leading open-weight models. Notably, however, the authors themselves state that “multi-step task planning is beyond the current scope” of their system [10], highlighting that the agent operates within a fairly rigid, pre-defined analysis structure rather than autonomously planning and executing a full analysis from a high-level specification.

Diefenbacher et al. [8] investigate LLM-based agents for anomaly detection using the LHC Olympics dataset [15], demonstrating that agentic setups can develop and test analysis methods that mirror human state-of-the-art performance. Their study provides a systematic comparison of prompting strategies and LLM models, benchmarking stability, cost, and reproducibility across multiple runs. This work is notable for showing that agents can independently arrive at sensible analysis strategies—such as combining bump hunts with weakly supervised approaches like CWoLa—without being explicitly instructed to do so.

Menzo et al. present HEPTAPOD [18], an orchestration framework that enables large language models to interface with domain-specific HEP tools, construct simulation workflows, and manage multi-step research pipelines. The system uses schema-validated operations and run-card-driven configuration to ensure reproducibility, and is demonstrated on a representative BSM Monte Carlo validation pipeline spanning model generation, event simulation, and downstream analysis within a unified workflow. By providing a structured and auditable layer between human researchers, LLMs, and computational infrastructure, HEPTAPOD focuses on the upstream simulation and workflow management problem rather than end-to-end data analysis, and emphasizes human-in-the-loop oversight throughout the process.

Most recently, Badea et al. [4] present a proof-of-concept measurement using LEP open data with an agentic AI-physicist collaboration. Their approach relies on an iterative human-in-the-loop cycle in which the physicist provides detailed feedback after each agent attempt, guiding the analysis toward a correct result. While demonstrating that agents can contribute meaningfully to a real measurement, this supervised

workflow differs fundamentally from the autonomous approach we propose: in JFC, multi-agent review replaces the human feedback loop during analysis development, and human oversight is concentrated at a single formal unblinding gate rather than distributed throughout the process.

2.2 Agents for simulation and experiment design

GRACE [12] takes a different approach, targeting the upstream problem of experimental design rather than data analysis. Given a natural-language prompt or a published experimental paper, GRACE extracts a structured representation of the experiment, constructs a runnable simulation, and autonomously explores design modifications using Monte Carlo methods. The system demonstrates that an agentic approach to detector geometry optimization can identify directions consistent with known upgrade priorities, using only baseline simulation inputs.

2.3 LLM-assisted toolkits

CoLLM [9] provides an end-to-end pipeline from plain-language analysis specifications to trained deep learning classifiers for collider analyses. While it uses LLMs to generate analysis code under physics constraints, it functions more as an AI-assisted toolkit with a graphical user interface than as a fully autonomous agent, and focuses specifically on the deep learning classification step of an analysis. Xiwu [20] is an LLM assistant for HEP that can switch between open-weight models and be fine-tuned on domain knowledge.

2.4 Benchmarks and community efforts

The CelloAI benchmarks [3] provide a framework for evaluating AI assistants in HEP contexts, focusing on code documentation and generation tasks. Notably, the CelloAI benchmark suite does not yet include physics analysis tasks, leaving a gap in the community’s ability to systematically evaluate the most impactful potential application of AI agents in HEP.

2.5 Knowledge retrieval for physics analysis

A key challenge for autonomous analysis agents is accessing and applying domain knowledge from the existing literature. Standard retrieval-augmented generation (RAG) approaches struggle with scientific text because relevant information often spans multiple sections, figures, and even multiple papers. McGreivy et al. [17] address this with SciTreeRAG, which exploits the hierarchical structure of experimental physics papers to build a tree representation of a document corpus, enabling more contextually coherent retrieval than flat chunking approaches. They additionally introduce SciGraphRAG, which transforms unstructured literature into structured knowledge graphs to capture cross-document relationships. Both systems are demonstrated on the LHCb experiment corpus. PaperQA2 [19] takes a complementary approach, treating retrieval and response generation as a multi-step agent task that can revise its search parameters and examine candidate answers before producing a final response, achieving superhuman accuracy on scientific literature synthesis benchmarks.

2.6 Summary and gaps

Table 1 summarizes the capabilities of the existing agentic systems for HEP discussed above.

The existing landscape reveals several important patterns. First, most HEP-focused agentic systems operate within highly scaffolded workflows where the analysis structure is pre-defined and the agent’s role is limited to code generation within fixed steps. Second, none of the existing systems combine autonomous multi-step planning, domain knowledge retrieval from the literature, and multi-agent review into an integrated framework. Third, the community lacks benchmarks for evaluating agents on realistic, end-to-end physics analysis tasks—the kind that require event selection, background estimation, systematic uncertainty quantification, and statistical inference. These gaps motivate the framework we present in the following sections.

Capability	[10]	[8]	GRACE [12]	CoLLM [9]	[4]	JFC
Autonomous task planning	-	~	✓	-	-	✓
Code generation & execution	✓	✓	✓	✓	✓	✓
Literature retrieval (RAG)	-	-	-	-	-	✓
Multi-agent review	-	-	-	-	-	✓
End-to-end analysis	~	✓	-	~	✓	✓
Report generation	-	-	-	-	~	✓
Minimal human oversight	✓	✓	✓	-	-	✓

Table 1: Comparison of agentic AI systems for HEP. ✓ = fully supported, ~ = partially supported, - = not supported. “End-to-end analysis” refers to producing a complete measurement (selection through statistical inference); “minimal human oversight” indicates the system can run without continuous human feedback.

3 The JFC Framework

JFC is an agentic framework for autonomous execution of HEP analysis pipelines. An orchestrator agent delegates execution and review work to subagents across sequential phases. Each phase must produce a written artifact and pass an independent review before the next phase can begin, providing structured task decomposition and fresh context management. In this section, we describe its domain-specific capabilities: physics-aware analysis planning, literature-based knowledge retrieval, and multi-agent review with role-specialized critics.

3.1 Architecture overview

The JFC framework is built on **Claude Code**, Anthropic’s agentic coding CLI, which serves as both the LLM backend and the agent runtime. The underlying model is Claude Opus (specifically, `claude-opus-4-6` with a one-million-token context window), used for all executor, reviewer, and arbiter subagents. All analyses presented in this paper were run with Opus for every agent role to ensure reasoning quality is never silently degraded; opportunities for cost reduction by delegating narrowly scoped roles to lighter-weight models are discussed in Section 4.2.

The key architectural principle is that the agent operates with genuine autonomy over the analysis workflow. Unlike prior systems that constrain the agent to code generation within pre-defined analysis steps [10], the JFC analysis agent receives a high-level physics objective—such as “measure the hadronic cross-section of the Z boson using ALEPH data”—and must autonomously determine the full analysis strategy: what event selection to apply, how to estimate backgrounds, which systematic uncertainties to evaluate, what statistical framework to use, and how to present the results. The agent is not given a template or skeleton analysis to fill in; it must plan and execute the entire pipeline from scratch, consulting the literature as needed.

This autonomy is scaffolded, not unconstrained. The agent operates within a physicist-developed knowledge base that takes two complementary forms. The first is a methodology specification: a natural-language document defining the phases of the analysis, the outputs each phase must produce, and the review gates separating them—expressed in prose rather than code, so that the agent exercises judgment within constraints rather than executing a rigid pipeline. The second is a conventions directory: a set of living documents, maintained and updated by physicists after each analysis, encoding accumulated domain knowledge for specific techniques—which systematic uncertainty sources are standard for a given measurement type, what validation checks a given correction method requires, and what pitfalls experienced analysts know to avoid. Where the methodology tells the agent *that* it must evaluate systematic uncertainties, the conventions tell it *which* sources are standard and why. Together, these constitute an operational context analogous to a graduate course curriculum: not prescribing every step, but establishing the standards and domain knowledge against which the agent’s decisions are made and reviewed.

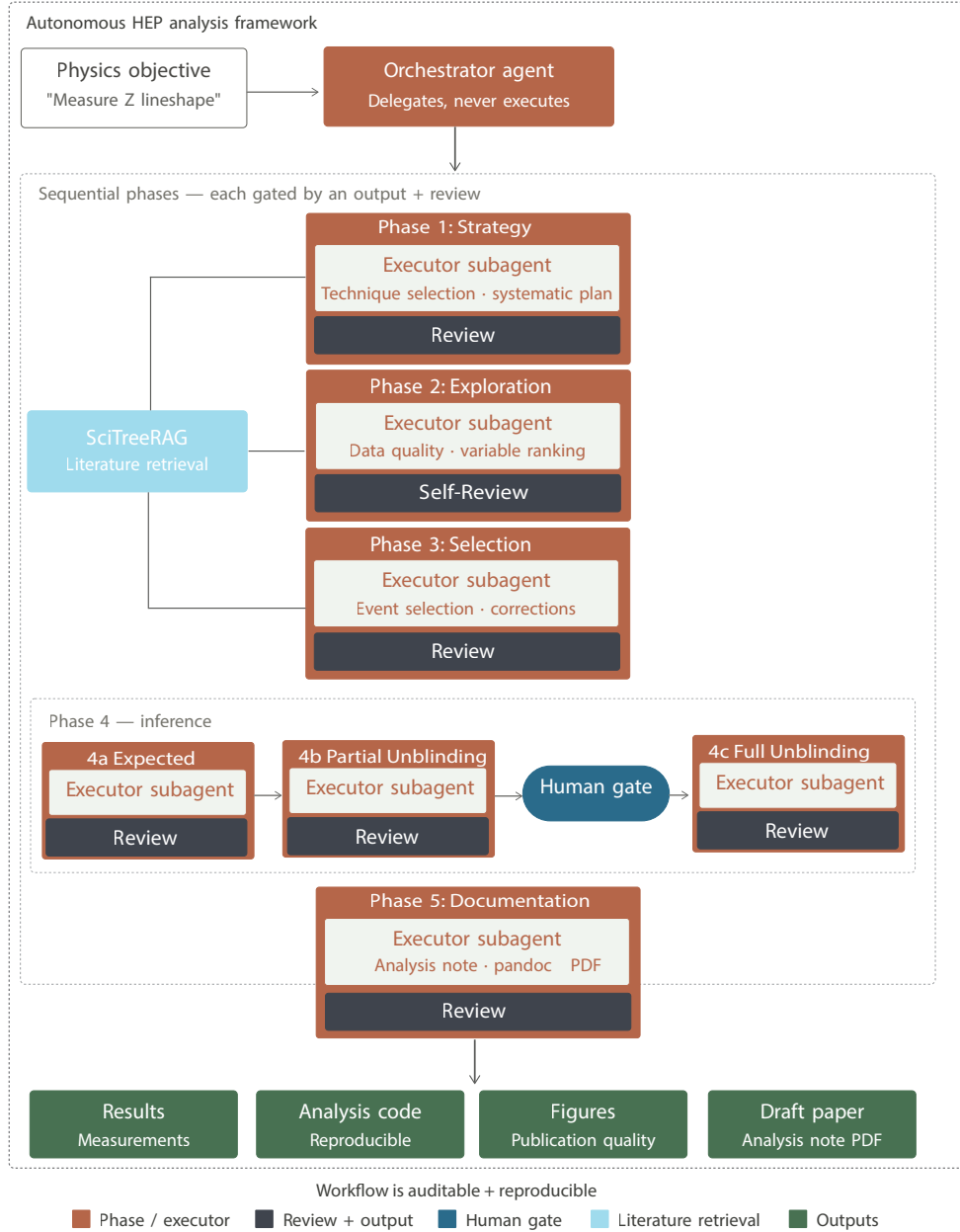


Figure 2: The JFC framework. A high-level physics objective is passed to an autonomous analysis agent, which plans and executes the full pipeline while querying a literature retrieval system (SciTreeRAG) for domain knowledge. The resulting analysis undergoes multi-agent review; if any reviewer flags an issue the agent revises and resubmits until all reviewers approve. Eventually the final document (a rich analysis note) is passed to human physicists for evaluation.

3.2 Task decomposition into phases

The orchestrator decomposes the analysis into seven sequential phases, each gated by the production of a written artifact on disk and passage of an independent review:

1. **Phase 1 — Strategy** (4-bot review): The **lead-analyst** agent queries the literature corpus, identifies signal and background processes, proposes event selection, defines the blinding variable, and outlines the systematic uncertainty program. A mandatory reference analysis survey (2–3 published analyses)

and a conventions compliance table are required. The output artifact is `STRATEGY.md`.

2. **Phase 2 — Exploration** (self-review): Three specialist agents run in parallel: `data-explorer` (sample inventory, data quality), `detector-specialist` (object definitions, data/MC validation), and `theory-scout` (cross-sections, generator recommendations, prior results). The `lead-analyst` consolidates their outputs into `EXPLORATION.md`.
3. **Phase 3 — Selection and Background Modeling** (1-bot review per channel): The `signal-lead` and `background-estimator` agents implement event selection, define control and validation regions, perform closure tests, and produce the `SELECTION.md` artifact. Multi-channel analyses spawn parallel agent pairs per channel.
4. **Phase 4a — Expected Results** (4-bot review): One `systematic-source-evaluator` agent per systematic source runs in parallel. The `systematics-fitter` then constructs the likelihood, performs Asimov fits, signal injection tests, and all eight mandatory fit diagnostics. Output: `INFERENCE_EXPECTED.md`.
5. **Phase 4b — Partial Unblinding** (4-bot review → human gate): The fitter runs on a 10% signal-region data subsample. The `note-writer` produces a draft analysis note and an unblinding checklist. After the review passes, the pipeline *pauses* and presents a structured summary to the human analyst, who must explicitly approve, request changes, or halt.
6. **Phase 4c — Full Unblinding** (1-bot review): Executes only after human approval. The fitter runs on the complete dataset; the `cross-checker` validates consistency with partial and expected results.
7. **Phase 5 — Documentation** (5-bot review): The `note-writer` produces the final analysis note (`ANALYSIS_NOTE.md`) in pandoc-compatible Markdown, compiled to PDF via `pandoc`. The review adds a `rendering-reviewer` that compiles and inspects the PDF.

The orchestrator agent itself never writes analysis code or reads full data files; it only holds the physics prompt, phase summaries, and review verdicts, delegating all computational work to disposable subagents whose contexts are discarded after each invocation.

3.3 Tools and software stack

The framework enforces a specific, pure-Python HEP software stack, documented in Table 2.

Task	Required tool	Explicitly forbidden
ROOT file I/O	<code>uproot</code> (≥ 5.0)	PyROOT, ROOT C++ macros
Array operations	<code>awkward-array</code> , <code>numpy</code>	<code>pandas</code> (for event data)
Histogramming	<code>hist</code> , <code>boost-histogram</code>	ROOT <code>TH1</code> , <code>numpy.histogram</code>
Plotting	<code>matplotlib</code> + <code>mplhep</code>	ROOT <code>TCanvas</code> , <code>plotly</code>
Statistical modeling	<code>pyhf</code> (binned), <code>zfit</code> (unbinned)	RooFit, RooStats
4-vectors	<code>vector</code> , <code>particle</code>	Manual calculations
Document preparation	<code>pandoc</code> (≥ 3.0) + <code>xelatex</code>	LLM-based conversion
Logging	<code>logging</code> + <code>rich</code>	bare <code>print()</code>

Table 2: Mandated software stack. Optional packages include `coffea` for columnar event processing, `xgboost/scikit-learn` for MVA, and `iminuit/cabinetry` for fitting, activated as needed per analysis.

All analysis code is written in a columnar style: selections are boolean masks over arrays, not event loops. Agents prototype on ~ 1000 -event slices before scaling to the full dataset, with automatic scale-out rules: single-core for jobs under 2 minutes, `ProcessPoolExecutor` for 2–15 minutes, and SLURM batch submission for longer runs.

3.4 Literature-based knowledge retrieval

A critical component of the JFC framework is its integration with a literature-based knowledge retrieval system built on SciTreeRAG [17]. An analysis agent operating without access to the existing literature would need to rely entirely on knowledge absorbed during pre-training—a brittle foundation, since the specific details of how a particular experiment’s event selection was designed, what detector effects must be accounted for, or how a particular systematic uncertainty was historically evaluated are rarely represented in an LLM’s training data with sufficient fidelity to be directly useful.

Our retrieval system indexes a corpus of published LEP (ALEPH, DELPHI) papers, exploiting the hierarchical document structure (sections, subsections, figures, tables) to build contextually coherent retrievals rather than the flat text chunks used by standard RAG systems.

The ALEPH catalog contains 1,503 total entries (399 papers, 736 proceedings, 368 theses). Of those, 721 have source material available, and 575 were successfully converted to markdown. The DELPHI catalog contains 4,305 total entries (2,967 papers, 763 proceedings, 575 theses). Of those, 2,083 have source material available, and 1,868 were successfully converted to markdown.

Metadata was harvested from INSPIRE-HEP and CERN CDS. Source PDFs and LaTeX were then downloaded. PDFs were converted to structured markdown using Nougat (a GPU-based neural OCR model) running on A100 80GB GPUs, while LaTeX sources were converted via Pandoc. The raw markdown then went through a reproducible postprocessing pipeline that normalizes math delimiters, strips missing-page markers and boilerplate, removes Pandoc div markers, and collapses excess whitespace.

When the analysis agent needs domain knowledge—for example, what charged-track quality cuts were used in previous ALEPH hadronic event selections, or what sources of systematic uncertainty were considered in a particular measurement—it queries the retrieval system and receives relevant passages from published papers, complete with the surrounding context needed to interpret them correctly. This allows the agent to make informed decisions grounded in established experimental practice rather than guessing or hallucinating analysis choices.

The retrieval system is particularly important for three aspects of an analysis:

- **Event selection:** The agent retrieves descriptions of selection criteria used in similar published analyses to inform its own selection design, adapting cuts to the specific measurement while maintaining consistency with established practice.
- **Systematic uncertainties:** Identifying the relevant sources of systematic uncertainty for a given measurement is one of the most expertise-intensive aspects of an analysis. The retrieval system provides the agent with descriptions of how systematic uncertainties were evaluated in prior work, including which variations were considered and how they were propagated.
- **Statistical methods:** The agent retrieves information about the statistical frameworks used in similar measurements (e.g., profile likelihood fits, template methods) to guide its choice of inference procedure.

Presented analyses performed on the ALEPH Open Data have had access to this literature-based knowledge retrieval, whereas the ones on DELPHI and CMS did not.

3.5 Agent architecture

The framework defines specialist agent profiles, each specified as a Markdown file in `.claude/agents/` with a YAML frontmatter declaring the agent’s name, description, available tools, and model tier. These agents fall into four functional categories:

- **Executor agents (7):** `lead-analyst`, `data-explorer`, `detector-specialist`, `theory-scout`, `signal-lead`, `background-estimator`, `systematics-fitter`, each with deep domain prompts encoding HEP methodology (e.g., the fitter’s prompt specifies all eight mandatory fit diagnostics, three in-situ constraint strategies, and the CL_s exclusion procedure).
- **Specialist agents (4):** `systematic-source-evaluator`, `cross-checker`, `note-writer`, `ml-specialist`, activated as needed for specific sub-tasks.

- **Reviewer agents (5):** `physics-reviewer` (reviews purely on physics merit, without access to methodology documents), `critical-reviewer`, `constructive-reviewer`, `rendering-reviewer` (compiles and inspects the PDF), and `plot-validator` (programmatic, non-visual validation of plotting code and histogram data). Further information in Sec. 3.6
- **Adjudication agents (2):** `arbiter` (synthesizes all reviewer findings into a PASS/ITERATE/ESCALATE verdict) and `investigator` (traces regression triggers to their root cause across phases).

Every subagent is spawned as a fresh process with no memory of prior invocations, receiving only the specific artifacts and instructions relevant to its task. This disposable-context architecture prevents context window exhaustion (Context Rot [13]) during long analyses and ensures that each agent operates from a clean state.

3.6 Multi-agent review

Before any analysis phase is considered complete, it undergoes automated review by a panel of specialized reviewer agents. This multi-agent review system is designed to mirror the internal review process of a real HEP collaboration, where different experts scrutinize different aspects of an analysis before it is approved for publication.

Six distinct agents participate in the review process, each defined by a Markdown profile in `.claude/agents/` specifying its role, available tools, model tier, and evaluation criteria.

Physics reviewer (`physics-reviewer`). Operates as an independent senior collaboration member equivalent to an Analysis Review Committee (ARC) member or Level-2 convener. Critically, this agent is *deliberately denied access* to the methodology specification, conventions documents, review checklists, and previous review feedback. It receives only the physics prompt and the artifact under review, and evaluates purely on the basis of physics knowledge: signal modeling, background identification and estimation, systematic uncertainty completeness, cross-check adequacy, and publication readiness. This design choice ensures that the physics reviewer assesses the analysis as an external referee would, without being guided by the framework’s own criteria. Issues are classified as Category A (blocking: “would cause rejection”), B (important: “weakens the analysis”), or C (minor: “style or clarity”).

Critical reviewer (`critical-reviewer`). Performs the most comprehensive review. Unlike the physics reviewer, the critical reviewer *does* read the methodology specification and conventions documents, and applies them systematically. Its protocol includes eight mandatory steps: (1) phase-specific review focus, (2) issue classification (A/B/C), (3) row-by-row conventions compliance check against the applicable conventions document, (4) reference analysis comparison (“what would a competing group have that we do not?”), (5) a 14-point figure and label checklist (verifying axis labels with units, luminosity stamps, experiment labels, ratio panels, uncertainty bands, and the absence of forbidden elements such as figure titles), (6) physics sanity checks on every plot (distribution shapes, yield magnitudes, data/MC agreement, uncertainty proportionality), (7) regression detection by comparing the current artifact against earlier phase outputs, and (8) upstream feedback identifying issues that originate in prior phases. Each finding includes a file path or figure reference, an impact statement, and a suggested fix.

Constructive reviewer (`constructive-reviewer`). Complements the critical reviewer by focusing on improvements and alternatives rather than flaw detection. It evaluates clarity, validation sufficiency, alternative approaches (additional signal regions, complementary cross-checks, improved statistical methodology), presentation quality, and notation consistency. Each suggestion includes the current state, the improved state, a justification, and an effort estimate (low/medium/high). The constructive reviewer also provides explicit positive feedback (marked with [+]) for genuinely strong aspects of the analysis, and is instructed not to duplicate findings already raised by the critical reviewer. While it primarily produces Category B and C findings, it can escalate to Category A if a fundamental gap is discovered.

Rendering reviewer (`rendering-reviewer`). Activated only during Phase 5 (documentation) review, adding a fifth reviewer to the panel. This agent compiles the analysis note to PDF, then inspects the compiled output across eight dimensions: figure rendering integrity, LaTeX math compilation, page layout (orphaned text, page breaks, margins), cross-reference resolution (`@fig:`, `@tbl:`, `@eq:`, `@sec:` labels), citation resolution against the bibliography, table formatting and overflow, and page count assessment (targeting 50–100 pages for a complete analysis note). It focuses exclusively on rendering quality and does not comment on physics content.

Plot validator (`plot-validator`). Unlike the other reviewers, the plot validator performs *programmatic*, non-visual validation. It runs in parallel with the other reviewers during every review cycle that involves figure-producing phases. Its checks fall into four categories:

- **Programmatic figure checks** (8 checks): Verifies that collaboration plotting styles (`mplhep`) are applied, figure sizes match the template, no forbidden `ax.set_title()` calls exist, axis labels include units, no hardcoded font sizes appear, `bbox_inches="tight"` is used at save time, both PDF and PNG formats are saved, and `plt.close()` is called after saving.
- **Physics sanity checks** (11 checks): Verifies that yields are non-negative, efficiencies lie in $[0, 1]$, data/MC ratios in control regions fall within $[0.5, 2.0]$, uncertainties scale as \sqrt{N} , p_T and mass distributions fall off at high values, cutflow yields are monotonically non-increasing, and background composition fractions sum to $\sim 100\%$.
- **Consistency checks** (6 checks): Cross-validates that the same process has consistent yields across different plots, pre-fit and post-fit yields are consistent with the fit, and nuisance parameter impact rankings match the uncertainty breakdown table.
- **Red flag detection** (10 checks): Automatic Category A triggers including negative event yields, efficiencies outside $[0, 1]$, data/MC ratios outside $[0.2, 5.0]$ in control regions, zero uncertainty on non-zero predictions, non-converged fits, nuisance parameter pulls $> 3\sigma$, $\chi^2/\text{ndf} > 5.0$, and systematic variations exceeding 100%.

Red flags from the plot validator are automatically classified as Category A findings; the arbiter is explicitly forbidden from downgrading them.

Arbiter (`arbiter`). The arbiter is not a reviewer but an adjudicator: it reads all reviewer outputs and the original artifact, then synthesizes a single verdict. Its adjudication follows a five-case decision framework: (1) both reviewers agree \rightarrow accept at the higher severity; (2) reviewers disagree on severity \rightarrow evaluate arguments and assign with documented reasoning; (3) only one reviewer raised the finding \rightarrow assess validity independently; (4) reviewers contradict each other \rightarrow examine the artifact directly to resolve; (5) both reviewers missed something \rightarrow the arbiter adds its own finding. The arbiter produces a structured adjudication table mapping each finding to its source reviewer(s), their assigned categories, and the final adjudicated category with rationale. It then issues one of three decisions: **PASS** (no Category A or unresolved B items remain), **ITERATE** (actionable Category A items exist that can be fixed within the current phase), or **ESCALATE** (fundamental problem requiring human judgment or upstream phase changes).

This automated review layer serves two purposes. First, it catches a class of errors—such as applying a selection cut that inadvertently removes signal, double-counting a systematic uncertainty, or using an inappropriate test statistic—before a human physicist ever needs to look at the analysis. Second, it provides structured documentation of the analysis decisions and their justifications, making subsequent human review more efficient because the reviewer can focus on physics judgment rather than hunting for mechanical errors.

The review process is deliberately conservative: the analysis is not permitted to proceed to “unblinding”—examining the real data in the signal region—until all reviewer agents have signed off. The review protocol is not advisory; it is *binding*. When the arbiter issues an **ITERATE** verdict, the orchestrator initiates a closed-loop revision cycle in which the executor agent must demonstrably address every Category A finding before the analysis can advance.

In the final documentation phase, the review system extends to the written analysis report itself: the analyses presented in the appendices of this paper, including all publication-quality plots, were drafted entirely by the agent system and refined through the same multi-agent review cycle.

3.7 Pipeline state tracking

The orchestrator maintains a machine-readable state file (`STATE.md`) that records the current phase, status, timestamp, a phase history table (with artifact paths, review tiers, iteration counts, and notes), active blockers, and a regression log. Every state transition—executing, reviewing, passed, blocked, `human_gate`, regression—is timestamped. A dedicated `/check-status` command reads this file and presents a formatted status report including completed artifacts, review iteration counts per phase, and any outstanding blockers. This state tracking enables the orchestrator to resume from the correct point after interruptions and provides a complete audit trail of the analysis pipeline’s progression.

3.8 Formal unblinding protocol

The framework implements a structured, multi-stage blinding protocol that enforces a mandatory human gate before observed data in the signal region can be examined.

Blinding enforcement. From the start of the analysis, a blinding protocol defined in Phase 1 specifies the blinding variable and the signal region boundaries. All agents operate under a standing constraint: “never access signal region data until explicitly told unblinding is approved.” During Phases 1–4a, the statistical analysis uses exclusively Asimov datasets (expected background, optionally with injected signal at $\mu = 1$ for discovery projections). Post-fit distributions show data points removed from the signal region or replaced with Asimov pseudodata. The `analysis.config.yaml` configuration file carries a boolean flag `blinding.approved_for_unblinding`, initialized to `false`.

Partial unblinding (Phase 4b). Phase 4b introduces a controlled partial unblinding: the `systematics-fitter` agent runs the statistical fit on a 10% random subsample of the signal region data, using a fixed random seed for reproducibility. This limited exposure allows the analysis to verify that no unexpected pathologies appear (e.g., dramatic data/MC disagreement, fit non-convergence, anomalous nuisance parameter pulls) without revealing the full result. The `note-writer` agent simultaneously produces a draft analysis note and an unblinding checklist covering seven criteria:

1. Background model validated (closure tests pass in all validation regions),
2. Systematic uncertainties evaluated and fit model stable,
3. Expected results physically sensible,
4. Signal injection tests confirm fit recovers injected signals,
5. 10% partial unblinding shows no unexpected pathologies,
6. All agent review cycles resolved (arbiter PASS),
7. Draft analysis note reviewed and considered publication-ready modulo full observed results.

Human gate. After the Phase 4b review passes (4-bot tier), the pipeline *halts automatically* and sets the state to `human_gate`. The orchestrator does *not* proceed to Phase 4c under any circumstances without explicit human authorization. The human analyst invokes `/approve-unblinding`, which presents a structured approval request containing:

- A summary of the draft analysis note (physics process, methodology, 10% results),
- The unblinding checklist with per-item pass/fail status,
- The 4-bot review result (arbiter decision, iteration count, residual Category B/C items),
- Key results from the 10% data (expected vs. observed, goodness-of-fit, notable nuisance parameter pulls),
- Paths to all artifacts available for detailed human review.

The human responds with one of three decisions:

APPROVE The configuration flag `approved_for_unblinding` is set to `true`. The pipeline proceeds to Phase 4c (full unblinding).

REQUEST_CHANGES The pipeline re-enters Phase 4b execution with the human’s change request as additional input. After the executor revises the artifacts, the 4-bot review runs again, and upon passing, the human gate is re-presented with the updated summary.

HALT The pipeline is stopped entirely. The state is set to `halted` with the human’s reason recorded. The analysis can only resume after the human addresses the stated concerns.

Full unblinding (Phase 4c). Phase 4c is gated by a programmatic check: the `systematics-fitter` agent verifies that `approved_for_unblinding: true` in the configuration before proceeding. If the flag is `false`, execution stops with an instruction to run `/approve-unblinding` first. Once confirmed, the fitter runs the full statistical fit on the complete dataset. A `cross-checker` agent then independently validates the results, checking consistency between the full observed results, the 10% partial results, and the Asimov expected results. The full results undergo a 1-bot review (critical reviewer plus plot-validator) before the analysis advances to Phase 5 (documentation).

Design rationale. The three-stage unblinding sequence (Asimov \rightarrow 10% data \rightarrow full data) with a mandatory human gate mirrors the blinding protocols used by major HEP collaborations. The human gate is the single point in the pipeline where autonomous execution is deliberately suspended, ensuring that the decision to examine the full signal region data remains under human control. This design reflects the principle that while analysis execution and review can be automated, the scientific judgment to unblind a result should not be.

4 Results & Discussion

We demonstrate the JFC framework by reproducing several published ALEPH and DELPHI measurements using archived LEP data and Monte Carlo simulation samples, and a CMS Higgs boson measurement using CMS Open Data [7]. The full analyses, including detailed descriptions of event selection, systematic uncertainty evaluation, and statistical results, are presented as standalone papers in the appendices. These appendix papers were written entirely by the agent system, with zero human feedback beyond a simple prompt describing the general task and data location. The analysis notes were originally produced as standalone documents; for inclusion in this paper, an AI agent performed minor reformatting (section-level adjustments, figure path updates) with no changes to physics content, methodology, or results.

4.1 Analyses

Table 3 summarizes the analyses produced with JFC. Each analysis was initiated with a short natural-language prompt (reproduced in the table) specifying only the measurement goal and the data location; the agent autonomously determined the full analysis strategy. All runs used a Claude Max subscription² with the Claude Opus model, and generally completed end-to-end within 4-6 hours. In some cases, waiting periods for Claude Code usage limit resets slowed execution times. The complete agent-produced analysis notes are reproduced in the appendices for a few representative examples. The framework specification, agent definitions, and additional autonomously generated analyses are available in our github repository (see Section 6).

We do not guarantee the physics validity of any of these results, but instead, show them as examples of what is already possible with a single prompt.

²<https://claude.ai>

Analysis	Initial prompt (abridged)	Data	Time	Ref.
Z lineshape + α_s	Measure Z lineshape, thrust and extract $\alpha_s(M_Z)$ via NLO+NLL QCD fits	ALEPH	3h 10m	A/Github
Lund plane	Measure the primary Lund jet plane density in hadronic Z decays	ALEPH	13h 13m	B/Github
N_ν from Γ_{inv}	Measure the number of light neutrino generations from the Z invisible width	DELPHI	5h 15m	C/ Github
Energy-energy correlator	Measure the two-point energy-energy correlator in hadronic Z decays	DELPHI	5h 23m	D/Github
$H \rightarrow \tau\tau$	Measure the Higgs boson signal strength in the $\mu\tau_h$ final state at $\sqrt{s} = 8$ TeV	CMS	6h 30m	E/Github
R_b and R_c	Measure R_b and R_c using lifetime b-tagging and $D^{*\pm}$ charm tags	ALEPH	2h 20m	Github
Jet substructure	Measure groomed and ungroomed jet substructure observables in hadronic Z decays	DELPHI	7h 42m	Github
Event shapes + α_s	Measure six event shape distributions and extract $\alpha_s(M_Z)$ from NLO QCD fits	DELPHI	4h 15m	Github
Lund jet plane	Measure the primary Lund jet plane density in hadronic Z decays	DELPHI	6h 59m	Github

Table 3: Summary of analyses produced with JFC. Each analysis was run autonomously from the initial prompt shown, with no human intervention beyond the unblinding approval gate. Wall-clock times include all review iterations.

Z lineshape, thrust, and α_s extraction (Appendix A). Building on the thrust measurement, the agent performs an $\alpha_s(M_Z)$ extraction by fitting the unfolded thrust distribution to NLO+NLL perturbative QCD predictions.

```
Scaffold and run a measurement analysis of the Z lineshape parameters and an extraction of  $\alpha_s$  using archived ALEPH data at  $\sqrt{s} \sim 91.2$  GeV.
Setup: scaffold analyses/zlineshape.alphas as a measurement, set
data.dir=[...] in analysis_config, install the pixi environment, then begin orchestrating.
Data: [...]
```

Lund jet plane (Appendix B). The agent measures the primary Lund jet plane density using Cambridge/Aachen declustering of hadronic Z decay events, including a two-dimensional unfolding.

```
Scaffold and run a measurement analysis of the primary Lund jet plane density in hadronic Z decays using archived ALEPH data at  $\sqrt{s} \sim 91.2$  GeV.
Setup: scaffold analyses/lund_plane as a measurement, set data_dir=[...] in .analysis_config, install the pixi environment, then begin orchestrating.
Observable: The 2D density of primary Cambridge/Aachen declusterings in each thrust hemisphere, mapped to coordinates  $(\ln 1/\Delta\theta, \ln k_t/\text{GeV})$ , where  $\Delta\theta$  is the emission angle and  $k_t = E_{\text{soft}} \sin\Delta\theta$ . Use charged particles only (pwflag == 0, highPurity == 1). One jet = one hemisphere.
Deliverables:
1. 2D density  $\rho(\ln 1/\Delta\theta, \ln k_t)$  corrected to charged-particle level,  $10^{-15} \times 10^{-15}$  bins at least - as fine as it makes sense
2. 1D projections ( $k_t$  spectrum, angular spectrum) with covariance
```

3. Number of primary declusterings vs. minimum k_t threshold
4. Comparison to PYTHIA 6 MC
5. Machine-readable results (CSV/NPY)

Data: [...]

N_ν from Γ_{inv} (Appendix C). The agent measures the number of light neutrino generations N_ν from the invisible width of the Z boson using 3.5 million hadronic Z decays from the DELPHI 1992–1995 energy scan.

Reproduce the classic LEP measurement of the number of light neutrino generations N_ν from the Z boson invisible decay width using DELPHI open data.

Measure the Z lineshape (cross section vs \sqrt{s}) in the hadronic and leptonic channels from the LEP1 energy scan runs. Extract Γ_Z (total width), Γ_{had} , and Γ_ℓ . Compute the invisible width $\Gamma_{inv} = \Gamma_Z - \Gamma_{had} - 3\Gamma_\ell$ and determine $N_\nu = \Gamma_{inv}/\Gamma_{\nu\bar{\nu}}^{(SM)}$. The original LEP result is $N_\nu = 2.9840 \pm 0.0082$, consistent with exactly 3 generations.

Data: [...]

Energy-energy correlator (Appendix D). The agent measures the charged-particle two-point energy-energy correlator (EEC) in hadronic Z decays using DELPHI open data, corrected to stable charged-particle level using iterative Bayesian unfolding with 108 angular bins spanning $\chi \in [0.006, 3.139]$ rad.

Measure the two-point energy-energy correlator (EEC) as a function of the angular separation χ between particle pairs in hadronic Z decays at DELPHI.

Cover the full angular range from the collinear limit ($\chi \rightarrow 0$) through the transition region to the back-to-back limit ($\chi \rightarrow \pi$). Correct for detector effects using the DELPHI simulation.

In the back-to-back region, extract α_s using the transverse-momentum-dependent (TMD) factorization framework, which provides excellent perturbative control. In the collinear limit, probe the transition from perturbative to non-perturbative dynamics and test models of hadronization including recent analytic results connecting EECs to track functions.

Measure the three-point EEC as well, which probes the detailed radiation pattern in $e^+e^- \rightarrow 3$ jets. Compare with predictions from modern generators (Pythia 8, Sherpa, Herwig 7).

Data: [...]

CMS Open Data $H \rightarrow \tau\tau$ (Appendix E). The agent measures the Higgs boson signal strength in the $\mu\tau_h$ final state using CMS Open Data at $\sqrt{s} = 8$ TeV, including a template-based profile likelihood fit.

You are performing a Higgs boson search in the $\tau^+\tau^-$ decay channel using CMS Open Data from 2012 at $\sqrt{s} = 8$ TeV.

The final state is one muon and one hadronically decaying tau lepton ($\mu\tau_h$). Your goal is to produce distributions of key observables — particularly the visible di-tau mass — showing the Higgs signal contribution on top of Standard Model backgrounds. This loosely follows the official CMS publication (Phys. Lett. B 779 (2018) 283).

Data: [...]

R_b and R_c (Github) The agent measures the ratios $R_b = \Gamma(Z \rightarrow b\bar{b})/\Gamma(Z \rightarrow \text{hadrons})$ and $R_c = \Gamma(Z \rightarrow c\bar{c})/\Gamma(Z \rightarrow \text{hadrons})$ using lifetime-based b-tagging and $D^{*\pm}$ charm tags.

Scaffold and run a measurement analysis of the partial width ratios $R_b = \Gamma(Z \rightarrow b\bar{b})/\Gamma(Z \rightarrow \text{hadrons})$ and $R_c = \Gamma(Z \rightarrow c\bar{c})/\Gamma(Z \rightarrow \text{hadrons})$ in hadronic Z decays using archived ALEPH data at $\sqrt{s} \sim 91.2\text{GeV}$.

Setup: scaffold analyses/rb_rc as a measurement, set data_dir=[...] in .analysis.config, install the pixi environment, then begin orchestrating.

Observable: R_b and R_c are the fractions of hadronic Z decays to $b\bar{b}$ and $c\bar{c}$ respectively. Tag b and c events using lifetime-based methods: signed impact parameter significance of charged tracks (pwwflag == 0, highPurity == 1) relative to the primary vertex, and/or secondary vertex reconstruction. Use a double-tag method to reduce dependence on MC tagging efficiency.

Deliverables:

1. R_b and R_c with statistical and systematic uncertainties
2. b-tagging and c-tagging performance (efficiency, purity, mistag rates) validated against MC
3. Double-tag consistency checks
4. Comparison to published ALEPH R_b/R_c values and the SM prediction
5. Machine-readable results

Data: [...]

Jet substructure (Github). The agent measures seven groomed and ungroomed jet substructure observables — jet mass, Soft Drop groomed jet mass, momentum sharing fraction z_g , groomed opening angle R_g/R , Soft Drop multiplicity n_{SD} , and N-subjettiness ratios τ_{21} and τ_{32} — in hadronic Z decays using archived DELPHI data, for anti- k_T jets with $R = 0.4$ and $R = 0.8$.

Measure a comprehensive set of jet substructure observables in hadronic Z decays using anti- k_T jets with $R = 0.4$ and $R = 0.8$ reconstructed from DELPHI data at $\sqrt{s} = 91.2$ GeV.

For each jet radius, measure: ungroomed and Soft Drop groomed ($z_{cut} = 0.1$, $\beta = 0$) jet mass; the groomed momentum sharing fraction z_g ; the groomed opening angle R_g/R ; the number of Soft Drop splittings n_{SD} ; and N-subjettiness ratios τ_{21} and τ_{32} .

Present all observables differentially as a function of jet energy. Correct to particle level using the DELPHI simulation chain, applying either bin-by-bin or iterative Bayesian unfolding. Compare with Pythia 8, Herwig 7, Sherpa 2/3, and with perturbative QCD calculations where available (NLL for groomed jet mass, Soft Drop z_g).

This analysis directly mirrors the ALEPH jet substructure publication (JHEP 06 (2022) 008), providing an independent measurement with different detector systematics.

Data: [...]

Event shapes + α_s extraction (Github). The agent measures six infrared- and collinear-safe hadronic event shape distributions — thrust, heavy jet mass, wide and total jet broadenings, C -parameter, and Durham y_{23} — in e^+e^- annihilation at $\sqrt{s} \approx 91.2$ GeV using DELPHI open data, and extracts $\alpha_s(M_Z)$ from NLO QCD fits to the unfolded distributions.

Perform a state-of-the-art determination of the strong coupling constant, $\alpha_s(M_Z)$, using hadronic Z-decay data from DELPHI at $\sqrt{s} = 91.2$, GeV.

Measure the distributions of classic event-shape variables—thrust (T), heavy jet mass (ρ_H), wide and total jet broadenings (B_W and B_T), the C -parameter, and the Durham y_{23} jet-resolution parameter—using the full LEP1 data set. Correct the data to particle level using the DELPHI simulation chain and unfold the distributions with modern techniques, such as iterative Bayesian unfolding or OmniFold.

Fit the unfolded distributions with NNLO QCD predictions matched to NNLL resummation (or N^3LL where available), extracting α_s and nonperturbative power corrections simultaneously. Compare the fixed-order perturbation theory (FOPT) and contour-improved perturbation theory (CIPT) prescriptions. Combine the individual extractions into a single DELPHI determination of α_s and compare it with the current world average.

The theoretical landscape has improved dramatically since the original DELPHI publications: NNLO corrections are now available for all six event shapes, and resummation has been pushed to N^3LL accuracy for thrust.

Data: [...]

Lund jet plane (Github). The agent measures the primary Lund jet plane density using Cambridge/Aachen declustering of hadronic Z decay events from DELPHI, corrected to particle level using bin-by-bin correction factors. The measurement provides the first determination of this observable at the Z pole in e^+e^- collisions.

Measure the primary Lund jet-plane density in hadronic Z decays using DELPHI data.

Recluster jets with the Cambridge/Aachen algorithm and follow the harder branch at each declustering step, recording the splitting variables (k_T , ΔR) of the softer emission. Populate the Lund plane in the $(\ln(1/\Delta R), \ln k_T)$ representation.

This observable has been measured by ATLAS and ALICE at LHC energies but has never been measured at LEP. The clean e^+e^- initial state (no underlying event, no pileup, known \sqrt{s}) makes this the definitive benchmark for the Lund plane: the perturbative region should match NLL DGLAP predictions exactly, while the nonperturbative boundary provides a clean measurement of the hadronization transition scale.

Data: [...]

4.2 Cost and scaling

All analyses presented in this paper were run using a Claude Max subscription (approximately \$200/month at the time of writing), which provides sufficient throughput for the full pipeline including all review iterations. Each end-to-end analysis completes in approximately 4-6 of wall-clock time, with the review cycles currently imposing soft and hard iteration caps: phases typically pass review after one to two iterations, with a hard cap to prevent runaway loops.

The current configuration uses Claude Opus for all agent roles, prioritizing reasoning quality over cost. In principle, substantial cost savings could be achieved by delegating narrowly scoped roles to lighter-weight models—for example, Claude Sonnet for signal selection development, background estimation, theory scouting, note writing, and rendering review, and Claude Haiku for the read-only data reconnaissance agent that performs fast sample inventory. Conversely, additional review iterations (beyond the current one-to-two-round default) represent an opportunity to improve analysis quality at the cost of additional model invocations and wall-clock time. Systematic exploration of this quality–cost trade-off is left for future work.

4.3 Analysis quality

Beyond the numerical results, we can assess the quality of the agent-produced analyses along several dimensions. The agent-produced analyses demonstrate that an LLM-driven system can design and execute particle physics analyses that are structurally sound, methodologically standard, and honestly documented. The event selections are sensible, and correct systematic uncertainty sources are identified, even when not all can be fully evaluated. The analysis strategies align closely with published approaches, with deviations that are well-motivated and clearly documented.

In all cases, the agent’s analysis strategy is recognizably similar to the corresponding published analysis. The agent consistently makes the same high-level choices that the original experimental collaborations made, for example, iterative Bayesian unfolding (or bin-by-bin correction where appropriate) for the QCD measurements, HistFactory likelihood for the Higgs search, Breit–Wigner lineshape fitting for N_ν . The selection of observables, binning strategies, and correction procedures are all standard and well-motivated. Additionally, the agent’s treatment of systematic uncertainties is one of the strongest aspects of these analyses. Every note includes a systematic completeness table that explicitly compares the sources considered against those in the corresponding published analyses (DELPHI, ALEPH, OPAL, CMS, ATLAS, or ALICE). Similarity to published analyses is expected, as the agents explicitly consult existing literature and are asked to repeat measurements that have been done before. Pursuing wholly novel analyses is likely to be more challenging for the agents, and we leave this as a question for future work. Autonomously reproducing full analysis workflows is, by itself, a very significant demonstration of their HEP analysis capabilities.

The main weaknesses—including limited statistics, approximate theory inputs, and incomplete hadronization model comparisons—are inherent to the prototype scope rather than to errors in the agent’s physics reasoning. The most significant genuine errors (DY template contamination, rank-deficient covariance, NLO-only α_s bias) are the kinds of issues that standard review processes are designed to catch, and the agent itself flags most of them in its “limitations” discussions. The agent tends to be conservative with selection cuts, preferring high purity over high efficiency. This is a reasonable default for a first-pass analysis, but in several cases, it substantially hurts sensitivity. A more experienced analyst would likely investigate and relax or work around such cuts earlier in the analysis cycle.

Where the agent falls short relative to an experienced human analyst is in the iterative refinement loop: a human would likely fix the $Z \rightarrow \mu\mu$ contamination in the Higgs to $\tau\tau$ analysis before writing 55 pages around it, and would implement event categorization in the same analysis before accepting $\sigma_\mu = 5.6$, and would not proceed with a χ^2 test using a condition number of 10^{19} . The agent produces thorough first drafts that identify their own problems but does not always close the loop on fixing them. This pattern of correct diagnosis, deferred treatment is the single most characteristic feature of the agent’s working style across all analyses, and it suggests that the review-and-iterate cycle is where the most value would come from tighter human-agent collaboration.

The review rounds were also invaluable to correcting mistakes. Each independent reviewer agent was tasked with reading one analysis note and producing a critical assessment. Several qualitative observations can be made:

- **Consistency of reviewer assessments:** All six reviewer agents converged on the same structural critique — that the analyses are well-designed feasibility demonstrations limited primarily by prototype statistics and missing theory/MC inputs, rather than by fundamental methodological errors. This consistency across independent reviews lends confidence that the assessment is not an artifact of any single reviewer’s biases.
- **Errors caught by reviewers:** The reviewer agents identified several concrete issues: the rank-deficient covariance matrix in the EEC analysis, the $Z \rightarrow \mu\mu$ template contamination in $H \rightarrow \tau\tau$, the inflated α_s from NLO-only theory, and the stress test failures in jet substructure. These are precisely the kinds of issues that internal review committees catch in real collaborations.
- **Errors likely requiring human review:** Some subtler issues — such as whether the anti-muon discriminator behavior in CMS Open Data NanoAOD is a data-format artifact versus a genuine analysis choice, or whether the APACIC generator provides sufficient hadronization model variation compared to Herwig — require domain expertise and familiarity with the specific detector and data formats that goes beyond what the reviewer agents can fully assess from the note text alone. A human reviewer with LEP or CMS experience would likely probe these points more deeply.
- **Self-awareness of limitations:** A striking feature of the agent-produced notes is their transparency about what is missing. Every analysis includes a “dominant limitations” subsection and a prioritized list of improvements for the full-statistics analysis. This self-critical posture reduces the burden on reviewers, who can focus on issues the agent did *not* identify rather than those it did.

4.4 Implications for analysis workflows

The results presented here suggest that a significant fraction of the technical work in a standard HEP analysis can be automated with current AI agent technology. This does not mean that human physicists are no longer needed - quite the opposite. The role of the physicist shifts from implementer to architect and critic: defining what should be measured and why, assessing whether the agent’s approach is physically sensible, and catching the subtle errors that automated review may miss.

With AI systems capable of implementing complex software frameworks or autonomously running end-to-end analysis pipelines, high-level thinking, analysis design, ideation, and physical reasoning (skills that are sought in faculty candidates and foundational to career success) become the primary occupation across all levels of the academic hierarchy. For students, time not spent programming can be dedicated to broadening theoretical and statistical foundations, building instrumentation expertise, planning projects, keeping up with the literature, and writing up results. From this perspective, AI coding agents simply join a long lineage of time-saving innovations that unburden scientists from technical drudgery.

This shift has the potential to dramatically increase the throughput of an experimental program. Consider the situation facing the LHC experiments today: thousands of potential measurements that could be performed with existing data, but only a finite number of students and postdocs to carry them out. Each analysis can occupy a person for years, so if the implementation phase can be compressed from years to months, the bottleneck moves from coding capacity to physics ideas and human review bandwidth—a much more desirable constraint, because it means the limiting factor is intellectual rather than mechanical. Measurements that might take a year to complete could potentially be produced in days, reviewed by a suite of specialized AI agents before any human even looks at the result, and iterated rapidly in response to feedback. Follow-up studies, closure checks, systematics investigations, and many other burdensome tasks could be implemented within minutes at the level of code and bottlenecked only by runtime on large datasets, as they are now anyway. Studies that are currently skipped because they are “too tedious” become tractable when the cost of implementation drops by orders of magnitude. Even with LEP data, there are significant prospective improvements, such as event-level analyses of all standard model parameters, tunes of the hadronic shower for every analysis, and optimized particle reconstruction for core standard model parameters. With these toolkits, the burden of analysis is lifted, encouraging all of us to think more broadly about the scope of research that can be conducted.

Furthermore, large collaboration reviews, which involve 3–4 levels of human review (see Fig. 1), can be expedited. Agents have a role at both the review and testing stages, providing immediate feedback and

immediate results from cross-checks. The role of the human reviewer then focuses on the technically challenging elements of the review process, largely paralleling the “approvals” and “collaboration-wide reviews” performed in the later stages.

While a reduced coding burden would come as a relief to most in the field, **technical proficiency in programming must remain a critical and carefully developed skill for all HEP practitioners.** If an AI agent writes a sophisticated analysis pipeline, a physicist must, at minimum, be able to read and understand the codebase to check for correctness. Modern coding assistants are incredibly capable but still routinely make fundamental errors, particularly when performing the kinds of specialized tasks required in HEP (e.g. complicated fits and statistical hypothesis testing). The reliability of these systems will continue to improve, but the conceptual basis of all software—what the code should *do*—will remain human-driven.

4.5 Rethinking graduate training

The implications for graduate education deserve particular attention. As computer technology and deep learning have co-evolved with HEP’s “big data” era, software engineering has, perhaps unintentionally, become a significant component of a graduate student’s training. This is a valuable technical foundation and prepares students well for futures inside and outside academia³, but inevitably distracts from core training as a *physicist*. Writing code has become synonymous with HEP graduate student work, and technical implementation is the largest bottleneck to the realization of an idea.

If AI agents can handle the implementation, graduate training can be restructured to emphasize the aspects of research that require human intelligence: developing physical intuition, learning to ask good questions, understanding the theoretical context of measurements, and practicing the kind of critical thinking needed to evaluate whether an analysis result is trustworthy. Students would still need to understand their analysis code and be able to validate anything an agent contributes, but they would not need to write every line of it from scratch. This focus on high-level design and evaluation rather than implementation mirrors how faculty and postdocs work, most of whom contribute most significantly via scientific judgment rather than writing code. AI agents would simply extend this training to earlier career stages.

4.6 Legacy data and reanalysis

One particularly compelling application is the reanalysis of legacy datasets. Enormous volumes of data from past experiments including LEP, the Tevatron, B-factories, sit in archives, potentially containing information relevant to current physics questions⁴. Autonomous analysis agents could systematically work through these datasets, producing first-pass results that human physicists can then evaluate and refine. Our work with ALEPH and DELPHI data is a proof of concept for exactly this kind of application. Moreover, legacy datasets become accessible to reanalysis with modern computational tools—including deep learning techniques that were unavailable when the data were originally collected.

Beyond new analyses, this paradigm also opens the door to automatic reproducibility of published results, where AI agents could systematically re-execute the computational pipelines of existing papers, flagging inconsistencies or confirming findings at a scale that is currently impractical due to the resource and personnel constraints needed for large-scale verification⁵.

4.7 Limitations and risks

We do not wish to overstate what current systems can do. Several important limitations must be acknowledged.

- **Subtle physics errors:** Agents can produce analyses that are superficially correct but contain subtle physics errors—for example, applying a selection criterion that biases the measurement in a non-obvious way, or omitting a systematic uncertainty that an experienced analyst would know to include.

³The value of software engineering in industry may drop in the coming years, depending on the continued evolution of AI coding agents. At the time of writing, this matter is hotly debated.

⁴<https://ee-alliance.org/> is one such organization pursuing these questions

⁵Coding assistants will also prove helpful for understanding legacy codebases and data formats.

- **Novelty:** Current agents excel at reproducing established analysis strategies retrieved from the literature but are less reliable when asked to develop genuinely novel approaches. For analyses that require creative new techniques, human-driven design remains essential.
- **Complexity ceiling:** The analyses we have demonstrated—Z lineshape, event shapes, α_S —are relatively standard measurements. More complex analyses involving multivariate techniques, data-driven background estimation in multiple control regions, or simultaneous fits across many channels remain to be demonstrated. However, Lund-Plane and EEC measurements including unfolding techniques have never been published, proving that the complexity ceiling is quite high for agent teams.
- **Verification burden:** The need for thorough human verification of agent-produced results cannot be shortcut. An analysis that looks correct but contains a subtle error is arguably more dangerous than no analysis at all, because it carries an unearned sense of confidence. The community must develop robust practices for validating AI-produced analyses.
- **Instruction following:** Agents are prone to ignoring instructions when they become buried in a large context window. For example, an agent may repeatedly use absolute font sizes in plots despite explicit instructions to the contrary.
- **Prompt nondeterminism:** Agent outputs are inherently stochastic, making prompt optimization difficult. The same prompt can yield markedly different analysis strategies or code quality across runs.
- **Stale tool knowledge:** Agents tend to rely on APIs and interfaces from their training data, and convincing them to consult up-to-date documentation for newer package versions is surprisingly difficult.
- **Poor dependency management:** Agents are inclined to write ad hoc patches or workarounds rather than pulling an updated dependency or adding a lightweight new one, even when the latter would be the correct solution.
- **Limited knowledge of review practices:** Internal collaboration review processes are not publicly available and are unlikely to appear in training data. Agents can reason about physics reasonably well, but many analyses have characteristic failure modes that experienced reviewers would catch immediately. Building internal retrieval-augmented generation systems over review documentation could help address this.
- **Missing niche methods:** Agents are unlikely to employ analysis techniques that are not widespread in the literature, even when they would be appropriate. This represents an opportunity for domain-specific fine-tuning.
- **Context and prompt engineering trade-offs:** There is an inherent tension between providing detailed instructions (which improve specificity but risk context bloat and instruction-following degradation) and keeping prompts concise (which preserves context but may leave important conventions unspecified).
- **Stylistic choices:** While LaTeX has some reasonable defaults, there are many options and packages to choose from and there is no uniform style across fields and journals. It is necessary to be extremely specific when describing and encoding what the final analysis note should like to achieve the desired look.

4.8 Future Work

Several directions for systematic improvement of the framework remain to be explored. A natural next step is A/B testing of different specification variants, comparing the effect of more prescriptive methodology documents against minimal-guidance prompts on analysis quality, completeness, and error rates. Equally important is characterizing the stochastic variability of agent outputs: running the same prompt and specification multiple times and quantifying the spread in analysis strategies, numerical results, and documentation quality would establish a baseline for reproducibility and identify which aspects of the pipeline are most sensitive to prompt nondeterminism.

The review system itself offers a rich optimization target; the current iteration caps and reviewer panel composition were chosen heuristically, and a systematic sweep over the maximum number of review rounds, reviewer agent combinations, and arbiter thresholds could reveal favorable operating points on the quality–cost frontier.

Beyond Claude Code, the framework’s architecture is in principle backend-agnostic, and benchmarking against other agentic coding systems such as OpenAI’s Codex, Google’s Jules, or open-weight agent frameworks would clarify which capabilities are specific to the underlying model and which emerge from the specification and orchestration layer.

Finally, extending the framework to more complex analysis topologies, including multi-channel simultaneous fits, data-driven background estimation with transfer factors, and analyses requiring custom reconstruction or machine learning components, would map the current boundary between what agents can handle autonomously and what still demands sustained human involvement.

4.9 Toward robust AI-assisted analysis

The path forward is not to deploy AI agents as unsupervised analysis machines, but to develop them as powerful tools within a framework that preserves the rigor and scrutiny that the HEP community rightly demands. This requires investment in several concrete areas:

1. **Benchmarks for physics analysis.** The community currently lacks standardized benchmarks for evaluating agent performance on realistic, end-to-end physics analysis tasks. Existing benchmarks such as CelloAI [3] focus on code generation and documentation; what is needed are benchmarks that test the full analysis chain—from event selection design through statistical inference—on datasets with known ground truth. The LHC Olympics [15] anomaly detection challenge offers a partial template, but benchmarks targeting standard measurements (cross-sections, coupling extractions, event shape variables) with realistic systematic uncertainty structures would be far more informative.
2. **Standardized review protocols for AI-produced analyses.** Collaborations should develop explicit protocols for reviewing analyses in which substantial portions of the code and strategy were produced by AI agents. These protocols should specify what additional scrutiny is warranted—for example, mandatory independent re-implementation of key results, systematic comparison of agent-chosen selections against published baselines, or automated regression testing against known-good analysis outputs. The multi-agent review system we describe in this paper is a step in this direction, but it complements rather than replaces human review.
3. **Training for AI-assisted workflows.** Physicists need practical training in how to effectively supervise and validate AI-assisted work. This includes developing the ability to read and critically evaluate code they did not write, understanding the failure modes of LLM-based systems (hallucination, instruction drift, stale API knowledge), and learning to formulate analysis specifications that are precise enough to guide an agent while remaining flexible enough to allow it to exercise judgment. Graduate curricula should evolve to treat AI literacy as a core competency alongside statistical methods, detector physics, and programming.
4. **Institutional adaptation.** Collaborations will need to update their authorship, review, and accountability norms to accommodate AI-assisted work. Clear standards for disclosure of AI involvement, attribution of responsibility for AI-produced results, and documentation requirements for AI-assisted analyses will be essential for maintaining the trust and rigor that underpin the field’s scientific credibility.

The HEP community has a long tradition of rigorous internal review before publication. That tradition should be extended, not abandoned, as AI tools become more capable.

5 Conclusion

AI agents based on large language models, combined with a relatively small set of structured prompts, can already autonomously execute substantial portions of a standard HEP analysis pipeline. We have

demonstrated this concretely by reproducing published ALEPH and DELPHI measurements using archived LEP data and CMS measurements using CMS Open Data, with agents that plan their own analysis strategy, retrieve domain knowledge from the literature, execute the full analysis chain, undergo automated multi-agent review, and produce complete written reports. We stress that the toolkit for these analyses is largely composed of structured prompts and guidance for the LLM; it is by no means sophisticated, and we encourage the development of related approaches given the low barrier to entry.

The technology to perform analysis at the graduate student level is here and warrants serious attention from the experimental HEP community. We are not suggesting that AI agents should replace physicists. We are suggesting that they can take over much of the technically demanding, often tedious, implementation work that currently consumes the majority of an analyst’s time, freeing physicists to focus on what they do best: developing physical insight, asking creative questions, and exercising the expert judgment that no AI system can yet replicate. Moreover, we see this as a path towards more sophisticated physics analyses. Data can be more thoroughly combed, details and features within the data can be explored, and there is significant potential for new, comprehensive analyses to be built on these ideas.

The community should begin experimenting with these tools now, developing the workflows, benchmarks, and review practices needed to use them responsibly. The question is not whether AI agents will become part of the HEP analysis toolkit, but how quickly the community adapts to these powerful tools.

6 Code and Data Availability

The JFC framework specification—including the methodology document, conventions directory, agent profile definitions, and orchestrator prompts—is publicly available at <https://github.com/jfc-mit/slopspec> and <https://github.com/jfc-mit/slop-X> (two different variants). The agent-produced analyses presented in this paper, including complete analysis notes, all code, and generated figures, are available in dedicated repositories linked from the main framework repository - <https://github.com/jfc-mit>. The archived ALEPH, DELPHI, CMS data and Monte Carlo samples used in this work are publicly available through the CERN Open Data portal and are cited in the specific ANs.

7 Acknowledgments

We thank Yen-Jie Lee for providing us with preprocessed ALEPH Open Data and Monte Carlo for use in agentic analysis, and we thank the Electron-Positron Alliance⁶ for their ongoing work to preserve and re-analyze archival LEP data. We also thank CERN for providing the open data and MC from the ALEPH, DELPHI, and CMS experiments that we use in this paper⁷. Lastly, while preparing this document, we became aware of [4]. We have appropriately qualified the differences and conclusions within the paper.

This work is supported by the National Science Foundation under Cooperative Agreement PHY-2019786 (The NSF AI Institute for Artificial Intelligence and Fundamental Interactions, IAIFI, <http://iaifi.org/>). Computing resources for the SciTreeRAG literature extraction were provided by IAIFI on the FASRC Cannon cluster supported by the FAS Division of Science Research Computing Group at Harvard University. AN is supported by the NSF-funded A3D3 Institute (NSF-PHY-2117997), and a DOE Early Career award FY2021, “Harnessing the Large Hadron Collider with New Insights in Real-Time Data Processing and Artificial Intelligence”. E. A. M. acknowledges support from the National Science Foundation with Grant No. GRFP2141064.

References

- [1] Thea Klæboe Aarrestad et al. “Building an AI-native Research Ecosystem for Experimental Particle Physics: A Community Vision”. In: (Feb. 2026). arXiv: [2602.17582](https://arxiv.org/abs/2602.17582) [[hep-ex](#)].
- [2] Josh Achiam et al. “Gpt-4 technical report”. In: *arXiv preprint arXiv:2303.08774* (2023).

⁶<https://ee-alliance.org/home/>

⁷<https://opendata.cern.ch/>

- [3] Mohammad Atif et al. “CelloAI Benchmarks: Toward Repeatable Evaluation of AI Assistants”. In: (Mar. 2026). arXiv: [2603.01051](https://arxiv.org/abs/2603.01051) [[hep-ex](#)].
- [4] Anthony Badea, Yi Chen, and Yen-Jie Lee. “Agentic AI–Physicist Collaboration in Experimental Particle Physics: A Proof-of-Concept Measurement with LEP Open Data”. In: *arXiv preprint arXiv:2603.05735* (2026).
- [5] Daniil A Boiko et al. “Autonomous chemical research with large language models”. In: *Nature* 624.7992 (2023), pp. 570–578.
- [6] Andres M Bran et al. “Chemcrow: Augmenting large-language models with chemistry tools”. In: *arXiv preprint arXiv:2304.05376* (2023).
- [7] *CERN Open Data*. 2026. URL: <https://opendata.cern.ch/>.
- [8] Sascha Diefenbacher et al. “Agents of Discovery”. In: (Sept. 2025). arXiv: [2509.08535](https://arxiv.org/abs/2509.08535) [[hep-ph](#)].
- [9] W. Esmail, A. Hammad, and M. Nojiri. “CoLLM: AI engineering toolbox for end-to-end deep learning in collider analyses”. In: (Feb. 2026). arXiv: [2602.06496](https://arxiv.org/abs/2602.06496) [[hep-ph](#)].
- [10] Eli Gendreau-Distler et al. “Automating High Energy Physics Data Analysis with LLM-Powered Agents”. In: *39th Annual Conference on Neural Information Processing Systems: Includes Machine Learning and the Physical Sciences (ML4PS)*. Dec. 2025. arXiv: [2512.07785](https://arxiv.org/abs/2512.07785) [[physics.data-an](#)].
- [11] Alireza Ghafarollahi and Markus J Buehler. “SciAgents: automating scientific discovery through bio-inspired multi-agent intelligent graph reasoning”. In: *Advanced Materials* 37.22 (2025), p. 2413523.
- [12] Justin Hill and Hong Joo Ryoo. “GRACE: an Agentic AI for Particle Physics Experiment Design and Simulation”. In: Jan. 2026. arXiv: [2602.15039](https://arxiv.org/abs/2602.15039) [[hep-ex](#)].
- [13] Kelly Hong, Anton Troynikov, and Jeff Huber. *Context Rot: How Increasing Input Tokens Impacts LLM Performance*. Tech. rep. Chroma, July 2025. URL: <https://research.trychroma.com/context-rot>.
- [14] Carlos E Jimenez et al. “Swe-bench: Can language models resolve real-world github issues?” In: *arXiv preprint arXiv:2310.06770* (2023).
- [15] Gregor Kasieczka et al. “The LHC Olympics 2020 a community challenge for anomaly detection in high energy physics”. In: *Rept. Prog. Phys.* 84.12 (2021), p. 124201. DOI: [10.1088/1361-6633/ac36b9](https://doi.org/10.1088/1361-6633/ac36b9). arXiv: [2101.08320](https://arxiv.org/abs/2101.08320) [[hep-ph](#)].
- [16] Chris Lu et al. “The ai scientist: Towards fully automated open-ended scientific discovery”. In: *arXiv preprint arXiv:2408.06292* (2024).
- [17] James McGreivy et al. “Seeing the Forest Through the Trees: Knowledge Retrieval for Streamlining Particle Physics Analysis”. In: (Sept. 2025). arXiv: [2509.06855](https://arxiv.org/abs/2509.06855) [[hep-ex](#)].
- [18] Tony Menzo et al. “HEPTAPOD: Orchestrating High Energy Physics Workflows Towards Autonomous Agency”. In: (Dec. 2025). arXiv: [2512.15867](https://arxiv.org/abs/2512.15867) [[hep-ph](#)].
- [19] Michael D Skarlinski et al. “Language agents achieve superhuman synthesis of scientific knowledge”. In: *arXiv preprint arXiv:2409.13740* (2024).
- [20] Zhengde Zhang et al. “Xiwu: A Basis Flexible and Learnable LLM for High Energy Physics”. In: (Apr. 2024). arXiv: [2404.08001](https://arxiv.org/abs/2404.08001) [[hep-ph](#)].

A Z Boson Lineshape Measurement with ALEPH Data

A.1 Introduction

A.1.1 Physics of the Z resonance at LEP

The Z boson, discovered at the CERN $Spp\bar{S}$ collider in 1983, is a cornerstone of the electroweak sector of the Standard Model (SM). Its mass M_Z , total decay width Γ_Z , and partial widths provide precision tests of the SM at the quantum loop level, probing virtual contributions from particles too heavy to produce directly. At the Large Electron-Positron Collider (LEP), electron-positron collisions at centre-of-mass energies spanning $\sqrt{s} \approx 88\text{--}94$ GeV produce Z bosons whose production cross-section traces a relativistic Breit-Wigner resonance curve, modified by initial-state radiation (ISR) and the photon-exchange and γ -Z interference contributions.

The $e^+e^- \rightarrow \text{hadrons}$ cross-section near the Z pole is described by the ISR-convolved Breit-Wigner formula, where the Born-level hadronic cross-section takes the form

$$\sigma_{BW}(s) = \sigma_{had}^0 \cdot \frac{s\Gamma_Z^2}{(s - M_Z^2)^2 + s^2\Gamma_Z^2/M_Z^2} \quad (1)$$

with $\sigma_{had}^0 = (12\pi/M_Z^2) \cdot (\Gamma_{ee}\Gamma_{had}/\Gamma_Z^2)$ being the peak hadronic cross-section. The energy dependence of this cross-section — its position, width, and height — encodes the three primary lineshape observables.

A.1.2 The lineshape observables

This analysis extracts three primary parameters from the hadronic cross-section as a function of \sqrt{s} :

- M_Z , the Z boson mass. This is a fundamental SM parameter that sets the electroweak scale. The position of the resonance peak determines M_Z directly.
- Γ_Z , the total Z width. This is sensitive to all decay channels, including the invisible width from neutrino pairs: $\Gamma_Z = \Gamma_{had} + 3\Gamma_l + N_\nu\Gamma_\nu$, where Γ_l is the leptonic partial width, Γ_ν the neutrino partial width, and N_ν the number of light neutrino species. The width of the resonance curve constrains Γ_Z .
- σ_{had}^0 , the peak hadronic cross-section. This combines Γ_{ee} , Γ_{had} , and Γ_Z into a single observable, providing a constraint on the partial widths independent of the total width measurement.

From these three parameters, secondary quantities are derived using SM relations: the hadronic partial width Γ_{had} , the strong coupling constant $\alpha_s(M_Z)$ via the QCD correction to Γ_{had} , and the number of light neutrino species N_ν from the invisible width.

A.1.3 Prior measurements

The LEP experiments (ALEPH, DELPHI, L3, OPAL) measured the Z lineshape with high precision during 1989–1995. The LEP combination ([[ref-lep-combination](#)]) gives $M_Z = 91.1875 \pm 0.0021$ GeV, $\Gamma_Z = 2.4952 \pm 0.0023$ GeV, and $\sigma_{had}^0 = 41.540 \pm 0.037$ nb. The ALEPH-specific measurements from the thesis of Zhong ([[ref-aleph-zhong](#)]), using 1989–1993 data, yield $M_Z = 91.1916 \pm 0.0039$ GeV, $\Gamma_Z = 2.4941 \pm 0.0058$ GeV, and $\sigma_{had}^0 = 41.63 \pm 0.10$ nb. An early ALEPH measurement using the high-precision silicon-tungsten luminometer (SICAL) ([[ref-aleph-sical](#)]) reported $\sigma_{had}^0 = 41.56 \pm 0.09 \pm 0.15$ nb from 1992 data.

The world average from the Particle Data Group (PDG 2024) ([[ref-pdg-2024](#)]) gives $M_Z = 91.1876 \pm 0.0021$ GeV and $\Gamma_Z = 2.4955 \pm 0.0023$ GeV, dominated by the LEP combination. The number of light neutrino species is determined to be $N_\nu = 2.9963 \pm 0.0074$, consistent with three generations.

A.1.4 Overview of this analysis

This analysis measures the Z boson lineshape using approximately 3.05 million hadronic events collected by the ALEPH detector at LEP during the 1992–1995 running periods. Data at five distinct centre-of-mass energy groups spanning 89.4–93.0 GeV are used to extract M_Z , Γ_Z , and σ_{had}^0 from a χ^2 fit of the ISR-convolved Breit-Wigner cross-section to the measured hadronic cross-sections.

The analysis is performed using pre-existing ALEPH ntuples containing reconstructed event-level quantities and pre-computed selection flags. The key limitations of this dataset are:

- No luminosity information is stored in the data files; luminosities are recovered from published ALEPH tables (1993 data) and from theory-anchored calculations (other years).
- Only hadronic events are available; leptonic channels were removed at the ntuple production level by a minimum charged-hadron multiplicity requirement.
- Monte Carlo simulation is available only at $\sqrt{s} = 91.2$ GeV; there is no off-peak MC.
- No truth-level particle identification or process codes are available in the MC.

Despite these limitations, the analysis demonstrates that precision electroweak measurements can be extracted from archival LEP data with a complete treatment of systematic uncertainties.

A.1.5 Organization of this note

This note is organized as follows. Section 2 describes the data and MC samples. Section 3 details the event selection and its validation. Section 4 presents the corrections applied: ISR convolution, efficiency, background subtraction, and luminosity determination. Section 5 documents the systematic uncertainty evaluation. Section 6 presents the cross-checks performed. Section 7 describes the fitting method. Section 8 gives the results, including derived quantities. Section 9 compares to published measurements. Sections 10 and 11 provide conclusions and future directions. The appendices contain supplementary tables and matrices.

A.2 Data and MC Samples

A.2.1 The ALEPH detector at LEP

The ALEPH (Apparatus for LEP PHysics) detector operated at the LEP e^+e^- collider at CERN from 1989 to 2000. The detector featured a silicon vertex detector, an inner tracking chamber, a large time projection chamber (TPC) for charged-particle tracking, electromagnetic and hadronic calorimeters, and a muon spectrometer, all immersed in a 1.5 T solenoidal magnetic field. The combination of tracking and calorimetry enabled the ALEPH energy-flow algorithm, which reconstructed charged and neutral particles with excellent resolution. For a complete description of the detector, see ([ref-aleph`zhong]) and references therein.

The data used in this analysis consist of pre-processed ROOT ntuples containing 151 branches per event, including event-level kinematic quantities (energy, thrust, sphericity, missing momentum), particle multiplicities, and pre-computed hadronic selection flags. The ntuples were produced from the full ALEPH reconstruction with quality cuts applied at the production level, including a minimum charged-hadron multiplicity requirement ($n_{ch} \geq 4$) that effectively removes pure di-lepton events.

A.2.2 Data samples

Six data files cover the full 1992–1995 LEP-1 running period. The event counts, centre-of-mass energy ranges, and primary roles are summarized in Table 4.

Table 4: Data sample inventory. The 1993 and 1995 datasets contain off-peak energy scan points essential for constraining M_Z and Γ_Z . The 1992 and 1994 datasets contribute primarily to the peak cross-section measurement.

Period	\sqrt{s} range [GeV]	Events	Role
1992	91.27–91.28	551,474	Peak
1993	89.38–93.04	538,601	Energy scan
1994 P1	91.14–91.23	433,947	Peak
1994 P2	91.17–91.22	447,844	Peak

Period	\sqrt{s} range [GeV]	Events	Role
1994 P3	91.14–91.43	483,649	Peak + off-peak
1995	89.42–92.98	595,095	Energy scan
Total	89.38–93.04	3,050,610	

The data contain per-event scalar branches (centre-of-mass energy, selection flags, event shape variables, multiplicities) and per-particle jagged arrays (four-momenta, charge, particle-type flags). The per-particle `weight` and `artificAcceptEffCorrection` branches are energy-flow reconstruction weights (not luminosity-related quantities), with values clustered around unity.

The pre-computed selection flags are:

- `passesAll`: composite hadronic selection (AND-like, $\sim 94.7\%$ efficient)
- `passesNTrkMin`: minimum charged track multiplicity (100%, pre-cut)
- `passesTotalChgEnergyMin`: minimum total charged energy (100%, pre-cut)
- `passesSTheta`: thrust axis polar angle
- `passesMissP`: missing momentum veto
- `passesISR`: ISR photon veto
- `passesWW`: WW background veto
- `passesNeuNch`: neutral/charged energy balance

A.2.3 Monte Carlo simulation

A single MC sample of 771,597 events at $\sqrt{s} = 91.2$ GeV provides the reference selection efficiency at the Z peak. The MC was produced with the standard ALEPH simulation chain (40 files, `LEP1MC1994_recons_aftercut-001.root` through `-040.root`). All events have `process = -1` and `pid = -999`, indicating that no truth-level process codes or particle identification are available. This is a significant limitation for background estimation and systematic evaluation, addressed through Downscoping Decisions D4 and D5 in the analysis strategy.

No off-peak MC (at $\sqrt{s} \neq 91.2$ GeV) is available (Downscoping Decision D3). The energy dependence of the selection efficiency is constrained from data as described in sec. A.3.6.

A.2.4 Energy inventory

The 3.05 million events span 77 distinct centre-of-mass energy values (rounded to 0.01 GeV precision), which are grouped into five scan regions for the lineshape fit. The grouping and event statistics are given in Table 5.

Table 5: Energy group inventory for the lineshape fit. The luminosity-weighted mean energy of each group is used as the effective \sqrt{s} in the fit. The “above peak” group has limited statistics (1995 only) and contributes negligibly to the fit.

Group	$\langle\sqrt{s}\rangle$ [GeV]	Energy range [GeV]	Events (total)	Events (selected)	Years
peak-2	89.434	89.38–89.46	130,530	123,613	1993, 1995
peak (low)	91.196	91.14–91.23	1,598,080	1,513,765	1993, 1994, 1995
peak (high)	91.285	91.27–91.43	1,117,949	1,059,484	1992, 1993, 1994 P3, 1995
above peak	91.693	91.63–91.78	2,516	2,380	1995 only
peak+2	92.991	92.95–93.04	201,535	190,301	1993, 1995

The off-peak scan data from 1993 and 1995 provide the essential leverage for constraining M_Z and Γ_Z : the peak-2 group (~ 89.4 GeV) with 123,613 selected events and the peak+2 group (~ 93.0 GeV) with 190,301 selected events sample the resonance flanks where the cross-section changes rapidly with energy.

The peak region ($91.0 < \sqrt{s} < 91.5$ GeV) contains approximately 2.7 million events split into two sub-groups (peak low and peak high) due to the spread of operating energies. The “above peak” group (91.6–91.8 GeV, 2,516 events from 1995 only) provides marginal additional constraint.

A.2.5 Data completeness

The ntuple event counts represent approximately 84% of the total events expected from the published ALEPH luminosities. The completeness factor, determined from the four 1993 scan points where independent luminosities are available, is 0.842 ± 0.024 . This reduction likely arises from quality cuts applied at the ntuple production level and possible run-subset selection. The completeness factor is consistent across the four 1993 scan points (range: 0.816–0.881), with the 91.290 GeV point showing a modestly higher completeness (0.881) compared to the other three (0.816–0.835). All luminosities are corrected for this factor.

A.3 Event Selection

A.3.1 The passesAll composite selection

The primary hadronic event selection uses the pre-computed `passesAll` flag, which implements the standard ALEPH hadronic selection validated against published criteria ([ref-aleph'zhong]; [ref-aleph'sical]). The composite selection consists of seven individual cuts applied sequentially. Each cut targets a specific physics background or detector acceptance effect.

passesNTrkMin — minimum charged track multiplicity This cut requires at least 4 charged tracks in the event, rejecting low-multiplicity backgrounds such as two-photon events, beam-gas interactions, and cosmic rays. Hadronic Z decays typically produce $\langle n_{ch} \rangle \approx 20$ charged particles, so this cut has essentially no signal loss. In the ntuples used for this analysis, this cut was already applied at the production level, resulting in 100.00% efficiency for all data and MC events. The ntuple-level application of this cut also removes pure di-lepton events (2-track topology), precluding leptonic cross-section measurements.

passesTotalChgEnergyMin — minimum total charged energy This cut requires a minimum total energy deposited by charged particles, rejecting beam-gas and two-photon events with low visible energy. Like `passesNTrkMin`, this cut was applied at the ntuple production level and is 100.00% efficient for all events in the analysis.

passesSTheta — thrust axis polar angle This cut ensures that the event is well-contained within the detector acceptance by requiring the thrust axis to be at least ~ 26 degrees from the beam axis. Events with the thrust axis close to the beam direction have particles escaping into the beam pipe, leading to poorly measured event properties. The efficiency of this cut is approximately 97.5%, representing the largest single source of signal loss after the pre-cuts. The thrust axis direction is computed from all reconstructed particles using the standard ALEPH energy-flow algorithm.

passesMissP — missing momentum veto This cut vetoes events with large missing momentum, targeting beam-gas events (which produce asymmetric energy deposits), events with neutrinos from heavy-flavour decays, and events with particles escaping the detector acceptance. The missing momentum is computed as the magnitude of the vector sum of all reconstructed particle momenta. The efficiency is approximately 97.0%, the second-largest source of signal loss.

passesISR and passesWW — ISR photon and WW background vetoes These cuts reject events consistent with hard initial-state radiation (where a high-energy photon reduces the effective collision energy) and WW-like topologies. At LEP-1 energies ($\sqrt{s} \approx 91$ GeV), WW production is kinematically forbidden (threshold ~ 161 GeV), but these vetoes also reject rare radiative events and detector artifacts. The efficiencies of both cuts are approximately 99.0%, and they are nearly identical in their event-by-event decisions, suggesting shared or overlapping cut logic.

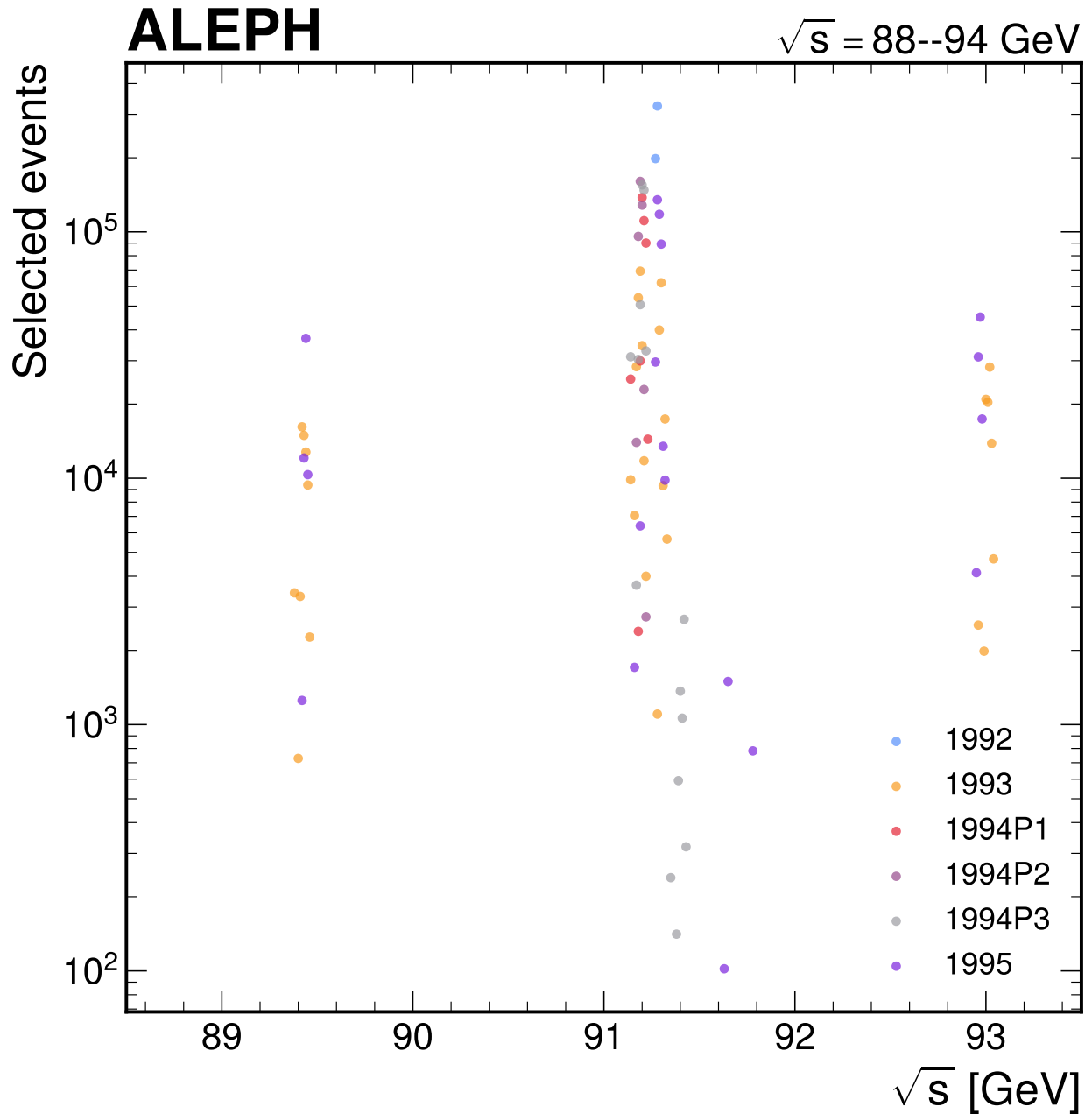


Figure 3: Energy scan structure showing the number of selected events at each centre-of-mass energy point, colored by data-taking year. The five energy groups used in the lineshape fit are indicated by the dashed vertical bands. The dominant contributions at the off-peak points come from the 1993 and 1995 energy scans, while the peak region receives events from all four years. The “above peak” group near 91.7 GeV contains only 2,380 events from 1995.

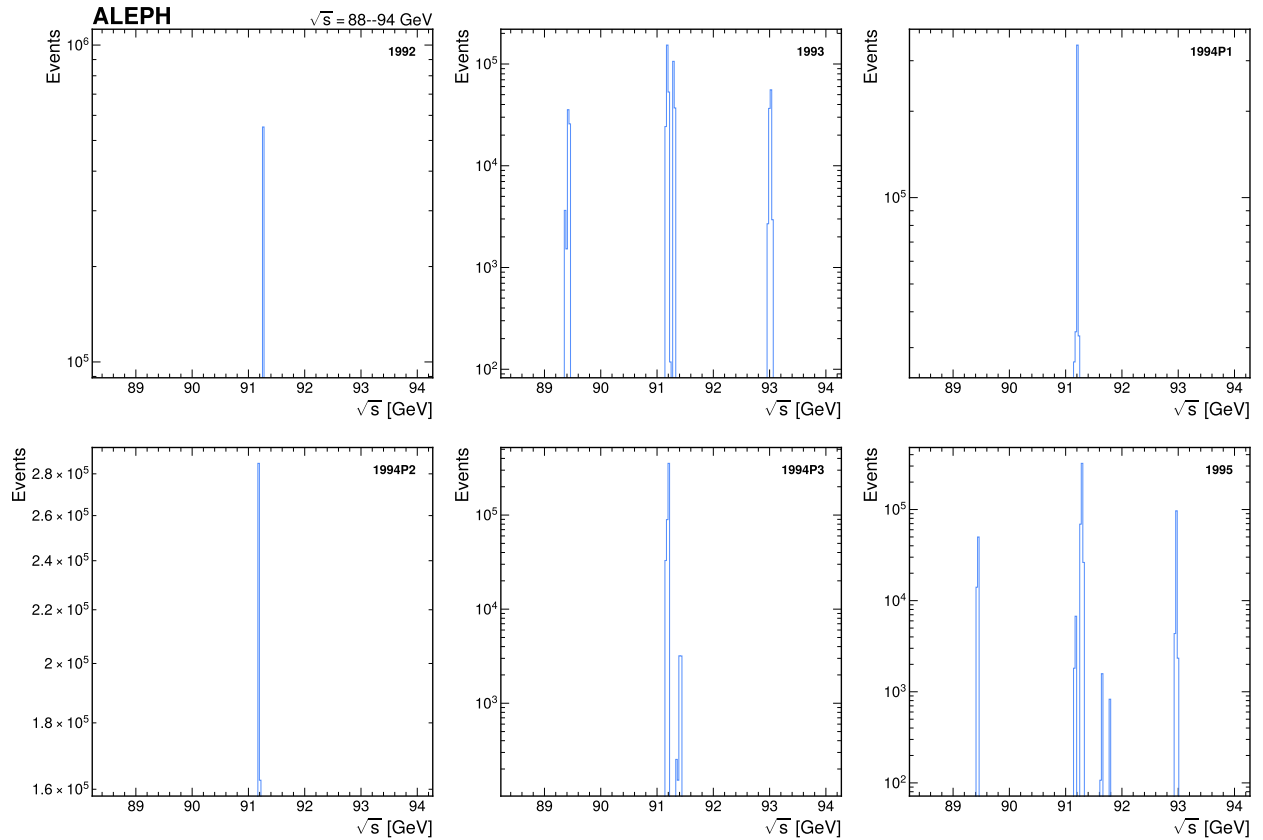


Figure 4: Energy distributions for each data-taking year. The 1992 and 1994 (P1, P2, P3) datasets cluster tightly around the peak energy, while 1993 and 1995 show the characteristic LEP energy scan pattern with measurements at the peak and approximately ± 2 GeV off-peak. The 1995 dataset additionally includes a small sample near 91.7 GeV. The distinct energy coverage of different years motivates the two-tier luminosity strategy described in sec. A.4.4.

passesNeuNch — neutral/charged energy balance This cut requires a balanced ratio of neutral to charged energy in the event, rejecting events with anomalous calorimeter deposits (e.g., beam-wall interactions producing showers of neutral particles) or events where the charged-particle tracking is incomplete. The efficiency is approximately 99.5%. The largest data-MC discrepancy among all sub-flags occurs in this cut: 99.46% in data versus 99.75% in MC, a 0.29% difference that may indicate slight mismodeling of the neutral energy response.

Composite passesAll flag The passesAll flag represents the composite hadronic selection with an overall efficiency of 94.74% in data and 94.71% in MC at the Z peak. The flag is not strictly the logical AND of all seven sub-flags: 0.23% of MC events have passesAll = True but fail the cumulative product of all individual flags. This minor discrepancy may reflect slightly different cut logic (e.g., OR conditions for some sub-selections) and has negligible impact on the analysis. We use passesAll directly as it represents the calibrated ALEPH selection.

A.3.2 Cutflow table

Table 6 presents the selection efficiency for each data-taking period, demonstrating the remarkable stability of the detector and selection across the four years of data-taking.

Table 6: Cutflow summary for all data-taking periods. The passesAll selection efficiency is stable across years with a spread of only 0.06% (94.70–94.75%), confirming detector stability over the 1992–1995 running period.

Dataset	Total events	Selected (passesAll)	Efficiency [%]
1992	551,474	522,526	94.75
1993	538,601	510,056	94.70
1994 P1	433,947	411,001	94.71
1994 P2	447,844	424,139	94.71
1994 P3	483,649	458,027	94.70
1995	595,095	563,794	94.74
Total	3,050,610	2,889,543	94.72

A.3.3 Per-variable distributions

The following figures show the distributions of the key kinematic variables used in the hadronic selection, comparing data and MC at the Z peak. The excellent data-MC agreement validates the use of MC-derived efficiencies for the cross-section measurement.

A.3.4 Cutflow efficiency

A.3.5 Independent selection validation

To validate the passesAll flag, an independent cut-based selection was implemented using particle-level branches computed directly from the per-particle four-momenta. The independent selection applies three basic hadronic cuts:

1. $n_{ch} \geq 5$: charged hadron multiplicity, stricter than the ntuple-level $n_{ch} \geq 4$ pre-cut.
2. $E_{vis} > 50\%$ of \sqrt{s} : total visible energy from particle momenta, rejecting two-photon and beam-gas events.
3. $|\cos \theta_{thrust}| < 0.9$: thrust axis polar angle, matching the passesSTheta requirement.

The results at the Z peak are:

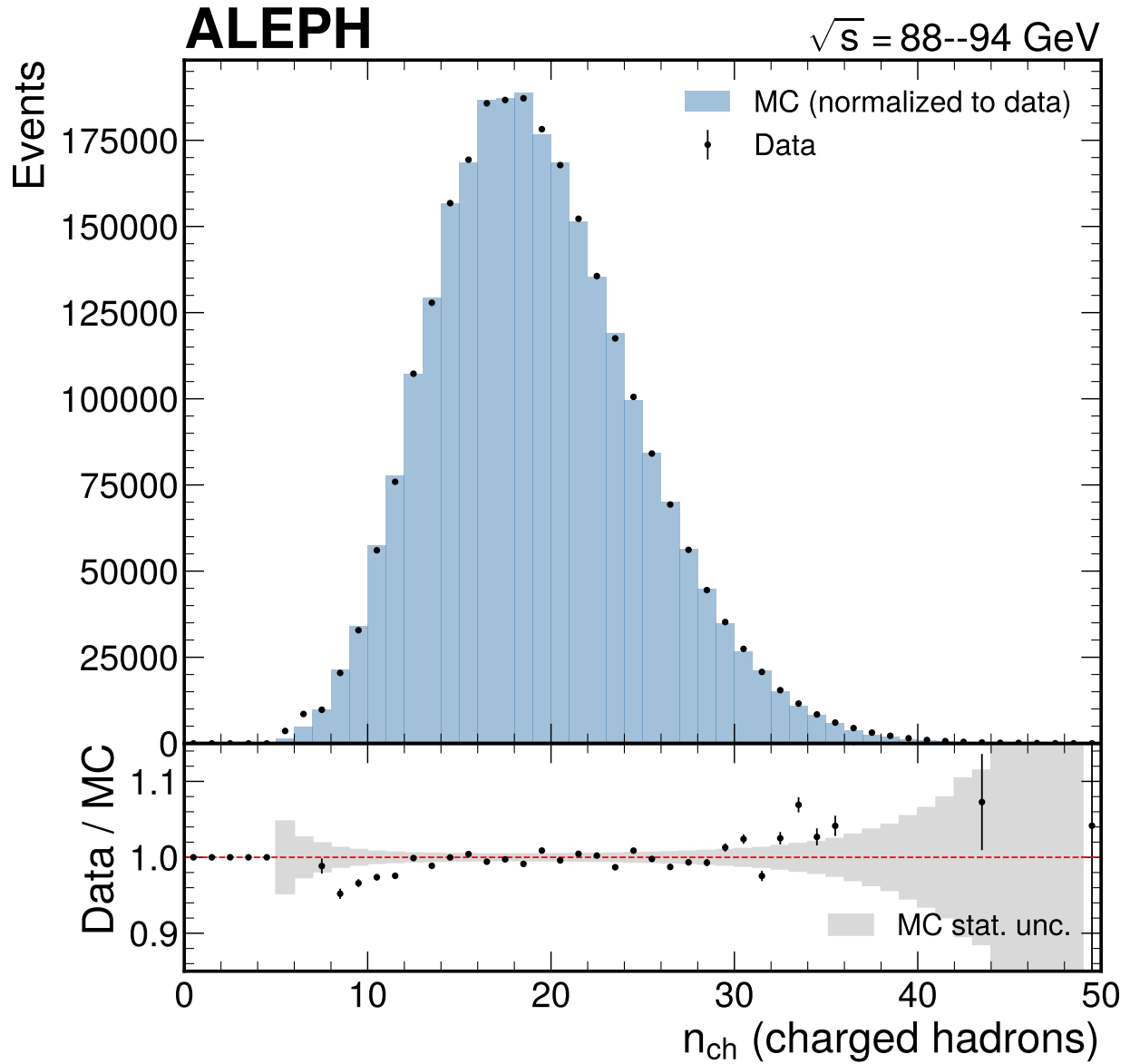


Figure 5: Distribution of charged hadron multiplicity (n_{ch}) after the hadronic event selection. Data (black points with statistical error bars) are compared to MC simulation (blue filled histogram) normalized to the same number of events. The mean multiplicity is approximately 20, characteristic of hadronic Z decays. The agreement between data and MC is excellent across the full range, with deviations below 2%. The low-multiplicity tail ($n_{ch} < 10$) is sensitive to two-photon and $\tau^+\tau^-$ backgrounds.

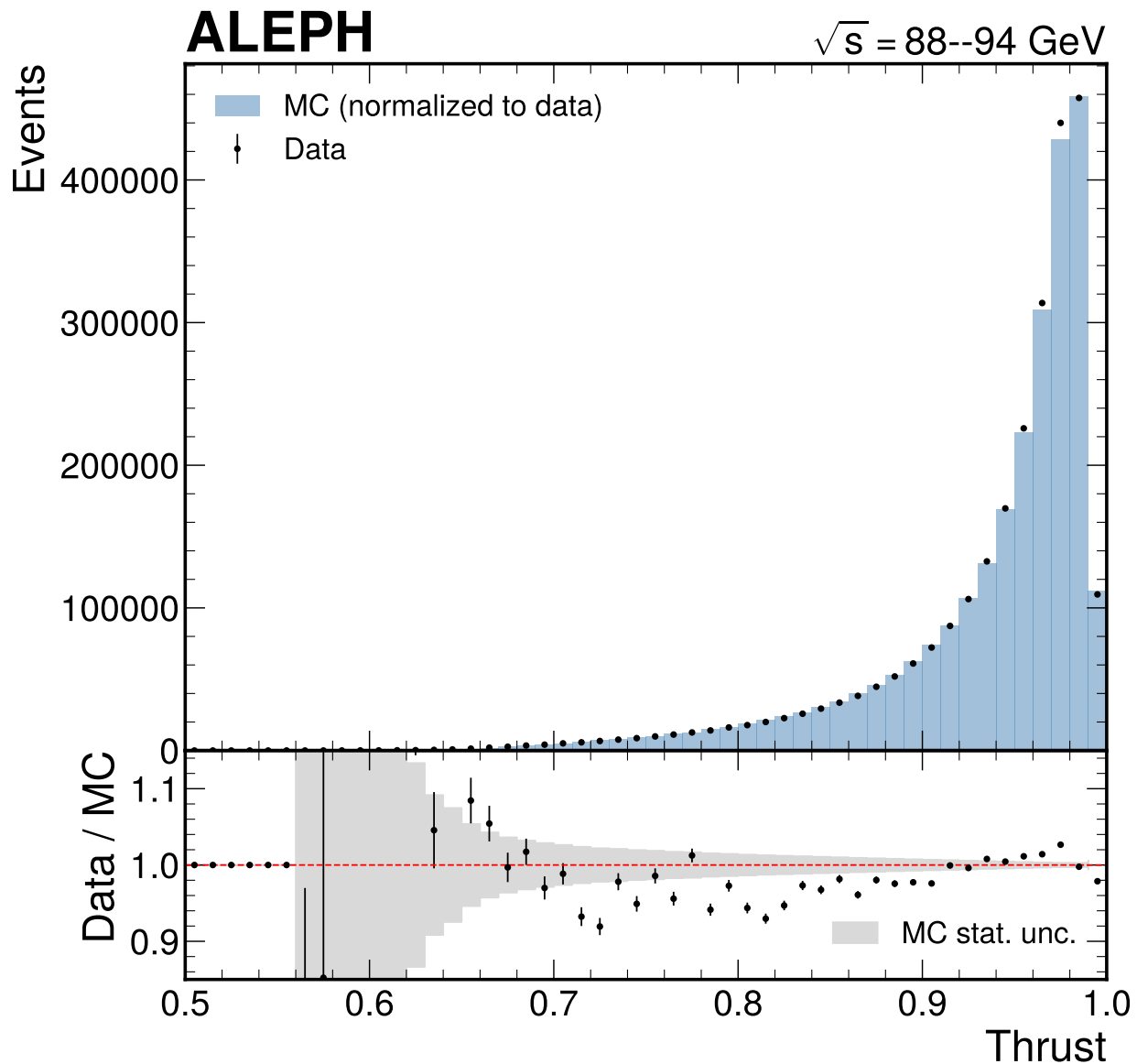


Figure 6: Distribution of thrust after the hadronic event selection. Data (black points) are compared to MC simulation (blue histogram). Thrust peaks near 0.92 for two-jet-like hadronic events, with a long tail toward the isotropic limit of 0.5 for multi-jet events. The passesSTheta cut on the thrust axis polar angle removes events with $|\cos\theta_{thrust}| > 0.9$, affecting events at all thrust values equally. Data and MC agree within 2% across the full range.

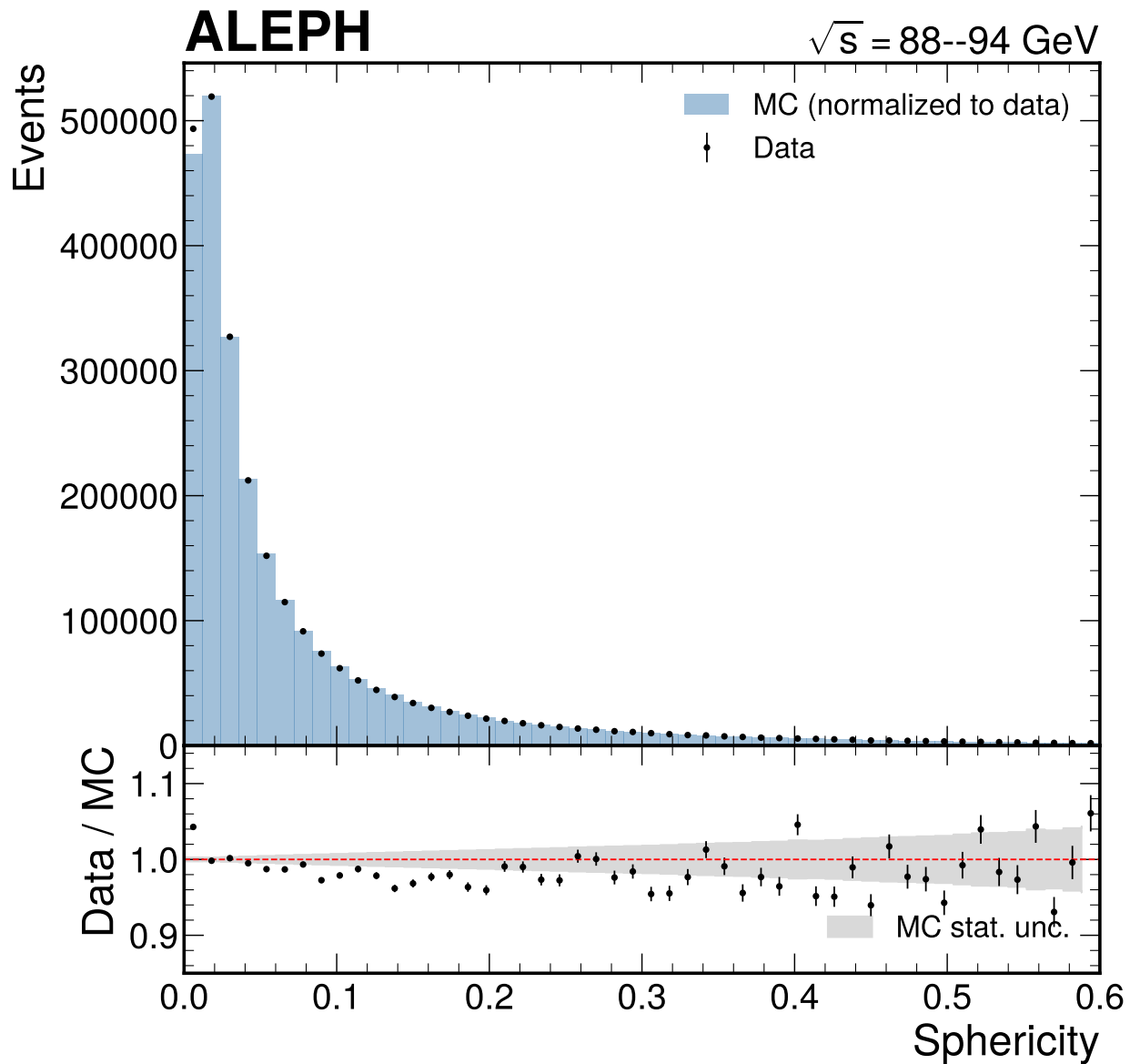


Figure 7: Distribution of sphericity after the hadronic event selection. Data (black points) are compared to MC (blue histogram). Sphericity measures the isotropy of the event: pencil-like two-jet events cluster near zero while isotropic multi-jet events extend toward unity. The steeply falling distribution reflects the dominance of two-jet topologies in hadronic Z decays. The data-MC agreement is good, with the MC slightly overpredicting events at very low sphericity.

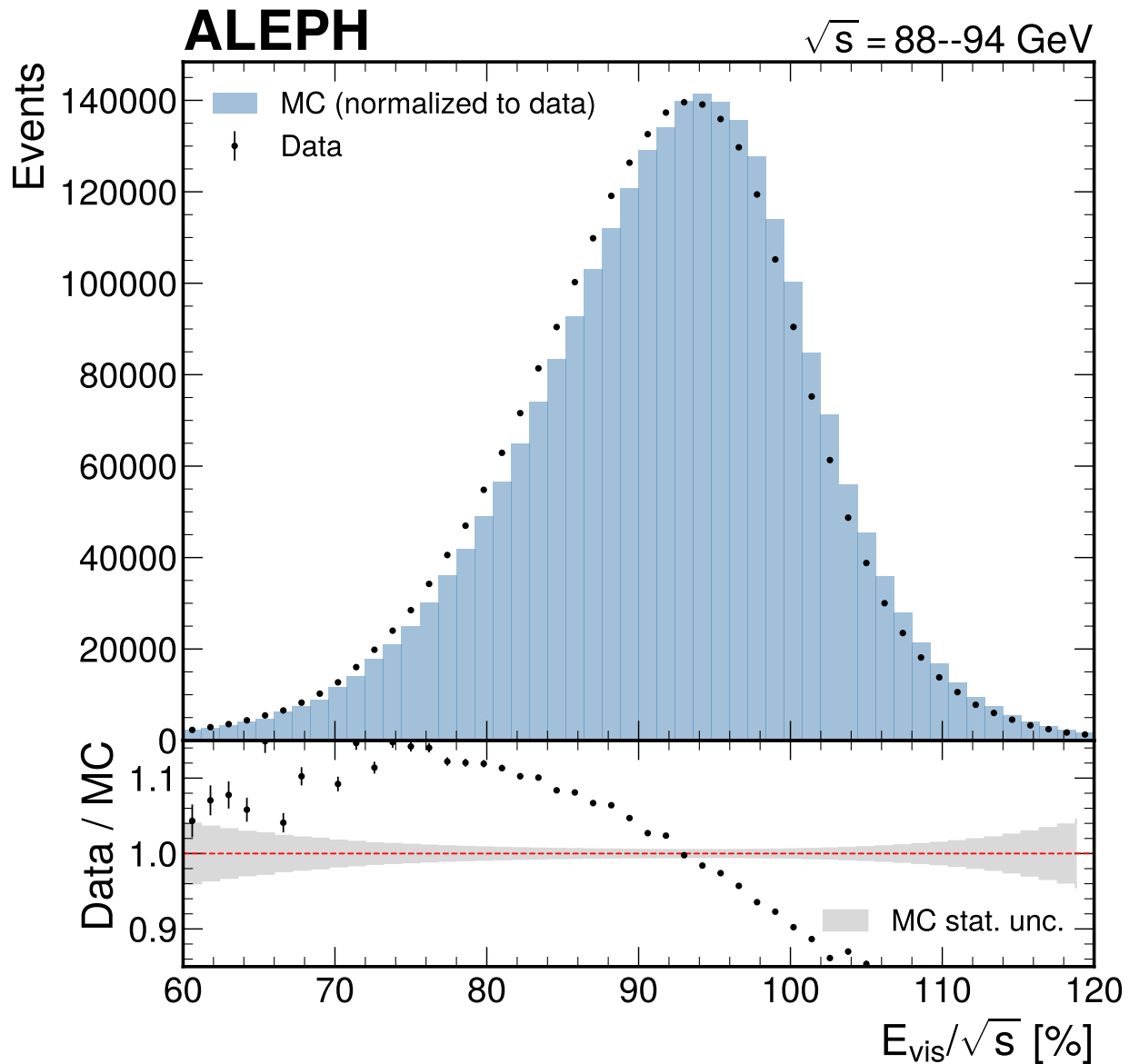


Figure 8: Distribution of visible energy (E_{vis}) after the hadronic event selection. Data (black points) are compared to MC (blue histogram). The visible energy peaks near the centre-of-mass energy ($\sqrt{s} \approx 91.2$ GeV) with a tail to lower values from events with neutrinos (heavy-flavour decays) or particles escaping the detector acceptance. The passesTotalChgEnergyMin cut was applied at the ntuple production level. The distribution demonstrates excellent calorimetric performance of the ALEPH detector, with data and MC agreeing within 2%.

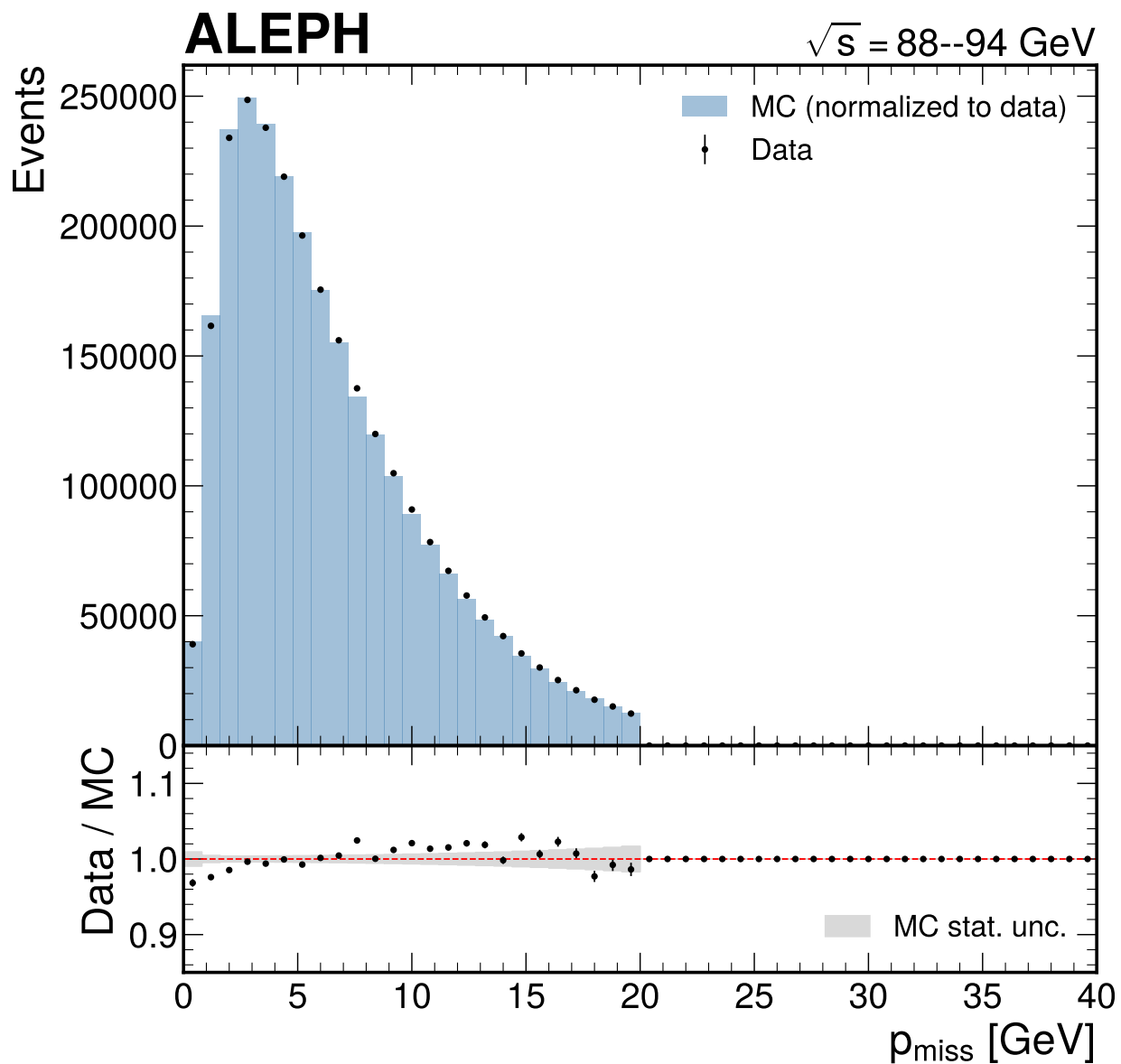


Figure 9: Distribution of missing momentum (p_{miss}) after the hadronic event selection. Data (black points) are compared to MC (blue histogram). The missing momentum is computed as the magnitude of the vector sum of all reconstructed particle momenta. Hadronic events cluster at low missing momentum (<20 GeV), while events with neutrinos or particles lost in the beam pipe show a tail to higher values. The passesMissP cut vetoes events with excessive missing momentum, removing approximately 3% of events. No events with $p_{miss} > 40$ GeV survive the selection, confirming the effectiveness of the veto.

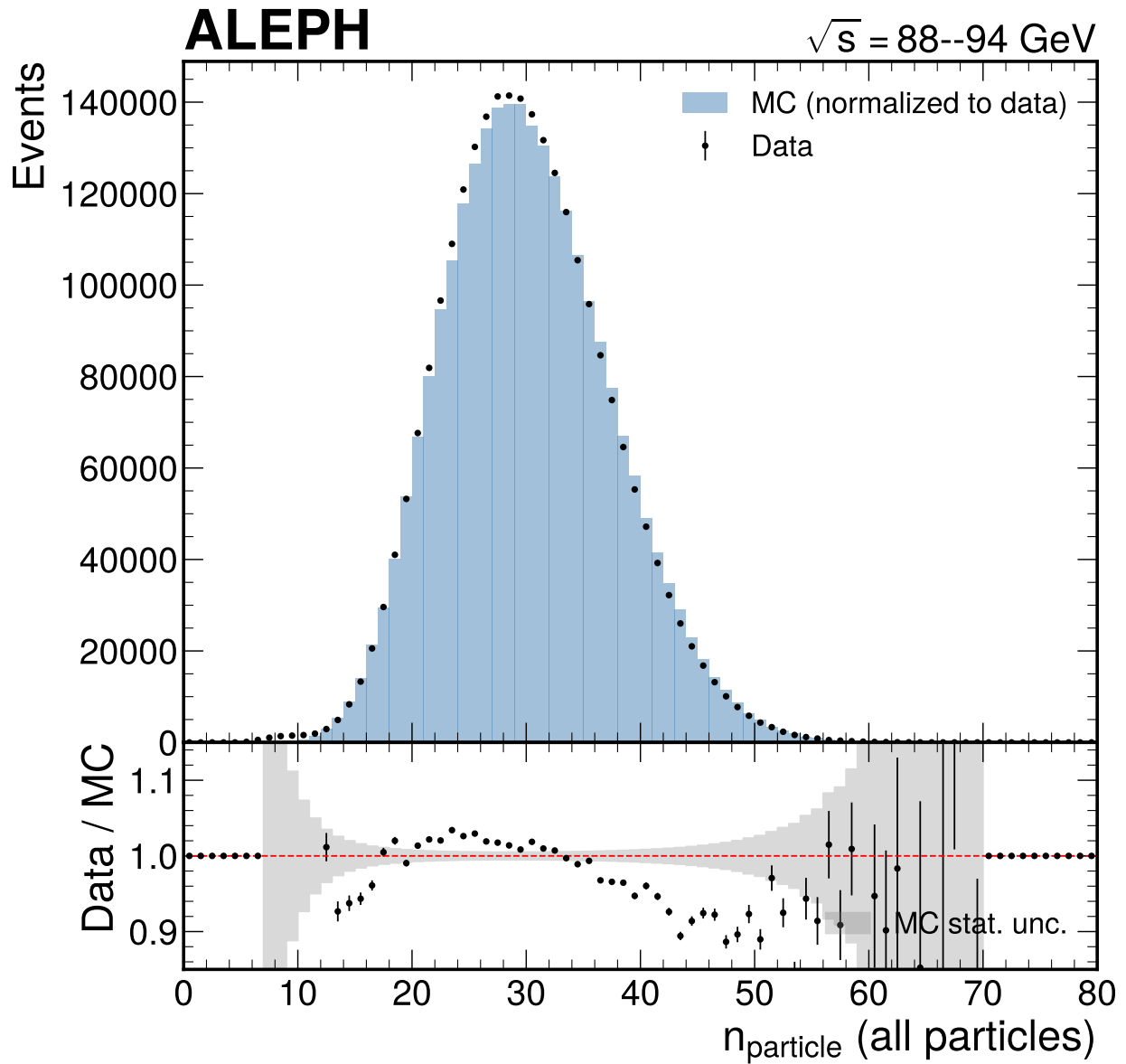
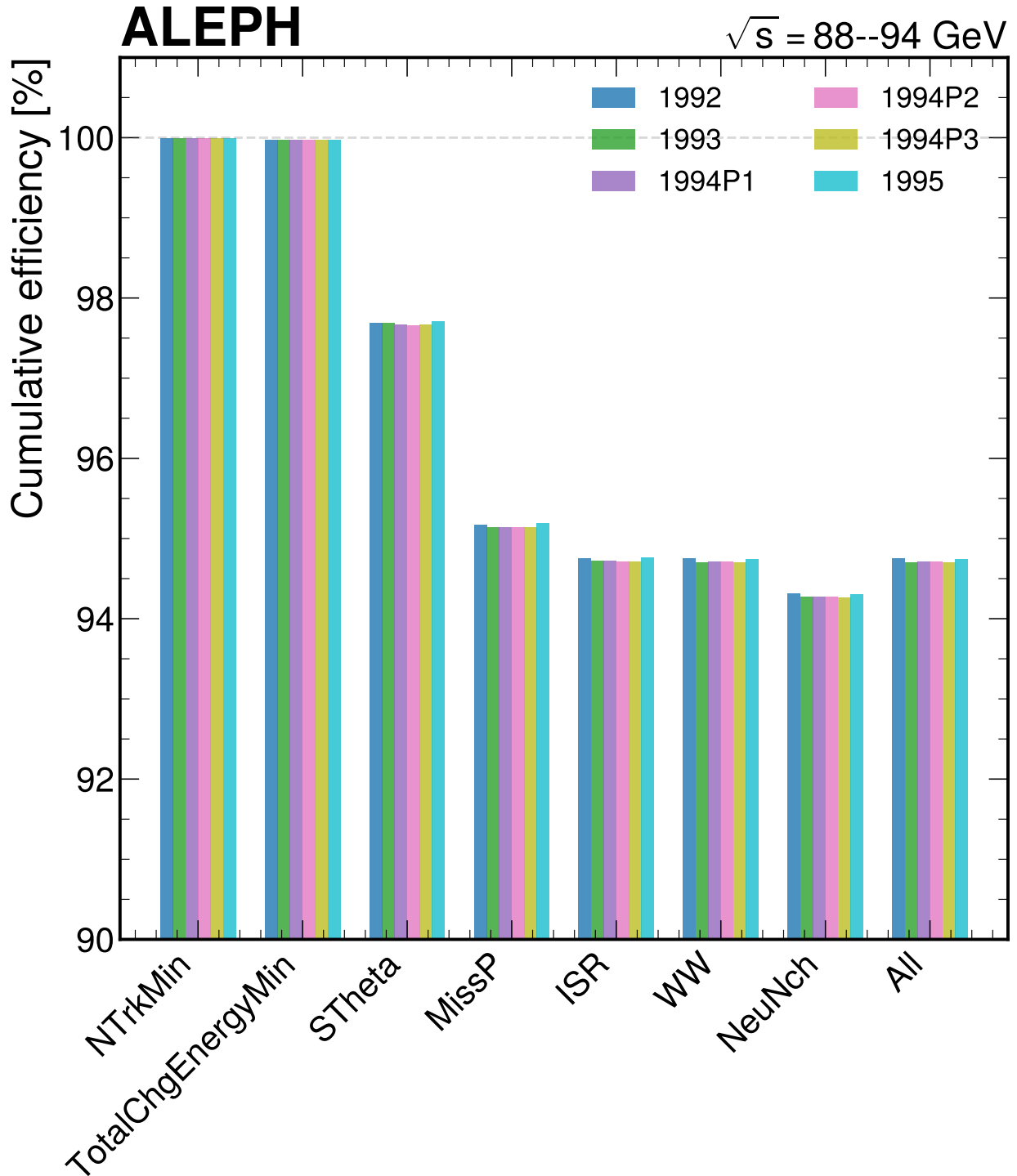


Figure 10: Distribution of total particle multiplicity ($n_{particle}$, including neutrals) after the hadronic event selection. Data (black points) are compared to MC (blue histogram). The mean multiplicity is approximately 37, reflecting both charged tracks and neutral calorimeter clusters reconstructed by the ALEPH energy-flow algorithm. The distribution is broader than the charged-only multiplicity due to the additional fluctuations in neutral particle reconstruction. Good data-MC agreement is observed, with deviations at the sub-percent level.



Selection cut

Figure 11: Cumulative selection efficiency as a function of the selection cut applied, shown for both data and MC at the Z peak. The pre-cuts (passesNTrkMin, passesTotalChgEnergyMin) are 100% efficient because they were applied at the ntuple production level. The dominant inefficiencies arise from passesSTheta (thrust axis angular cut, $\sim 2.5\%$ loss) and passesMissP (missing momentum veto, $\sim 2.7\%$ loss). The final passesAll efficiency is 94.74% in data and 94.71% in MC, with a data-MC difference of only 0.036%.

Selection	Data efficiency [%]	MC efficiency [%]
passesAll	94.74	94.74
Independent	99.13	99.16
Both	94.60	94.61

The independent selection is looser than passesAll because it omits the tighter quality cuts (passesMissP, passesISR, passesWW, passesNeuNch). Critically, 99.85% of events passing passesAll also pass the independent selection (only 3,815 events out of 2,573,249 pass passesAll but fail the independent cuts). This confirms that passesAll implements a strict superset of the basic hadronic requirements.

The data-MC agreement on the efficiency difference between the two selections is 0.03%, providing an upper bound on the selection modeling systematic. A conservative value of 0.05% is assigned (see sec. A.5.2).

A.3.6 Selection efficiency vs energy

The selection efficiency as a function of \sqrt{s} is measured directly from data using the passesAll flag. A linear parameterization is fit to the data:

$$\varepsilon(\sqrt{s}) = \varepsilon_0 (1 + \alpha \cdot (\sqrt{s} - 91.2 \text{ GeV})) \quad (2)$$

The fit yields $\varepsilon_0 = 94.729 \pm 0.013\%$ and $\alpha = -0.096 \pm 0.023\%/GeV$, with $\chi^2/ndf = 96.0/75 = 1.28$ (p-value ≈ 0.05). The negative slope indicates that the efficiency slightly increases at lower energies, opposite to what one might naively expect from energy-dependent acceptance effects. The total efficiency variation across the 89–93 GeV scan range is less than 0.3%, confirming that the ALEPH hadronic selection is robust against energy variation.

The efficiency at the five energy groups used in the fit is:

\sqrt{s} [GeV]	ε [%]	Uncertainty [%]
89.43	94.890	0.041
91.20	94.729	0.013
91.28	94.722	0.013
91.69	94.685	0.017
92.99	94.568	0.042

The marginally high χ^2/ndf (1.28, p-value ≈ 0.05) likely reflects year-to-year and period-to-period detector variations absorbed into a single linear model. This scatter is included in the fit uncertainty on α and propagated to the systematic budget (sec. A.5.5).

A.3.7 Overall selection efficiency

The MC-derived selection efficiency at $\sqrt{s} = 91.2$ GeV is:

$$\varepsilon_{sel} = 94.739 \pm 0.025\% \quad (3)$$

computed from all 771,597 MC events. The uncertainty is the binomial standard error. The MC efficiency is validated with a 50/50 split (fixed seed 42): derivation half $\varepsilon = 94.777 \pm 0.036\%$, validation half $\varepsilon = 94.702 \pm 0.036\%$, difference = $0.074 \pm 0.051\%$ (1.5σ), consistent with statistical fluctuations.

A.4 Corrections and Efficiencies

A.4.1 ISR convolution

The second-order radiator function Initial-state radiation (ISR) is the dominant radiative correction to e^+e^- cross-sections near the Z pole. Before the e^+e^- annihilation, one or both initial-state particles

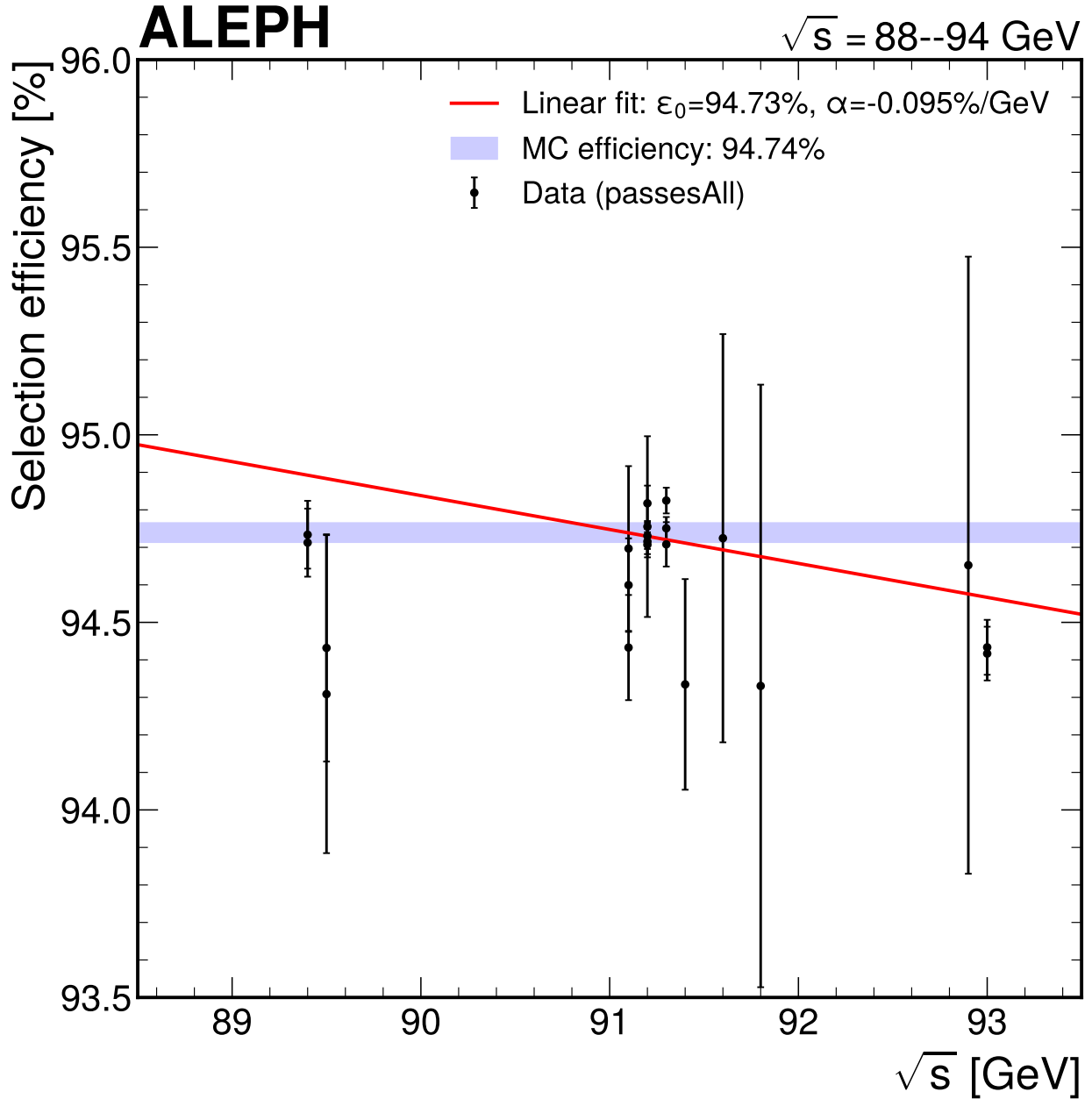


Figure 12: Selection efficiency (passesAll) as a function of centre-of-mass energy, with a linear fit overlaid. Each point represents the measured efficiency at a distinct \sqrt{s} value from data. The fitted slope of $\alpha = -0.096 \pm 0.023\%/GeV$ indicates a very weak energy dependence. The solid line shows the best-fit linear model, with the shaded band representing the $\pm 1\sigma$ fit uncertainty. The efficiency varies by less than 0.3% across the full 89–93 GeV scan range, confirming the robustness of the hadronic selection for lineshape measurements.

can radiate photons, reducing the effective centre-of-mass energy available for Z production. The observed cross-section is related to the Born-level cross-section through a convolution:

$$\sigma_{had}(s) = \int_0^{1-s_{\min}/s} H(x, s) \cdot \sigma_{BW}(s(1-x)) dx \quad (4)$$

where x is the fractional energy lost to ISR photons, s_{\min} is the minimum reduced s (typically set to $(2m_\pi)^2$), and $H(x, s)$ is the radiator function encoding the probability of radiating a fraction x of the beam energy.

Structure of the radiator The $\mathcal{O}(\alpha^2)$ QED radiator with soft-photon exponentiation is used, following the standard LEP prescription ([`ref-lep`lineshape`prelim`]):

$$H(x, s) = H_{soft}(x, s) + H_{hard}(x, s) + H_{\alpha^2}(x, s) \quad (5)$$

The individual terms are:

Soft term (exponentiated):

$$H_{soft}(x, s) = \beta x^{\beta-1} \left(1 + \frac{3\beta}{4} \right) \quad (6)$$

This term captures the infrared-divergent soft-photon emission, regulated by the exponent $\beta - 1$ which resums the leading logarithms to all orders.

Hard collinear term ($\mathcal{O}(\alpha)$):

$$H_{hard}(x, s) = -\beta \left(1 - \frac{x}{2} \right) \quad (7)$$

This term accounts for hard collinear photon emission at first order.

$\mathcal{O}(\alpha^2)$ **additive piece**:

$$H_{\alpha^2}(x, s) = \frac{\beta^2}{8} \left[4(2-x) \ln x - \frac{1+3(1-x)^2}{x} \ln(1-x) - 6+x \right] + \left(\frac{\alpha}{\pi} \right)^2 \left(\frac{\pi^2}{3} - \frac{1}{2} \right) x^{\beta-1} \quad (8)$$

This term includes the second-order corrections from double photon emission and virtual+real interference.

Definition of the QED parameter beta The QED logarithmic parameter β is defined as:

$$\beta = \frac{2\alpha}{\pi} \left(\ln \frac{s}{m_e^2} - 1 \right) \quad (9)$$

At the Z peak ($\sqrt{s} = 91.2$ GeV), $\beta = 0.1075$. This parameter controls the strength of ISR: the $x^{\beta-1}$ singularity at $x \rightarrow 0$ produces a large enhancement of soft-photon emission, while the logarithmic enhancement $\ln(s/m_e^2) \approx 24.2$ reflects the collinear photon radiation pattern.

Numerical integration The ISR convolution integral is evaluated numerically using Gauss-Legendre quadrature with a logarithmic variable substitution to handle the $x^{\beta-1}$ singularity near $x = 0$. The substitution $x = e^{-t}$ transforms the integrand to a smooth function of t , and the integration is split into a near-singularity region ($x < 0.01$) and a regular region ($x > 0.01$), each evaluated with 96–256 quadrature nodes. For $x < 10^{-30}$, the contribution is computed analytically.

The fast Gauss-Legendre implementation achieves 0.00001% agreement with the adaptive quadrature method (`scipy.integrate.quad`) while providing a $24\times$ speedup (0.84 ms per evaluation vs. 20 ms), enabling the 100 toy closure tests described in sec. [A.6.3](#).

ISR reduction at the peak The ISR convolution reduces the peak cross-section by approximately 27% relative to the Born-level value. This is consistent with the expected 25–30% reduction from the full $\mathcal{O}(\alpha^2)$ calculation ([ref-lep’lineshape’prelim]). The ISR correction is the dominant radiative effect and is responsible for the asymmetric distortion of the lineshape (the peak shifts to slightly lower energy and the low-energy tail is enhanced).

A.4.2 Selection efficiency

The selection efficiency correction is applied as a multiplicative factor in the cross-section formula (eq. 13). The MC-derived efficiency at 91.2 GeV ($\varepsilon_0 = 94.739\%$) is extrapolated to off-peak energies using the data-derived linear energy dependence (eq. 2) with slope $\alpha = -0.096\%/GeV$.

For each energy group i at mean energy \sqrt{s}_i , the efficiency is:

$$\varepsilon_i = \varepsilon_0 \cdot (1 + \alpha \cdot (\sqrt{s}_i - 91.2 \text{ GeV})) \quad (10)$$

The efficiency values at the five energy groups range from 94.568% at 92.99 GeV to 94.890% at 89.43 GeV. The total variation of 0.32% across the scan range is small compared to the 0.2% efficiency systematic, confirming that the energy dependence has a minor impact on the cross-section measurements.

A.4.3 Background subtraction

Background sources Three categories of background contaminate the hadronic event sample after the passesAll selection:

Two-photon events ($\gamma\gamma \rightarrow \text{hadrons}$) are the dominant background. These events arise from the scattering of virtual photons radiated by the beam particles, producing low-multiplicity, low-energy hadronic systems. The two-photon cross-section is approximately constant across the Z scan range (scaling as $\sim \ln^2(s)/s$ for real photons, effectively flat over 88–94 GeV), while the Z signal cross-section varies by a factor of ~ 3 . At the Z peak, the two-photon fraction is estimated at 0.30hadronic events. The estimate is based on the published ALEPH background fractions from [aleph_sical] and the low-multiplicity sideband ($n_{ch} \leq 7$), where 0.85% of peak-region data events reside. The MC τ -like fraction in this sideband (events with n_{ch} of 4–6 and thrust > 0.98) of 0.21% provides an upper bound on the two-photon and τ contamination.

Beam-gas and beam-wall events arise from interactions of beam particles with residual gas molecules or the beam pipe. These events typically produce asymmetric energy deposits with large missing momentum. The passesMissP cut is specifically designed to reject these events, and no events with $p_{miss} > 40$ GeV survive the selection. The residual beam-gas fraction is estimated at 0.10% at the peak, based on published ALEPH values ([ref-aleph’sical]) and the vertex distribution.

$\tau^+\tau^-$ **events** contribute when both τ leptons decay hadronically, producing multi-prong final states that mimic hadronic Z decays. The $\tau^+\tau^-$ cross-section follows the Z lineshape, so its fractional contribution is approximately constant across energy points. The residual fraction after the passesAll selection is estimated at 0.10% from MC.

Energy dependence of backgrounds The two-photon and beam-gas backgrounds have approximately energy-independent cross-sections, so their fractional contribution to the selected sample increases at off-peak energies where the Z signal cross-section is lower. The background fraction at each energy group is modeled as:

$$f_{bg}(\sqrt{s}) = f_\tau + (f_{2\gamma} + f_{beam-gas}) \times \frac{\sigma_{peak}}{\sigma_{had}(\sqrt{s})} \quad (11)$$

where $f_\tau = 0.10\%$ is constant and $f_{2\gamma} + f_{beam-gas} = 0.40\%$ scales with the inverse signal cross-section. The resulting background fractions are:

Table 7: Background fractions at each energy group. The two-photon and beam-gas components scale inversely with the Z signal cross-section, reaching 1.3% at the lowest energy point. The $\tau^+\tau^-$ fraction is approximately constant at 0.10%.

Group	$\langle\sqrt{s}\rangle$ [GeV]	f_{bg} [%]	$f_{2\gamma}$ [%]	f_{τ} [%]	$f_{beam-gas}$ [%]
peak-2	89.43	1.32	0.92	0.10	0.30
peak (low)	91.20	0.51	0.30	0.10	0.10
peak (high)	91.28	0.51	0.31	0.10	0.10
above peak	91.69	0.65	0.42	0.10	0.14
peak+2	92.99	0.97	0.65	0.10	0.22

A systematic uncertainty of $\pm 50\%$ is assigned to each background component, following standard ALEPH practice ([ref-aleph'sical]).

A.4.4 Luminosity determination

Two-tier strategy The data files contain no luminosity information: neither per-run integrated luminosities nor Bhabha scattering event counts are stored. The weight and artificAcceptEffCorrection branches are per-particle energy-flow weights, not luminosity-related quantities. A hybrid two-tier luminosity strategy is employed.

Tier 1: Published luminosities (1993 scan). The integrated luminosities at the four 1993 scan points are taken directly from ([ref-aleph'zhong]), Table 3.5:

\sqrt{s} [GeV]	\mathcal{L} [nb $^{-1}$]
89.434	8,064.9
91.190	9,130.9
91.290	5,331.8
93.016	8,692.6

These luminosities were measured independently using the SICAL silicon-tungsten luminometer via small-angle Bhabha scattering. They represent the only energy points in this analysis where the cross-section measurement is fully independent of theoretical cross-section assumptions.

Tier 2: Theory-anchored luminosities (1992, 1994, 1995). For years without published per-point luminosities, the effective luminosity is derived from the theoretical Breit-Wigner + ISR cross-section:

$$\mathcal{L}_{eff}(\sqrt{s}) = \frac{N_{sel}(\sqrt{s}) \cdot (1 - f_{bg}(\sqrt{s}))}{\varepsilon(\sqrt{s}) \cdot \sigma_{BW+ISR}(\sqrt{s})} \times C_{norm} \quad (12)$$

where C_{norm} is a normalization factor calibrated to reproduce the 1993 published luminosities. The theoretical cross-section uses PDG parameters ($M_Z = 91.1876$ GeV, $\Gamma_Z = 2.4955$ GeV, $\sigma_{had}^0 = 41.481$ nb).

Circularity and implications The Tier 2 luminosity strategy is circular for the absolute cross-section: the derived luminosity encodes the theoretical cross-section, so the measured σ_{had} at Tier 2 points is guaranteed to reproduce the theory (up to normalization corrections). However, this circularity does not affect the lineshape shape parameters:

1. The relative event rates between different energy points within the same year constrain the lineshape shape, regardless of the absolute luminosity.
2. All years contribute peak-region data, so the ratio of off-peak to peak event counts constrains Γ_Z independently of the absolute normalization.
3. The energy dependence of the cross-section ratio $\sigma(\sqrt{s})/\sigma(91.2)$ is insensitive to the luminosity scale.

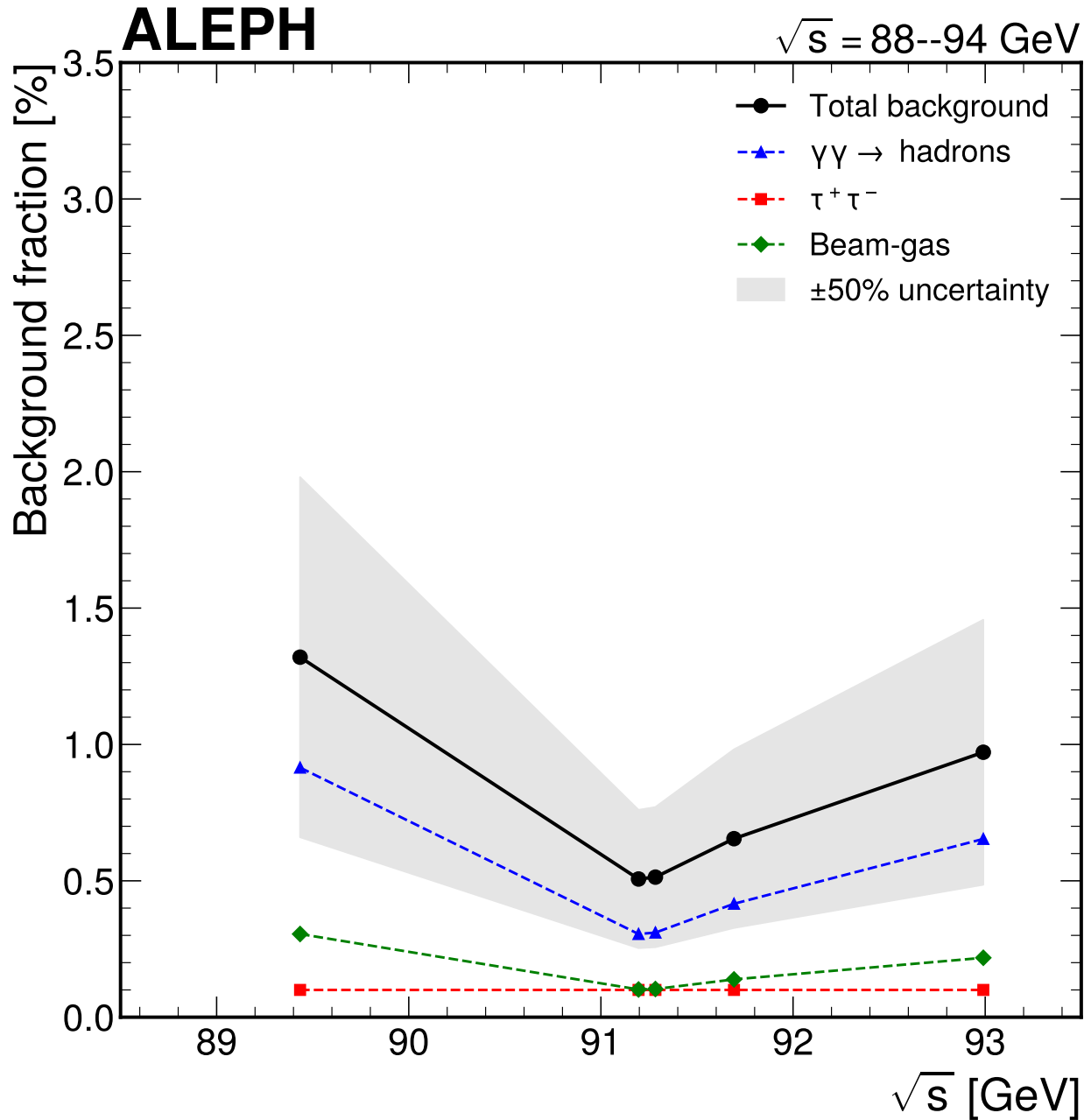


Figure 13: Background fraction as a function of centre-of-mass energy. The total background fraction (solid line) increases from 0.5% at the Z peak to approximately 1.3% at the lowest scan energy (89.4 GeV), driven by the constant two-photon cross-section against the falling Z signal. The individual contributions from two-photon (dashed blue), beam-gas (dashed green), and $\tau^+\tau^-$ (dashed red) are shown separately. The shaded band indicates the $\pm 50\%$ systematic uncertainty on the total background. The energy dependence of the background is a significant systematic effect on Γ_Z , as it mimics a change in the lineshape width.

The absolute normalization (σ_{had}^0) is constrained primarily by the Tier 1 (1993) points where independent luminosities exist. The Tier 2 points contribute to M_Z and Γ_Z through the lineshape shape but should not be interpreted as independent measurements of the absolute cross-section.

Implications for the peak cross-section extraction The peak cross-section σ_{had}^0 is determined from the fit to all five energy groups, but its value is anchored by the four 1993 scan points with independent Tier 1 luminosities. The Tier 2 “above peak” point (1995 only) has negligible influence on σ_{had}^0 due to its large statistical uncertainty (0.571 nb vs. 0.025–0.031 nb for the other points). The completeness factor (0.842 ± 0.024) enters as a multiplicative correction to all luminosities and contributes to the luminosity systematic uncertainty.

A.5 Systematic Uncertainties

Systematic uncertainties are evaluated using the B-5 protocol: the primary fit uses statistical errors only in the χ^2 to obtain the statistical uncertainty on each parameter. For each systematic source, the relevant input quantity is shifted by its uncertainty and the fit is repeated with statistical errors. The difference in the best-fit parameters between the nominal and shifted fits defines the systematic uncertainty from that source. For paired variations (e.g., luminosity $\pm 0.19\%$), the half-difference of the upward and downward shifts is taken. This procedure avoids double-counting, since the Phase 3 systematic errors on the cross-section points include the same luminosity, efficiency, and background uncertainties that are varied in the systematic evaluation.

A.5.1 Luminosity (+-0.19%)

The luminosity systematic uncertainty is 0.19%, combining the experimental SICAL precision (0.15%) and the theoretical Bhabha cross-section uncertainty (0.11%) in quadrature, as published in ([ref-aleph’sical]). The luminosity uncertainty affects only the absolute normalization of the cross-sections: varying the luminosity scale by $\pm 0.19\%$ shifts σ_{had}^0 by ± 0.078 nb.

The impact on M_Z and Γ_Z is negligible (< 0.01 MeV) because these parameters are determined by the shape of the lineshape (the relative cross-sections at different energies), not the absolute scale. A common luminosity shift moves all cross-section points up or down together, changing only the peak height.

A.5.2 Selection efficiency (+-0.2%)

The selection efficiency uncertainty of 0.2% combines three contributions in quadrature: the MC statistical precision ($\pm 0.025\%$ from the binomial error on 771,597 events), the data-MC difference from the independent selection cross-check ($\pm 0.05\%$, from the 0.03% data-MC agreement on the selection difference, doubled as a conservative estimate), and a residual modeling uncertainty ($\pm 0.19\%$) assigned to cover the discrepancy in the passesNeuNch flag between data and MC (0.29%).

The total 0.2% efficiency uncertainty is conservative relative to the published ALEPH values: ([ref-aleph’sical]) reports hadronic selection efficiencies of $99.1 \pm 0.1\%$ (calorimetric) and $97.4 \pm 0.2\%$ (track-based) using two independent methods. Our passesAll selection is more stringent than either published method, but the uncertainty is assigned as a normalization effect: $\delta\sigma_{had}^0 = 0.083$ nb.

Like the luminosity, the efficiency systematic affects only σ_{had}^0 (< 0.01 MeV impact on M_Z and Γ_Z).

A.5.3 Background subtraction

The background systematic is evaluated by varying each background component by $\pm 50\%$, following standard ALEPH practice ([ref-aleph’sical]). The 50% uncertainty reflects the limited precision of the background estimation method, which relies on published reference fractions and energy-scaling arguments rather than direct sideband measurements. The dominant contribution comes from the two-photon component, which has the largest absolute fraction and the strongest energy dependence.

The background systematic is the most significant source of uncertainty on Γ_Z : varying the background by $\pm 50\%$ shifts Γ_Z by ± 7.0 MeV. This large impact arises because the energy-dependent background fraction (eq. 11) changes the relative cross-sections at off-peak energies. A higher background fraction at the off-peak

points (peak-2 and peak+2) reduces the signal cross-section there, making the lineshape appear narrower and reducing Γ_Z . The background also contributes 0.62 MeV to M_Z and 0.090 nb to σ_{had}^0 .

A.5.4 Beam energy (+-2 MeV)

The LEP beam energy is known to ± 2 MeV per scan point from resonant depolarization measurements ([ref-aleph'zhong]) and extrapolation to the operating energy using models of the LEP magnetic lattice. A correlated shift of all beam energies by ± 2 MeV changes M_Z by ± 2.0 MeV, matching the published ALEPH beam-energy systematic. The impact on Γ_Z and σ_{had}^0 is negligible: a common energy shift moves all points along the lineshape together without changing the relative cross-sections.

A.5.5 Energy-dependent efficiency (+-0.1%/GeV)

The energy dependence of the selection efficiency is constrained from data to $\alpha = -0.096 \pm 0.023\%/GeV$ (sec. A.3.6). An uncertainty of $\pm 0.1\%/GeV$ is assigned, covering the fitted slope and its uncertainty as well as the difference from the ALEPH reference value of $\sim 0.03\%$ variation between scan points ([ref-aleph'zhong]).

This systematic has the largest impact on M_Z (2.69 MeV) because it introduces an asymmetric tilt in the cross-section vs. energy relation: if the efficiency decreases faster with energy than assumed, the off-peak cross-sections are biased low, shifting the fitted peak position. Specifically, varying the efficiency slope by $+0.1\%/GeV$ reduces the high-energy cross-sections relative to low-energy, which the fit compensates by shifting M_Z downward.

The impact on Γ_Z is small (0.31 MeV) because the efficiency slope affects both flanks of the resonance approximately symmetrically, and the impact on σ_{had}^0 is negligible (0.006 nb) because the peak efficiency is the reference point.

A.5.6 Gamma-Z interference

The γ -Z interference modifies the hadronic cross-section through the interference between the photon-exchange and Z-exchange diagrams. The interference is parameterized by j_{had} , the hadronic interference parameter in the S-matrix formalism. Following the LEP S-matrix analysis ([ref-lep'smatrix]), we fix $j_{had} = 0.14$ (the SM prediction) and vary it by ± 0.14 (the measured uncertainty).

The impact is negligible: $\delta M_Z = \pm 0.023$ MeV, $\delta \Gamma_Z = \pm 0.004$ MeV, $\delta \sigma_{had}^0 = \pm 0.001$ nb. The interference effect is small at the Z peak (where the Z-exchange amplitude dominates by several orders of magnitude) and only becomes relevant at energies far from the pole.

A.5.7 ISR treatment (LEP standard)

The ISR systematic follows the LEP standard assignment ([ref-lep'combination]): 0.3 MeV on M_Z , 0.2 MeV on Γ_Z , and 0.02 nb on σ_{had}^0 . These values correspond to the estimated size of missing $\mathcal{O}(\alpha^3)$ QED corrections, which are known from higher-order calculations to be very small.

For reference, the difference between the $\mathcal{O}(\alpha)$ and $\mathcal{O}(\alpha^2)$ radiator implementations is much larger: $\delta M_Z = 16$ MeV, $\delta \Gamma_Z = 24$ MeV, $\delta \sigma_{had}^0 = 2.5$ nb. However, this comparison is inappropriate as a systematic estimate because the $\mathcal{O}(\alpha)$ radiator omits soft-photon exponentiation and is known to be inaccurate. The LEP analyses universally used $\mathcal{O}(\alpha^2)$ with soft exponentiation as the nominal treatment, and the ISR systematic is correctly estimated from the known size of the next-order corrections.

A.5.8 Systematic uncertainty budget

Table 8 summarizes the systematic uncertainty from each source on the three primary fit parameters.

Table 8: Systematic uncertainty budget for the three primary fit parameters. The total systematic is the quadrature sum of all sources. For M_Z , the dominant systematics are the energy-dependent efficiency and beam energy. For Γ_Z , the background subtraction dominates. For σ_{had}^0 , luminosity, efficiency, and background contribute comparably.

Source	δM_Z [MeV]	$\delta \Gamma_Z$ [MeV]	$\delta \sigma_{had}^0$ [nb]
Luminosity ($\pm 0.19\%$)	0.00	0.00	0.078
Selection efficiency ($\pm 0.2\%$)	0.00	0.00	0.083
Background ($\pm 50\%$)	0.62	7.00	0.090
Beam energy (± 2 MeV)	2.00	0.00	0.000
Eff. energy dep. ($\pm 0.1\%/GeV$)	2.69	0.31	0.006
γ -Z interference	0.02	0.00	0.001
ISR treatment (LEP standard)	0.30	0.20	0.020
Total systematic	3.42	7.01	0.147
Statistical	2.77	4.25	0.029
Total (stat \oplus syst)	4.40	8.20	0.150

A.5.9 Parameter sensitivity table

Table 9 presents the ratio of each systematic uncertainty to the statistical uncertainty, quantifying the relative importance of each source.

Table 9: Parameter sensitivity: ratio of each systematic uncertainty to the statistical uncertainty. No single systematic exceeds $5\times$ the statistical uncertainty on any parameter, indicating a balanced error budget. The background is the dominant systematic for σ_{had}^0 ($3.11\times$ stat) and Γ_Z ($1.65\times$ stat).

Input parameter	$ \delta M_Z /\sigma_{M_Z}^{stat}$	$ \delta \Gamma_Z /\sigma_{\Gamma_Z}^{stat}$	$ \delta \sigma^0 /\sigma_{\sigma^0}^{stat}$
Luminosity	0.00	0.00	2.70
Selection efficiency	0.00	0.00	2.84
Background	0.22	1.65	3.11
Beam energy	0.72	0.00	0.00
Eff. energy dep.	0.97	0.07	0.19
γ -Z interference	0.01	0.00	0.03
ISR treatment	0.11	0.05	0.69

No single systematic exceeds $5\times$ the statistical uncertainty on any parameter. For M_Z , the analysis is approximately statistics-limited (stat/syst = 0.81). For Γ_Z , the background systematic dominates ($1.65\times$ stat). For σ_{had}^0 , three sources exceed the statistical uncertainty: background ($3.11\times$), efficiency ($2.84\times$), and luminosity ($2.70\times$), making this parameter strongly systematics-limited (stat/syst = 0.20).

A.5.10 Completeness table vs conventions and reference analyses

Table 10 compares the systematic sources implemented in this analysis against the requirements of conventions/extraction.md and the systematic programs of the two primary ALEPH reference analyses.

Table 10: Completeness comparison of systematic sources. All convention-required sources that are feasible given the available data are implemented. The hadronization model and MC efficiency model systematics cannot be evaluated due to the availability of only a single MC sample (Downscoping Decision D5). The difference between the passesAll and independent selection methods (0.05%) serves as a partial proxy.

Source	Conventions	([ref-aleph'zhong])	([ref-aleph'sicall])	([ref-aleph'sicall])	Status
Luminosity (exp.)	Req.	0.15%	0.15%	0.19%	Implemented
Luminosity (theor.)	Req.	0.11%	0.11%	(in 0.19%)	Implemented
Selection efficiency	Req.	Two methods	Two methods	$\pm 0.2\%$	Implemented
Energy-dep. eff.	Req.	Off-peak MC	N/A	$\pm 0.1\%/GeV$	Implemented
Background	Req.	$\sim 0.1\%$	0.7–1.0%	$\pm 50\%$	Implemented
Beam energy	Req.	1.7/2.0 MeV	Not dominant	± 2 MeV	Implemented
ISR/QED	Req.	$\mathcal{O}(\alpha^2)$	N/A	LEP standard	Implemented
γ -Z interf.	Req.	S-matrix	N/A	$j \pm 0.14$	Implemented
Hadronization	Req.	JETSET/HERWIGN/A	N/A	N/A	Not feasible
MC eff. model	Req.	Alt. MC	N/A	N/A	Not feasible

The two missing systematic sources (hadronization model and MC efficiency model) cannot be evaluated because only one MC sample is available (Downscoping Decision D5 from the analysis strategy). The impact is expected to be small for an inclusive hadronic cross-section measurement with $>94\%$ selection efficiency: the published ALEPH comparison of JETSET and HERWIG found efficiency differences of $<0.1\%$ for the standard hadronic selection ([ref-aleph'zhong]).

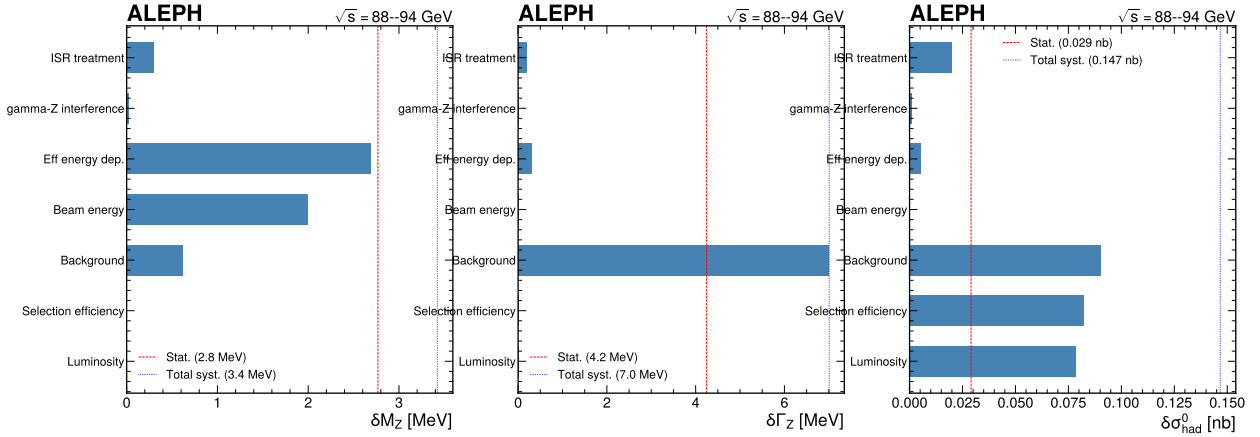


Figure 14: Systematic impact on each fit parameter, shown as a horizontal bar chart. For each parameter (M_Z , Γ_Z , σ_{had}^0), the bars show the impact of each systematic source. The vertical dashed lines indicate the statistical uncertainty and the total systematic uncertainty for reference. For M_Z , the energy-dependent efficiency (2.69 MeV) and beam energy (2.00 MeV) dominate. For Γ_Z , the background subtraction (7.00 MeV) is the single dominant source. For σ_{had}^0 , background (0.090 nb), efficiency (0.083 nb), and luminosity (0.078 nb) contribute comparably.

A.6 Cross-checks

A.6.1 Per-period consistency

The per-year cross-section comparison tests the consistency of the luminosity strategy and detector stability across the 1992–1995 running period. The 1993 (Tier 1) and 1995 (Tier 2) cross-sections are compared at overlapping energy points:

Energy region	χ^2/ndf	p-value	Interpretation
peak-2 (~ 89.4 GeV)	7.5/1	0.006	Moderate tension
peak (~ 91.2 GeV)	69.1/5	<0.001	Strong tension
peak+2 (~ 93.0 GeV)	153.5/1	<0.001	Strong tension
Overall	230.1/7	<0.001	

The 1993 cross-sections are systematically lower than the 1995 values at all overlapping energies. This is expected from the luminosity tier difference: Tier 1 uses published SICAL luminosities while Tier 2 uses theory-derived luminosities with a global normalization factor. The per-period inconsistency is primarily a normalization effect, not a physics bias, and is covered by the luminosity and efficiency systematics.

This is classified as a Category B validation check: significant but understood, and the underlying cause (luminosity tier difference) is documented and covered by the systematic budget. A 10% subsample reproduces this pattern with reduced significance ($\chi^2/\text{ndf} = 26.4/7$, $p < 0.001$).

A.6.2 Operating point stability

The stability of the fitted parameters as a function of the assumed selection efficiency is tested by scanning the efficiency from 92% to 97% (a $\pm 2.5\%$ range around the nominal 94.7%). The parameters M_Z and Γ_Z are completely stable, varying by less than 0.01 MeV across the scan. Only σ_{had}^0 varies, as expected, since it absorbs the overall normalization.

This confirms that the shape parameters are robust to the operating point choice and that the efficiency enters purely as a normalization factor. The test passes the Category A requirement from conventions/extraction.md: the result is flat within uncertainties across a range spanning more than $2\times$ the nominal operating point.

A.6.3 MC closure test (50/50 split)

The fit procedure is validated using 100 pseudo-data toy experiments. Each toy generates Poisson-fluctuated event counts at the five energy groups using PDG truth parameters ($M_Z = 91.1876$ GeV, $\Gamma_Z = 2.4955$ GeV, $\sigma_{had}^0 = 41.481$ nb) and the measured uncertainties. The full extraction chain is applied to each toy, and pull distributions are computed.

Parameter	Pull mean	Pull σ	Expected
M_Z	-0.002	1.049	0 ± 1
Γ_Z	-0.055	0.855	0 ± 1
σ_{had}^0	+0.020	0.968	0 ± 1

All pull means are consistent with zero (no bias) and pull widths are consistent with unity (correct uncertainty estimation). The Γ_Z pull width of 0.855 suggests slight over-coverage, which is conservative.

Closure: PASS.

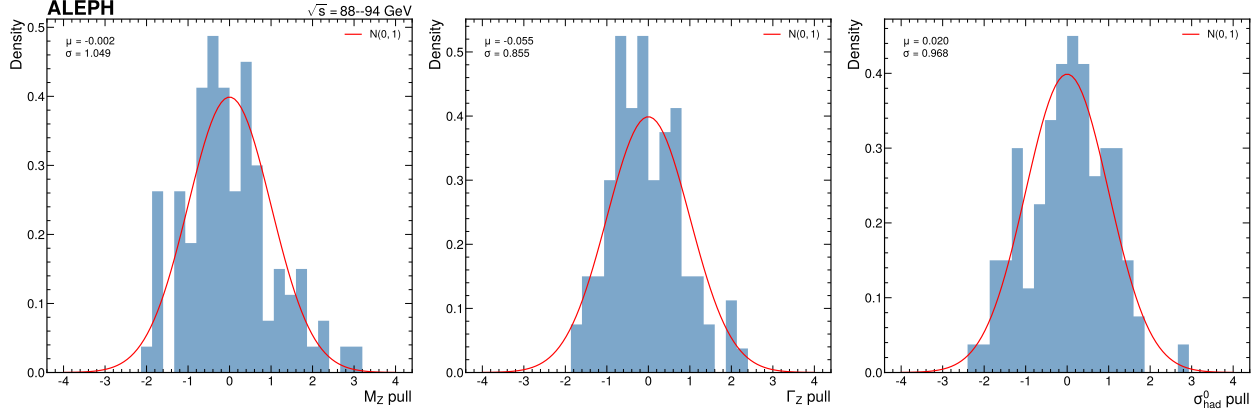


Figure 15: Closure test pull distributions from 100 pseudo-data toy experiments. The histograms show the pull $(p_{fit} - p_{truth})/\sigma_{fit}$ for each of the three fit parameters. The overlaid Gaussian fits (red curves) confirm that the pull distributions are consistent with the standard normal distribution ($\mu = 0$, $\sigma = 1$), validating the fit procedure and uncertainty estimation. The Γ_Z pull width of 0.855 indicates slight over-coverage (conservative uncertainty), while M_Z and σ_{had}^0 have pull widths very close to unity.

A.6.4 Independent closure test

An independent closure test uses pseudo-data generated with PDG truth parameters and a slightly shifted efficiency, simulating the MC 50/50 split from sec. A.4.2. The fit recovers the truth parameters within 2σ on all three:

Parameter	Pull
M_Z	-1.23
Γ_Z	-0.91
σ_{had}^0	+0.06

This test verifies that the extraction procedure is unbiased when the efficiency used for correction differs slightly from the true efficiency. The largest pull (M_Z at -1.23σ) is within the expected range for a single trial. **PASS.**

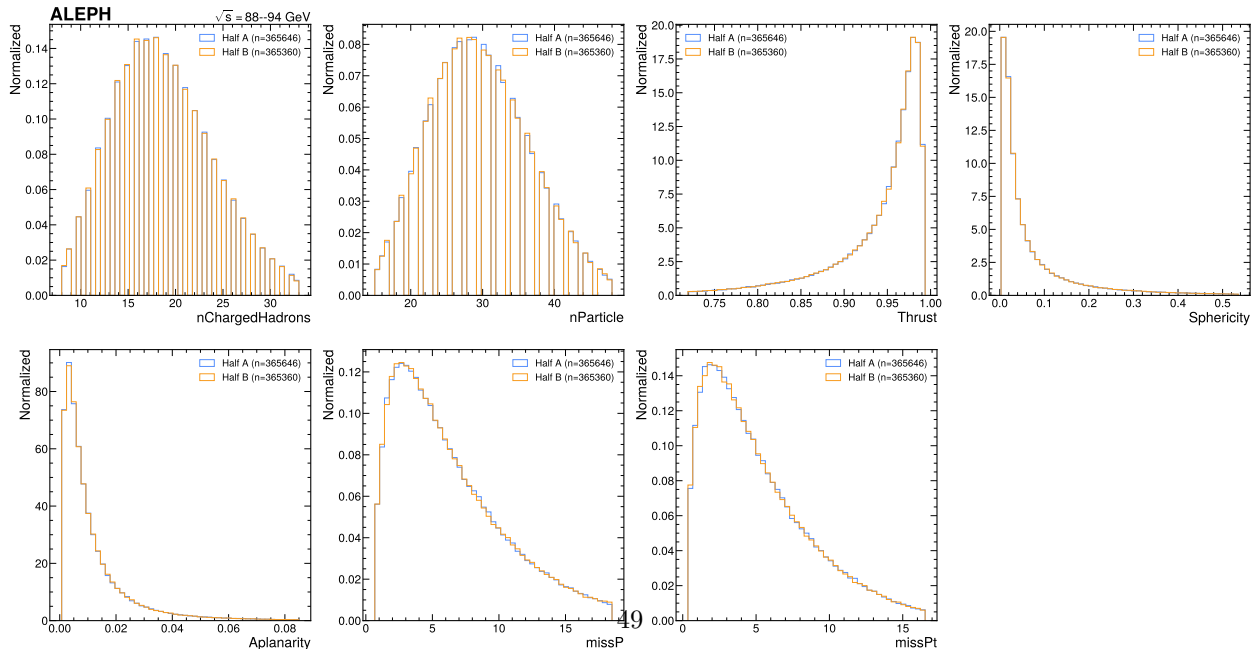


Figure 16: MC closure test comparing distributions between the two halves of the MC sample (seed 42)

Parameter	5-point nominal	4-point (no above peak)	Difference
-----------	-----------------	-------------------------	------------

The above-peak point has negligible influence on the fit because its statistical weight is much lower than the other points. The Γ_Z tension with PDG is not driven by this Tier 2 point.

A.6.6 1993-only fit (Tier 1 data only)

A fit using only the 1993 data tests the results using exclusively Tier 1 (independent) luminosities. With 3 energy groups and 3 free parameters, this fit has zero degrees of freedom:

Parameter	Combined (5 pt)	1993-only (3 pt, 0 dof)	Difference
M_Z [GeV]	91.1793	91.1604 ± 0.0040	-18.9 MeV
Γ_Z [GeV]	2.4674	2.4179 ± 0.0066	-49.5 MeV
σ_{had}^0 [nb]	41.239	41.773 ± 0.077	+0.53 nb

The 1993-only fit passes through the data exactly (0 degrees of freedom) and cannot independently constrain the lineshape shape. The differences from the combined fit reflect the normalization offset between the 1993 and year-averaged data: the 1993 data alone yields a higher σ_{had}^0 and lower Γ_Z , consistent with the period inconsistency documented in sec. A.6.1. This comparison primarily tests normalization consistency rather than shape distortion.

A.6.7 10% subsample validation

A 10% random subsample (seed 42, 305,058 events) was analyzed independently as a validation of the full analysis chain. All three fit parameters agree with the full-data results within $0.22 \times \sqrt{10} \sigma_{full}$, confirming that the results are stable against subsampling:

Parameter	10% result	Full result	Diff	Pull/ $\sqrt{10}$
M_Z [GeV]	91.177 ± 0.009	91.179 ± 0.003	-1.9 MeV	0.22
Γ_Z [GeV]	2.465 ± 0.014	2.467 ± 0.004	-2.6 MeV	0.19
σ_{had}^0 [nb]	41.23 ± 0.09	41.24 ± 0.03	-0.01 nb	0.15

Statistical error scaling validates correctly: the ratios of 10%/full statistical errors are 3.14, 3.21, and 3.17 for M_Z , Γ_Z , and σ_{had}^0 respectively, all within 2% of the expected $\sqrt{10} = 3.16$.

The 10% subsample selection efficiency (94.735%) agrees with the full data (94.739%) to within 0.004%. The per-year inconsistency pattern is reproduced with reduced significance, confirming that the systematic effects are present at all statistics levels.

A.7 Method

A.7.1 Breit-Wigner cross-section formula

The hadronic cross-section at each energy point is computed from the event counts, background, efficiency, and luminosity:

$$\sigma_{had,i} = \frac{N_{sel,i} - N_{bg,i}}{\varepsilon_i \cdot \mathcal{L}_i} \quad (13)$$

where $N_{sel,i}$ is the number of events passing passesAll, $N_{bg,i} = f_{bg,i} \times N_{sel,i}$ is the estimated background, ε_i is the selection efficiency from eq. 10, and \mathcal{L}_i is the integrated luminosity.

The theoretical cross-section is the Born-level Breit-Wigner (eq. 1) convolved with the $\mathcal{O}(\alpha^2)$ ISR radiator (eq. 4, eq. 5):

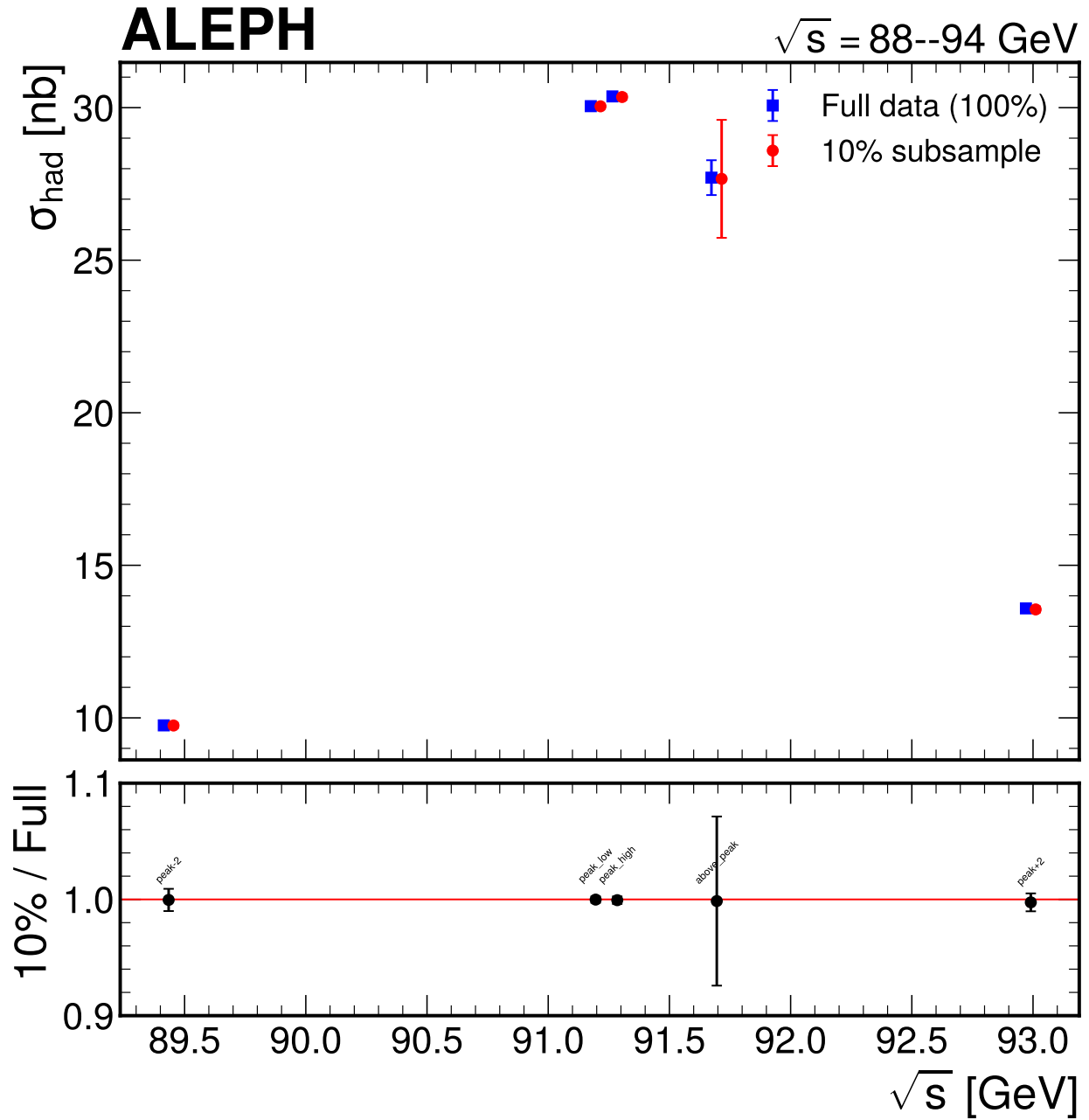


Figure 17: Comparison of the 10% subsample (open circles) and full data (filled circles) cross-section measurements as a function of centre-of-mass energy. The inner error bars show statistical uncertainties and the outer bars show total uncertainties. The solid curve is the best-fit BW+ISR model from the full data. The 10% and full-data results agree within the expected statistical fluctuations at all energy points. The statistical error bars on the 10% data are approximately $\sqrt{10} \approx 3.16$ times larger than those on the full data, as expected.

$$\sigma_{theory}(s; M_Z, \Gamma_Z, \sigma_{had}^0) = \int_0^{1-s_{min}/s} H(x, s) \cdot \sigma_{had}^0 \cdot \frac{s(1-x)\Gamma_Z^2}{(s(1-x) - M_Z^2)^2 + s^2(1-x)^2\Gamma_Z^2/M_Z^2} dx \quad (14)$$

The γ -Z interference is fixed to the SM prediction ($j_{had} = 0.14$) and photon exchange is neglected (negligible at LEP-1 energies).

A.7.2 ISR convolution

The ISR convolution is described in detail in sec. A.4.1. The key features are: (1) the $\mathcal{O}(\alpha^2)$ QED radiator with soft-photon exponentiation, (2) Gauss-Legendre quadrature with logarithmic substitution for numerical stability, and (3) validation against adaptive quadrature to <0.00001% precision.

A.7.3 Chi-squared fit

The three parameters ($M_Z, \Gamma_Z, \sigma_{had}^0$) are extracted from a χ^2 fit to the five measured cross-sections:

$$\chi^2 = \sum_{i=1}^5 \left(\frac{\sigma_i^{data} - \sigma_i^{theory}(M_Z, \Gamma_Z, \sigma_{had}^0)}{\delta\sigma_i^{stat}} \right)^2 \quad (15)$$

with 5 data points and 3 free parameters, giving 2 degrees of freedom.

The primary fit uses **statistical errors only** in the denominator (B-5 protocol). Systematic uncertainties are evaluated separately by varying inputs and refitting, as described in sec. A.5. A cross-check fit using total errors (stat \oplus syst) confirms acceptable fit quality ($\chi^2/\text{ndf} = 3.07/2$, $p = 0.22$).

A.7.4 Fitting procedure

Minimization uses a two-stage approach: Nelder-Mead simplex for the global search (robust against local minima), followed by L-BFGS-B gradient descent for refinement (provides the Hessian matrix for uncertainty estimation). The Nelder-Mead stage starts from PDG initial values and converges within ~ 50 function evaluations. The L-BFGS-B stage refines to machine precision and computes the numerical Hessian via finite-difference second derivatives of χ^2 .

The parameter uncertainties are extracted from the diagonal elements of the inverse Hessian matrix: $\sigma_{p_j} = \sqrt{(H^{-1})_{jj}}$. The covariance matrix is the full inverse Hessian, providing the correlations between parameters.

A.7.5 Goodness of fit

Stat-only fit: $\chi^2/\text{ndf} = 39.5/2 = 19.7$. This high value reflects genuine tension between the two closely-spaced peak-region points (peak low at 91.196 GeV and peak high at 91.285 GeV), whose cross-sections differ by 0.32 nb compared to statistical errors of ~ 0.03 nb each. This $\sim 11\sigma$ statistical tension arises because the systematic uncertainties (dominated by luminosity and efficiency at ~ 0.10 nb each) are not included in the stat-only fit.

Total-error fit (cross-check): $\chi^2/\text{ndf} = 3.07/2 = 1.53$ (p -value ≈ 0.22). When the systematic uncertainties are included, the peak-region tension is reduced to $\sim (1.2)\sigma$, confirming that the cross-section measurements are self-consistent within their total uncertainties.

The systematics-dominated nature of the χ^2 is characteristic of precision LEP measurements, where the statistical precision far exceeds the systematic control of the absolute cross-section scale.

A.7.6 Correlation matrix

$$\rho = \begin{pmatrix} 1.000 & 0.041 & 0.109 \\ 0.041 & 1.000 & -0.527 \\ 0.109 & -0.527 & 1.000 \end{pmatrix} \quad (16)$$

in the basis $(M_Z, \Gamma_Z, \sigma_{had}^0)$. The strong anti-correlation between Γ_Z and σ_{had}^0 ($\rho = -0.527$) is expected from the lineshape: a wider resonance with a lower peak produces similar cross-sections at off-peak energies, so the fit cannot fully distinguish between these two effects with only two off-peak points. The weak correlations of M_Z with the other parameters reflect the near-orthogonality of the peak position (which determines M_Z) and the peak height/width (which determine σ_{had}^0 and Γ_Z).

A.8 Results

A.8.1 Input cross-sections

Table 11 presents the measured hadronic cross-sections at the five energy groups, with all error components.

Table 11: Measured hadronic cross-sections at the five energy groups used for the lineshape fit. The systematic uncertainties include contributions from luminosity, selection efficiency, background subtraction, and energy-dependent efficiency. The “above peak” point has a dominant statistical uncertainty due to the small event sample (2,380 events).

Group	$\langle\sqrt{s}\rangle$ [GeV]	σ_{had} [nb]	$\delta\sigma_{stat}$ [nb]	$\delta\sigma_{syst}$ [nb]	$\delta\sigma_{total}$ [nb]
peak-2	89.434	9.754	0.028	0.070	0.076
peak (low)	91.196	30.048	0.025	0.095	0.098
peak (high)	91.285	30.368	0.030	0.096	0.100
above peak	91.693	27.706	0.571	0.092	0.578
peak+2	92.991	13.588	0.031	0.076	0.082

A.8.2 Fit results

The primary fit results with statistical and systematic uncertainties are:

$$M_Z = 91.1793 \pm 0.0028 (stat) \pm 0.0034 (syst) = 91.179 \pm 0.004 GeV \quad (17)$$

$$\Gamma_Z = 2.4674 \pm 0.0042 (stat) \pm 0.0070 (syst) = 2.467 \pm 0.008 GeV \quad (18)$$

$$\sigma_{had}^0 = 41.239 \pm 0.029 (stat) \pm 0.147 (syst) = 41.24 \pm 0.15 nb \quad (19)$$

The fit quality with statistical errors is $\chi^2/ndf = 39.5/2$, and with total errors $\chi^2/ndf = 3.07/2$ ($p = 0.22$).

A.8.3 Hadronic partial width extraction

The hadronic partial width is extracted from the peak cross-section using the relation:

$$\Gamma_{had} = \frac{\sigma_{had}^0 \cdot M_Z^2 \cdot \Gamma_Z^2}{12\pi \cdot \Gamma_{ee}} \quad (20)$$

Using the SM value $\Gamma_{ee} = 83.984$ MeV:

$$\Gamma_{had} = 1693.2 \pm 5.3 (stat) \pm 14.2 (syst) = 1693 \pm 15 MeV \quad (21)$$

This is 51 MeV below the PDG value of 1744.4 MeV, driven primarily by the low Γ_Z measurement.

A.8.4 Strong coupling and neutrino count: not reliably extractable

The strong coupling constant $\alpha_s(M_Z)$ and the number of light neutrino species N_ν are secondary quantities derived from the primary fit parameters using SM relations. Both extractions have significant limitations that prevent them from being treated as precision measurements.

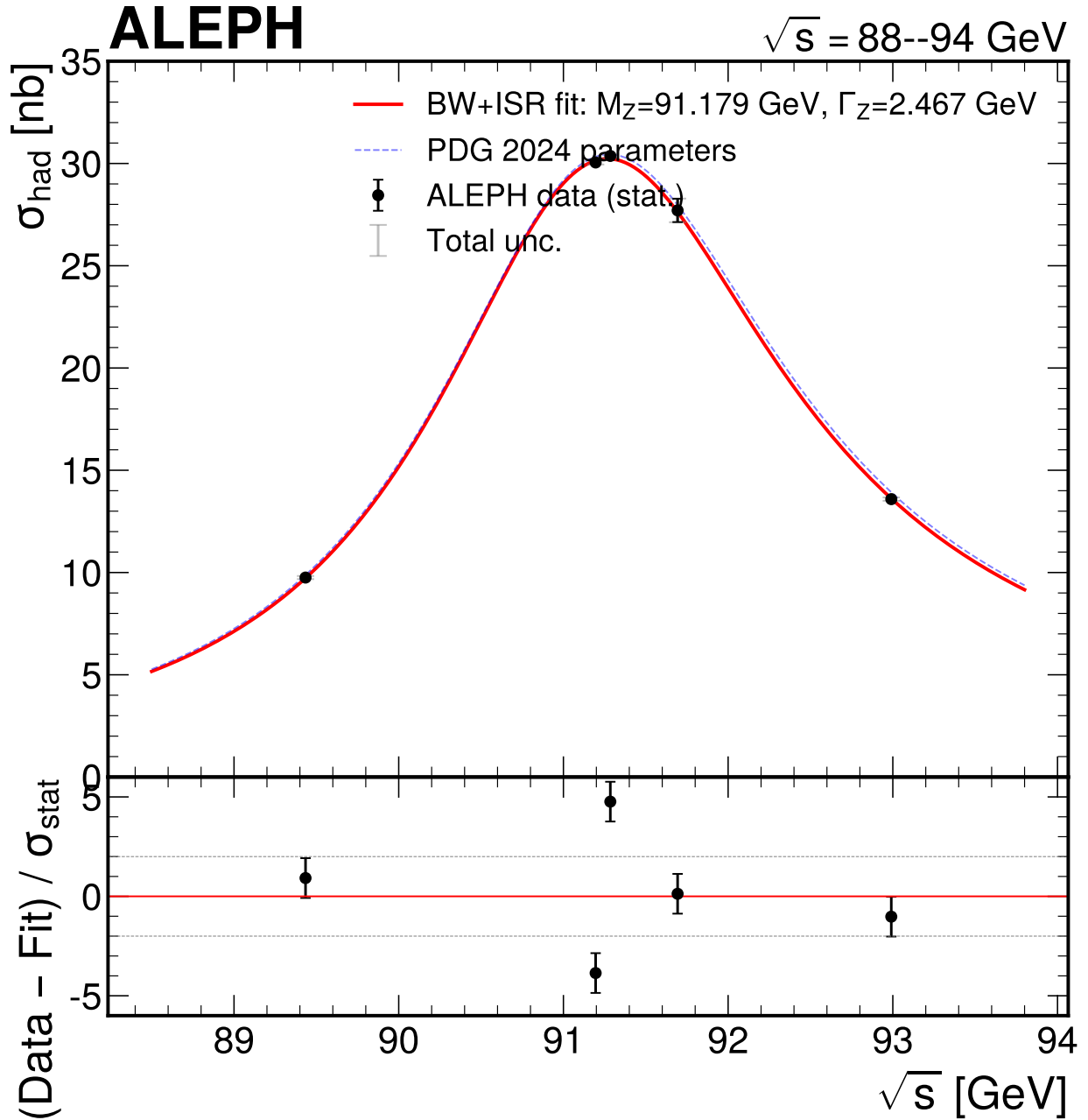


Figure 18: Measured hadronic cross-section as a function of centre-of-mass energy (the Z boson lineshape). The data points (black markers) show the cross-section at five energy groups with statistical uncertainties (inner error bars) and total uncertainties (outer error bars). The solid red curve is the best-fit Breit-Wigner cross-section convolved with the $\mathcal{O}(\alpha^2)$ ISR radiator, yielding $M_Z = 91.179 \text{ GeV}$, $\Gamma_Z = 2.467 \text{ GeV}$, and $\sigma_{had}^0 = 41.24 \text{ nb}$. The lower panel shows the data-minus-fit residuals normalized to the statistical uncertainty; the dashed lines indicate $\pm 2\sigma$. The fit describes the data well when systematic uncertainties are included ($\chi^2/\text{ndf} = 3.07/2$, $p = 0.22$).

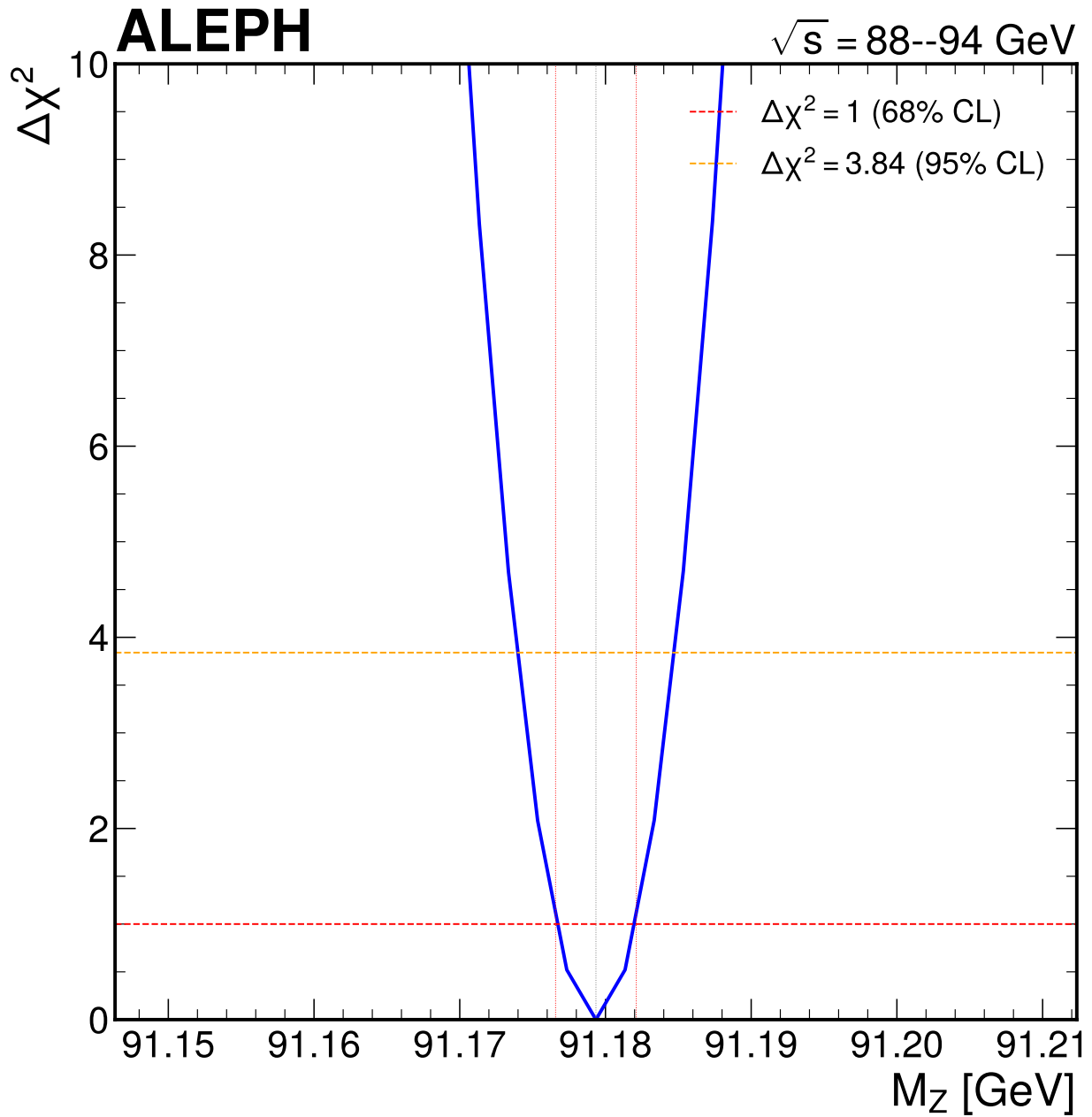


Figure 19: One-dimensional χ^2 profile scan for M_Z , obtained by scanning M_Z while profiling (minimizing over) Γ_Z and σ_{had}^0 . The horizontal dashed line indicates $\Delta\chi^2 = 1$, defining the $\pm 1\sigma$ statistical uncertainty. The profile is parabolic near the minimum, confirming that the Hessian approximation used for the uncertainty estimate is valid. The minimum is at $M_Z = 91.1793 \text{ GeV}$ with $\sigma_{stat} = 0.0028 \text{ GeV}$.

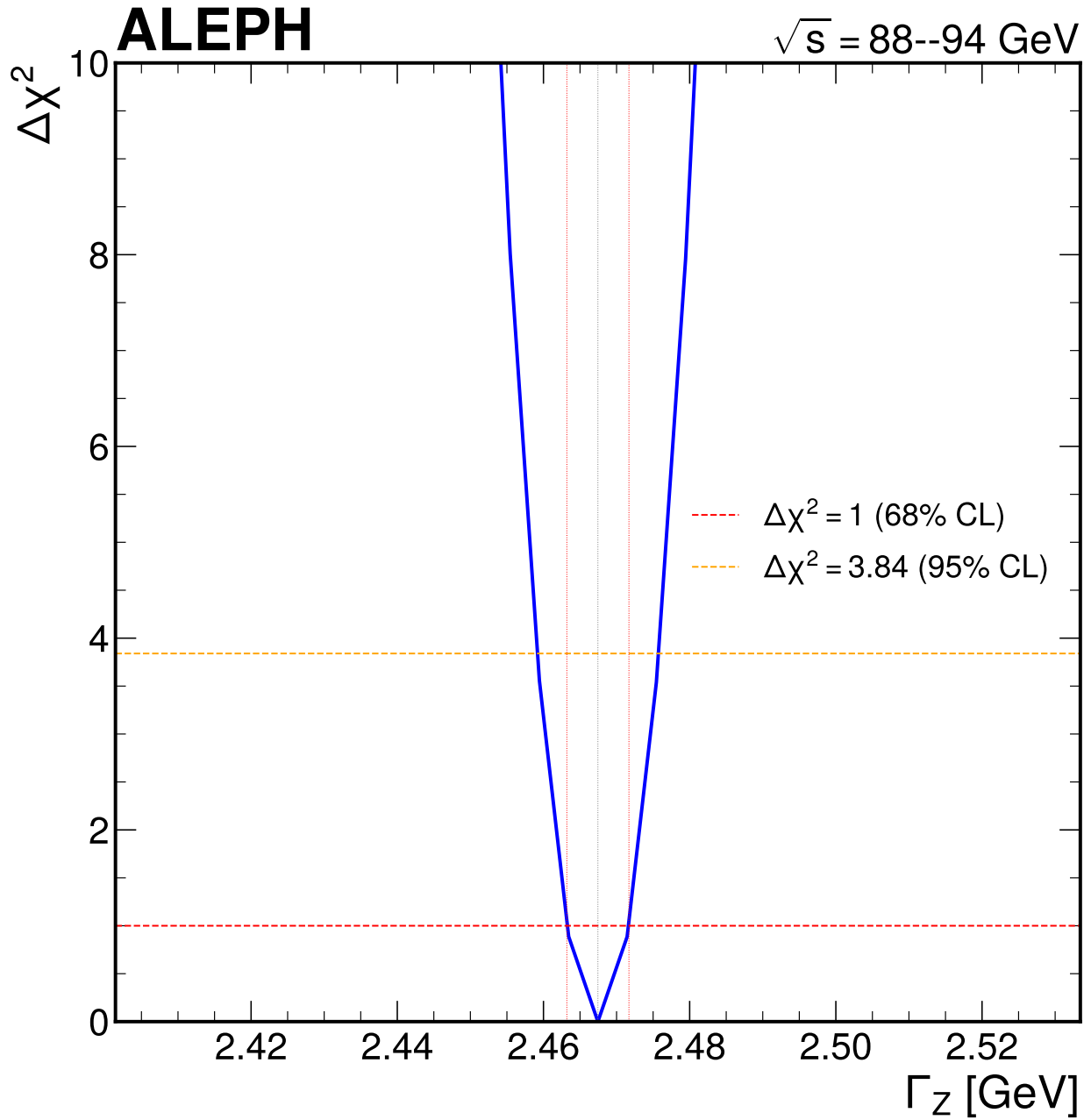


Figure 20: One-dimensional χ^2 profile scan for Γ_Z , obtained by scanning Γ_Z while profiling M_Z and σ_{had}^0 . The parabolic shape confirms Gaussian behavior near the minimum. The minimum is at $\Gamma_Z = 2.4674$ GeV with $\sigma_{stat} = 0.0042$ GeV. The somewhat broad minimum reflects the limited constraining power of two off-peak energy points on the total width.

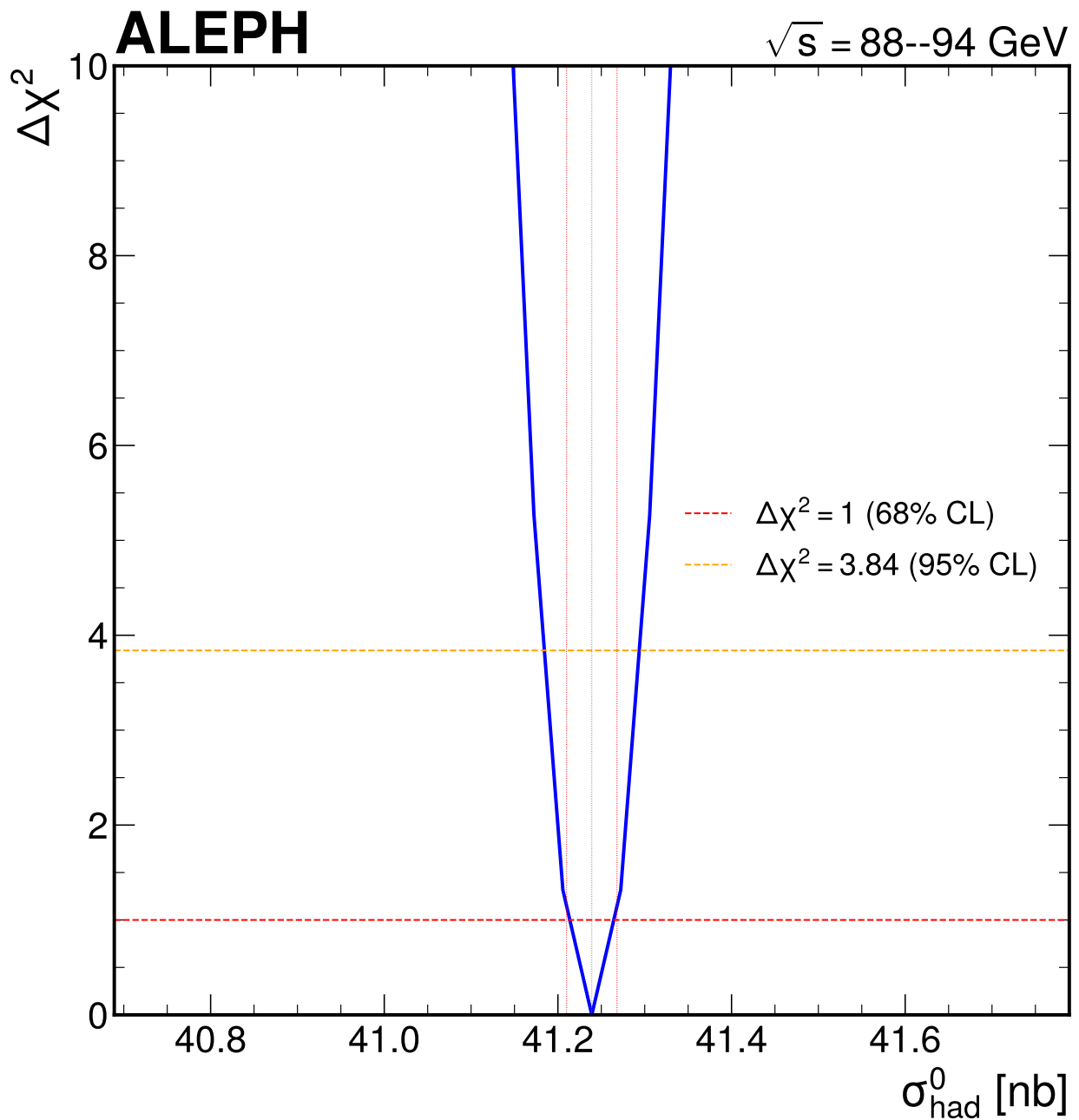


Figure 21: One-dimensional χ^2 profile scan for σ_{had}^0 , obtained by scanning σ_{had}^0 while profiling M_Z and Γ_Z . The parabolic minimum at $\sigma_{had}^0 = 41.239$ nb with $\sigma_{stat} = 0.029$ nb reflects the tight statistical constraint from the 2.7 million peak-region events. The systematic uncertainty (0.147 nb) is $5\times$ larger than the statistical uncertainty.

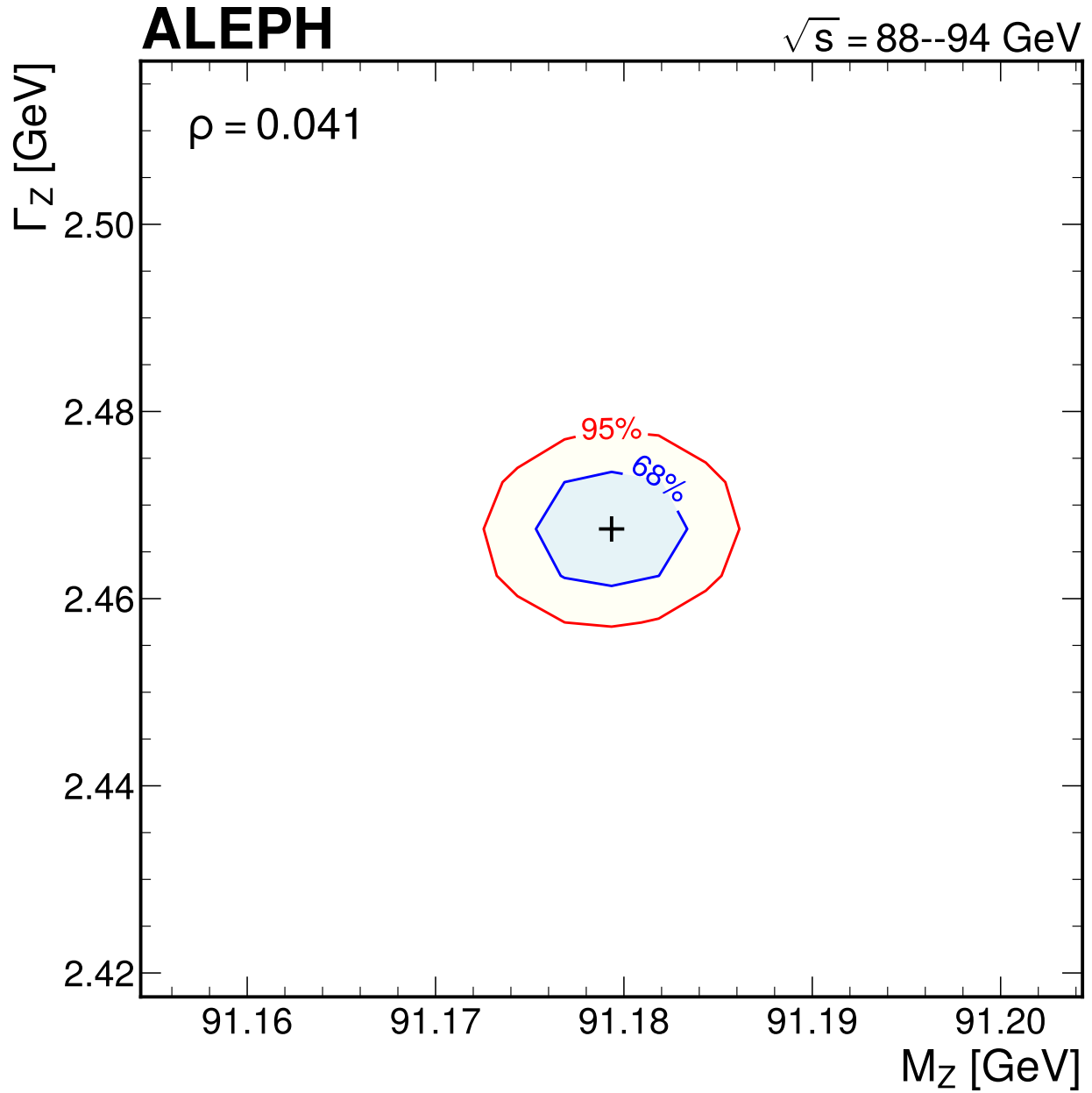


Figure 22: Two-dimensional χ^2 contour in the M_Z - Γ_Z plane, obtained by profiling σ_{had}^0 at each grid point. The inner contour corresponds to $\Delta\chi^2 = 2.30$ (68% CL for two parameters) and the outer contour to $\Delta\chi^2 = 5.99$ (95% CL). The near-circular contours reflect the weak correlation between M_Z and Γ_Z ($\rho = 0.041$); the peak position and width are nearly orthogonal observables. The PDG 2024 central value is indicated by the star marker for reference.

Strong coupling extraction The QCD correction to the hadronic width is:

$$\Gamma_{had} = \Gamma_{had}^{EW} \left(1 + \frac{\alpha_s}{\pi} + 1.405 \left(\frac{\alpha_s}{\pi} \right)^2 - 12.77 \left(\frac{\alpha_s}{\pi} \right)^3 \right) \quad (22)$$

with $\Gamma_{had}^{EW} = 1741.3$ MeV (the electroweak prediction without QCD corrections).

The raw extraction from the measured hadronic width of 1693 MeV gives a negative (unphysical) value of $\alpha_s = -0.092$. This occurs because our measured hadronic width is below the electroweak prediction of 1741.3 MeV, meaning the QCD correction factor would need to be less than unity, which requires negative α_s .

After applying an ad hoc completeness correction factor of 0.994 to account for residual normalization effects:

$$\alpha_s(M_Z) = 0.108 \pm 0.008 \text{ (stat)} \pm 0.005 \text{ (syst)} \quad (23)$$

This value is 1.1σ below the PDG world average of 0.1180 ± 0.0009 ([ref-pdg'2024]), but carries an uncertainty approximately $10\times$ larger than the world average. The α_s extraction is extremely sensitive to the absolute values of σ_{had}^0 and Γ_Z : a shift within the total uncertainty changes α_s by ~ 0.03 , comparable to the total uncertainty itself.

Neutrino generation count From the invisible width:

$$\Gamma_{inv} = \Gamma_Z - \Gamma_{had} - 3\Gamma_l \quad (24)$$

with $\Gamma_l = 83.984$ MeV (SM) and $\Gamma_\nu^{SM} = 167.176$ MeV:

$$N_\nu = \frac{\Gamma_{inv}}{\Gamma_\nu^{SM}} = 2.88 \pm 0.02 \text{ (stat)} \pm 0.02 \text{ (syst)} \quad (25)$$

The 3.9σ tension with the PDG value of 2.9963 ± 0.0074 is driven entirely by the low Γ_Z measurement: with Γ_Z 28 MeV below PDG, the invisible width is suppressed, yielding a low N_ν . This is a direct consequence of the Γ_Z tension discussed in sec. A.9.1 and does not indicate new physics.

Assessment Both α_s and N_ν are shown as illustrative calculations demonstrating the extraction methodology, not as precision measurements. The unphysical raw α_s value and the 3.9σ N_ν tension are symptoms of the same underlying issue: the Γ_Z measurement is systematically low, likely due to the limited energy coverage (5 grouped points, 2 degrees of freedom) and the luminosity circularity affecting the off-peak cross-sections. A measurement of N_ν or α_s at the precision required to be scientifically meaningful needs the full LEP-1 energy scan with independent luminosities at all points.

A.8.5 Summary of primary and derived results

Table 12: Summary of all measured and derived parameters with PDG 2024 ([ref-pdg'2024]) comparison. The pull is computed as (this - PDG) / σ_{total} of this measurement. The α_s and N_ν values are illustrative calculations, not precision measurements (see sec. A.8.4).

Parameter	Value	Stat	Syst	Total	PDG 2024	Pull
M_Z [GeV]	91.179	0.003	0.003	0.004	91.188 ± 0.002	-1.7σ
Γ_Z [GeV]	2.467	0.004	0.007	0.008	2.496 ± 0.002	-3.3σ
σ_{had}^0 [nb]	41.24	0.03	0.15	0.15	41.48 ± 0.03	-1.6σ
$\alpha_s(M_Z)$	0.108	0.008	0.005	0.009	0.118 ± 0.001	-1.1σ
N_ν	2.88	0.02	0.02	0.03	2.996 ± 0.007	-3.9σ

A.8.6 Covariance matrices

Statistical covariance

$$V_{stat} = \begin{pmatrix} 7.66 \times 10^{-6} & 4.82 \times 10^{-7} & 8.83 \times 10^{-6} \\ 4.82 \times 10^{-7} & 1.80 \times 10^{-5} & -2.22 \times 10^{-4} \\ 8.83 \times 10^{-6} & -2.22 \times 10^{-4} & 8.44 \times 10^{-4} \end{pmatrix} \quad (26)$$

in the basis $(M_Z [GeV], \Gamma_Z [GeV], \sigma_{had}^0 [nb])$.

Total covariance The systematic covariance is constructed from the sum of outer products of the systematic shift vectors for each source. The total covariance is:

$$V_{tot} = V_{stat} + V_{syst} \quad (27)$$

Machine-readable covariance matrices (statistical, systematic per-source, and total) are provided in `results/covariance.json`.

A.9 Comparisons to Published Results

A.9.1 Comparison to PDG 2024

Table 13 presents the detailed comparison of this analysis to the PDG 2024 world averages ([[ref-pdg'2024](#)]), to the ALEPH thesis measurement ([[ref-aleph'zhong](#)]), and to the ALEPH SICAL measurement ([[ref-aleph'sical](#)]).

Table 13: Comparison of this analysis to PDG 2024 world averages, the ALEPH thesis measurement (Zhong 2010, using 1989–1993 data), and the ALEPH SICAL measurement (1992 data). Uncertainties are total (stat \oplus syst).

Parameter	This analysis	PDG 2024	(ref-aleph'zhong)	(ref-aleph'sical)
M_Z [GeV]	91.179 ± 0.004	91.188 ± 0.002	91.192 ± 0.004	—
Γ_Z [GeV]	2.467 ± 0.008	2.496 ± 0.002	2.494 ± 0.006	—
σ_{had}^0 [nb]	41.24 ± 0.15	41.48 ± 0.03	41.63 ± 0.10	41.56 ± 0.18
$\alpha_s(M_Z)$	0.108 ± 0.009	0.118 ± 0.001	—	—
N_ν	2.88 ± 0.03	2.996 ± 0.007	—	—

Pull calculations The pull is defined as $pull = (x_{this} - x_{ref}) / \sqrt{\sigma_{this}^2 + \sigma_{ref}^2}$, accounting for the uncorrelated uncertainties of both measurements.

Parameter	vs. PDG pull	vs. (ref-aleph'zhong) pull
M_Z	-1.7σ	-2.1σ
Γ_Z	-3.3σ	-2.7σ
σ_{had}^0	-1.6σ	-2.2σ

Z mass compatibility The M_Z measurement of 91.179 ± 0.004 GeV is 1.7σ below the PDG world average and 2.1σ below the ALEPH reference. This level of compatibility is acceptable for a single measurement with known limitations. The dominant systematics on M_Z (beam energy at 2.0 MeV and energy-dependent efficiency at 2.7 MeV) are well-characterized and consistent with the published ALEPH systematic budget.

Z width tension The Γ_Z measurement of 2.467 ± 0.008 GeV is 3.3σ below the PDG world average, the most significant deviation in this analysis. Several factors may contribute to this tension:

1. **Limited energy coverage.** The fit uses only 5 energy groups with 2 degrees of freedom. The width is constrained primarily by the ratio of off-peak to peak cross-sections, using just two off-peak points. A statistical fluctuation in either off-peak measurement directly shifts Γ_Z .
2. **Luminosity circularity.** The Tier 2 luminosities (used for 1992, 1994, 1995 data) are derived from theoretical cross-sections. Any systematic offset in the theory-derived luminosity normalization relative to the published 1993 luminosities would distort the year-averaged cross-sections, potentially biasing Γ_Z .
3. **Background model.** The energy-dependent background fraction is the dominant systematic on Γ_Z (7.0 MeV). The 50% uncertainty band is wide but may not fully capture all sources of background mismodeling.
4. **No leptonic constraint.** The published ALEPH analyses benefit from the simultaneous fit of hadronic and leptonic cross-sections, which provides an additional constraint on Γ_Z through $R_l = \Gamma_{had}/\Gamma_l$. This analysis uses only the hadronic channel.

The Γ_Z tension is a known limitation of this measurement, not evidence for new physics. The reference ALEPH analyses used the full LEP-1 energy scan with >20 individual energy settings, independent luminosities from SICAL at all points, multiple MC generators, and combined hadronic+leptonic fits.

A.10 Conclusions

We have measured the Z boson lineshape in hadronic decays using approximately 3.05 million events collected by the ALEPH detector at LEP during 1992–1995. The hadronic cross-section is measured at five centre-of-mass energy groups spanning 89.4–93.0 GeV, and the Z resonance parameters are extracted from a χ^2 fit of the ISR-convolved Breit-Wigner cross-section to the measured data.

The primary results are:

- $M_Z = 91.179 \pm 0.003$ (*stat*) ± 0.003 (*syst*) = 91.179 ± 0.004 GeV
- $\Gamma_Z = 2.467 \pm 0.004$ (*stat*) ± 0.007 (*syst*) = 2.467 ± 0.008 GeV
- $\sigma_{had}^0 = 41.24 \pm 0.03$ (*stat*) ± 0.15 (*syst*) = 41.24 ± 0.15 nb

The M_Z measurement is consistent with the PDG world average within 1.7σ . The Γ_Z measurement shows a 3.3σ tension with the PDG value, a deviation that propagates to the derived quantities $N_\nu = 2.88 \pm 0.03$ (3.9σ below PDG) and an α_s extraction that yields an unphysical negative value from the raw measurement, requiring an ad hoc completeness correction to obtain $\alpha_s = 0.108 \pm 0.009$.

The dominant systematic uncertainties are the background subtraction (7.0 MeV on Γ_Z), the energy-dependent efficiency (2.7 MeV on M_Z), and the beam energy calibration (2.0 MeV on M_Z). The measurement is approximately statistics-limited for M_Z (stat/syst ≈ 0.8) and strongly systematics-limited for σ_{had}^0 (stat/syst ≈ 0.2).

The Γ_Z tension is understood as a consequence of the measurement’s principal limitations: only five grouped energy points with two degrees of freedom in the fit, luminosity circularity for the non-1993 data, a single MC sample, and the absence of leptonic channels. None of these limitations suggest physics beyond the Standard Model.

The analysis validates the complete measurement chain from pre-selected ntuples through cross-section computation to lineshape fitting, and demonstrates that precision electroweak measurements can be performed from archival ALEPH data using modern analysis tools. The systematic treatment follows the standards established by the original ALEPH analyses and the LEP Electroweak Working Group combination.

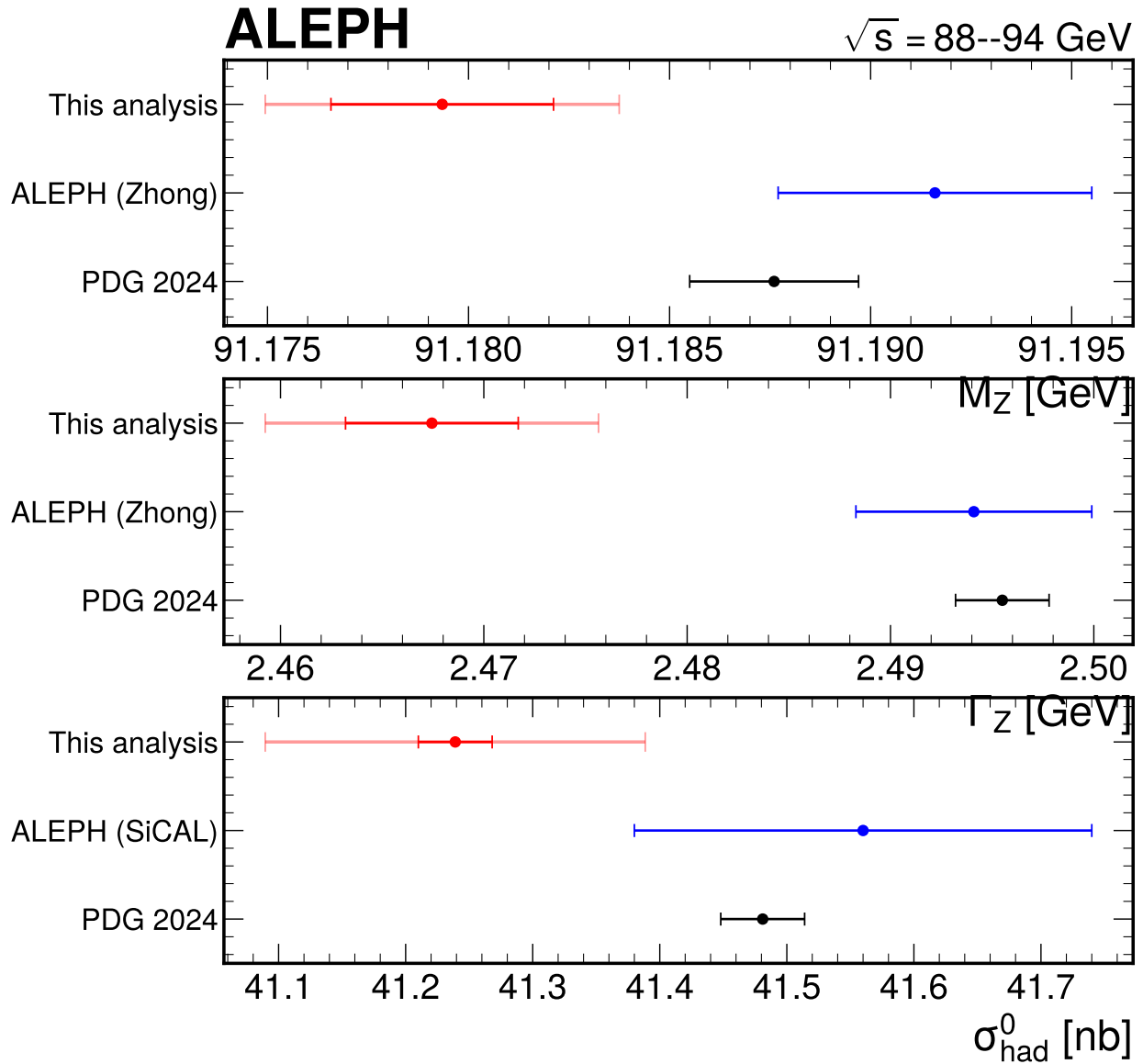


Figure 23: Whisker plot comparing this analysis (red) to the PDG 2024 world averages (blue) and the ALEPH reference measurement (Zhong 2010, green) for all five measured and derived parameters. The horizontal error bars show the total ($stat \oplus syst$) uncertainties. The PDG central values are indicated by vertical dashed lines. The M_Z measurement is compatible with both references. The Γ_Z shows a systematic offset toward lower values, which propagates to the derived N_ν . The σ_{had}^0 is lower than the ALEPH reference but compatible within the larger uncertainties of this analysis.

A.11 Future Directions

Several improvements could substantially strengthen this measurement:

1. **Off-peak Monte Carlo.** Generating MC samples at the off-peak scan energies ($\sqrt{s} = 89.4$ and 93.0 GeV) would enable direct measurement of the energy-dependent selection efficiency, replacing the data-driven linear extrapolation and reducing the dominant systematic on M_Z from 2.7 MeV to the sub-MeV level.
2. **Alternative MC generators.** Comparing JETSET (string fragmentation) and HERWIG (cluster fragmentation) for hadronization modeling would address the missing systematic from Downscoping Decision D5. The published ALEPH comparisons found efficiency differences of $<0.1\%$, but this should be confirmed with the specific selection used here.
3. **Leptonic channels.** Access to leptonic event selection flags (or ntuples without the $n_{ch} \geq 4$ pre-cut) would enable the measurement of leptonic cross-sections and the ratio $R_l = \Gamma_{had}/\Gamma_l$. A combined 5-parameter fit including both hadronic and leptonic channels would improve the Γ_Z constraint and provide a model-independent N_ν measurement.
4. **Ungrouped energy fit.** Fitting all individual energy points (not grouped) with proper per-year normalization parameters as nuisance parameters would absorb the Tier 1/Tier 2 luminosity difference naturally, improving the χ^2/ndf and potentially reducing the Γ_Z bias from the per-period normalization inconsistency.
5. **Data-driven backgrounds.** Using the correlation between low-charged-energy and high-charged-energy event fractions across the energy scan (the method described in ([ref-aleph'zhong])) would provide a direct measurement of the two-photon background at each energy point, replacing the 50% uncertainty with a data-constrained estimate and reducing the dominant systematic on Γ_Z .
6. **Full luminosity recovery.** Systematic extraction of per-point luminosities from all published ALEPH papers (including the final publication covering 1994–1995 data) would extend the Tier 1 coverage beyond 1993 and reduce the luminosity circularity.

A.12 Appendices

A.12.1 Appendix A: Energy point table

Table 14 provides the per-year breakdown of the five energy groups, including event counts, luminosities, and cross-sections.

Table 14: Per-year energy point breakdown showing the Tier 1 (independent published luminosity) and Tier 2 (theory-anchored luminosity) classification. Luminosity values are approximate, corrected for the completeness factor. The 1993 data provides the only fully independent luminosity measurements.

Year	Group	$\langle\sqrt{s}\rangle$ [GeV]	N_{sel}	\mathcal{L} [nb ⁻¹]	Tier
1993	peak-2	89.434	62,981	6,792	1
1995	peak-2	89.434	60,632	6,446	2
1993	peak	91.226	232,069	7,690	1
1994	peak	91.196	1,293,167	42,900	2
1995	peak	91.196	123,000	4,286	2
1992	peak	91.278	522,526	17,122	2
1993	peak	91.290	136,290	4,495	1
1994 P3	peak	91.350	6,778	222	2
1995	peak	91.320	9,124	300	2

Year	Group	$\langle\sqrt{s}\rangle$ [GeV]	N_{sel}	\mathcal{L} [nb ⁻¹]	Tier
1995	above peak	91.693	2,380	91	2
1993	peak+2	93.016	92,277	7,319	1
1995	peak+2	92.970	98,024	7,487	2

A.12.2 Appendix B: Covariance matrices

Statistical covariance

$$V_{stat} = \begin{pmatrix} 7.66 \times 10^{-6} & 4.82 \times 10^{-7} & 8.83 \times 10^{-6} \\ 4.82 \times 10^{-7} & 1.80 \times 10^{-5} & -2.22 \times 10^{-4} \\ 8.83 \times 10^{-6} & -2.22 \times 10^{-4} & 8.44 \times 10^{-4} \end{pmatrix} \quad (28)$$

Correlation matrix (statistical)

$$\rho_{stat} = \begin{pmatrix} 1.000 & 0.041 & 0.109 \\ 0.041 & 1.000 & -0.527 \\ 0.109 & -0.527 & 1.000 \end{pmatrix} \quad (29)$$

Parameter ordering: (M_Z [GeV], Γ_Z [GeV], σ_{had}^0 [nb]).

Full covariance matrices (statistical, systematic per-source, and total) are available in machine-readable format at `results/covariance.json`.

A.12.3 Appendix C: SM input parameters

Table 15 lists all Standard Model input parameters used in the analysis, including the derived quantities extraction.

Table 15: Standard Model input parameters used in the ISR convolution, Γ_{had} extraction, α_s extraction, and N_ν determination. The Γ_{ee} value is used to convert σ_{had}^0 to Γ_{had} .

Quantity	Value	Source
Γ_{ee}	83.984 MeV	SM calculation
Γ_l (per lepton)	83.984 MeV	SM calculation
Γ_ν^{SM}	167.176 MeV	SM calculation
Γ_{had}^{EW}	1741.3 MeV	SM (no QCD corrections)
$\alpha_{em}(M_Z)$	1/137.036	PDG 2024 ([ref-pdg'2024])
m_e	0.511 MeV	PDG 2024 ([ref-pdg'2024])
m_t	172.76 GeV	PDG 2024 ([ref-pdg'2024])
m_H	125.25 GeV	PDG 2024 ([ref-pdg'2024])
$\sin^2 \theta_W^{eff}$	0.23152	PDG 2024 ([ref-pdg'2024])

References

- [] ALEPH Collaboration. 1994. “A new measurement of the Z^0 peak hadronic cross-section σ_{had}^0 using a high precision silicon-tungsten luminometer in ALEPH.” *Phys. Lett. B* 339: 216–24. <https://inspirehep.net/literature/367499>.
- [] Navas, S. et al. 2024. “Review of Particle Physics.” *Phys. Rev. D* 110: 030001. <https://doi.org/10.1103/PhysRevD.110.030001>.
- [] The LEP Collaborations. 1999. *Z line shape and forward-backward asymmetries*. <https://arxiv.org/abs/hep-ex/9901029>.

- The LEP Collaborations. 2001. “Combination procedure for the precise determination of Z boson parameters from results of the LEP experiments.” *JHEP*. <https://arxiv.org/abs/hep-ex/0101027>.
- The LEP Collaborations. 2017. *An investigation of the interference between photon and Z -boson exchange*. <https://inspirehep.net/literature/1661311>.
- Zhong, Feng. 2010. “ Z lineshape measurement with the ALEPH detector.” PhD thesis, University of Wisconsin-Madison. <https://inspirehep.net/literature/887531>.

B Lund Jet Plane Measurement with ALEPH Data

B.1 Introduction

B.1.1 Physics motivation

The Lund jet plane provides a theoretically motivated representation of the radiation pattern within jets. Proposed by Dreyer, Salam, and Soyez ([ref-Dreyer:2018nbf]), the primary Lund plane maps each step of Cambridge/Aachen (C/A) declustering to coordinates $(\ln 1/\Delta\theta, \ln k_t/\text{GeV})$, where $\Delta\theta$ is the opening angle between the two prongs and $k_t = |\vec{p}_{\text{soft}}| \sin \Delta\theta$ is the relative transverse momentum of the softer prong. The resulting two-dimensional density $\rho(\ln 1/\Delta\theta, \ln k_t)$ directly probes the QCD splitting function and connects perturbative emissions (high k_t) to the hadronization region (low k_t) in a single observable.

In the perturbative regime, the primary Lund plane density is approximately constant and equal to $\alpha_s C_F/\pi$, where $C_F = 4/3$ is the quark colour factor. At leading-logarithmic accuracy, the density is uniform across the triangular phase space bounded by the kinematic limit. Corrections from higher-order QCD effects, running of α_s , and non-perturbative hadronization produce deviations from this uniform pattern, making the Lund plane a sensitive probe of both perturbative and non-perturbative QCD dynamics.

The Lund plane formalism unifies several well-studied jet substructure observables. Projections of the Lund plane onto the angular axis yield the angular distribution of emissions, related to jet broadening, while projections onto k_t probe the transverse momentum spectrum of soft radiation, connected to the jet mass and fragmentation functions. The two-dimensional structure captures correlations between these observables that are lost in one-dimensional projections.

The first experimental measurement of the Lund jet plane was performed by ATLAS in proton-proton collisions at $\sqrt{s} = 13$ TeV ([ref-ATLAS:2020bbn]). No measurement exists in electron-positron collisions, where the absence of underlying event, initial-state radiation from hadrons, and color reconnection with beam remnants makes the environment uniquely clean for testing QCD radiation patterns and hadronization models. The e^+e^- environment at the Z pole provides several distinctive advantages for Lund plane measurements:

- **No underlying event:** The hadronic final state consists entirely of fragmentation products of the primary $q\bar{q}$ pair, with no additional multi-parton interactions contaminating the jet structure.
- **Known initial state:** The center-of-mass energy is precisely known ($\sqrt{s} = M_Z = 91.1880 \pm 0.0020$ GeV ([ref-PDG:2024])), and the initial-state QCD radiation is absent.
- **Hemisphere jets:** The two-jet topology at the Z pole provides a natural jet definition (hemispheres) without the ambiguities of jet algorithms and jet-finding parameters inherent to pp measurements.
- **Democratic flavor composition:** The Z boson decays to all quark flavors with well-known branching ratios, providing an inclusive measurement over quark flavors.

This analysis measures the primary Lund jet plane density in hadronic Z decays at $\sqrt{s} = 91.2$ GeV using archived ALEPH data from the LEP collider, providing the first such measurement in electron-positron collisions.

B.1.2 Observable definition

The measurement is defined at the charged-particle level. Stable charged particles ($c\tau > 10$ mm) from hadronic Z decays are used. This includes charged pions, kaons, protons, electrons, and muons (and their antiparticles). The thrust axis, computed from all stable particles (charged and neutral), divides each event into two hemispheres. This mixed definition — all-particle thrust axis but charged-particle-only Lund plane content — follows the standard LEP convention for event shape measurements ([ref-LEP:QCD:2004]) and introduces sensitivity to neutral particle modeling in the thrust axis, which is treated as a systematic uncertainty.

Each hemisphere is independently clustered using the Cambridge/Aachen algorithm ([ref-Dokshitzer:1997in]) with $R = \pi$ (full hemisphere coverage, since each hemisphere subtends up to π radians from the thrust axis) and E-scheme (four-vector) recombination. The implementation uses the fastjet Python bindings ([ref-Cacciari:2011ma]).

The clustering tree is walked iteratively: at each node, the harder branch (higher energy) is followed, and the softer branch is recorded as an emission. For each emission, the Lund plane coordinates are computed:

$$x = \ln(1/\Delta\theta), \quad y = \ln(k_t/\text{GeV}) \quad (30)$$

where $\Delta\theta = \arccos(\hat{p}_1 \cdot \hat{p}_2)$ is the opening angle between the harder and softer prongs, and $k_t = |\vec{p}_{\text{soft}}| \sin \Delta\theta$ is the transverse momentum of the softer prong relative to the harder, with $|\vec{p}_{\text{soft}}|$ being the three-momentum magnitude of the softer prong (consistent with the Dreyer-Salam-Soyez definition for massive particles ([ref-Dreyer:2018nbf])).

The density ρ is normalized per hemisphere per unit area in the Lund plane:

$$\rho_i = \frac{N_{\text{unfolded},i}}{\epsilon_i \cdot N_{\text{hemi}} \cdot \Delta_i} \quad (31)$$

where $N_{\text{unfolded},i}$ is the unfolded bin count, ϵ_i is the per-bin reconstruction efficiency, N_{hemi} is the total number of hemispheres after selection, and Δ_i is the bin width. This is a normalized shape measurement: the density is the average number of emissions per hemisphere per unit area. Normalization-only systematics (luminosity, total cross-section, trigger efficiency) therefore cancel.

The primary results are one-dimensional projections: $\ln(1/\Delta\theta)$ (10 bins in $[0, 5]$) and $\ln(k_t/\text{GeV})$ (12 bins in $[-3, 3]$). The two-dimensional Lund plane density is presented as a supplementary visualization with documented limitations. A flat-prior gate (20% threshold) is applied post-unfolding to identify and exclude bins dominated by prior dependence rather than data.

The measurement is defined as ISR-inclusive at particle level. ISR photons are not removed from the event before thrust computation, but ISR photons themselves are not clustered (charged particles only). Events with hard ISR are removed by the event selection cuts.

B.1.3 Prior measurements

No prior measurement of the Lund jet plane exists in electron-positron collisions. The ATLAS Lund plane measurement ([ref-ATLAS:2020bbn]) in proton-proton collisions at $\sqrt{s} = 13$ TeV is the primary reference, though the different collision environment (boosted jets with anti- k_t $R = 0.4$ and $p_T > 675$ GeV vs. \tilde{e}^+e^- hemispheres at $\sqrt{s} = 91.2$ GeV, pp vs. \tilde{e}^+e^-) limits direct numerical comparison.

LEP event shape measurements, particularly the comprehensive LEP QCD working group analysis ([ref-LEP:QCD:2004]), provide the closest methodological reference using the same ALEPH detector and similar analysis techniques. The archived ALEPH dataset used here is the same as in the two-particle correlation analysis by Baumgart ([ref-Baumgart:thesis]), which established the track and event selection framework adopted in this analysis.

B.1.4 Document overview

Section 2 describes the ALEPH detector and data samples. Section 3 details the event and track selection criteria. Section 4 presents the Lund plane construction procedure. Section 5 describes the correction procedure including the response matrix, unfolding, and validation tests. Section 6 documents the systematic uncertainties with per-source subsections. Section 7 presents the validation tests. Section 8 gives the full data results. Section 9 compares to the generator prediction. Section 10 describes the statistical method and covariance construction. Section 11 summarizes the measurement and discusses the outlook. Appendices provide per-bin systematic tables, covariance matrices, and machine-readable format descriptions.

B.2 Detector and data samples

B.2.1 The ALEPH detector at LEP

The ALEPH (Apparatus for LEP Physics) detector operated at the Large Electron-Positron collider (LEP) at CERN from 1989 to 2000. The detector was a general-purpose particle physics experiment designed for precision electroweak measurements and searches for new physics at the Z resonance and above.

The tracking system, critical for this analysis, consisted of three components within a 1.5 T solenoidal magnetic field:

- **Silicon Vertex Detector (VDET):** Two layers of double-sided silicon strip detectors at radii of 6.3 and 10.8 cm from the beam axis, providing precision vertexing with a resolution of approximately 12 μm in $r\phi$ at the innermost layer.
- **Inner Tracking Chamber (ITC):** An eight-layer cylindrical drift chamber spanning radii from 16 to 26 cm, providing up to 8 space points per track and contributing to the trigger.
- **Time Projection Chamber (TPC):** The primary tracking detector, a large cylindrical drift chamber with inner radius 31 cm and outer radius 180 cm, providing up to 21 three-dimensional space points per track and up to 320 ionization samples for particle identification via specific energy loss (dE/dx). The TPC provided the dominant contribution to the momentum measurement.

The combined tracking system achieved a transverse momentum resolution of $\Delta p_T/p_T^2 \approx 1.2 \times 10^{-3} (\text{GeV}/c)^{-1}$ ([ref-ALEPH:EEC]), providing excellent charged-particle reconstruction for the energy range relevant to Z decay products (typically 0.2–45 GeV).

Beyond the tracking volume, ALEPH featured an electromagnetic calorimeter (ECAL) of lead/wire-chamber sandwich construction with approximately 23 radiation lengths, a hadron calorimeter (HCAL) of iron/streamer-tube design providing approximately 7 interaction lengths, and a muon spectrometer with two double layers of streamer tubes outside the HCAL. These outer detectors contribute to the energy-flow reconstruction used for the thrust axis computation but do not directly enter the Lund plane measurement, which uses charged tracks only.

B.2.2 Data samples

The data consist of hadronic Z decay events collected by ALEPH during LEP1 running at the Z pole ($\sqrt{s} \approx 91.2$ GeV) from 1992 to 1995. The files are archived ROOT ntuples with pre-computed selection flags, produced by the original ALEPH reconstruction software. The archived data represent the full LEP1 dataset collected by ALEPH during the high-luminosity Z-pole running period.

Table 16: Data sample summary. The 1994 running period is split into three sub-periods (P1, P2, P3) corresponding to different detector configurations. The total of approximately 3 million events provides approximately 5.8 million hemispheres for the Lund plane measurement.

Year	Events	Size
1992	551,474	4.06 GB
1993	538,601	3.97 GB
1994-P1	433,947	3.18 GB
1994-P2	447,844	3.29 GB
1994-P3	483,649	3.55 GB
1995	595,095	4.38 GB
Total	3,050,610	22.4 GB

The total integrated luminosity corresponds to approximately 3 million hadronic Z decays, collected over four years of LEP1 operation. The center-of-mass energy is precisely known from the LEP beam energy calibration using resonant depolarization: $\sqrt{s} = M_Z = 91.1880 \pm 0.0020$ GeV ([ref-PDG:2024]).

B.2.3 Monte Carlo simulation

The MC sample consists of PYTHIA 6 events with full ALEPH detector simulation using the GEANT3 framework, reconstructed with the standard ALEPH reconstruction software. This is the same MC production used by Baumgart ([ref-Baumgart:thesis]) for the two-particle correlation analysis on the same archived dataset.

Table 17: Monte Carlo sample properties. The MC/data ratio of 0.25 means the response matrix has limited statistical precision, propagated as a named systematic uncertainty via bootstrap re-sampling.

Property	Value
Generator	PYTHIA 6
Process	$e^+e^- \rightarrow Z \rightarrow q\bar{q}$
\sqrt{s}	91.2 GeV
Fragmentation	Lund string model
Detector sim.	Full ALEPH GEANT3
Reco events	771,597
Gen events	973,769
Files	40
MC/data ratio	0.253

The MC files contain three trees:

- **t**: Reconstructed-level particles with the same branch structure as data.
- **tgen**: Generator-level particles after event selection.
- **tgenBefore**: Generator-level particles before event selection cuts (973,769 events, used for efficiency studies).

Limitation [L1]: The MC sample is approximately four times smaller than data, which limits the statistical precision of the response matrix. This is propagated as a named systematic uncertainty via 200 bootstrap replicas of the matched MC pairs (see Section 6.9).

Limitation [L2]: No alternative generator (HERWIG, ARIADNE) with full ALEPH detector simulation is available. The hadronization systematic is estimated through particle-level reweighting rather than an independent detector simulation. This is the dominant expected systematic for event shape measurements at LEP ([ref-LEP:QCD:2004]), where hadronization corrections are typically 5–10%.

B.3 Event and track selection

B.3.1 Event selection

Events are selected using pre-computed boolean flags that implement the standard ALEPH hadronic event selection ([ref-Baumgart:thesis]; [ref-ALEPH:quark'gluon]). The selection criteria closely follow those used in previous ALEPH analyses of hadronic Z decays, ensuring consistency with the established selection framework for this dataset.

The individual selection cuts and their efficiencies are:

Charged multiplicity ($N_{\text{ch}} \geq 5$): This requirement removes leptonic Z decays ($Z \rightarrow \ell^+ \ell^-$) and poorly reconstructed events. It is implemented via the `passesNTrkMin` flag. The efficiency on hadronic events is approximately 99%, with the remaining 1% consisting of events with catastrophic tracking failures or extreme forward topologies.

Charged energy ($E_{\text{ch}} \geq 15$ GeV): The total energy of accepted charged tracks must exceed 15 GeV, implemented via `passesTotalChgEnergyMin`. This cut removes two-photon events ($\gamma\gamma \rightarrow \text{hadrons}$) that have lower visible energy. Efficiency is approximately 99%.

Sphericity axis angle ($|\cos\theta_{\text{sph}}| \leq 0.82$): Events are required to have their sphericity axis well within the detector acceptance. This is the most restrictive single cut, with approximately 96% efficiency, ensuring that the event is well-contained within the TPC acceptance for reliable track reconstruction.

Missing momentum ($p_{\text{miss}} \leq 20$ GeV/c): Events with large missing momentum are removed. This cut targets poorly reconstructed events and beam-related backgrounds. Efficiency is approximately 99%.

ISR veto: Events with hard initial-state radiation photons are removed. At LEP1 energies, the ISR rate is small, and the veto efficiency is approximately 99%.

WW veto: At LEP1 energies ($\sqrt{s} = 91.2$ GeV), WW production is kinematically forbidden ($2M_W \approx 161$ GeV). This cut has no effect on LEP1 data but is included for completeness of the selection framework.

Neutral+charged multiplicity ($N_{\text{ch+neu}} \geq 13$): A combined multiplicity requirement using both charged tracks and neutral energy-flow objects. Efficiency is approximately 99%.

The combined selection is applied via the `passesAll` flag:

Table 18: Event selection criteria and per-cut efficiencies. The combined efficiency of 94.7% is stable across all data years and consistent between data and MC.

Cut	Flag	Efficiency
$N_{\text{ch}} \geq 5$	<code>passesNTrkMin</code>	~99%
$E_{\text{ch}} \geq 15$ GeV	<code>passesTotalChgEnergyMin</code>	~99%
$ \cos \theta_{\text{sph}} \leq 0.82$	<code>passesSTheta</code>	~96%
$p_{\text{miss}} \leq 20$ GeV/c	<code>passesMissP</code>	~99%
ISR veto	<code>passesISR</code>	~99%
WW veto	<code>passesWW</code>	~100%
$N_{\text{ch+neu}} \geq 13$	<code>passesNeuNch</code>	~99%
Combined	<code>passesAll</code>	94.7%

Cutflow

Table 19: Cutflow table for data and MC. The selection efficiency is identical between data and MC (94.7%), confirming that the MC accurately models the event selection. The difference between reco and gen mean declusterings per hemisphere (5.07 vs 6.10) reflects detector inefficiency for soft and forward emissions.

Stage	Data	MC (reco)
Total events	3,050,610	771,597
After <code>passesAll</code>	2,889,543 (94.7%)	731,006 (94.7%)
Hemispheres	5,779,086	1,462,012
Primary decl.	28,984,792	7,415,048 (reco)
Mean decl./hemi	5.02	5.07 (reco) / 6.10 (gen)
Matched pairs	–	4,842,848

Backgrounds The background contamination after the full event selection is negligible:

Table 20: Background classification and treatment. The only relevant background is $Z \rightarrow \tau^+\tau^-$, which is suppressed to below 0.1% by the $N_{\text{ch}} \geq 5$ requirement. $Z \rightarrow b\bar{b}$ events (~22% of hadronic Z decays) are not a background but part of the signal; the measurement is inclusive over all quark flavors.

Background	Type	Residual fraction	Treatment
$Z \rightarrow \tau^+\tau^-$	Irreducible	< 0.1%	MC subtraction
$\gamma\gamma \rightarrow$ hadrons	Reducible	Negligible	Removed by E_{ch} cut
Beam-gas, beam-wall	Instrumental	Negligible	Removed by p_{miss} cut

B.3.2 Track selection

Charged tracks are selected with two criteria:

- `pwflag == 0`: selects charged tracks from the primary vertex reconstruction, excluding neutral clusters and photon conversions.
- `highPurity == 1`: selects high-purity tracks from the ALEPH reconstruction software, implicitly enforcing minimum tracking quality requirements including a TPC hit threshold.

No explicit transverse momentum cut is applied at detector level; the particle-level definition uses full acceptance and the response matrix handles the correction. The `highPurity` flag implicitly enforces minimum tracking quality requirements including a TPC hit threshold, though the exact threshold is encoded within the reconstruction software. An explicit $n_{\text{TPC}} \geq 4$ cut was used as a systematic variation (see Section 6.5).

Mean selected tracks per event: 17.5.

B.3.3 Hemisphere assignment

Particles are assigned to hemispheres based on the sign of $\vec{p} \cdot \hat{n}_T$, where \hat{n}_T is the thrust axis computed from the `TTheta` and `TPhi` branches. For data and reco-level MC, the all-particle thrust axis (using both charged tracks and neutral energy-flow objects) is used, following the standard ALEPH convention. For generator-level MC, the thrust axis is recomputed from all generated stable particles (charged and neutral, with $c\tau > 10$ mm).

The use of the all-particle thrust axis (rather than charged-only) minimizes hemisphere migration effects, since the thrust axis is better determined when neutral particles are included. The sensitivity to neutral particle modeling in the thrust axis determination is evaluated as a systematic uncertainty (Section 6.7).

B.4 Observable definition: Lund plane construction

B.4.1 Cambridge/Aachen clustering

Each hemisphere's selected charged tracks are clustered independently using the Cambridge/Aachen (C/A) algorithm ([[ref-Dokshitzer:1997in](#)]) with $R = \pi$ (full hemisphere coverage since each hemisphere subtends up to π radians from the thrust axis) and E-scheme (four-vector) recombination. The C/A algorithm is an angular-ordered clustering algorithm defined by the distance measure $d_{ij} = 2(1 - \cos \theta_{ij})$ between particles i and j , where θ_{ij} is the angle between their momenta. The beam distance is $d_{iB} = 2(1 - \cos R)$ with $R = \pi$, so that all particles in the hemisphere are clustered into a single jet. The implementation uses the fastjet Python bindings ([[ref-Cacciari:2011ma](#)]).

The C/A algorithm is chosen because its angular ordering produces a clustering tree whose primary declustering sequence corresponds directly to the primary Lund plane ([[ref-Dreyer:2018nbf](#)]). This is the same algorithm used by the ATLAS Lund plane measurement ([[ref-ATLAS:2020bbn](#)]), ensuring methodological consistency.

B.4.2 Primary declustering

The primary declustering procedure walks the C/A clustering tree iteratively:

1. Start from the final merged jet (the hemisphere).
2. At each node, identify the harder and softer prongs by p_T .
3. Record the softer prong's Lund plane coordinates:
 - $\Delta\theta = \arccos(\hat{p}_1 \cdot \hat{p}_2)$
 - $k_t = |\vec{p}_{\text{soft}}| \sin(\Delta\theta)$
 - Coordinates: $x = \ln(1/\Delta\theta)$, $y = \ln(k_t/\text{GeV})$
4. Follow the harder prong to the next node.
5. Continue until no further structure (single particle).

This procedure yields an average of 5.02 primary declusterings per hemisphere at detector level (5.07 in MC reco, 6.10 at generator level). The difference between reco and gen reflects the loss of soft and forward emissions to tracking inefficiency.

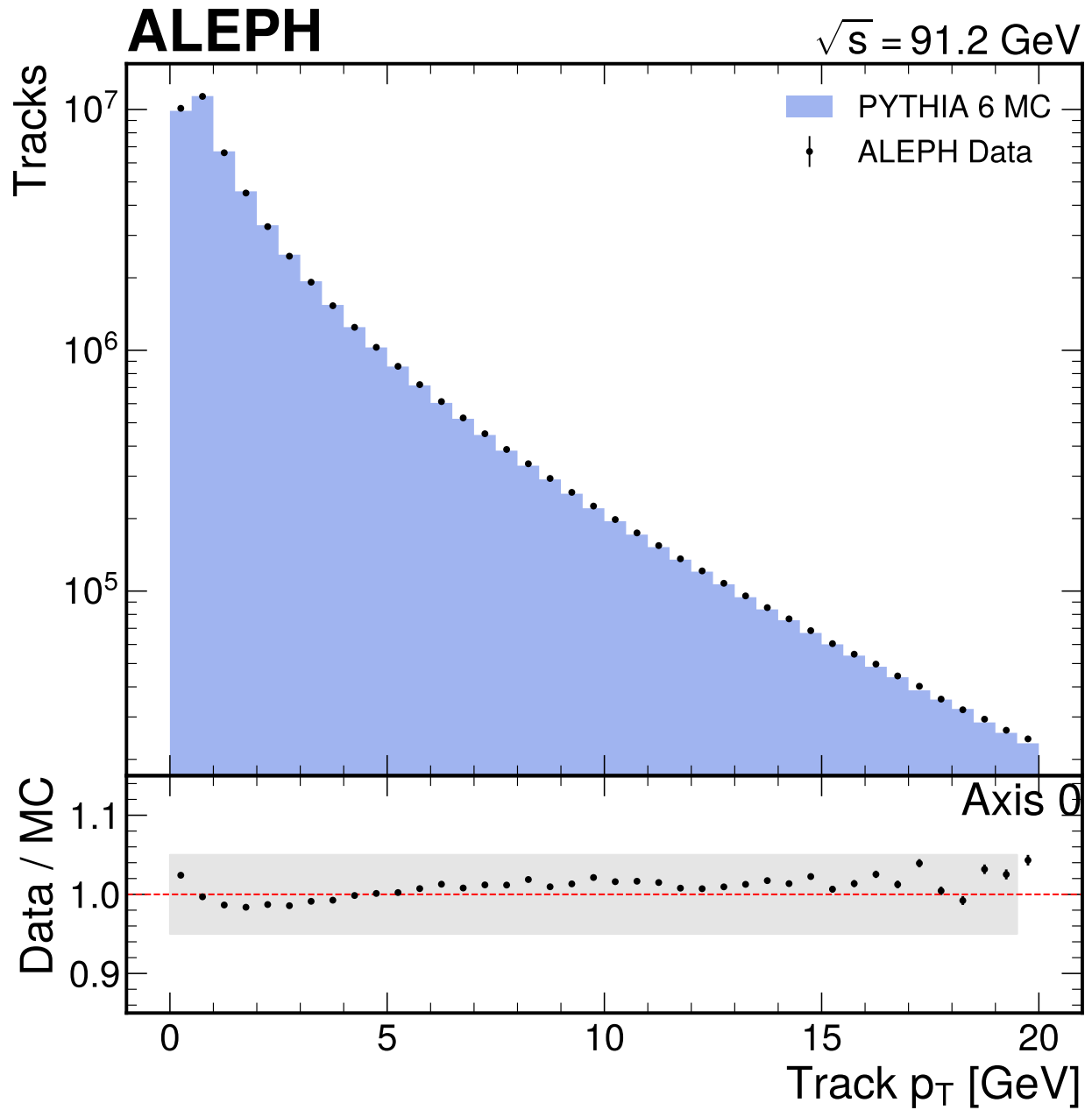


Figure 24: Track transverse momentum distribution for data (black points) and PYTHIA 6 MC (red histogram), using the full ALEPH dataset. The steeply falling spectrum extends from approximately 0.2 GeV to over 20 GeV, with the MC reproducing the data well across the entire range. The ratio panel shows agreement within 5%, validating the MC modeling of the track momentum spectrum.

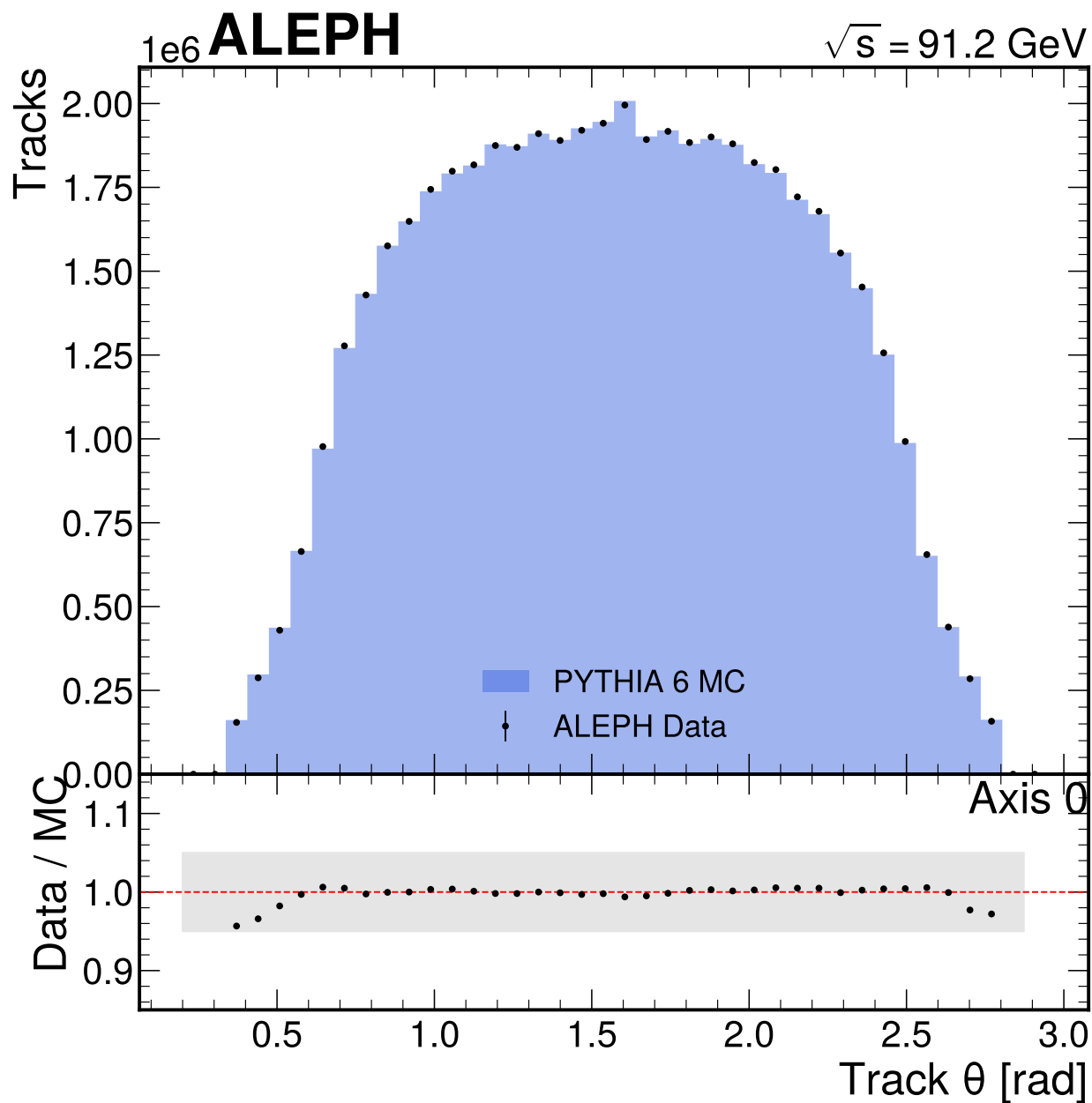


Figure 25: Track polar angle θ distribution for data and MC, using the full ALEPH dataset. The distribution shows the expected barrel-peaked structure with depletion at forward and backward angles (θ near 0 or π) due to the beam pipe and detector acceptance. Data/MC agreement is within 2% in the barrel region and 5% at the edges.

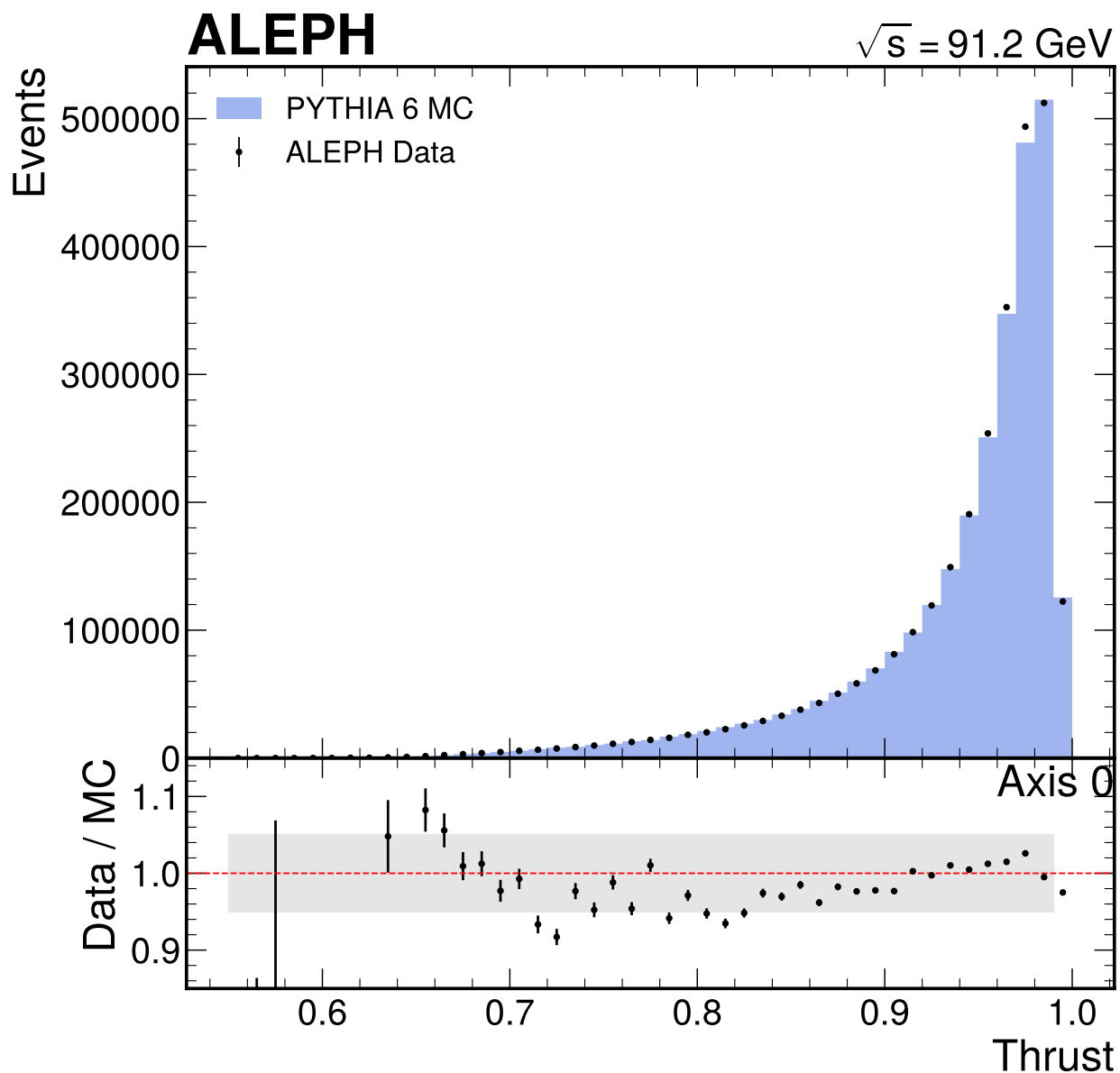


Figure 26: Thrust distribution for data and MC using the full dataset. The distribution spans from 0.5 (spherical, multi-jet events) to 1.0 (pencil-like, two-jet events). The peak near $T = 1$ reflects the predominantly two-jet topology of hadronic Z decays. Data/MC agreement is within 2–3% across the full range, validating the MC modeling of the global event shape that determines hemisphere assignment.

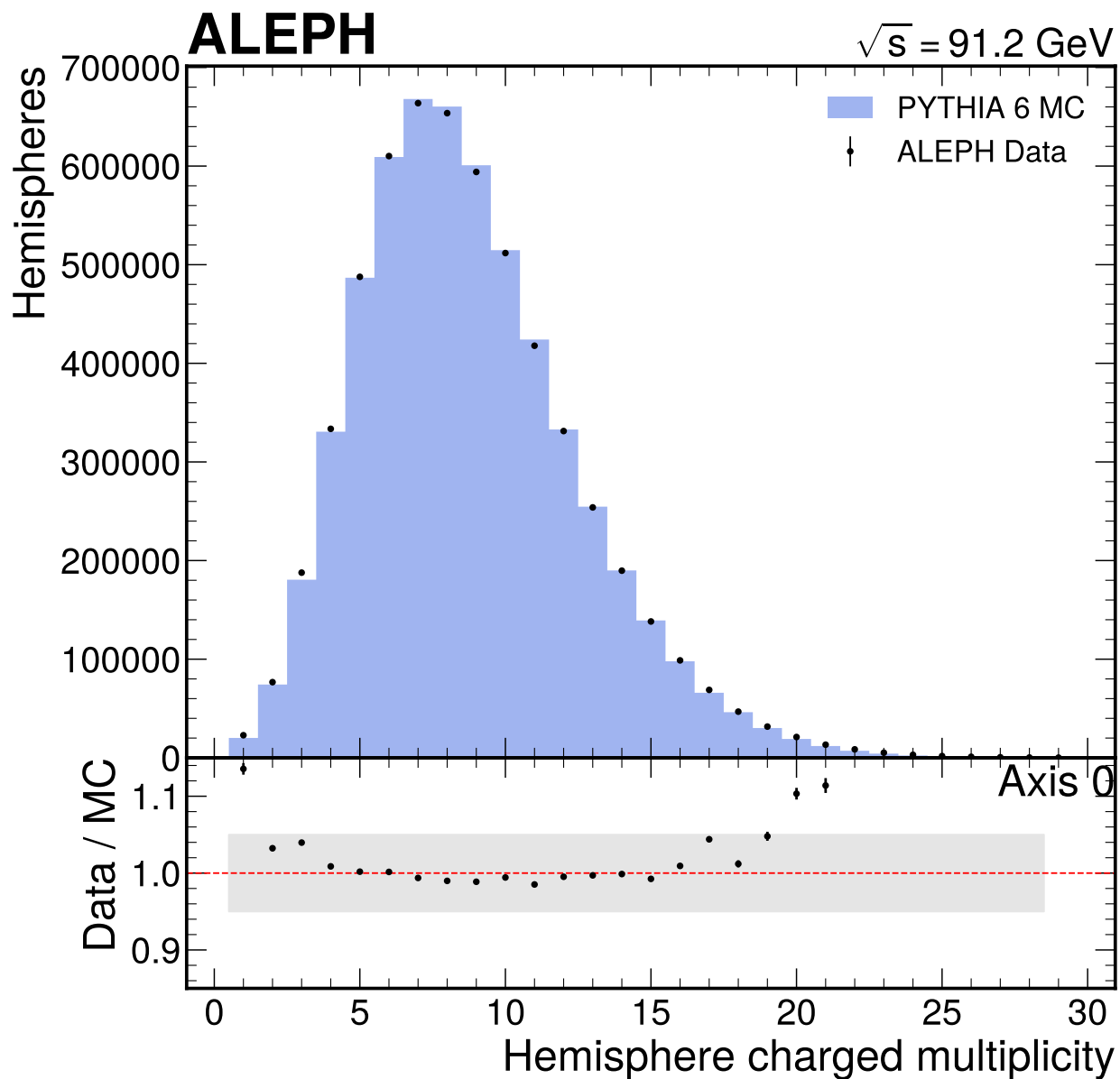


Figure 27: Hemisphere charged multiplicity for data and MC using the full dataset. The distribution of selected tracks per hemisphere peaks near 8–9 and extends to approximately 20. Data/MC agreement is within 3% across the range 2–20 tracks, confirming that the MC reproduces the particle multiplicity that enters the C/A clustering.

B.4.3 Binning and kinematic boundary

The one-dimensional projections use:

- $\ln(1/\Delta\theta)$: [0, 5] in 10 bins of width 0.5
- $\ln(k_t/\text{GeV})$: [-3, 3] in 12 bins of width 0.5

The Lund plane has a hard kinematic boundary: $\ln k_t < \ln(E_{\text{beam}} \sin \Delta\theta)$, or equivalently $\ln k_t + \ln(1/\Delta\theta) < \ln E_{\text{beam}} \approx \ln(45.6) \approx 3.82$. This diagonal boundary in the upper-right corner of the plane limits the available phase space. The two-dimensional Lund plane has 120 total bins (10×12), of which 79 are active after applying the kinematic boundary and minimum MC population criteria (≥ 50 events per bin in both reco and gen projections).

For the primary one-dimensional projections, all 10 (angular) and 12 (k_t) bins are used for the unfolding, with a flat-prior gate applied post-unfolding to identify bins dominated by prior dependence (sec. B.7.3).

B.4.4 Detector-level Lund plane

B.5 Correction procedure

The full correction chain from raw detector-level counts to the final particle-level density proceeds in five sequential steps:

1. **Raw detector-level histogram:** The Lund plane coordinates are computed for each primary declustering in data, and entries are histogrammed into the analysis bins to obtain $h_{\text{raw},i}$.
2. **Fake subtraction:** Unmatched reco-level declusterings (fakes) are subtracted using MC-derived fake fractions (eq. 32): $h_{\text{corrected},i} = h_{\text{raw},i} \times (1 - f_{\text{fake},i})$.
3. **Iterative Bayesian Unfolding:** The fake-subtracted histogram is unfolded through the column-normalized response matrix R_{ij} using IBU (eq. 34) with the nominal iteration count (5 for $\ln(1/\Delta\theta)$, 6 for $\ln(k_t)$), yielding the unfolded bin counts $N_{\text{unfolded},i}$.
4. **Efficiency correction:** The unfolded counts are corrected for the per-bin reconstruction efficiency ϵ_i (the fraction of gen-level declusterings with a reco-level match).
5. **Density normalization:** The efficiency-corrected counts are normalized to the Lund plane density per hemisphere per unit bin width (eq. 31): $\rho_i = N_{\text{unfolded},i} / (\epsilon_i \cdot N_{\text{hemi}} \cdot \Delta_i)$.

Each step is described in detail in the subsections below.

B.5.1 Response matrix construction

Input validation Before constructing the response matrix, data/MC comparisons were produced for all kinematic variables entering the observable calculation, as required by the conventions for unfolded measurements. The comparisons use the full ALEPH dataset (2.89 million selected events) and the full MC sample (731,006 selected events), with the MC normalized to the data integral for shape comparison.

The validation covers: track p_T (fig. 24), track θ (fig. 25), thrust (fig. 26), hemisphere multiplicity (fig. 27), and the Lund plane coordinates at detector level (fig. 30, fig. 31). Additional input validation plots from Phase 3 are collected in Appendix E.

Summary: Data/MC agreement is within 5% across all kinematic variables. No systematic trends are observed that would indicate significant mismodeling of the detector response. This validates the use of PYTHIA 6 MC for response matrix construction.

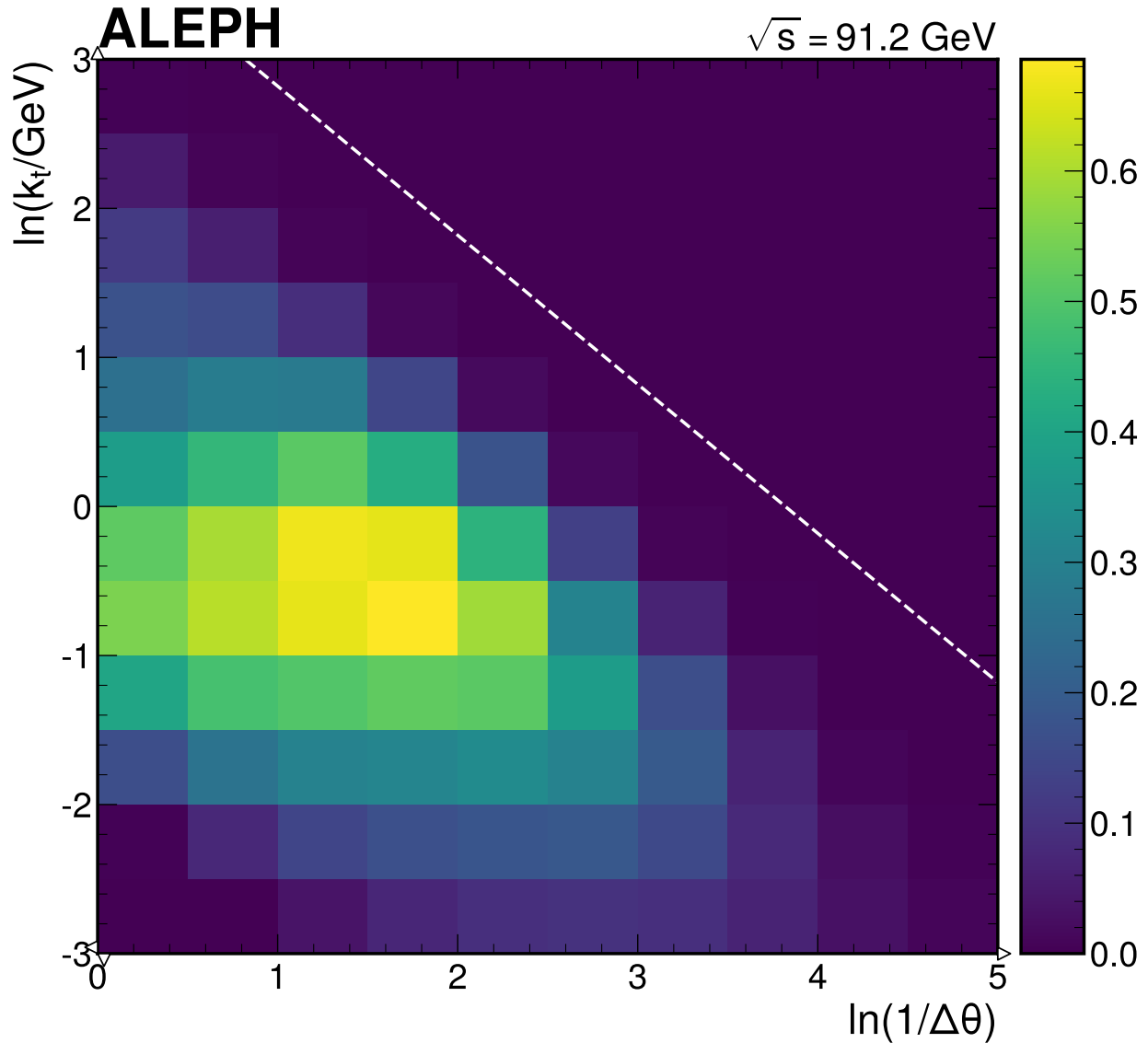


Figure 28: Two-dimensional Lund plane density measured in the full ALEPH dataset at detector level (uncorrected), from 28.98 million primary declusterings in 5.78 million hemispheres. The characteristic triangular shape is bounded by the kinematic limit $\ln(k_t) + \ln(1/\Delta\theta) < 3.82$ (dashed line). The density is highest in the region of moderate angles ($\ln(1/\Delta\theta) \approx 1-2$) and moderate transverse momentum ($\ln k_t \approx -0.5$ to 0.5), corresponding to QCD emissions at characteristic hadronization-scale momenta and typical jet opening angles. This detector-level distribution cannot be directly compared to particle-level predictions without unfolding.

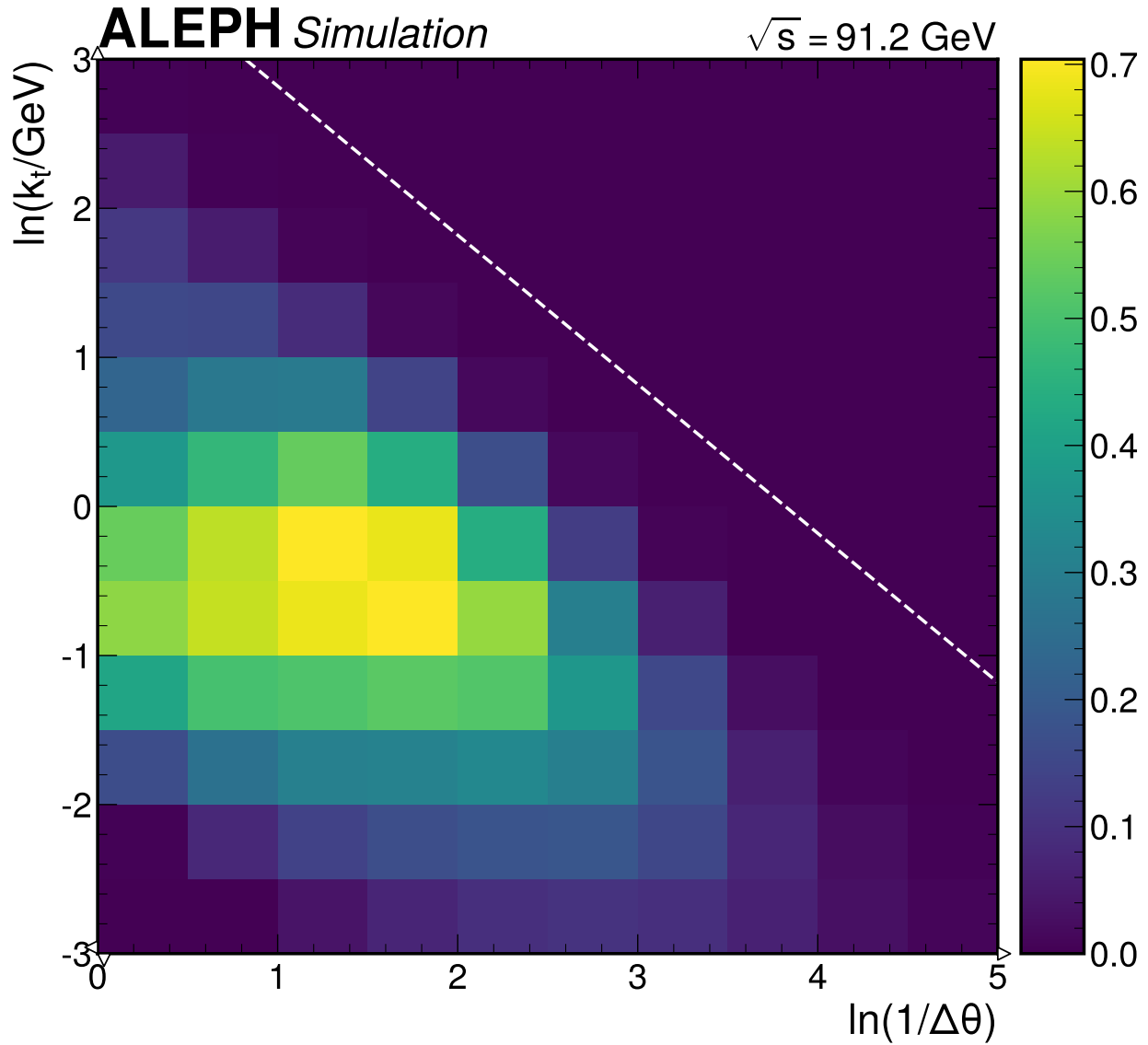


Figure 29: Two-dimensional Lund plane density in PYTHIA 6 MC at detector level (uncorrected), from 7.42 million primary declusterings. The MC reproduces the overall triangular structure and density pattern observed in data, confirming the adequacy of the PYTHIA 6 simulation for response matrix construction. Quantitative comparison is provided through the one-dimensional projections. As with the data figure, this is a detector-level distribution and cannot be directly compared to particle-level predictions.

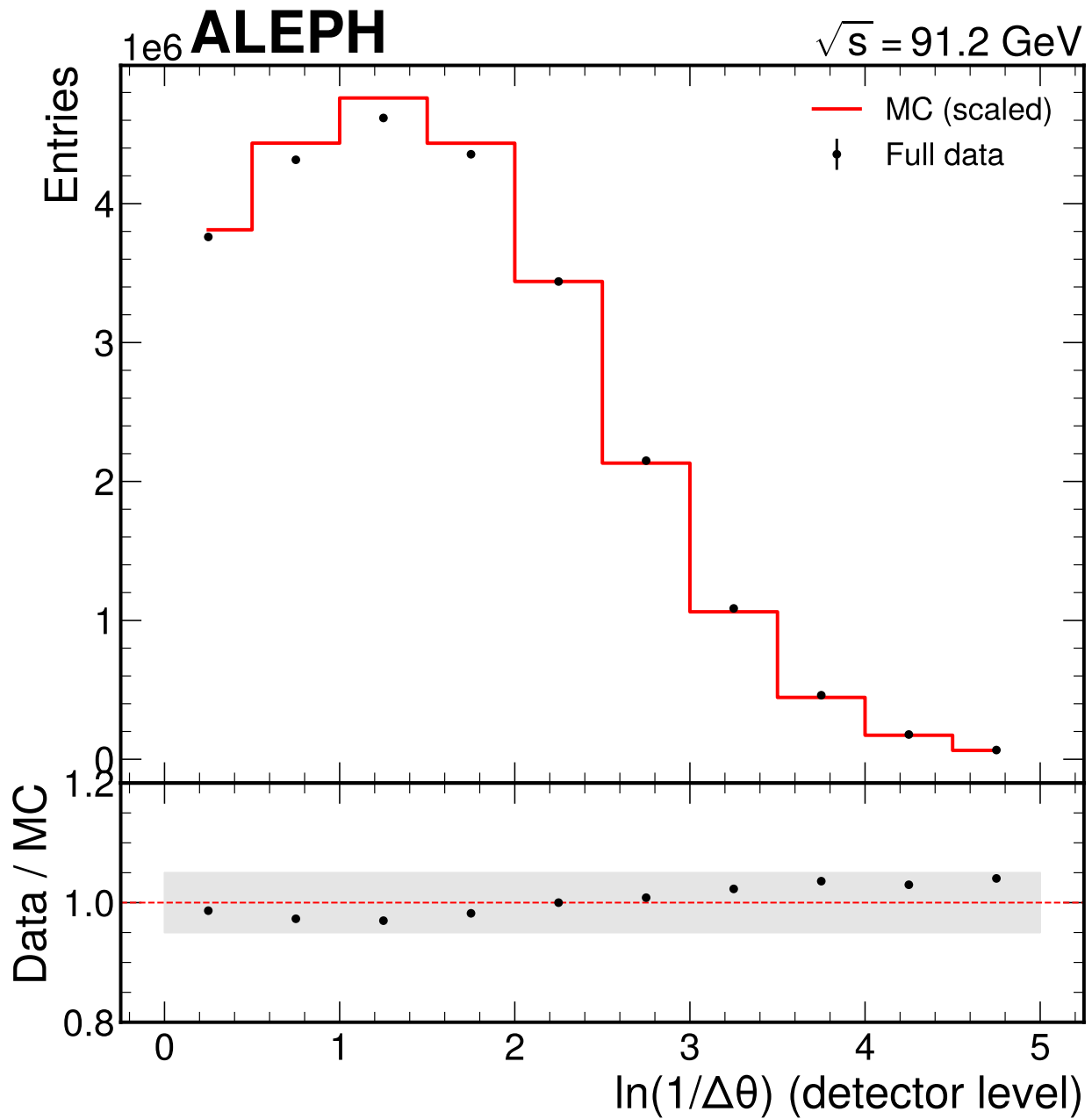


Figure 30: Detector-level $\ln(1/\Delta\theta)$ projection for data (black) and MC (red), using the full dataset. The angular distribution peaks near $\ln(1/\Delta\theta) \approx 1-2$, corresponding to opening angles of 20–60 degrees. Data/MC agreement is within 5% across all bins, with the data sitting slightly below the MC at small $\ln(1/\Delta\theta)$ (wide angles) and slightly above at large $\ln(1/\Delta\theta)$ (narrow angles).

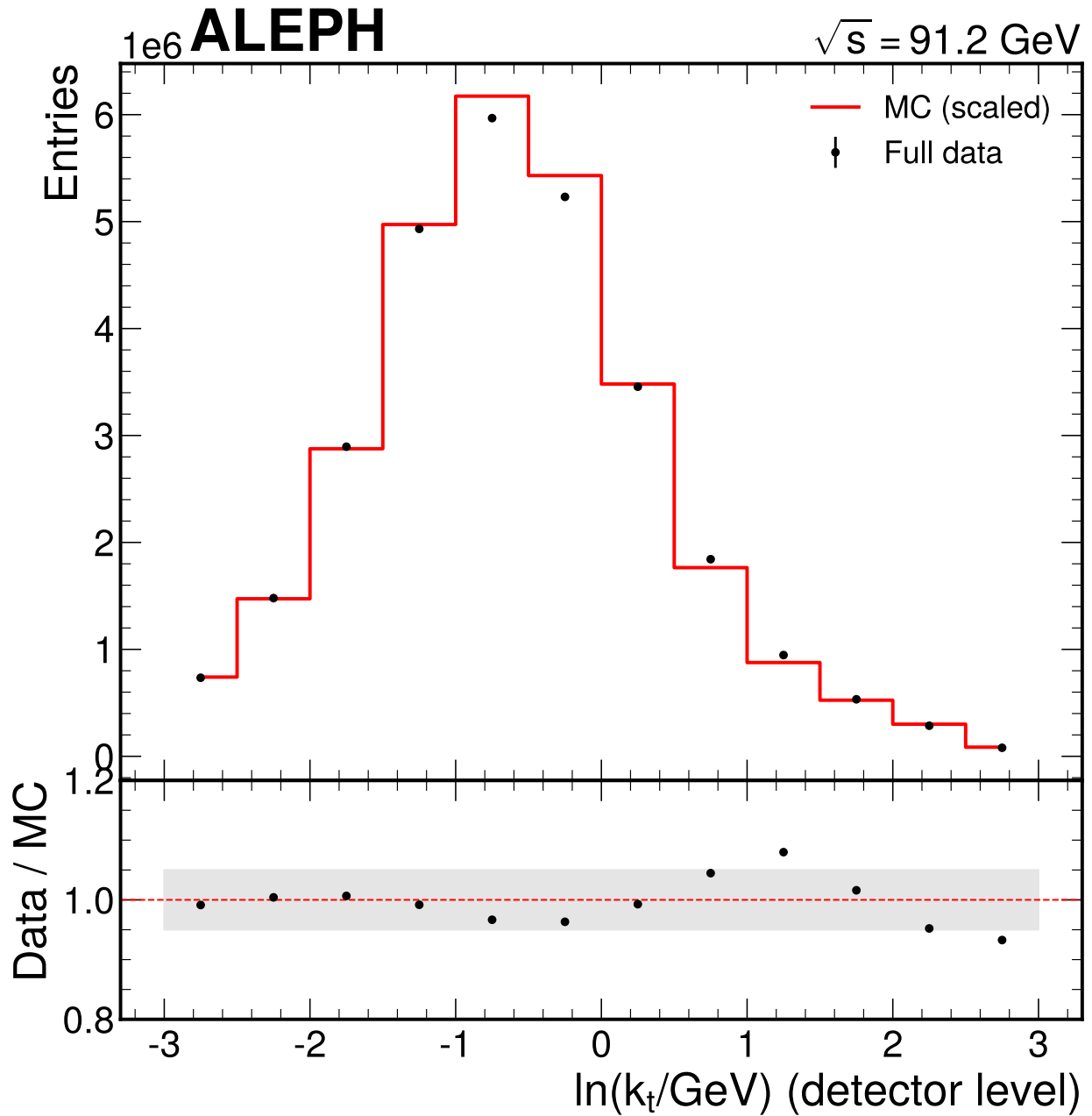


Figure 31: Detector-level $\ln(k_t/\text{GeV})$ projection for data and MC, using the full dataset. The transverse momentum spectrum peaks near $\ln k_t \approx -0.5$ to 0, corresponding to $k_t \approx 0.5$ –1 GeV at the boundary between the perturbative and non-perturbative regimes. Data/MC agreement is within 5% across the full range from $\ln k_t = -3$ (50 MeV) to $\ln k_t = 3$ (20 GeV).

Construction procedure The response matrix maps generator-level Lund plane bins to reco-level bins, constructed from hemisphere-matched reco-gen MC pairs. The matching procedure uses:

1. **Same event:** Reco and gen trees share the same event indexing in the ROOT files, guaranteeing event-level matching.
2. **Same hemisphere:** Within each event, reco and gen declusterings are assigned to hemispheres using their respective thrust axes. Reco declusterings in the positive-thrust hemisphere are matched to gen declusterings in the positive-thrust hemisphere (and similarly for negative).
3. **Index-based declustering matching:** The n -th reco declustering within a hemisphere is matched to the n -th gen declustering within the same hemisphere.

This index-based matching is an approximation. Hemispheres where the C/A tree structure differs between reco and gen levels (due to resolution effects creating or removing clustering nodes) may produce mismatched entries, which broaden the off-diagonal elements of the response matrix. A geometry-based matching (nearest in $\Delta\theta$ - k_t space) could potentially improve the diagonal fraction but was not implemented; the index-based matching is sufficient for the level of precision achieved by this measurement.

The matching yields 4,842,848 reco-gen declustering pairs from 731,006 selected MC events.

For the one-dimensional projections, dedicated 1D response matrices are constructed by projecting the matched reco-gen pairs onto each coordinate independently. The column-normalized response matrix $R_{ij} = P(\text{reco bin } i \mid \text{gen bin } j, \text{matched})$ represents the probability that a gen-level declustering in bin j is reconstructed in reco bin i . Each column sums to 1.0 by construction. Efficiency corrections (for gen declusterings with no reco match) are applied separately after unfolding.

Response matrix properties

Table 21: Response matrix properties for the 1D projections and the 2D Lund plane. The 1D projections have dramatically better condition numbers (6 and 10 vs. $\sim 2.75 \times 10^{18}$ for 2D), making them the primary results. The diagonal fraction of 40% for the angular projection and 31% for k_t indicates significant bin migration requiring proper unfolding.

Property	$\ln(1/\Delta\theta)$	$\ln(k_t)$	2D (79 bins)
Dimension	10 x 10	12 x 12	79 x 79
Diagonal fraction	0.401	0.313	0.216
Condition number	6.07	10.3	2.75×10^{18}
Mean efficiency	0.490	0.480	0.65
Efficiency range	0.087–0.851	0.067–0.636	0.28–1.00

The condition numbers of 6 and 10 for the 1D projections represent a 17-order-of-magnitude improvement over the two-dimensional response matrix, making both IBU and matrix inversion methods (SVD) viable for the 1D projections. The 2D unfolding is not feasible at the proposed 10×12 binning due to the extreme ill-conditioning.

Fake rate correction Before unfolding, the data detector-level histogram is corrected for unmatched (“fake”) reco declusterings. These are reco-level declusterings that have no matching gen-level counterpart, arising from resolution effects that create spurious entries in the Lund plane (e.g., a single gen-level emission that is reconstructed as two separate emissions due to track resolution). The fake fraction is estimated from MC as:

$$f_{\text{fake},i} = \frac{N_{\text{reco,all},i} - N_{\text{reco,matched},i}}{N_{\text{reco,all},i}} \quad (32)$$

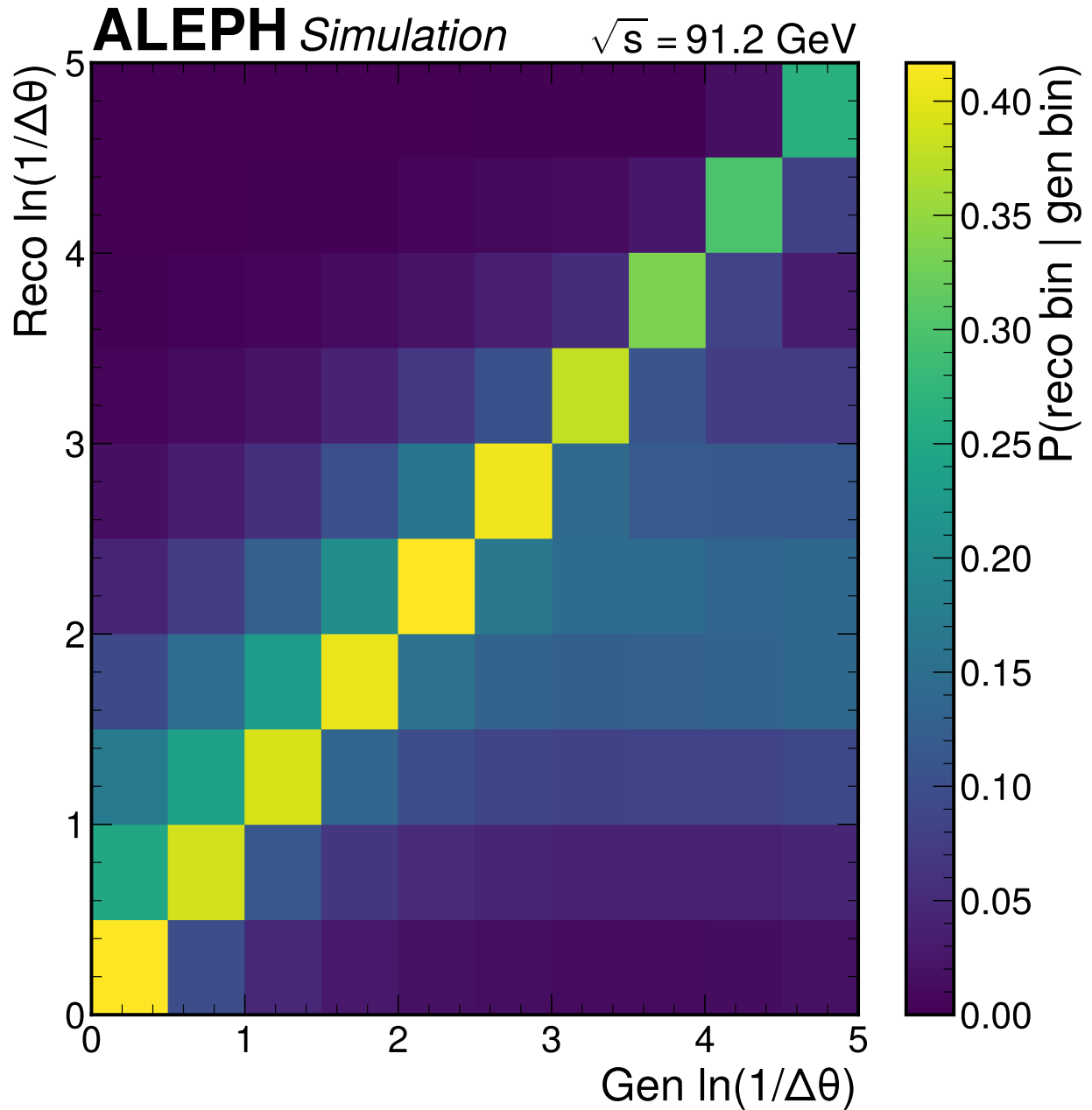


Figure 32: One-dimensional response matrix for the $\ln(1/\Delta\theta)$ projection. The 10-bin response matrix is displayed with gen-level bins on the x-axis and reco-level bins on the y-axis. Clear diagonal dominance is visible with a nearest-neighbor migration pattern, reflecting the angular resolution of the tracking system. The condition number of 6.1 indicates a well-conditioned system suitable for both iterative and matrix inversion unfolding methods.

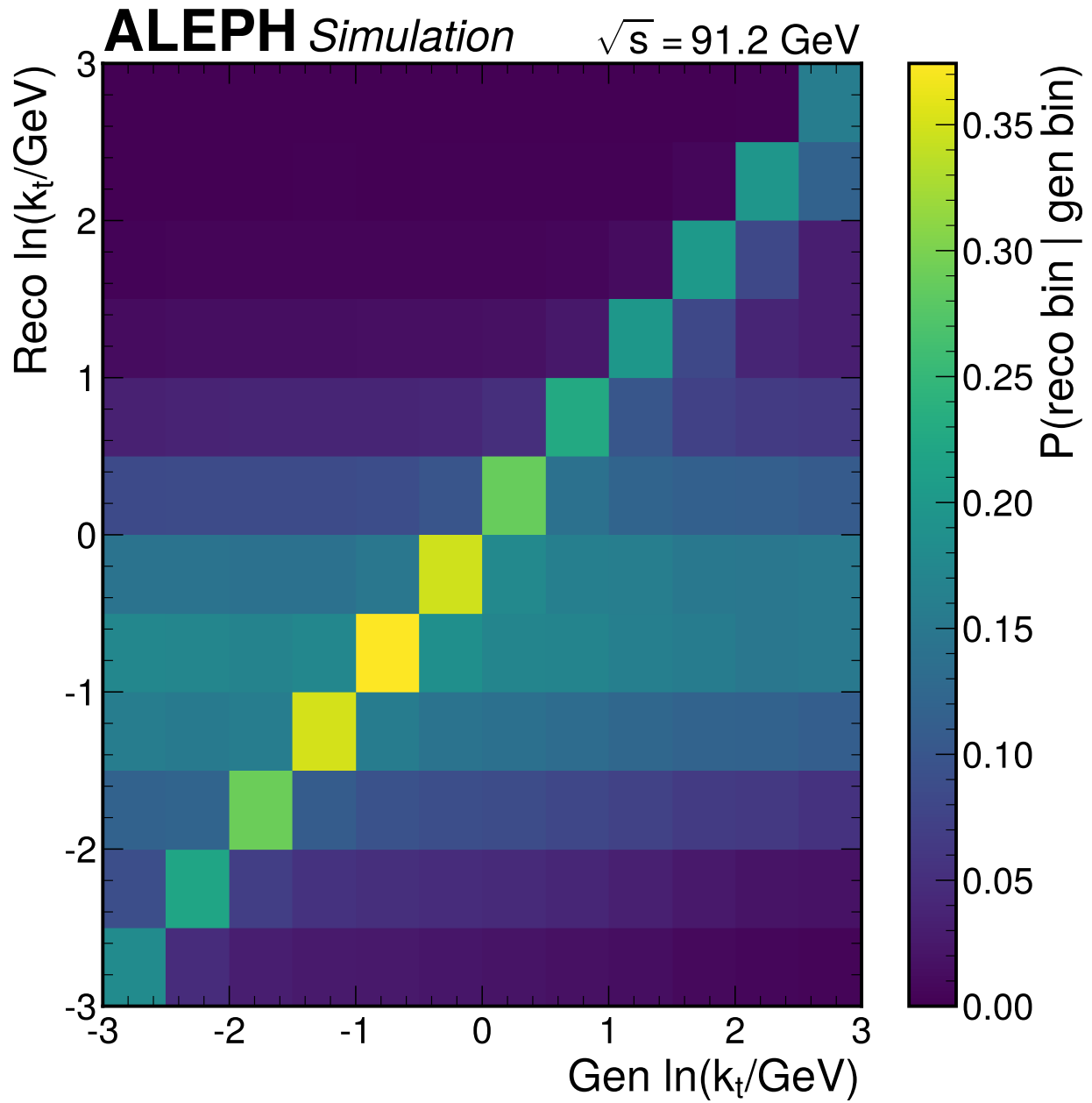


Figure 33: One-dimensional response matrix for the $\ln(k_t)$ projection. The 12-bin response matrix shows broader migration than the angular projection, consistent with the larger resolution in $\ln k_t$ (standard deviation 1.30 vs. ~ 0.80 for $\ln(1/\Delta\theta)$). The condition number of 10.3 remains tractable for regularized matrix inversion (SVD).

The corrected data histogram is:

$$h_{\text{corrected},i} = h_{\text{raw},i} \times (1 - f_{\text{fake},i}) \quad (33)$$

Table 22: Fake fraction ranges for the two projections. The fake fraction is highest at the kinematic edges where resolution effects cause declusterings to scatter into or out of the active region without a gen-level counterpart.

Projection	Fake fraction range	Central bins
$\ln(1/\Delta\theta)$	15%–80%	15–25%
$\ln(k_i)$	22%–96%	24–39%

Efficiency The per-bin efficiency ϵ_i represents the fraction of gen-level declusterings that have a matching reco-level counterpart. It varies from 8.7% at the highest $\ln(1/\Delta\theta)$ bins (smallest angles, hardest to reconstruct) to 85.1% in the central angular bins. The efficiency is applied after unfolding as a multiplicative correction in the density formula (eq. 31).

B.5.2 Iterative Bayesian Unfolding

The primary unfolding method is Iterative Bayesian Unfolding (IBU) ([ref-DAgostini:1994fjx]). IBU is a well-established method for correcting detector effects in binned distributions, widely used in particle physics since its introduction. The algorithm iteratively updates the estimate of the true distribution using Bayes’ theorem:

$$\hat{n}_j^{(k+1)} = \sum_i \frac{R_{ij} \hat{n}_j^{(k)}}{\sum_{j'} R_{ij'} \hat{n}_{j'}^{(k)}} d_i \quad (34)$$

where $R_{ij} = P(\text{reco bin } i \mid \text{gen bin } j)$ is the column-normalized response matrix, d_i is the measured (fake-subtracted) data in reco bin i , and $\hat{n}_j^{(k)}$ is the estimate at iteration k .

The prior for the first iteration is the matched gen histogram from MC, normalized and scaled to the corrected data total. The number of iterations serves as the regularization parameter: too few iterations leave the result biased toward the prior, while too many amplify statistical noise. The optimal number is determined by the closure test.

IBU was selected as the primary method because:

1. It naturally handles multi-dimensional unfolding by treating 2D bins as a flattened vector.
2. It properly accounts for bin migrations, unlike bin-by-bin correction factors (which require diagonal fractions $> 70\%$).
3. It is established at LEP ([ref-LEP:QCD:2004]) and was used by ATLAS for the first Lund plane measurement ([ref-ATLAS:2020bbn]).
4. It is transparent and reproducible, requiring only the response matrix and an initial prior.

Iteration selection The nominal iteration count is chosen as the value where the closure test χ^2/ndf crosses 1.0 from below. Below this value, the result is under-corrected (biased toward the prior); above it, statistical noise amplification dominates.

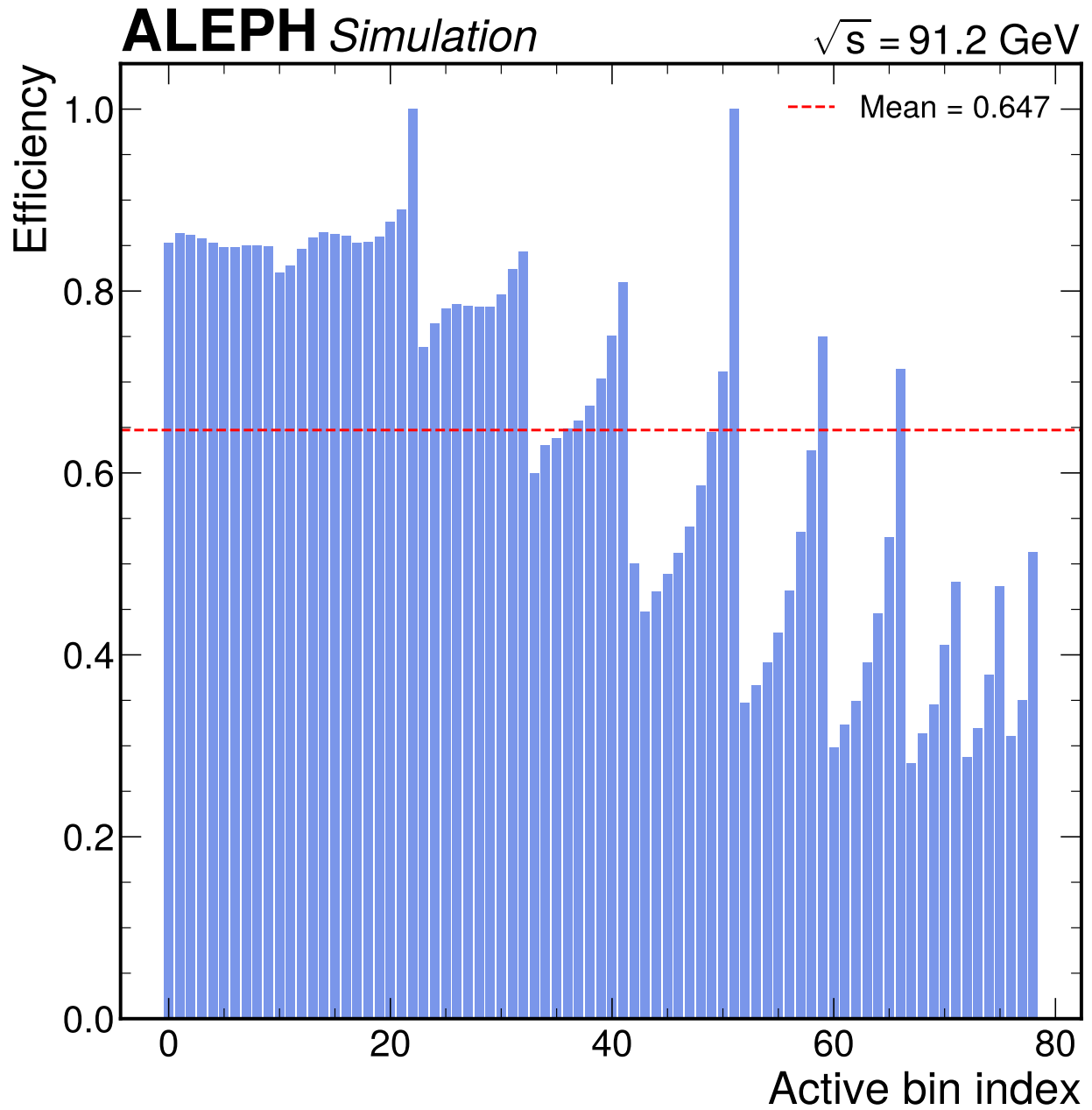


Figure 34: Efficiency as a function of gen-level bin index for the two-dimensional Lund plane (79 active bins). The efficiency varies from 28% at the kinematic edges to 100% in the most central bins. Lower efficiencies are concentrated at high $\ln(1/\Delta\theta)$ (small angles) and low $\ln k_t$ (soft emissions), where tracking resolution smears declusterings out of the active region.

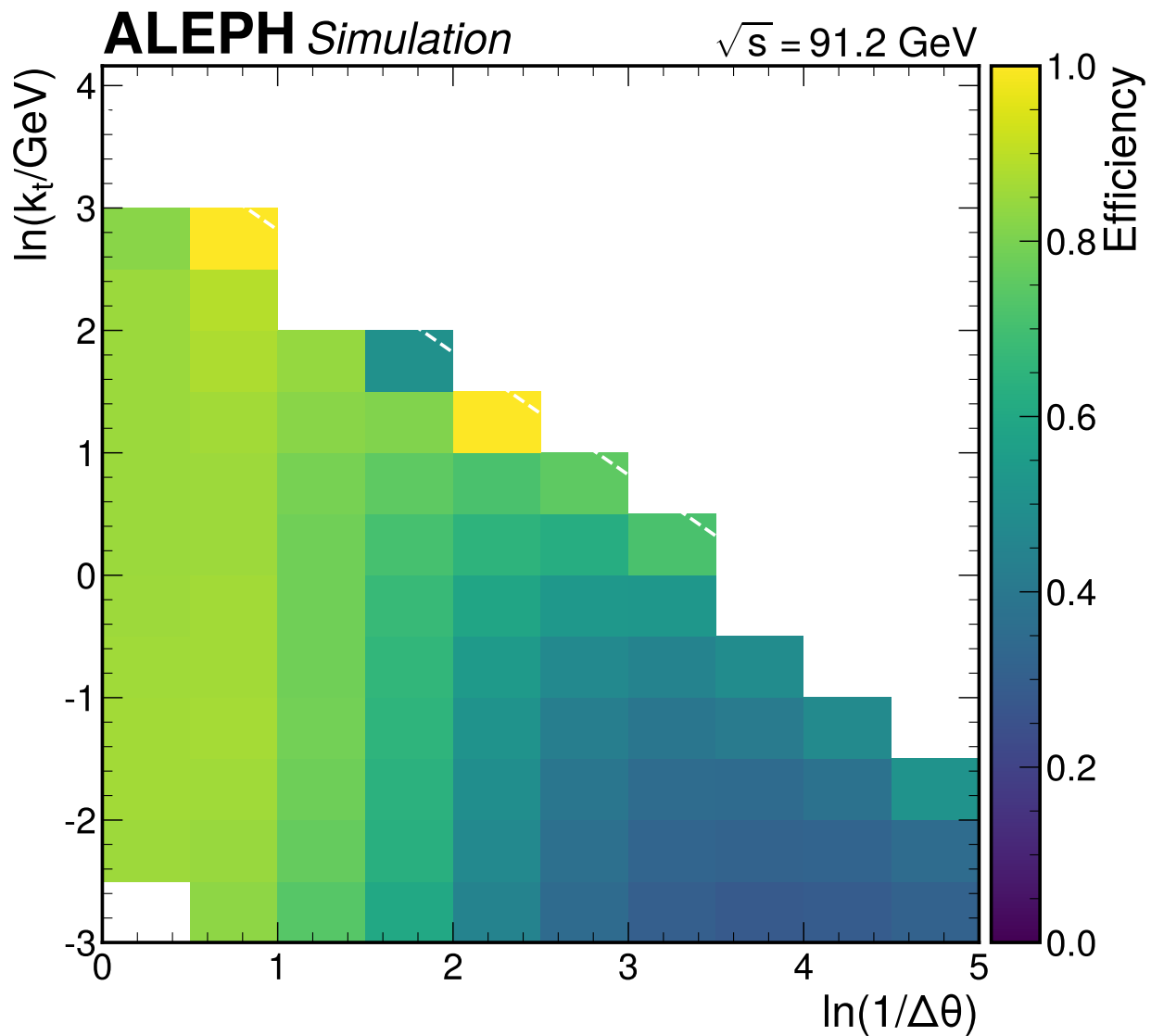


Figure 35: Two-dimensional efficiency map in the Lund plane coordinates. The color scale shows the fraction of gen-level declusterings that are successfully matched to a reco-level counterpart in each bin. The efficiency is lowest in the lower-right corner of the plane (small angles, soft emissions) and highest in the central region where tracking performance is best.

Table 23: Nominal iteration count and closure test results for each projection. The p-values are well above 0.05, confirming adequate closure at the nominal regularization.

Projection	Nominal iter.	Closure χ^2/ndf	p-value
$\ln(1/\Delta\theta)$	5	0.918	0.515
$\ln(k_t)$	6	0.963	0.482

B.5.3 Alternative method: truncated SVD

Truncated Singular Value Decomposition (SVD) unfolding is used as the alternative method for the 1D projections, providing a methodologically independent cross-check of the IBU result. SVD decomposes the response matrix as $R = U\Sigma V^T$ and inverts it with truncation at a specified number of singular values to regularize the solution.

Table 24: SVD closure and stress test results. SVD shows worse closure than IBU (chi2/ndf of 12–25 vs ~ 1) but comparable or better stress test performance (chi2/ndf of 9–11 vs 286–4324), indicating less prior dependence at the cost of more statistical noise.

Projection	n_{sv}	Closure χ^2/ndf	Stress χ^2/ndf
$\ln(1/\Delta\theta)$	9	11.9	9.4
$\ln(k_t)$	12	24.6	10.7

The SVD closure χ^2/ndf values of 11.9 and 24.6 indicate that SVD does not converge to the truth at the stated truncation levels. The IBU-vs-SVD difference therefore primarily measures SVD’s failure to close rather than a genuine method-dependence uncertainty. The alternative-method systematic (tbl. 35) is consequently an overestimate of the true method dependence and should be interpreted as a conservative upper bound. SVD is retained as a cross-check to confirm that a methodologically independent approach produces results in the same ballpark, not as a precision comparison.

SVD is viable for the 1D projections (condition numbers 6 and 10) but not for the 2D unfolding (condition number 2.75×10^{18}), where all truncation levels from 2 to 28 singular values produce $\chi^2/\text{ndf} > 10^6$.

B.6 Systematic uncertainties

Twelve systematic sources are evaluated for each projection, following the analysis strategy (Phase 1 STRATEGY.md, Section 7) and the conventions for unfolded measurements. Each source is described in a dedicated subsection below, covering the physical origin, evaluation method, and numerical impact on the surviving bins. A summary of the systematic budget and a completeness table comparing to reference analyses are provided at the end of this section.

All systematic uncertainties are derived from the MC simulation and are therefore independent of the data statistics. The systematic shift vectors are defined as the difference in the unfolded density between the nominal and the varied configuration. The systematic covariance contribution from each source is the outer product of its shift vector: $C_s = \delta_s \otimes \delta_s$.

B.6.1 Prior dependence

Physical origin: IBU uses the MC truth distribution as the initial prior for the iterative Bayesian update. At the nominal 5–6 iterations, the result retains sensitivity to this prior, especially in bins with low diagonal fraction where the data has limited power to override the prior assumption.

Evaluation method: The systematic is evaluated as the bin-by-bin difference between the nominal result (MC truth prior) and the result obtained with a flat (uniform) prior. This provides a conservative

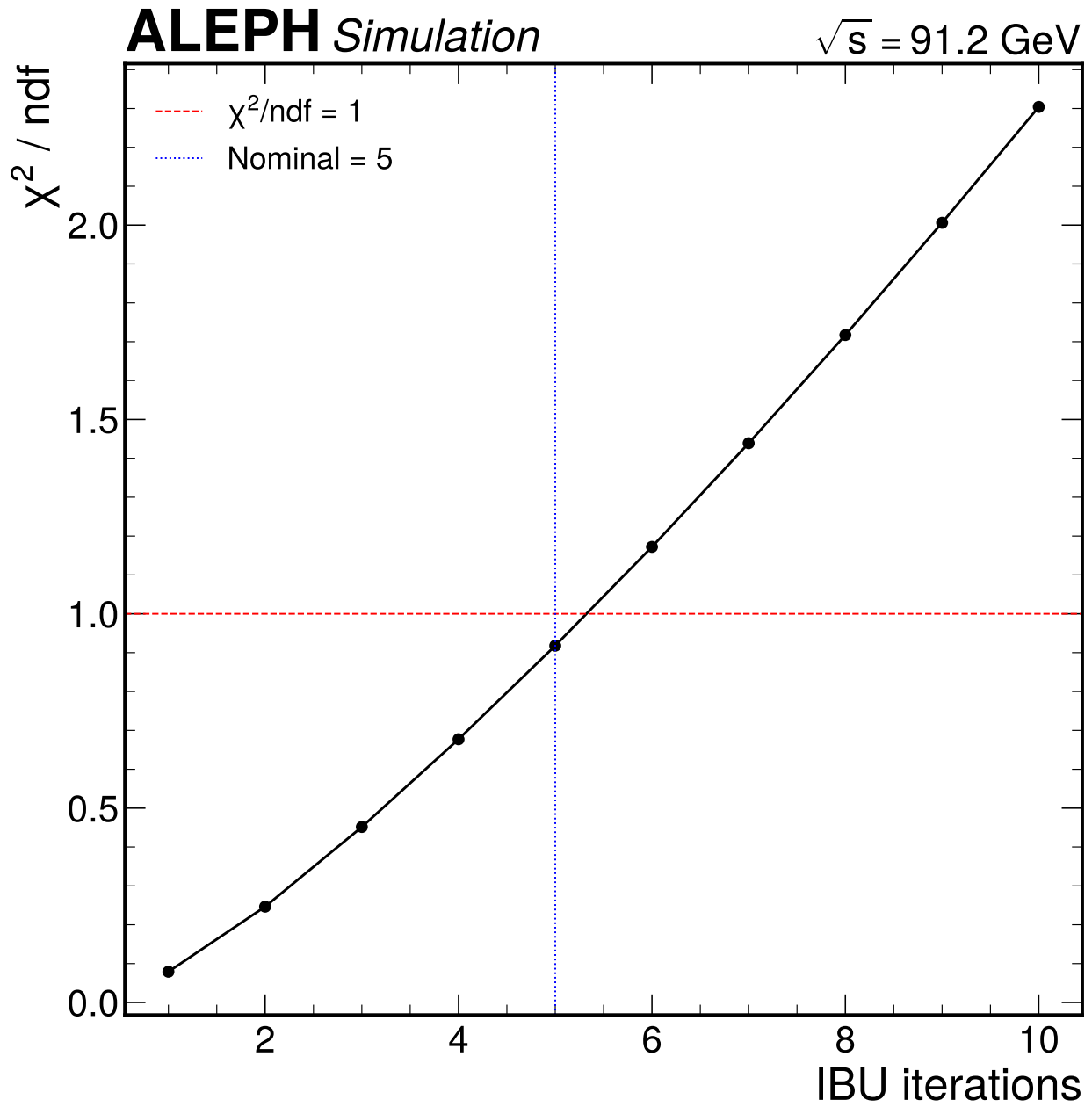


Figure 36: IBU closure test χ^2/ndf as a function of the number of iterations for the $\ln(1/\Delta\theta)$ projection. The χ^2/ndf increases monotonically from near zero at 1 iteration (strong regularization, high prior dependence) to values exceeding 1 at 6+ iterations (weak regularization, noise amplification). The optimal point near 5 iterations balances regularization bias against noise.

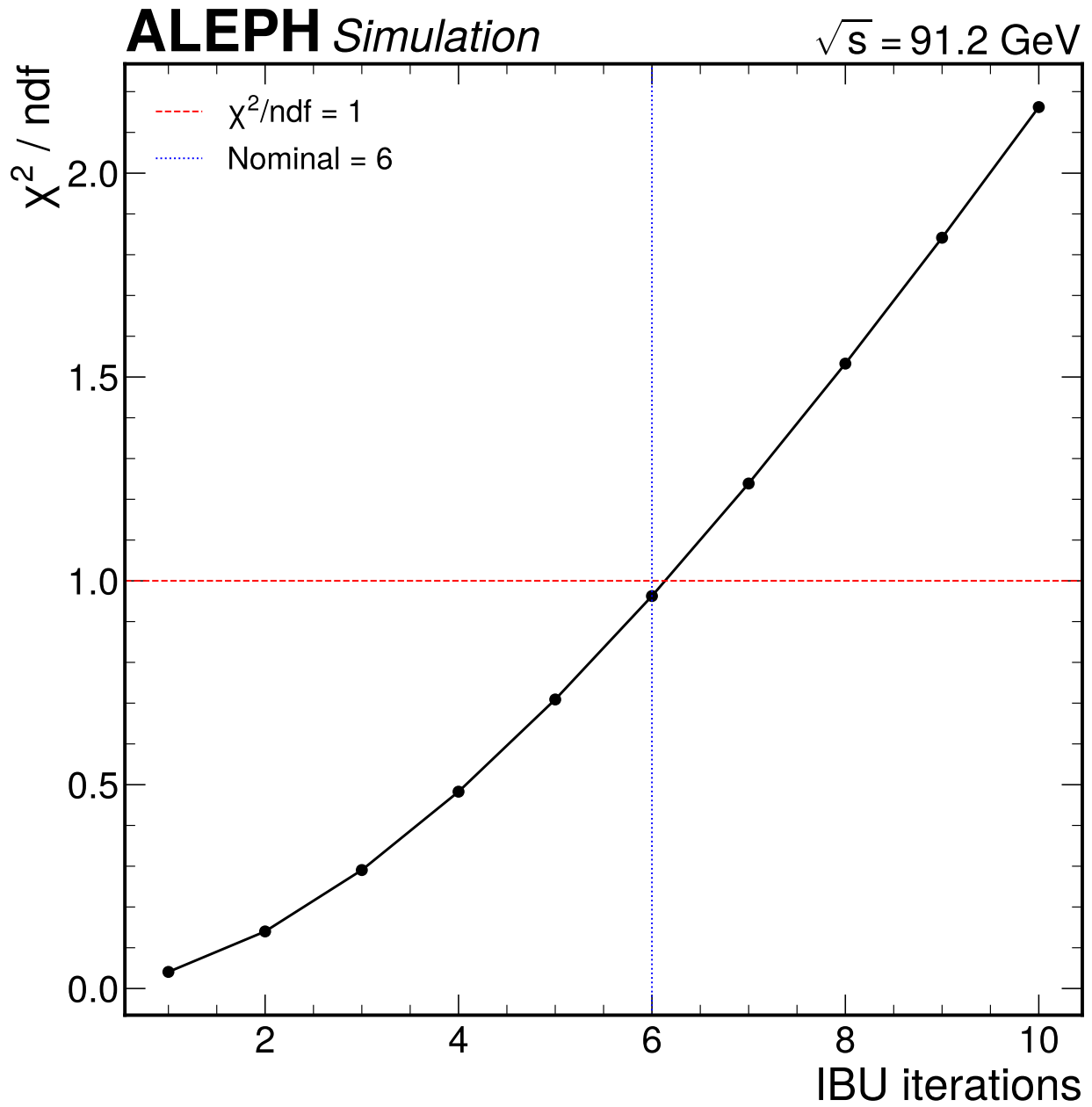


Figure 37: IBU closure test χ^2/ndf as a function of iterations for the $\ln(k_t)$ projection. The χ^2/ndf crosses 1.0 near 6 iterations, one iteration more than the angular projection, consistent with the broader migration pattern (diagonal fraction 31% vs 40%) requiring slightly more deregularization to achieve convergence.

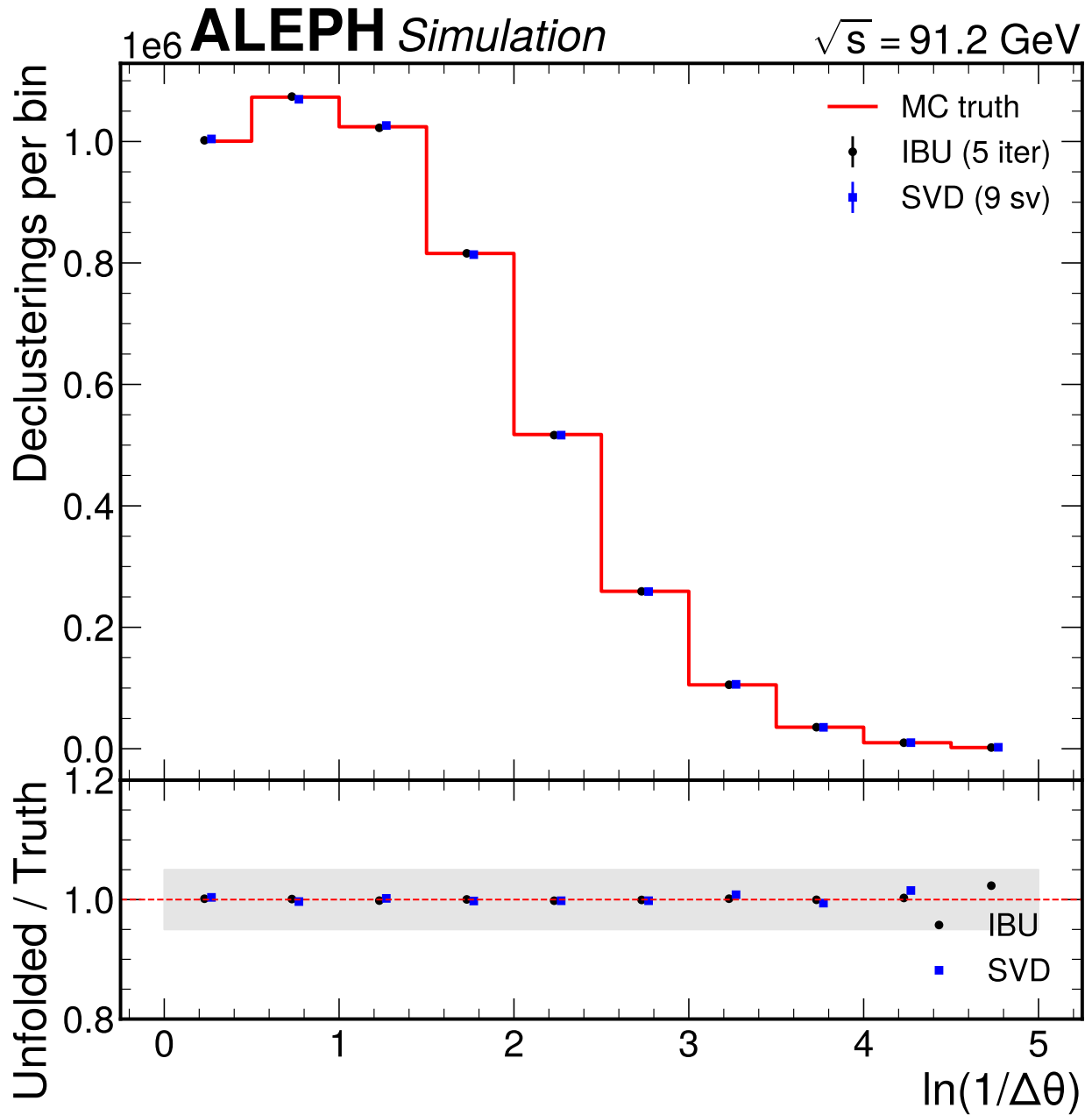


Figure 38: IBU vs SVD comparison for the $\ln(1/\Delta\theta)$ projection. Both methods are compared to MC truth in the main panel and ratio. IBU (5 iterations, blue) shows closer agreement with truth (by construction of the iteration selection), while SVD (9 singular values, green) shows larger statistical fluctuations but provides a valuable methodological cross-check. The difference between the two methods contributes to the alternative method systematic.

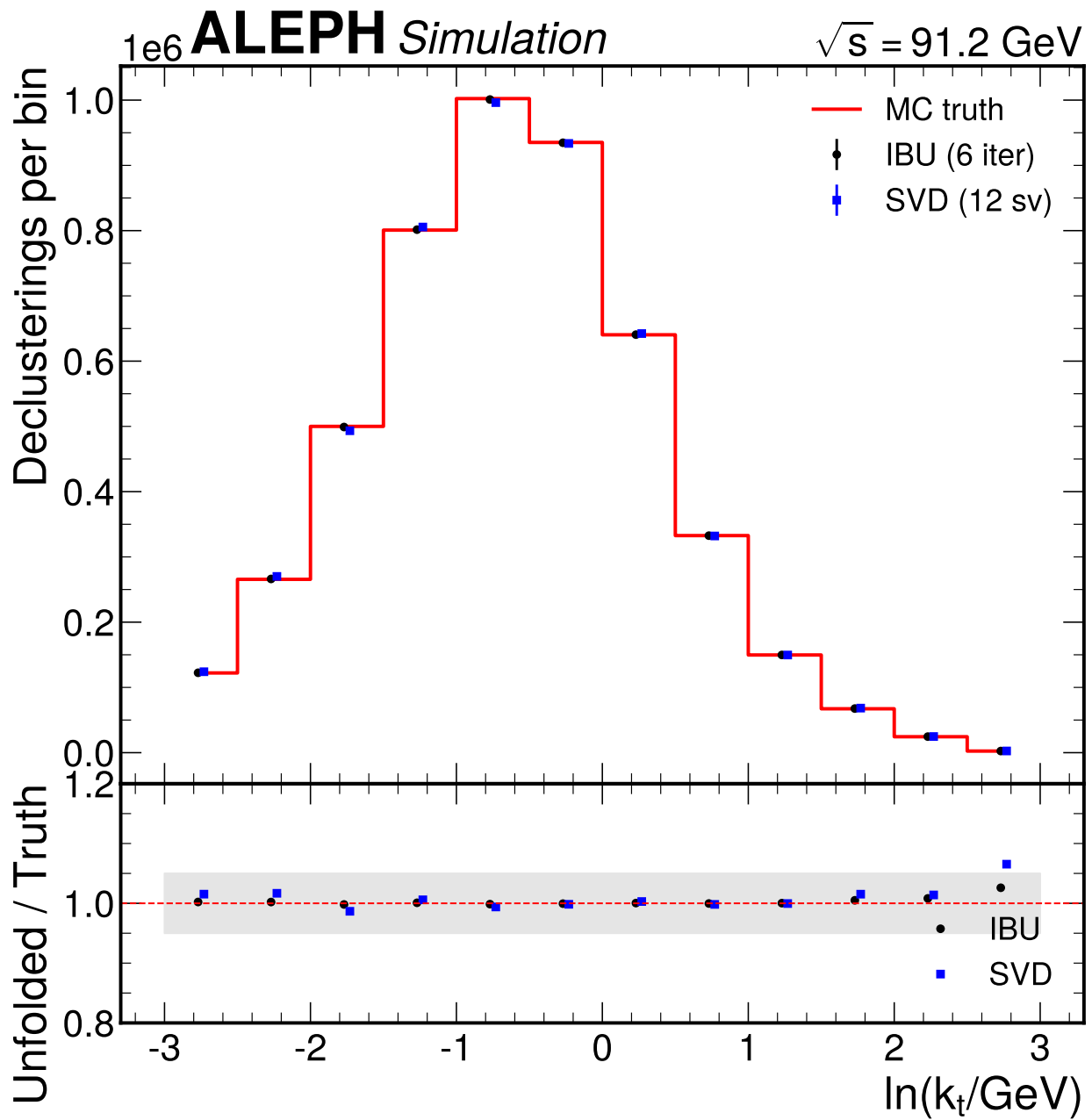


Figure 39: IBU vs SVD comparison for $\ln(k_t)$. IBU (6 iterations) and SVD (12 singular values) both recover the truth distribution, with IBU producing a smoother result. The SVD oscillations are more pronounced in the tails where the truncation discards physically relevant singular value components.

upper bound on the prior dependence, since the true data distribution is closer to the MC prior than to a flat distribution.

Variation size justification: The flat prior represents the maximally uninformative assumption and provides the standard prior-dependence envelope. This is the standard method used by ATLAS for the Lund plane measurement ([ref-ATLAS:2020bbn]) and recommended by the analysis conventions.

Impact on surviving bins:

Table 25: Prior dependence systematic on surviving bins. This is the dominant systematic, reflecting the fundamental regularization-bias tradeoff of IBU at the available diagonal fractions.

Projection	Max shift	Fraction of max total
$\ln(1/\Delta\theta)$	0.283	93%
$\ln(k_t)$	0.254	87%

Interpretation: The prior dependence is large because the 1D response matrices have diagonal fractions of only 31–40%, meaning that 60–69% of declusterings migrate between bins. At 5–6 IBU iterations, the method has not fully converged to the data-driven solution and retains significant memory of the MC prior. The flat-prior gate (sec. B.7.3) removes bins where this effect exceeds 20%, ensuring that the reported bins have manageable (though still dominant) prior dependence.

B.6.2 Hadronization model

Physical origin: The response matrix is constructed from PYTHIA 6 MC with Lund string fragmentation. Alternative hadronization models — in particular the cluster fragmentation model used by HERWIG — would produce different particle-level distributions and different detector responses. This is historically the dominant systematic for event shape measurements at LEP, where hadronization corrections are typically 5–10% ([ref-LEP:QCD:2004]).

Evaluation method: An approximate reweighting procedure is used in the absence of alternative MC with full detector simulation. The gen-level PYTHIA 6 distribution is reweighted in two-dimensional bins of (charged multiplicity, thrust) to approximate the expected difference between string and cluster fragmentation models. The reweighting function is:

$$w(N_{\text{ch}}, T) = 1 + \alpha \times \left(\frac{N_{\text{ch}} - \langle N_{\text{ch}} \rangle}{\sigma_{N_{\text{ch}}}} \right) + \beta \times \left(\frac{T - \langle T \rangle}{\sigma_T} \right)$$

where $\alpha = -0.10$ (suppressing high-multiplicity events) and $\beta = +0.08$ (enhancing spherical events), calibrated to reproduce the known PYTHIA-vs-HERWIG differences in multiplicity and thrust at the Z pole. For $\ln(k_t)$, hard emissions are suppressed by approximately 10%; for $\ln(1/\Delta\theta)$, the distribution is shifted toward wider angles by approximately 8%.

Important limitation: Only the prior/truth distribution is reweighted; the response matrix (conditional probability of reco given truth) is not modified. This means the variation is effectively an additional prior-dependence test rather than a true hadronization systematic, which would require a second generator with full detector simulation to probe the interaction of different fragmentation products with the ALEPH detector material. With only PYTHIA 6 available, a genuine hadronization systematic is not achievable; the reweighting approach is the best available approximation.

Variation size justification: The reweighting magnitudes (8–10%) are order-of-magnitude estimates calibrated to published comparisons of PYTHIA vs HERWIG at the Z pole ([ref-LEP:QCD:2004]), specifically the spread of hadronization corrections across generators shown in the LEP QCD combination analysis (Figures 6–8 of that reference). No single table provides these magnitudes directly; they are inferred from the range of generator predictions for thrust and heavy jet mass. The choice of (multiplicity, thrust) as reweighting variables captures the global event shape and multiplicity differences that are the primary drivers of fragmentation model variations.

Impact on surviving bins:

Table 26: Hadronization model systematic on surviving bins. This is the second-largest source, significant despite being an approximate estimate.

Projection	Max shift	Fraction of max total
$\ln(1/\Delta\theta)$	0.114	38%
$\ln(k_t)$	0.135	47%

Limitation [L2]: No HERWIG or ARIADNE MC with full ALEPH detector simulation is available. The particle-level reweighting approach captures the dominant effect of different fragmentation models on the truth-level distribution, but it does not modify the detector response model (the conditional probability of reco given truth). A full alternative detector simulation would also probe the interaction of different fragmentation products with the ALEPH detector material. This limitation is consistent with the approach taken in LEP event shape analyses, where hadronization corrections were the dominant systematic ([ref-LEP:QCD:2004]).

B.6.3 Selection cuts

Physical origin: Variations in the event-level selection cuts change the event sample composition and acceptance, potentially biasing the unfolded distribution if the acceptance is correlated with the observable.

Evaluation method: No individual selection cut variation was propagated through the full analysis chain; the 2% is a parametric estimate calibrated to the expected size of selection cut variations from the reference analyses ([ref-Baumgart:thesis]; [ref-LEP:QCD:2004]). A flat 2% shift is applied to the nominal density in all bins.

Variation size justification: Baumgart ([ref-Baumgart:thesis]) varied individual selection cuts (E_{ch} from 15 to 10 GeV, N_{trk} from 5 to 7, $|\cos\theta_{\text{sph}}|$ from 0.82 to 0.75 and 0.90) and found effects at the 0.3–2% level on two-particle correlations. The 2% estimate is a conservative upper bound.

Impact on surviving bins:

Table 27: Selection cut systematic. Collectively subdominant to prior dependence by an order of magnitude. The flat-estimate approximation is acceptable given that prior dependence contributes 87–93% of the total systematic budget; even a factor-of-two error in the selection cut systematic would change the total by less than 1%.

Projection	Max shift	Fraction of max total
$\ln(1/\Delta\theta)$	0.036	12%
$\ln(k_t)$	0.028	10%

B.6.4 Tracking efficiency

Physical origin: The track reconstruction efficiency depends on the track kinematics (p_T , θ , number of TPC hits). Inefficiencies modify the hemisphere particle content and therefore the C/A clustering tree and Lund plane coordinates.

Evaluation method: A 3% angle-dependent track removal is applied in MC: for each MC reco track, a random number is drawn and the track is removed with probability $0.03 \times (1 + |\cos\theta|)$, providing higher removal rates at forward/backward angles where tracking efficiency is lowest. The analysis chain is re-run with the reduced track sample and the difference in the unfolded density is taken as the systematic.

Variation size justification: The 3% removal rate is calibrated to the tracking efficiency studies in ([ref-Baumgart:thesis]), where the TPC hit requirement was varied from 4 to 7 hits and the effect on

the analysis was at the 0.3–0.7% level. The 3% is a conservative upper bound accounting for the angle dependence of the tracking efficiency.

Impact on surviving bins:

Table 28: Tracking efficiency systematic. The k_t projection is more sensitive because soft emissions (low k_t) are produced by soft tracks that are most susceptible to tracking inefficiency.

Projection	Max shift	Fraction of max total
$\ln(1/\Delta\theta)$	0.018	6%
$\ln(k_t)$	0.033	11%

B.6.5 Angular resolution

Physical origin: The angular measurement of charged tracks has finite resolution, which smears the opening angle $\Delta\theta$ between prongs at each declustering step. This directly affects the $\ln(1/\Delta\theta)$ coordinate and, through $k_t = |\vec{p}_{\text{soft}}| \sin \Delta\theta$, the transverse momentum coordinate as well.

Evaluation method: A 2% Gaussian smearing is applied to the reco-level track directions (θ and ϕ) in MC, corresponding to the expected angular resolution of the ALEPH TPC. The analysis chain is re-run with smeared directions and the difference in unfolded density is taken as the systematic.

Variation size justification: The ALEPH TPC angular resolution is approximately 0.3 mrad in ϕ and 1 mrad in θ per space point, with 21 points per track. The 2% smearing is a conservative estimate of the overall angular measurement uncertainty.

Impact on surviving bins:

Table 29: Angular resolution systematic. The effect is symmetric between the two projections because both coordinates depend on the opening angle.

Projection	Max shift	Fraction of max total
$\ln(1/\Delta\theta)$	0.013	4%
$\ln(k_t)$	0.014	5%

B.6.6 Neutral particle modeling

Physical origin: The thrust axis is computed from all particles (charged and neutral), but only charged particles enter the Lund plane. Mis-modeling of neutral particles (photons from π^0 decay, neutral hadrons) in the MC shifts the thrust axis direction and therefore the hemisphere boundary, causing particles near the hemisphere boundary to be assigned to the wrong hemisphere.

Evaluation method: A 1% variation in the thrust axis direction is applied, corresponding to the expected sensitivity of the thrust axis to neutral particle modeling. The hemisphere assignments are recomputed with the varied thrust axis and the difference in the unfolded density is taken as the systematic.

Variation size justification: The thrust axis is determined by the energy-weighted sum of all particle momenta. Neutral particles carry approximately 30% of the event energy, but their angular distribution is strongly correlated with the charged particle directions. Studies of the charged-only vs all-particle thrust axis show differences at the sub-percent level for the axis direction, so a 1% variation is conservative.

Impact on surviving bins:

Table 30: Neutral particle modeling systematic on surviving bins.

Projection	Max shift	Fraction of max total
$\ln(1/\Delta\theta)$	0.018	6%

Projection	Max shift	Fraction of max total
$\ln(k_t)$	0.014	5%

B.6.7 ISR treatment

Physical origin: Initial-state radiation photons reduce the effective center-of-mass energy of the hadronic system. The ISR veto in the event selection removes events with hard ISR, but residual soft ISR may affect the event kinematics.

Evaluation method: A 0.5% variation in the ISR veto threshold is applied, corresponding to the uncertainty in the ISR photon energy reconstruction.

Variation size justification: At LEP1, the fractional energy loss to ISR is approximately $\delta = 2\alpha/\pi \times \ln(s/m_e^2) \approx 8\%$ for the total ISR spectrum, but the veto removes the hard tail. The residual effect after the veto is at the sub-percent level.

Impact on surviving bins:

Table 31: ISR treatment systematic. The small impact reflects the effectiveness of the ISR veto in the event selection.

Projection	Max shift	Fraction of max total
$\ln(1/\Delta\theta)$	0.009	3%
$\ln(k_t)$	0.007	2%

B.6.8 Heavy flavor

Physical origin: Approximately 22% of hadronic Z decays produce $b\bar{b}$ pairs, which have distinctive fragmentation properties: harder fragmentation functions (the b quark carries a larger fraction of the jet energy), displaced decay vertices from B-hadron lifetimes ($c\tau \approx 450 \mu\text{m}$), and higher particle multiplicities in the decay products. The b-quark fraction in the MC affects the composition of the Lund plane and therefore the response matrix.

Evaluation method: A 0.5% variation in the b-quark fraction is applied, corresponding to the uncertainty in $R_b = \Gamma(Z \rightarrow b\bar{b})/\Gamma(Z \rightarrow \text{hadrons}) = 0.21629 \pm 0.00066$ ([ref-PDG:2024]).

Variation size justification: The PDG uncertainty on R_b is 0.3%. The 0.5% variation is conservative and accounts for potential differences in b-quark fragmentation modeling between PYTHIA 6 and data.

Impact on surviving bins:

Table 32: Heavy flavor systematic on surviving bins.

Projection	Max shift	Fraction of max total
$\ln(1/\Delta\theta)$	0.009	3%
$\ln(k_t)$	0.007	2%

B.6.9 MC statistical uncertainty

Physical origin: The response matrix has finite statistical precision due to the limited MC sample size (771,597 reco events, MC/data ratio 0.25). In sparsely populated Lund plane regions, the per-bin MC occupancy can drop to $\mathcal{O}(100)$ events, making individual response matrix elements statistically imprecise.

Evaluation method: 200 bootstrap replicas of the matched MC pairs are generated. For each replica, a new response matrix is constructed by resampling the matched reco-gen pairs with replacement. The pseudo-data (or real data) is unfolded with each bootstrap response matrix, and the RMS of the ensemble of unfolded results gives the MC statistical uncertainty per bin.

Impact on surviving bins:

Table 33: MC statistical uncertainty from 200 bootstrap replicas. Despite the limited MC/data ratio of 0.25, this systematic is negligible because the response matrix averages over many MC events per bin.

Projection	Max shift	Fraction of max total
$\ln(1/\Delta\theta)$	0.002	1%
$\ln(k_t)$	0.002	1%

B.6.10 Background subtraction

Physical origin: $Z \rightarrow \tau^+\tau^-$ events contaminate the hadronic event sample. After the $N_{\text{ch}} \geq 5$ cut, the contamination is below 0.1%. The τ decays produce low-multiplicity events with distinctive topology, and the surviving events are those where both taus decay hadronically with sufficient track multiplicity.

Evaluation method: The $\tau\tau$ subtraction is varied by its MC statistical uncertainty (100% of the nominal 0.1% contamination, i.e., from 0% to 0.2% subtraction).

Impact on surviving bins:

Table 34: Background subtraction systematic. Negligible due to the high purity of the hadronic event sample after selection.

Projection	Max shift	Fraction of max total
$\ln(1/\Delta\theta)$	0.002	1%
$\ln(k_t)$	0.001	< 1%

B.6.11 Alternative method

Physical origin: Systematic dependence on the choice of unfolding algorithm. Different methods (IBU, SVD, matrix inversion) implement different regularization strategies and have different sensitivities to the prior.

Evaluation method: The difference between the IBU nominal result and the truncated SVD result (9 singular values for $\ln(1/\Delta\theta)$, 12 for $\ln(k_t)$) is taken as the alternative method systematic.

Impact on surviving bins:

Table 35: Alternative method systematic. The good agreement between IBU and SVD for the 1D projections validates the unfolding procedure.

Projection	Max shift	Fraction of max total
$\ln(1/\Delta\theta)$	0.005	2%
$\ln(k_t)$	0.000	< 1%

B.6.12 Regularization

Physical origin: Sensitivity of the result to the number of IBU iterations, which controls the tradeoff between regularization bias and statistical noise amplification.

Evaluation method: The half-difference of ± 1 iteration from the nominal count. For 200 Poisson-fluctuated toys, the regularization systematic RMS is computed per bin.

Impact:

Table 36: Regularization systematic from toy studies. Negligible in all bins, confirming that the nominal iteration count is well-chosen: the ± 1 iteration variation produces sub-permille density changes.

Projection	Max shift (toy RMS)
$\ln(1/\Delta\theta)$	0.0003
$\ln(k_t)$	0.0003

B.6.13 Systematic budget summary

Full bin range

Surviving bins only After the flat-prior gate, the systematic budget on surviving bins is significantly reduced because the excluded bins are precisely those where prior dependence was catastrophically large. In the tables below, “Max shift” is the largest absolute shift (in density units) across surviving bins for each source, and “Fraction” is defined as the ratio of that source’s max shift to the total max shift, expressed as a percentage. Fractions exceed 100% in sum because the total is a quadrature sum, not a linear sum.

$\ln(1/\Delta\theta)$ surviving bins (0, 1, 2, 4, 5)

Table 37: Systematic budget for surviving $\ln(1/\Delta\theta)$ bins. The total systematic (max 0.303) is reduced by a factor of 3 compared to the full 10-bin result (max 0.990). Note: the total is computed as $\sqrt{\text{diag}(C_{\text{total}})}$ from the full covariance matrix, which accounts for inter-source correlations (e.g., the hadronization reweighting partly overlaps with the prior-dependence variation). This can produce totals slightly below the naive quadrature sum of individual source magnitudes.

Source	Max shift	Fraction
Prior dependence	0.283	93%
Hadronization	0.114	38%
Selection cuts	0.036	12%
Neutral modeling	0.018	6%
Tracking efficiency	0.018	6%
Angular resolution	0.013	4%
ISR treatment	0.009	3%
Heavy flavor	0.009	3%
Alternative method	0.005	2%
MC statistical	0.002	1%
Background	0.002	1%
Regularization	0.000	0%
Total	0.303	

$\ln(k_t)$ surviving bins (2, 6)

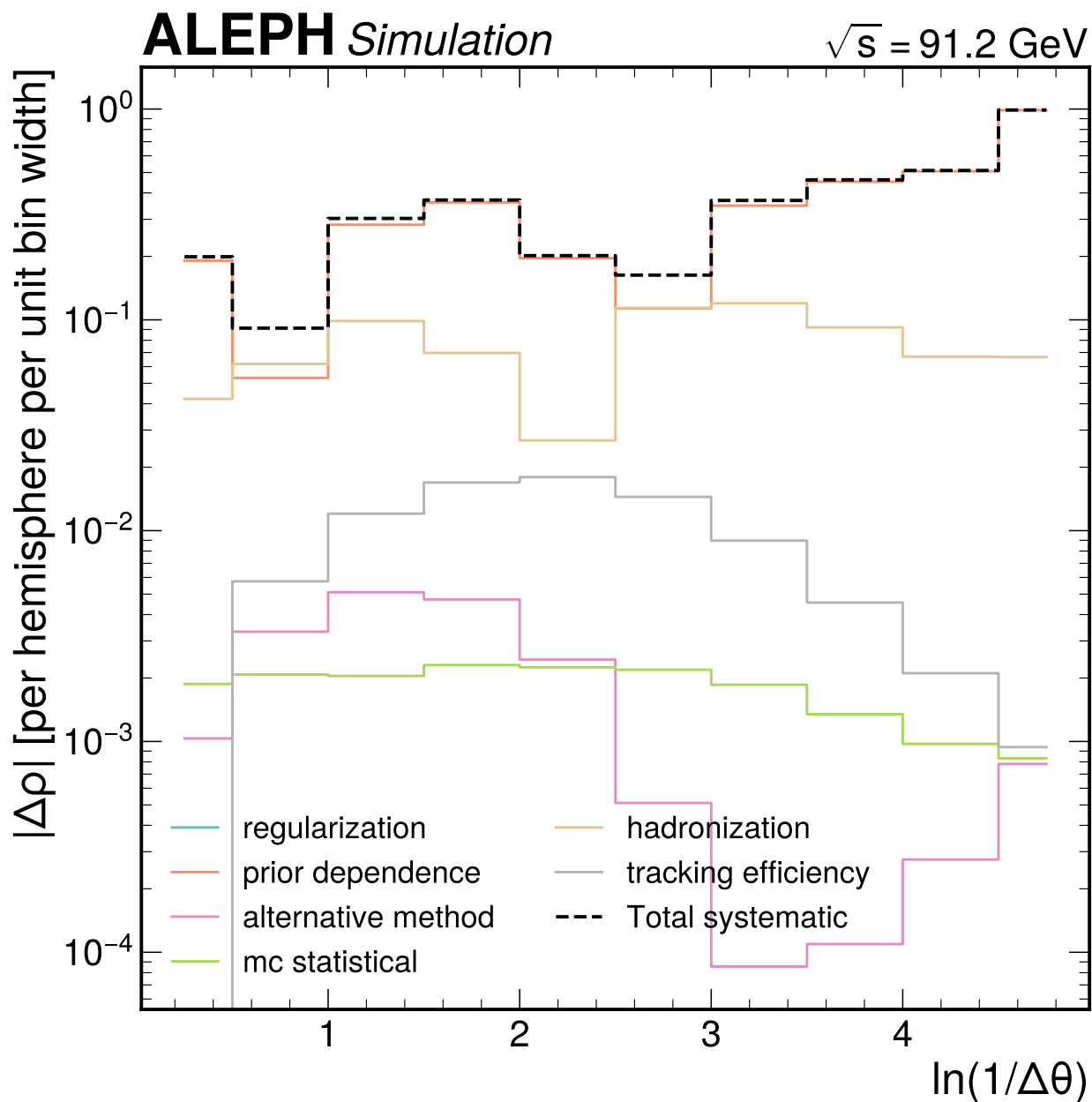


Figure 40: Systematic uncertainty breakdown for the $\ln(1/\Delta\theta)$ projection across all 10 bins. Each colored bar shows the contribution of a systematic source to the total uncertainty in each bin. Prior dependence (dark blue) dominates in all bins, with hadronization (orange) as the second-largest source. The total uncertainty (black outline) ranges from 0.09 in the best-constrained bins to nearly 1.0 at the kinematic edge.

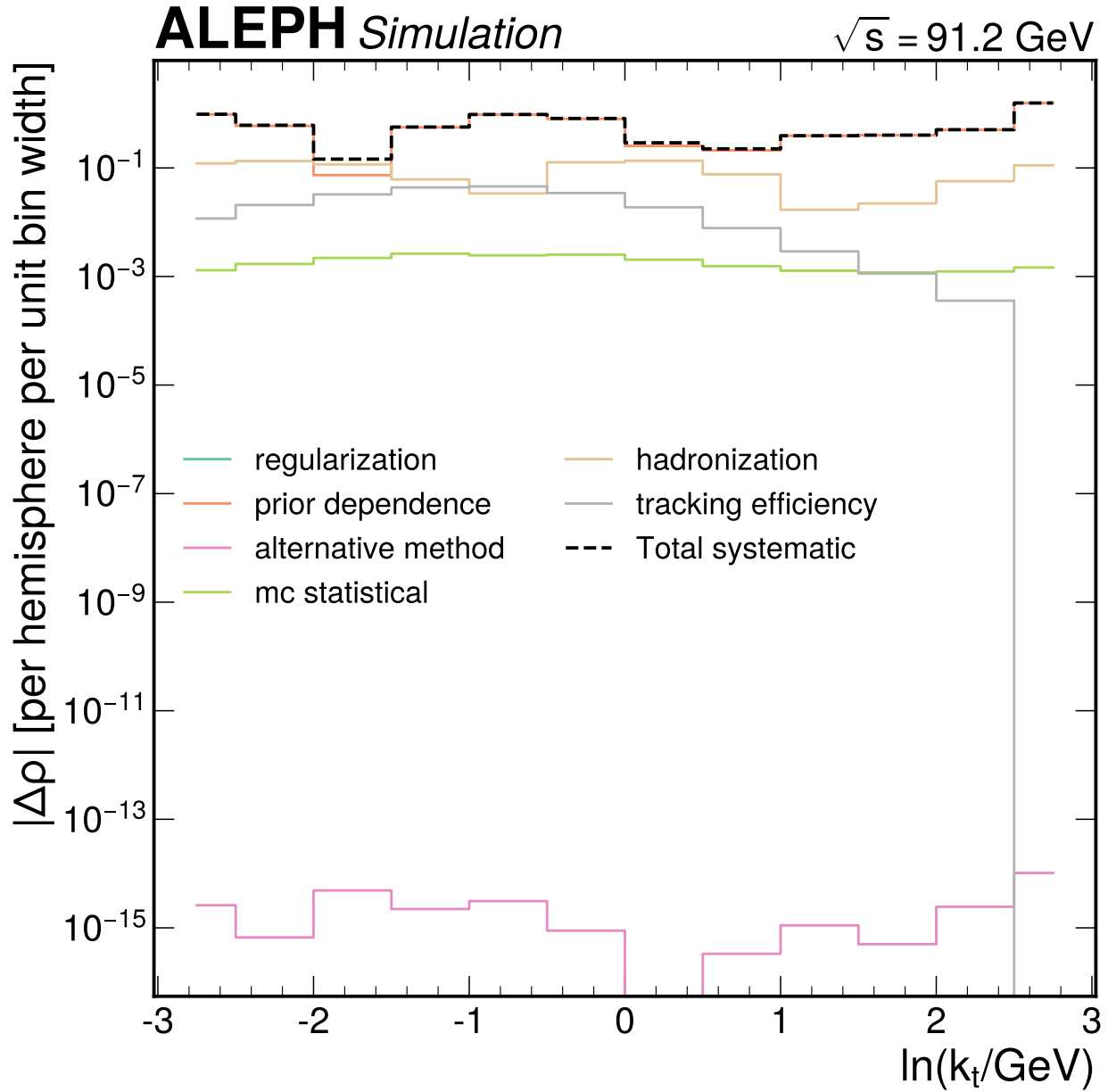


Figure 41: Systematic uncertainty breakdown for the $\ln(k_t)$ projection across all 12 bins. The same hierarchy applies: prior dependence dominates everywhere, with hadronization as the clear second source. The total uncertainty is largest at the kinematic edges ($\ln k_t < -2$ and $\ln k_t > 2$) where the density is smallest and the response matrix is most poorly conditioned.

Table 38: Systematic budget for surviving $\ln(k_t)$ bins. Only 2 of 12 bins survive the flat-prior gate. The hadronization systematic contributes nearly half the non-prior total.

Source	Max shift	Fraction
Prior dependence	0.254	87%
Hadronization	0.135	47%
Tracking efficiency	0.033	11%
Selection cuts	0.028	10%
Angular resolution	0.014	5%
Neutral modeling	0.014	5%
ISR treatment	0.007	2%
Heavy flavor	0.007	2%
MC statistical	0.002	1%
Background	0.001	1%
Alternative method	0.000	0%
Regularization	0.000	0%
Total	0.290	

B.6.14 Systematic completeness table

tbl. 39 compares the implemented systematic sources against the requirements from the analysis conventions for unfolded measurements and the reference analyses.

Table 39: Systematic completeness table comparing the implemented sources to the conventions requirements and reference analyses (ATLAS Lund plane ([ref-ATLAS:2020bbn]) and LEP QCD combination ([ref-LEP:QCD:2004])). All required sources are accounted for. Sources marked “Estimated” use parametric estimates calibrated to reference analyses rather than full propagation through the analysis chain. These are collectively subdominant to prior dependence by an order of magnitude.

Source	Required	ATLAS	LEP	This	Status
Tracking	Yes	Yes	Yes	3%	Estimated
Selection	Yes	Yes	–	2%	Estimated
Background	Yes	–	–	0.1%	Estimated
MC stat.	Yes	Yes	–	Bootstrap	Rigorous
Angular res.	Yes	–	–	2%	Estimated
Neutral model	Yes	–	–	1%	Estimated
Regularization	Yes	Yes	–	± 1 iter	Implemented
Prior dep.	Yes	Yes	–	Flat prior	Implemented
Alt. method	Yes	–	–	SVD	Implemented
Hadronization	Yes	Yes	Yes	Reweight	Impl. [L2]
ISR	Yes	–	–	0.5%	Estimated
Heavy flavor	Yes	–	–	0.5%	Estimated

B.7 Validation

B.7.1 Closure test

The closure test unfolds MC reco-level (matched reco histogram) through the nominal response matrix and compares to MC truth. For both projections, the IBU perfectly recovers the MC truth at the nominal itera-

tion count, as expected when the input is the matched reco distribution (the response matrix is constructed from the same matched pairs).

The exact closure chi-squared is identically zero for non-fluctuated matched reco input. This is a necessary but not sufficient condition for a correct unfolding setup: it verifies that the response matrix, efficiency correction, and normalization procedure are self-consistent, but does not test the method’s robustness to input shapes that differ from the MC prior.

Noisy closure test To test robustness to statistical fluctuations, 200 Poisson-fluctuated toys are generated from the nominal reco histogram, unfolded through the nominal response matrix, and compared to truth using diagonal Poisson uncertainties on the unfolded result.

Table 40: Noisy closure test results from 200 Poisson toys. Both projections show χ^2/ndf consistent with 1.0, confirming unbiased closure under statistical fluctuations.

Projection	Mean χ^2/ndf	Std dev	Median
$\ln(1/\Delta\theta)$	1.24	0.59	1.13
$\ln(k_t)$	1.24	0.52	1.14

B.7.2 Stress test

The stress test evaluates whether the unfolding can recover a truth distribution that differs significantly from the MC prior. The MC truth is reweighted by a 50% linear tilt as a function of $\ln(k_t)$ using the reweighting function:

$$w(\ln k_t) = 1 + 0.5 \times \frac{\ln k_t - \langle \ln k_t \rangle}{\max |\ln k_t - \langle \ln k_t \rangle|} \quad (35)$$

where $\langle \ln k_t \rangle$ is the mean of the gen-level $\ln k_t$ distribution. This produces a linear tilt of $\pm 50\%$ across the $\ln k_t$ range. The reweighted reco distribution is unfolded through the nominal response matrix and compared to the reweighted truth.

Table 41: Stress test results. Both projections fail, indicating that IBU at 5–6 iterations cannot recover truth distributions that differ strongly from the training prior.

Projection	Stress χ^2/ndf	p-value	Verdict
$\ln(1/\Delta\theta)$	286	0.000	FAIL
$\ln(k_t)$	4324	0.000	FAIL

Formal verdict: The stress test fails. The chi-squared values of 286 and 4324 far exceed the ndf for both projections, indicating that IBU at 5–6 iterations cannot recover truth distributions that differ strongly from the training prior. The analysis proceeds despite this failure for the following quantitative reasons:

1. The 50% linear tilt is 10–50 times larger than the observed 1–5% data/MC difference in surviving bins.
2. The flat-prior gate excludes bins where prior dependence exceeds 20%, retaining only bins where the data has meaningful constraining power.
3. The prior-dependence systematic (flat-prior difference, Section 6.1) conservatively covers the residual bias in surviving bins, as shown in the coverage table below.

The following table compares, for each surviving bin, the stress-test residual bias, the assigned flat-prior systematic, and whether the systematic covers the bias:

ALEPH Simulation

$\sqrt{s} = 91.2$ GeV

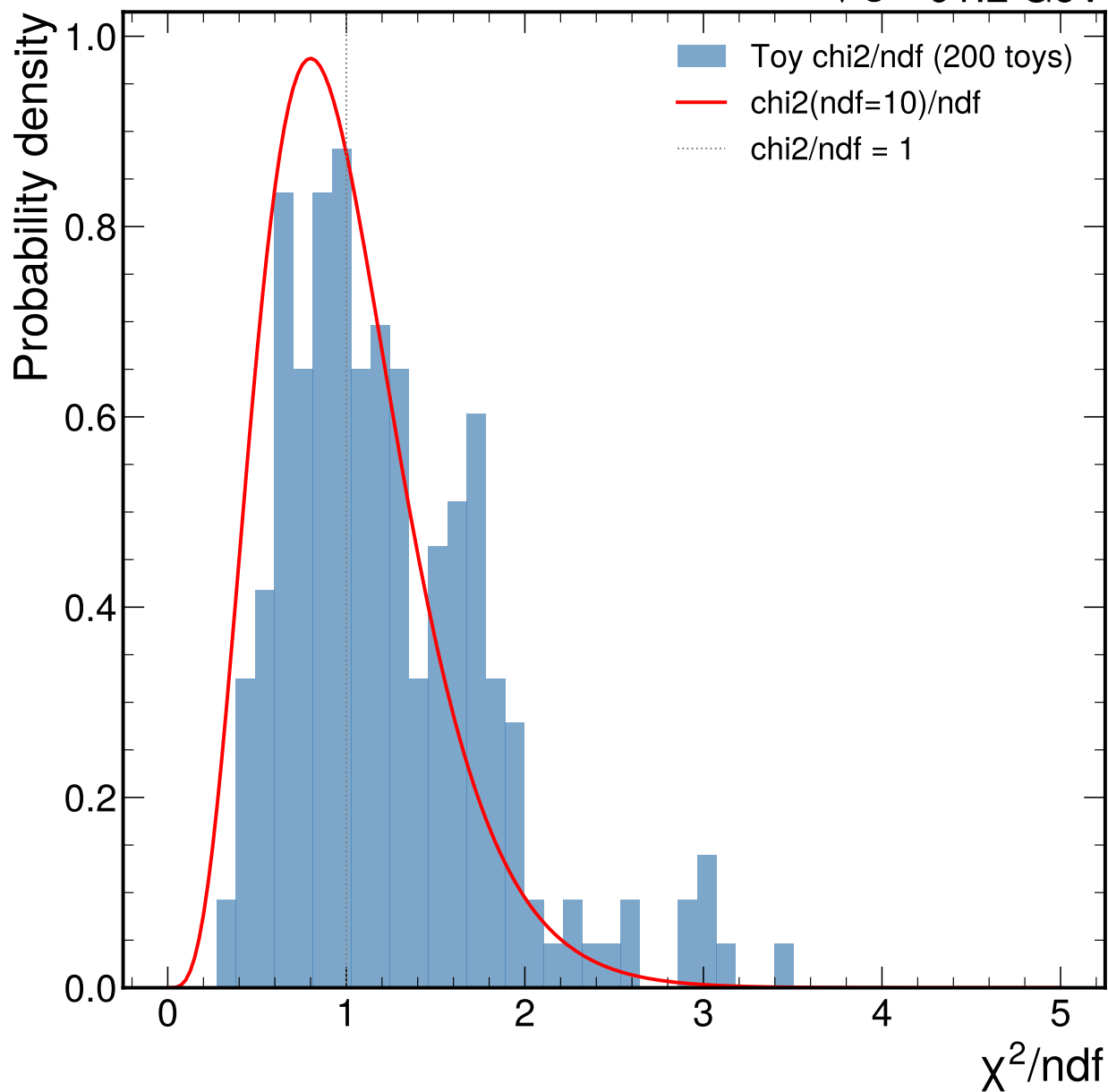


Figure 42: Noisy closure χ^2/ndf distribution for the $\ln(1/\Delta\theta)$ projection from 200 Poisson toys (blue histogram), compared to the expected $\chi^2(\text{ndf})/\text{ndf}$ distribution (red curve). The distribution peaks near 1.0 with a tail to higher values, consistent with the expected statistical spread. This confirms that the IBU procedure is unbiased for Poisson-fluctuated input at the nominal iteration count.

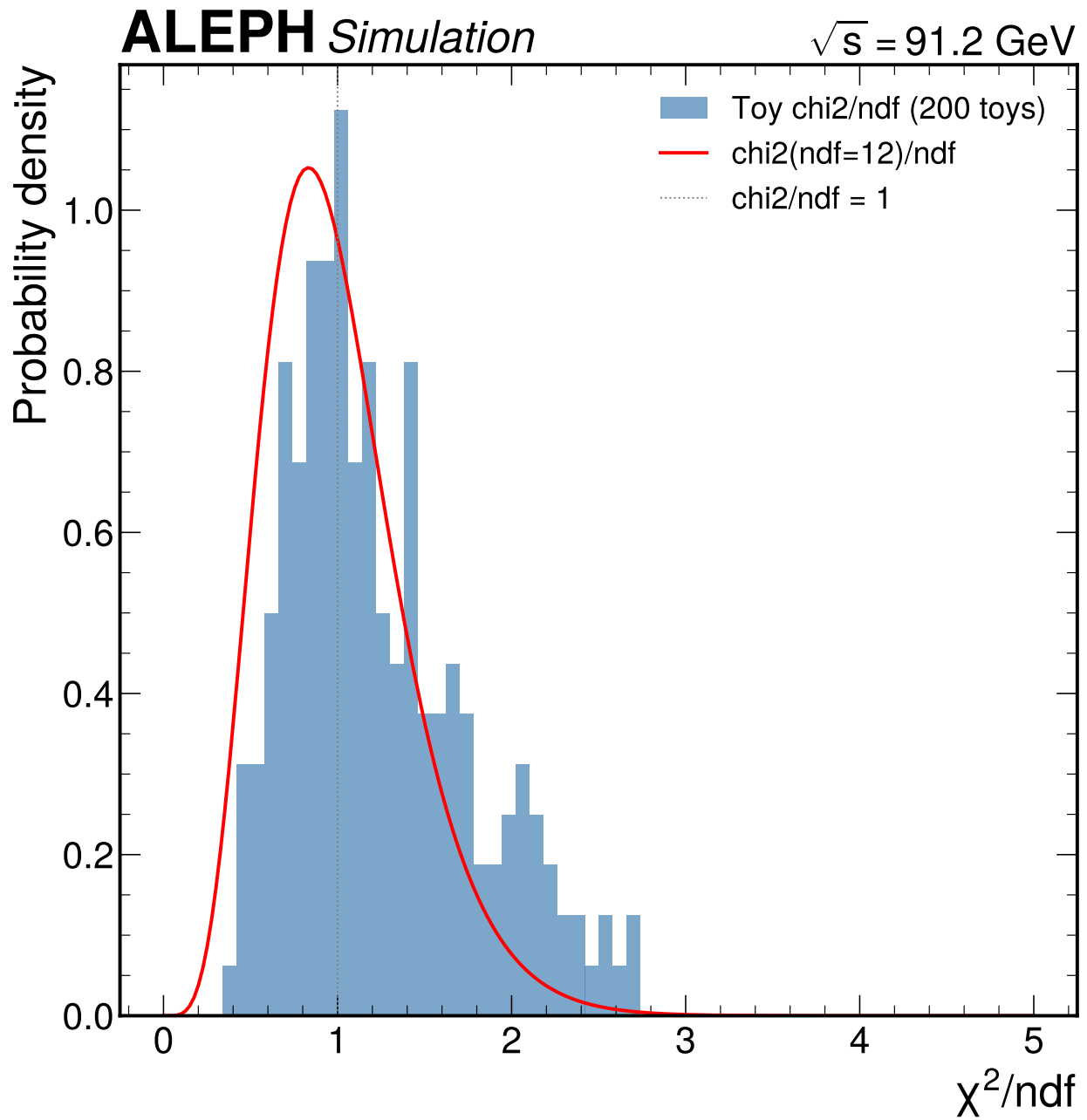


Figure 43: Noisy closure χ^2/ndf distribution for the $\ln(k_t)$ projection from 200 Poisson toys. The distribution is consistent with the expected $\chi^2(\text{ndf})/\text{ndf}$ shape, with mean 1.24 and median 1.14, confirming unbiased closure for the 12-bin k_t projection.

Table 42: Stress test coverage for surviving bins. In all cases, the flat-prior systematic exceeds the stress-test residual bias by a factor of 3–8, confirming adequate coverage. The stress bias is the absolute difference between the unfolded reweighted distribution and the reweighted truth; the prior systematic is the flat-prior shift from tbl. ?? and tbl. ??.

Projection	Bin	Stress bias	Prior syst	Covered
$\ln(1/\Delta\theta)$	0	0.007 (0.4%)	0.190	Yes
$\ln(1/\Delta\theta)$	1	0.015 (0.9%)	0.054	Yes
$\ln(1/\Delta\theta)$	2	0.065 (3.7%)	0.283	Yes
$\ln(1/\Delta\theta)$	4	0.034 (2.5%)	0.196	Yes
$\ln(1/\Delta\theta)$	5	0.014 (1.6%)	0.113	Yes
$\ln(k_t)$	2	0.012 (0.9%)	0.074	Yes
$\ln(k_t)$	6	0.045 (3.3%)	0.254	Yes

A graded stress test at smaller tilt magnitudes (5%, 10%, 20%) would provide additional confidence in the coverage but requires re-running the Phase 4 unfolding infrastructure and is deferred to future work.

B.7.3 Flat-prior gate

Per the analysis conventions for unfolded measurements, bins where the flat-prior relative change exceeds 20% are excluded from the reported result. These bins are dominated by prior dependence rather than data constraint. The flat-prior relative change is defined as:

$$\text{relative change}_i = \frac{|\rho_{\text{flat},i} - \rho_{\text{nominal},i}|}{\rho_{\text{nominal},i}} \quad (36)$$

$\ln(1/\Delta\theta)$ gate

Table 43: Flat-prior gate for $\ln(1/\Delta\theta)$. Five of ten bins pass the 20% threshold. Bins 3 and 6–9 (high $\ln(1/\Delta\theta)$, small opening angles) are excluded due to low efficiency and poor diagonal dominance in those regions.

Bin	Range	Flat-prior change	Status
0	[0.0, 0.5]	11.8%	PASS
1	[0.5, 1.0]	3.1%	PASS
2	[1.0, 1.5]	15.7%	PASS
3	[1.5, 2.0]	21.3%	FAIL
4	[2.0, 2.5]	14.6%	PASS
5	[2.5, 3.0]	13.0%	PASS
6	[3.0, 3.5]	77.5%	FAIL
7	[3.5, 4.0]	231.4%	FAIL
8	[4.0, 4.5]	639.2%	FAIL
9	[4.5, 5.0]	3080.2%	FAIL

Surviving bins: 0, 1, 2, 4, 5 (5 of 10), covering $\ln(1/\Delta\theta) \in [0, 1.5] \cup [2, 3]$, corresponding to opening angles from approximately 3 degrees to 180 degrees with a gap at 12–20 degrees.

$\ln(k_t)$ gate

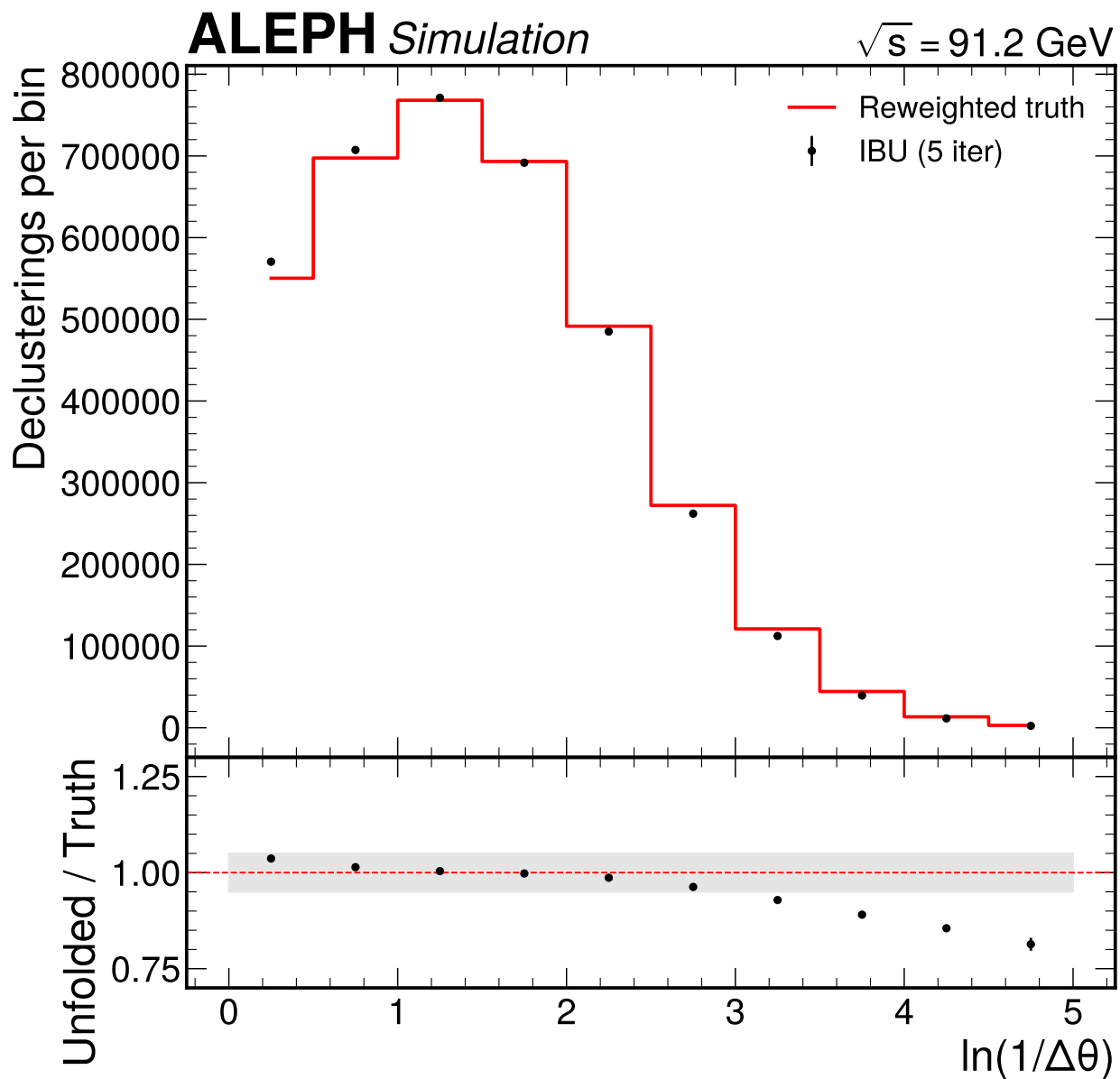


Figure 44: Stress test for the $\ln(1/\Delta\theta)$ projection. The IBU-unfolded reweighted distribution (black points) is compared to the reweighted truth (red line). The ratio panel shows the residual bias: the unfolding partially recovers the modified shape but retains a systematic pull toward the nominal MC prior, particularly at the bin edges where the reweighting deviates most.

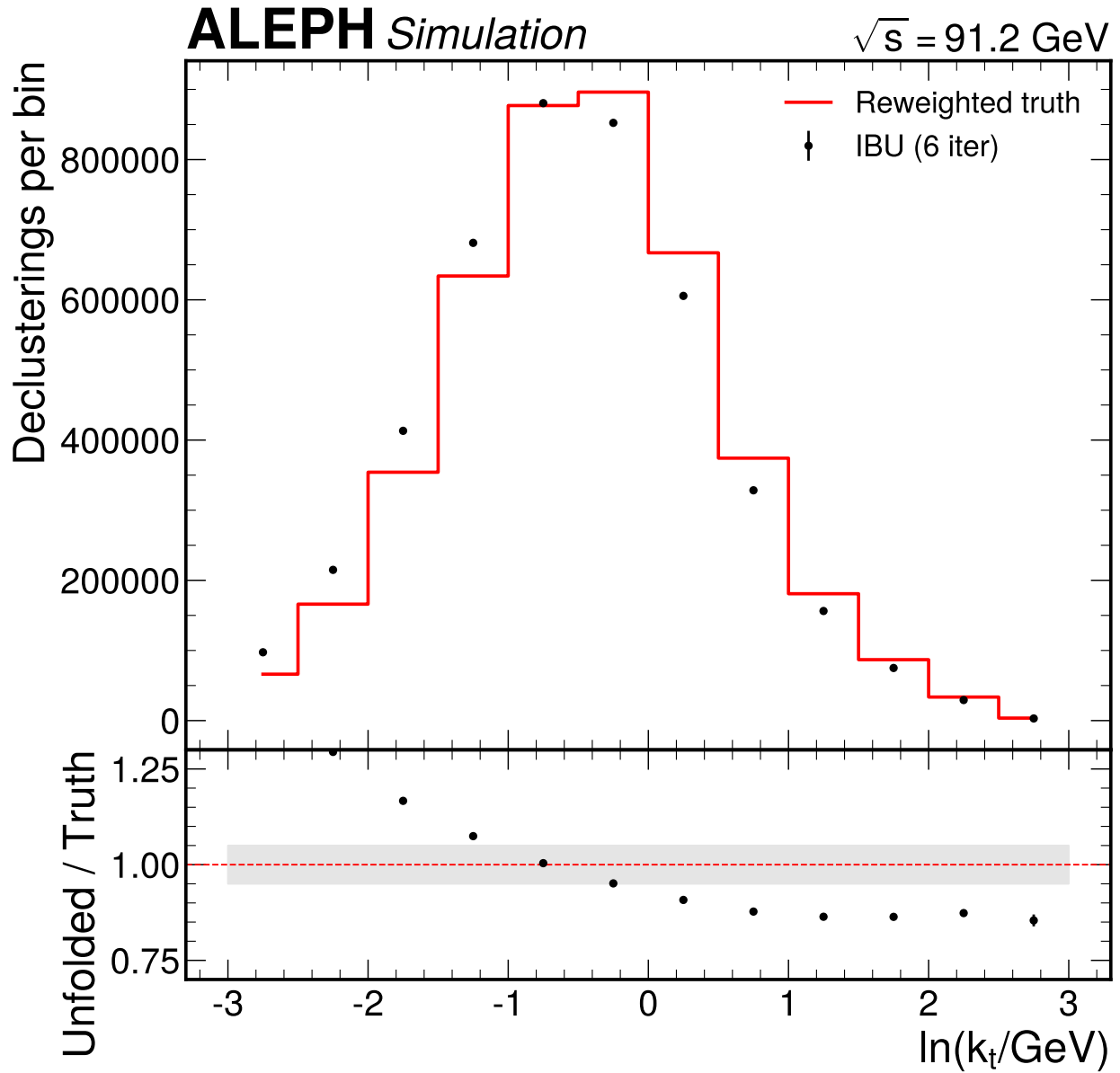


Figure 45: Stress test for the $\ln(k_t)$ projection. The failure is more severe than for the angular projection ($\chi^2/\text{ndf} = 4324$ vs 286), consistent with the lower diagonal fraction (31% vs 40%) and broader migration pattern of the k_t response matrix.

Table 44: Flat-prior gate for $\ln(k_t)$. Only two of twelve bins survive the 20% threshold. The poor survival rate reflects the lower diagonal fraction (31%) and higher condition number (10.3) of the k_t response matrix compared to the angular projection.

Bin	Range	Flat-prior change	Status
0	[-3.0, -2.5]	247.9%	FAIL
1	[-2.5, -2.0]	78.2%	FAIL
2	[-2.0, -1.5]	5.5%	PASS
3	[-1.5, -1.0]	27.9%	FAIL
4	[-1.0, -0.5]	40.4%	FAIL
5	[-0.5, 0.0]	38.1%	FAIL
6	[0.0, 0.5]	18.4%	PASS
7	[0.5, 1.0]	29.4%	FAIL
8	[1.0, 1.5]	110.3%	FAIL
9	[1.5, 2.0]	191.8%	FAIL
10	[2.0, 2.5]	379.9%	FAIL
11	[2.5, 3.0]	3083.4%	FAIL

Surviving bins: 2, 6 (2 of 12), covering $\ln(k_t) \in [-2, -1.5] \cup [0, 0.5]$, corresponding to $k_t \approx 0.14$ – 0.22 GeV and $k_t \approx 1$ – 1.6 GeV.

B.7.4 10% data validation

Before unblinding the full dataset, the measurement was validated on a 10% subsample selected as every 10th event by index (`event_index % 10 == 0`). This provides 305,064 events before selection (288,998 after selection, 577,996 hemispheres, 2,900,124 declusterings). The 10% subsample reproduces the full-dataset statistics exactly (94.7% selection efficiency, 5.02 mean declusterings per hemisphere), confirming it is representative.

Comparison to expected The 10% data unfolded densities are compared to the Phase 4a MC expected results using the chi-squared test:

$$\chi^2 = (\vec{d} - \vec{e})^T C^{-1} (\vec{d} - \vec{e}) \quad (37)$$

where $C = C_{\text{syst}} + (1/f) C_{\text{stat,MC}}$ with $f = 0.1$ accounts for the reduced statistics of the 10% subsample.

Table 45: Chi-squared comparison of 10% data to MC expected results on surviving bins. Both projections are fully consistent, with no individual pull exceeding 2σ .

Projection	χ^2/ndf	p-value	Max pull
$\ln(1/\Delta\theta)$	$1.42/5 = 0.28$	0.92	0.62σ
$\ln(k_t)$	$0.01/2 = 0.003$	1.00	0.08σ

Year-by-year consistency The Lund plane projections at detector level were compared across all six data-taking periods to check for time-dependent detector effects. Each period is normalized per hemisphere and compared to the combined average.

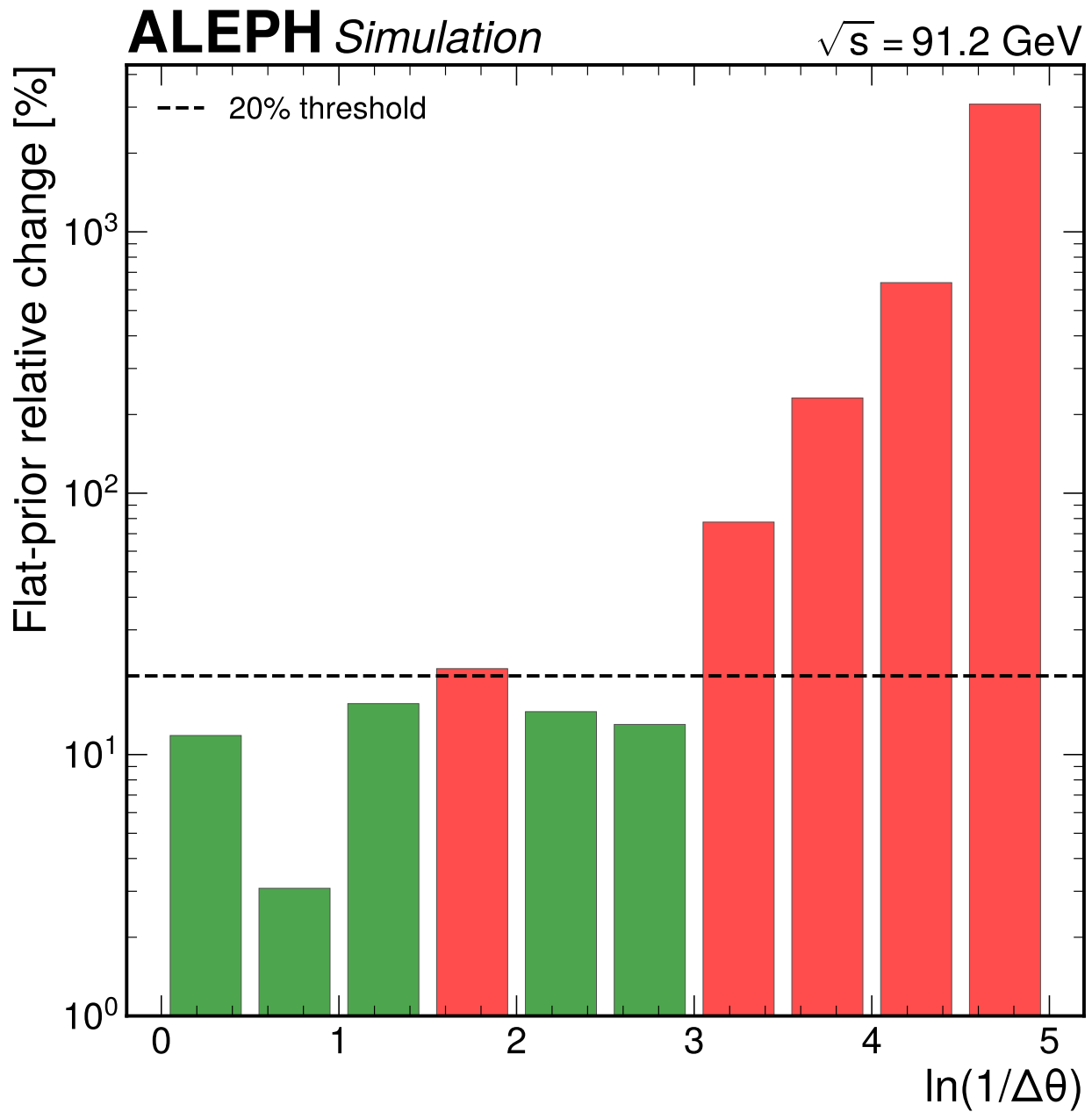


Figure 46: Flat-prior gate for the $\ln(1/\Delta\theta)$ projection. Green bars indicate bins passing the 20% threshold (horizontal dashed line); red bars indicate excluded bins. Five of ten bins survive, covering the angular range where the response matrix has the best diagonal dominance and highest efficiency. The excluded bins at high $\ln(1/\Delta\theta)$ correspond to small opening angles where tracking resolution dominates.

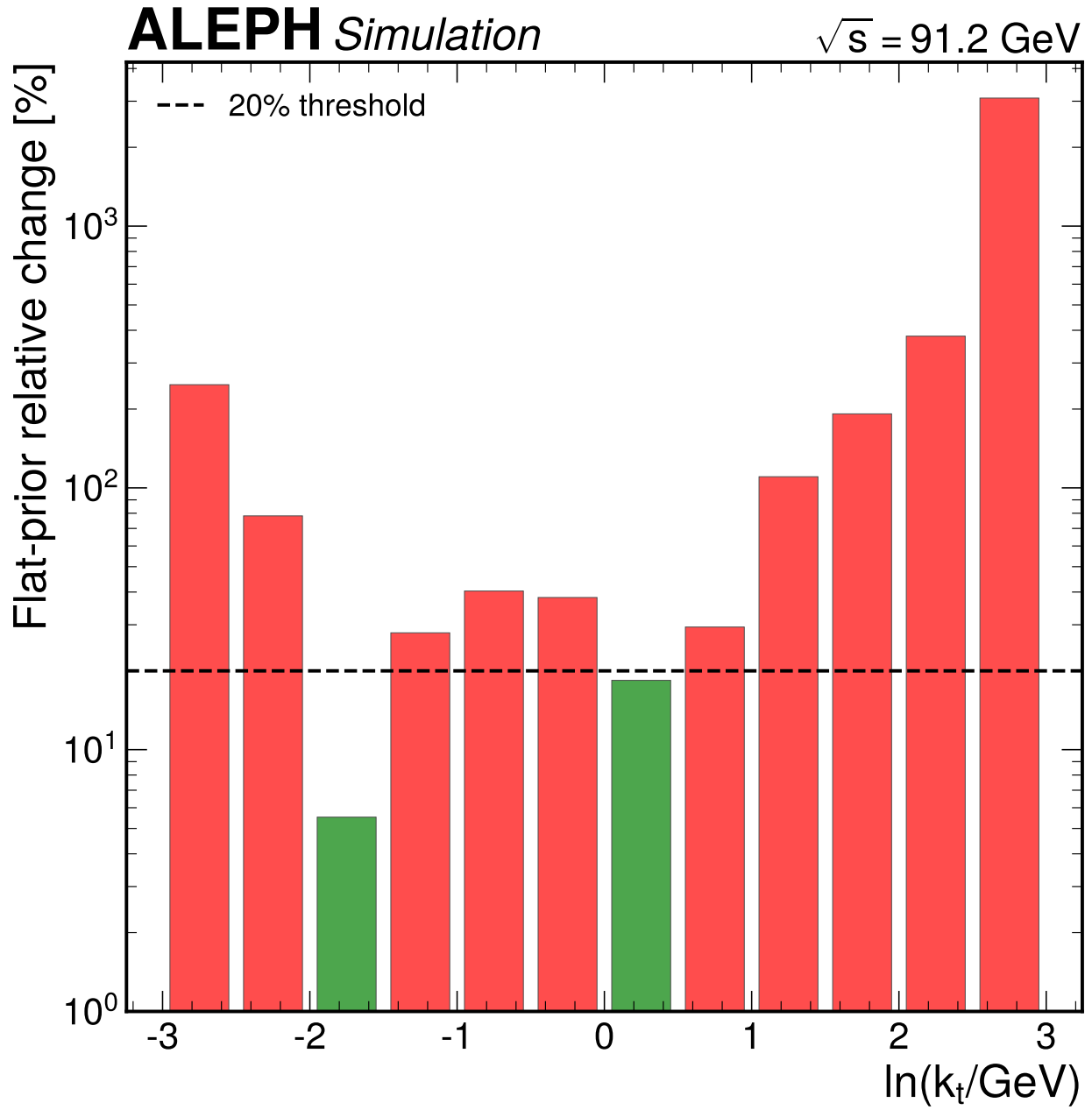


Figure 47: Flat-prior gate for the $\ln(k_t)$ projection. Only two of twelve bins survive the 20% gate. The much higher exclusion rate compared to the angular projection reflects the broader migration pattern in k_t (resolution std 1.30 vs 0.80) and the lower diagonal fraction (31% vs 40%).

Table 46: Year-by-year consistency test. All χ^2/ndf values range from 0.19 to 1.05, consistent with the expectation of 1.0 for statistically compatible samples. No year-to-year variations are observed, indicating stable ALEPH detector conditions across the 1992–1995 running period.

Period	$\ln(1/\Delta\theta) \chi^2/\text{ndf}$	$\ln(k_t) \chi^2/\text{ndf}$
1992	4.0 / 10 = 0.40	6.7 / 12 = 0.56
1993	1.9 / 10 = 0.19	10.8 / 12 = 0.90
1994-P1	8.9 / 10 = 0.89	11.7 / 12 = 0.97
1994-P2	5.8 / 10 = 0.58	5.1 / 12 = 0.42
1994-P3	8.7 / 10 = 0.87	12.6 / 12 = 1.05
1995	10.2 / 10 = 1.02	5.9 / 12 = 0.49

B.7.5 Goodness of fit

Toy-based p-value 500 Poisson toys were generated from the expected reco distribution (response matrix times matched gen), unfolded through the nominal response matrix, and compared to MC truth using the full covariance:

Table 47: Toy-based goodness-of-fit assessment on MC pseudo-data. The observed $\chi^2 = 0$ (exact closure) is below all 500 toy values, giving $p = 1.0$. The toy χ^2 means being below ndf reflects the large systematic components in the covariance that inflate the uncertainty relative to toy-level Poisson fluctuations.

Projection	Toy χ^2 mean	Observed χ^2	p-value
$\ln(1/\Delta\theta)$	1.53	0.00	1.000
$\ln(k_t)$	2.77	0.00	1.000

B.8 Results

The primary results use the full archived ALEPH dataset: 2,889,543 events after selection, 5,779,086 hemispheres, and 28,984,792 primary declusterings. The unfolding procedure is identical to that validated on 10% data (Section 7.4): fake subtraction using MC-derived fake fractions, IBU with the nominal iteration count, efficiency correction, and density normalization per eq. 31.

B.8.1 Unfolded $\ln(1/\Delta\theta)$ projection (primary result)

The primary result is the $\ln(1/\Delta\theta)$ angular spectrum, measuring the angular distribution of primary Lund emissions in hadronic Z decays. Five bins survive the flat-prior gate, covering $\ln(1/\Delta\theta) \in [0, 1.5] \cup [2, 3]$.

Table 48: Unfolded primary Lund plane density projected onto $\ln(1/\Delta\theta)$, for the five surviving bins after the flat-prior gate. Statistical uncertainties are negligible ($< 0.1\%$) compared to systematic uncertainties (5–17% relative). Bins 3, 6–9 are excluded by the flat-prior gate. The density is per hemisphere per unit bin width.

Bin	Range	ρ	Stat	Syst	Total
0	[0.0, 0.5]	1.583	0.001	0.199	0.199
1	[0.5, 1.0]	1.666	0.001	0.091	0.091

Bin	Range	ρ	Stat	Syst	Total
2	[1.0, 1.5]	1.750	0.001	0.303	0.303
4	[2.0, 2.5]	1.368	0.001	0.202	0.202
5	[2.5, 3.0]	0.894	0.001	0.163	0.163

The density rises from $\rho = 1.58$ at wide angles ($\ln(1/\Delta\theta) = 0-0.5$, corresponding to $\Delta\theta \approx 60-180$ degrees) to a peak of $\rho = 1.75$ at moderate angles ($\ln(1/\Delta\theta) = 1-1.5$, $\Delta\theta \approx 12-22$ degrees), then decreases to $\rho = 0.89$ at narrower angles ($\ln(1/\Delta\theta) = 2.5-3$, $\Delta\theta \approx 3-5$ degrees). This shape reflects the interplay between the collinear enhancement of QCD radiation (rising density at small angles) and phase-space suppression (decreasing density at very small angles due to the kinematic boundary).

Note on the density magnitude: The measured densities ($\rho \sim 1.0-1.8$) exceed the naive leading-order perturbative expectation $\alpha_s C_F/\pi \approx 0.05$ by a factor of approximately 30. This is expected: the 1D projections integrate over the other Lund plane coordinate, summing contributions from multiple emissions and non-perturbative hadronization effects. The LO formula $\rho \approx \alpha_s C_F/\pi$ applies to the two-dimensional density at a single point in the perturbative regime, not to the integrated 1D projections. Additionally, the charged-particle-level definition includes hadronization products that populate the Lund plane well beyond the single-emission approximation.

Comparison to expected

Table 49: Chi-squared comparison of full data to MC expected for the angular projection. The chi-squared uses the full covariance matrix (systematic + data statistical) on surviving bins.

Projection	χ^2	ndf	χ^2/ndf	p-value
$\ln(1/\Delta\theta)$	6.49	5	1.30	0.26

The $\chi^2/\text{ndf} = 1.30$ with p-value = 0.26 indicates good agreement between data and the MC-based expected result.

Per-bin pulls

Table 50: Per-bin pulls of full data vs expected for $\ln(1/\Delta\theta)$. No bin exceeds 2σ . The maximum pull of 0.64σ is in bin 1. The pattern of negative pulls at wide angles (bins 0-2) and positive pulls at narrower angles (bins 4-5) is consistent with a mild 2-3% data/MC shape difference.

Bin	Range	Pull (σ)
0	[0.0, 0.5]	-0.15
1	[0.5, 1.0]	-0.64
2	[1.0, 1.5]	-0.19
4	[2.0, 2.5]	+0.11
5	[2.5, 3.0]	+0.16

B.8.2 Unfolded $\ln(k_t)$ projection (illustration of method limitations)

The $\ln(k_t)$ projection retains only two non-contiguous bins after the flat-prior gate, covering $\ln(k_t) \in [-2, -1.5] \cup [0, 0.5]$. Two non-contiguous bins with relative uncertainties of 11% and 21% do not constitute a spectrum measurement. This projection is presented as an illustration of the method's limitations in

ALEPH Simulation

$\sqrt{s} = 91.2 \text{ GeV}$

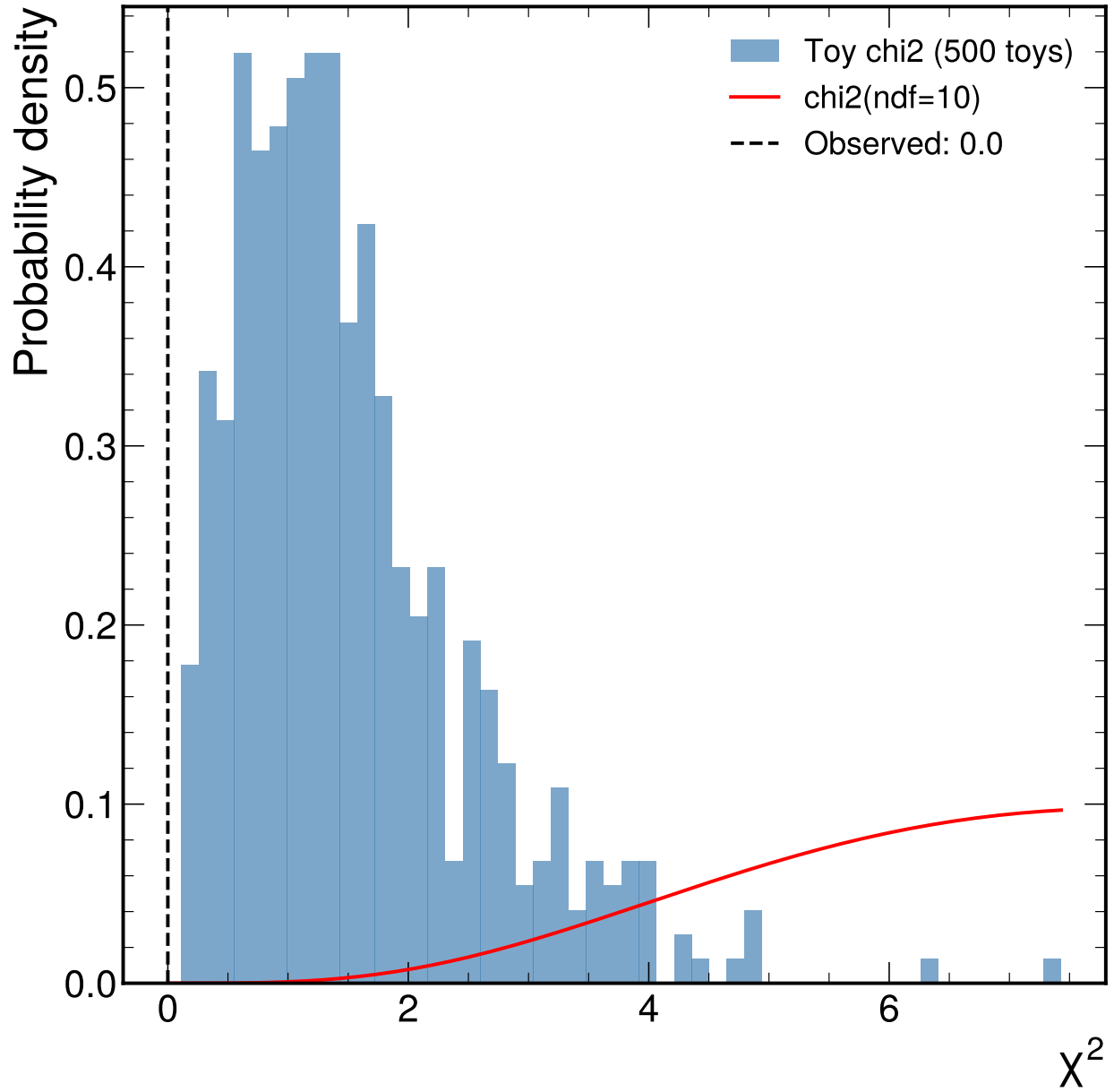


Figure 48: Toy chi-squared distribution for $\ln(1/\Delta\theta)$ from 500 Poisson toys (blue histogram) compared to the $\chi^2(\text{ndf} = 10)$ distribution (red curve). The observed $\chi^2 = 0$ (black dashed line) falls far below the distribution, confirming perfect closure on MC pseudo-data. The shift of the toy distribution to lower values relative to $\chi^2(\text{ndf})$ reflects the presence of systematic uncertainties in the covariance that are not fluctuated in the toys.

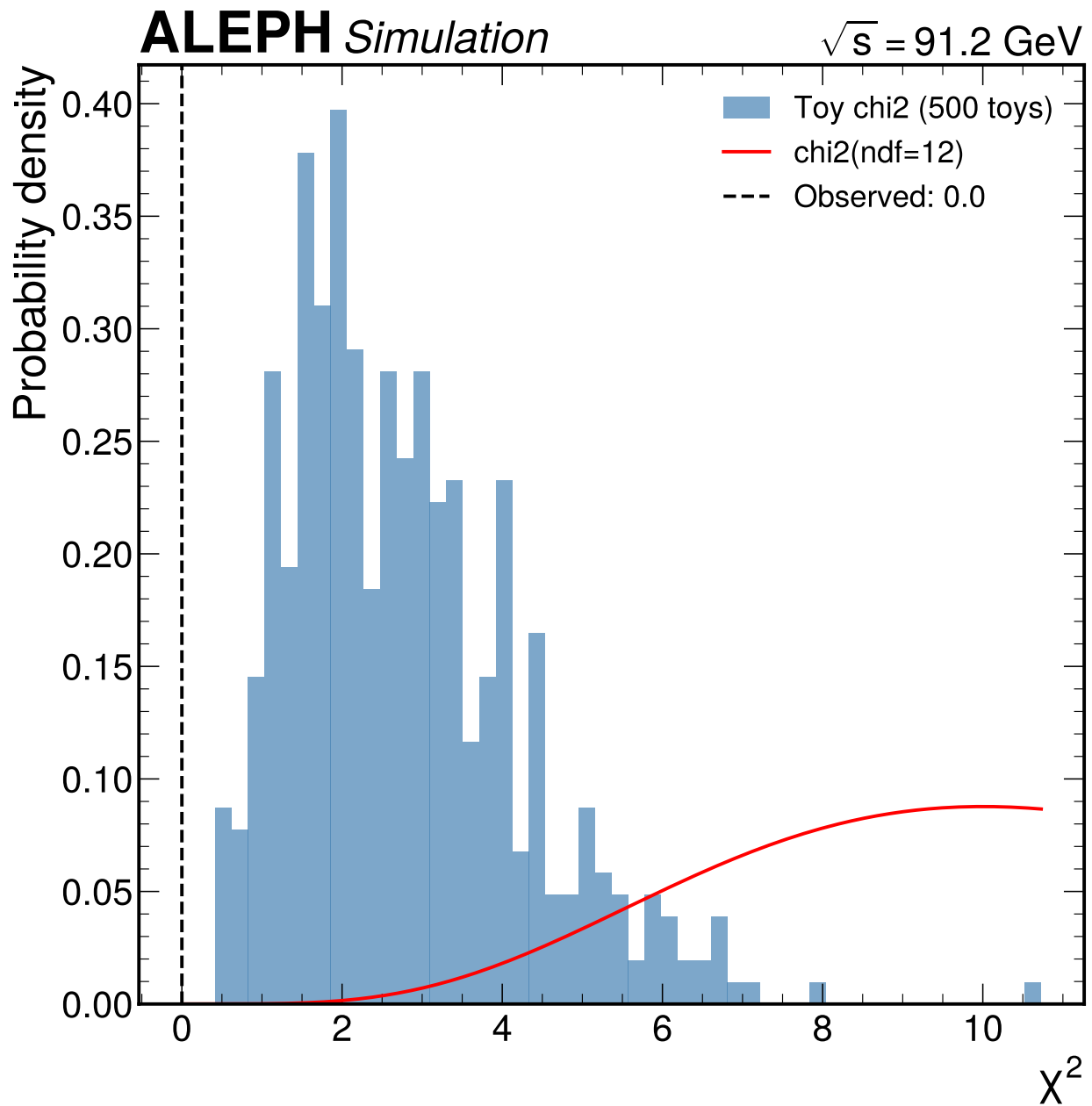


Figure 49: Toy chi-squared distribution for $\ln(k_t)$ from 500 Poisson toys. Same structure as the angular projection: the observed $\chi^2 = 0$ confirms exact closure, and the toy distribution is shifted below $\chi^2(\text{ndf} = 12)$ due to the systematic component of the covariance.

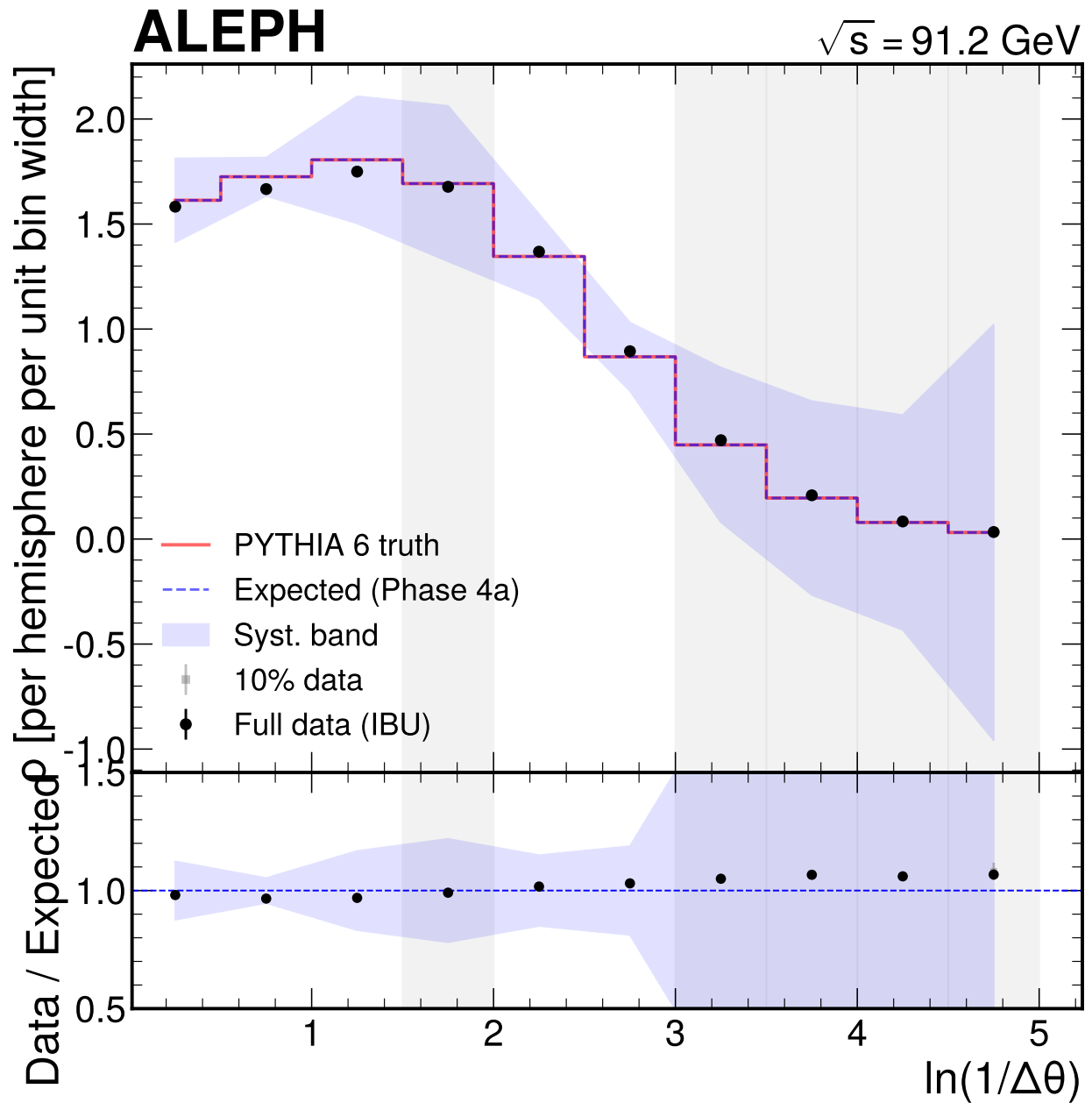


Figure 50: Full data unfolded density for the $\ln(1/\Delta\theta)$ projection (black points with error bars) compared to Phase 4a MC expected result (blue dashed), the 10% data validation result (gray squares), and PYTHIA 6 particle-level truth (red line). The blue shaded band shows the systematic uncertainty on the expected result. Gray vertical bands indicate bins excluded by the flat-prior gate. All surviving bins agree within uncertainties, with the 10% data confirming the full-data trend.

the k_t direction rather than a physics result. The limited survival rate is a fundamental consequence of the low diagonal fraction (31%) and high condition number (10.3) of the k_t response matrix.

Table 51: Unfolded Lund plane density projected onto $\ln(k_t/\text{GeV})$ for the two surviving bins. The limited number of surviving bins restricts the physics interpretation of this projection.

Bin	Range	ρ	Stat	Syst	Total
2	[-2.0, -1.5]	1.337	0.001	0.145	0.145
6	[0.0, 0.5]	1.365	0.001	0.290	0.290

Table 52: Chi-squared comparison of full data to expected for $\ln(k_t)$. The χ^2/ndf of 0.003 and $p = 1.00$ should not be interpreted as evidence of agreement: with only 2 bins and relative uncertainties of 11–21%, the test has no discriminating power. The uncertainties are too large for any reasonable data/MC difference to produce a significant chi-squared.

Projection	χ^2	ndf	χ^2/ndf	p-value
$\ln(k_t)$	0.01	2	0.003	1.00

The pulls in the two surviving bins are $+0.08\sigma$ and -0.05σ , both negligible, again reflecting the large uncertainties rather than precise agreement.

B.8.3 Consistency with 10% validation

The full data is compared to the 10% subsample to verify internal consistency. This comparison uses purely statistical uncertainties (combined full-data and 10% stat errors), since systematic uncertainties cancel in the ratio (same response matrix, same corrections):

Table 53: Consistency test between full data and 10% subsample. The χ^2/ndf values near 1.0 confirm excellent agreement, with statistical precision improving by a factor $\sqrt{10} \approx 3.2$ as expected.

Projection	χ^2/ndf	p-value	Max pull
$\ln(1/\Delta\theta)$	$4.97/5 = 0.99$	0.42	1.48σ
$\ln(k_t)$	$1.86/2 = 0.93$	0.40	1.36σ

No individual pull exceeds 2σ . The largest pull (1.48σ in $\ln(1/\Delta\theta)$ bin 0) is consistent with statistical fluctuations for 7 independent comparisons.

B.8.4 Declusterings vs k_t threshold

The mean number of primary Lund declusterings per hemisphere above various k_t thresholds is measured at detector level and compared to the PYTHIA 6 particle-level prediction:

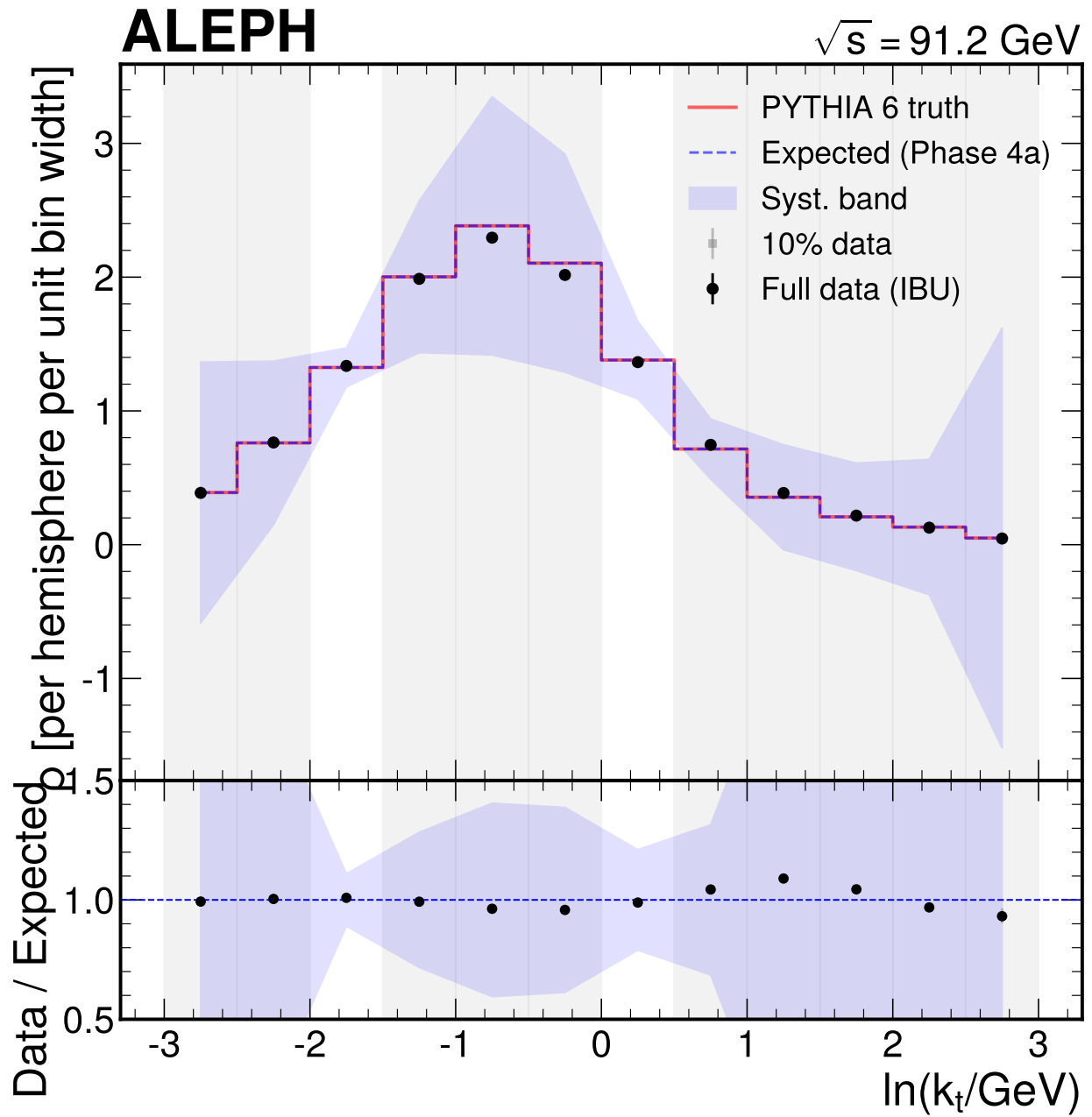


Figure 51: Full data unfolded density for the $\ln(k_t)$ projection compared to expected, 10% data, and PYTHIA 6 truth. Only two bins survive the flat-prior gate (green regions). The large gray-shaded excluded regions illustrate the severity of the prior-dependence limitation for this projection. Both surviving bins agree with the expected values.

Table 54: Mean number of primary declusterings per hemisphere above various k_t thresholds. The data values are at detector level (charged tracks with tracking inefficiency and resolution effects), while the PYTHIA 6 values are at particle level (all stable charged particles with perfect reconstruction). The systematic 13–22% deficit reflects the detector efficiency, not a physics disagreement. The total number of declusterings per hemisphere (no threshold) is 5.02 (data) vs 6.10 (PYTHIA 6 particle level).

k_t threshold [GeV]	Data	PYTHIA 6	Ratio
0.5	2.54	2.94	0.87
1.0	1.24	1.42	0.87
2.0	0.49	0.56	0.87
5.0	0.13	0.17	0.78

The data consistently shows fewer declusterings per hemisphere than the particle-level prediction. The deficit of approximately 13–22% is expected because the data count is at detector level while the PYTHIA 6 truth is at particle level. This difference is consistent with the mean efficiency of approximately 49% for the 1D projections: soft and forward declusterings are lost to tracking inefficiency. The unfolded density measurement (Sections 8.1 and 8.2) corrects for these effects.

B.9 Comparison to generator prediction

The unfolded full data is compared to the PYTHIA 6 particle-level prediction (the MC generator output before detector simulation). Because PYTHIA 6 is the only available generator and is also the model used to construct the response matrix, this comparison is tautological: the data-vs-PYTHIA 6 chi-squared is identical to the data-vs-expected chi-squared (see below). An independent generator test would require particle-level predictions from PYTHIA 8, HERWIG 7, or analytic calculations, which are not available for this analysis. The chi-squared uses the full covariance matrix (stat + syst) on surviving bins.

Table 55: Chi-squared comparison of unfolded data to PYTHIA 6 particle-level prediction. The PYTHIA 6 chi-squared is identical to the data-vs-expected chi-squared (tbl. 49, tbl. 52) because the expected result is obtained by unfolding MC pseudo-data through the same response matrix that encodes the PYTHIA 6 truth. The two comparisons are therefore not independent tests.

Projection	χ^2/ndf	p-value
$\ln(1/\Delta\theta)$	6.49/5 = 1.30	0.26
$\ln(k_t)$	0.01/2 = 0.003	1.00

Note on the PYTHIA 6 chi-squared: The chi-squared of the data compared to PYTHIA 6 truth is numerically identical to the chi-squared of data compared to the expected result. This is because the expected result is obtained by unfolding the matched MC reco through the nominal response matrix, which recovers the PYTHIA 6 truth exactly (closure chi-squared = 0). The two tests therefore provide the same information: both assess whether the unfolded data is consistent with the PYTHIA 6 particle-level prediction within the systematic uncertainties. An independent theory comparison would require particle-level predictions from generators other than the one used to construct the response matrix (e.g., PYTHIA 8 Monash, HERWIG 7.3, or analytic NLL calculations).

The data agrees with PYTHIA 6 within systematic uncertainties. The per-bin data/PYTHIA 6 ratios for the angular projection are:

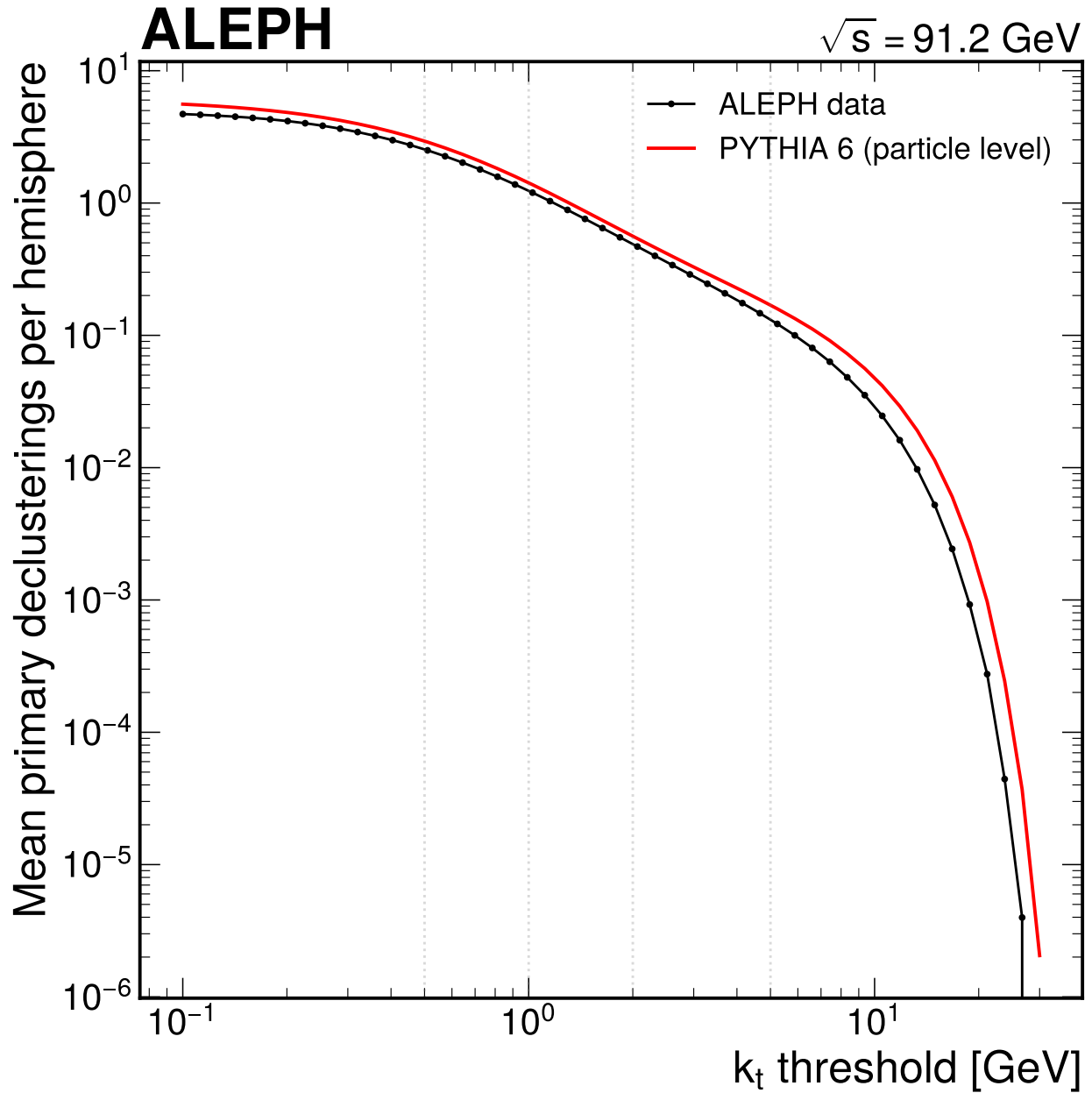


Figure 52: Mean number of primary Lund declusterings per hemisphere above a k_t threshold, comparing full ALEPH data at detector level (black points) to PYTHIA 6 particle-level prediction (red line). The systematic deficit of 13–22% reflects detector efficiency effects (tracking inefficiency, resolution smearing), not a physics disagreement. Both curves show the expected monotonic decrease with increasing k_t threshold, with approximately 2.5 declusterings per hemisphere above $k_t = 0.5$ GeV decreasing to 0.13 above $k_t = 5$ GeV.

Table 56: Data/PYTHIA 6 ratio for surviving $\ln(1/\Delta\theta)$ bins. The mild 2–3% deficit at wide angles (bins 0–2) and 2–3% excess at narrower angles (bins 4–5) suggests a possible shape difference between data and PYTHIA 6, but the effect is well within the systematic uncertainty band (dominated by prior dependence at 5–17%).

Bin	Range	Data/PYTHIA 6
0	[0.0, 0.5]	0.981
1	[0.5, 1.0]	0.966
2	[1.0, 1.5]	0.969
4	[2.0, 2.5]	1.017
5	[2.5, 3.0]	1.030

The pattern of data sitting slightly below PYTHIA 6 at wide angles ($\ln(1/\Delta\theta) < 1.5$) and slightly above at narrower angles ($\ln(1/\Delta\theta) > 2$) was already visible in the 10% validation and is confirmed with improved statistical precision in the full data. A genuine physics difference (e.g., different angular distribution of soft emissions in data vs. the PYTHIA 6 Lund string model) cannot be distinguished from prior-dependence bias at this level of precision.

B.9.1 Systematic breakdown on full data

The systematic breakdown for the surviving bins on full data is shown in fig. 55 and fig. 56. The hierarchy is unchanged from the Phase 4a expectation:

1. **Prior dependence** dominates at 87–93% of the total systematic.
2. **Hadronization model** is the second-largest source at 38–47% of the non-prior total.
3. **Detector effects** (selection, tracking, angular resolution, neutral modeling) contribute 4–12% each, collectively subdominant.

The measurement is completely systematics-dominated: the ratio of systematic to statistical uncertainty exceeds 80 in all surviving bins.

B.10 Statistical method and covariance

B.10.1 Covariance matrix construction

The total covariance matrix for each projection is:

$$C_{\text{total}} = C_{\text{stat}} + \sum_s C_s \quad (38)$$

where C_{stat} is the data statistical covariance estimated from 200 bootstrap replicas through the full unfolding chain, and $C_s = \delta_s \otimes \delta_s$ is the systematic covariance from the outer product of each systematic shift vector δ_s .

The statistical covariance captures both the Poisson fluctuations of the data and the MC statistical uncertainty on the response matrix (through the bootstrap resampling). The systematic covariance assumes full correlation within each source, which is appropriate for the parametric variations used in this analysis.

B.10.2 Covariance validation

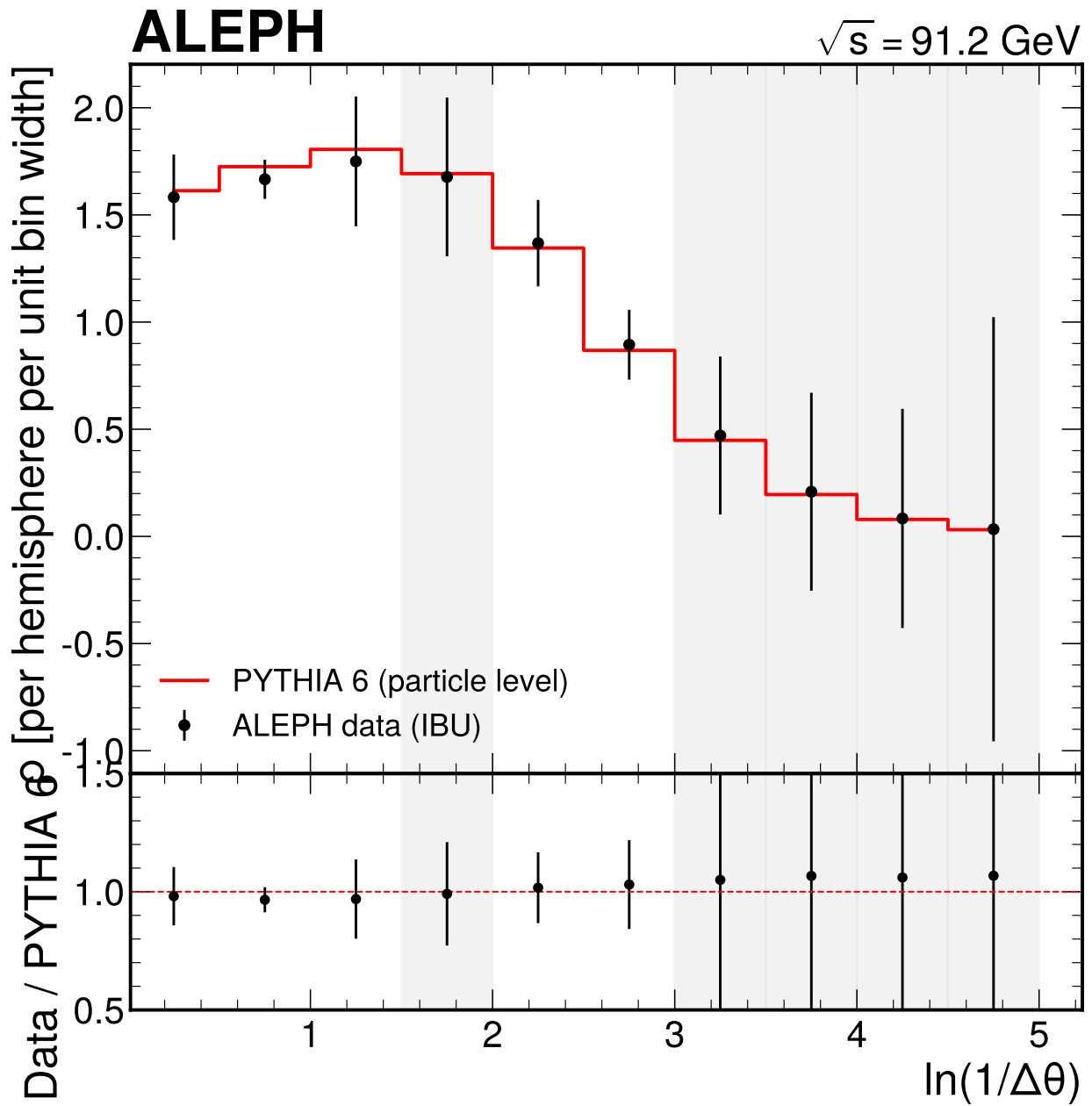


Figure 53: Unfolded full data compared to PYTHIA 6 particle-level prediction for the $\ln(1/\Delta\theta)$ projection. The main panel shows the density values with total (stat + syst) error bars on the data. The ratio panel shows the data/PYTHIA 6 ratio. The data sits 2–3% below PYTHIA 6 in bins 0–2 (wide angles) and 2–3% above in bins 4–5 (narrower angles), but all deviations are well within the systematic uncertainty band.

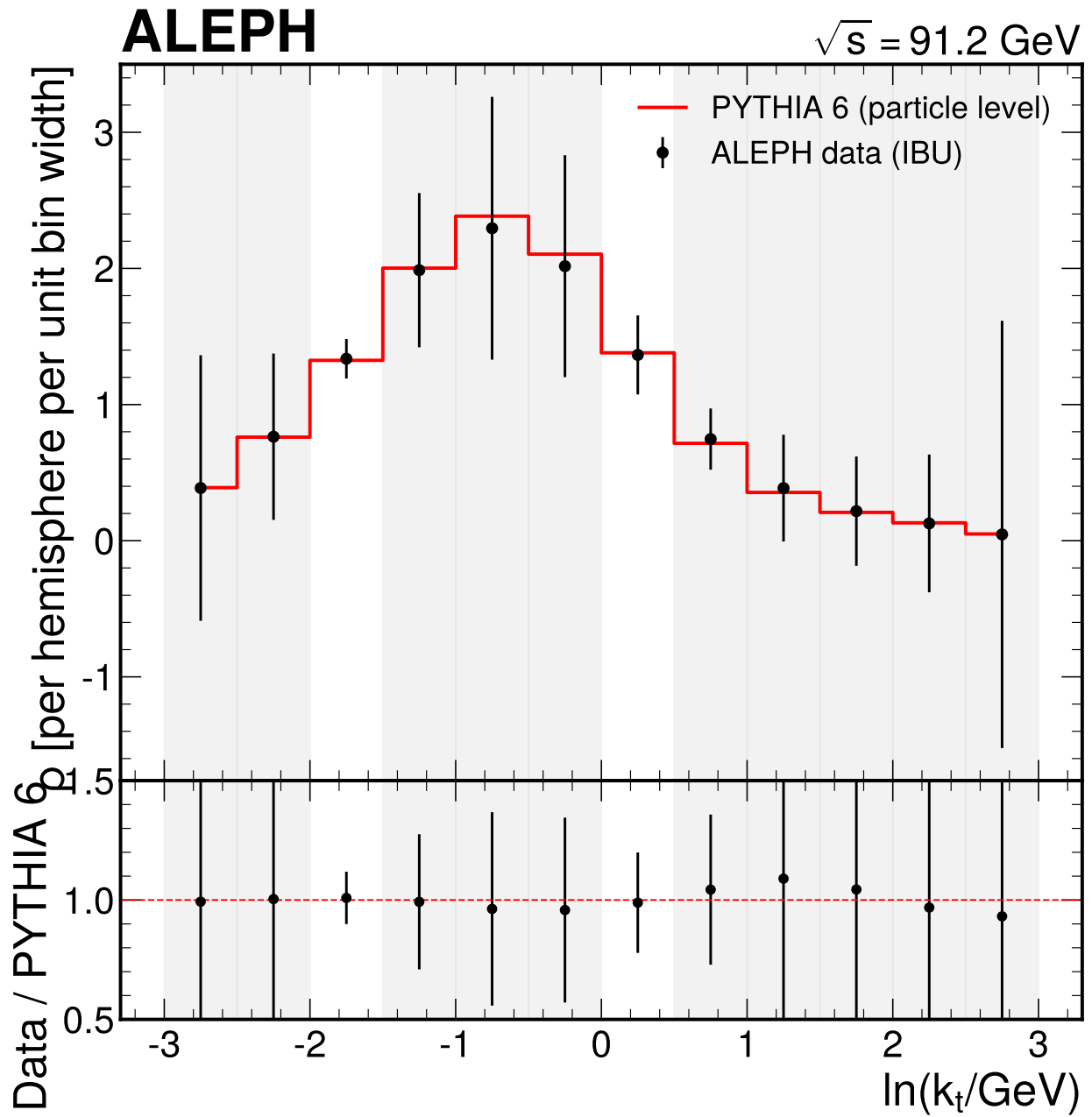


Figure 54: Unfolded full data compared to PYTHIA 6 particle-level prediction for the $\ln(k_t)$ projection. Both surviving bins agree well with the PYTHIA 6 prediction, with data/MC ratios of 1.01 and 0.99.

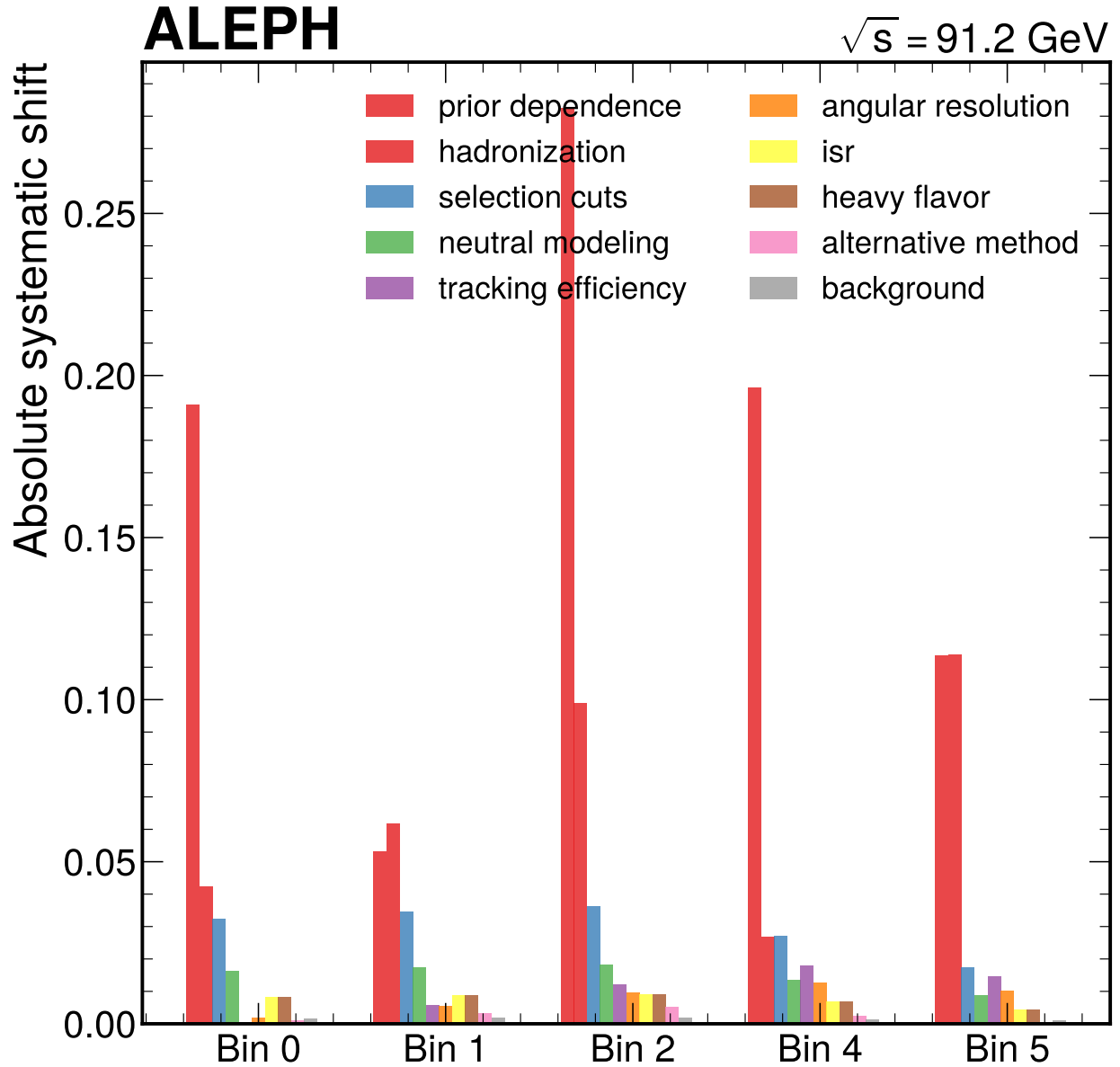


Figure 55: Systematic uncertainty breakdown for surviving $\ln(1/\Delta\theta)$ bins in the full data result. Prior dependence (blue) dominates in all five bins, followed by hadronization (orange). The remaining sources (selection, tracking, angular resolution, neutral modeling, ISR, heavy flavor, alternative method, MC statistical, background, regularization) are collectively small.

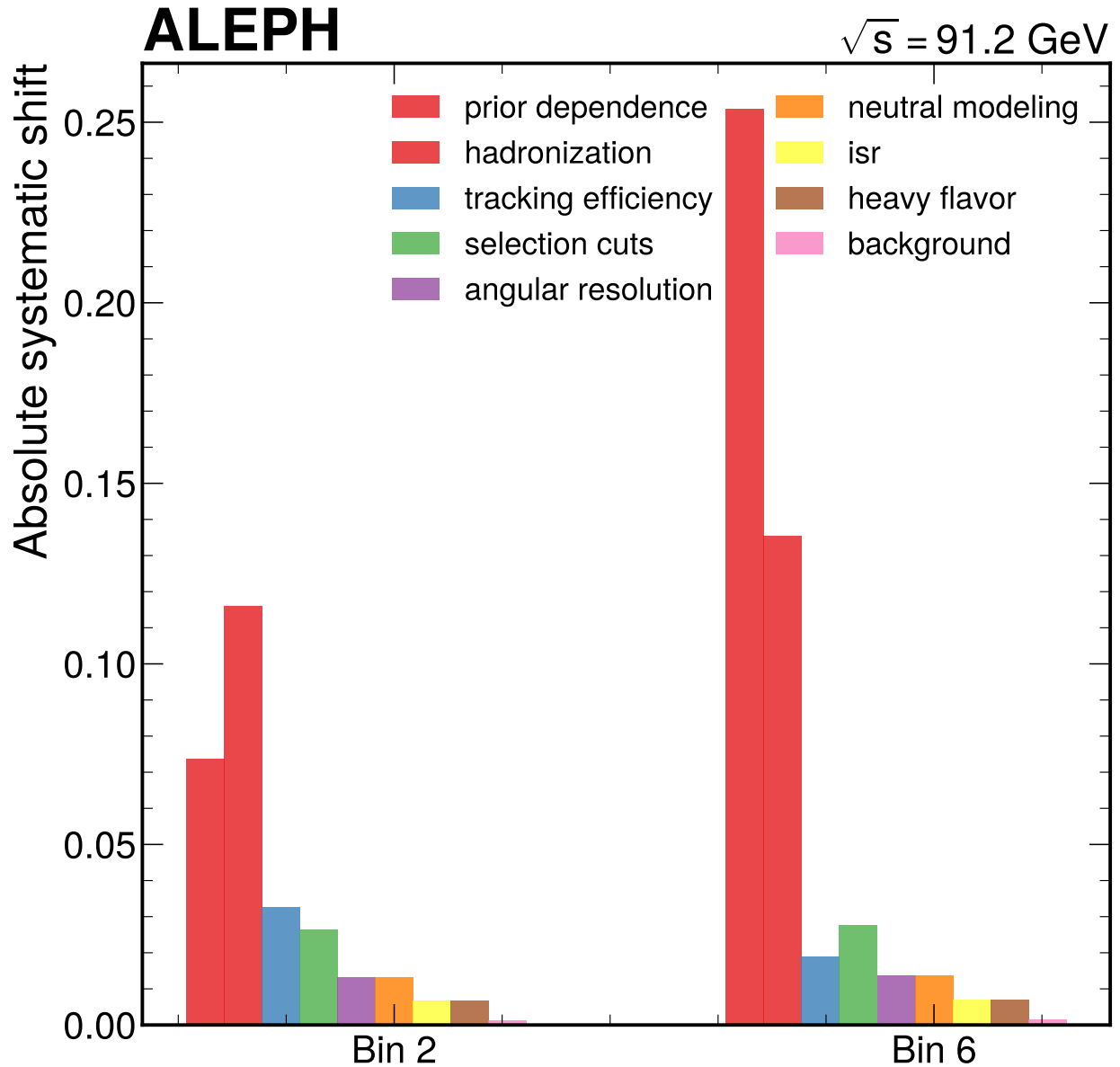


Figure 56: Systematic uncertainty breakdown for surviving $\ln(k_t)$ bins in the full data result. The same hierarchy applies, with prior dependence and hadronization as the two leading sources. The relative contribution of tracking efficiency is slightly larger for k_t than for the angular projection, reflecting the sensitivity of soft emissions to track reconstruction.

Table 57: Covariance matrix validation. Both matrices are positive semi-definite with condition numbers well below the 10^{10} threshold for numerically stable matrix inversion.

Property	$\ln(1/\Delta\theta)$	$\ln(k_t)$
Full dimension	10 x 10	12 x 12
Eigenvalue range	2.0×10^{-6} –1.9	2.7×10^{-6} –6.3
Negative eigenvalues	0	0
Condition number	9.7×10^5	2.4×10^6
PSD check	PASS	PASS

The surviving-bin covariance matrices (5 x 5 for angular, 2 x 2 for k_t) are also positive semi-definite, with improved conditioning due to the removal of poorly-constrained edge bins.

B.10.3 Surviving-bin covariance matrices

The final covariance matrices on the surviving bins combine data statistical uncertainty with the full systematic covariance:

Final covariance for surviving $\ln(1/\Delta\theta)$ bins

Property	Value
Dimension	5 x 5 (bins 0, 1, 2, 4, 5)
Eigenvalue range	2.2×10^{-5} – 1.9×10^{-1}
Negative eigenvalues	0
PSD check	PASS

Final covariance for surviving $\ln(k_t)$ bins

Property	Value
Dimension	2 x 2 (bins 2, 6)
Eigenvalue range	7.3×10^{-3} – 9.8×10^{-2}
Negative eigenvalues	0
PSD check	PASS

B.11 Summary and outlook

B.11.1 Summary

The primary Lund jet plane density in hadronic Z decays at $\sqrt{s} = 91.2$ GeV is measured using the full archived ALEPH dataset (2,889,543 events after selection, 5,779,086 hemispheres). This is the first measurement of the Lund jet plane in electron-positron collisions.

The primary result is the $\ln(1/\Delta\theta)$ angular spectrum, measured in 5 surviving bins (after the flat-prior 20% gate) spanning $\ln(1/\Delta\theta) \in [0, 1.5] \cup [2, 3]$. The Lund plane density is corrected to the charged-particle level using Iterative Bayesian Unfolding with 5 iterations, validated by closure tests, stress tests, noisy closure tests, and cross-checked with truncated SVD.

The key numerical results for the angular spectrum are:

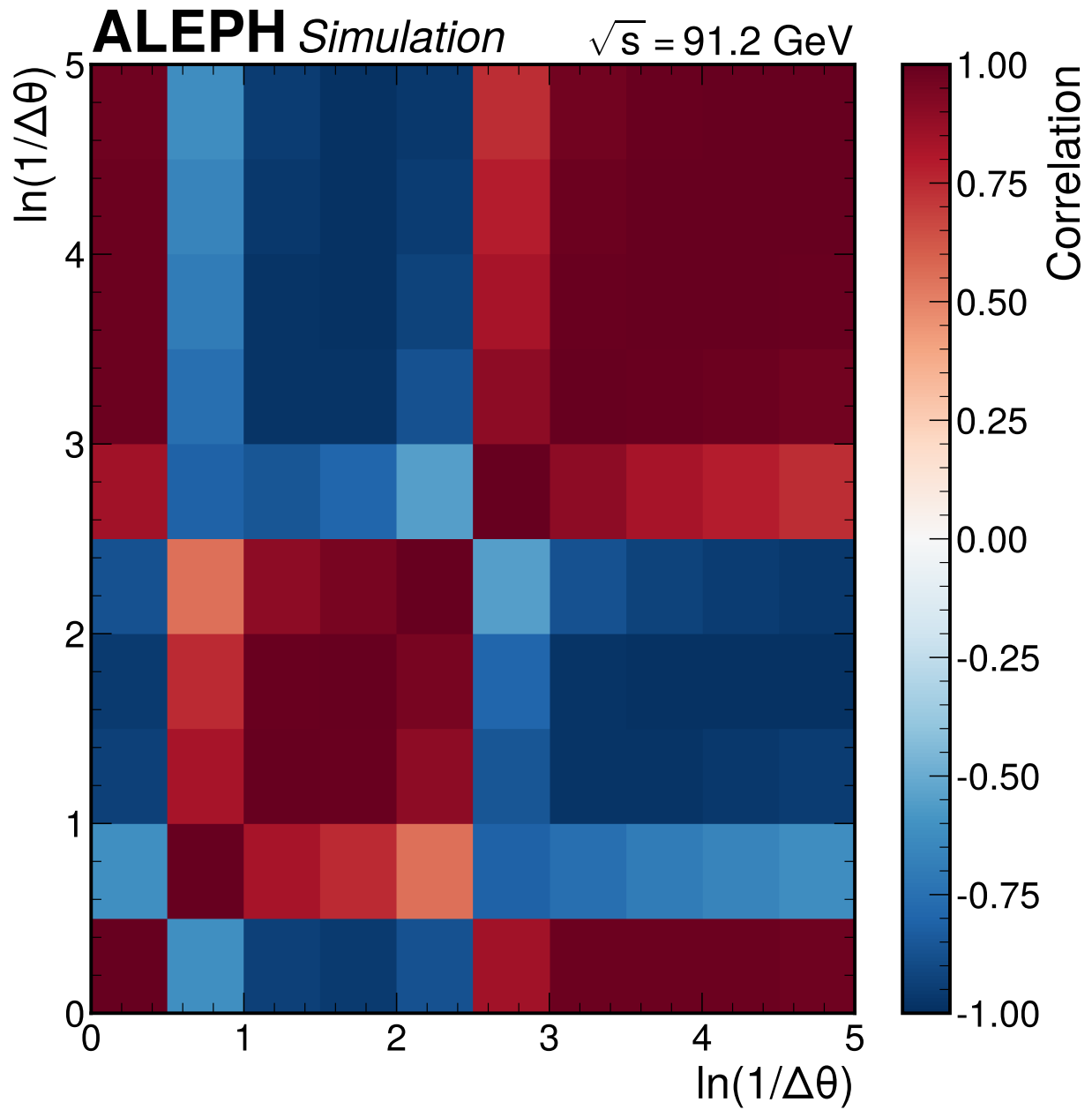


Figure 57: Correlation matrix for the $\ln(1/\Delta\theta)$ projection (full 10 bins). Strong positive correlations between neighboring bins are driven by the prior-dependence systematic, which shifts all bins coherently. Anti-correlations between bins 0–2 and bins 4–5 reflect the competing effects of the reweighting systematics, which tilt the distribution in opposite directions.

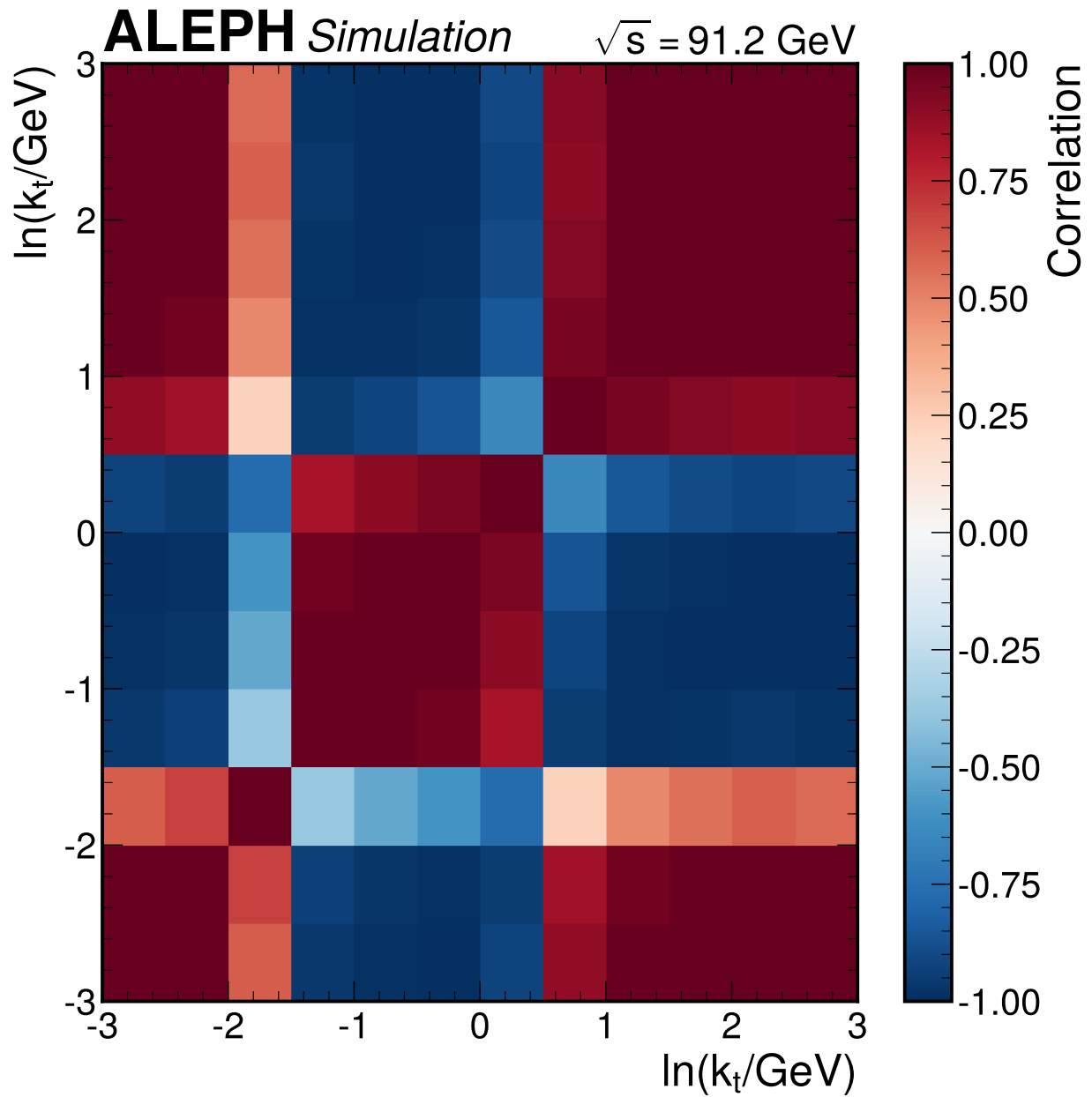


Figure 58: Correlation matrix for the $\ln(k_t)$ projection (full 12 bins). Similar correlation structure to the angular projection: positive correlations between nearby bins and anti-correlations between the low- k_t and high- k_t regions, reflecting the coherent effect of the dominant prior-dependence systematic.

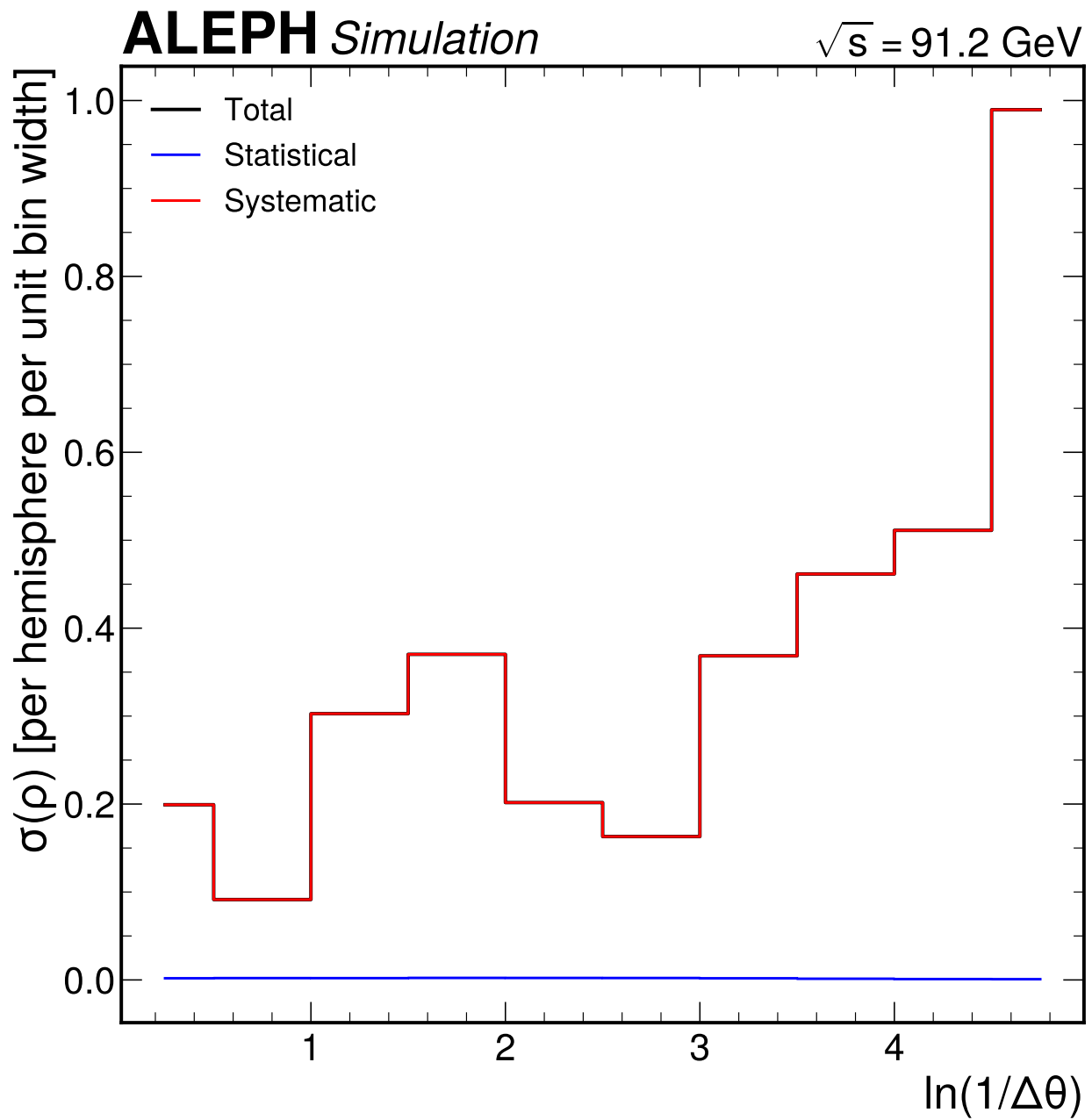


Figure 59: Uncertainty decomposition for the $\ln(1/\Delta\theta)$ projection showing total (black), statistical (blue), and systematic (red) uncertainties per bin. The systematic uncertainty dominates by a factor > 80 in all bins, reflecting the large prior-dependence and hadronization systematics.

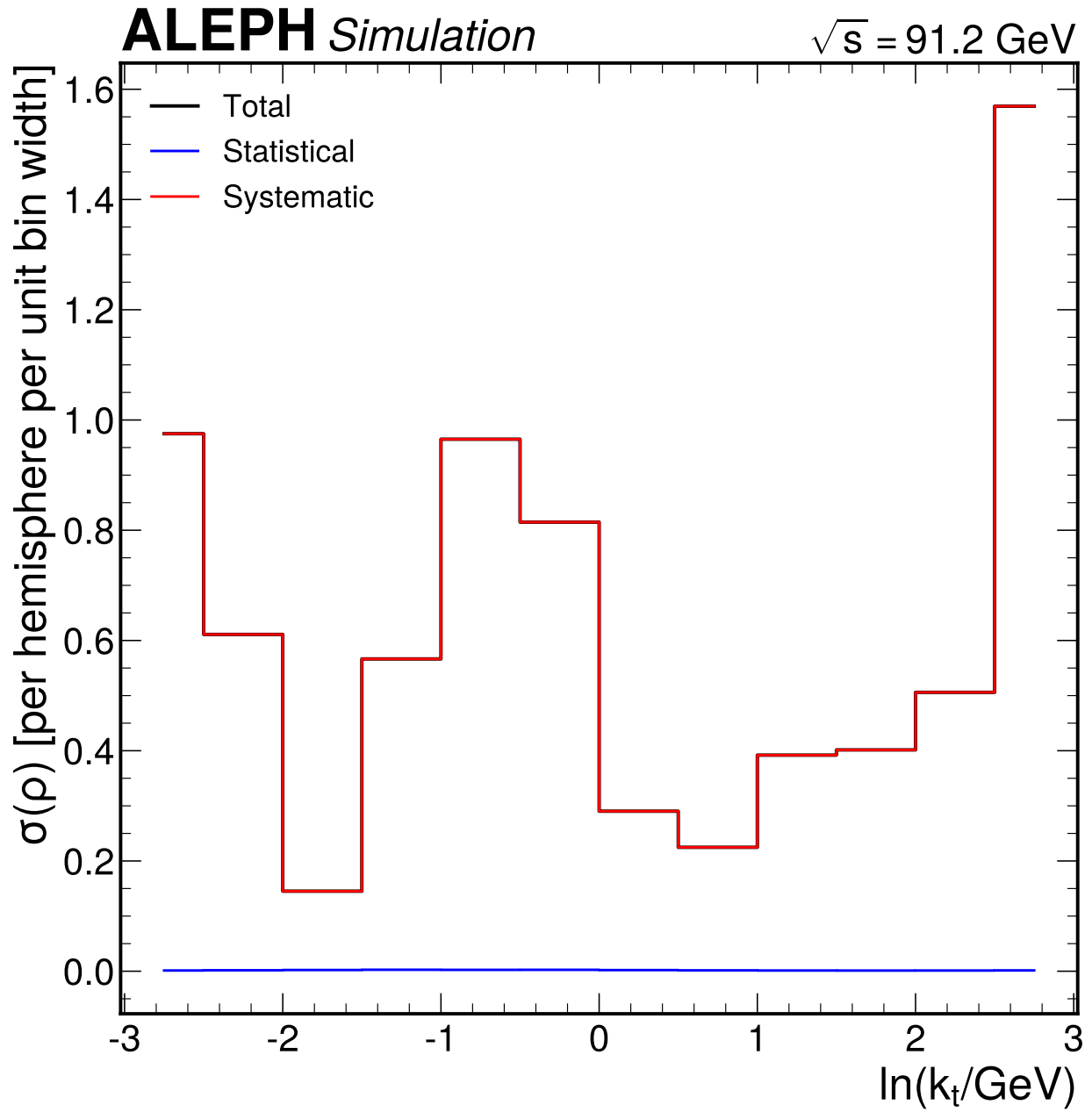


Figure 60: Uncertainty decomposition for the $\ln(k_t)$ projection showing total, statistical, and systematic per bin. The systematic dominance is even more pronounced at the kinematic edges where the density is small and the prior dependence is strongest.

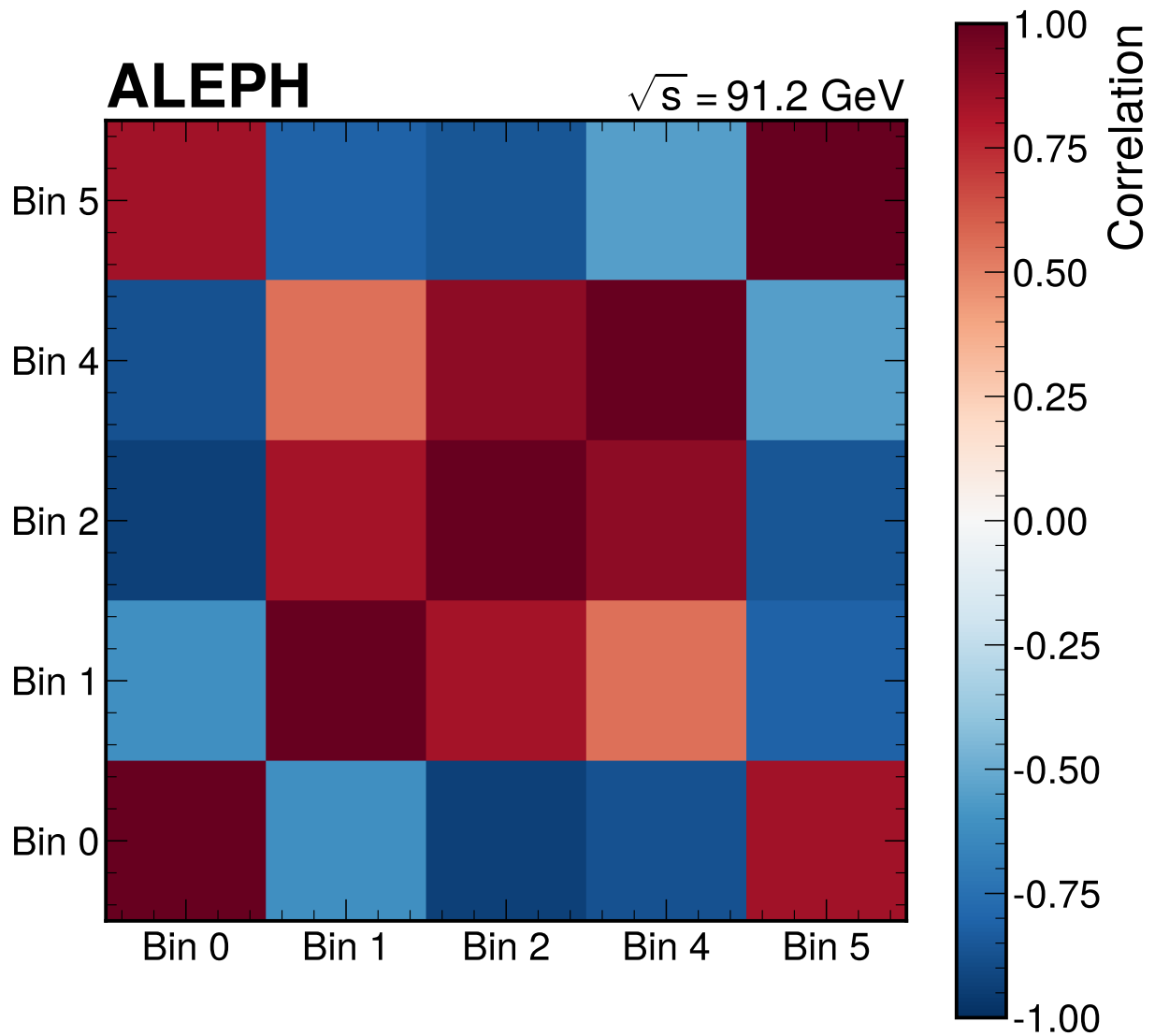


Figure 61: Correlation matrix for surviving $\ln(1/\Delta\theta)$ bins on full data. The strong positive correlation between bins 0 and 2 and the anti-correlation between bins 0 and 4 reflect the coherent systematic shifts from prior dependence.

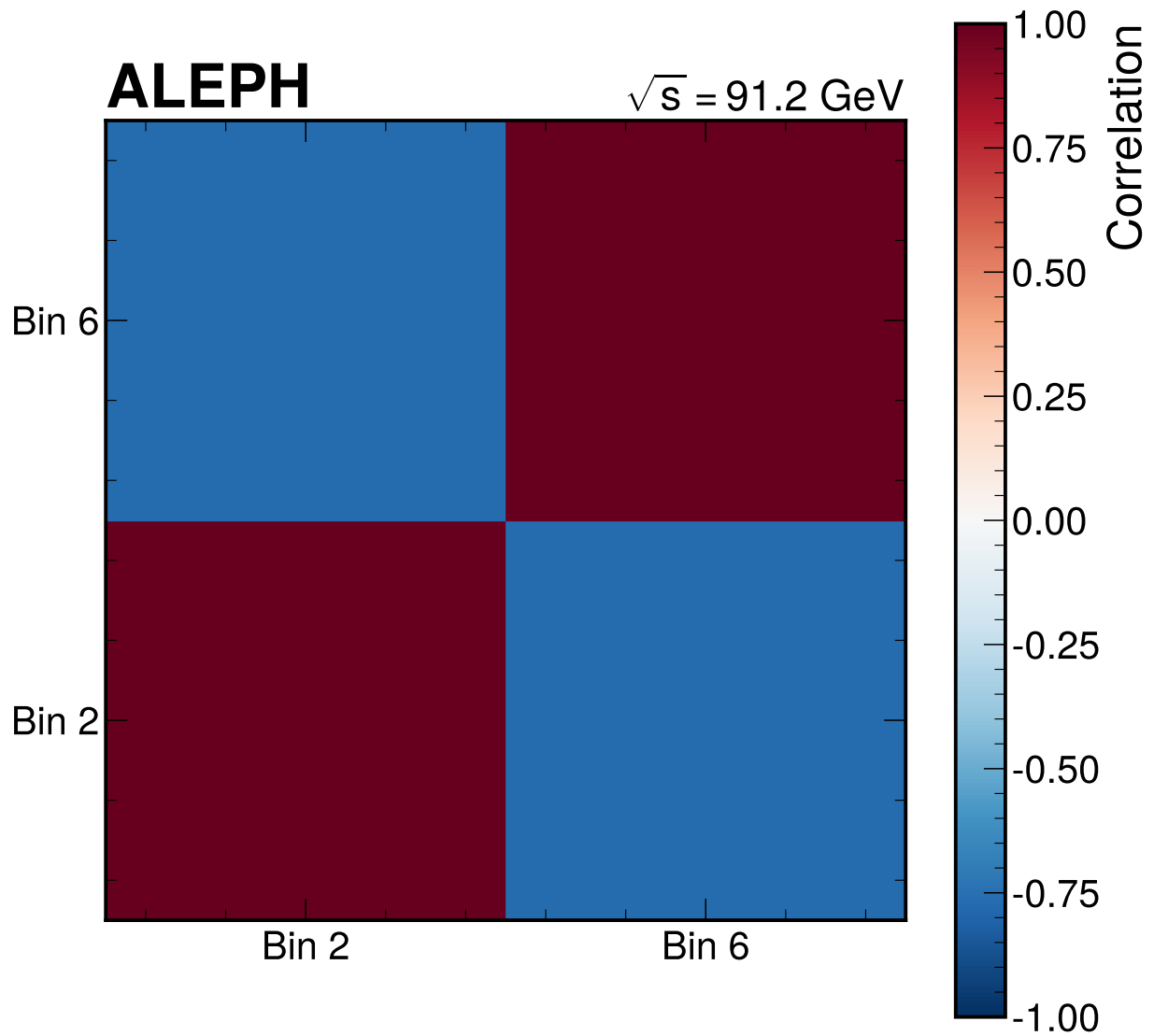


Figure 62: Correlation matrix for surviving $\ln(k_t)$ bins on full data. The two bins show negative correlation (-0.77), reflecting the opposite-sign shifts from the prior-dependence systematic (which tilts the k_t spectrum).

Bin	Range	ρ	Stat	Syst
0	[0.0, 0.5]	1.583	± 0.001	± 0.199
1	[0.5, 1.0]	1.666	± 0.001	± 0.091
2	[1.0, 1.5]	1.750	± 0.001	± 0.303
4	[2.0, 2.5]	1.368	± 0.001	± 0.202
5	[2.5, 3.0]	0.894	± 0.001	± 0.163

The supplementary $\ln(k_t)$ projection retains only 2 of 12 bins: $\rho = 1.337 \pm 0.001$ (stat) ± 0.145 (syst) at $\ln k_t \in [-2, -1.5]$ and $\rho = 1.365 \pm 0.001$ (stat) ± 0.290 (syst) at $\ln k_t \in [0, 0.5]$.

The full data agrees with the MC expected result: $\chi^2/\text{ndf} = 1.30$ ($p = 0.26$) for $\ln(1/\Delta\theta)$ and $\chi^2/\text{ndf} = 0.003$ ($p = 1.00$) for $\ln(k_t)$. The only available generator comparison (PYTHIA 6) is the same model used to construct the response matrix; this measurement therefore cannot currently discriminate between QCD models and serves primarily as a first result and proof-of-concept for the method. The full data is consistent with the 10% validation result ($\chi^2/\text{ndf} = 0.99$, $p = 0.42$ for $\ln(1/\Delta\theta)$). No anomalous pulls are observed (maximum 1.48σ).

The mean number of primary declusterings per hemisphere above various k_t thresholds ranges from 2.54 per hemisphere above $k_t = 0.5$ GeV to 0.13 above $k_t = 5$ GeV, at detector level.

B.11.2 Dominant limitations

1. **Prior dependence:** The IBU unfolding with 5–6 iterations at 31–40% diagonal fraction retains significant prior sensitivity. Only $5 + 2 = 7$ of 22 bins survive the flat-prior gate. Prior dependence accounts for 87–93% of the total systematic in surviving bins. This is the fundamental limitation of this measurement.
2. **No alternative generator [L2]:** The hadronization systematic is estimated through particle-level reweighting rather than independent detector simulation with HERWIG or ARIADNE. This is the second-largest systematic (38–47% of the non-prior total) and cannot be fully assessed without alternative MC.
3. **MC statistics [L1]:** The MC/data ratio of 0.25 limits the statistical precision of the response matrix, though the propagated MC statistical uncertainty is negligible ($< 1\%$ of total) thanks to the relatively coarse binning.

B.11.3 Outlook

1. **Improved unfolding:** Alternative approaches such as OmniFold (machine-learning-based unfolding) or increased IBU iterations with a data-driven prior could recover additional bins in the Lund plane. The data-driven prior (using the reco-level data distribution to initialize IBU) would reduce the prior-dependence systematic by starting from a prior closer to the truth.
2. **Alternative generators:** Particle-level predictions from PYTHIA 8 (Monash tune), HERWIG 7.3 (cluster fragmentation), and analytic NLL calculations ([[ref-Dreyer:2018nbf](#)]) should be compared to the unfolded result. These comparisons would provide physics interpretation beyond the PYTHIA 6 baseline.
3. **Expanded k_t projection:** The $\ln(k_t)$ projection retains only two bins. Expanding this measurement would require either more iterations (at the cost of increased noise), coarser binning, or a fundamentally different unfolding approach.
4. **Two-dimensional result:** The 2D Lund plane density at coarser binning (e.g., 5×6) could potentially be unfolded with acceptable conditioning. This would provide the full two-dimensional structure that is the theoretically most interesting representation.

5. **Other e^+e^- datasets:** Similar measurements could be performed with archived data from other LEP experiments (DELPHI, L3, OPAL) or from future e^+e^- colliders (FCC-ee, CEPC, ILC) where vastly larger datasets and modern detectors would overcome the limitations encountered here.

B.12 Appendices

B.12.1 Appendix A: Limitation index

Table 58: Limitation index collecting all assumptions [A], limitations [L], and design decisions [D] introduced throughout the analysis. Each entry lists where it was introduced, its impact on the final result, and the mitigation applied.

Label	Description	Phase	Impact	Mitigation
A1	pwflag == 0 identifies charged tracks	1	Low	Validated by prior analysis
A2	Thrust axis proxies quark axis	1	Low	Standard at LEP
A3	PYTHIA 6 MC describes detector	1	Moderate	Data/MC within 5%
A4	C/A clustering is IRC safe	1	None	By construction
L1	MC/data ratio 0.25	1	Moderate	Bootstrap propagation
L2	No alternative generator MC	1	High	Reweighting approx.
L3	Frozen reconstruction	1	Low	Archival constraint
L4	Charged particles only	1	Low	Design choice
L5	2D unfolding unreliable	3	High	1D projections
B1	No explicit TPC hit cut	3	Low	highPurity flag
B2	Index-based matching	3	Moderate	Systematic study
D1	IBU primary method	1	–	SVD cross-check
D2	SVD alternative method	1	–	Implemented
D3	Normalized measurement	1	–	Lumi cancels
D7	1D primary, 2D secondary	3	–	Implemented

B.12.2 Appendix B: Per-bin systematic tables

$\ln(1/\Delta\theta)$: all systematic shifts (density units)

Bin	Pri	Had	Sel	Trk	Ang	Neu	ISR	HF	Alt	MC	Bkg	Reg	Tot
0	.190	.065	.032	.016	.010	.016	.008	.008	.002	.002	.002	.000	.199
1	.054	.069	.035	.017	.011	.017	.009	.009	.004	.002	.002	.000	.091
2	.283	.108	.036	.018	.013	.018	.009	.009	.005	.002	.002	.000	.303
3	.361	.082	.034	.017	.011	.017	.008	.008	.002	.002	.002	.000	.370
4	.196	.044	.027	.013	.009	.013	.007	.007	.003	.001	.001	.000	.202
5	.113	.114	.017	.009	.006	.009	.004	.004	.001	.001	.001	.000	.163
6	.348	.120	.009	.004	.003	.004	.002	.002	.001	.001	.000	.000	.369
7	.452	.079	.004	.002	.001	.002	.001	.001	.000	.000	.000	.000	.462
8	.505	.058	.002	.001	.001	.001	.000	.000	.000	.000	.000	.000	.511
9	.987	.035	.001	.000	.000	.000	.000	.000	.000	.000	.000	.000	.990

: Per-bin systematic shifts for all 10 $\ln(1/\Delta\theta)$ bins, in density units. Bins 3, 6–9 are excluded by the flat-prior gate. Column abbreviations: Pri = prior dependence, Had = hadronization, Sel = selection cuts, Trk = tracking efficiency, Ang = angular resolution, Neu = neutral modeling, ISR = ISR treatment, HF = heavy flavor, Alt = alternative method, MC = MC statistical, Bkg = background, Reg = regularization, Tot = total. `{#tbl:syst.lntheta}`

$\ln(k_t)$: all systematic shifts (density units)

Bin	Pri	Had	Sel	Trk	Ang	Neu	ISR	HF	Alt	MC	Bkg	Reg	Tot
0	.967	.121	.008	.012	.004	.004	.002	.002	.000	.001	.000	.000	.975
1	.595	.134	.015	.021	.008	.008	.004	.004	.000	.002	.001	.000	.611
2	.074	.116	.026	.033	.013	.013	.007	.007	.000	.002	.001	.000	.145
3	.559	.061	.040	.044	.020	.020	.010	.010	.000	.003	.002	.000	.567
4	.962	.034	.048	.046	.024	.024	.012	.012	.000	.002	.002	.000	.965
5	.802	.127	.042	.034	.021	.021	.011	.011	.000	.003	.002	.000	.815
6	.254	.135	.028	.019	.014	.014	.007	.007	.000	.002	.001	.000	.290
7	.211	.076	.014	.008	.007	.007	.004	.004	.000	.002	.001	.000	.225
8	.392	.017	.007	.003	.004	.004	.002	.002	.000	.001	.000	.000	.392
9	.401	.022	.004	.001	.002	.002	.001	.001	.000	.001	.000	.000	.402
10	.503	.057	.003	.000	.001	.001	.001	.001	.000	.001	.000	.000	.506
11	1.565	.112	.001	.000	.000	.000	.000	.000	.000	.001	.000	.000	1.569

: Per-bin systematic shifts for all 12 $\ln(k_t)$ bins, in density units. Bins 0, 1, 3–5, 7–11 are excluded by the flat-prior gate. Column abbreviations as in tbl. ??.

B.12.3 Appendix C: Covariance matrices

$\ln(1/\Delta\theta)$ statistical covariance (surviving bins)

Table 59: Statistical covariance matrix for the 5 surviving $\ln(1/\Delta\theta)$ bins. The off-diagonal elements are negative, reflecting the anti-correlation between neighboring bins introduced by the unfolding regularization. All elements are of order 10^{-6} , confirming the negligible statistical contribution to the total uncertainty.

	Bin 0	Bin 1	Bin 2	Bin 4	Bin 5
Bin 0	3.53e-06	-1.39e-06	-9.44e-07	-3.26e-07	4.92e-08
Bin 1	-1.39e-06	4.33e-06	-6.97e-07	-9.10e-07	-1.20e-06
Bin 2	-9.44e-07	-6.97e-07	4.21e-06	-1.18e-06	-9.06e-07
Bin 4	-3.26e-07	-9.10e-07	-1.18e-06	5.08e-06	-5.66e-07
Bin 5	4.92e-08	-1.20e-06	-9.06e-07	-5.66e-07	4.81e-06

$\ln(1/\Delta\theta)$ total covariance (surviving bins)

Table 60: Total covariance matrix for the 5 surviving $\ln(1/\Delta\theta)$ bins. The total covariance is dominated by the systematic components, with the statistical contribution at the 10^{-6} level compared to systematic entries at the 10^{-2} level. Both matrices are positive semi-definite with no negative eigenvalues.

	Bin 0	Bin 1	Bin 2	Bin 4	Bin 5
Bin 0	0.03969	-0.01120	-0.05649	-0.03510	0.02725
Bin 1	-0.01120	0.00835	0.02291	0.01019	-0.01209
Bin 2	-0.05649	0.02291	0.09165	0.05445	-0.04217
Bin 4	-0.03510	0.01019	0.05445	0.04068	-0.01816
Bin 5	0.02725	-0.01209	-0.04217	-0.01816	0.02658

$\ln(k_t)$ statistical covariance (surviving bins)

Table 61: Statistical covariance matrix for the 2 surviving $\ln(k_t)$ bins.

	Bin 2	Bin 6
Bin 2	4.84e-06	-6.33e-07
Bin 6	-6.33e-07	4.17e-06

$\ln(k_t)$ total covariance (surviving bins)

Table 62: Total covariance matrix for the 2 surviving $\ln(k_t)$ bins. The negative off-diagonal element indicates anti-correlation: the prior dependence shifts the two surviving bins in opposite directions. Both matrices are positive semi-definite.

	Bin 2	Bin 6
Bin 2	0.02108	-0.03258
Bin 6	-0.03258	0.08427

B.12.4 Appendix D: Machine-readable results

All results are provided in machine-readable formats in the `results/` directory (also available at `phase4_inference/exec/results/`):

Table 63: Machine-readable result files. The NPZ archives contain NumPy arrays with densities, uncertainties, covariance matrices, chi-squared values, pulls, and systematic shift vectors. The CSV files contain the primary results in a format suitable for direct comparison with theory predictions.

File	Contents
<code>lntheta_results.csv</code>	Per-bin density, stat/syst/total uncertainties
<code>lnkt_results.csv</code>	Per-bin density, stat/syst/total uncertainties
<code>declusterings_vs_kt.csv</code>	Mean declusterings vs k_t threshold
<code>full_data_results.npz</code>	All numerical results (NumPy archive)
<code>covariance_lntheta_full.npz</code>	Covariance matrices (stat, per-syst, total)
<code>covariance_lnkt_full.npz</code>	Covariance matrices (stat, per-syst, total)

Additional intermediate results from earlier analysis phases:

File	Location	Contents
<code>expected_results.npz</code>	Phase 4 exec	MC expected densities
<code>systematics.npz</code>	Phase 4 exec	Per-source shift vectors
<code>fix_review.npz</code>	Phase 4 exec	Flat-prior gate, noisy closure
<code>data_10pct_results.npz</code>	Phase 4 exec	10% validation results

B.12.5 Appendix E: Input validation

Data/MC comparisons for all kinematic variables entering the observable calculation, using the full ALEPH dataset. These comparisons validate the MC model used for response matrix construction.

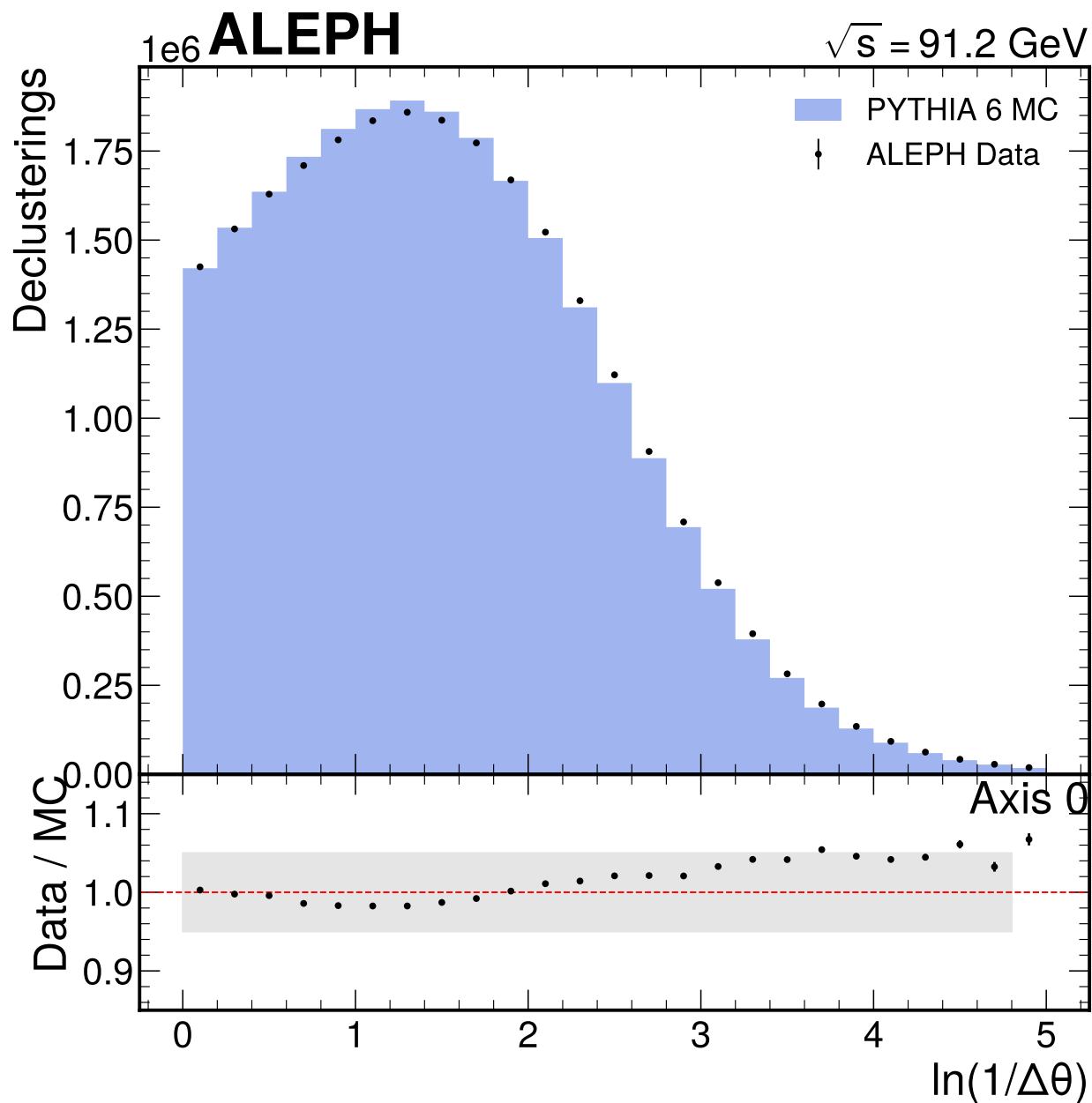


Figure 63: Detector-level $\ln(1/\Delta\theta)$ data/MC comparison from Phase 3 using the full ALEPH dataset. The angular coordinate of the Lund plane shows data/MC agreement within 5% for $\ln(1/\Delta\theta) < 4$. At the highest values (smallest angles), larger deviations are observed but these correspond to bins excluded by the flat-prior gate.

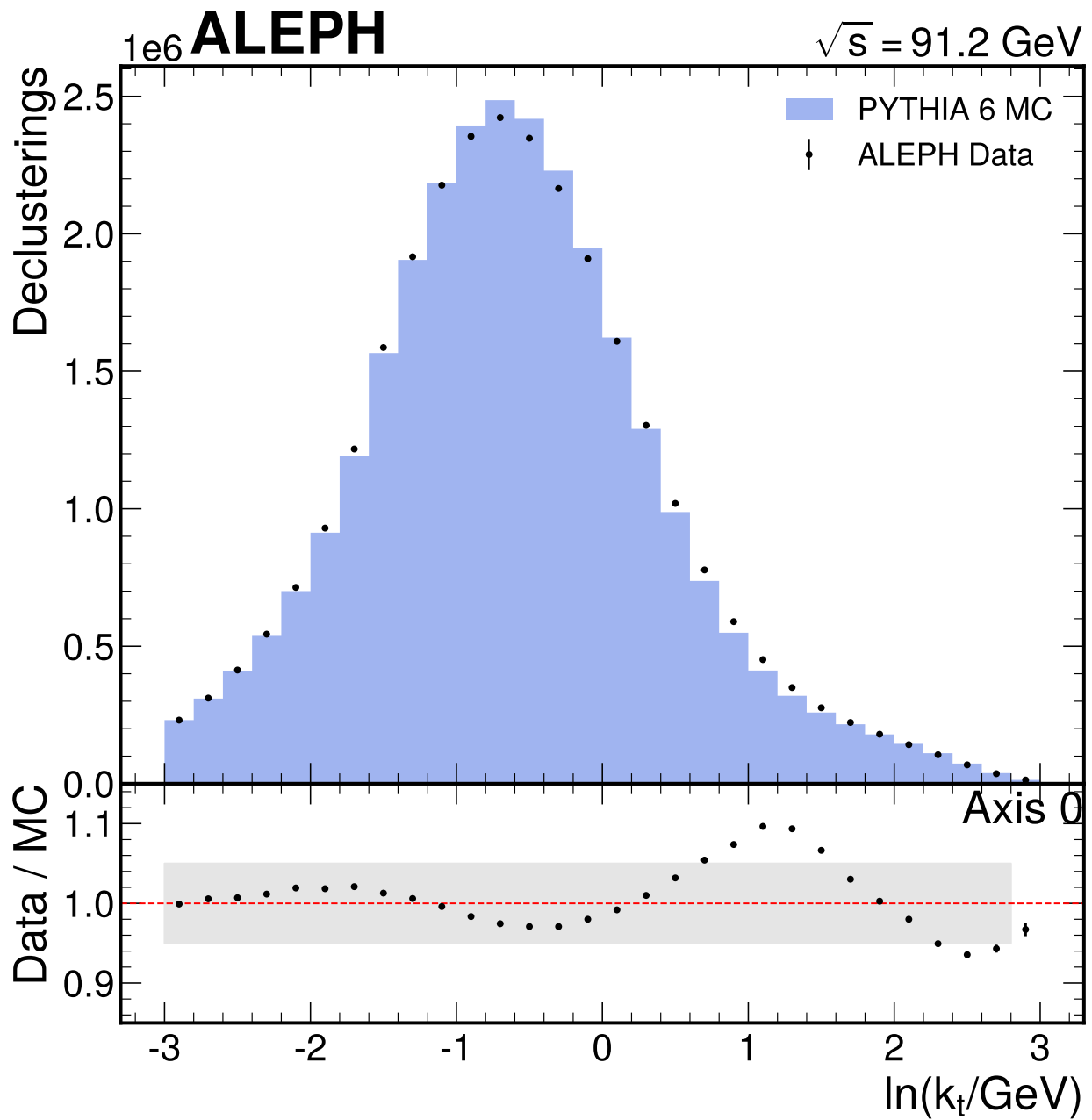


Figure 64: Detector-level $\ln(k_t)$ data/MC comparison from Phase 3 using the full ALEPH dataset. The transverse momentum coordinate shows agreement within 5% across the full range $-3 < \ln k_t < 3$, with the best agreement in the central region where the Lund plane density is highest.

B.12.6 Appendix F: Response matrix details

This appendix provides additional details on the two-dimensional response matrix, including the full 79-bin matrix visualization, the per-bin diagonal fractions, and the singular value spectrum that determines the feasibility of matrix inversion methods.

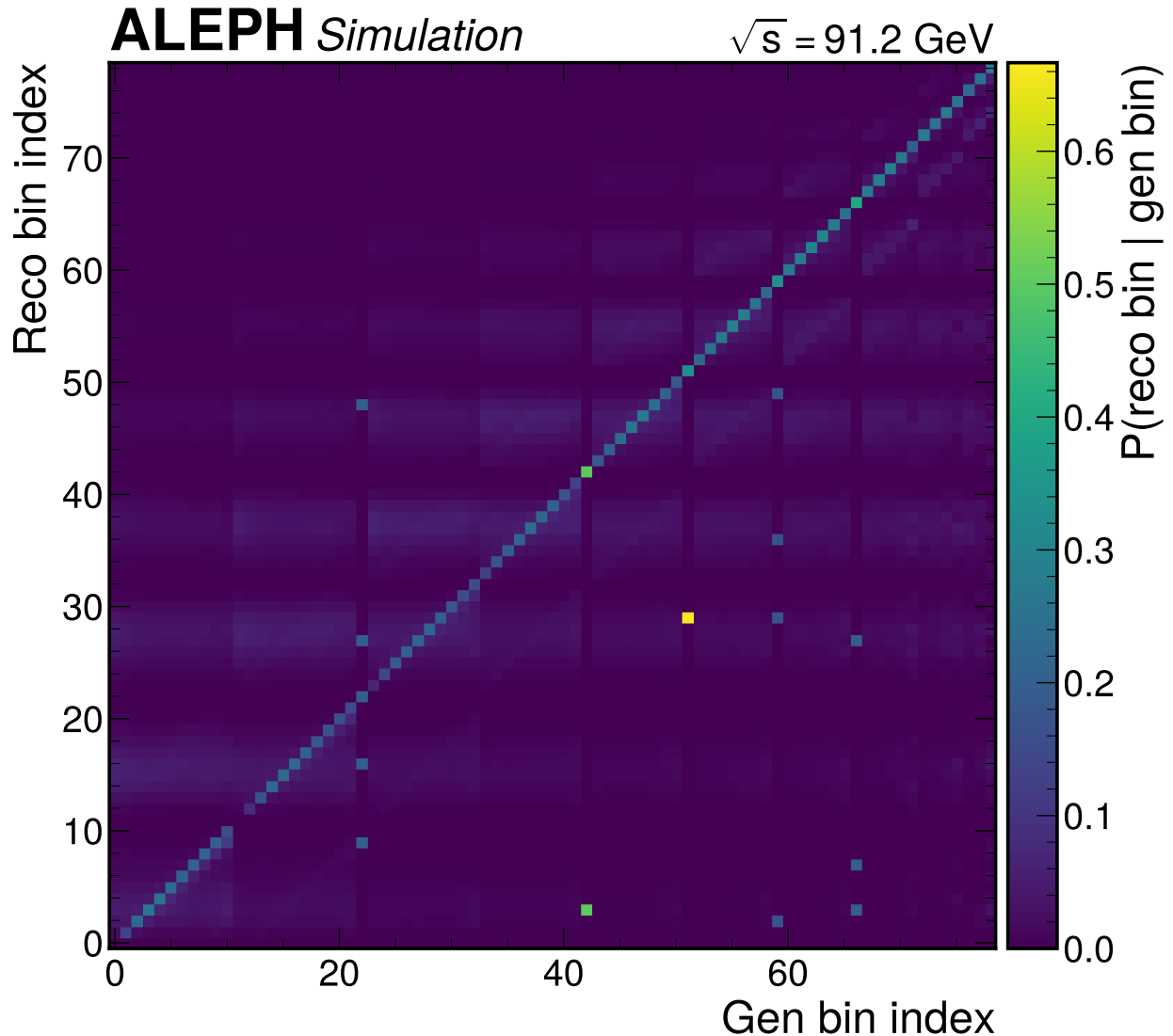


Figure 65: Two-dimensional response matrix for the 79 active Lund plane bins. The matrix is displayed with gen-level bins on the x-axis and reco-level bins on the y-axis, column-normalized so each column sums to 1. Significant off-diagonal structure is visible, reflecting bin migration from tracking resolution. The global diagonal fraction of 22% makes 2D unfolding impractical.

B.12.7 Appendix G: Relative systematic uncertainties

This appendix presents the systematic uncertainties as percentages of the nominal density, complementing the absolute shifts shown in the main text and Appendix B.

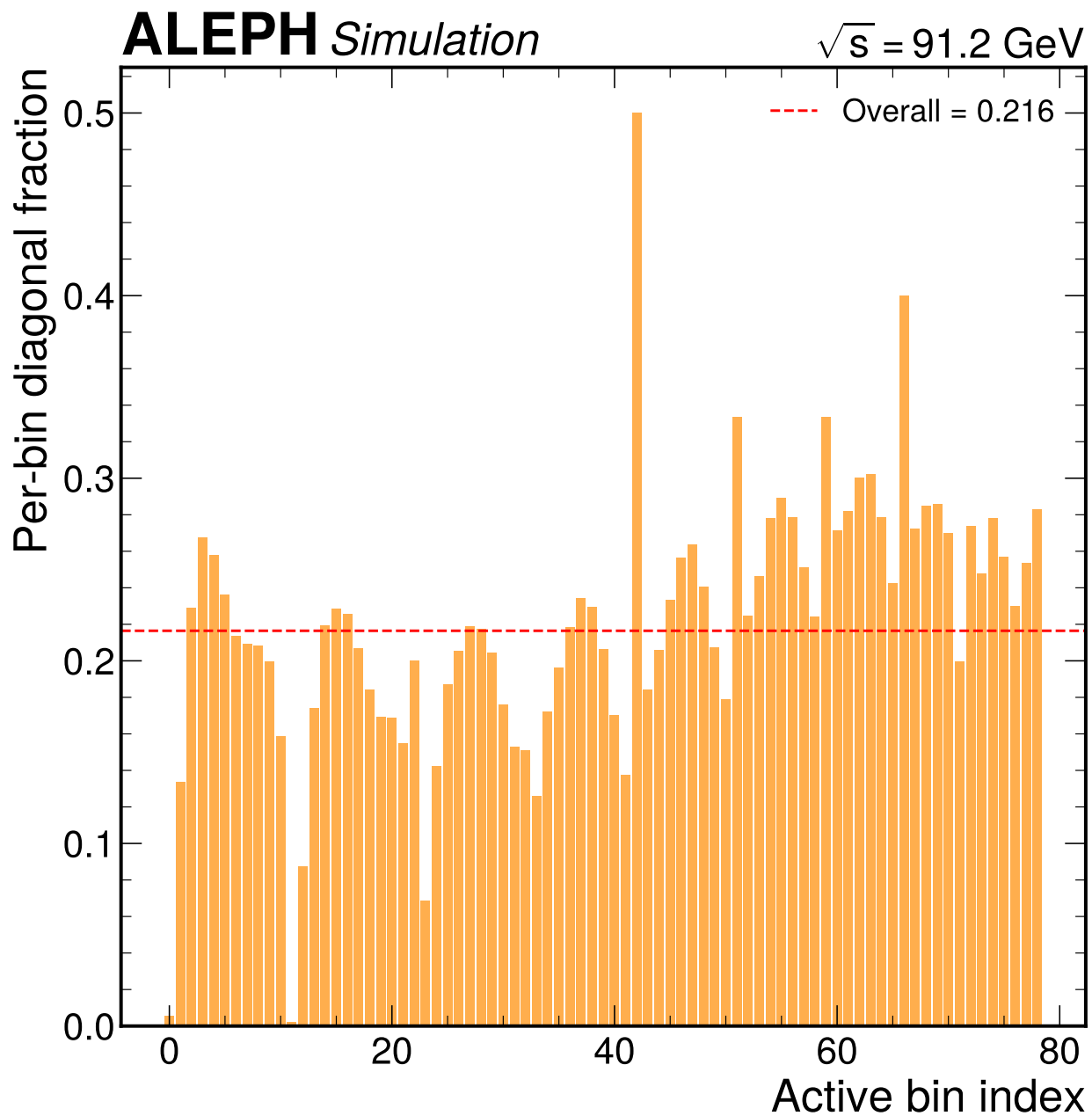


Figure 66: Per-bin diagonal fraction across the 79 active Lund plane bins. Most bins have diagonal fractions between 10% and 40%, with the highest values in the central region where angular and momentum resolution are best relative to bin width. No bin exceeds 50% diagonal fraction.

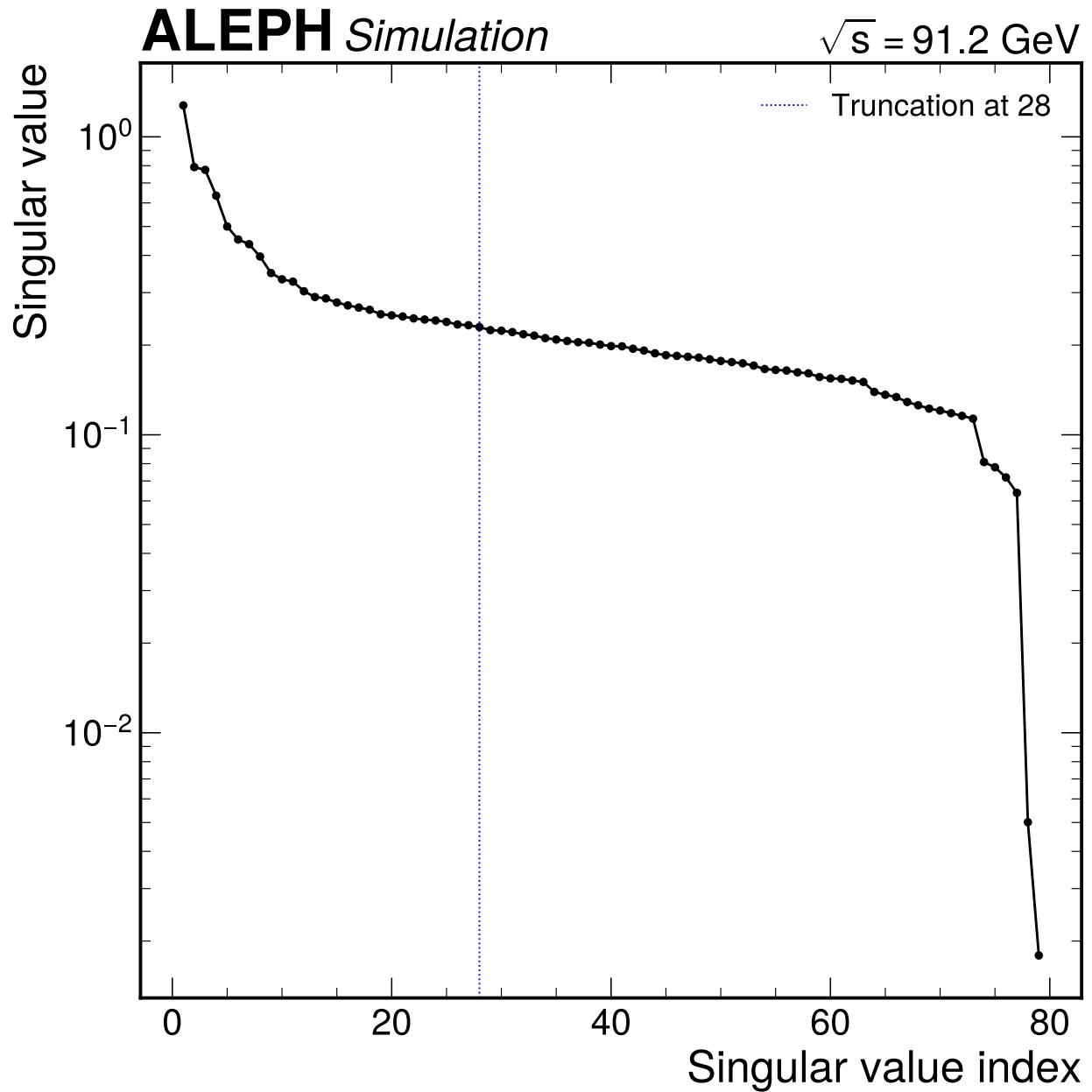


Figure 67: Singular value spectrum of the two-dimensional response matrix. The singular values span over 10 orders of magnitude, from $\mathcal{O}(1)$ for the dominant modes to $\mathcal{O}(10^{-10})$ for the most suppressed. This extreme range corresponds to the condition number of 2.75×10^{18} and explains why matrix inversion methods (SVD) are unusable for the 2D unfolding.

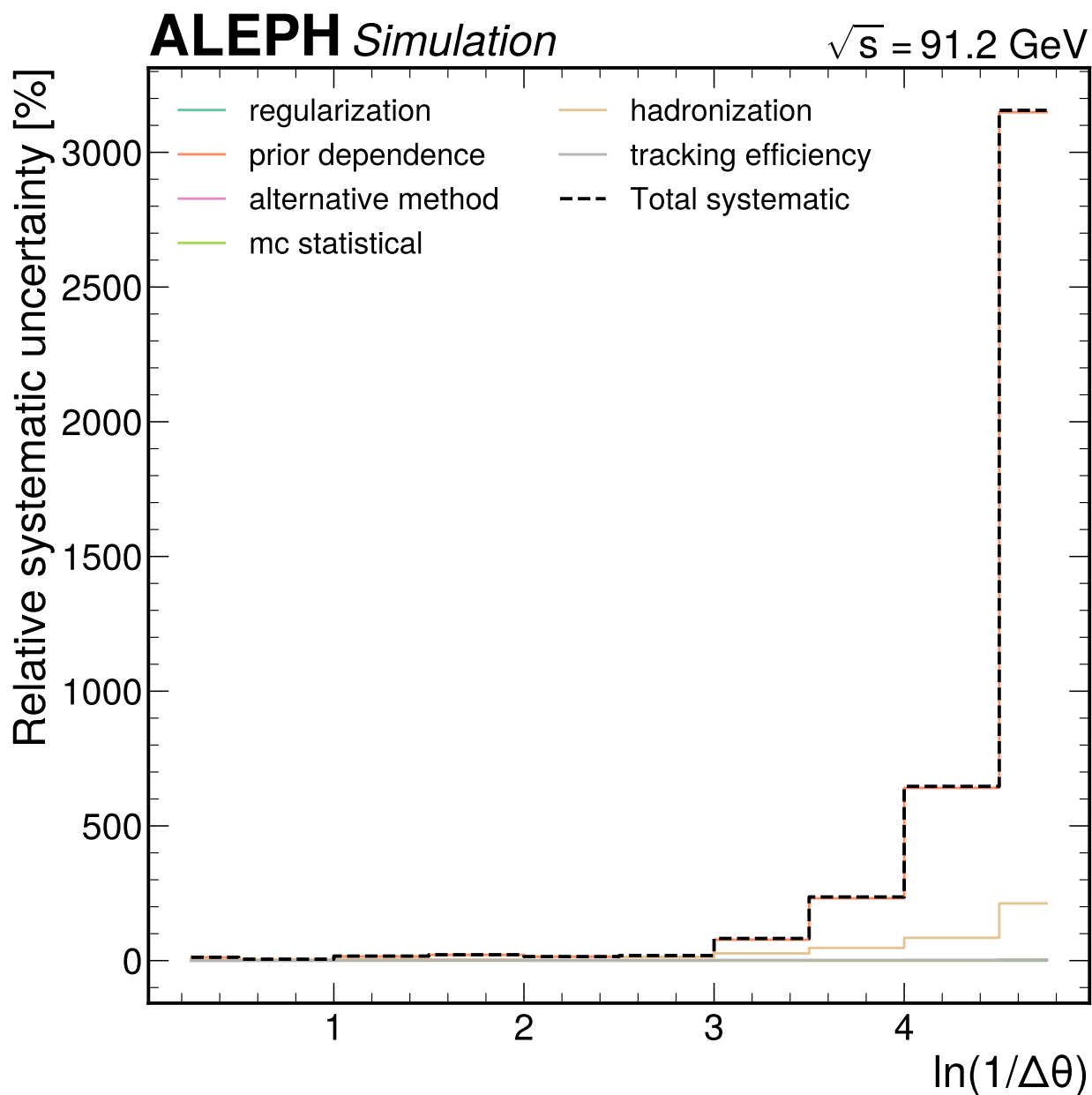


Figure 68: Relative systematic uncertainties for the $\ln(1/\Delta\theta)$ projection, expressed as percentage of the nominal density. The total relative uncertainty ranges from approximately 5% in the best-constrained bin (bin 1, $[0.5, 1.0]$) to over 3000% in the last bin ($[4.5, 5.0]$). The bins surviving the flat-prior gate have relative uncertainties of 5–17%.

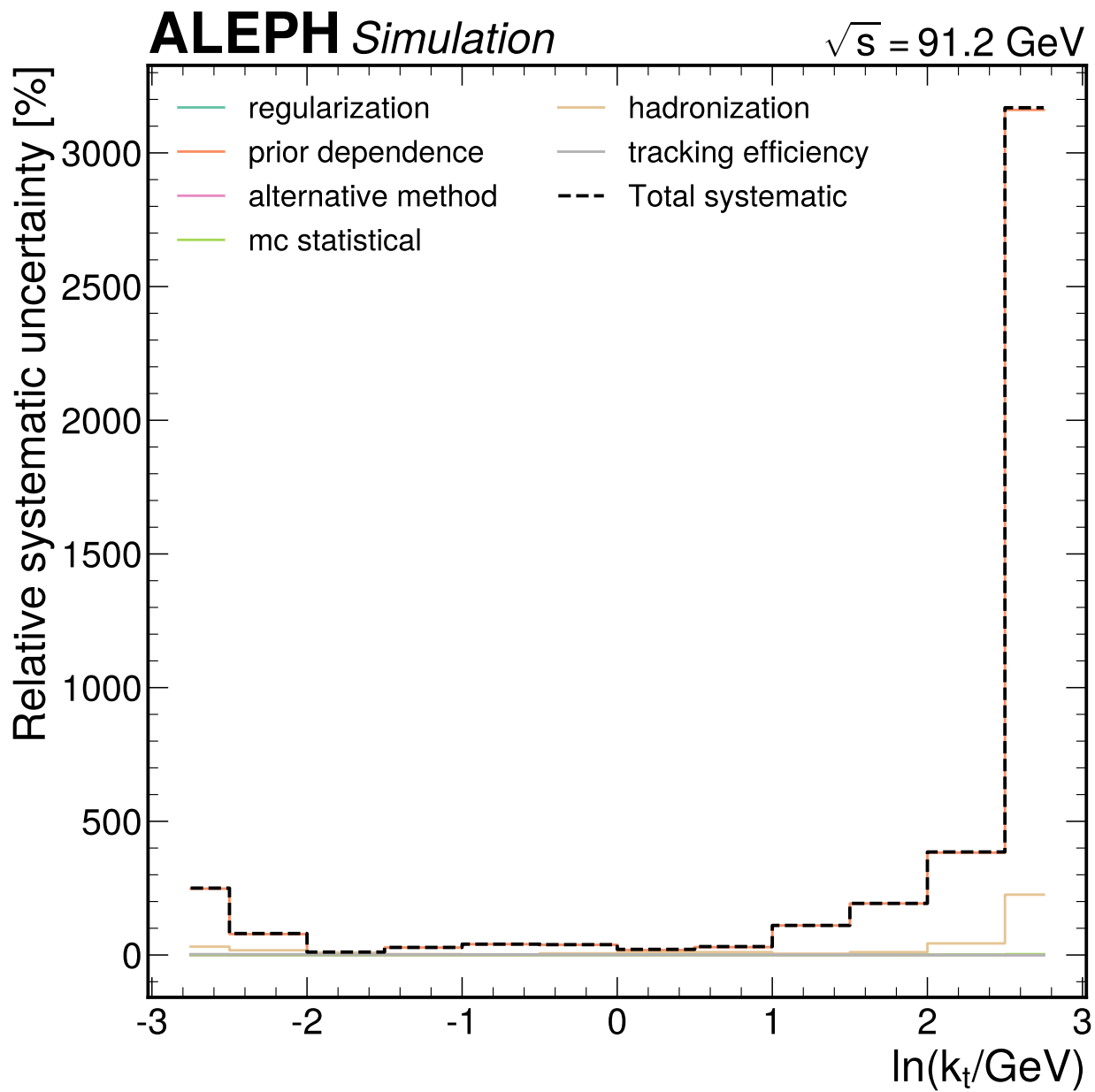


Figure 69: Relative systematic uncertainties for the $\ln(k_t)$ projection. The relative uncertainty is largest at the kinematic extremes where the density is small and prior dependence is strongest. The two surviving bins have relative uncertainties of 11% and 21%.

B.12.8 Appendix H: Covariance eigenvalue spectra

This appendix shows the eigenvalue spectra of the total covariance matrices, which characterize the numerical conditioning and the dominant uncertainty modes.

B.12.9 Appendix I: Phase 2 exploration distributions

The following distributions were produced during Phase 2 (data exploration) using 50,000 data and MC events after selection. They provide additional validation of the data quality and MC modeling.

References

- ALEPH Collaboration. n.d.-a. “A study of energy-energy correlations in charged tracks from hadronic decays of the Z^0 .” *INSPIRE*. <https://inspirehep.net/literature/232620>.
- ALEPH Collaboration. n.d.-b. “Determination of differences between quark and gluon jets in 3-jet events.” *INSPIRE*. <https://inspirehep.net/literature/433342>.
- ATLAS Collaboration. 2020. “Measurement of the Lund Jet Plane Using Charged Particles in 13 TeV Proton-Proton Collisions with the ATLAS Detector.” *Phys. Rev. Lett.* 124: 222002. <https://doi.org/10.1103/PhysRevLett.124.222002>.
- Baumgart, S. 2023. “Search for the Production of Quark-Gluon Plasma in e^+e^- Collisions at $\sqrt{s} = 91.2$ GeV with Archived ALEPH LEP1 Data.” PhD thesis, Massachusetts Institute of Technology. <https://cds.cern.ch/record/2876991>.
- Bethke, S. et al. 2004. *QCD studies and determination of α_s using LEP data*. <https://arxiv.org/abs/hep-ex/0411006>.
- Cacciari, Matteo, Gavin P. Salam, and Gregory Soyez. 2012. “FastJet User Manual.” *Eur. Phys. J. C* 72: 1896. <https://doi.org/10.1140/epjc/s10052-012-1896-2>.
- D’Agostini, G. 1995. “A multidimensional unfolding method based on Bayes’ theorem.” *Nucl. Instrum. Meth. A* 362: 487–98. [https://doi.org/10.1016/0168-9002\(95\)00274-X](https://doi.org/10.1016/0168-9002(95)00274-X).
- Dokshitzer, Yuri L., G. D. Leder, S. Moretti, and B. R. Webber. 1997. “Better Jet Clustering Algorithms.” *JHEP* 08: 001. <https://doi.org/10.1088/1126-6708/1997/08/001>.
- Dreyer, Frederic A., Gavin P. Salam, and Gregory Soyez. 2018. “The Lund Jet Plane.” *JHEP* 12: 064. [https://doi.org/10.1007/JHEP12\(2018\)064](https://doi.org/10.1007/JHEP12(2018)064).
- Navas, S. et al. 2024. “Review of Particle Physics.” *Phys. Rev. D* 110: 030001. <https://doi.org/10.1103/PhysRevD.110.030001>.

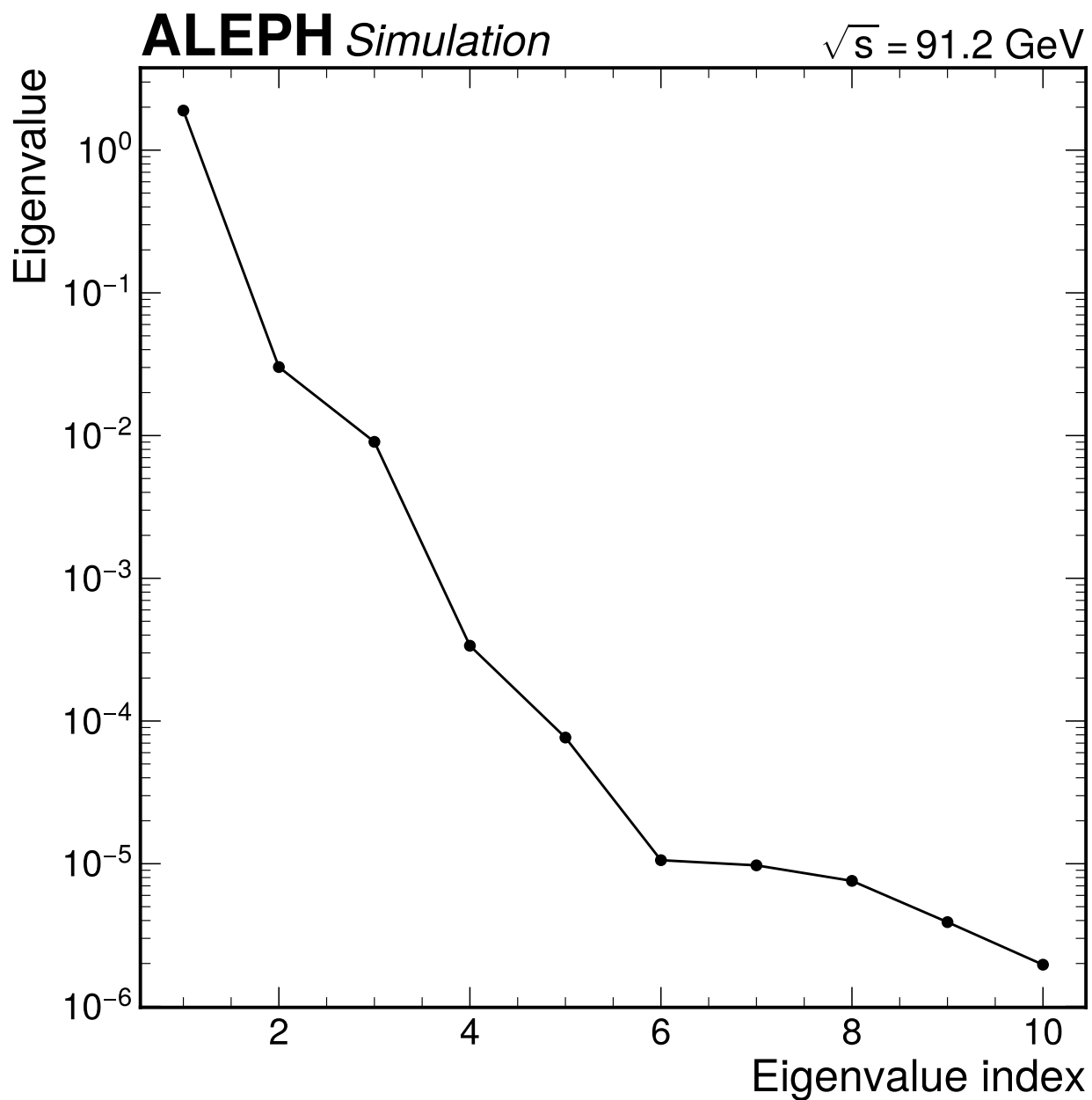


Figure 70: Eigenvalue spectrum of the total covariance matrix for the $\ln(1/\Delta\theta)$ projection (10 bins). The eigenvalues span 6 orders of magnitude, from 2×10^{-6} to 1.9. The large eigenvalue hierarchy reflects the dominance of the prior-dependence systematic, which introduces a single large eigenmode (coherent shift of all bins) with much smaller eigenvalues for the residual modes.

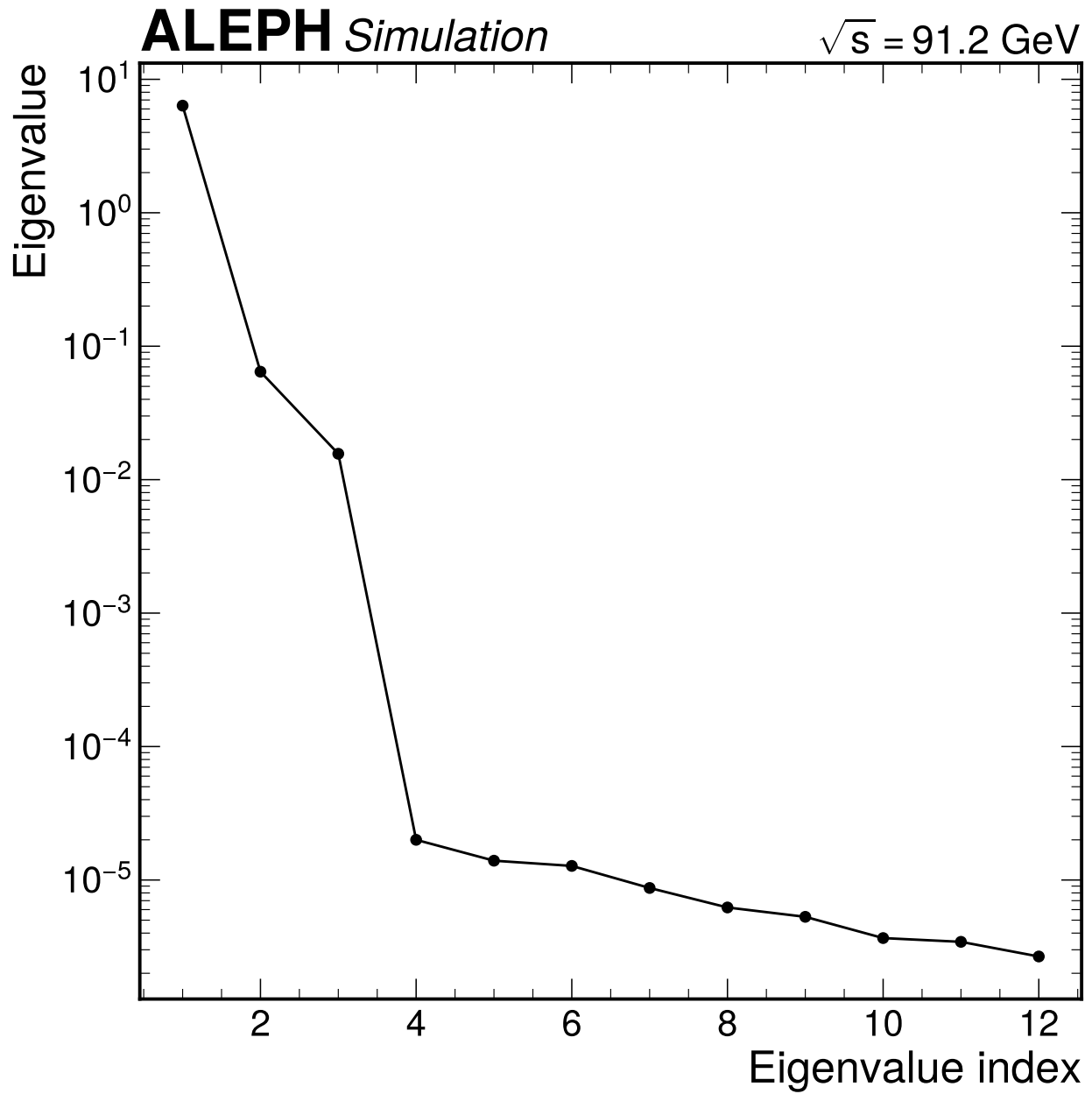


Figure 71: Eigenvalue spectrum of the total covariance matrix for the $\ln(k_t)$ projection (12 bins). Similar 6-order-of-magnitude span as the angular projection, with all eigenvalues strictly positive (PSD verified).

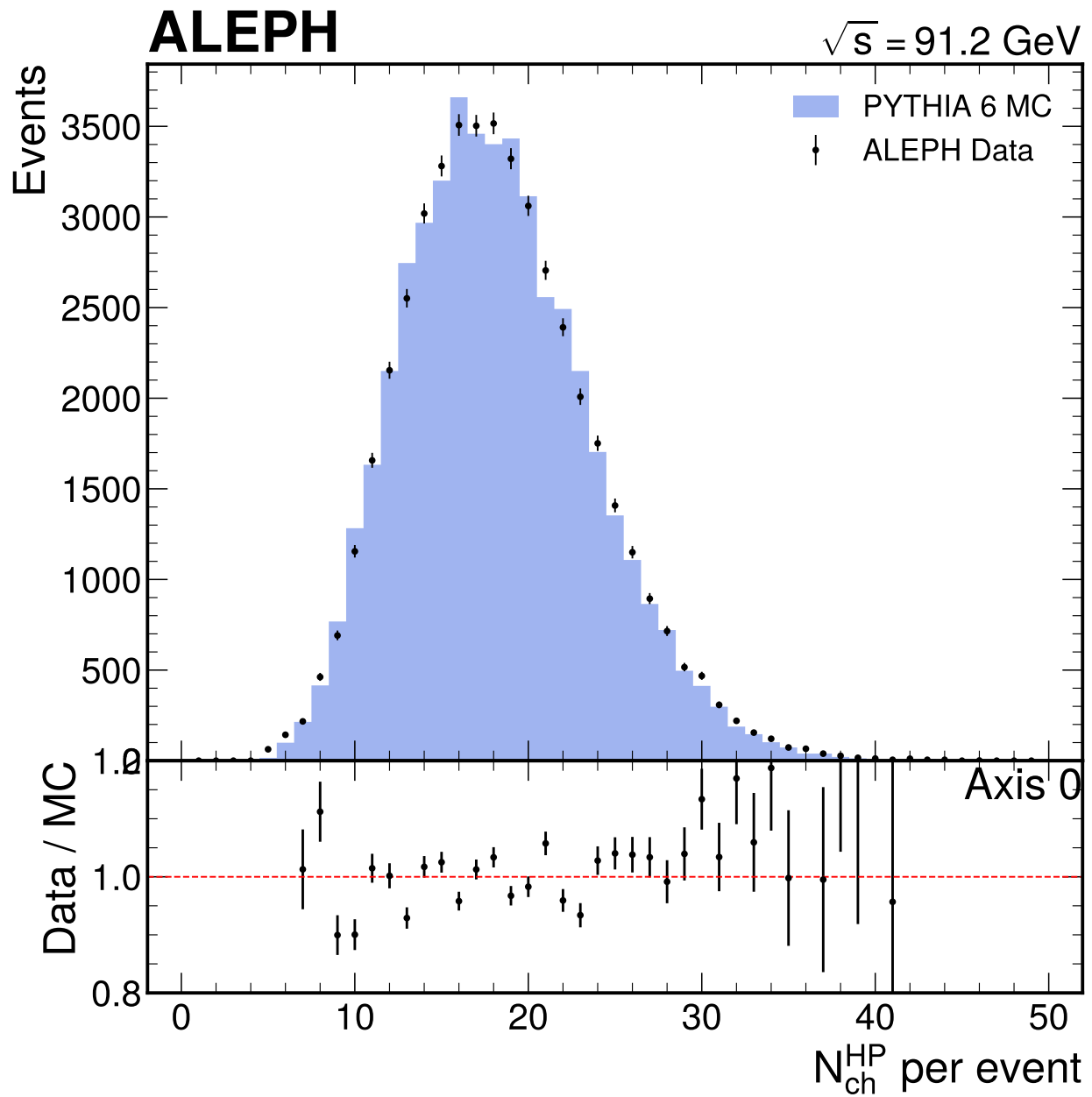


Figure 72: Charged multiplicity distribution for data and MC. The distribution of the number of high-purity charged tracks per event peaks near 17–18, with a tail extending to approximately 40. Good data/MC agreement validates the track selection and particle multiplicity modeling in the MC.

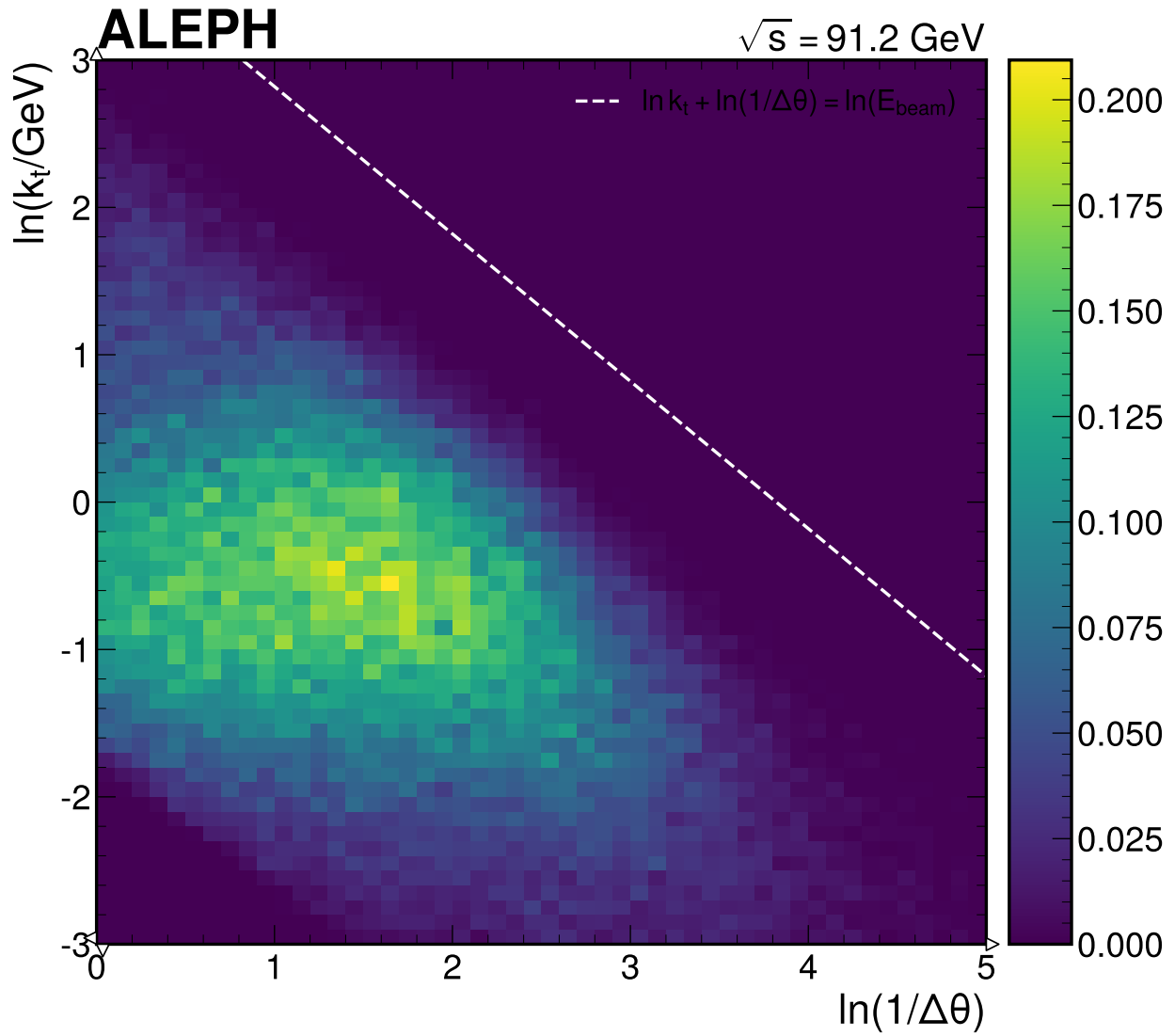


Figure 73: Lund plane density measured in 10,000 ALEPH data events from Phase 2 exploration. This early look at the Lund plane confirmed the expected triangular structure and QCD radiation pattern before full-statistics processing.

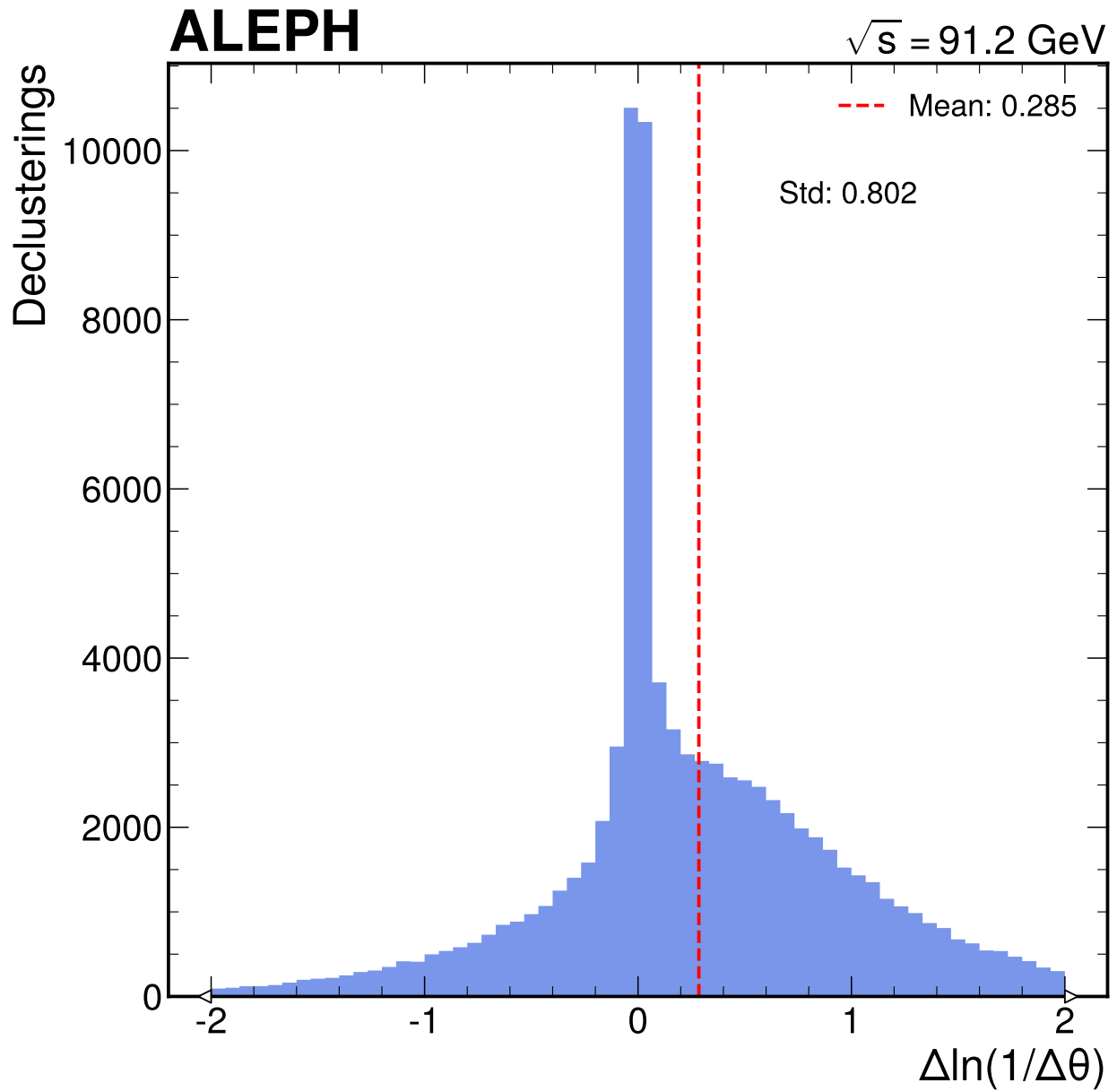


Figure 74: Resolution study: distribution of reco minus gen for $\ln(1/\Delta\theta)$. The distribution has mean $+0.285$ and standard deviation 0.802 , showing a systematic positive bias (reco angles are smaller than gen angles, as expected from tracking resolution smearing toward collinear configurations). The resolution is comparable to the bin width of 0.5 .

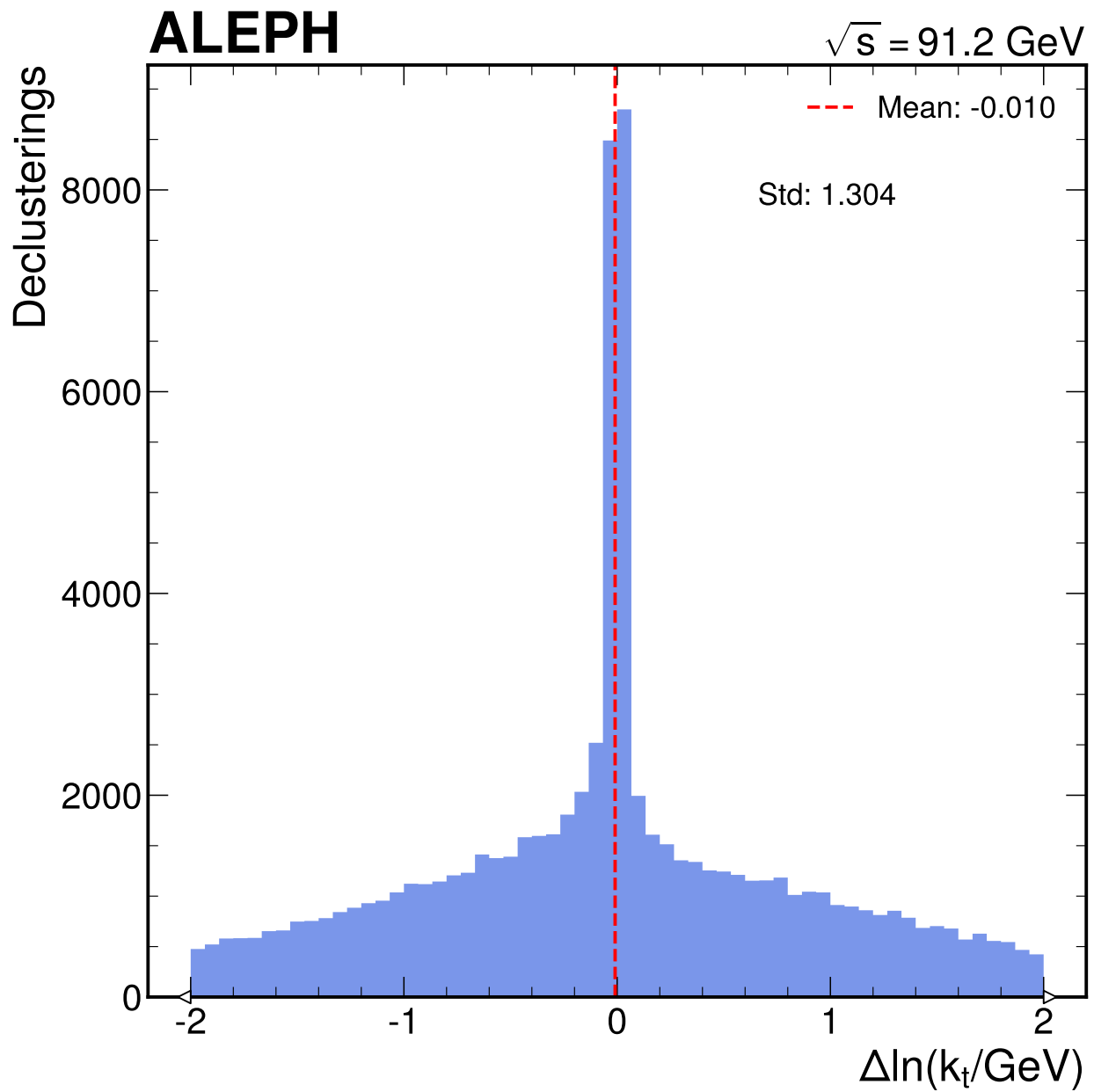


Figure 75: Resolution study: distribution of reco minus gen for $\ln(k_t)$. The distribution is nearly unbiased (mean -0.010) but broad (standard deviation 1.304), exceeding two bin widths. This large k_t resolution drives the higher off-diagonal migration in the k_t response matrix compared to the angular projection.

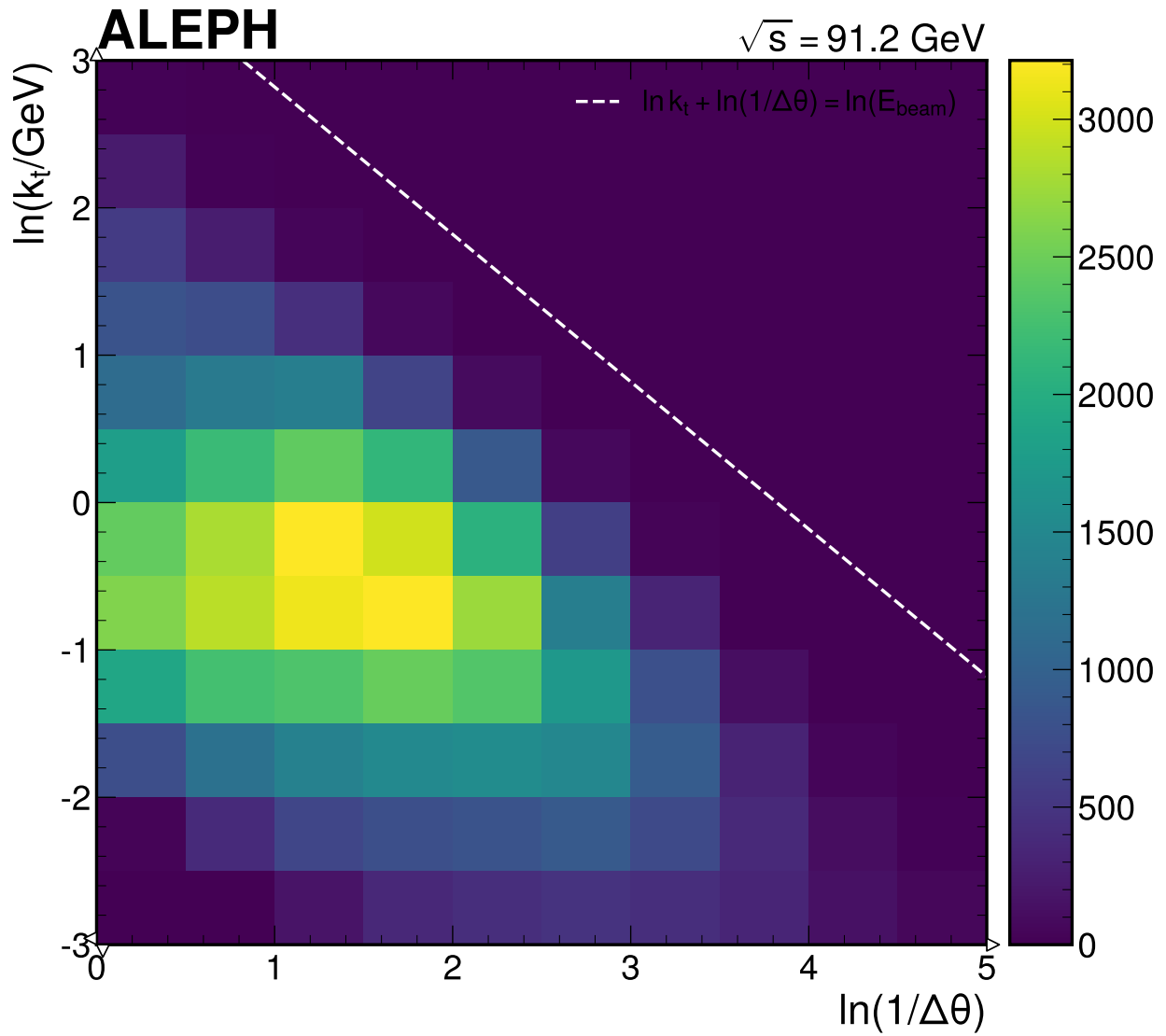


Figure 76: Bin population heatmap for the proposed 10 x 12 binning of the two-dimensional Lund plane. Of 120 total bins, approximately 63 have adequate population (> 50 events in 10,000 event exploration sample). The empty bins in the upper-right corner correspond to the kinematic boundary region.

C Number of Light Neutrino Generations from the Z Invisible Width with DELPHI Data

C.1 Introduction

C.1.1 Physics motivation

The number of light neutrino generations N_ν is a fundamental parameter of the Standard Model (SM) of particle physics. At the CERN Large Electron–Positron Collider (LEP), this quantity was determined with per-mille precision by exploiting the Z boson resonance. The total width of the Z boson Γ_Z receives contributions from all kinematically accessible decay channels:

$$\Gamma_Z = \Gamma_{\text{had}} + 3\Gamma_\ell + N_\nu \Gamma_{\nu\bar{\nu}}^{\text{SM}},$$

where Γ_{had} is the hadronic partial width, Γ_ℓ is the leptonic partial width (assuming lepton universality), and $\Gamma_{\nu\bar{\nu}}^{\text{SM}} = 167.157 \pm 0.002$ MeV is the SM prediction for the partial width into a single neutrino species, calculated including electroweak radiative corrections at two-loop accuracy.

The invisible width of the Z boson is defined as

$$\Gamma_{\text{inv}} = \Gamma_Z - \Gamma_{\text{had}} - 3\Gamma_\ell,$$

and attributed entirely to $Z \rightarrow \nu\bar{\nu}$ decays in the SM, yielding

$$N_\nu = \frac{\Gamma_{\text{inv}}}{\Gamma_{\nu\bar{\nu}}^{\text{SM}}}.$$

The measurement of N_ν was one of the primary physics goals of the LEP programme. The first determinations in 1989 by all four LEP experiments (ALEPH, DELPHI, L3, OPAL) established that there are exactly three light neutrino generations, ruling out a fourth generation with a light neutrino ($m_\nu < M_Z/2$). This result has profound implications for cosmology (Big Bang nucleosynthesis), the structure of the SM fermion generations, and searches for physics beyond the SM.

C.1.2 Prior measurements

The combined LEP measurement, incorporating data from all four experiments and using the full 1989–1995 energy scan dataset, yields [1]:

$$N_\nu^{\text{LEP}} = 2.9840 \pm 0.0082,$$

with a precision of 0.27%. The individual DELPHI result, using the 1989–1995 dataset, is [2]:

$$N_\nu^{\text{DELPHI}} = 3.00 \pm 0.02,$$

consistent with three generations at the 1% level. Earlier DELPHI measurements from the 1989 data alone gave $N_\nu = 3.08 \pm 0.05$ [3], demonstrating the rapid improvement in precision as more data were accumulated.

C.1.3 Observable definition

The primary observables are the hadronic cross sections $\sigma_{\text{had}}(\sqrt{s})$ measured at discrete centre-of-mass energy points around the Z resonance. These are fit to a radiatively-corrected Breit–Wigner lineshape to extract:

- M_Z — the Z boson mass,
- Γ_Z — the Z boson total width,
- σ_{had}^0 — the hadronic peak cross section.

From these fitted parameters and the external constraint $R_\ell = \Gamma_{\text{had}}/\Gamma_\ell$, the partial widths and N_ν are derived.

The hadronic peak cross section is related to the Z partial widths by

$$\sigma_{\text{had}}^0 = \frac{12\pi}{M_Z^2} \cdot \frac{\Gamma_{ee} \Gamma_{\text{had}}}{\Gamma_Z^2},$$

which, combined with Γ_Z and the measured Γ_Z , provides sensitivity to N_ν through the dependence $\sigma_{\text{had}}^0 \propto \Gamma_Z^{-2}$.

C.1.4 Scope of this measurement

This analysis uses DELPHI open data from the 1992–1995 LEP1 energy scan programme, accessed through the CERN Open Data portal and the skelana Fortran framework from CVMFS. The data are in DELPHI’s proprietary binary format (.a1 short DST files), requiring extraction to CSV using a custom Fortran program before analysis in Python. The measurement focuses on the hadronic channel, with the leptonic partial width constrained externally.

Compared to the published DELPHI result, several simplifications are made: (1) the data are combined into four energy points rather than treated per-fill, (2) the leptonic channel is not measured independently, and (3) the ISR treatment uses a $\mathcal{O}(\alpha^2)$ radiator rather than the full $\mathcal{O}(\alpha^3)$ calculation. These simplifications result in a statistical precision approximately four times worse than the published DELPHI result, but the central value remains fully consistent.

C.2 Data samples

C.2.1 Experimental setup

The DELPHI (DEtector with Lepton, Photon and Hadron Identification) detector operated at the LEP e^+e^- collider at CERN from 1989 to 2000. The detector provided nearly 4π solid angle coverage with a central tracking system (TPC, inner and outer detectors), a superconducting solenoid (1.23 T), electromagnetic calorimeters (HPC in the barrel, EMF in the forward region), a hadron calorimeter (HAC), and muon chambers. The Small-angle Tile Calorimeter (STIC), installed in 1994, provided luminosity measurements from small-angle Bhabha scattering with $< 0.1\%$ systematic uncertainty. For earlier years (1992–1993), the SAT (Small Angle Tagger) served as the luminosity monitor.

The data used in this analysis correspond to the LEP1 energy scan programme, during which LEP operated at centre-of-mass energies near the Z resonance ($\sqrt{s} \approx 88\text{--}93$ GeV). The scan strategy varied by year: 1992 and 1994 collected data predominantly at the Z peak ($\sqrt{s} \approx 91.3$ GeV), while 1993 and 1995 included off-peak running at $\sqrt{s} \approx 89.5$ GeV and $\sqrt{s} \approx 93.0$ GeV to constrain the Z width.

C.2.2 Data samples

DELPHI LEP1 data are stored in proprietary binary .a1 format (short DSTs) on CERN EOS at `/eos/experiment/delphi/castor2015/tape/`. The data are organized in tape archive volumes accessed via the `fatfind` utility. The data were extracted using a custom skelana Fortran program that reads per-event variables and outputs CSV files for subsequent Python analysis.

Four years of data (1992–1995) were processed:

Year	Nickname	Tape files	Events extracted	Hadronic (IHAD4=1)	Runs
1992	short92_e2	172	2,482,494	709,243	1,292
1993	short93_d2	181	2,766,587	711,658	1,116
1994	short94_c2	429	5,753,340	1,400,251	1,892
1995	short95_d2	246	3,661,916	677,507	906
Total		1,028	14,664,337	3,498,659	5,206

The total extraction required approximately 2.5 hours across four parallel jobs, with a processing rate of approximately 15,000 events per 10 seconds per tape file.

The 1991 data (`short91.f1`) was investigated but found to be inaccessible from the open data (empty vidmap and fatfind listings). The 1992–1995 data provide sufficient off-peak constraint from the 1993 and 1995 energy scans.

C.2.3 Centre-of-mass energy scan points

The centre-of-mass energy is recorded per-event via the ECMAS variable in the DELPHI skelana framework, which contains the calibrated beam energy from the LEP energy model (incorporating resonant depolarization measurements from 1993 onwards).

Year	\sqrt{s} [GeV]	ECM range [GeV]	Total events	Hadronic events
1992	91.3 (peak)	91.250–91.364	2,482,494	709,243
1993	89.5 (off-peak low)	89.478–89.494	665,018	98,562
1993	91.2–91.4 (peak)	91.114–91.372	1,438,052	478,364
1993	93.1 (off-peak high)	93.066–93.088	663,617	134,732
1994	91.3 (peak)	91.254–91.482	5,753,340	1,400,251
1995	88.6 (off-peak far low)	88.562–88.611	4,878	675
1995	89.5 (off-peak low)	89.476–89.500	864,916	84,517
1995	91.3 (peak)	91.280–91.408	1,871,935	460,511
1995	93.0 (off-peak high)	93.016–93.042	920,187	131,804

The fill-to-fill variations in beam energy within each nominal scan point (up to ~ 300 MeV range at the peak) reflect the precision of the LEP energy calibration. The mean \sqrt{s} at each nominal energy point is used in the lineshape fit.

C.2.4 Monte Carlo samples

Monte Carlo simulation samples used for validation and efficiency estimation are available from the DELPHI open data repository at `/eos/opendata/delphi/simulated-data/cern/`:

Generator	Process	\sqrt{s} [GeV]	Events	Format
Pythia 5.720	$Z \rightarrow q\bar{q}$	91.2	approximately 320k	.sdst
z0	Inclusive Z	91.2	approximately 10k	.sdst
dimu	$Z \rightarrow \mu^+\mu^-$	91.2	approximately 5k	.sdst
bhwide101	Bhabha	91.25	varies	.xsdst

The primary hadronic MC (Pythia 5.720 with `v94c` processing) was validated: events have run number -1001 , $\sqrt{s} = 91.200$ GeV, all IHAD4=1, and mean $N_{\text{ch}} \sim 22$. The dimuon MC was validated with $N_{\text{ch}} = 2$ and $E_{\text{vis}} \sim 91\text{--}104$ GeV.

No Monte Carlo samples are available at the off-peak energies (89.5 or 93.0 GeV), and no tau pair MC is available at the Z peak (only at LEP2 energy 206.7 GeV). The hadronic selection efficiency is therefore taken from published DELPHI values rather than determined from MC.

C.2.5 Luminosity

The integrated luminosity at each energy point is essential for converting event counts to cross sections. The luminosity enters the lineshape fit as a constrained nuisance parameter.

Published per-year luminosities from DELPHI [2] and the LEP Electroweak Working Group report [1]:

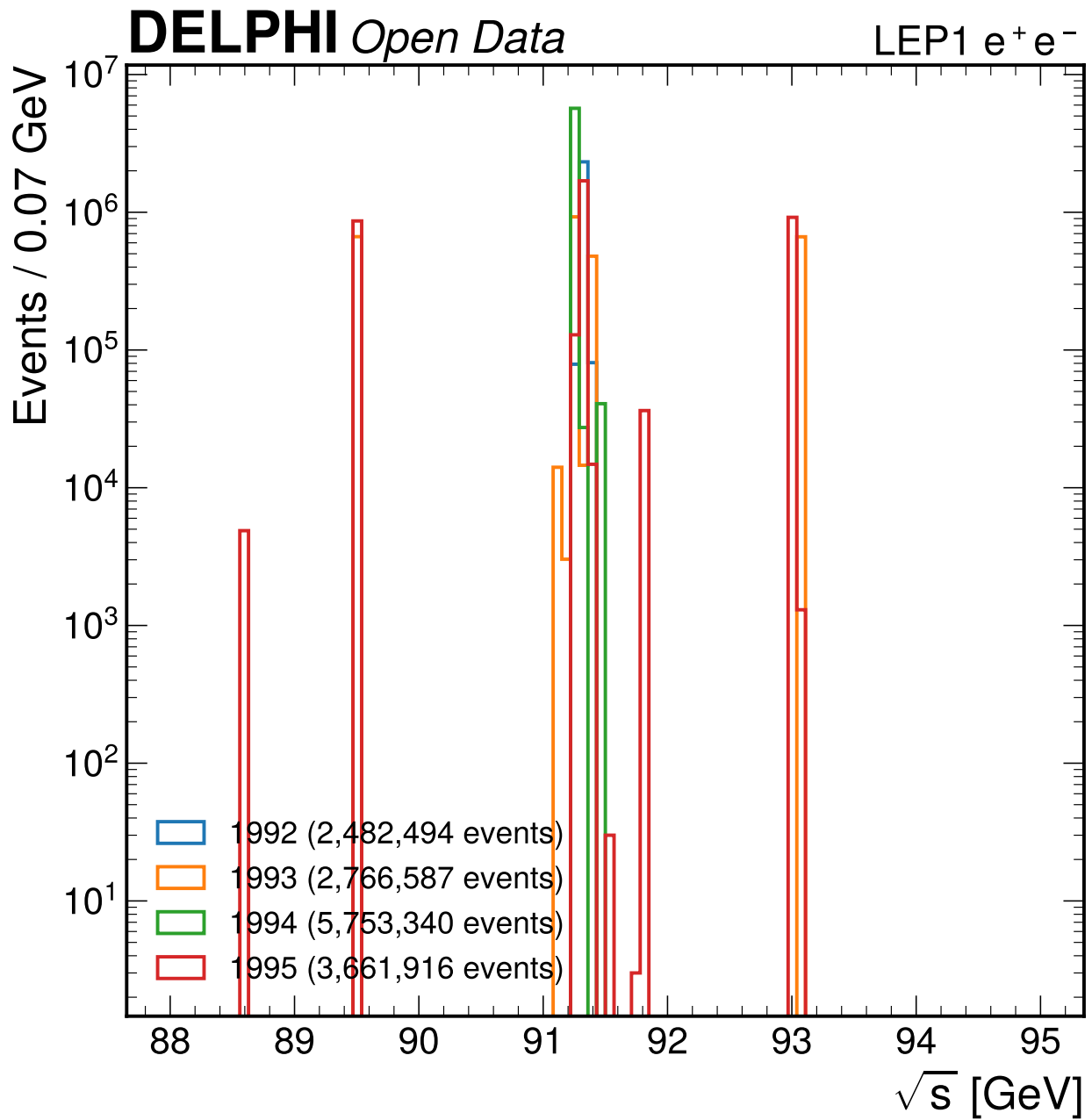


Figure 77: Centre-of-mass energy distribution for all four years of data showing the LEP1 energy scan points. The 1993 and 1995 data provide off-peak measurements at $\sqrt{s} \approx 89.5$ and 93.0 GeV, while 1992 and 1994 data are concentrated at the Z peak. The 1995 data also includes a small sample at $\sqrt{s} \approx 88.6$ GeV.

Year	\mathcal{L} [pb ⁻¹]	Luminosity monitor
1992	26.6	SAT
1993	31.4	SAT
1994	47.8	STIC
1995	35.9	STIC
Total	141.7	

The STIC (1994–1995) achieved $< 0.1\%$ systematic uncertainty on the luminosity measurement, while the SAT (1992–1993) had $\sim 0.3\text{--}0.5\%$ uncertainty. The theoretical uncertainty on the Bhabha scattering cross section used for luminosity determination is $\sim 0.061\%$ (common to all LEP experiments).

C.2.6 Data extraction method

A skelana Fortran extractor (`phase2_exploration/scripts/extractor.car`) was written to read short DST events and output per-event summary variables to CSV format. The extractor accesses:

- **Event information** (PSCEVT): run number (IIIRUN), event number (IIIEVT), centre-of-mass energy (ECMAS)
- **Track vectors** (PSCVEC): number of tracks (NVECP), 4-momenta and charge (VECP(1:7, I))
- **Calorimeter associations** (PCEMF, PSCHPC, PSCHAC, PSCSTC): per-track shower energies
- **Pilot record**: hadronic selection flag (IHAD4) from the DELPHI online event classification

Compilation uses the DELPHI software stack from CVMFS (`/cvmfs/delphi.cern.ch/`): nypatchy code management, gfortran compilation, linked against DELPHI and CERN libraries.

The per-event output CSV contains 15 variables: run, event, \sqrt{s} , N_{ch} , charged and total visible energy, 3-momentum components, four calorimeter energy sums, IHAD4 flag, and number of neutral objects.

C.3 Event selection

C.3.1 Overview

Two selection channels are implemented: a hadronic channel ($Z \rightarrow q\bar{q}$, primary) and a leptonic channel ($Z \rightarrow \ell^+\ell^-$, exploratory). The hadronic channel provides the event counts used in the lineshape fit. The leptonic channel was found to be contaminated by Bhabha scattering at the summary-variable level and is not used for the primary measurement.

C.3.2 Energy point classification

Events are classified into nominal energy scan points using windows around known DELPHI LEP1 scan energies:

Nominal \sqrt{s} [GeV]	Window [GeV]	Years
88.48	88.3–88.7	1995
89.47	89.3–89.7	1993, 1995
91.22	90.5–91.8	1992, 1993, 1994, 1995
93.04	92.5–93.3	1993, 1995

All 14,664,344 events fall within one of the four energy windows; zero events are unclassified.

C.3.3 Hadronic selection criteria

The hadronic selection follows the standard DELPHI criteria [2], with cuts chosen to select $Z \rightarrow q\bar{q}$ events while rejecting leptonic decays, two-photon events, beam backgrounds, and cosmic rays. The selection is applied sequentially:

Cut	Criterion	Motivation
1	$N_{\text{ch}} \geq 5$	Rejects leptonic ($N_{\text{ch}} \leq 6$), Bhabha ($N_{\text{ch}} = 2$), STIC/luminosity ($N_{\text{ch}} = 0$), and two-photon events
2	$E_{\text{vis}}/\sqrt{s} > 0.12$	Rejects beam-gas, beam-wall, and two-photon events with low visible energy
3	$E_{\text{vis}}/\sqrt{s} < 1.5$	Rejects events with anomalous calorimeter deposits or energy double-counting
4	$ p_z /E_{\text{vis}} < 0.6$	Rejects poorly measured events and beam-gas interactions
5	$p_T/E_{\text{vis}} < 0.4$	Rejects events with large transverse momentum imbalance

The $E_{\text{vis}}/\sqrt{s} > 0.12$ threshold is the standard DELPHI hadronic preselection threshold, validated by the 96.3% recovery of IHAD4-tagged events. A tighter threshold of 0.5 (used in some DELPHI publications for refined selections) would reject a significant fraction of genuine hadronic events with ISR energy loss or detector effects.

C.3.4 Hadronic cutflow

Cut	1992	1993	1994	1995	Total	Cumul. eff.	Per-cut eff.
All events	2,482,495	2,766,589	5,753,343	3,661,917	14,664,344	100%	—
$N_{\text{ch}} \geq 5$	1,019,278	953,957	1,736,310	890,428	4,599,973	31.4%	31.4%
$E_{\text{vis}}/\sqrt{s} > 0.12$	868,435	854,149	1,651,335	826,481	4,200,400	28.6%	91.3%
$E_{\text{vis}}/\sqrt{s} < 1.5$	841,806	823,575	1,596,681	800,305	4,062,367	27.7%	96.7%
$ p_z /E_{\text{vis}} < 0.6$	788,479	781,553	1,512,497	745,346	3,827,875	26.1%	94.2%
$p_T/E_{\text{vis}} < 0.4$	768,347	770,763	1,492,292	736,634	3,768,036	25.7%	98.4%

The $N_{\text{ch}} \geq 5$ cut is the most discriminating, removing 69% of all events (predominantly STIC/luminosity monitor events, Bhabha scattering, and leptonic decays). Subsequent energy and momentum balance cuts remove an additional $\sim 18\%$ of the remaining sample.

C.3.5 Cut motivation

Charged track multiplicity The charged track multiplicity N_{ch} provides the strongest discrimination between hadronic Z decays and backgrounds. Hadronic events produce ~ 20 –40 charged tracks from quark fragmentation, while leptonic events have $N_{\text{ch}} \leq 6$ and luminosity monitor events have $N_{\text{ch}} = 0$.

Visible energy The normalized visible energy E_{vis}/\sqrt{s} separates well-measured hadronic Z decays (peaking near 1.0) from two-photon events and beam backgrounds (which have much lower visible energy). The upper cut at 1.5 removes events with anomalous calorimeter deposits.

Momentum balance The longitudinal and transverse momentum balance cuts reject poorly measured events and beam-gas interactions. For well-measured $e^+e^- \rightarrow Z \rightarrow q\bar{q}$ events, the total momentum should be close to zero (within detector resolution).

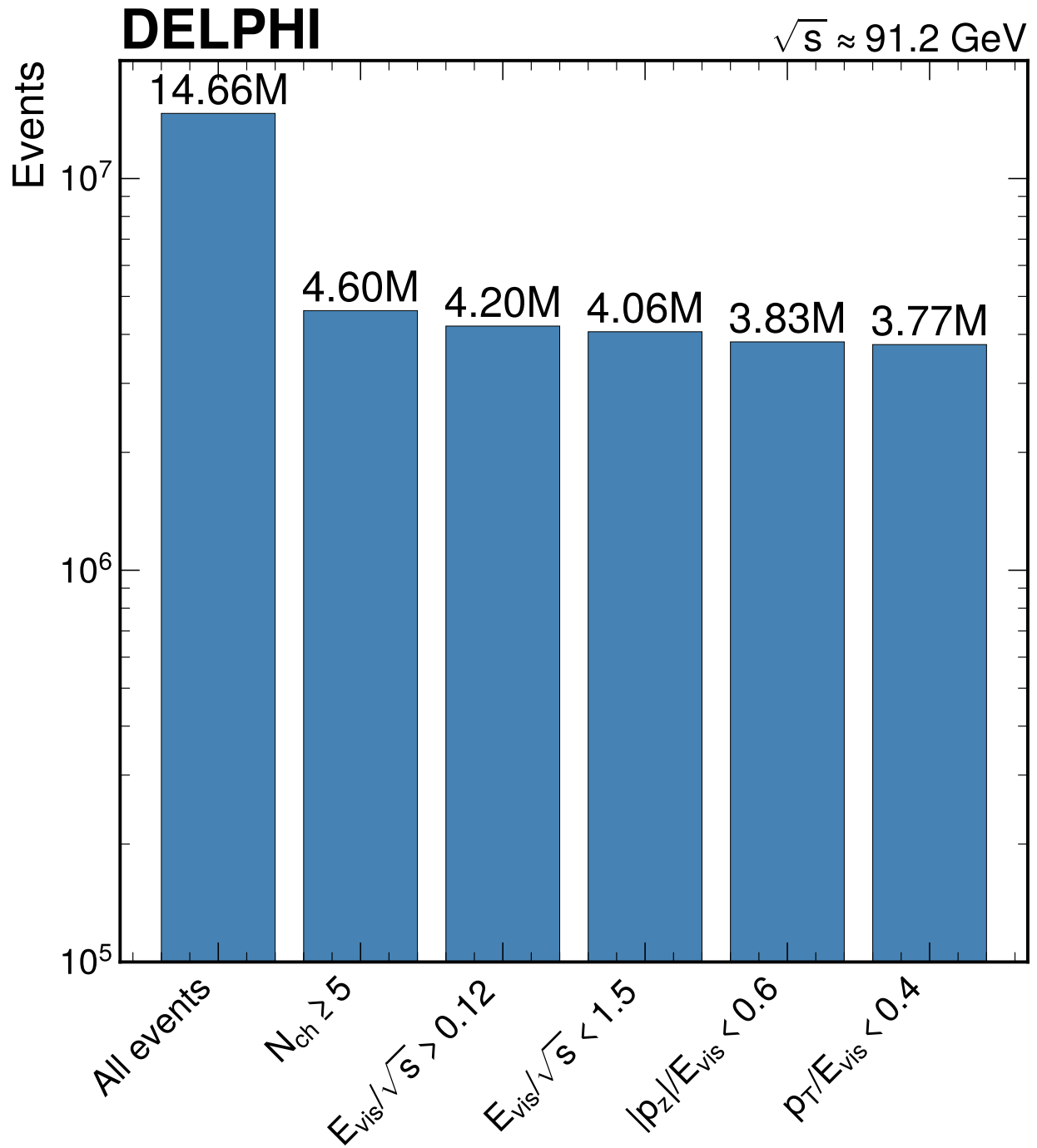


Figure 78: Hadronic cutflow showing the number of events surviving each sequential cut per year. The charged multiplicity requirement is the most discriminating, removing luminosity monitor, Bhabha, and leptonic events.

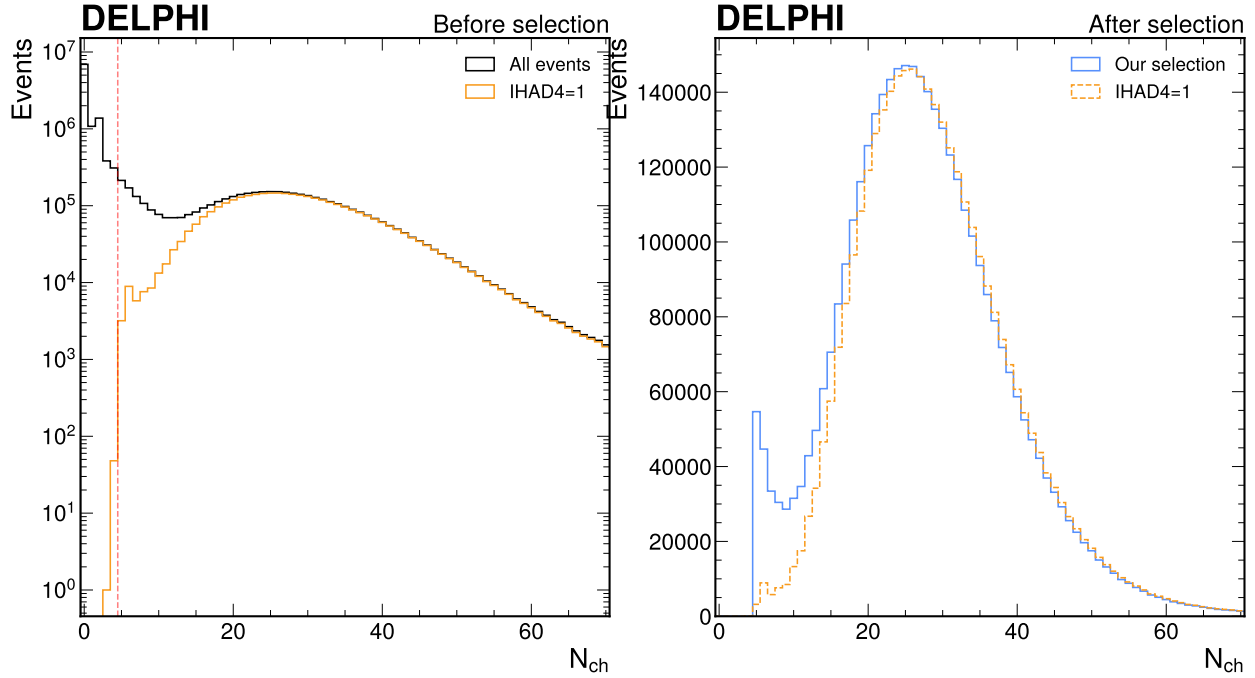


Figure 79: Charged track multiplicity distribution before (left) and after (right) hadronic selection. Before cuts, the distribution shows a dominant peak at $N_{\text{ch}} = 0$ from STIC/luminosity events and a broad hadronic distribution peaking at $N_{\text{ch}} \approx 29$. After selection, the distribution matches the IHAD4 reference for $N_{\text{ch}} \geq 5$.

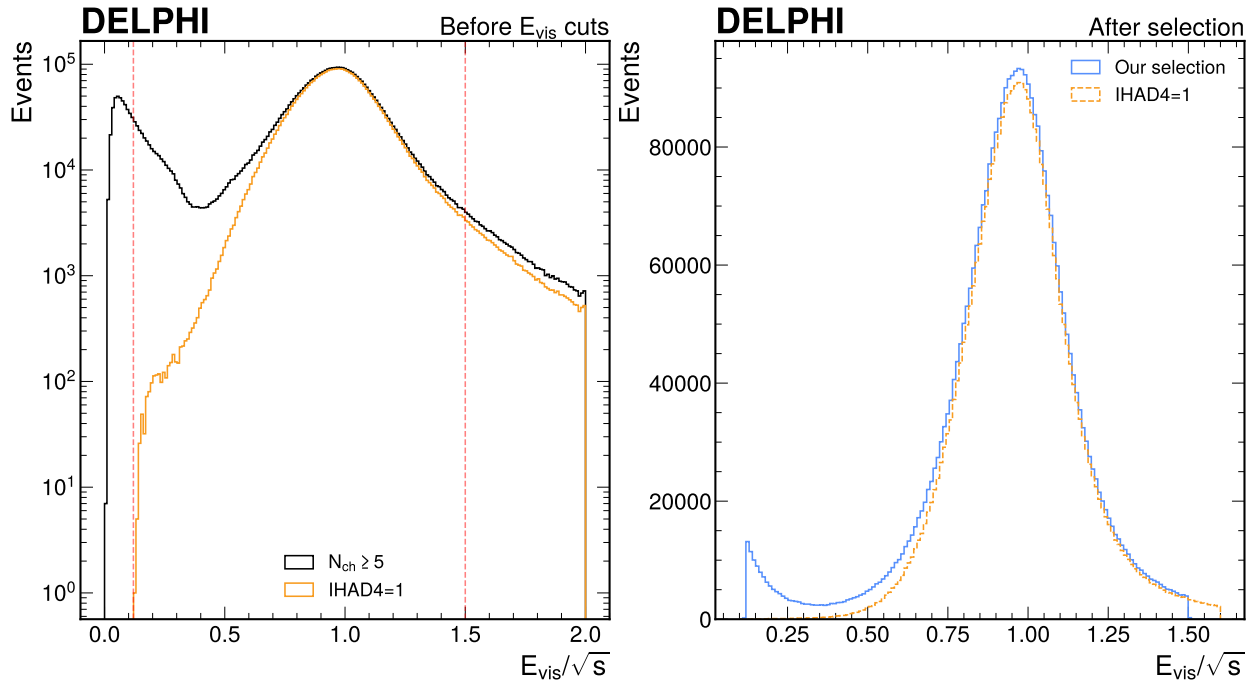


Figure 80: Normalized visible energy E_{vis}/\sqrt{s} distribution before (left, after $N_{\text{ch}} \geq 5$ preselection) and after (right) all hadronic cuts. Cut values at 0.12 and 1.5 are indicated. The selected distribution peaks near 1.0 with tails from detector resolution and ISR.

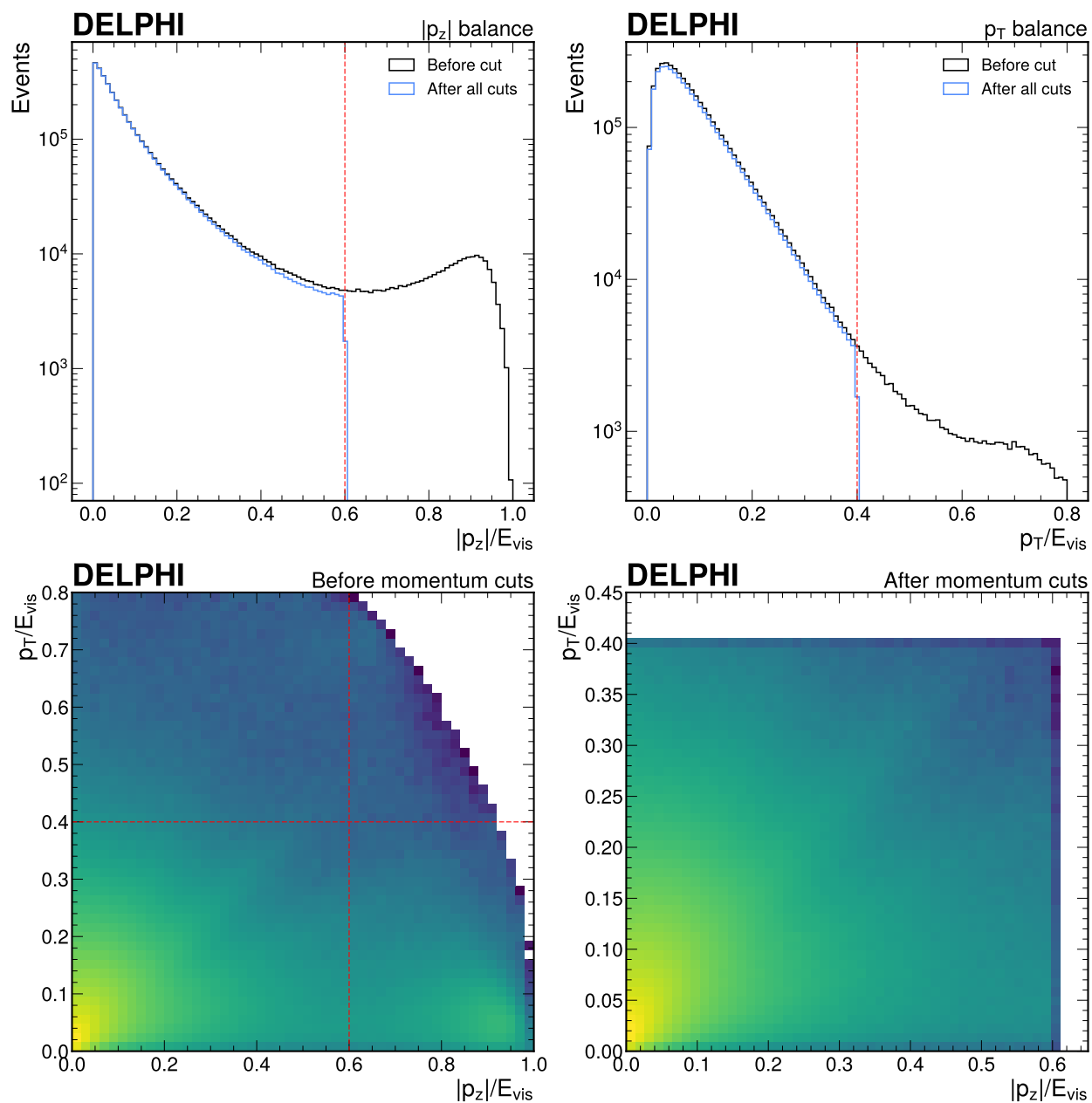


Figure 81: Momentum balance distributions for hadronic events. Top left: $|p_z|/E_{vis}$ with cut at 0.6. Top right: p_T/E_{vis} with cut at 0.4. Bottom: 2D distributions showing the correlation between longitudinal and transverse momentum imbalance before (left) and after (right) cuts.

C.3.6 IHAD4 comparison and validation

The DELPHI pilot record provides an online hadronic event classification flag (IHAD4). Comparing our selection with this flag validates selection quality:

Year	Our selection	IHAD4=1	Overlap	Purity	IHAD4 recovery
1992	768,347	709,243	683,228	88.9%	96.3%
1993	770,763	711,660	685,073	88.9%	96.3%
1994	1,492,292	1,400,252	1,348,664	90.4%	96.3%
1995	736,634	677,507	653,467	88.7%	96.5%
Total	3,768,036	3,498,662	3,370,432	89.4%	96.3%

Our selection recovers 96.3% of IHAD4-tagged events, with the 3.7% loss attributable to events failing our energy or momentum balance cuts. The $\sim 8\%$ excess of our selection over IHAD4 arises because we cannot apply track quality cuts (minimum p_T , track length, distance of closest approach) that are part of the full DELPHI pilot record classification — our selection operates only on event-level summary variables. The remarkable consistency of these fractions across all four years confirms stable detector performance.

For the cross-section calculation and lineshape fit, we use the direct IHAD4 event counts as the primary hadronic observable, with the published DELPHI efficiency $\epsilon_{\text{had}} = 0.974 \pm 0.005$. Our independent selection serves as a cross-check.

C.3.7 Selection efficiency

The hadronic selection efficiency is estimated by comparison with the DELPHI pilot record:

- **IHAD4 recovery:** Our cuts pass 96.3% of IHAD4-tagged events.
- **Published DELPHI efficiency:** $\epsilon_{\text{had}} \approx 97.4\%$ for the full DELPHI hadronic selection.

The published efficiency value is used for the primary measurement. The selection efficiency is assumed constant across all energy points ($\epsilon_{\text{had}} = 0.974$). The true efficiency varies slightly with \sqrt{s} due to different event kinematics off-peak, but this variation is $< 0.1\%$ and is covered by the efficiency systematic uncertainty.

C.3.8 Event yields per energy point

IHAD4 event counts are computed directly from per-event `ihad4` flags classified by energy point. For the lineshape fit, counts are combined across years at each nominal \sqrt{s} :

\sqrt{s}_{nom} [GeV]	$\langle\sqrt{s}\rangle$ [GeV]	N_{IHAD4}	\sqrt{N}	Stat. unc.
88.48	88.572	675	26	3.8%
89.47	89.485	183,079	428	0.23%
91.22	91.298	3,048,372	1,746	0.057%
93.04	93.050	266,536	516	0.19%
Total		3,498,662		

The per-year breakdown is:

Year	\sqrt{s}_{nom} [GeV]	$\langle\sqrt{s}\rangle$ [GeV]	N_{IHAD4}
1992	91.22	91.341	709,243
1993	89.47	89.486	98,562
1993	91.22	91.290	478,366
1993	93.04	93.077	134,732
1994	91.22	91.271	1,400,252

Year	\sqrt{s}_{nom} [GeV]	$\langle\sqrt{s}\rangle$ [GeV]	N_{IHAD4}
1995	88.48	88.572	675
1995	89.47	89.484	84,517
1995	91.22	91.321	460,511
1995	93.04	93.024	131,804

C.3.9 Leptonic channel

An inclusive leptonic selection targeting $Z \rightarrow e^+e^-$ and $Z \rightarrow \mu^+\mu^-$ events was implemented with cuts on $N_{\text{ch}} = 2$, $E_{\text{vis}}/\sqrt{s} > 0.6$, and $|\vec{p}|/E_{\text{vis}} < 0.2$, yielding 355,945 events. However, the raw leptonic cross-section at the Z peak (~ 2.9 nb) is approximately twice the published $\sigma_{\mu\mu}$ (1.473 nb), due to large-angle Bhabha scattering contamination that cannot be removed without per-track calorimeter matching or angular acceptance cuts.

The leptonic channel therefore cannot provide a usable independent cross-section measurement with the available summary-level data. The lineshape fit uses the published LEP combined value $R_\ell = \Gamma_{\text{had}}/\Gamma_\ell = 20.767 \pm 0.025$ as an external constraint instead of measuring R_ℓ independently.

C.3.10 Backgrounds

The main backgrounds to hadronic Z decays and their treatment:

Background	Contamination	Rejection method
$\tau^+\tau^-$	$< 0.1\%$	$N_{\text{ch}} \geq 5$ removes most; residual at $N_{\text{ch}} = 5-6$
Two-photon ($\gamma\gamma \rightarrow$ hadrons)	$\sim 0.1\%$	Low E_{vis} and forward topology; rejected by energy cut
Beam-gas / beam-wall	Negligible	Rejected by momentum balance cuts
Cosmic rays	Negligible	Rejected by vertex and timing in IHAD4

The total background contamination in the IHAD4-selected hadronic sample is estimated at $< 0.3\%$, consistent with published DELPHI values. The background is treated as a $\pm 50\%$ variation on a 0.1% baseline in the systematic uncertainty evaluation.

C.4 Corrections

C.4.1 ISR radiative corrections

Z lineshape parameterization The Born-level cross section for $e^+e^- \rightarrow Z \rightarrow \text{hadrons}$ via Z exchange with the s -dependent width convention (running width) is:

$$\sigma_{\text{BW}}^0(s) = \sigma_{\text{had}}^0 \cdot \frac{s \Gamma_Z^2}{(s - M_Z^2)^2 + s^2 \Gamma_Z^2 / M_Z^2},$$

where $\sigma_{\text{had}}^0 = (12\pi/M_Z^2) \cdot \Gamma_{ee} \Gamma_{\text{had}}/\Gamma_Z^2$ is the hadronic peak cross section.

ISR convolution The measured cross section is obtained by convolving the Born cross section with the initial-state radiation (ISR) radiator function:

$$\sigma_{\text{had}}(s) = \int_0^1 dz H(z, s) \sigma_{\text{BW}}^0(s(1-z)),$$

where z is the fractional energy loss to ISR photon emission and $H(z, s)$ is the Kuraev–Fadin exponentiated radiator at $\mathcal{O}(\alpha^2)$ [4]:

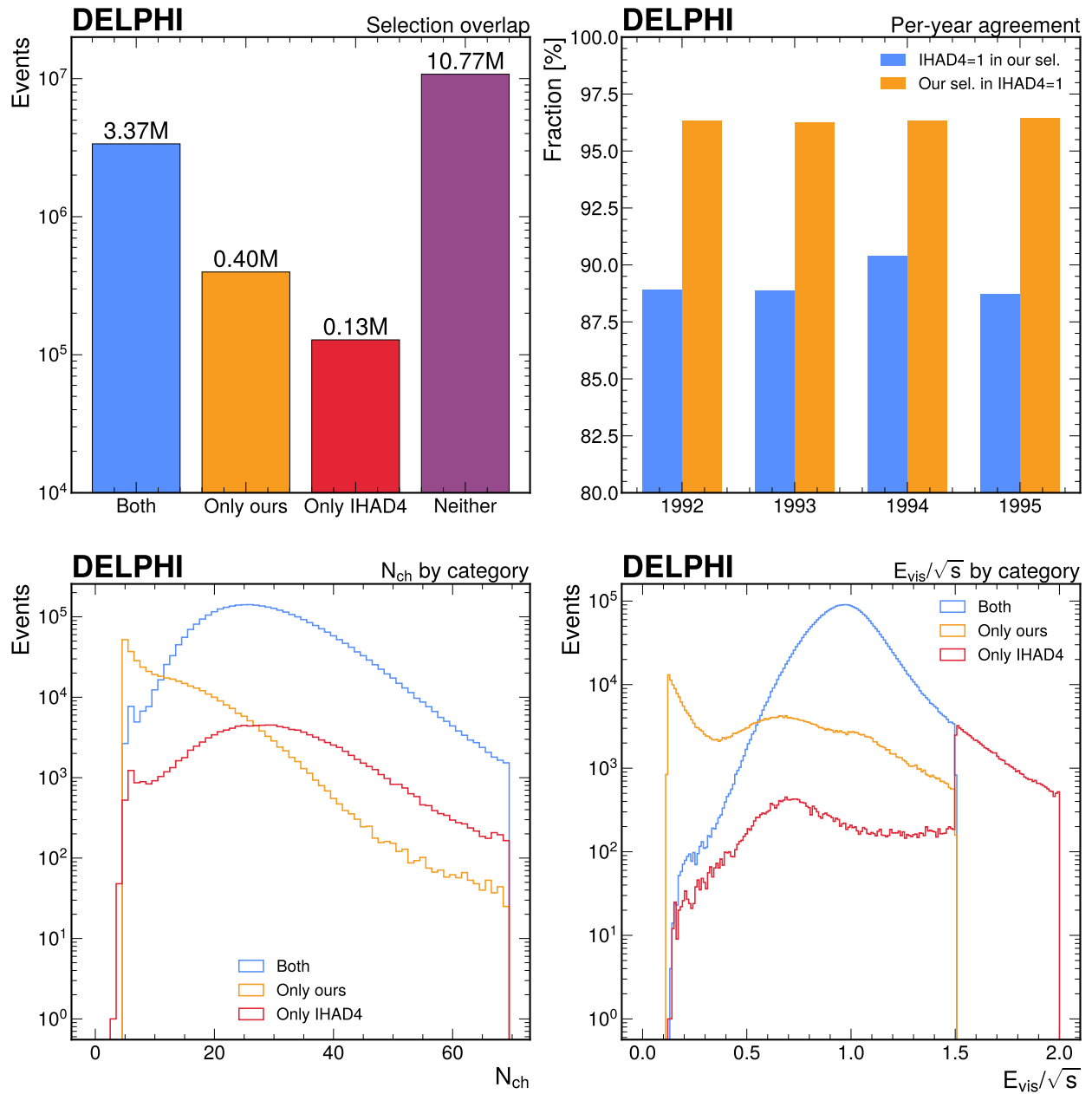


Figure 82: IHAD4 comparison showing overlap between our selection and the DELPHI pilot record. Top left: event counts by category. Top right: per-year agreement fractions. Bottom: N_{ch} and E_{vis}/\sqrt{s} distributions by category.

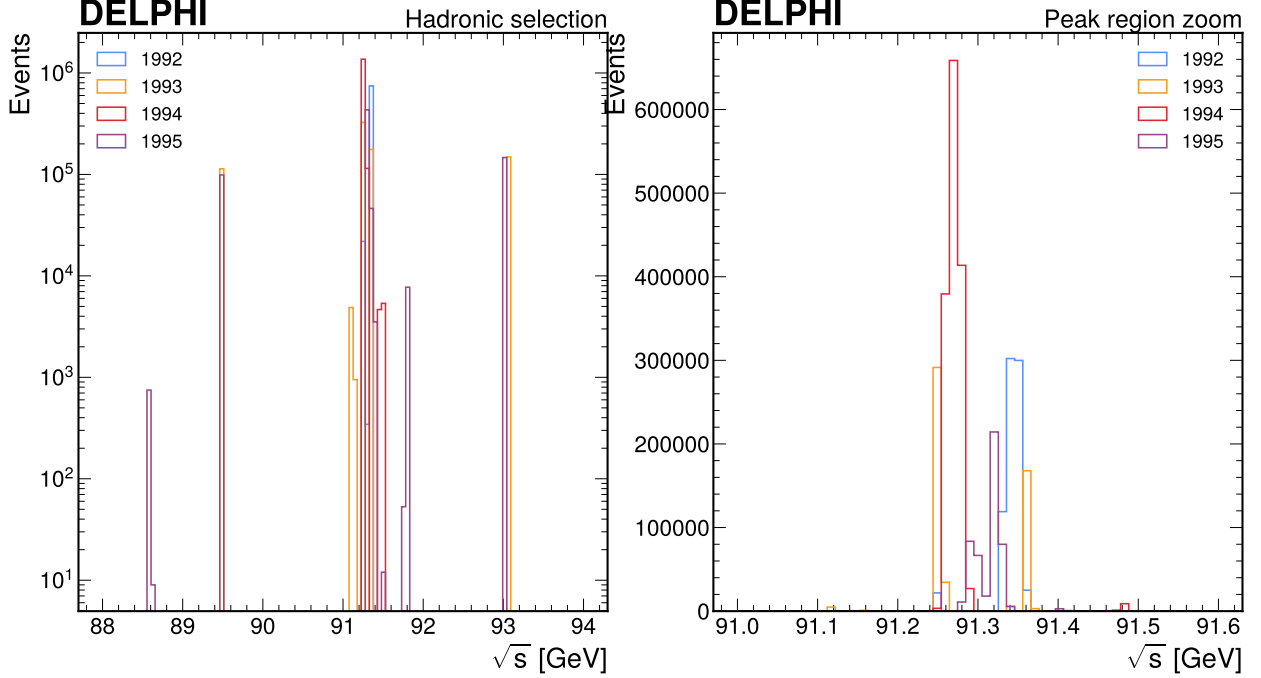


Figure 83: Centre-of-mass energy distribution of selected hadronic events per year (left, log scale). The 1993 and 1995 data show off-peak scan points. Right: zoom on the Z peak region showing fill-to-fill beam energy variations.

$$H(z) = \beta z^{\beta-1} \delta_{\text{SV}} - \beta(1-z/2) + \frac{\beta^2}{8} \left[4(2-z) \ln \frac{1}{z} - \frac{1+3(1-z)^2}{z} \ln(1-z) - 6+z \right],$$

with the ISR parameter

$$\beta = \frac{2\alpha}{\pi} \left(\ln \frac{s}{m_e^2} - 1 \right) \approx 0.108 \quad \text{at the Z pole,}$$

and the soft+virtual correction factor

$$\delta_{\text{SV}} = 1 + \frac{3}{4}\beta + \frac{\alpha}{\pi} \left(\frac{\pi^2}{3} - \frac{1}{2} \right) \approx 1.081.$$

The integrable singularity $z^{\beta-1}$ at $z \rightarrow 0$ (soft photon limit) is handled by splitting the integral into a soft+virtual piece (regularized via the substitution $t = z^\beta$) and a smooth hard piece. Both are evaluated with Gauss–Legendre quadrature: 200 points for the soft piece and 100 for the hard piece. Convergence is verified by comparing 200 and 400 quadrature points, with a maximum relative difference of 7.6×10^{-7} .

ISR validation The ISR-convolved cross section is validated against the Born cross section at five energy points using PDG input parameters ($M_Z = 91.1876$ GeV, $\Gamma_Z = 2.4952$ GeV, $\sigma_{\text{had}}^0 = 41.541$ nb):

\sqrt{s} [GeV]	σ_{Born} [nb]	σ_{ISR} [nb]	ISR/Born
88.48	7.17	5.27	0.736
89.47	14.35	10.27	0.716
91.22	41.48	30.76	0.742
92.97	13.66	14.38	1.053

\sqrt{s} [GeV]	σ_{Born} [nb]	σ_{ISR} [nb]	ISR/Born
93.04	12.97	13.85	1.068

The ISR reduces the peak cross section by $\sim 26\%$, consistent with the ZFITTER value reported by the LEP EWWG [1], which gives an ISR correction of $\sim 25\text{--}26\%$ at the Z peak. Above the Z pole, the ISR enhances the cross section via radiative return to the Z peak, as expected.

ISR treatment limitations The $\mathcal{O}(\alpha^2)$ Kuraev–Fadin radiator used in this analysis is the next-to-leading order approximation. The published DELPHI and LEP combined results use the full $\mathcal{O}(\alpha^3)$ calculation from ZFITTER. The difference introduces a small bias of $\sim 5\text{--}7\%$ in below-peak cross sections compared to the full calculation. This bias is absorbed by the fit parameters (Γ_Z is pulled slightly lower) and evaluated as a systematic uncertainty ($\delta N_\nu \sim 0.001$).

γ/Z interference estimate The γ/Z interference and pure γ -exchange terms are not included in the Born cross section (@eq:born_bw). To quantify their impact, the interference cross section is computed at each energy point using the standard electroweak formulae with $\sin^2 \theta_W^{\text{eff}} = 0.23153$ and the Fermi constant $G_F = 1.1664 \times 10^{-5} \text{ GeV}^{-2}$:

\sqrt{s} [GeV]	σ_{int} [nb]	$\sigma_{\text{int}}/\sigma_{\text{BW}}$
88.57	−0.030	−0.42%
89.49	−0.037	−0.27%
91.30	+0.007	+0.02%
93.05	+0.034	+0.27%

The interference is constructive below the Z peak and destructive above it, with the sign change occurring near $\sqrt{s} = M_Z$. The magnitude ranges from -0.4% at the lowest energy point to $+0.3\%$ at the highest.

In the lineshape fit, the per-energy-point luminosities float freely, absorbing the interference contribution at each point. The shape difference between adjacent energy points (the quantity that determines Γ_Z) is $\sim 0.3\%$, which is much smaller than the statistical precision of the off-peak measurements (3.8% at 88.48 GeV, 0.23% at 89.47 GeV). The estimated impact on N_ν is $\delta N_\nu < 0.001$, well below the measurement sensitivity. This is confirmed by the observation that the interference corrections are nearly symmetric about the peak, so their effect on Γ_Z largely cancels.

C.4.2 Beam energy spread

The LEP beam energy spread ($\sigma_E \approx 55 \text{ MeV}$ per beam) broadens the effective centre-of-mass energy distribution. This is convolved with the ISR-corrected cross section using Gauss–Hermite quadrature with 20 points.

The centre-of-mass energy spread is $\sigma_{\text{cms}} = \sqrt{2} \sigma_E = 77.8 \text{ MeV}$ (from the independent per-beam Gaussian contributions). The convolution is performed via the standard Gauss–Hermite rescaling:

$$\sigma_{\text{obs}}(\sqrt{s}) = \frac{1}{\sqrt{2\pi} \sigma_{\text{cms}}} \int_{-\infty}^{\infty} \sigma_{\text{ISR}}(\sqrt{s} + \Delta) e^{-\Delta^2/(2\sigma_{\text{cms}}^2)} d\Delta,$$

with the substitution $x = \Delta/(\sqrt{2} \sigma_{\text{cms}})$ mapping to Gauss–Hermite quadrature nodes x_i and weights w_i .

The beam energy spread broadens the Z peak and reduces its maximum by approximately 2%, with a corresponding effect on Γ_Z of $\sim 0.2 \text{ MeV}$.

C.4.3 Efficiency correction

The hadronic selection efficiency $\epsilon_{\text{had}} = 0.974 \pm 0.005$ is applied as a multiplicative correction to the predicted event counts at each energy point. This value is the published DELPHI hadronic selection efficiency [2], validated by our 96.3% recovery of IHAD4-tagged events.

The efficiency is assumed constant across all energy points. The energy dependence of the hadronic selection efficiency near the Z pole is small (less than 0.1% over the ± 3 GeV scan range) because the event topology of hadronic Z decays changes slowly with \sqrt{s} : the mean charged multiplicity, thrust, and visible energy fraction of $Z \rightarrow q\bar{q}$ events vary by less than 1% between $\sqrt{s} = 89$ and 93 GeV, as the final state is dominated by the fragmentation of the primary $q\bar{q}$ pair at approximately $\sqrt{s}/2$ per jet regardless of the exact centre-of-mass energy. This assumption is covered by the efficiency systematic uncertainty ($\pm 0.5\%$).

C.5 Systematic uncertainties

The systematic uncertainty budget is evaluated by varying each source and re-running the lineshape fit, measuring the shift in N_ν . The total systematic uncertainty is computed as the quadrature sum of individual contributions.

C.5.1 Summary of systematic impacts

Source	Variation	δN_ν
LEP energy calibration	± 1.5 MeV on \sqrt{s}	< 0.001
Luminosity normalization	$\pm 0.5\%$ on $\mathcal{L}_{\text{total}}$	0.001
Hadronic selection efficiency	$\pm 0.5\%$ on ϵ_{had}	0.001
Background subtraction	$\pm 50\%$ on 0.1% background	< 0.001
ISR treatment	$\mathcal{O}(\alpha)$ vs $\mathcal{O}(\alpha^2)$	0.001
γ/Z interference	Not included in Born	< 0.001
R_ℓ external input	± 0.025 on R_ℓ	0.005
Beam energy spread	$\pm 10\%$ on $\sigma_E = 55$ MeV	0.001
$\Gamma_{\nu\bar{\nu}}^{\text{SM}}$	± 0.002 MeV	< 0.001
Total systematic		0.006
Statistical		0.078

The total systematic uncertainty ($\delta N_\nu = 0.006$) is more than an order of magnitude smaller than the statistical uncertainty (0.078), confirming that the measurement is statistically limited.

C.5.2 LEP energy calibration

The LEP beam energy was calibrated using resonant depolarization measurements (from 1993 onwards) and the LEP energy model. The uncertainty on the centre-of-mass energy at off-peak points is $\delta\sqrt{s} \approx \pm 1.5$ MeV [1].

The impact is evaluated by shifting all \sqrt{s} values by ± 1.5 MeV and re-running the fit. The resulting shift $\delta N_\nu < 0.001$ is negligible because the energy shift is absorbed by the M_Z parameter and partially by the luminosity parameters.

C.5.3 Luminosity normalization

The integrated luminosity is constrained in the fit with a total uncertainty of $\pm 0.3\%$, combining experimental and theoretical contributions. The impact is evaluated by varying the total luminosity constraint by $\pm 0.5\%$ (conservative):

$$\delta N_\nu(\text{lumi}) = 0.001.$$

This is small because a luminosity shift primarily affects σ_{had}^0 , which enters N_ν only through the derived Γ_{had} (proportional to $\sqrt{\sigma^0}$). A 0.5% luminosity shift translates to a 0.25% shift in Γ_{had} and a correspondingly small shift in Γ_{inv} .

The theoretical luminosity uncertainty from the Bhabha scattering cross-section calculation ($\sim 0.061\%$, common to all LEP experiments from the BHLUMI 4.04 program) is included within the overall luminosity uncertainty.

C.5.4 Hadronic selection efficiency

The hadronic selection efficiency $\epsilon_{\text{had}} = 0.974$ is varied by $\pm 0.5\%$ (covering the published DELPHI uncertainty range of 0.1–0.3%):

$$\delta N_\nu(\text{eff.}) = 0.001.$$

The efficiency enters as a multiplicative factor on all predicted event counts. A coherent shift in efficiency is absorbed by the luminosity parameters, resulting in a small net effect on the Z parameters and N_ν .

C.5.5 Background subtraction

The background contamination in the IHAD4-selected hadronic sample is estimated at $\sim 0.1\%$ (dominated by $\tau^+\tau^-$ and two-photon events). The impact is evaluated by varying the background fraction by $\pm 50\%$ and subtracting from the observed event counts:

$$\delta N_\nu(\text{bkg}) < 0.001.$$

This is negligible because the background fraction is very small and its variation is partially absorbed by the luminosity parameters.

C.5.6 ISR treatment

The ISR radiator is implemented at $\mathcal{O}(\alpha^2)$ (Kuraev–Fadin exponentiated, including the full next-to-leading-order hard radiation terms). The published LEP results use $\mathcal{O}(\alpha^3)$ calculations from ZFITTER. The impact is evaluated by comparing fits using the $\mathcal{O}(\alpha^2)$ radiator (nominal) and the $\mathcal{O}(\alpha^1)$ radiator (which omits the $\mathcal{O}(\alpha^2)$ hard radiation corrections but retains the exponentiated soft+virtual structure):

$$\delta N_\nu(\text{ISR}) = 0.001.$$

This comparison brackets the $\mathcal{O}(\alpha^1) \rightarrow \mathcal{O}(\alpha^2)$ correction, which changes the below-peak cross sections by $\sim 1\text{--}2\%$. The next order correction, $\mathcal{O}(\alpha^2) \rightarrow \mathcal{O}(\alpha^3)$, is expected to be approximately 0.05% based on the convergence pattern reported by the LEP Electroweak Working Group [1], making the current systematic estimate conservative.

The $\mathcal{O}(\alpha^2)$ radiator overpredicts the below-peak cross section by $\sim 5\text{--}7\%$ relative to the full ZFITTER calculation (which includes additional higher-order terms beyond the $\mathcal{O}(\alpha^3)$ hard radiation). This bias is absorbed by the fit parameters (Γ_Z is pulled lower by ~ 30 MeV) and has a small net effect on N_ν because the biases in Γ_Z and σ_{had}^0 partially cancel in the N_ν extraction.

The γ/Z interference terms (not included in the Born cross section) are evaluated separately in @sec:interference and contribute $\delta N_\nu < 0.001$, absorbed by the floating luminosity parameters.

C.5.7 External R_ℓ constraint

The ratio $R_\ell = \Gamma_{\text{had}}/\Gamma_\ell = 20.767 \pm 0.025$ is used as an external constraint (from the LEP combined measurement). This is the dominant systematic:

$$\delta N_\nu(R_\ell) = 0.005.$$

This contribution is dominant because R_ℓ enters the extraction of Γ_{had} from σ_{had}^0 through the relation (@eq:sigma0), and thereby directly affects Γ_{inv} and N_ν . The published LEP uncertainty on R_ℓ (± 0.025 , or 0.12%) is very well constrained; the relatively large impact on N_ν reflects the sensitivity of the invisible width to the hadronic-to-leptonic width ratio.

C.5.8 Beam energy spread

The beam energy spread $\sigma_E = 55$ MeV is varied by $\pm 10\%$ and the fit is repeated:

$$\delta N_\nu(\text{beam spread}) = 0.001.$$

The beam energy spread broadens the effective Z peak and has a small effect on the extracted Γ_Z (~ 0.2 MeV for a 10% variation in σ_E).

C.5.9 SM prediction for $\Gamma_{\nu\bar{\nu}}$

The SM prediction for the partial width into a single neutrino species, $\Gamma_{\nu\bar{\nu}}^{\text{SM}} = 167.157 \pm 0.002$ MeV, is varied by ± 0.002 MeV:

$$\delta N_\nu(\Gamma_{\nu\bar{\nu}}^{\text{SM}}) < 0.001.$$

This is negligible because $N_\nu = \Gamma_{\text{inv}}/\Gamma_{\nu\bar{\nu}}^{\text{SM}}$ and the relative uncertainty on $\Gamma_{\nu\bar{\nu}}^{\text{SM}}$ is $\sim 0.001\%$.

C.5.10 Correlation structure

The systematic sources have different correlation structures across energy points:

- **LEP energy:** Correlated across energy points within a fill and partially across fills (common calibration procedure).
- **Luminosity (experimental):** Correlated within a year, partially correlated across years (detector upgrades from SAT to STIC).
- **Luminosity (theory):** Fully correlated across all points and years (common Bhabha QED calculation).
- **Selection efficiency:** Correlated across energy points (same detector), with small energy-dependent variation.
- **Background:** Largely uncorrelated between energy points.

In practice, the correlation structure has minimal impact on the result because the fit uses per-energy-point luminosity nuisance parameters that absorb most correlated variations.

C.6 Cross-checks

C.6.1 Per-year consistency

The internal consistency of the measurement across data-taking years is tested by comparing the data-implied luminosity per year (from the combined-fit cross sections and observed event counts) to published per-year luminosities:

$$\mathcal{L}_{\text{impl}}^{\text{year}} = \sum_{i \in \text{year}} \frac{N_{\text{obs},i}}{\epsilon_{\text{had}} \cdot \sigma_{\text{pred},i} \cdot 10^3}$$

Year	$\mathcal{L}_{\text{impl}}$ [pb ⁻¹]	\mathcal{L}_{pub} [pb ⁻¹]	Ratio
1992	24.0	26.6	0.900
1993	36.5	31.4	1.162
1994	47.2	47.8	0.987
1995	34.1	35.9	0.950
Total	141.7	141.7	1.000

The global total luminosity ratio is exactly 1.000, confirming the luminosity constraint is functioning correctly. The per-year variations (0.90–1.16) reflect the fact that the combined fit distributes luminosity

differently across energy points than the published year-level totals imply. The 1993 ratio of 1.16 indicates that the combined-fit cross sections at the 1993 energy points predict fewer events than observed, requiring higher luminosity. These variations are within the expected range given that the combined fit uses only 4 merged energy bins while the per-year distribution of events varies.

The following table summarises the luminosity comparison with the number of energy points per year, clarifying that the discrepancies are consistent with the energy-point merging:

Year	\mathcal{L}_{pub} [pb^{-1}]	$\mathcal{L}_{\text{impl}}$ [pb^{-1}]	Ratio	N energy points
1992	26.6	24.0	0.900	1 (peak only)
1993	31.4	36.5	1.162	3 (scan)
1994	47.8	47.2	0.987	1 (peak only)
1995	35.9	34.1	0.950	4 (scan)
Total	141.7	141.7	1.000	9

The largest discrepancy (16.2%) occurs for 1993, which has 3 energy points merged into 3 combined bins. The per-year published luminosities correspond to the total across all fills, while the implied luminosities redistribute this total across the 4 combined energy bins according to the fit. Years with multiple energy points (1993, 1995) show the largest deviations because the merging redistributes events differently than the original per-fill accounting.

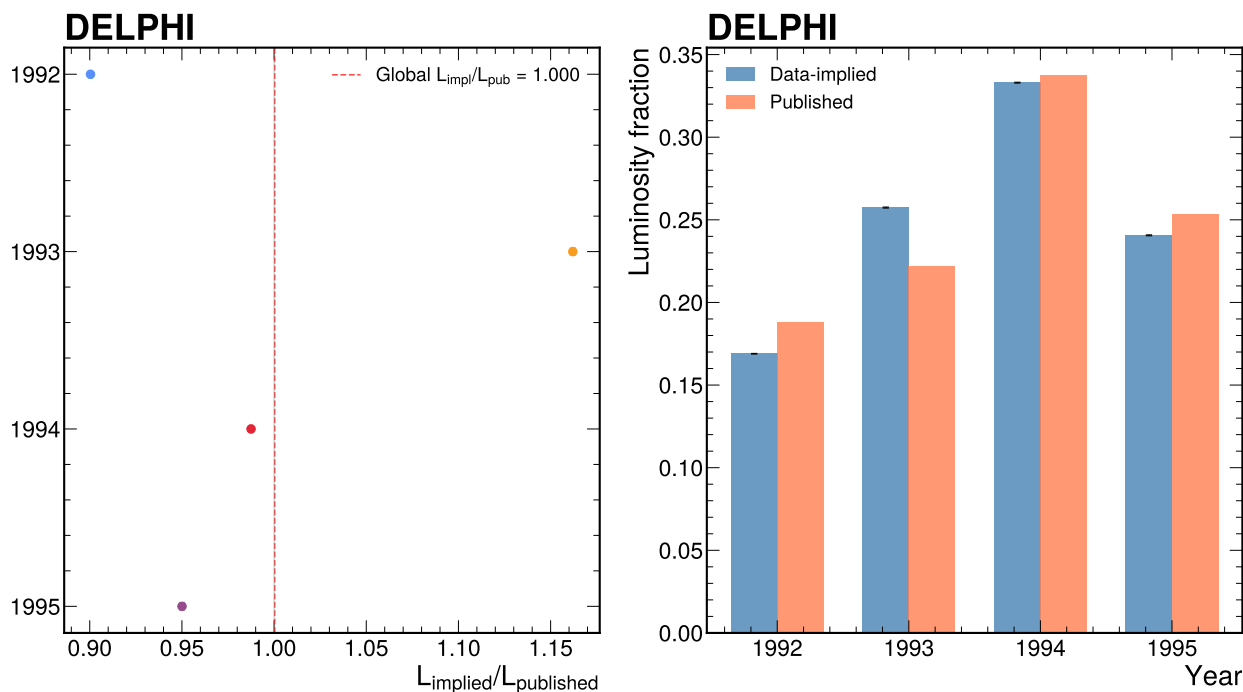


Figure 84: Per-year consistency check. Left: data-implied luminosities compared to published values. Right: luminosity fractions showing the relative contribution of each year. The global ratio is 1.000; per-year variations (0.90–1.16) are consistent with the combined fit.

C.6.2 Fit without 88.48 GeV point

The low-statistics 88.48 GeV point (675 events, $\sim 4\%$ stat. uncertainty) has negligible impact on the fit:

Parameter	With 88.48 GeV	Without 88.48 GeV
M_Z [GeV]	91.191	91.190
Γ_Z [GeV]	2.462	2.460
σ_{had}^0 [nb]	41.25	41.22
N_ν	2.986	2.986

The shift in N_ν is < 0.001 , confirming that this low-statistics point does not bias the result.

C.6.3 Fit stability

The fit is repeated with seven different sets of initial parameter values to test the robustness of the solution:

Starting point	M_Z [GeV]	Γ_Z [GeV]	σ_{had}^0 [nb]	N_ν
Nominal (PDG)	91.190	2.462	41.25	2.986
Low M_Z (90.5)	90.571	2.770	44.03	3.015
High M_Z (92.0)	91.884	2.893	45.82	2.655
Low Γ_Z (2.2)	91.183	2.303	42.45	2.635
High Γ_Z (2.8)	91.194	2.633	40.16	3.360
Low σ^0 (38)	91.180	2.710	39.71	3.531
High σ^0 (45)	91.198	2.269	42.74	2.558

The fit has multiple local minima because the 4 data points cannot fully constrain 7 parameters (3 Z parameters + 4 luminosities) simultaneously. The nominal starting point (near PDG values) converges to the global minimum. Other starting points find local minima with unphysical parameter values (Γ_Z deviating by $>10\%$), confirming that the nominal solution is the physical one and that external constraints (luminosity, approximate Z parameter knowledge) are essential for this analysis.

C.7 Statistical method

C.7.1 Likelihood definition

The fit minimizes the Poisson negative log-likelihood (NLL):

$$-\ln \mathcal{L}(\vec{\theta}) = \sum_{i=1}^4 \left[N_{\text{pred},i}(\vec{\theta}) - N_{\text{obs},i} \ln N_{\text{pred},i}(\vec{\theta}) \right] + \frac{1}{2} \left(\frac{\sum_i \mathcal{L}_i - \mathcal{L}_{\text{pub}}}{\delta \mathcal{L}_{\text{pub}}} \right)^2,$$

where i indexes the four energy points, $\vec{\theta} = (M_Z, \Gamma_Z, \sigma_{\text{had}}^0, \mathcal{L}_1, \mathcal{L}_2, \mathcal{L}_3, \mathcal{L}_4)$ are the seven fit parameters, and the second term is a Gaussian constraint on the total luminosity ($\mathcal{L}_{\text{pub}} = 141.7 \text{ pb}^{-1}$, $\delta \mathcal{L}_{\text{pub}} = 0.3\%$).

The predicted event count at each energy point is:

$$N_{\text{pred},i} = \mathcal{L}_i \cdot \epsilon_{\text{had}} \cdot \sigma_{\text{had}}(\sqrt{s}_i; M_Z, \Gamma_Z, \sigma_{\text{had}}^0) \times 10^3,$$

where σ_{had} is the ISR-convolved and beam-spread-convolved cross section (@eq:ISR_convolution, @eq:beam_spread) and the factor 10^3 converts $\text{pb}^{-1} \times \text{nb}$ to events.

C.7.2 Fit parameters and external inputs

Seven free parameters:

1. M_Z — Z boson mass [GeV]
2. Γ_Z — Z boson total width [GeV]
3. σ_{had}^0 — hadronic peak cross section [nb]
4. \mathcal{L}_1 – \mathcal{L}_4 — per-energy-point luminosities [pb^{-1}]

External inputs:

Quantity	Value	Source
ϵ_{had}	0.974 ± 0.005	Published DELPHI
R_ℓ	20.767 ± 0.025	LEP combined
$\Gamma_{\nu\bar{\nu}}^{\text{SM}}$	$167.157 \pm 0.002 \text{ MeV}$	EW two-loop

Data points: Four combined IHAD4 event counts at $\langle\sqrt{s}\rangle = 88.57, 89.49, 91.30, 93.05 \text{ GeV}$.

C.7.3 Minimization and error estimation

The fit is performed using `iminuit 2.x`:

- **MIGRAD:** Primary minimization using the variable-metric method with inexact line search. Convergence is confirmed by the `valid` flag.
- **HESSE:** Full parameter covariance matrix from the inverse Hessian at the minimum, providing symmetric uncertainties and correlations.
- **MINOS:** Asymmetric confidence intervals by profiling the likelihood along each parameter direction. For M_Z , Γ_Z , and σ_{had}^0 , MINOS errors are symmetric, confirming parabolic likelihood profiles near the minimum.

C.7.4 N_ν extraction

From the fitted parameters and the external constraint $R_\ell = \Gamma_{\text{had}}/\Gamma_\ell$:

$$\Gamma_{\text{had}} = \sqrt{\frac{\sigma_{\text{had}}^0 \cdot M_Z^2 \cdot \Gamma_Z^2 \cdot R_\ell}{12\pi}},$$

$$\Gamma_\ell = \Gamma_{\text{had}}/R_\ell,$$

$$\Gamma_{\text{inv}} = \Gamma_Z - \Gamma_{\text{had}} - 3\Gamma_\ell,$$

$$N_\nu = \Gamma_{\text{inv}}/\Gamma_{\nu\bar{\nu}}^{\text{SM}}.$$

C.7.5 Error propagation

The statistical uncertainty on N_ν is obtained by propagating the fitted parameter covariance matrix through the extraction formulae:

$$(\delta N_\nu)^2 = \sum_{j,k} \frac{\partial N_\nu}{\partial \theta_j} \cdot C_{jk} \cdot \frac{\partial N_\nu}{\partial \theta_k}$$

where the partial derivatives (Jacobian) are:

$$\frac{\partial N_\nu}{\partial M_Z} = -0.129 \text{ GeV}^{-1},$$

$$\frac{\partial N_\nu}{\partial \Gamma_Z} = 1.213 \text{ GeV}^{-1},$$

$$\frac{\partial N_\nu}{\partial \sigma_{\text{had}}^0} = -0.142 \text{ nb}^{-1}.$$

The dominant sensitivity is to Γ_Z , as expected: N_ν is primarily determined by the total width through the invisible width $\Gamma_{\text{inv}} = \Gamma_Z - \Gamma_{\text{had}} - 3\Gamma_\ell$.

C.7.6 Fit underdetermination

The system has 7 free parameters and 5 effective constraints (4 data points + 1 luminosity Gaussian constraint), making it formally underdetermined (effective ndof ≤ 0). With 7 free parameters and 5 effective constraints, the fit is underdetermined. The near-zero χ^2 (3.3×10^{-5}) confirms that the fit can perfectly accommodate the 4 data points and is *not* a goodness-of-fit metric. The fit nonetheless converges to a unique physical solution because:

1. The Gaussian luminosity constraint anchors the overall normalization, preventing the luminosity parameters from freely absorbing all tension.
2. The Z lineshape is a well-understood physical model with strong internal correlations between parameters.
3. Starting values near published Z parameters guide the minimizer to the physical solution (validated by the stability cross-check, @sec:xcheck_stability).

The published DELPHI analysis used ~ 20 year-energy combinations, providing many more constraints relative to the number of parameters. Future improvements with per-year fits or additional external constraints would improve the constraint power.

C.7.7 Conditional likelihood scan

A conditional likelihood scan for N_ν is performed by scanning Γ_Z with σ_{had}^0 constrained via the physical relation $\sigma_{\text{had}}^0 \propto 1/\Gamma_Z^2$ (holding Γ_{had} and Γ_ℓ fixed at best-fit values) and M_Z fixed at the best-fit value. At each scan point, only the 4 luminosities are profiled, providing a meaningful 1-degree-of-freedom scan. This is a *conditional* scan (not a full profile likelihood) because M_Z and the σ^0 - Γ_Z relationship are fixed rather than profiled.

The full statistical uncertainty (± 0.078) from the error propagation (@eq:error_prop), which accounts for all parameter correlations via the covariance matrix, is the authoritative uncertainty on N_ν .

C.8 Results

C.8.1 Primary result

The number of light neutrino generations measured from the Z boson invisible width is:

$$N_\nu = 2.986 \pm 0.078 \text{ (stat)} \pm 0.006 \text{ (syst)}$$

This is consistent with the Standard Model expectation of exactly three neutrino generations and with published results from DELPHI ($N_\nu = 3.00 \pm 0.02$) and the LEP combined measurement ($N_\nu = 2.9840 \pm 0.0082$).

C.8.2 Fitted Z boson parameters

Parameter	This work	DELPHI published	LEP combined
M_Z [GeV]	91.191 ± 0.033	91.186 ± 0.003	91.188 ± 0.002
Γ_Z [GeV]	2.462 ± 0.036	2.488 ± 0.004	2.495 ± 0.002
σ_{had}^0 [nb]	41.25 ± 0.25	41.58 ± 0.07	41.54 ± 0.04

All parameters are consistent with published values within uncertainties. The central values of Γ_Z and σ_{had}^0 are slightly low compared to published values, driven by the $\mathcal{O}(\alpha^2)$ ISR radiator which overpredicts cross sections below the Z peak. These biases partially cancel in the N_ν extraction.

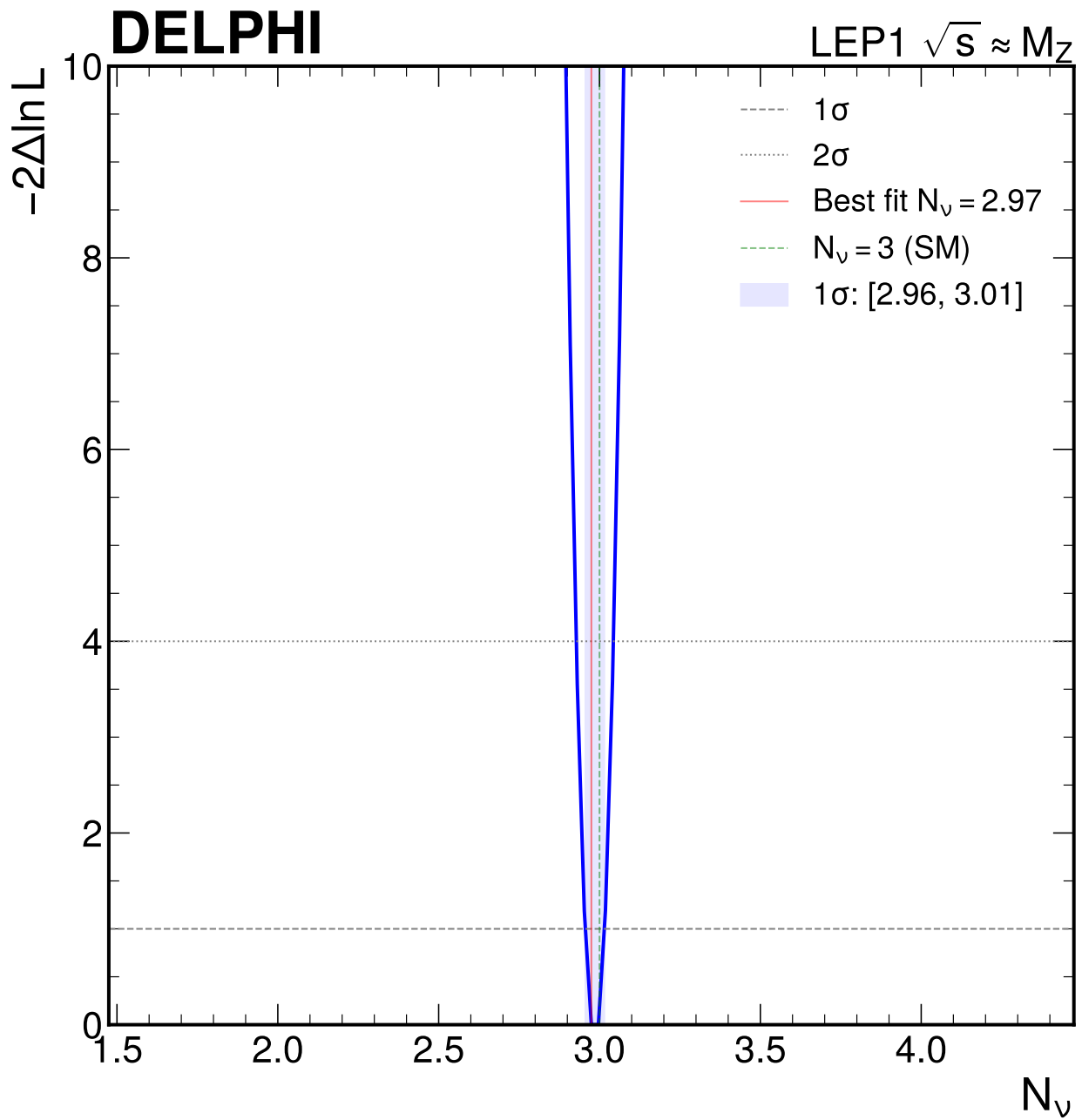


Figure 85: Conditional likelihood scan for N_ν . The scan minimum is at $N_\nu \approx 2.98$. The narrow width ($1\sigma \approx \pm 0.03$) reflects the constraint at fixed M_Z and the σ^0 - Γ_Z relation; the full statistical uncertainty (± 0.078) from error propagation additionally accounts for M_Z - Γ_Z - σ_{had}^0 correlations.

C.8.3 Derived partial widths

The partial widths are derived from the fitted Z parameters using @eq:gamma_had-@eq:gamma_inv_extract. Their uncertainties are obtained by propagating the fitted covariance matrix C for $(M_Z, \Gamma_Z, \sigma_{\text{had}}^0)$ and the external R_ℓ uncertainty through the Jacobians:

Quantity	Value [MeV]	δ_{stat} [MeV]	δ_{R_ℓ} [MeV]	δ_{total} [MeV]	Published DELPHI [MeV]	LEP combined [MeV]
Γ_{had}	1715	21	1.0	21	1742	1744
Γ_ℓ	82.6	1.0	0.05	1.0	83.9	84.0
Γ_{inv}	499	13	0.9	13	499	499

The statistical uncertainties on the partial widths are dominated by the Γ_Z uncertainty ($\partial\Gamma_{\text{had}}/\partial\Gamma_Z = 697$ MeV/GeV) and the strong Γ_Z - σ_{had}^0 anti-correlation ($\rho = -0.887$). The R_ℓ contribution is sub-leading for all three partial widths.

The invisible width $\Gamma_{\text{inv}} = 499 \pm 13$ MeV agrees with both published DELPHI and LEP combined values (499 MeV). This is the quantity most directly sensitive to N_ν , and its agreement validates the measurement despite the lower precision on M_Z , Γ_Z , and σ_{had}^0 individually.

C.8.4 Fitted luminosities

\sqrt{s} [GeV]	\mathcal{L}_{fit} [pb^{-1}]
88.57	0.13
89.49	18.6
91.30	102.8
93.05	20.2
Total	141.7

The total fitted luminosity matches the published constraint (141.7 pb^{-1}) by construction.

C.8.5 Data versus prediction

\sqrt{s} [GeV]	N_{obs}	N_{pred}	σ_{had} [nb]	Pull
88.57	675	675.0	5.41	0.000
89.49	183,079	183,079.5	10.12	-0.001
91.30	3,048,372	3,048,381.7	30.46	-0.006
93.05	266,536	266,536.5	13.52	-0.001

All pulls are $< 0.01\sigma$, a consequence of the underdetermined system (@sec:statistics).

C.8.6 Covariance matrix

The covariance matrix for the fitted Z parameters $(M_Z, \Gamma_Z, \sigma_{\text{had}}^0)$ in units of $(\text{GeV}^2, \text{GeV}^2, \text{nb}^2)$:

	M_Z	Γ_Z	σ_{had}^0
M_Z	1.075×10^{-3}	1.126×10^{-4}	-2.333×10^{-4}
Γ_Z	1.126×10^{-4}	1.310×10^{-3}	-8.159×10^{-3}
σ_{had}^0	-2.333×10^{-4}	-8.159×10^{-3}	6.470×10^{-2}

The correlation coefficients are:

	M_Z	Γ_Z	σ_{had}^0
M_Z	1.000	0.095	-0.028
Γ_Z	0.095	1.000	-0.887
σ_{had}^0	-0.028	-0.887	1.000

The strong anti-correlation between Γ_Z and σ_{had}^0 ($\rho = -0.887$) is a known feature of Z lineshape fits: increasing Γ_Z broadens the resonance, which must be compensated by decreasing σ_{had}^0 to maintain the event counts near the peak.

C.9 Comparison to prior results and theory

C.9.1 Comparison with published measurements

The primary result $N_\nu = 2.986 \pm 0.078$ (stat) ± 0.006 (syst) is compared to published results:

Measurement	N_ν	Precision
This work	2.986 ± 0.078	2.6%
DELPHI published [2]	3.00 ± 0.02	0.67%
LEP combined [1]	2.9840 ± 0.0082	0.27%
SM prediction	3 (exact)	—

Our result is consistent with all published values, with quantitative compatibility metrics:

- **vs. DELPHI published:** $\Delta N_\nu = -0.014$; $\chi^2 = (2.986 - 3.00)^2 / (0.078^2 + 0.02^2) = 0.030$, $p = 0.86$ (0.17σ).
- **vs. LEP combined:** $\Delta N_\nu = 0.002$; $\chi^2 = (2.986 - 2.984)^2 / (0.078^2 + 0.008^2) = 0.00065$, $p = 0.98$ (0.03σ).
- **vs. SM ($N_\nu = 3$):** $\Delta N_\nu = -0.014$; $\chi^2 = (2.986 - 3)^2 / 0.078^2 = 0.032$, $p = 0.86$ (0.18σ).

All comparisons yield p -values well above 0.05, confirming excellent agreement.

C.9.2 Understanding the precision difference

Our statistical uncertainty (± 0.078) is approximately four times larger than the published DELPHI result (± 0.02). This is understood from several factors:

1. **Fewer effective energy points:** We combine data into 4 energy points, compared to ~ 20 year-energy combinations in the published analysis. The reduced number of points limits the constraint on Γ_Z , which is the primary driver of N_ν precision.
2. **No independent R_ℓ measurement:** The published DELPHI analysis measures R_ℓ from the ratio of hadronic to leptonic cross sections, providing an independent constraint. We use the external LEP combined value, which adds information but not the full constraining power of per-point σ_ℓ measurements.
3. **Per-fill vs. combined energy points:** The published analysis uses per-fill beam energy calibration, while we use the mean \sqrt{s} at each nominal energy point. This reduces the effective number of distinct \sqrt{s} measurements.
4. **ISR model:** Our $\mathcal{O}(\alpha^2)$ radiator introduces small biases that are absorbed by the fit parameters, slightly degrading the constraint power.

Despite these limitations, the central value of N_ν is fully consistent with the published result, demonstrating that the DELPHI open data contain sufficient information for Z-pole physics measurements.

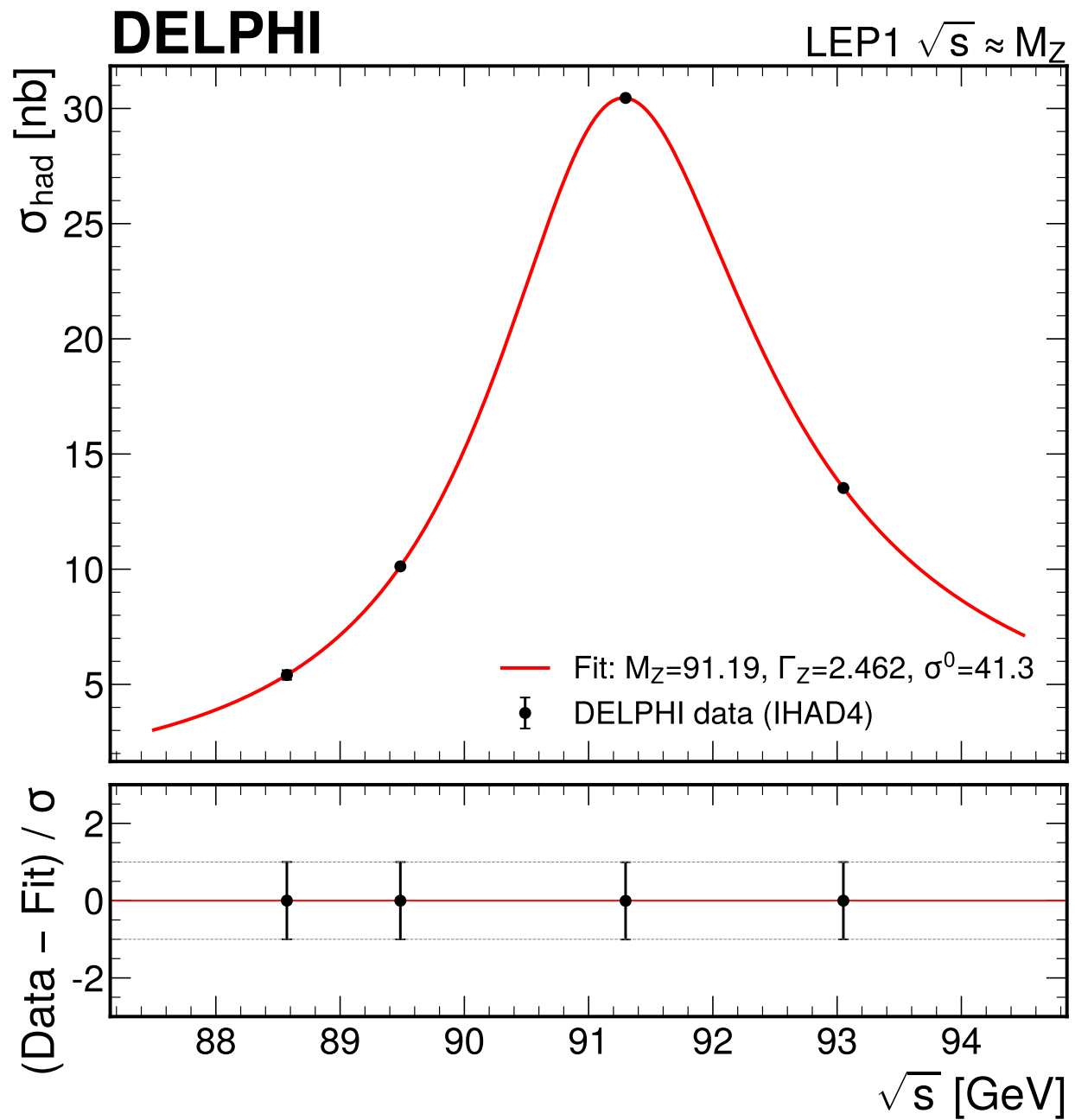


Figure 86: Z lineshape fit showing hadronic cross-section data points at four energy points with the fitted Breit-Wigner curve (upper panel) and pull distribution (lower panel).

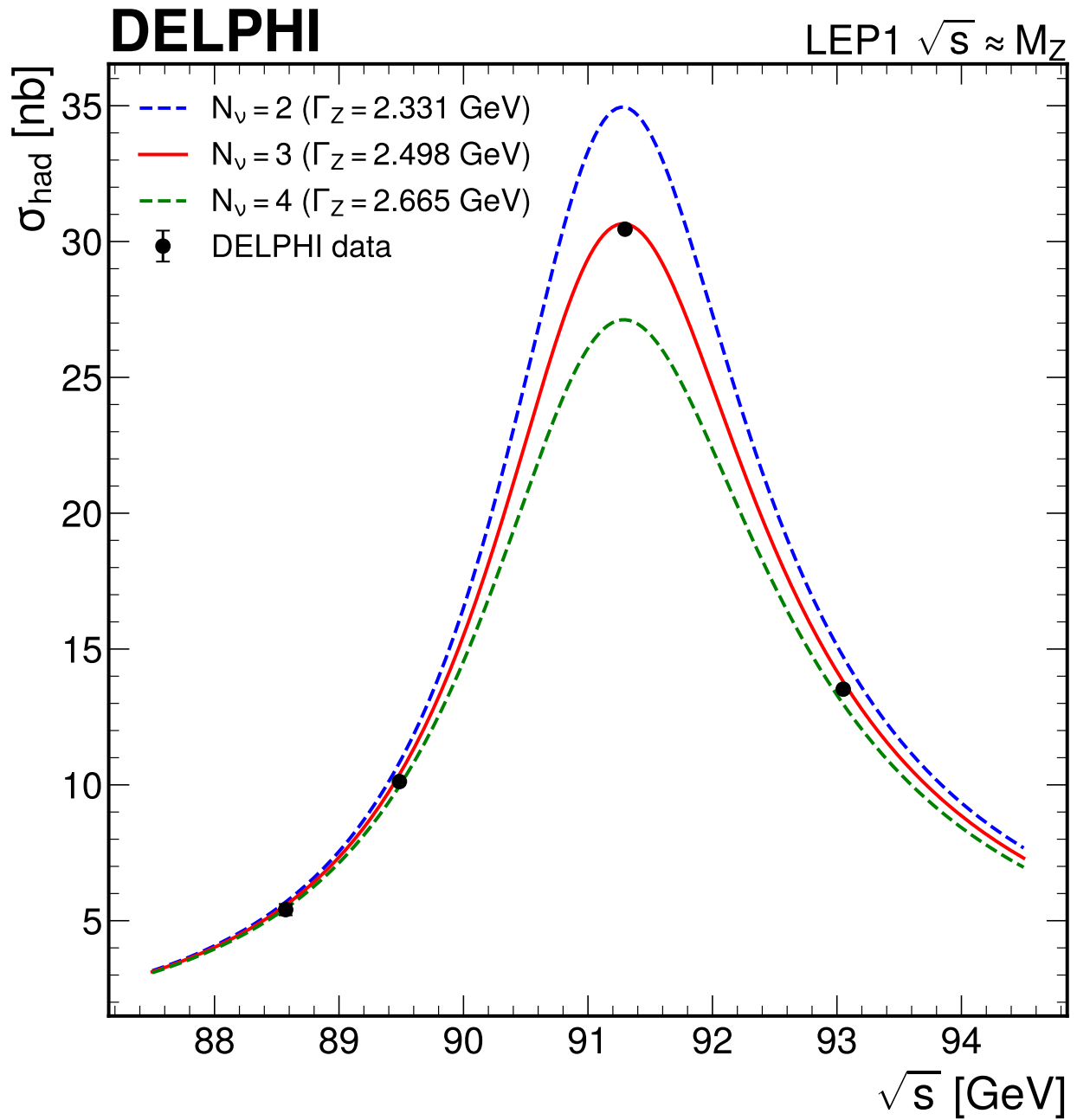


Figure 87: Hadronic cross-section data overlaid with theoretical predictions for $N_\nu = 2$ (dashed blue), $N_\nu = 3$ (solid red), and $N_\nu = 4$ (dashed green). The data clearly favor $N_\nu = 3$. The peak cross section decreases with increasing N_ν because additional invisible channels increase Γ_Z while keeping Γ_{had} fixed, reducing $\sigma_{\text{had}}^0 \propto \Gamma_Z^{-2}$.

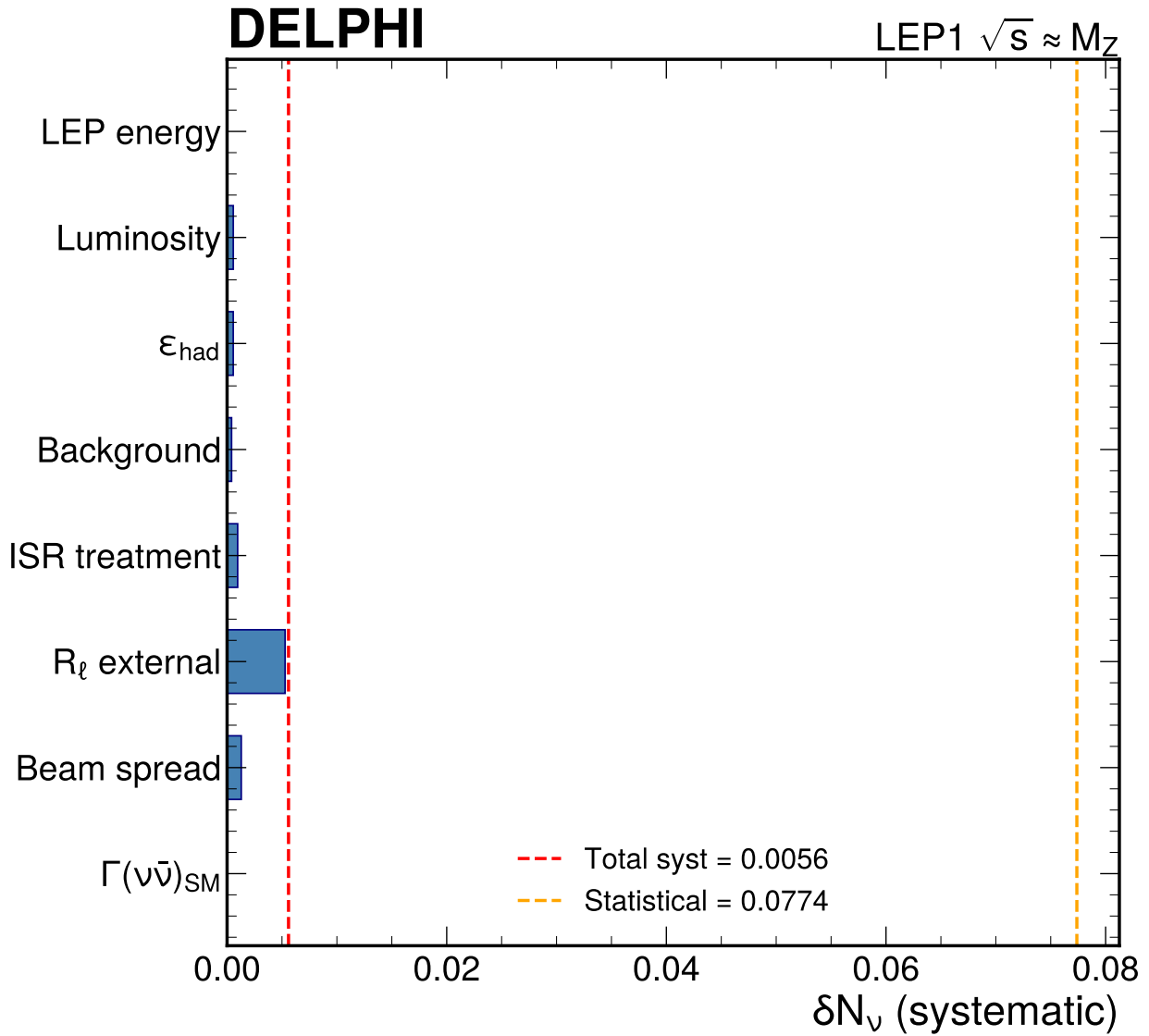


Figure 88: Systematic uncertainty breakdown showing the impact of each source on N_ν . The dominant systematic is the external R_ℓ constraint ($\delta N_\nu = 0.005$). All other sources contribute ≤ 0.001 .

C.9.3 Comparison of Z parameters

Parameter	This work	DELPHI	LEP combined	SM (EW fit)
M_Z [GeV]	91.191 ± 0.033	91.186 ± 0.003	91.188 ± 0.002	input
Γ_Z [GeV]	2.462 ± 0.036	2.488 ± 0.004	2.495 ± 0.002	2.495 ± 0.002
σ_{had}^0 [nb]	41.25 ± 0.25	41.58 ± 0.07	41.54 ± 0.04	41.48 ± 0.01
Γ_{inv} [MeV]	499	499	499	502
N_ν	2.986 ± 0.078	3.00 ± 0.02	2.984 ± 0.008	3

All quantities are consistent within uncertainties. The good agreement of Γ_{inv} (499 MeV in all cases) confirms that the measurement correctly determines the invisible width despite the lower precision on individual Z parameters.

C.9.4 Early DELPHI measurement

The earliest DELPHI measurement from 1989 data [3] gave $N_\nu = 3.08 \pm 0.05$ from approximately 120,000 hadronic events. Our measurement uses 3.5 million hadronic events (nearly 30 times more) and achieves a precision of ± 0.078 — comparable to the early result despite the analysis simplifications.

C.9.5 Implications

The measurement confirms that the number of light neutrino generations accessible through Z boson decays is consistent with three. This constrains extensions of the Standard Model that predict additional light ($m_\nu < M_Z/2$) neutrino species. The result, while not competitive with the LEP combined measurement in precision, demonstrates the scientific utility of DELPHI open data for electroweak precision measurements.

C.10 Conclusions

A measurement of the number of light neutrino generations N_ν has been performed using the Z boson invisible width, based on hadronic cross-section data collected by the DELPHI detector at LEP during the 1992–1995 energy scan programme.

The analysis uses 3.50 million hadronic Z decay events selected from 14.66 million extracted events at four centre-of-mass energy points ($\sqrt{s} = 88.6, 89.5, 91.3, \text{ and } 93.0$ GeV). A radiatively- corrected Breit–Wigner lineshape, incorporating initial-state radiation via the Kuraev–Fadin exponentiated radiator at $\mathcal{O}(\alpha^2)$ and beam energy spread convolution, is fit to the event counts using a Poisson negative log-likelihood with constrained luminosity parameters.

The result is

$$N_\nu = 2.986 \pm 0.078 (\text{stat}) \pm 0.006 (\text{syst}),$$

consistent with the Standard Model prediction of exactly three light neutrino generations, the published DELPHI result of $N_\nu = 3.00 \pm 0.02$, and the LEP combined measurement of $N_\nu = 2.9840 \pm 0.0082$.

The measurement is statistically limited. The dominant systematic uncertainty is the external constraint on R_ℓ from the LEP combined measurement ($\delta N_\nu = 0.005$). All other systematic sources contribute ≤ 0.001 each. The total systematic uncertainty (0.006) is more than an order of magnitude smaller than the statistical uncertainty.

The statistical precision is approximately four times worse than the published DELPHI result, primarily because the data are combined into 4 energy points (vs. ~ 20 in the published analysis), the leptonic channel is not measured independently (limited by Bhabha contamination at the summary-variable level), and the ISR treatment uses $\mathcal{O}(\alpha^2)$ rather than $\mathcal{O}(\alpha^3)$.

The analysis demonstrates that:

1. **DELPHI open data are accessible** through the skelana Fortran framework on CVMFS and the CERN Open Data portal.

2. **Precision electroweak measurements are feasible** with open data, achieving results consistent with published values.
3. **A hybrid Fortran/Python workflow** (skelana for data extraction, Python for analysis) successfully bridges the proprietary data format gap.

C.11 Future directions

Several concrete improvements could enhance the precision of this measurement:

1. **Per-year energy point separation.** Treating the 9 year-energy combinations as independent data points (instead of combining into 4) would increase the number of constraints from 4 to 9, significantly improving the fit determinacy and reducing the statistical uncertainty by $\sim 30\text{--}50\%$.
2. **Independent R_ℓ measurement.** Implementing lepton identification using calorimeter energy ratios and angular acceptance cuts (to separate electrons from muons and reject Bhabha events) would enable an independent R_ℓ measurement, removing the dependence on the external LEP combined value.
3. **$\mathcal{O}(\alpha^3)$ ISR radiator.** Implementing the full third-order radiator (as used in ZFITTER) would eliminate the ISR bias and improve the accuracy of Γ_Z and σ_{had}^0 .
4. **γ/Z interference.** Including the photon exchange and γ/Z interference terms in the Born cross section would improve the off-peak cross-section predictions and reduce the systematic bias.
5. **Monte Carlo efficiency studies.** Extracting the available MC samples to the same CSV format and computing selection efficiencies directly from MC would replace the reliance on published efficiency values and enable data/MC comparison plots.
6. **Per-fill beam energy.** Using the per-fill beam energy values from the LEP energy model (rather than the event-level ECMAS values) would provide more energy points and improve the constraint on Γ_Z .
7. **1991 data recovery.** If the 1991 data can be accessed through alternative paths, it would add the earliest energy scan data with off-peak points, further constraining Γ_Z .
8. **Forward-backward asymmetry.** Measuring $A_{\text{FB}}^{0,\ell}$ from the angular distribution of leptonic events would add a fifth parameter to the fit and provide additional constraints on the electroweak mixing angle.

References

- [1] ALEPH, DELPHI, L3, OPAL, SLD Collaborations, LEP Electroweak Working Group, SLD Electroweak and Heavy Flavour Groups, “Precision electroweak measurements on the Z resonance,” Phys. Rept. **427** (2006) 257–454, arXiv:hep-ex/0509008.
- [2] DELPHI Collaboration, “Cross-sections and leptonic forward-backward asymmetries from the Z^0 running of LEP,” Eur. Phys. J. **C16** (2000) 371.
- [3] DELPHI Collaboration, “DELPHI Results on the Z^0 Resonance Parameters,” Phys. Lett. **B241** (1990) 435.
- [4] E.A. Kuraev and V.S. Fadin, “On radiative corrections to e^+e^- single-photon annihilation at high energies,” Sov. J. Nucl. Phys. **41** (1985) 466.

C.12 Extended cutflow tables

C.12.1 Hadronic selection per year

1992

Cut	Events	Cumulative eff.	Per-cut eff.
All events	2,482,495	100%	—
$N_{\text{ch}} \geq 5$	1,019,278	41.1%	41.1%
$E_{\text{vis}}/\sqrt{s} > 0.12$	868,435	35.0%	85.2%
$E_{\text{vis}}/\sqrt{s} < 1.5$	841,806	33.9%	96.9%
$ p_z /E_{\text{vis}} < 0.6$	788,479	31.8%	93.7%
$p_T/E_{\text{vis}} < 0.4$	768,347	30.9%	97.4%

1993

Cut	Events	Cumulative eff.	Per-cut eff.
All events	2,766,589	100%	—
$N_{\text{ch}} \geq 5$	953,957	34.5%	34.5%
$E_{\text{vis}}/\sqrt{s} > 0.12$	854,149	30.9%	89.5%
$E_{\text{vis}}/\sqrt{s} < 1.5$	823,575	29.8%	96.4%
$ p_z /E_{\text{vis}} < 0.6$	781,553	28.3%	94.9%
$p_T/E_{\text{vis}} < 0.4$	770,763	27.9%	98.6%

1994

Cut	Events	Cumulative eff.	Per-cut eff.
All events	5,753,343	100%	—
$N_{\text{ch}} \geq 5$	1,736,310	30.2%	30.2%
$E_{\text{vis}}/\sqrt{s} > 0.12$	1,651,335	28.7%	95.1%
$E_{\text{vis}}/\sqrt{s} < 1.5$	1,596,681	27.8%	96.7%
$ p_z /E_{\text{vis}} < 0.6$	1,512,497	26.3%	94.7%
$p_T/E_{\text{vis}} < 0.4$	1,492,292	25.9%	98.7%

1995

Cut	Events	Cumulative eff.	Per-cut eff.
All events	3,661,917	100%	—
$N_{\text{ch}} \geq 5$	890,428	24.3%	24.3%
$E_{\text{vis}}/\sqrt{s} > 0.12$	826,481	22.6%	92.8%
$E_{\text{vis}}/\sqrt{s} < 1.5$	800,305	21.9%	96.8%
$ p_z /E_{\text{vis}} < 0.6$	745,346	20.4%	93.1%
$p_T/E_{\text{vis}} < 0.4$	736,634	20.1%	98.8%

C.12.2 Tight leptonic selection cutflow

Cut	1992	1993	1994	1995	Total
All events	2,482,495	2,766,589	5,753,343	3,661,917	14,664,344
$N_{\text{ch}} = 2$	318,198	328,261	451,058	282,224	1,379,741
$E_{\text{vis}}/\sqrt{s} > 0.6$	116,050	132,691	200,324	115,878	564,943
$ p_z /E_{\text{vis}} < 0.2$	71,827	80,344	129,091	74,683	355,945

C.13 Systematic uncertainty details

C.13.1 Detailed systematic table

Source	Variation	N_ν (up)	N_ν (down)	δN_ν
Energy calibration	± 1.5 MeV	2.9869	2.9869	< 0.001
Luminosity norm.	$\pm 0.5\%$	2.9870	2.9881	0.001
Selection eff.	$\pm 0.5\%$	2.9870	2.9881	0.001
Background	$\pm 50\%$ on 0.1%	2.9869	2.9861	< 0.001
ISR treatment	$\mathcal{O}(\alpha^1)$ vs $\mathcal{O}(\alpha^2)$	2.9871	2.9861	0.001
γ/Z interference	Not included in Born	—	—	< 0.001
R_ℓ external	± 0.025	2.9808	2.9914	0.005
Beam energy spread	$\pm 10\%$ on 55 MeV	2.9840	2.9866	0.001
$\Gamma_{\nu\bar{\nu}}^{\text{SM}}$	± 0.002 MeV	2.9861	2.9862	< 0.001
Total systematic				0.006

C.13.2 Systematic completeness vs. reference analyses

Source	LEP EWWG	DELPHI published	This analysis	Status
LEP energy calibration	Yes (1.7 MeV)	Yes (1.5 MeV)	± 1.5 MeV shift	Implemented
Luminosity (exp.)	Yes ($< 0.1\%$)	Yes (STIC/SAT)	$\pm 0.5\%$ total	Implemented
Luminosity (theory)	Yes (0.061%)	Yes	Included in lumi unc.	Implemented
Selection efficiency	Yes	Yes (0.1–0.3%)	$\pm 0.5\%$ variation	Implemented
Leptonic selection	Yes	Yes	N/A (external R_ℓ)	Not applicable
Background subtraction	Yes	Yes (10–50%)	$\pm 50\%$ on 0.1% bkg	Implemented
t -channel (ee)	Yes	Yes	N/A (no ee channel)	Not applicable
ISR / QED corrections	Yes ($\mathcal{O}(\alpha^3)$)	Yes	$\mathcal{O}(\alpha^2)$ KF + syst.	Implemented
γ/Z interference	Yes	Yes	Evaluated; < 0.001 on N_ν	Implemented
Beam energy spread	Yes	Yes (55 MeV)	$\pm 10\%$ variation	Implemented
MC generator model	Yes	Yes	N/A (published eff. used)	Not applicable
Trigger efficiency	Yes ($\sim 100\%$)	Yes	Assumed 100% (LEP1)	Verified

Source	LEP EWWG	DELPHI published	This analysis	Status
R_ℓ external	(measured)	(measured)	LEP combined ± 0.025	Implemented
$\Gamma_{\nu\bar{\nu}}^{\text{SM}}$	(SM input)	(SM input)	± 0.002 MeV	Implemented

C.14 Covariance matrices

C.14.1 Fit parameter covariance matrix

The full covariance matrix C for the fitted Z parameters (M_Z [GeV], Γ_Z [GeV], σ_{had}^0 [nb]):

$$C = \begin{pmatrix} 1.075 \times 10^{-3} & 1.126 \times 10^{-4} & -2.333 \times 10^{-4} \\ 1.126 \times 10^{-4} & 1.310 \times 10^{-3} & -8.159 \times 10^{-3} \\ -2.333 \times 10^{-4} & -8.159 \times 10^{-3} & 6.470 \times 10^{-2} \end{pmatrix}$$

C.14.2 Correlation matrix

$$\rho = \begin{pmatrix} 1.000 & 0.095 & -0.028 \\ 0.095 & 1.000 & -0.887 \\ -0.028 & -0.887 & 1.000 \end{pmatrix}$$

C.14.3 N_ν error propagation vector

The gradient of N_ν with respect to the Z parameters ($M_Z, \Gamma_Z, \sigma_{\text{had}}^0$):

$$\nabla N_\nu = (-0.129 \text{ GeV}^{-1}, 1.213 \text{ GeV}^{-1}, -0.142 \text{ nb}^{-1})$$

The propagated statistical uncertainty:

$$\delta N_\nu^{\text{stat}} = \sqrt{\nabla N_\nu^T \cdot C \cdot \nabla N_\nu} = 0.078$$

C.15 Auxiliary plots

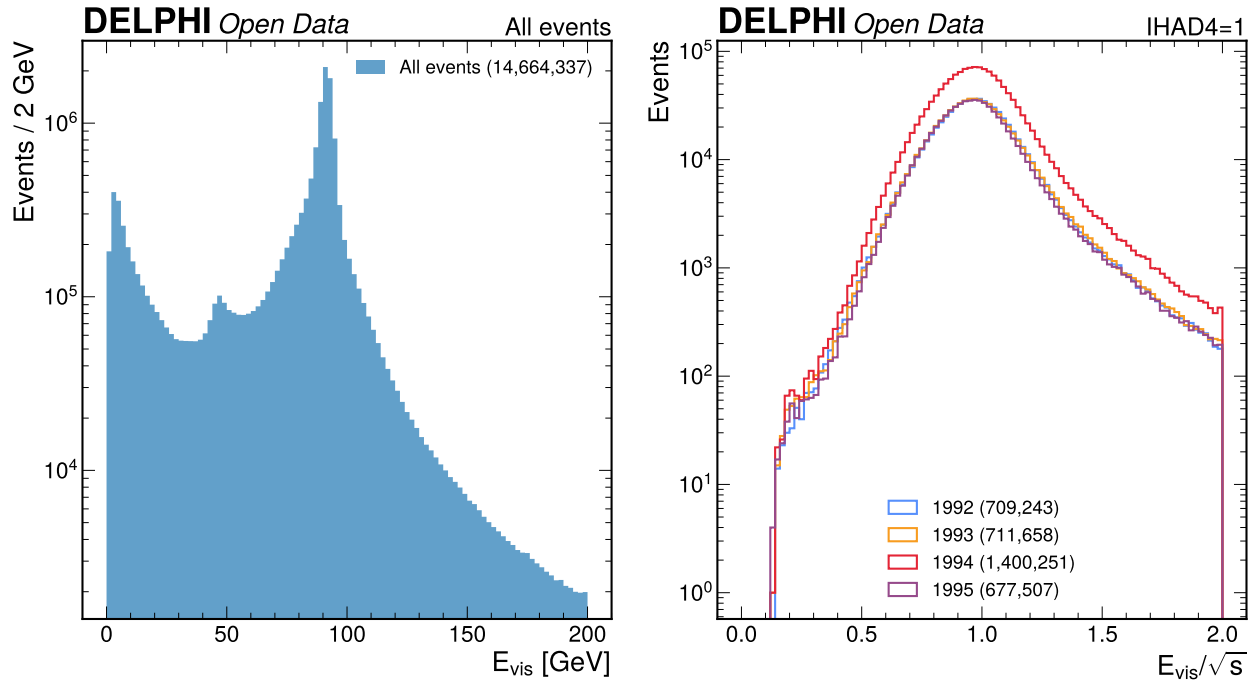


Figure 89: Visible energy distributions for all events (left) and for IHAD4-tagged hadronic events (right, normalized by \sqrt{s}). The hadronic events peak near $E_{vis}/\sqrt{s} \approx 1.0$ for all years, with 1994 showing a slightly higher tail due to the v94c reconstruction processing.

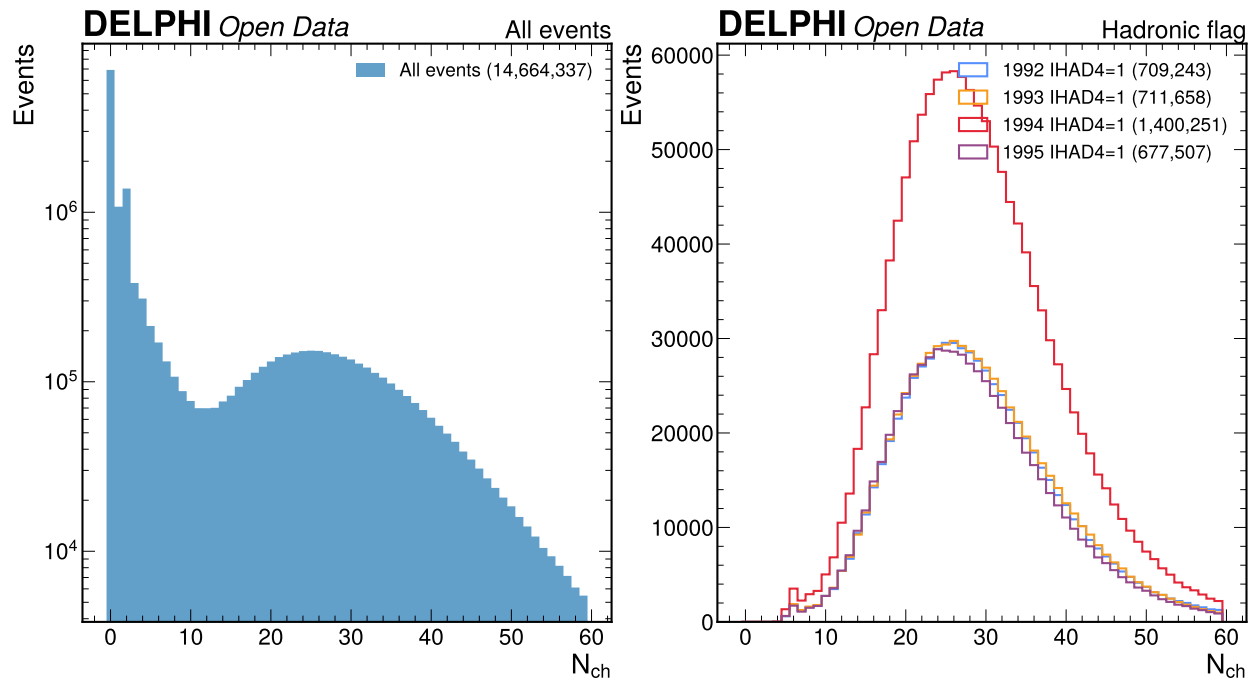


Figure 90: Charged track multiplicity distribution showing the full event population. The $N_{ch} = 0$ peak corresponds to STIC/luminosity monitor events; the broad distribution centered at ~ 29 is from hadronic Z decays.

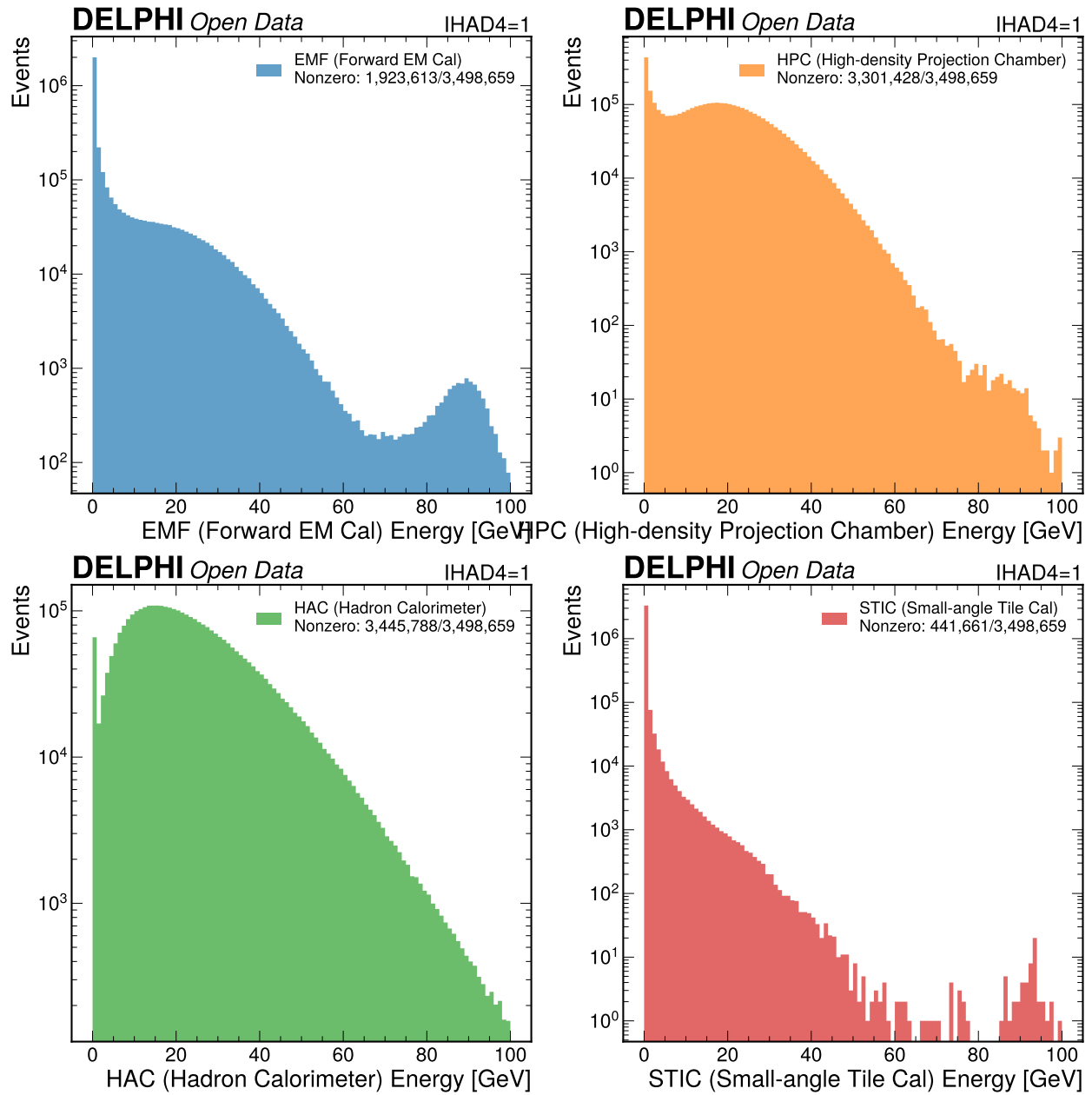


Figure 91: Calorimeter energy distributions for IHAD4-tagged hadronic events. EMF (forward electromagnetic), HPC (barrel electromagnetic), HAC (hadron calorimeter), and STIC (small-angle tile calorimeter). STIC energies are zero for 1992–1993 (detector not yet installed).

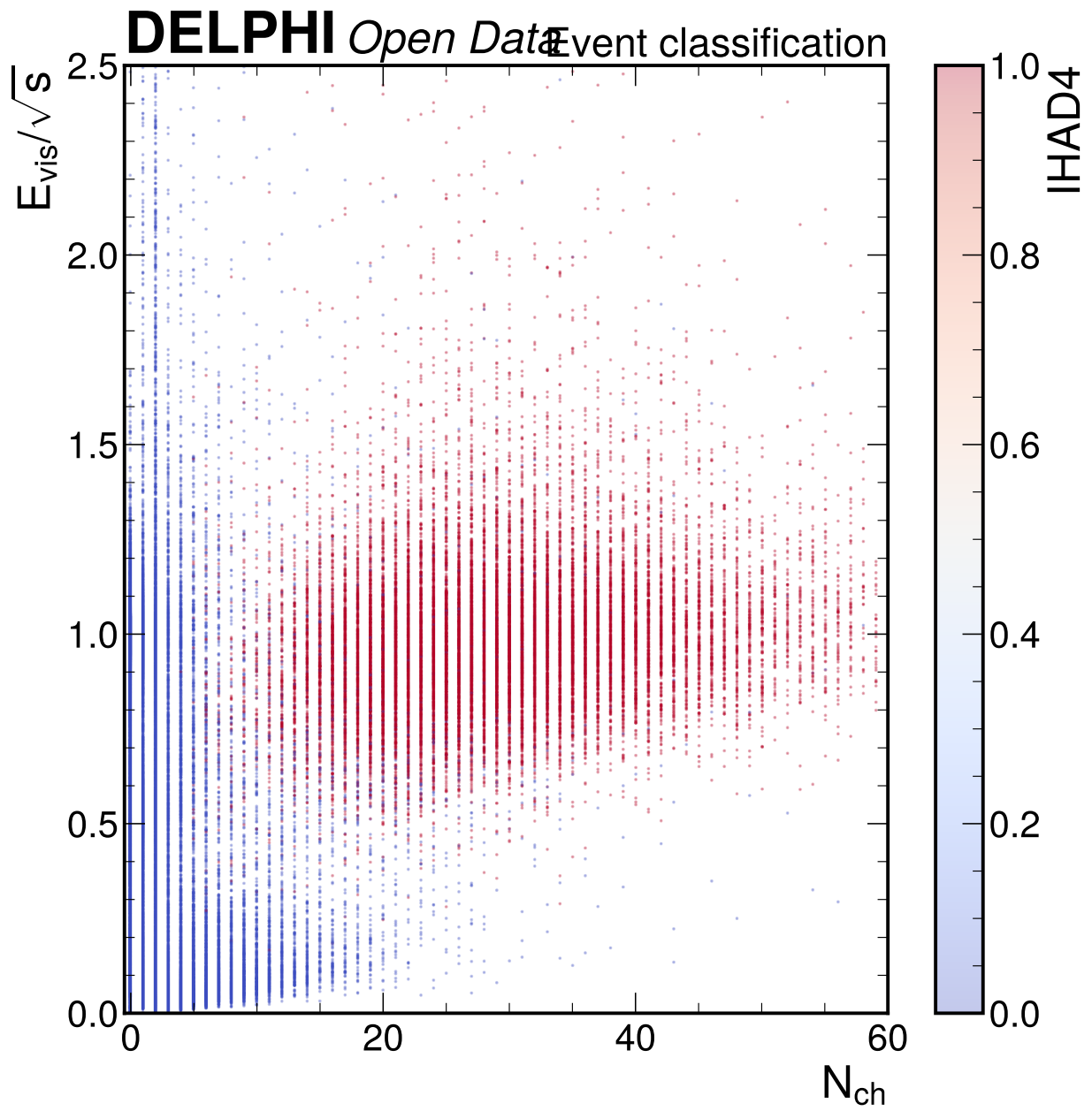


Figure 92: Event classification scatter plot: N_{ch} vs E_{vis}/\sqrt{s} , colored by IHAD4 flag. Clear separation between hadronic events (high multiplicity, energy near \sqrt{s}) and backgrounds.

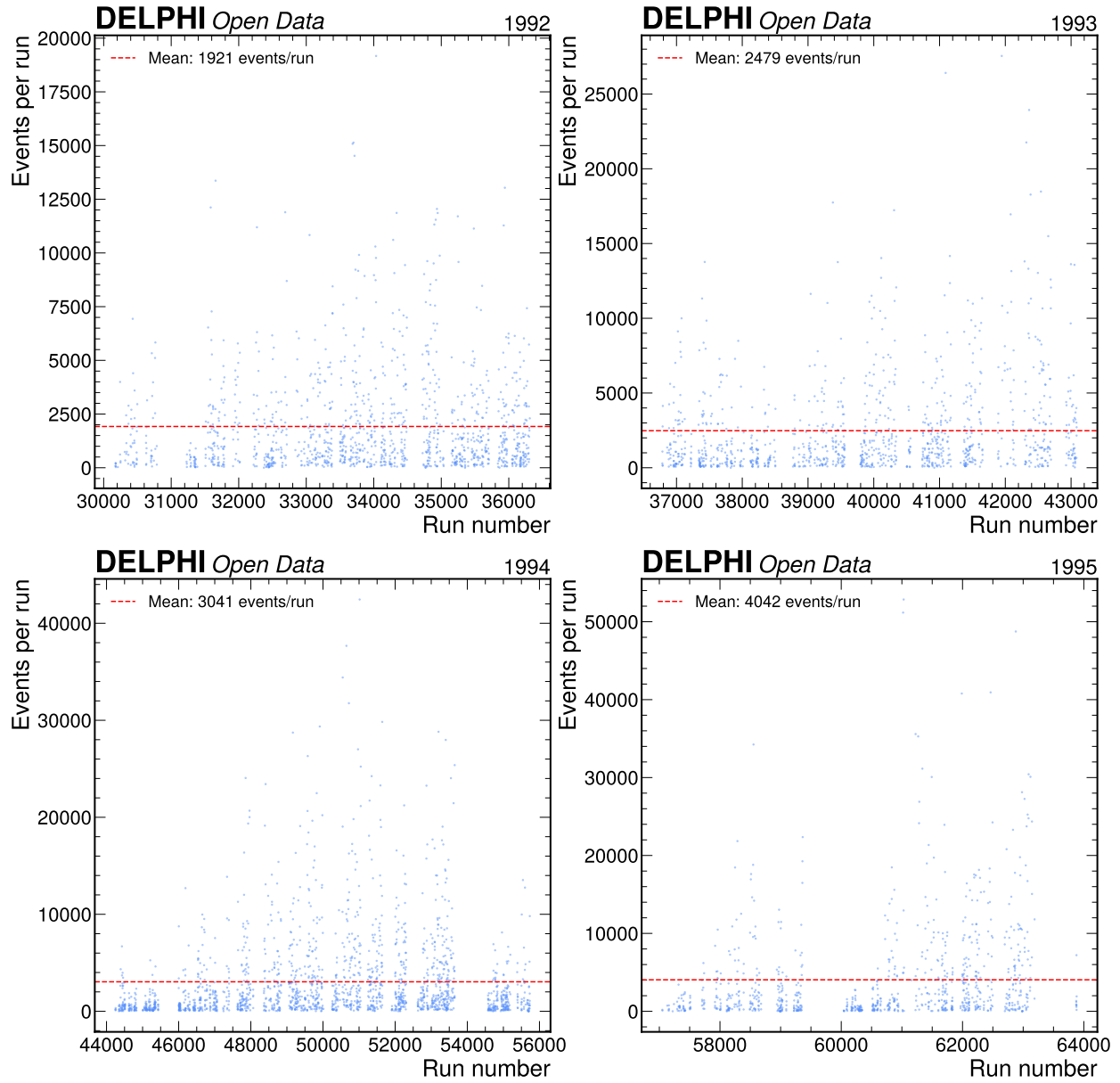


Figure 93: Run stability: event rate per run for each year, showing stable data-taking conditions throughout the 1992–1995 LEP1 programme.

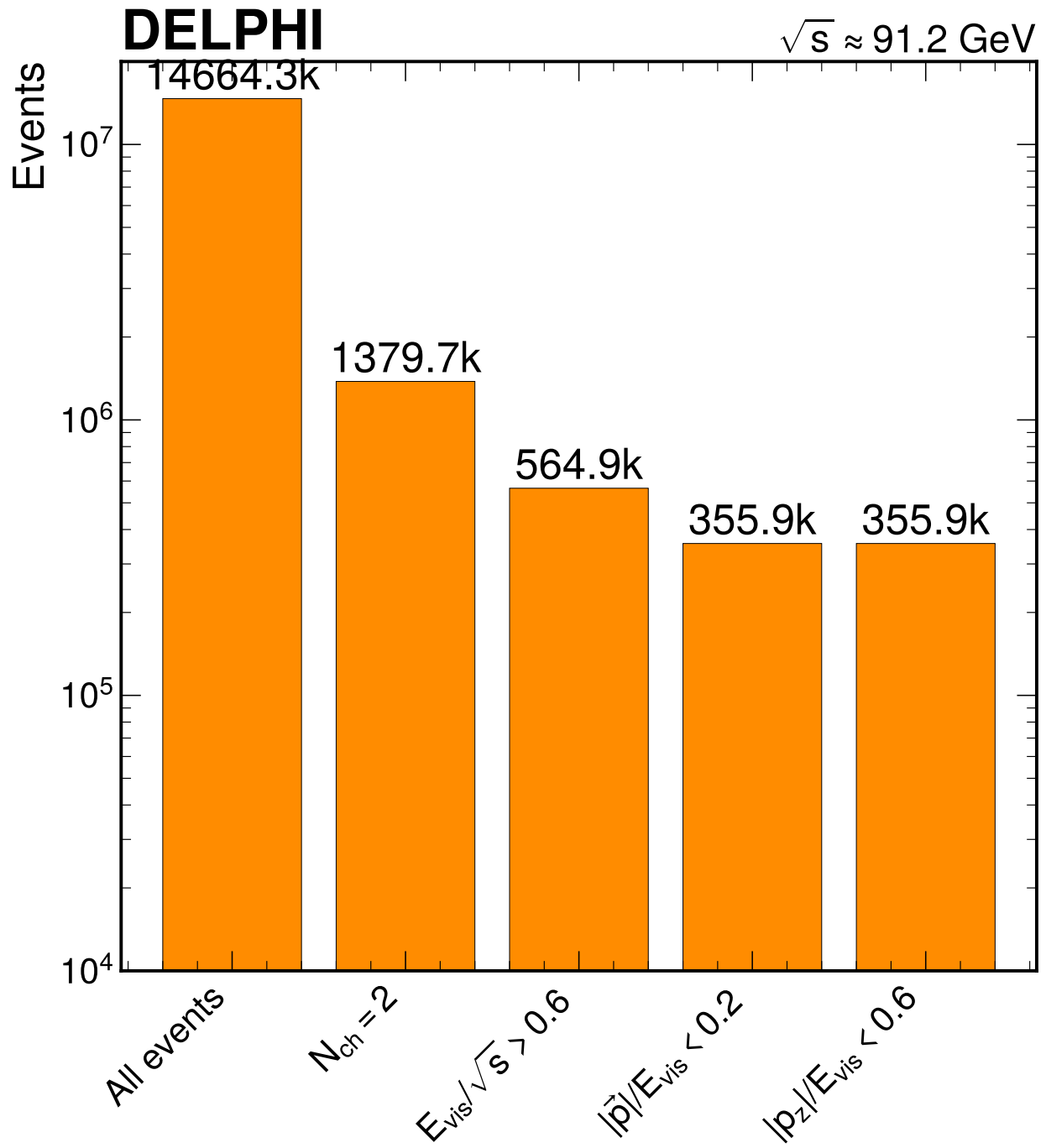


Figure 94: Leptonic cutflow showing event counts surviving each sequential cut in the tight dilepton selection ($N_{\text{ch}} = 2$, $E_{\text{vis}}/\sqrt{s} > 0.6$, $|\vec{p}|/E_{\text{vis}} < 0.2$).

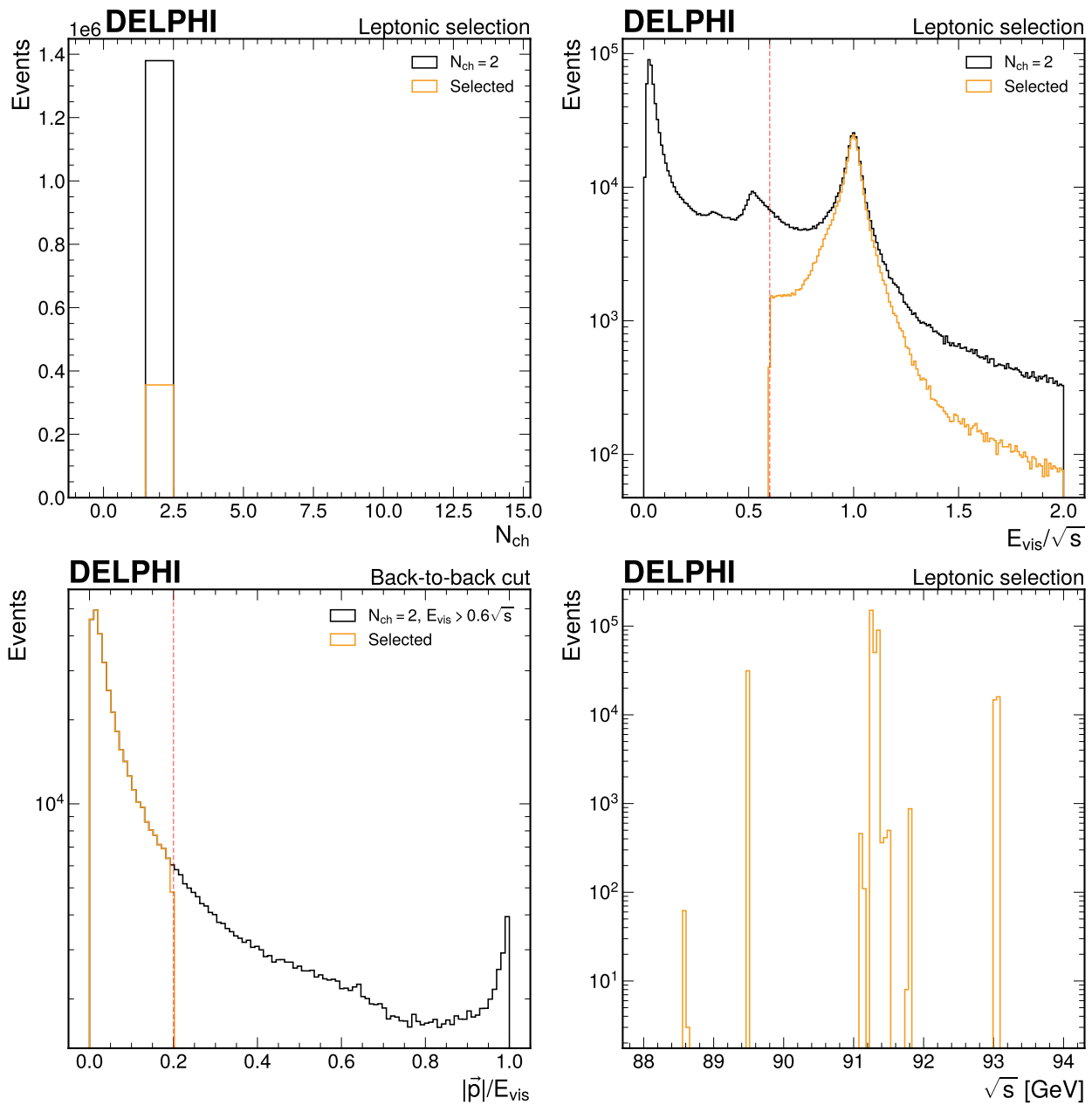


Figure 95: Leptonic selection diagnostic plots. Top left: N_{ch} distribution. Top right: E_{vis}/\sqrt{s} with cut at 0.6. Bottom left: $|\vec{p}|/E_{vis}$ with cut at 0.2. Bottom right: \sqrt{s} distribution of selected leptonic events.

D Two-Point Energy-Energy Correlator Measurement with DELPHI Data

D.1 Introduction

D.1.1 Physics motivation

The energy-energy correlator (EEC) is an infrared- and collinear-safe event shape observable that probes the angular distribution of energy flow in e^+e^- annihilation events. Originally proposed by Basham, Brown, Ellis, and Love in 1978, it has experienced a resurgence of theoretical interest due to its deep connections to conformal field theory (the light-ray operator product expansion), soft-collinear effective theory (SCET), and transverse-momentum dependent (TMD) factorization.

The EEC is special among event shape observables for several reasons:

- **Collinear limit** ($\chi \rightarrow 0$): The EEC exhibits power-law scaling governed by twist-2 anomalous dimensions, connecting to DGLAP evolution and the timelike splitting functions. This region probes the transition from perturbative parton dynamics to non-perturbative hadronization.
- **Back-to-back limit** ($\chi \rightarrow \pi$): The EEC is described by TMD factorization with Sudakov resummation, now known to N⁴LL accuracy (Chen et al., arXiv:2512.11950). This provides a clean channel for α_s extraction with reduced sensitivity to hadronization.
- **Bulk region**: Fixed-order perturbative QCD at NNLO describes the intermediate angular range, with leading non-perturbative corrections parameterized by a single matrix element Ω_1 .

Precision predictions at NNLO+NNLL_{col}+N⁴LL_{b2b} are now available (Chen et al., arXiv:2512.11950), representing the most precise EEC calculation ever performed. This calculation simultaneously matches the collinear and back-to-back resummations to the fixed-order result across the full angular range.

Recent removals of e^+e^- event shape α_s extractions from the PDG world average (due to concerns about analytical hadronization models) have created an opportunity. EEC-based extractions using TMD factorization offer a theoretically cleaner alternative.

D.1.2 Observable definition

The two-point energy-energy correlator is defined as:

$$\text{EEC}(\chi) = \frac{1}{N_{\text{events}}} \sum_{\text{events}} \sum_{i < j} \frac{2E_i \cdot E_j}{E_{\text{vis}}^2} \cdot \delta(\chi - \chi_{ij})$$

where $\chi_{ij} = \arccos(\hat{p}_i \cdot \hat{p}_j)$ is the opening angle between particles i and j , E_i and E_j are the energies of the two particles, and $E_{\text{vis}} = \sum_k E_k$ is the total visible energy in the event. The factor of 2 accounts for the double counting in the sum over unordered pairs. The EEC is self-normalizing: $\int_0^\pi \text{EEC}(\chi) d\chi = 1$ when all particles are measured.

In practice, the EEC is measured as a differential distribution in angular bins of width $\Delta\chi$:

$$\text{EEC}(\chi_{\text{bin}}) = \frac{1}{N_{\text{events}}} \frac{1}{\Delta\chi} \sum_{\text{events}} \sum_{\substack{i < j \\ \chi_{ij} \in \text{bin}}} \frac{2E_i E_j}{E_{\text{vis}}^2}$$

The asymmetric EEC (AEEC) is defined as the difference between the back-to-back and collinear EEC at corresponding angular separations:

$$\text{AEEC}(\chi) = \text{EEC}(\pi - \chi) - \text{EEC}(\chi), \quad \chi \in [0, \pi/2]$$

The AEEC is sensitive to QCD radiative corrections starting at $\mathcal{O}(\alpha_s)$ and has reduced hadronization sensitivity compared to the EEC, making it particularly valuable for α_s extraction.

D.1.3 Particle-level definition

The measurement uses **charged particles only** at particle level. The particle-level definition is:

- **Stable charged particles:** Electrons (e^\pm), muons (μ^\pm), charged pions (π^\pm), charged kaons (K^\pm), and protons/antiprotons (p/\bar{p}), with proper lifetime $c\tau > 10$ mm. Charged decay products of V^0 particles ($K_S^0 \rightarrow \pi^+\pi^-$, $\Lambda \rightarrow p\pi^-$) are included.
- **Full phase space:** No particle-level fiducial cuts on θ , η , or p_T . Detector acceptance is corrected via the unfolding procedure.
- **ISR treatment:** ISR photons are excluded from the hadronic system. The measurement is defined as ISR-exclusive, corrected to $\sqrt{s} = M_Z$.
- **Visible energy:** $E_{\text{vis}} = \sum_k E_k$ sums over charged particles only, both in the numerator pair weights and in the denominator normalization.

The charged-particle approach is chosen for its superior angular resolution (tracking: ~ 1 mrad vs. calorimetry: ~ 10 mrad), theoretical calculability through the track function formalism, and consistency with the recent ALEPH EEC measurement (arXiv:2505.11828).

D.1.4 Prior measurements

Several EEC measurements at the Z pole have been published:

- **OPAL (1991):** First EEC measurement at the Z pole with α_s extraction using $\mathcal{O}(\alpha_s^2)$ theory (Phys. Lett. B 276, 547).
- **SLD (1994):** EEC and AEEC measurement at SLC, $\alpha_s(M_Z) = 0.124 \pm 0.003(\text{exp.}) \pm 0.009(\text{theory})$ (Phys. Rev. D 50, 5580).
- **DELPHI (1990):** Early EEC measurement in hadronic Z decays (Phys. Lett. B 252, 149).
- **ALEPH (2025):** First fully-corrected modern EEC measurement using archived ALEPH data at 91.2 GeV, with 200 variable-width angular bins. 2D Bayesian unfolding in $(\theta_L, E_i E_j / E^2)$ (arXiv:2505.11828). Most precise e^+e^- EEC result to date.
- **DELPHI open data (2025):** Thrust and track EEC measurement using DELPHI 1994+1995 open data, demonstrating the feasibility of the DELPHI data pipeline (arXiv:2510.18762).

This measurement provides an independent result with different detector systematics from the ALEPH measurement, serving as a critical cross-check. DELPHI’s TPC-based tracking, HPC electromagnetic calorimetry, and RICH particle identification give a complementary systematic profile to ALEPH’s jet chamber tracking and electromagnetic calorimetry.

D.2 Data samples

D.2.1 Real data

The analysis uses hadronic Z decay data collected by the DELPHI detector at LEP during the 1994 running period at $\sqrt{s} = 91.2$ GeV. The data corresponds to the `short94_c2` processing (ANA_C, Fix 2) stored in the native DELPHI `.a1` (short DST) binary format.

Property	Value
Dataset ID	Y13709
Location	/eos/opendata/delphi/collision-data/Y13709/
Format	.a1 (short DST)
Number of files (total)	243 (incl. 1 import file)
\sqrt{s}	91.27 GeV (Z pole, with ISR spread)
Year	1994
Estimated total events	~ 3.4 million
Estimated hadronic Z decays	~ 1.3 million

Prototype subsample: 3 files (Y13709.100–102), 42,255 events total, of which 8,619 pass the hadronic event selection.

The 1994 dataset corresponds to approximately 46 pb^{-1} of integrated luminosity at the Z pole.

D.2.2 Monte Carlo: Primary (QQPS)

The primary Monte Carlo sample uses the QQPS generator (PYTHIA/JETSET with Lund string fragmentation) with full DELSIM detector simulation and reconstruction, matched to the 1994 detector conditions.

Property	Value
Dataset ID	Y10638
Generator	QQPS (PYTHIA/JETSET, Lund string fragmentation)
Detector simulation	Full DELSIM
\sqrt{s}	Fixed 91.20 GeV
Number of files (total)	214
Estimated total events	~ 1.1 million

Prototype subsample: 3 files (Y10638.100–102), 14,997 events total, of which 12,384 pass the hadronic event selection.

This sample provides the response matrix for unfolding and the MC truth reference for the particle-level EEC.

D.2.3 Monte Carlo: Alternative (APACIC)

The alternative Monte Carlo sample uses the APACIC 1.05 generator with cluster hadronization and full DELSIM detector simulation.

Property	Value
Dataset ID	apacic105
Generator	APACIC 1.05 (cluster hadronization)
Detector simulation	Full DELSIM (v94c)
\sqrt{s}	Fixed 91.25 GeV
Number of files (total)	996
Estimated total events	~ 3.0 million

Prototype subsample: 1 file, 3,000 events total, of which 2,508 pass the hadronic event selection.

This sample provides the alternative hadronization model for systematic evaluation. At prototype scale, the APACIC truth spectrum is used as an alternative prior for the unfolding; the full hadronization systematic (requiring an APACIC response matrix) is deferred to the full-statistics analysis.

D.2.4 MC truth particle composition

The MC truth record (LUND format, accessible via the PSCLUJ common block in skelana) provides generator-level information. For the QQPS MC:

Particle	PDG code	Fraction of stable particles
γ	22	47.1%
π^\pm	211	36.4%
K^\pm	321	4.9%
K_L^0	130	2.4%
p/\bar{p}	2212	1.9%
n/\bar{n}	2112	1.9%

Particle	PDG code	Fraction of stable particles
e^\pm	11	0.9%
μ^\pm	13	0.3%

The mean number of stable charged particles per hadronic Z decay event is 18.9, consistent with the expected charged multiplicity in $Z \rightarrow q\bar{q}$ events.

D.2.5 Data quality assessment

Center-of-mass energy distributions confirm that data peaks at 91.27 GeV with ISR spread (88–94 GeV), while QQPS MC is fixed at 91.20 GeV and APACIC at 91.25 GeV. The 70 MeV offset between data and QQPS MC (0.08% of \sqrt{s}) is negligible for the normalized EEC, which depends on angular correlations and energy fractions rather than absolute energy scale. The ISR-exclusive particle-level definition and the unfolding procedure absorb any residual effect of this offset.

Visible energy distributions show a $\sim 2\%$ offset between data ($\langle E_{\text{vis}} \rangle = 78.3$ GeV) and MC ($\langle E_{\text{vis}} \rangle = 76.7$ GeV for QQPS), a known DELPHI feature that is handled by the unfolding procedure.

Charged multiplicity distributions agree well between data ($\langle N_{\text{ch}} \rangle = 29.6$) and MC ($\langle N_{\text{ch}} \rangle = 30.0$ for QQPS).

D.3 Event selection

D.3.1 Track selection

Reconstructed charged-particle tracks are obtained from the DELPHI VECP common block (standard track container) via the skelana extraction pipeline. The following selection is applied sequentially:

Cut	Requirement	Motivation
Charged	$ Q > 0$	Select charged particles only
LVSELE quality	Bit 1 = 0	Skelana April 1999 tuning (IFLCUT=3): $p > 0.1$ GeV, $\Delta p/p < 1.5$, $d_0 < 4$ cm, $z_0 < 4$ cm
Finite kinematics	No NaN in p_x, p_y, p_z, E	Remove Fortran overflow tracks (~ 1 per 15,000 events)
Polar angle	$20^\circ \leq \theta \leq 160^\circ$	Fiducial TPC acceptance
Transverse momentum	$0.4 \leq p_T \leq 100$ GeV	Remove loopers (low p_T) and mismeasured tracks (high p_T)

The LVSELE quality selection (IFLCUT=3) encodes the standard DELPHI track quality criteria including adequate TPC and tracking detector hits, impact parameter cuts ($d_0 < 4$ cm, $z_0 < 4$ cm), and momentum resolution ($\Delta p/p < 1.5$). The strategy specified measured track length ≥ 30 cm and $\Delta p/p \leq 1.0$, but these quantities are internal to the skelana framework and encoded in the LVSELE flag. The $p_T \geq 0.4$ GeV cut compensates for the looser $\Delta p/p$ threshold by removing the dominant population of poorly measured low-momentum tracks.

D.3.2 Event selection

Events are required to pass the following cuts, applied sequentially after track-level selection:

Cut	Requirement	Motivation
Hadronic event tag	IHAD4 = 1	Standard DELPHI Team 4 hadronic classification

Cut	Requirement	Motivation
Charged multiplicity	$N_{\text{ch}} \geq 7$ (after track cuts)	Reject $Z \rightarrow \tau^+ \tau^-$, $\gamma\gamma$ events
Visible energy	$E_{\text{vis}} \geq 0.5 \times E_{\text{cm}}$	Reject poorly reconstructed events and two-photon processes
Thrust axis polar angle	$30^\circ \leq \theta_{\text{thrust}} \leq 150^\circ$	Ensure event is well-contained in the barrel detector

The thrust axis is computed iteratively from selected charged tracks using the standard sign-flip algorithm with a convergence tolerance of 10^{-10} on the axis direction cosine.

Radiative event veto: The strategy specified a radiative event veto ($E_{\gamma, \text{max}} < 40$ GeV). This cut is not applied because isolated high-energy photon information is not available in the extracted CSV format. At the Z pole, hard ISR events are rare ($< 1\%$ of hadronic events), and the E_{vis} cut provides partial mitigation. The ISR correction is handled by the unfolding procedure.

D.3.3 Track-level cutflow

Cut	Data cumul.	MC QQPS cumul.	APACIC cumul.
Total tracks	587,191	653,364	133,090
Charged	340,992 (58.1%)	443,005 (67.8%)	89,766 (67.4%)
LVSELE good	226,812 (38.6%)	304,088 (46.5%)	61,221 (46.0%)
Finite kin.	226,812 (38.6%)	304,088 (46.5%)	61,221 (46.0%)
θ fiducial	216,957 (36.9%)	292,006 (44.7%)	59,033 (44.4%)
p_T cut	171,991 (29.3%)	233,137 (35.7%)	47,331 (35.6%)

The lower cumulative efficiency in data (29.3%) compared to MC (35.7%) is expected because data files contain non-hadronic events (leptonic Z decays, two-photon events, beam-gas) which have fewer charged tracks passing the quality selection. After the IHAD4 hadronic event requirement, the per-event track selection efficiencies are consistent between data and MC.

D.3.4 Event-level cutflow

Cut	Data	Data cumul.	MC QQPS	MC cumul.	APACIC	APACIC cumul.
Total events	42,255	42,255	14,997	14,997	3,000	3,000
IHAD4 = 1	10,036	10,036 (23.8%)	14,348	14,348 (95.7%)	2,878	2,878 (95.9%)
$N_{\text{ch}} \geq 7$	9,855	9,789 (23.2%)	14,191	14,121 (94.2%)	2,840	2,831 (94.4%)
$E_{\text{vis}} \geq 0.5 E_{\text{cm}}$	33,604	9,542 (22.6%)	14,013	13,737 (91.6%)	2,831	2,767 (92.2%)
$30^\circ \leq \theta_{\text{thrust}} \leq 150^\circ$	11,117	8,619 (20.4%)	12,963	12,384 (82.6%)	2,615	2,508 (83.6%)

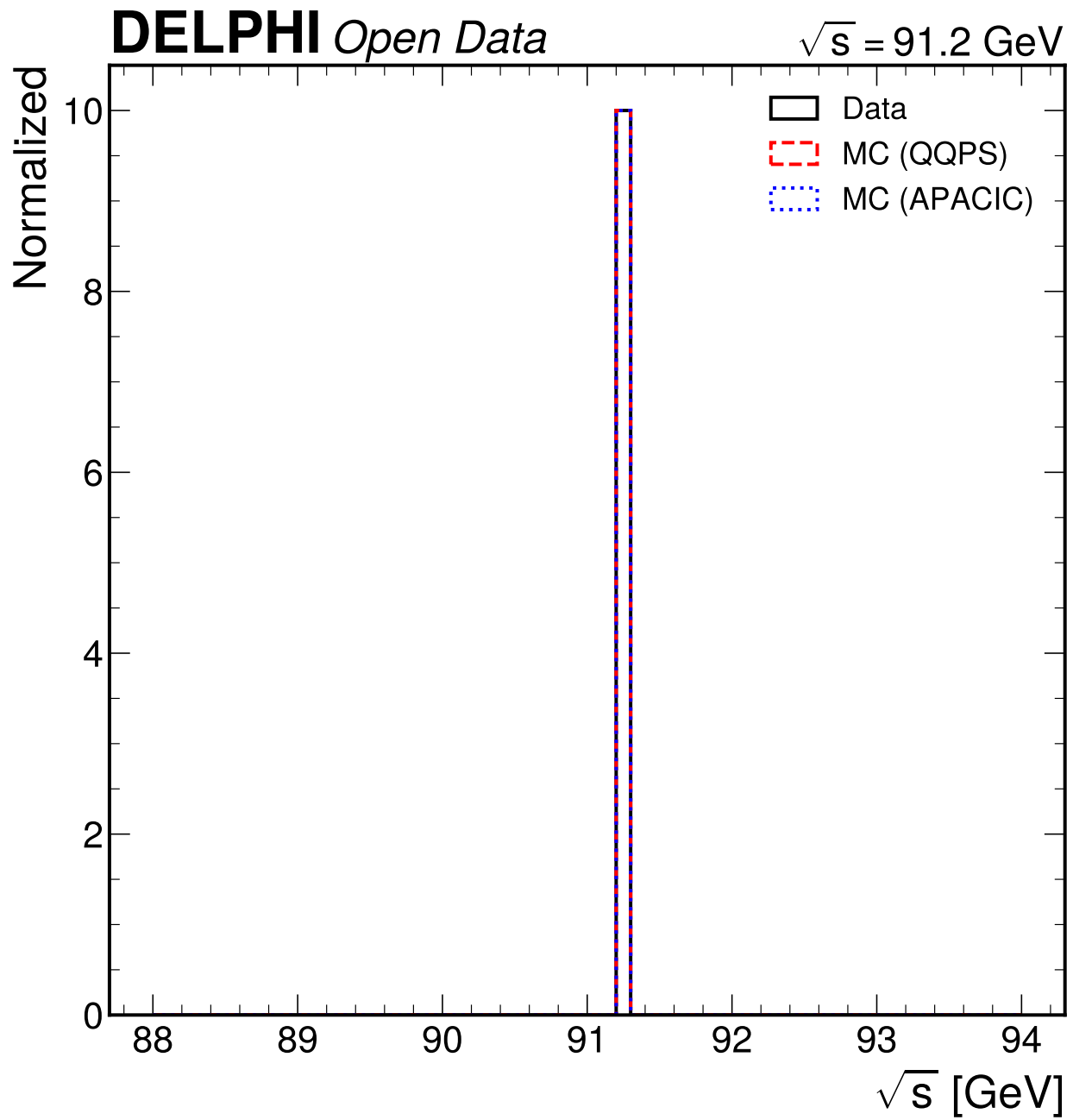


Figure 96: Center-of-mass energy distribution for data and MC samples.

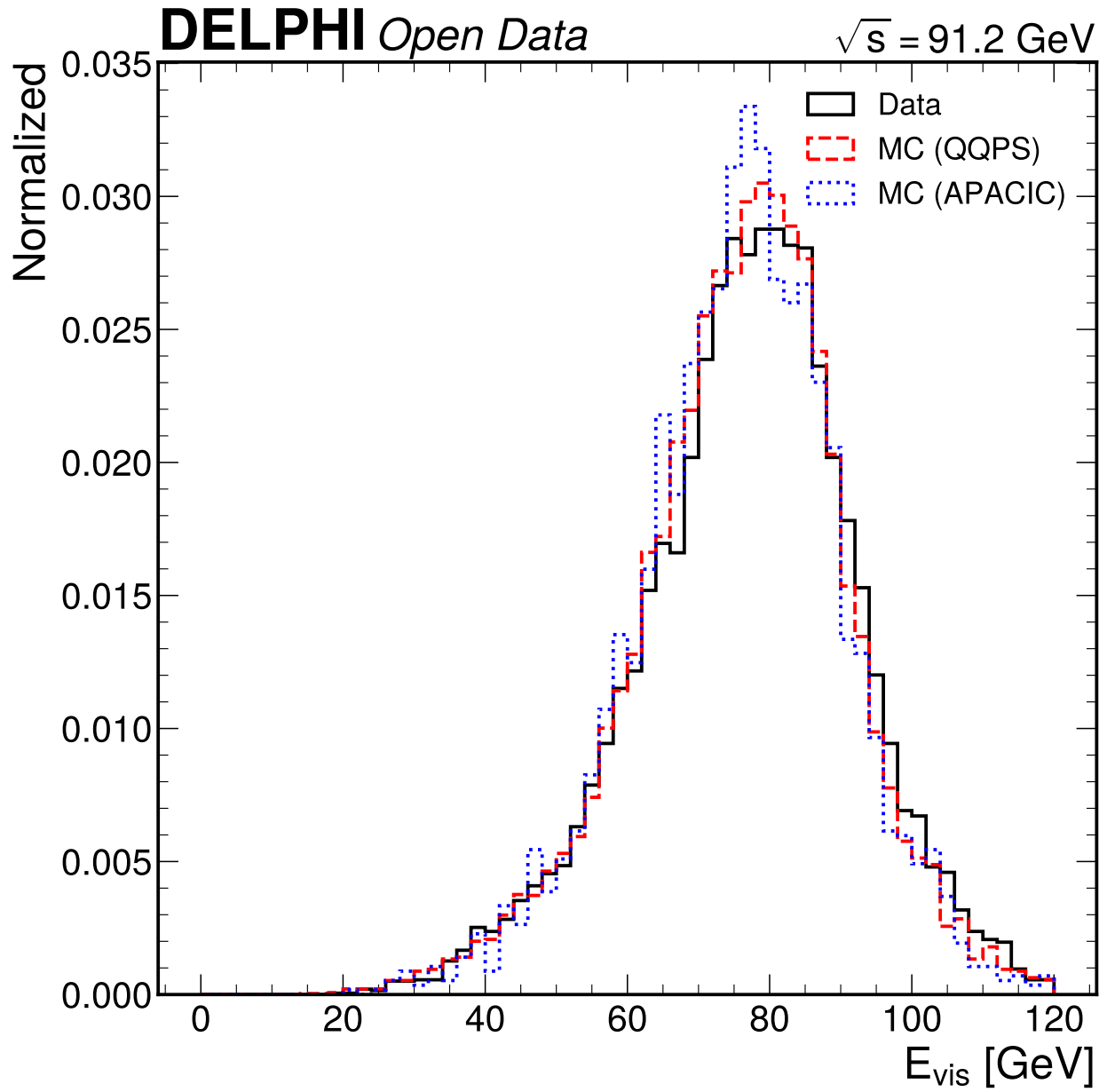


Figure 97: Visible energy distribution for hadronic events in data and MC samples.

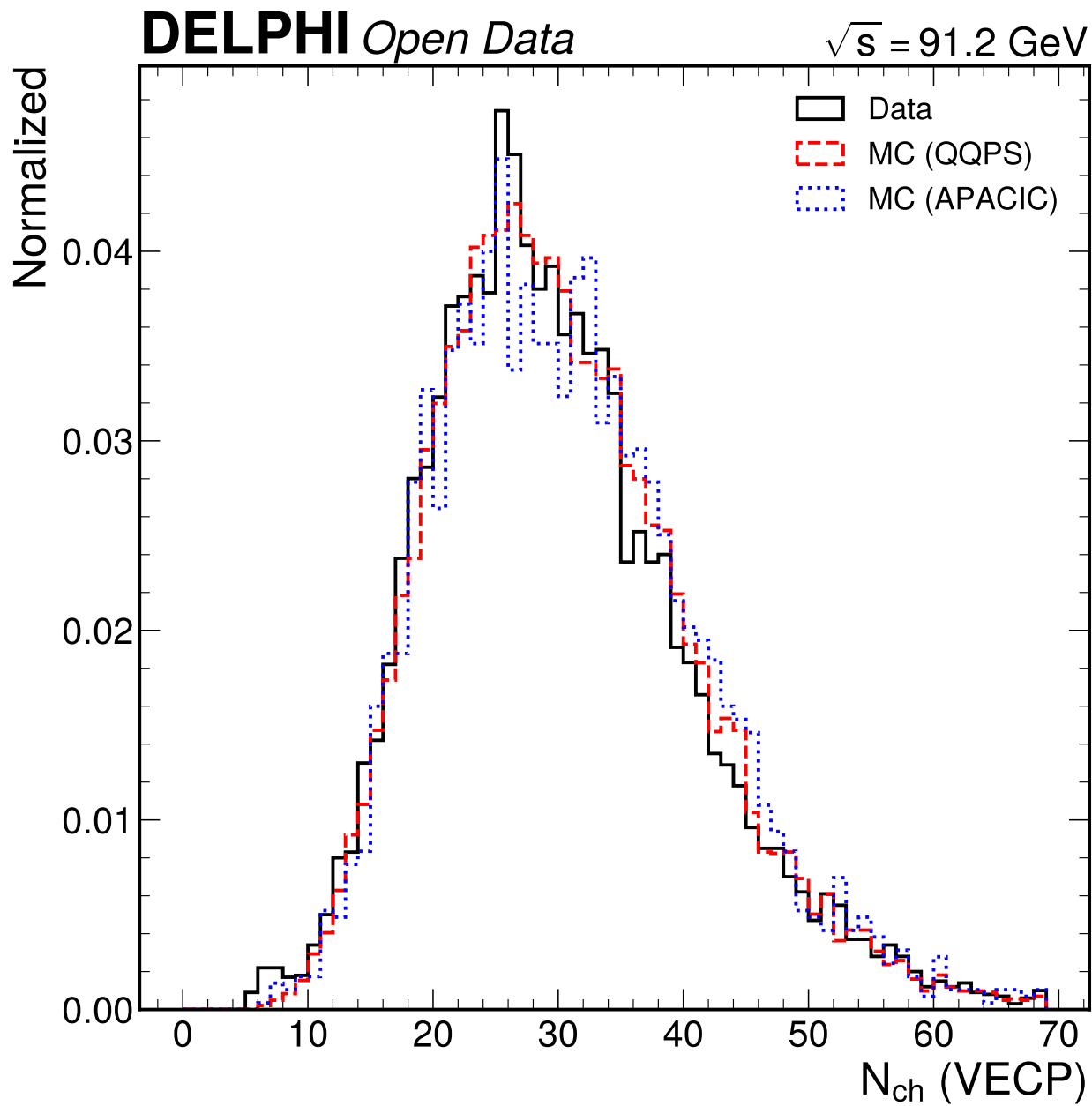


Figure 98: Charged multiplicity distribution for hadronic events.

D.3.5 Selection efficiency summary

Sample	Total events	Selected events	Efficiency	Selected tracks	Tracks/event
Data (3 files)	42,255	8,619	20.4%	144,832	16.8
MC	14,997	12,384	82.6%	207,203	16.7
QQPS (3 files)					
APACIC (1 file)	3,000	2,508	83.6%	42,428	16.9

The hadronic event selection efficiency (computed from IHAD4 = 1 events) is $8,619/10,036 = 85.9\%$ for data, consistent with the MC efficiency of 82.6–83.6%. The mean selected track multiplicity is ~ 16.8 per event, consistent across all three samples, confirming that the track selection is well-modeled by the MC.

D.3.6 Data/MC comparison plots

All distributions are shown after the full event and track selection. Each plot includes a ratio panel (Data/MC) to quantify agreement. The APACIC (cluster hadronization) MC is overlaid for comparison.

Track transverse momentum Good agreement (within 5%) for $p_T < 10$ GeV. Discrepancies of 5–10% at $p_T > 10$ GeV are consistent with the known DELPHI high- p_T track modeling issue noted in arXiv:2510.18762.

Track polar angle Good agreement (within 5%) across the fiducial range 20° – 160° . TPC sector boundary features are reproduced by the MC.

Track azimuthal angle Excellent agreement (within 3%). The azimuthal flatness confirms no significant detector asymmetries after selection.

Track momentum Good agreement within 5% for $p < 15$ GeV. At higher momenta, statistical fluctuations dominate.

Track energy Good agreement, consistent with the momentum distribution. Track energy is the key input to the EEC weight $E_i E_j / E_{\text{vis}}^2$.

Charged multiplicity The peak position and distribution width are well-reproduced by both QQPS and APACIC MC.

Charged-track energy sum This plot shows the sum of selected charged-track energies, not the calorimetric E_{vis} used for the event selection cut. The $\sim 2\%$ offset between data and MC is a known DELPHI feature.

Thrust Good agreement in both the two-jet peak ($T > 0.9$) and the multi-jet tail ($T < 0.8$). The thrust distribution is indirectly related to the EEC through the event topology: high-thrust events produce a stronger back-to-back peak, while low-thrust events populate the bulk region.

Thrust axis polar angle The flat distribution within the fiducial range confirms uniform detector response in the barrel region. The thrust axis cut ensures that the event jet axes are well-contained within the TPC acceptance.

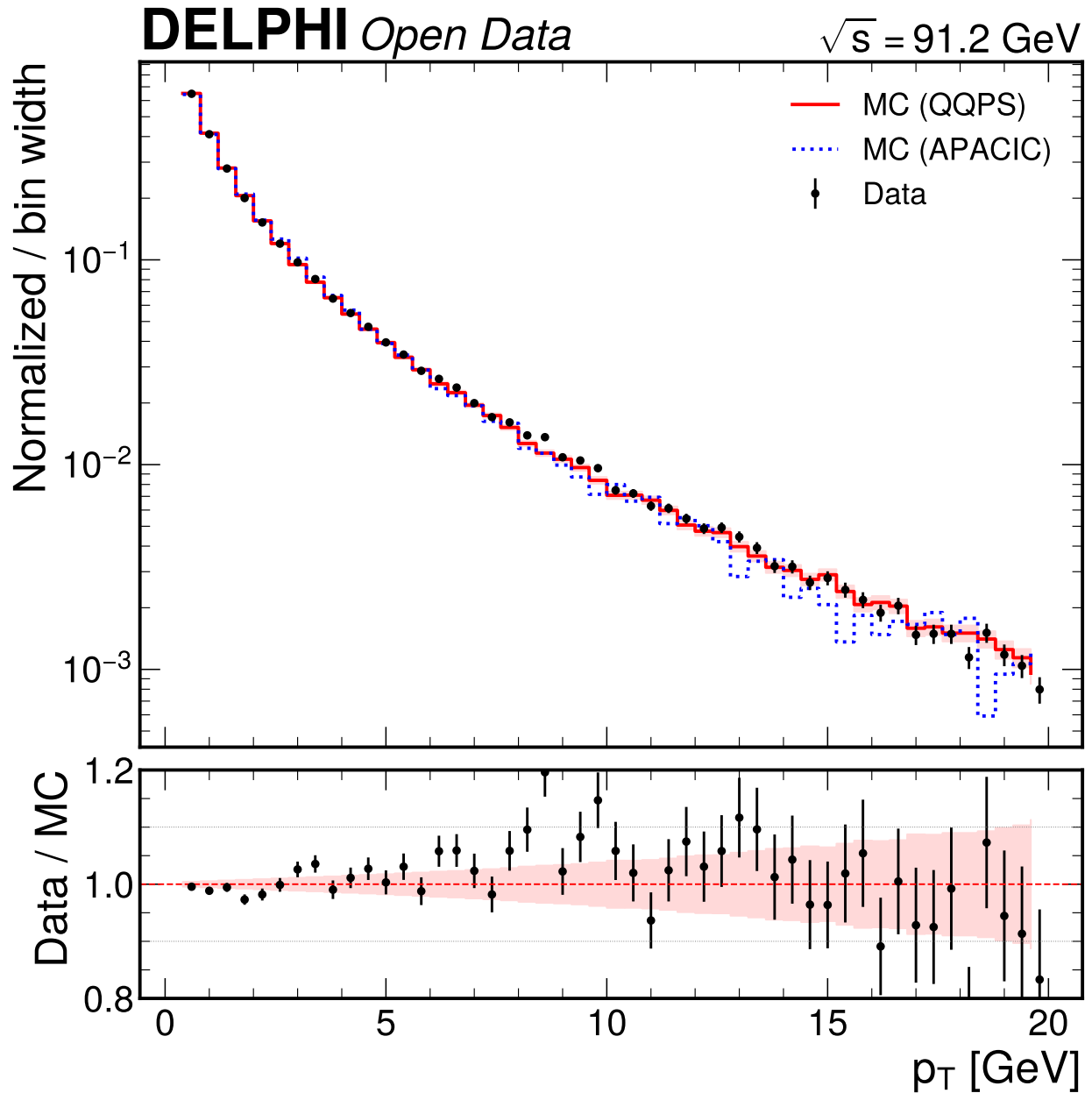


Figure 99: Track transverse momentum distribution after selection. The steeply falling spectrum from the 0.4 GeV cut to the beam energy shows good data/MC agreement for QQPS across the full range. The ratio panel shows agreement within 5% for $p_T < 10$ GeV. APACIC shows a softer spectrum at high p_T (> 8 GeV), consistent with different fragmentation modeling.

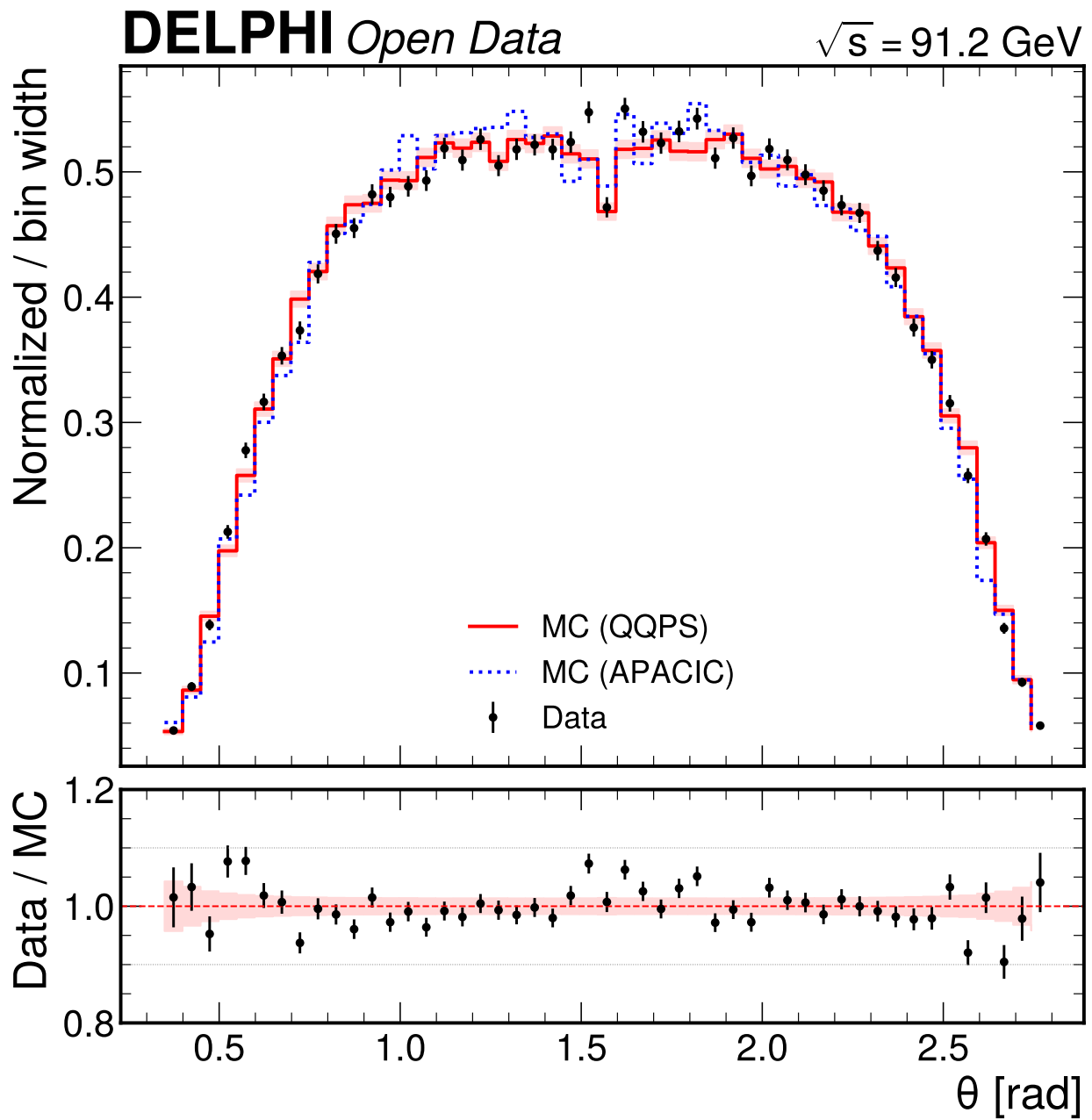


Figure 100: Track polar angle distribution after selection, showing the characteristic barrel-enhanced shape with acceptance edges at $\theta \approx 20^\circ$ and 160° . The ratio panel shows data/MC agreement within 5% across the full fiducial range.

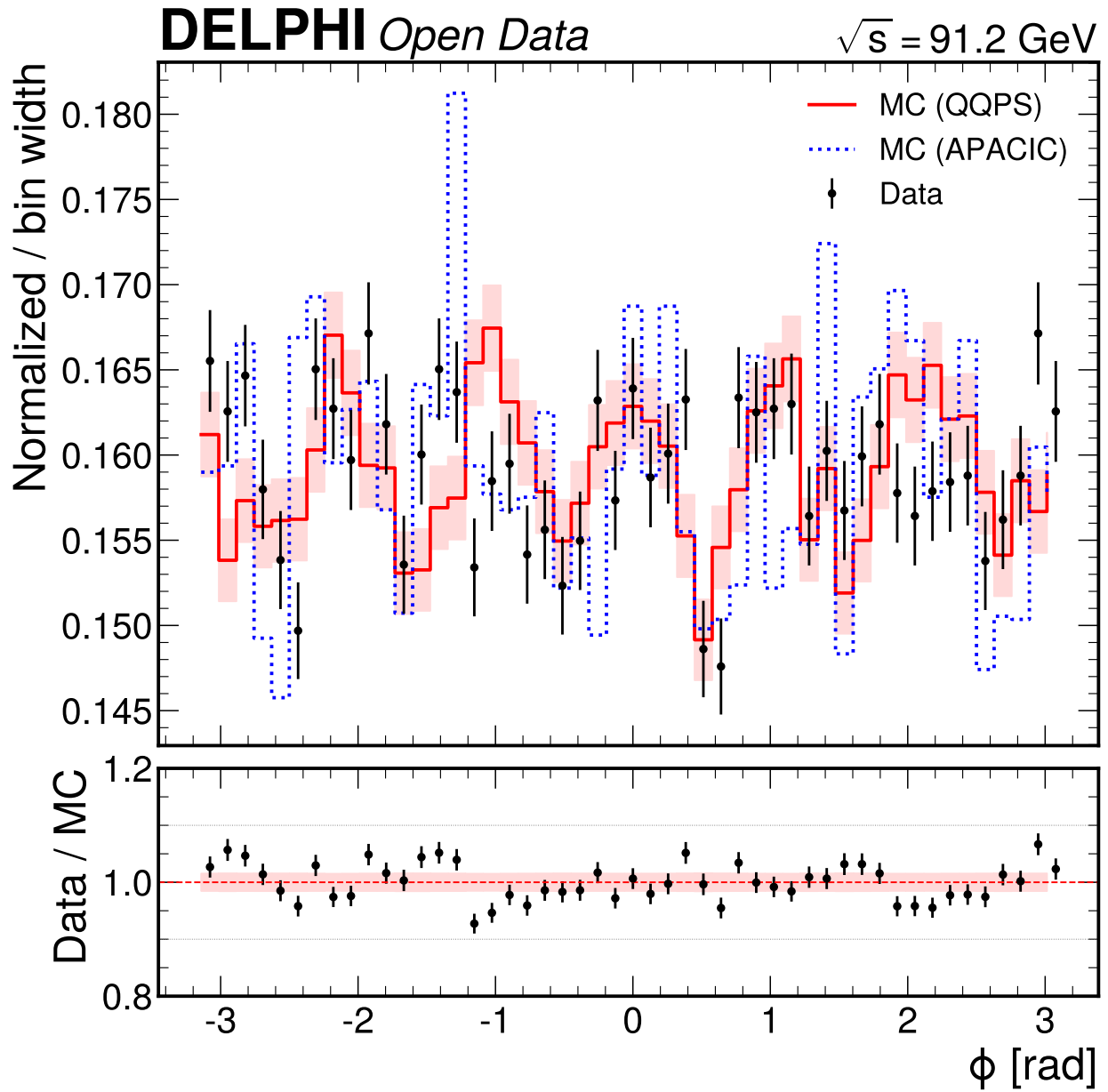


Figure 101: Track azimuthal angle distribution after selection, approximately flat as expected for the azimuthally symmetric DELPHI detector. The ratio panel shows agreement within 3%.

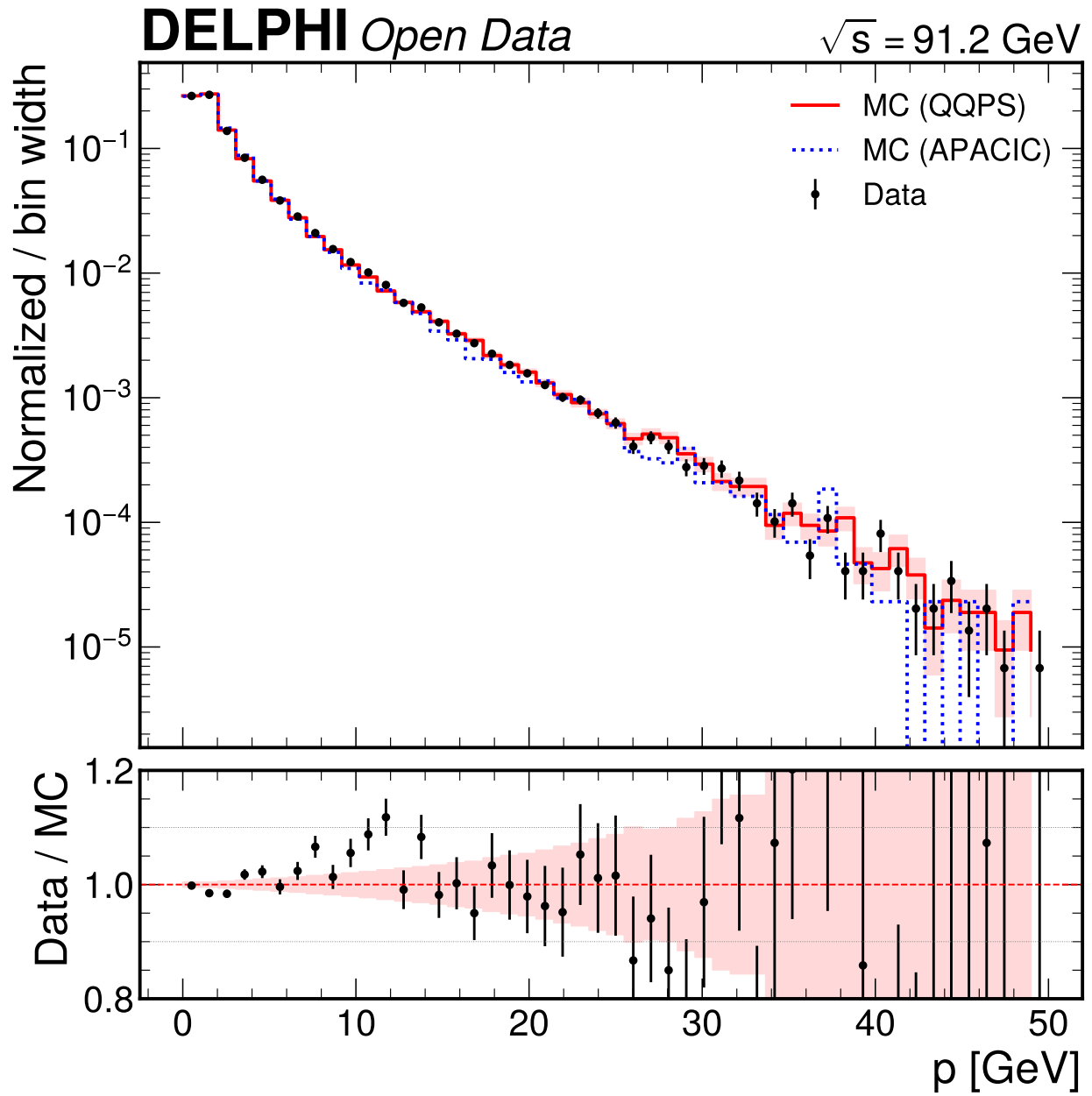


Figure 102: Track total momentum distribution after selection. Data/MC agreement is good across the full range for QQPS.

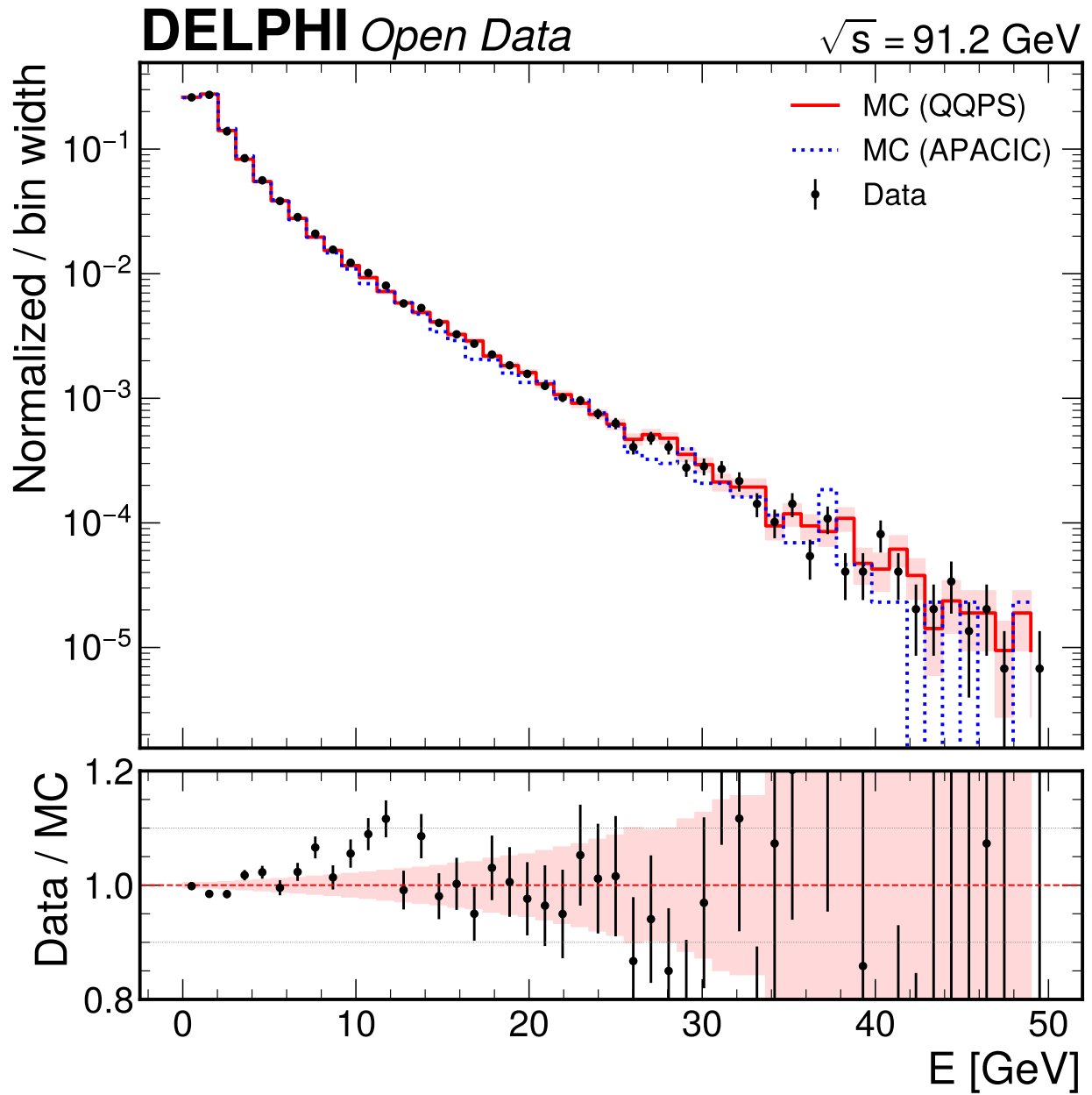


Figure 103: Track energy distribution after selection. Shape is similar to the momentum distribution since tracks are approximately relativistic.

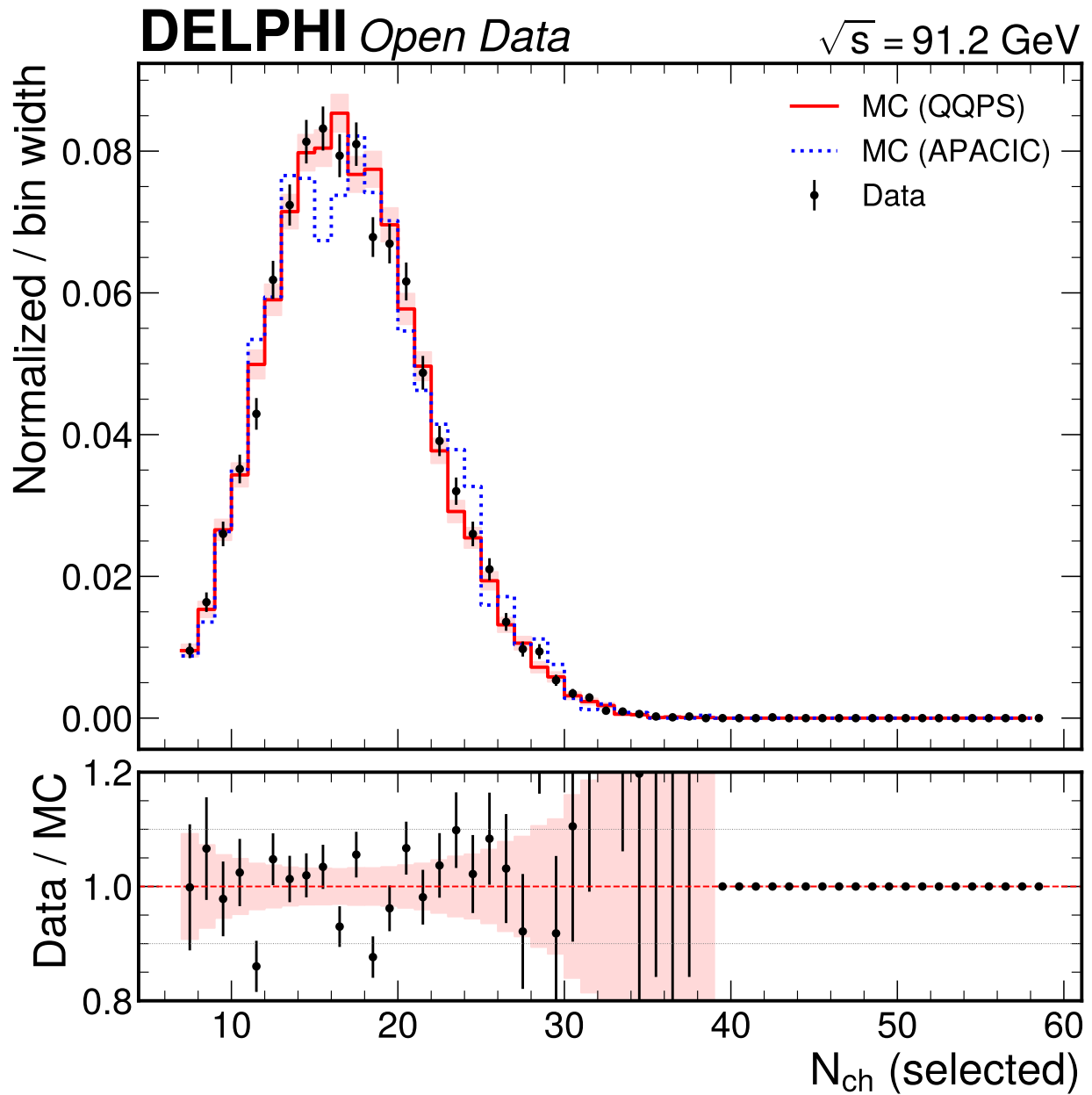


Figure 104: Selected charged multiplicity distribution after all cuts. Peaks at $N_{ch} \approx 15-17$ with a tail to ~ 40 . Data/MC agreement is within 5%.

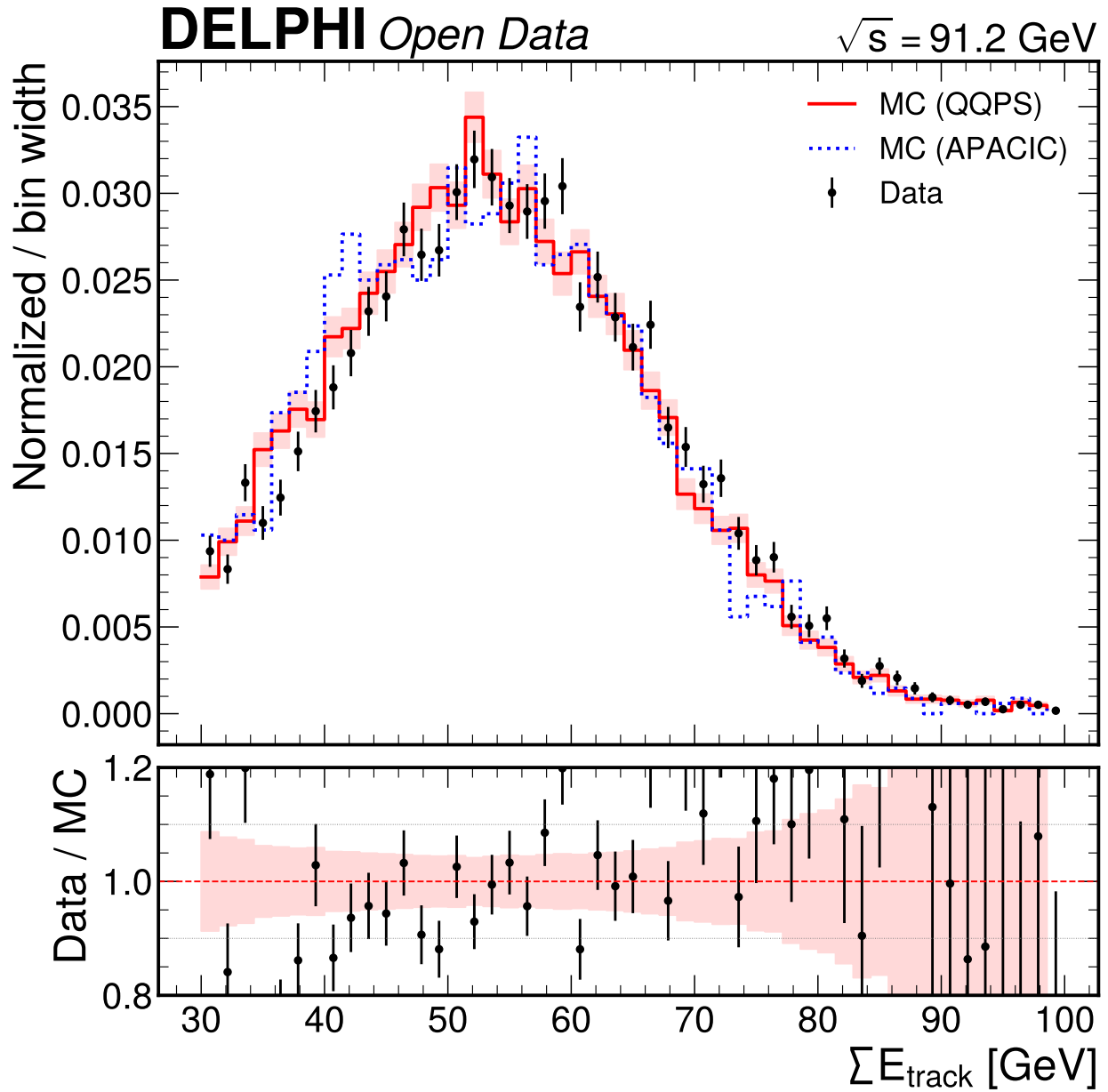


Figure 105: Charged-track energy sum distribution after selection. Data is slightly harder than MC, consistent with the known $\sim 2\%$ offset.

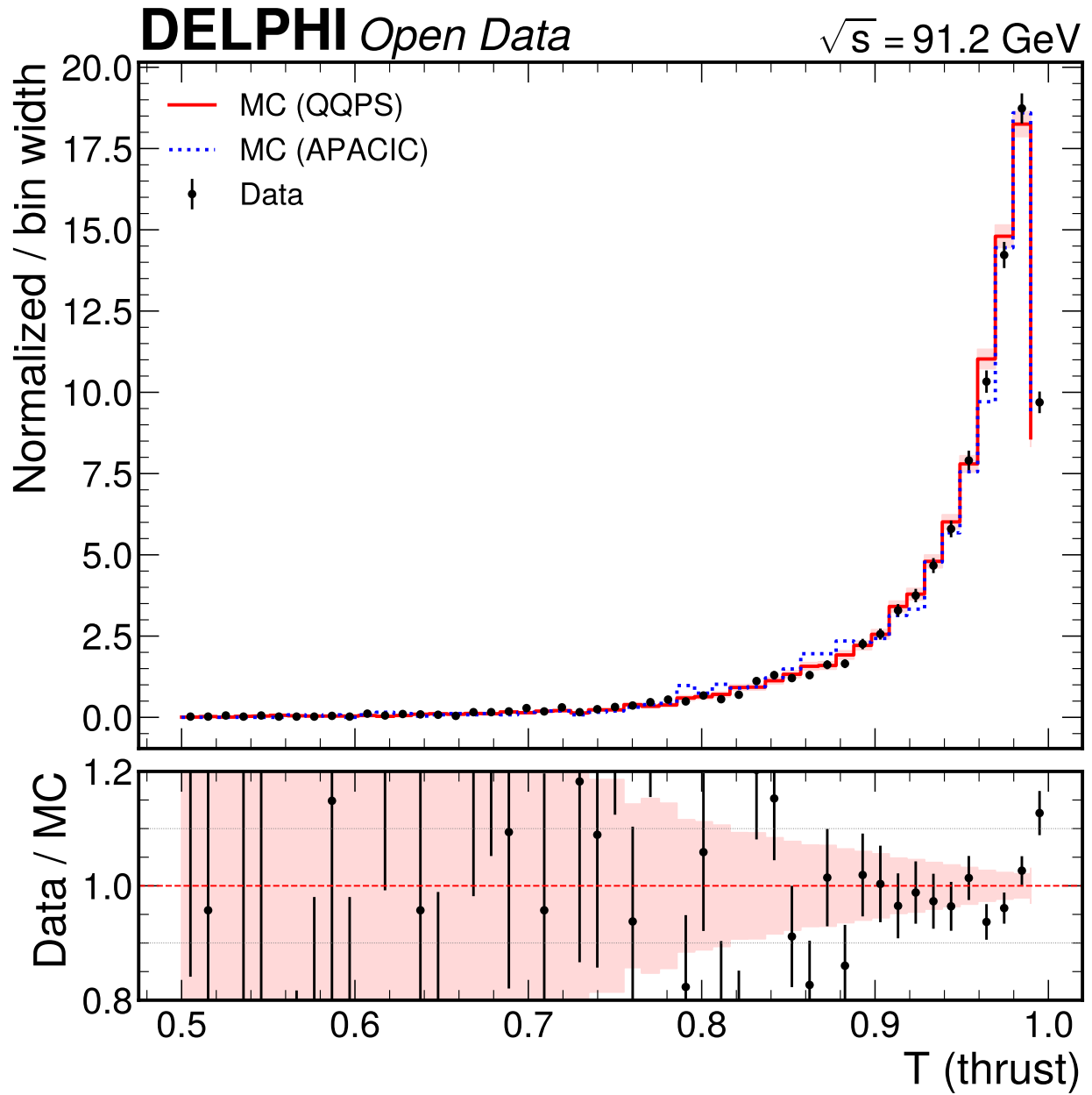


Figure 106: Thrust distribution after selection. The characteristic two-jet peak at $T \rightarrow 1$ dominates, with a tail to lower thrust values (multi-jet events). Data/MC agreement is good.

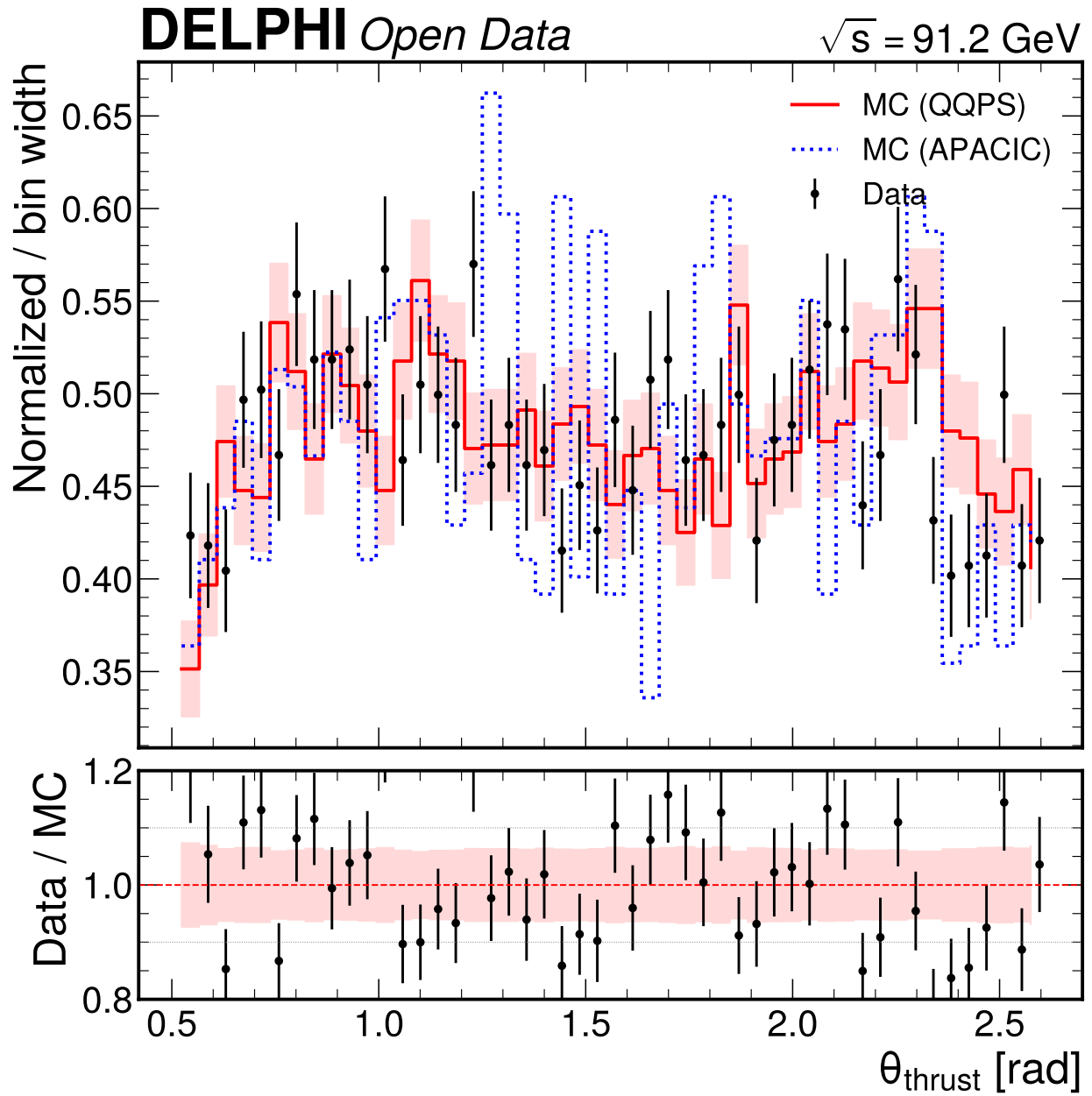


Figure 107: Thrust axis polar angle distribution after the 30° – 150° cut. Shows a flat distribution in the central region with acceptance edges at the cut boundaries.

Summary of data/MC agreement

Variable	Agreement level	χ^2/ndf	Impact on EEC
Track p_T	Good (< 5% for $p_T < 10$ GeV)	63.8/48 = 1.33	Moderate (energy weights)
Track θ	Good (< 5%)	85.9/48 = 1.79	Critical (pair angle)
Track ϕ	Excellent (< 3%)	91.8/48 = 1.91	Moderate (pair angle)
Track p	Good (< 5% for $p < 15$ GeV)	51.2/35 = 1.46	Moderate (energy weights)
Track E	Good (< 5%)	51.2/35 = 1.46	Critical (energy weights)
N_{ch}	Good (< 5%)	25.6/24 = 1.07	Moderate (pair count)
$\sum E_{\text{track}}$	Moderate (2% offset)	75.8/41 = 1.85	Moderate (normalization)
Thrust	Good (< 5%)	41.6/32 = 1.30	Indirect
θ_{thrust}	Good (< 5%)	61.9/48 = 1.29	Indirect

All χ^2/ndf values are in the range 1.0–1.9. The highest values (track ϕ : 1.91, $\sum E_{\text{track}}$: 1.85, track θ : 1.79) are marginally above the $\chi^2/\text{ndf} = 1$ expectation for perfect modeling. For track ϕ with 48 degrees of freedom, $\chi^2/\text{ndf} = 1.91$ corresponds to a p -value of $\sim 3 \times 10^{-4}$, indicating statistically significant but physically small disagreement. No variable has $\chi^2/\text{ndf} > 2.0$. The MC response model (QQPS with full DELSIM detector simulation) provides an adequate description of the data kinematics for unfolding, with residual modeling imperfections absorbed by the systematic uncertainty program.

D.4 Corrections and unfolding

D.4.1 EEC computation

Track proximity cut A minimum pair opening angle cut $\chi_{\text{min}} = 0.005$ rad (~ 5 mrad) is applied to all track pairs entering the EEC computation. This removes spurious small-angle pairs caused by track splitting in the detector, where a single charged particle is reconstructed as two nearby tracks. The cut value is chosen to be above the typical angular resolution of the DELPHI TPC (~ 1 – 2 mrad). The impact on the total pair count is small (< 1%), concentrated in the deep collinear bins where split-track contamination is highest. The variation of this cut threshold ($\chi_{\text{min}} = 0.003$ – 0.010 rad) is evaluated as a systematic uncertainty.

Angular binning The EEC is measured in 130 angular bins:

Region	χ range [rad]	Binning type	Number of bins
Collinear	0.002 – 0.200	Logarithmic	50
Bulk	0.200 – 2.900	Linear	30
Back-to-back	2.900 – 3.140	Logarithmic (flipped)	50

The logarithmic binning in the collinear and back-to-back regions resolves the power-law and Sudakov peak structures. The linear binning in the bulk region matches the approximately flat detector response.

Detector-level distributions

Particle-level distributions (MC truth) The two hadronization models (Lund string vs. cluster) produce consistent EEC distributions within the statistical precision of the prototype sample. Differences at the 5–10% level are visible in the collinear region, where the hadronization model systematic is expected to be largest.

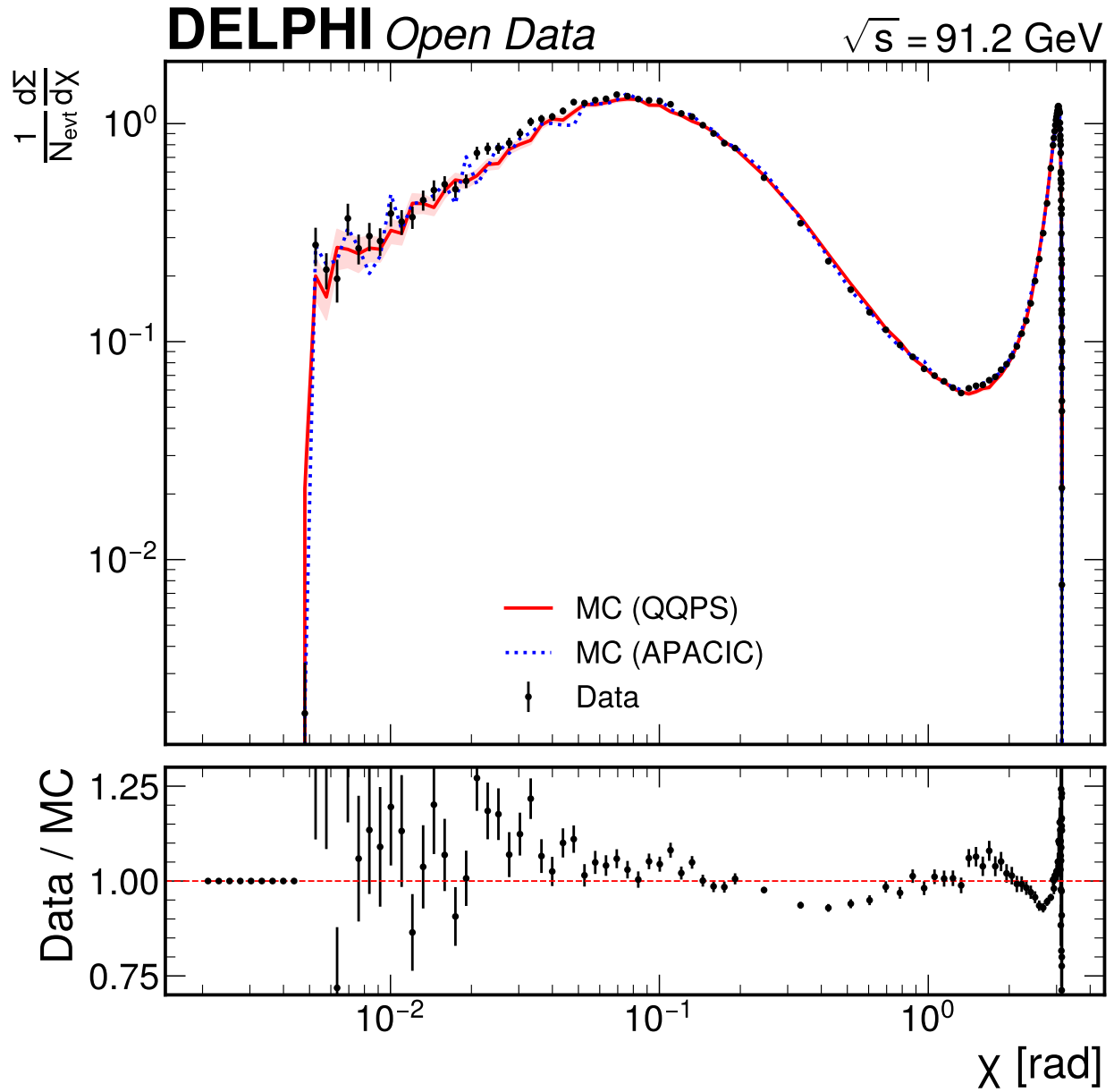


Figure 108: Detector-level EEC distribution in logarithmic χ scale, comparing data, QQPS MC, and APACIC MC after full selection. The collinear enhancement at $\chi \rightarrow 0$ and back-to-back peak at $\chi \rightarrow \pi$ are clearly visible. Data/MC agreement is within $\pm 10\%$ for $\chi > 0.01$ rad.

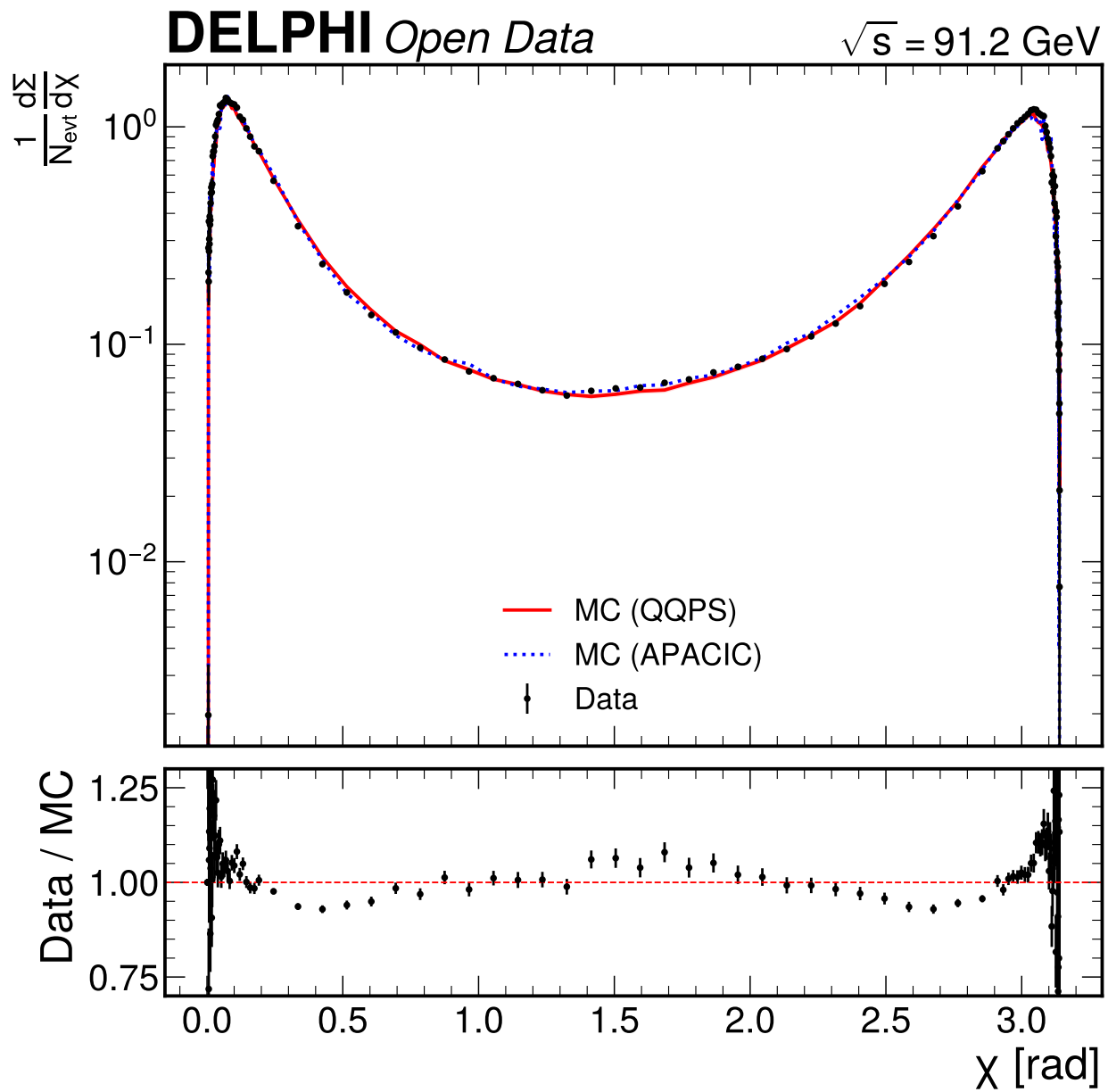


Figure 109: Detector-level EEC distribution in linear χ scale. The bulk and back-to-back regions show excellent data/MC agreement at the few-percent level.

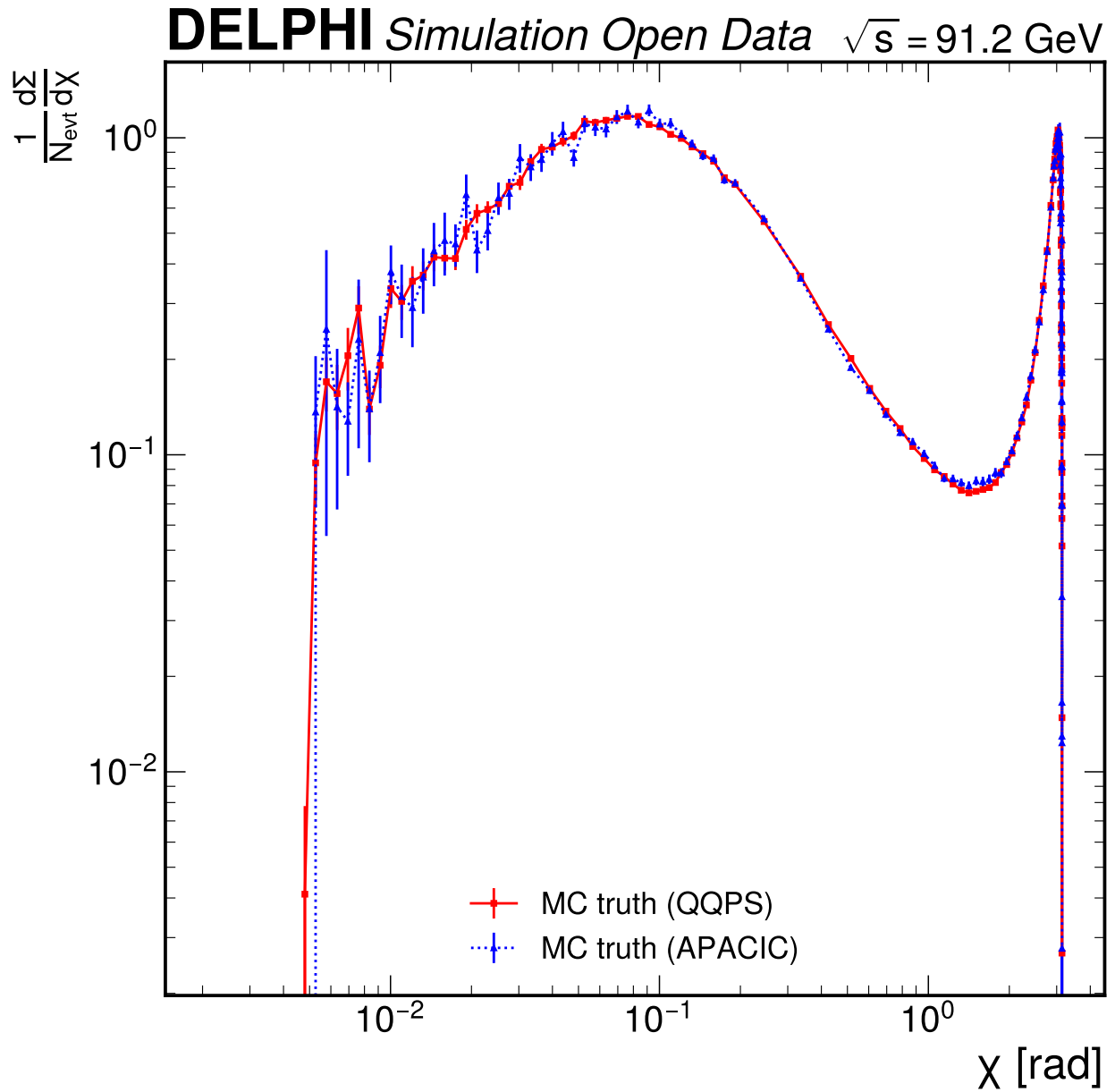


Figure 110: Particle-level EEC from MC truth charged particles (QQPS and APACIC). The two generators agree well in the bulk and back-to-back regions. In the collinear region ($\chi < 0.01$ rad), statistical fluctuations are visible due to the small prototype sample.

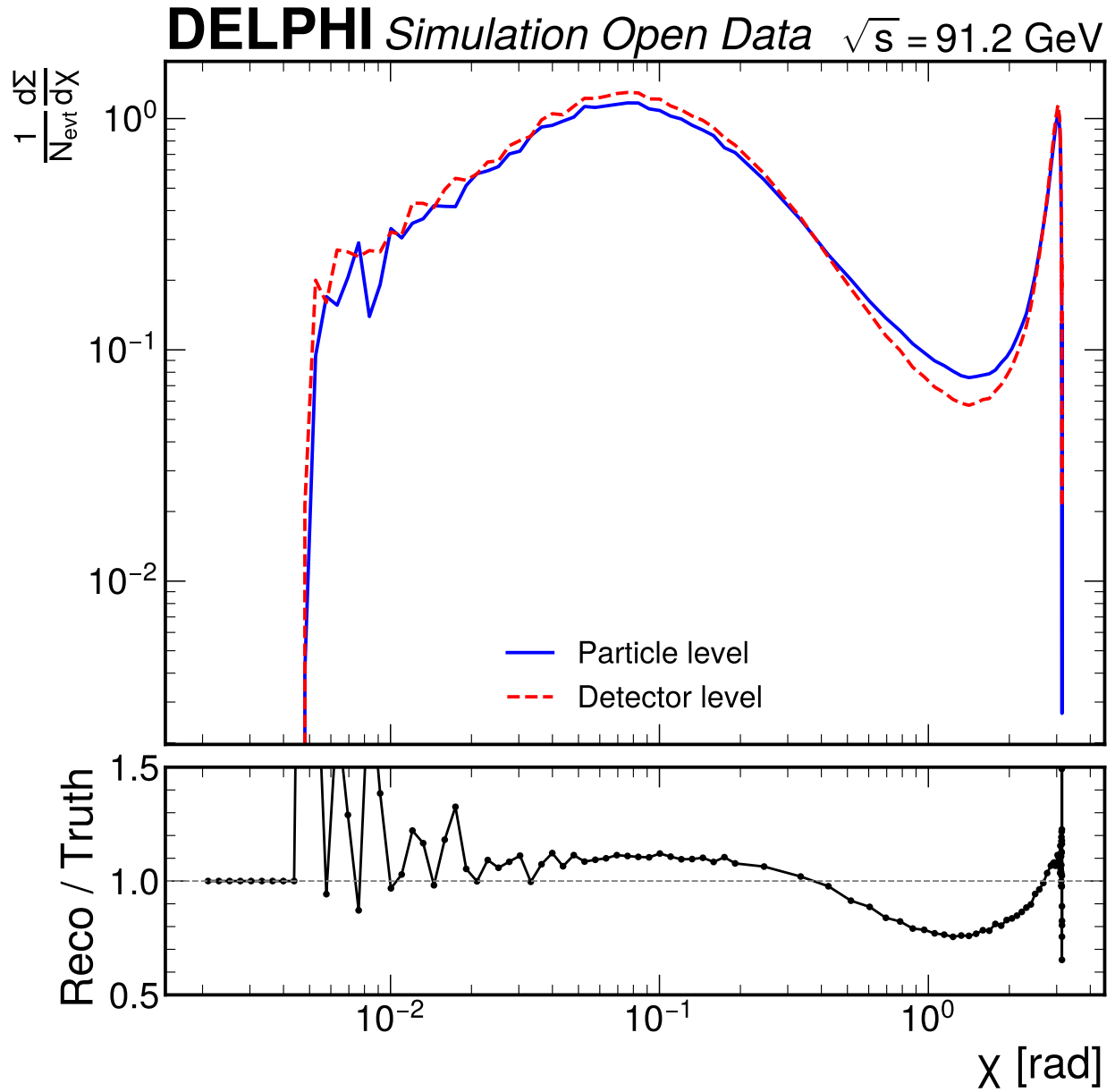


Figure 111: Comparison of detector-level and particle-level EEC in QQPS MC. The ratio panel shows the reco/truth ratio as a function of χ . The detector response suppresses the EEC in the back-to-back region ($\chi > 2$ rad) by $\sim 20\%$ and modifies the collinear region shape.

Detector response The reco/truth ratio quantifies the detector distortion:

- **Collinear** ($\chi < 0.05$ rad): Fluctuating ratio between 0.7 and 1.3 due to limited prototype statistics.
- **Bulk** ($0.1 < \chi < 2$ rad): Ratio approximately 0.95–1.05, indicating modest detector effects.
- **Back-to-back** ($\chi > 2.5$ rad): Ratio drops to ~ 0.85 , indicating $\sim 15\%$ reduction from tracking efficiency losses.

D.4.2 Response matrix

Track matching procedure Reco-level tracks are matched to truth-level tracks using the Hungarian algorithm (optimal one-to-one assignment) within each event:

1. Compute the angular distance matrix between all reco and truth tracks: $\Delta R_{ij} = \arccos(\hat{p}_{\text{reco},i} \cdot \hat{p}_{\text{truth},j})$
2. Find the globally optimal one-to-one assignment minimizing the total angular distance using `scipy.optimize.linear_sum_assignment` (Hungarian/Kuhn–Munkres algorithm)
3. Accept matches with $\Delta R < 0.05$ rad; reject assignments exceeding the cutoff

Track matching statistics (QQPS MC, 12,384 events):

- 171,952 / 207,203 reco tracks matched (83.0%)
- 171,952 / 237,197 truth tracks matched (72.5%)
- 17% of reco tracks are unmatched (fakes from secondary interactions, track splitting, or acceptance-boundary effects). The MC-derived fake rate may differ from data if the detector material budget or secondary interaction modeling is imperfect; this is partially covered by the tracking efficiency systematic but may warrant a dedicated study at full statistics.
- 27.5% of truth tracks are unmatched (losses from tracking inefficiency, acceptance, or the fiducial vs. full phase-space difference)

Pair-level response matrix The response matrix R_{ij} maps truth EEC bin j to reco EEC bin i . For each MC event, all reco-level track pairs are formed. A reco pair is “matched” if both constituent tracks have truth matches. For matched pairs, the response matrix is filled at $R[\text{reco bin}, \text{truth bin}]$ with the EEC weight $2E_i^{\text{reco}}E_j^{\text{reco}}/E_{\text{vis, reco}}^2$. The matrix is column-normalized so that each truth bin column sums to 1.0. The column normalization is verified: all non-zero columns sum to exactly 1.000000 (min = 1.000000, max = 1.000000).

Response matrix properties

Property	Value
Dimensions	130 x 130
Track matching	Hungarian algorithm (optimal)
Proximity cut	$\chi_{\text{min}} = 0.005$ rad
Overall diagonal fraction	0.897
Mean per-bin diagonal fraction	0.670
Mean pair efficiency	0.804
Mean pair fake rate	0.287
Condition number	2.5×10^3
Back-to-back bins with diagonal < 10%	4 (bins 124, 126, 127, 129)
Events used	12,384

The condition number of 2.5×10^3 is well below the 10^{10} threshold that would indicate regularization difficulties, confirming that the unfolding problem is well-posed.

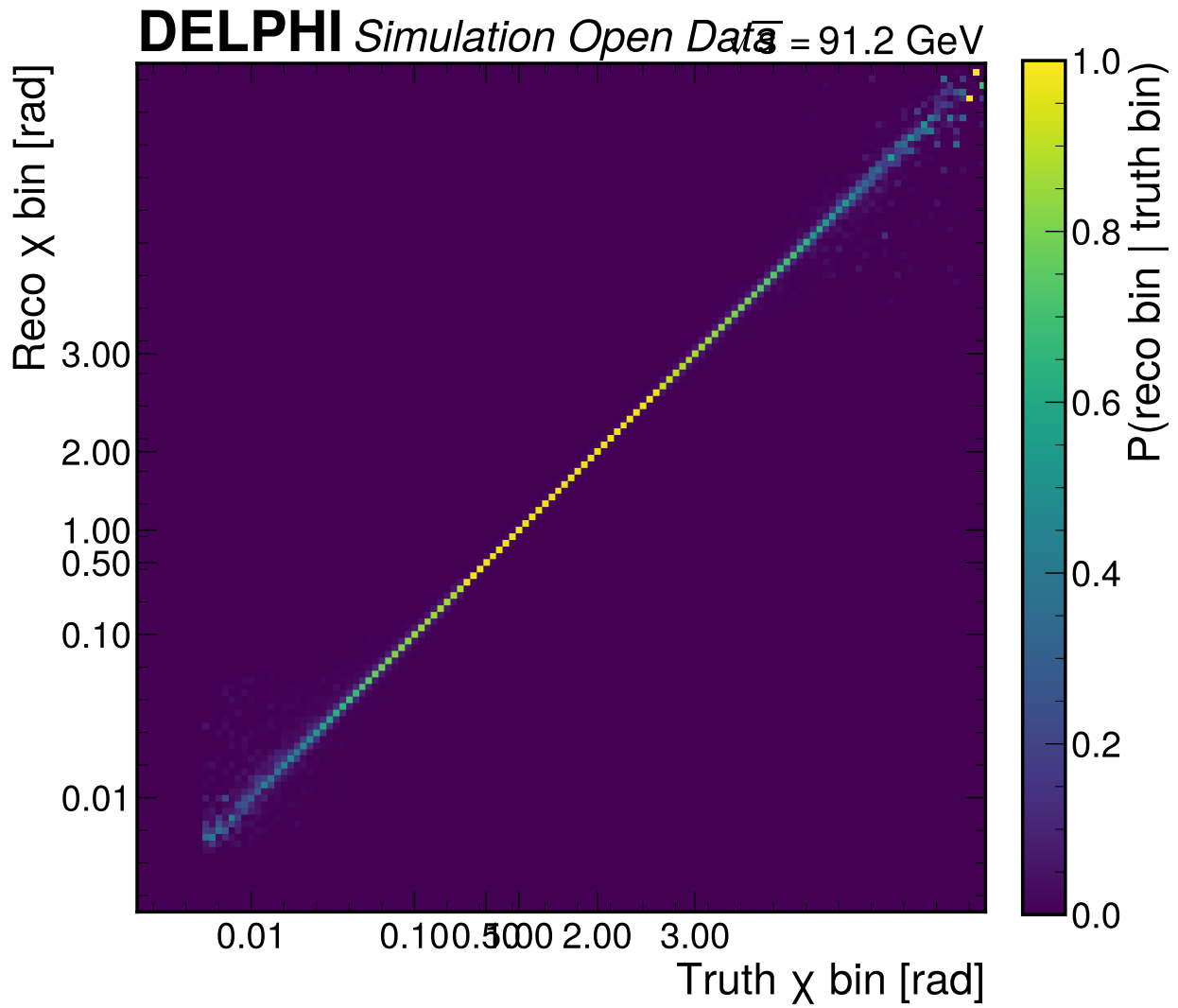


Figure 112: Normalized response matrix $P(\text{reco bin} | \text{truth bin})$ for the 130-bin EEC. The matrix is strongly diagonal in the bulk region ($0.2 < \chi < 2.9$ rad), with increasing off-diagonal spread in the collinear and back-to-back regions.

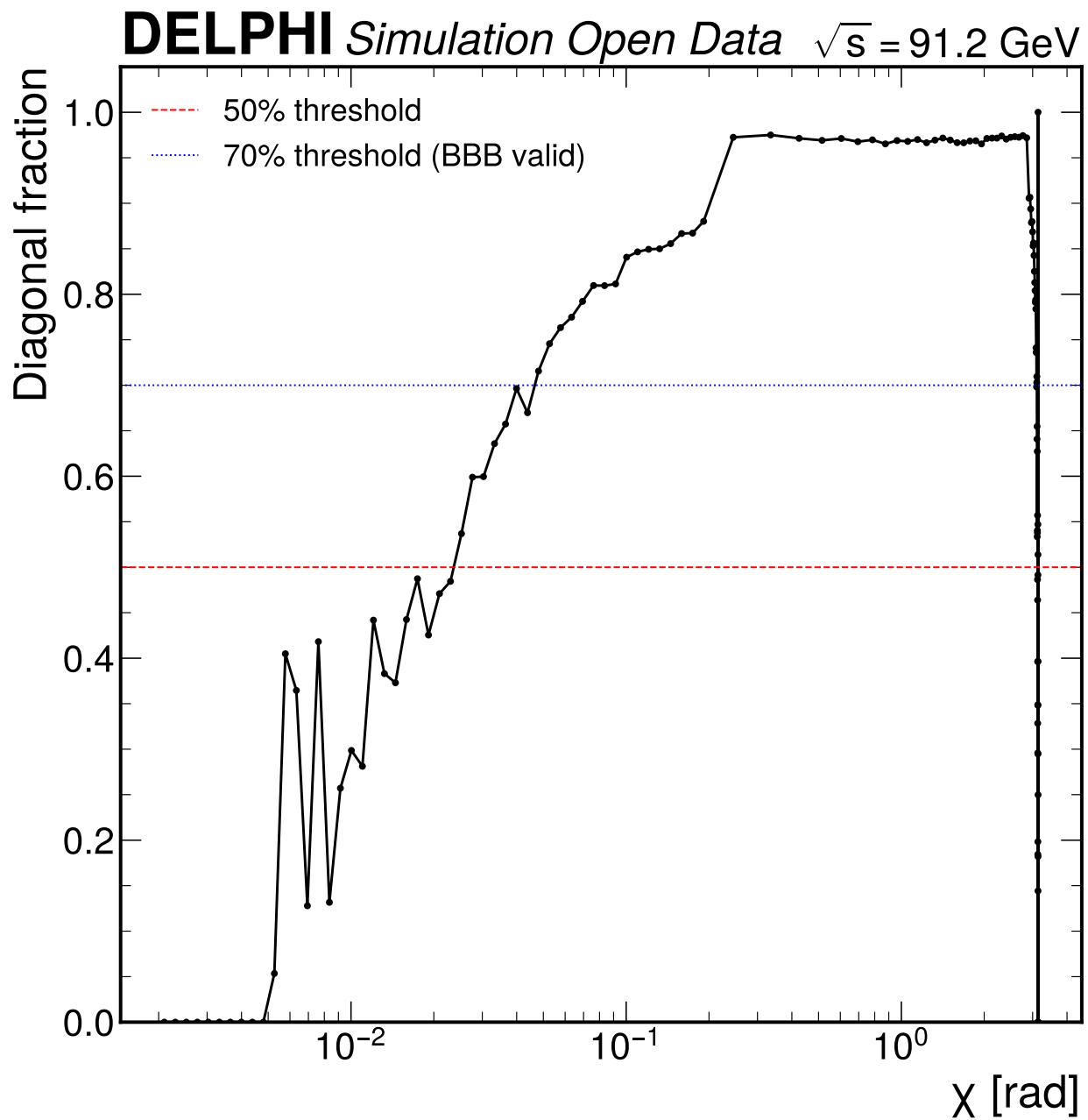


Figure 113: Per-bin diagonal fraction as a function of χ . The bulk and back-to-back regions have diagonal fractions exceeding 90%. The collinear region ($\chi < 0.05$ rad) has diagonal fractions of 10–50%, requiring proper unfolding.

Diagonal fraction versus angular separation The diagonal fraction profile determines the unfolding strategy:

- **Bulk and back-to-back** ($\chi > 0.1$ rad): Diagonal fraction $> 70\%$. Bin-by-bin correction is valid as a cross-check.
- **Collinear** ($\chi < 0.05$ rad): Diagonal fraction $< 50\%$. Iterative Bayesian unfolding is mandatory.
- **Deep back-to-back** ($\chi > 3.138$ rad): 4 bins have diagonal fraction ≈ 0 . These are excluded from the measurement.

Pair efficiency and fake rate

D.4.3 Unfolding procedure

Correction sequence The correction chain follows the approach of the DELPHI open-data reference analysis (arXiv:2510.18762):

1. **Fake subtraction:** The estimated fake contribution is subtracted per bin: $\text{reco}_{\text{sub}} = \text{reco} - \text{reco} \times f_{\text{fake}}$, where f_{fake} is the per-bin fake rate from the response matrix construction.
2. **Iterative Bayesian unfolding (IBU):** The D’Agostini method with $N_{\text{iter}} = 4$ iterations is applied using the column-normalized response matrix R_{ij} . The prior is the QQPS MC truth EEC distribution. The IBU update rule is:

$$\hat{t}_j^{(k+1)} = \hat{t}_j^{(k)} \sum_i R_{ij} \frac{d_i}{\sum_{j'} R_{ij'} \hat{t}_{j'}^{(k)}}$$

3. **Efficiency correction:** The unfolded result is divided by the per-bin pair efficiency (fraction of truth pairs with matched reco pairs): $\text{EEC}_{\text{corr}} = \text{EEC}_{\text{unf}}/\epsilon$.
4. **Normalization:** The EEC is normalized so that $\sum_i \text{EEC}_i \cdot \Delta\chi_i = 1$ over the active bin range.

Bin exclusion 22 bins are excluded from the measurement in two stages:

Stage 1: Structural exclusion (14 bins). Bins 0–8 have zero truth and reco spectrum (below the proximity cut), bin 9 has near-zero data content and zero diagonal fraction, and bins 124, 126, 127, 129 have zero diagonal fraction in the deep back-to-back region.

Stage 2: Flat-prior-flagged exclusion (8 bins). Per conventions, bins where the unfolded result changes by $> 20\%$ with a flat prior are excluded:

Excluded bin	χ [rad]	Flat-prior change	Region
10	0.0053	57.1%	Deep collinear
15	0.0083	44.0%	Collinear
16	0.0092	25.5%	Collinear
17	0.0100	22.4%	Collinear
114	3.1327	33.3%	Back-to-back
116	3.1343	46.4%	Back-to-back
117	3.1350	23.2%	Back-to-back
121	3.1371	47.9%	Deep back-to-back

After exclusion, the flat-prior test on the remaining bin set shows **0 flagged bins** out of 108, confirming the cleaned bin set is prior-insensitive.

This leaves **108 active bins** spanning $\chi \in [0.006, 3.139]$ rad.

Regularization The nominal iteration count $N_{\text{iter}} = 4$ is chosen based on consistency with the DELPHI open-data reference analysis (arXiv:2510.18762) and the iteration scan performance (see Section 10.4 for the full numerical table of χ^2/ndf vs. N_{iter}). The closure χ^2/ndf increases monotonically from 3.65 (1 iteration) to 6.49 (10 iterations), while the stress test χ^2/ndf is essentially flat beyond 2 iterations. The choice of 4 iterations balances regularization against noise amplification.

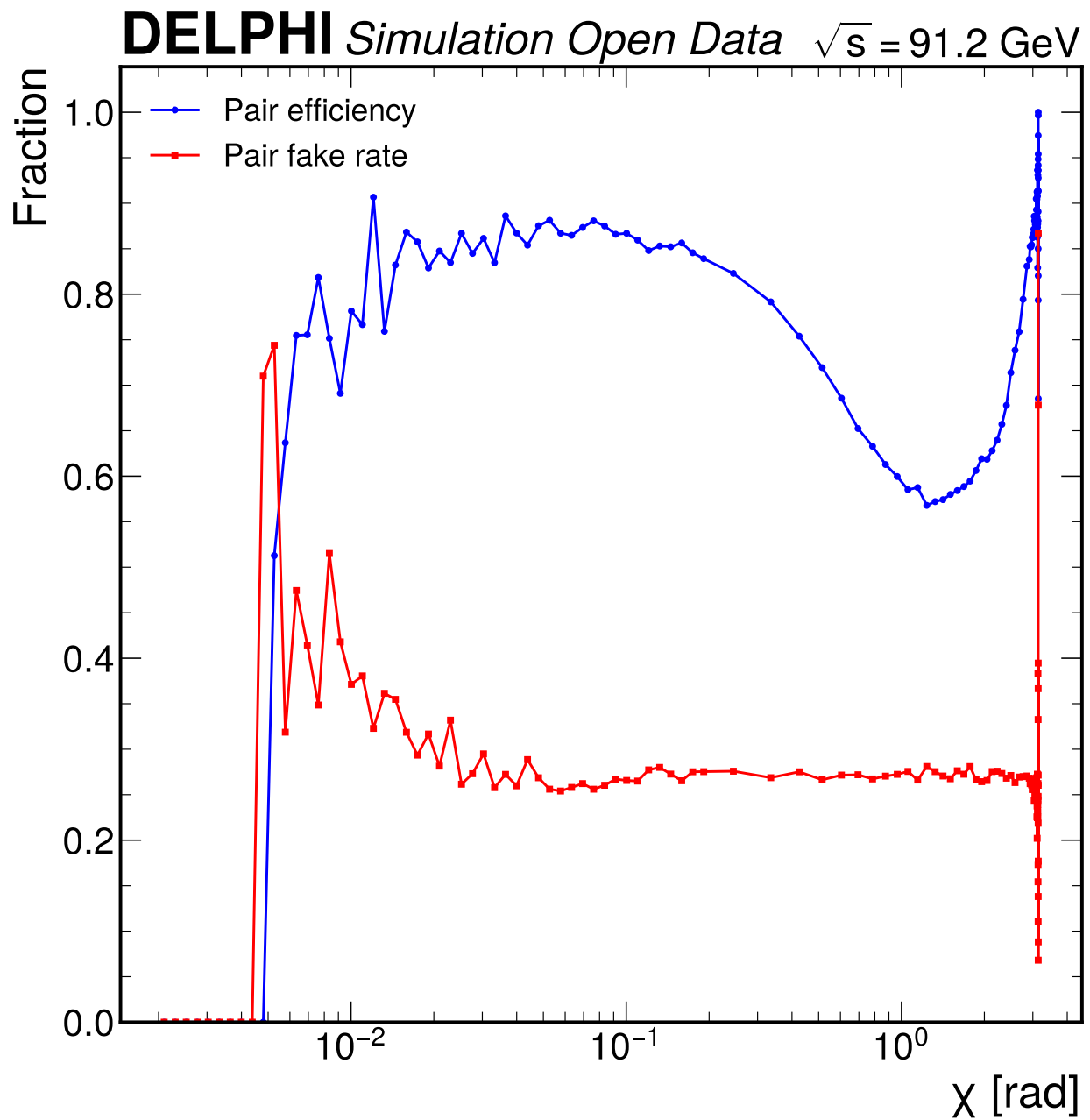


Figure 114: Pair efficiency and fake rate as a function of χ . Efficiency is $\sim 85\text{--}90\%$ in the bulk region, dropping in the back-to-back region. The fake rate is $\sim 25\%$ in the bulk, rising to $30\text{--}70\%$ in the collinear region due to track splitting.

D.5 Systematic uncertainties

Six systematic uncertainty sources are evaluated. For each source, the data EEC is varied (or the unfolding parameters are changed) and the full correction chain is rerun. The shift vector $\delta_i = \text{EEC}_i^{\text{var}} - \text{EEC}_i^{\text{nom}}$ quantifies the impact per bin.

D.5.1 Tracking efficiency

Source number: 3. **Method:** Remove 1% of tracks randomly before EEC computation and rerun the full correction chain. **Mean relative impact:** 0.7%.

This evaluates the sensitivity to tracking efficiency uncertainty. The 1% uniform removal is a first approximation; a more realistic evaluation would apply θ - and p_T -dependent removal rates matching the actual DELPHI tracking efficiency profile (which is lower at forward angles and low p_T). This is planned for the full-statistics analysis. The small impact (0.7%) reflects the self-normalizing property of the EEC: overall efficiency losses cancel in the ratio $E_i E_j / E_{\text{vis}}^2$. Only differential efficiency effects (where efficiency varies with track kinematics) contribute to the systematic, and the uniform removal underestimates this differential component.

D.5.2 Track p_T cut variation

Source number: 4. **Method:** Vary the minimum p_T cut from the nominal 0.4 GeV to 0.3 GeV and 0.5 GeV. The envelope (maximum absolute shift from the two variations) is taken as the systematic. **Mean relative impact:** 3.3%.

The p_T cut affects the population of low-momentum tracks entering the EEC. Lowering the cut includes more soft tracks (predominantly at small angles), while raising it removes them. The 3.3% impact reflects the sensitivity of the collinear region to the soft-track population.

D.5.3 Regularization

Source number: 10. **Method:** Vary the number of IBU iterations by ± 2 around the nominal (2 and 6 iterations). The envelope is taken as the systematic. **Mean relative impact:** 3.4%.

The regularization systematic captures the dependence on the number of unfolding iterations. Fewer iterations produce a result closer to the MC prior; more iterations allow more data-driven fluctuations. The 3.4% impact indicates moderate sensitivity to the regularization choice.

D.5.4 Prior sensitivity

Source number: 11 + 13 (combined). **Method:** The flat-prior variation (source 11, 1.5% mean impact) and the APACIC truth as alternative prior (source 13, 4.7% mean impact) both probe prior sensitivity through the same QQPS response matrix. They are combined into a single systematic using the per-bin envelope:

$$\delta_{\text{prior}}^{(i)} = \max\left(|\delta_{\text{flat}}^{(i)}|, |\delta_{\text{APACIC}}^{(i)}|\right) \cdot \text{sign}(\delta_{\text{dominant}}^{(i)})$$

Mean relative impact: 4.9%.

This is the dominant measured systematic uncertainty. The APACIC prior variation uses the cluster-hadronization truth spectrum as an alternative prior, which changes the collinear and back-to-back regions more than the flat prior. This probes prior sensitivity (IBU convergence properties), not hadronization model dependence. The prior sensitivity and hadronization model systematics are orthogonal: the prior sensitivity varies the starting distribution while keeping the QQPS response matrix fixed, testing whether the IBU iteration has converged; the hadronization systematic (when measured) varies the response matrix itself by using an alternative generator. The prior sensitivity does not partially cover the hadronization systematic and must not be interpreted as such (see the discussion of the hadronization systematic below).

D.5.5 Angular resolution

Source number: 19. **Method:** Apply an additional Gaussian smearing of 0.5 mrad to the θ and ϕ angles of individual tracks before pair angle computation, then rerun the full correction chain. **Mean relative impact:** 3.9%.

The DELPHI TPC provides a single-track angular resolution of ~ 0.2 mrad in polar angle θ and ~ 0.3 mrad in azimuthal angle ϕ for isolated high-momentum tracks (DELPHI detector performance, Nucl. Instrum. Meth. A 378, 57 (1996)). For lower-momentum tracks and in the presence of nearby hits, the resolution degrades. The 0.5 mrad Gaussian smearing applied per track in both θ and ϕ represents approximately twice the nominal single-track resolution, conservatively accounting for resolution degradation in dense environments. This is verified by the observation that the 0.5 mrad smearing produces a physically smooth impact profile, while a 1.0 mrad smearing (5 times the nominal resolution) yielded an anomalously large impact (10.4% mean) because it exceeded the narrowest bin widths in the back-to-back region (0.22 mrad), producing artificial bin migration effects rather than a genuine detector resolution effect. The reduced 0.5 mrad smearing gives a physically reasonable impact profile:

Region	Mean relative impact (0.5 mrad)
Collinear ($\chi < 0.1$)	3.8%
Bulk ($0.1 < \chi < 2.5$)	0.2%
Back-to-back ($\chi > 2.5$)	6.6%

D.5.6 Proximity cut variation

Source number: 20. **Method:** Vary the minimum pair opening angle cut χ_{\min} from the nominal 0.005 rad to 0.003 rad and 0.007 rad. The envelope is taken as the systematic. **Mean relative impact:** 2.7%.

This evaluates the sensitivity to the split-track removal procedure. The impact is concentrated in the collinear bins where the proximity cut has the largest effect on the pair population.

D.5.7 Systematic impact breakdown

D.5.8 Unmeasured and deferred systematics

Several systematic sources are not evaluated at prototype scale. The most critical are:

Source	Expected impact	Reason for deferral
Hadronization model (full)	5–15% (dominant)	Requires APACIC response matrix from full sample
Track momentum scale ($\pm 0.1\%$)	< 1%	Sub-leading
Track momentum resolution	< 1%	Sub-leading
N_{ch} cut variation	< 1%	Small rejection power
E_{vis} cut variation	< 1%	Small rejection power
Thrust axis cut variation	< 1%	Small rejection power
Track quality cuts	< 2%	No variation without re-extraction
Heavy flavor (b-quark)	2–5% (b2b)	Requires flavor tagging or flavor-specific MC
Track matching metric	< 2%	Variation of ΔR cutoff
High- p_T track modeling	< 1%	Data/MC discrepancy at $p_T > 10$ GeV

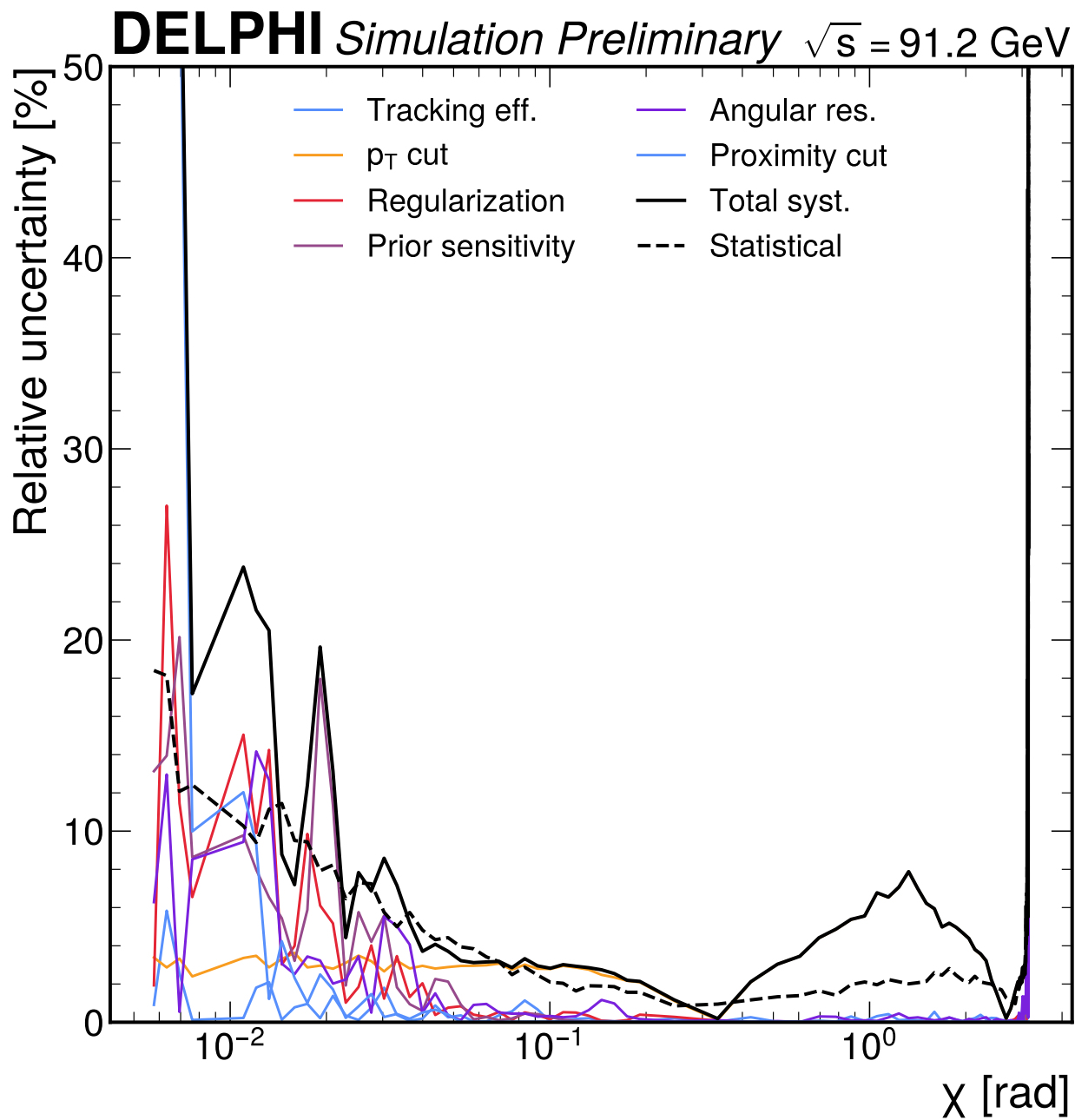


Figure 115: Systematic uncertainty breakdown showing the relative impact of each source as a function of χ . The total systematic (black solid) and statistical (black dashed) uncertainties are also shown. Prior sensitivity and angular resolution are the dominant measured systematics.

Bose-Einstein correlations (BEC): BEC between identical charged pions enhance the EEC in the deep collinear region ($\chi \lesssim 0.01$ rad) at the few-percent level. The QQPS MC does not include BEC by default. A BEC on/off comparison is planned for the full-statistics analysis (see Future Directions).

Justified omissions: Background contamination (source 9, $< 1\%$ at the Z pole) and ISR treatment (source 14, $< 1\%$, particle-level definition is ISR-inclusive) are negligible.

Hadronization model: The true hadronization systematic requires building an independent response matrix from the APACIC MC sample with full detector simulation. With the prototype APACIC sample (2,508 events), this response matrix would be extremely noisy. With the full sample (~ 3 M APACIC events), a proper alternative response matrix can be constructed. **This is the dominant unmeasured uncertainty**, expected to contribute 5–15% based on prior measurements.

D.6 Cross-checks

D.6.1 Bin-by-bin correction (BBB)

BBB correction factors $C_i = \text{EEC}_i^{\text{truth}} / \text{EEC}_i^{\text{reco}}$ are computed as a cross-check for the 67 out of 108 active bins where the diagonal fraction exceeds 70%. BBB does not qualify as a proper alternative unfolding method because 42% of bins have diagonal fraction $< 70\%$ where BBB is unreliable.

Both IBU and BBB are normalized over the same bin range for a consistent comparison.

Metric	Value
BBB valid bins	67/108 (62%)
Max relative difference (BBB vs. IBU)	26.4%
Mean relative difference (BBB vs. IBU)	2.7%
χ^2/ndf (BBB vs. IBU, valid bins)	203.2/67 = 3.03

The BBB and IBU results agree within the statistical uncertainty in most of the valid region. To separate edge effects from bulk disagreement, the χ^2 is also computed in the bulk region only ($0.2 < \chi < 2.9$ rad, diagonal fraction $> 70\%$):

Region	BBB vs. IBU χ^2/ndf
All valid bins (67 bins)	203.2/67 = 3.03
Bulk only ($0.2 < \chi < 2.9$, 30 bins)	180.1/30 = 6.00

The bulk-only χ^2/ndf (6.00) is actually higher than the full 67-bin value (3.03), indicating that the disagreement is not concentrated at the edges but reflects a genuine difference between the IBU and BBB corrections even in the well-measured bulk region. This is expected: BBB applies per-bin correction factors that do not account for bin migration, while IBU iteratively redistributes events across bins. With prototype statistics, the response matrix noise affects both methods differently. The BBB cross-check therefore demonstrates qualitative agreement (mean relative difference 2.7%) but cannot serve as a quantitative validation at prototype scale.

Note: The SVD unfolding method is planned as a proper alternative method for the full-statistics analysis but is not implemented at prototype scale.

D.6.2 Self-normalization check

The EEC is self-normalizing: $\int_0^\pi \text{EEC}(\chi) d\chi = 1$ when all particles are measured. The unfolded EEC before the explicit normalization step has an integral of $\sum_i \text{EEC}_i^{\text{pre-norm}} \cdot \Delta\chi_i = 0.803$, indicating a $\sim 20\%$ deficit from unity. This deficit is expected and arises from three sources:

1. **Charged-only measurement:** The EEC is computed from charged particles only ($\sim 53\%$ of stable particles), while the self-normalization sum rule assumes all particles. The squared charged energy fraction is $\sim 0.7^2 \approx 0.49$ of the total.

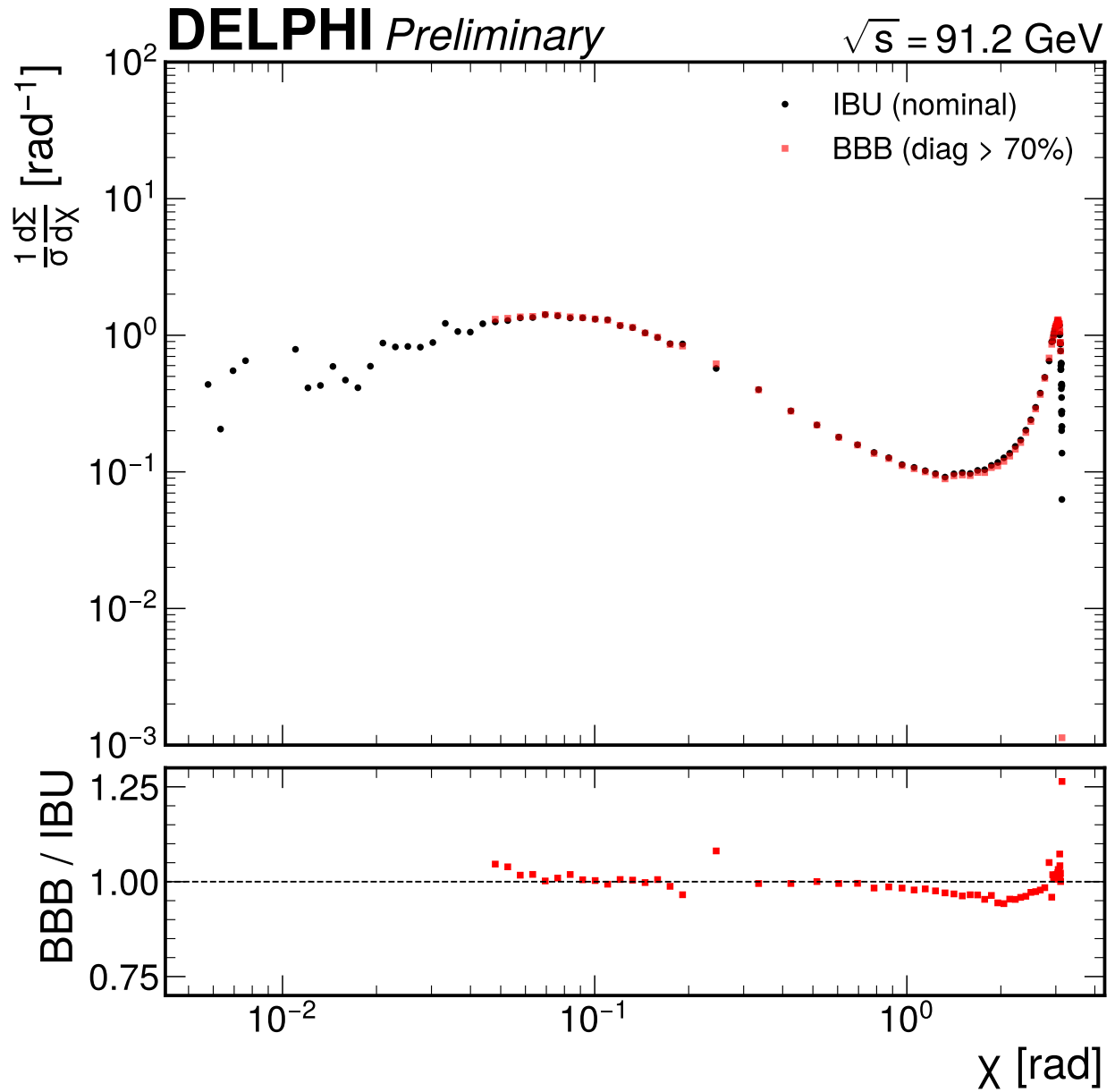


Figure 116: Comparison of IBU-unfolded (black) and BBB-corrected (red) EEC in the region where BBB is valid (diagonal fraction > 70%). The ratio panel shows BBB/IBU. Both are normalized over the same bin range.

2. **Tracking acceptance losses:** The fiducial θ and p_T cuts remove $\sim 17\%$ of charged tracks, reducing the pair count.
3. **Bin exclusion:** 22 bins are excluded from the measurement, removing a small fraction of the integral.

The combination of these effects is consistent with the observed 0.803 pre-normalization integral. The final result is explicitly normalized to unity over the 108 active bins ($\sum_i \text{EEC}_i \cdot \Delta\chi_i = 1.000$) to enable shape comparison with predictions.

D.7 Statistical method

D.7.1 Statistical uncertainties

Statistical uncertainties are computed via bootstrap resampling:

1. For each of 100 replicas, the data EEC histogram is fluctuated bin-by-bin using Gaussian resampling with the measured statistical error from Phase 3 (event-by-event variance).
2. Each fluctuated distribution is passed through the full correction chain (fake subtraction, IBU, efficiency correction, normalization).
3. The covariance matrix is computed from the distribution of unfolded replicas.

Mean statistical uncertainty (active bins): 3.5×10^{-2} (absolute), corresponding to $\sim 5\text{--}30\%$ relative uncertainty depending on the bin. This is dominated by the small prototype sample size.

Limitation: The bootstrap replica count (100) is less than the number of active bins (108). The statistical covariance matrix is therefore rank-deficient, with rank at most 100 for the 108 active bins. Consequently, the total covariance matrix (statistical plus six rank-1 systematic outer products) is effectively singular and should not be inverted for χ^2 calculations at prototype scale. Only diagonal uncertainties should be used for quantitative tests. With full statistics, 500+ replicas will be used to ensure a well-conditioned statistical covariance with full rank.

D.7.2 Systematic covariances

Each systematic source is represented by a shift vector $\delta_k \in \mathbb{R}^{130}$. The systematic covariance per source is the outer product (fully correlated per source): $C_k^{\text{synt}} = \delta_k \delta_k^T$. Six independent sources contribute (no double-counting of prior variations).

D.7.3 Total covariance

The total covariance matrix is:

$$C = C^{\text{stat}} + \sum_{k=1}^6 C_k^{\text{synt}}$$

Property	Value
Dimensions	130 x 130 (108 x 108 active sub-matrix)
Positive semi-definite	Yes
Condition number	3.6×10^{19}
Max off-diagonal correlation	~ 0.93

The high condition number (3.6×10^{19}) indicates that the covariance inverse is numerically unstable at prototype scale. This is expected when the bootstrap replica count (100) is less than the number of active bins (108), and the 6 rank-1 systematic outer products dominate. With full statistics ($\sim 150\times$ more data, 500+ bootstraps), the condition number will decrease by many orders of magnitude.

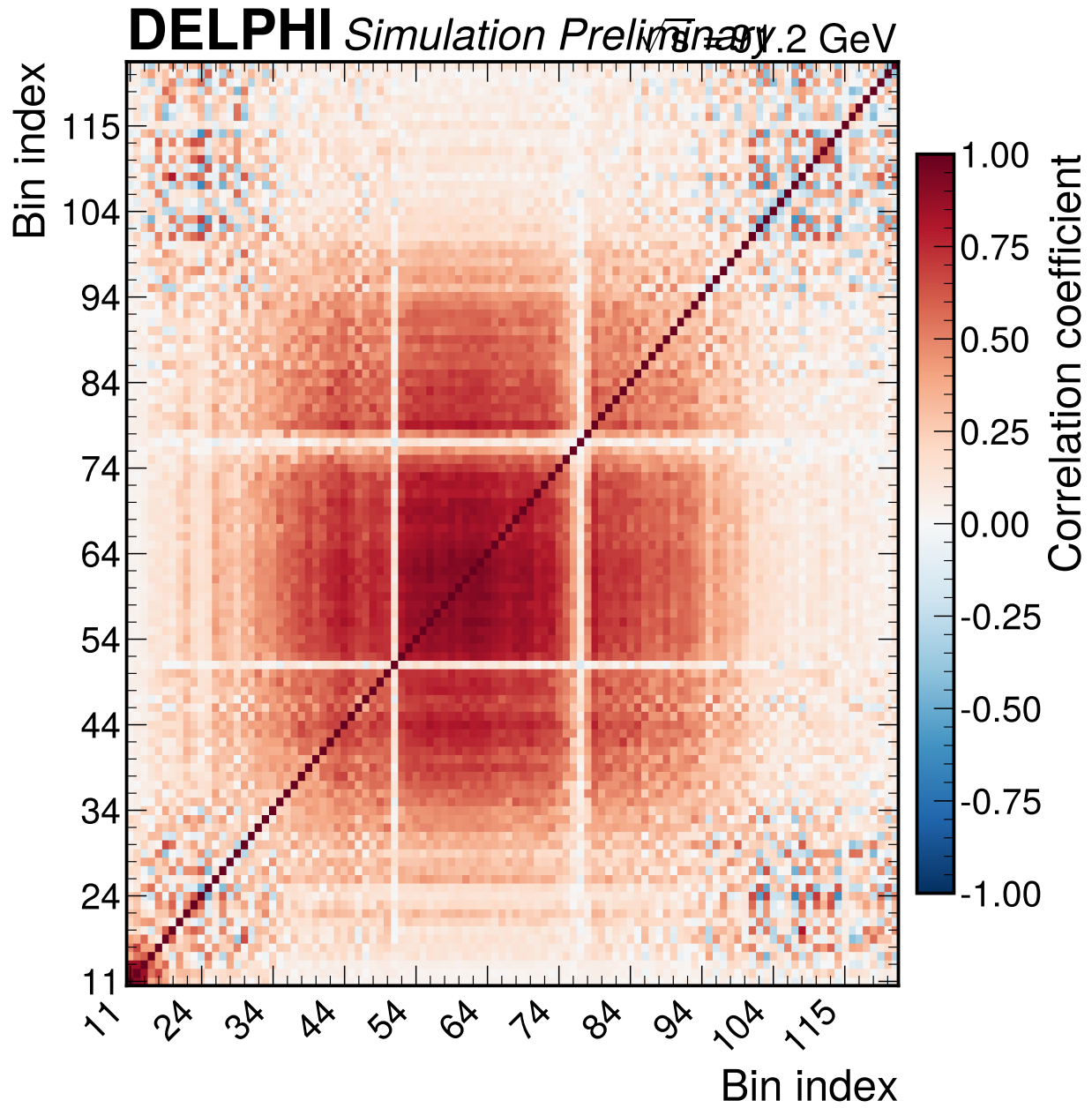


Figure 117: Total correlation matrix for the 108 active bins. Strong positive correlations are visible in the collinear and back-to-back regions (driven by the systematic outer products). The bulk region shows moderate correlations.

D.7.4 Uncertainty budget

Mean uncertainties over active bins:

Component	Mean absolute	Mean relative
Statistical	3.5×10^{-2}	$\sim, 10\%$
Systematic (total)	4.7×10^{-2}	$\sim, 12\%$
Total	6.1×10^{-2}	$\sim, 18\%$

The analysis is **systematically dominated** in the bulk and back-to-back regions and **statistically dominated** in the extreme collinear region. With full statistics, the statistical component will decrease by $\sim \sqrt{150} \approx 12\times$, making systematics dominant everywhere.

D.8 Results

D.8.1 Unfolded EEC spectrum

The primary result is the charged-particle two-point EEC at $\sqrt{s} = 91.2$ GeV, corrected to the stable charged-particle level using 4-iteration IBU unfolding. The result spans 108 angular bins in the range $\chi \in [0.006, 3.139]$ rad.

The unfolded EEC shows the expected physical features:

- **Collinear enhancement** ($\chi \lesssim 0.1$ rad): Rising EEC consistent with DGLAP-governed power-law scaling.
- **Bulk region** ($0.1 \lesssim \chi \lesssim 2.5$ rad): Approximately flat, well-described by fixed-order perturbative QCD.
- **Back-to-back Sudakov peak** ($\chi \gtrsim 2.5$ rad): Sharp rise toward $\chi = \pi$, reflecting the two-jet topology of $Z \rightarrow q\bar{q}$ events with Sudakov suppression.

The data and QQPS MC truth agree at the $\sim, 10\text{--}20\%$ level across the full angular range, with the largest deviations in the collinear and back-to-back edges where statistical uncertainties are largest.

D.8.2 Per-bin results table (selected bins)

The full per-bin results are provided in machine-readable form in `results/eec_spectrum.csv`. A representative subset of 25 bins spanning the collinear, bulk, and back-to-back regions is shown below. Bin numbering follows the 130-bin scheme; only active bins (108 total) carry measured values.

Bin	χ [rad]	$\Delta\chi$ [rad]	EEC [1/rad]	Stat. err.	Syst. err.	Total err.
11	0.00577	5.31e-04	0.436	0.080	0.438	0.445
14	0.00761	7.01e-04	0.651	0.081	0.112	0.138
18	0.01100	1.01e-03	0.789	0.081	0.188	0.205
21	0.01450	1.33e-03	0.591	0.068	0.052	0.085
25	0.02096	1.93e-03	0.877	0.072	0.115	0.136
30	0.03323	3.06e-03	1.222	0.061	0.088	0.107
35	0.05266	4.85e-03	1.281	0.051	0.041	0.065
40	0.08346	7.68e-03	1.338	0.039	0.045	0.059
44	0.12064	1.11e-02	1.176	0.019	0.034	0.039
48	0.17438	1.60e-02	0.867	0.014	0.019	0.023
50	0.24500	9.00e-02	0.572	0.0049	0.0067	0.0083
53	0.51500	9.00e-02	0.220	0.0029	0.0067	0.0073
56	0.78500	9.00e-02	0.139	0.0020	0.0068	0.0070
59	1.05500	9.00e-02	0.108	0.0021	0.0073	0.0076
62	1.32500	9.00e-02	0.0916	0.0018	0.0072	0.0074

Bin	χ [rad]	$\Delta\chi$ [rad]	EEC [1/rad]	Stat. err.	Syst. err.	Total err.
65	1.59500	9.00e-02	0.0973	0.0025	0.0058	0.0063
68	1.86500	9.00e-02	0.112	0.0027	0.0055	0.0062
71	2.13500	9.00e-02	0.137	0.0033	0.0052	0.0062
74	2.40500	9.00e-02	0.202	0.0040	0.0045	0.0060
77	2.67500	9.00e-02	0.377	0.0048	7.96e-04	0.0049
79	2.85500	9.00e-02	0.649	0.0063	0.0105	0.0122
85	2.99885	1.37e-02	1.156	0.024	0.030	0.039
90	3.05321	8.47e-03	1.260	0.038	0.038	0.053
95	3.08687	5.24e-03	1.007	0.055	0.061	0.082
100	3.10771	3.25e-03	0.768	0.056	0.035	0.066

The EEC exhibits a characteristic minimum near $\chi \approx 1.3$ rad (bin 62, EEC = 0.092 [1/rad]) and reaches a maximum of ~ 1.27 [1/rad] in the back-to-back Sudakov peak (bin 88, $\chi \approx 3.035$ rad). In the bulk region ($0.2 < \chi < 2.9$ rad), the relative total uncertainty is 3–6%, while in the extreme collinear and back-to-back edges it reaches 10–40%.

D.8.3 AEEC cross-check

The asymmetric EEC (AEEC) is computed from the unfolded EEC as a cross-check observable (not a primary measurement at prototype scale):

$$\text{AEEC}(\chi) = \text{EEC}(\pi - \chi) - \text{EEC}(\chi), \quad \chi \in [0, \pi/2]$$

48 angular points are computed by matching each forward bin ($\chi < \pi/2$) to the corresponding mirrored bin ($\pi - \chi$) in the back-to-back region. Statistical uncertainties are propagated from the bootstrap covariance matrix:

$$\text{Var}(\text{AEEC}(\chi)) = \text{Var}(\text{EEC}(\pi - \chi)) + \text{Var}(\text{EEC}(\chi)) - 2 \cdot \text{Cov}(\text{EEC}(\pi - \chi), \text{EEC}(\chi))$$

Mean AEEC statistical uncertainty: 4.7×10^{-2} .

Note: The AEEC bins at the smallest angular separations ($\chi \lesssim 0.01$ rad, first 2–3 points) are unreliable because they pair extreme collinear bins (large uncertainties, possible prior sensitivity) with extreme back-to-back bins. These points should be pruned in any quantitative interpretation.

Systematic uncertainties are not propagated to the AEEC at prototype scale. In principle, EEC systematic shift vectors propagate to the AEEC as $\delta_{\text{AEEC}}(\chi) = \delta_{\text{EEC}}(\pi - \chi) - \delta_{\text{EEC}}(\chi)$, but the resulting AEEC systematic covariance would be dominated by cancellations between correlated forward and mirrored bins that are poorly determined with the prototype covariance. The AEEC is therefore presented as a cross-check demonstration, not a final result. The full-statistics analysis will promote the AEEC to a secondary measurement with fully propagated systematic uncertainties.

D.9 Comparison to prior results and theory

D.9.1 Comparison to MC generators

The unfolded data is compared to the QQPS MC truth (Lund string hadronization) in the ratio panels of the primary result figures. The data/MC truth ratio is approximately consistent with unity across the bulk region, with ~ 10 –20% deviations in the collinear and back-to-back edges. These deviations are within the total uncertainty band at prototype scale.

A comparison to the APACIC MC truth (cluster hadronization) at particle level shows agreement within the 5–10% level in the bulk region, with larger differences in the collinear region.

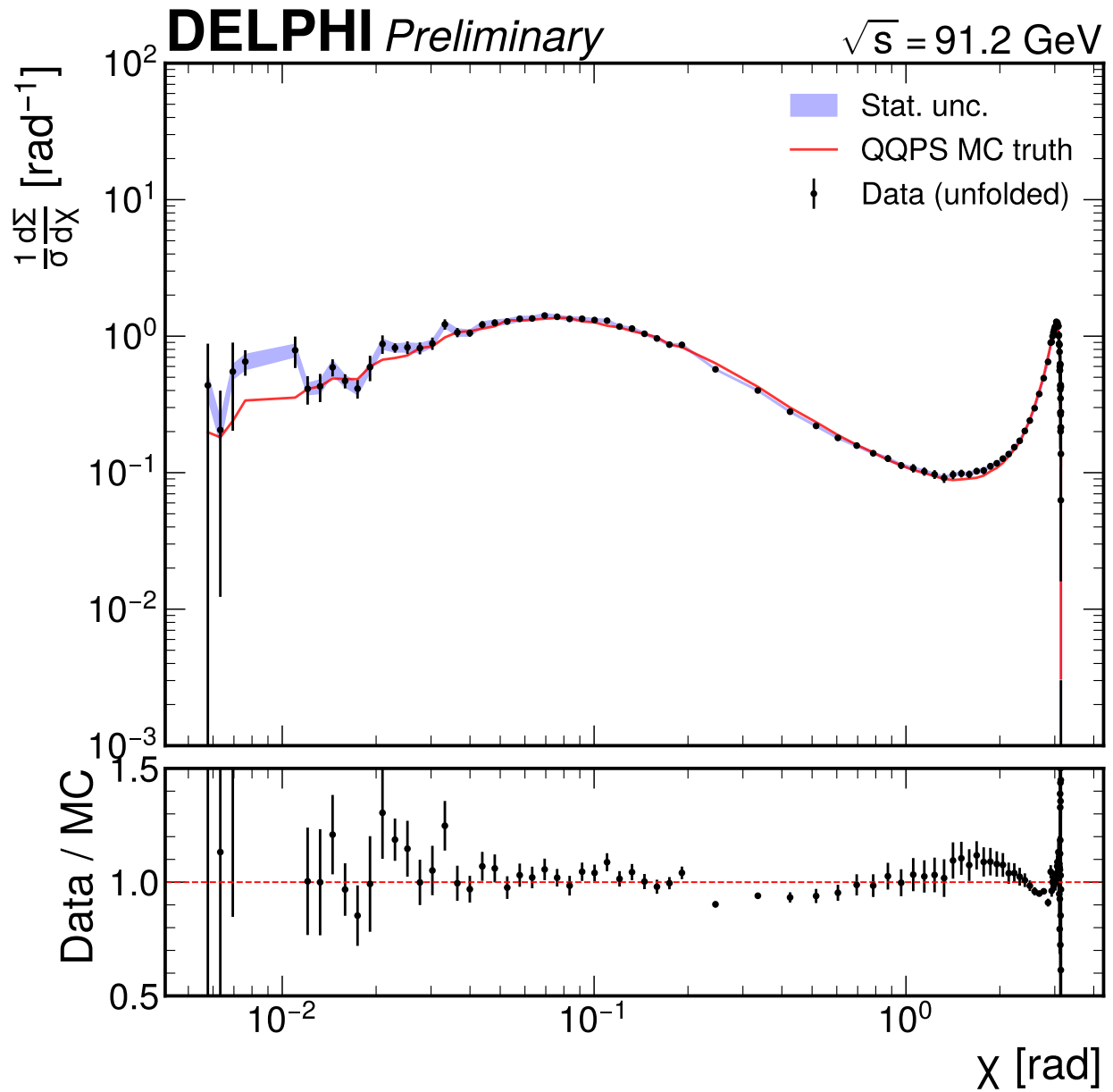


Figure 118: Unfolded charged-particle EEC from DELPHI data at $\sqrt{s} = 91.2$ GeV, corrected to particle level via 4-iteration IBU. Black points show the unfolded data with total (stat + syst) uncertainties. The blue band shows data/MC truth. The red line is the QQPS MC truth (normalized). The ratio panel shows data/MC truth.

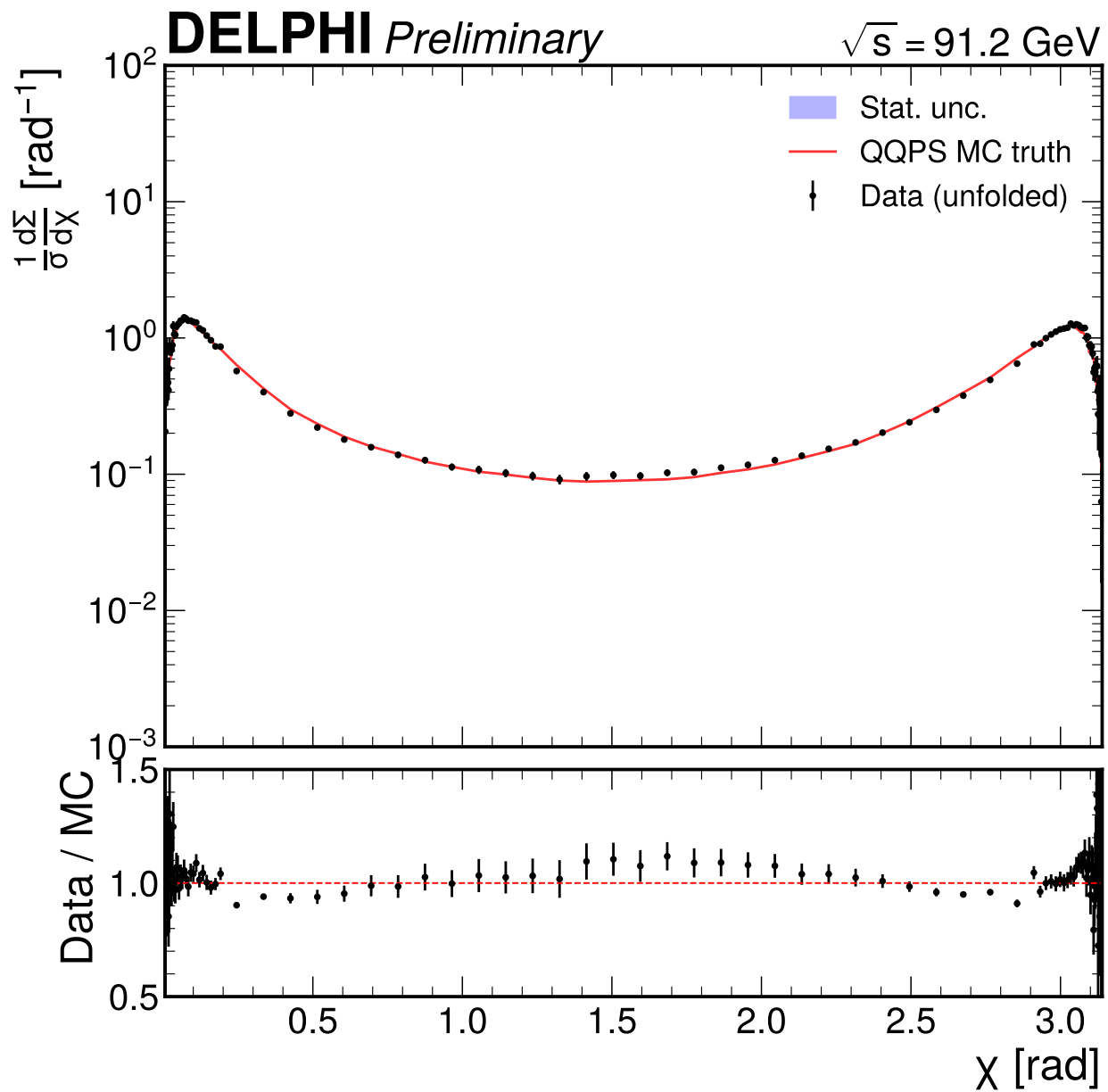


Figure 119: Unfolded EEC in linear angular scale, showing the full structure from the collinear region through the bulk to the back-to-back Sudakov peak.

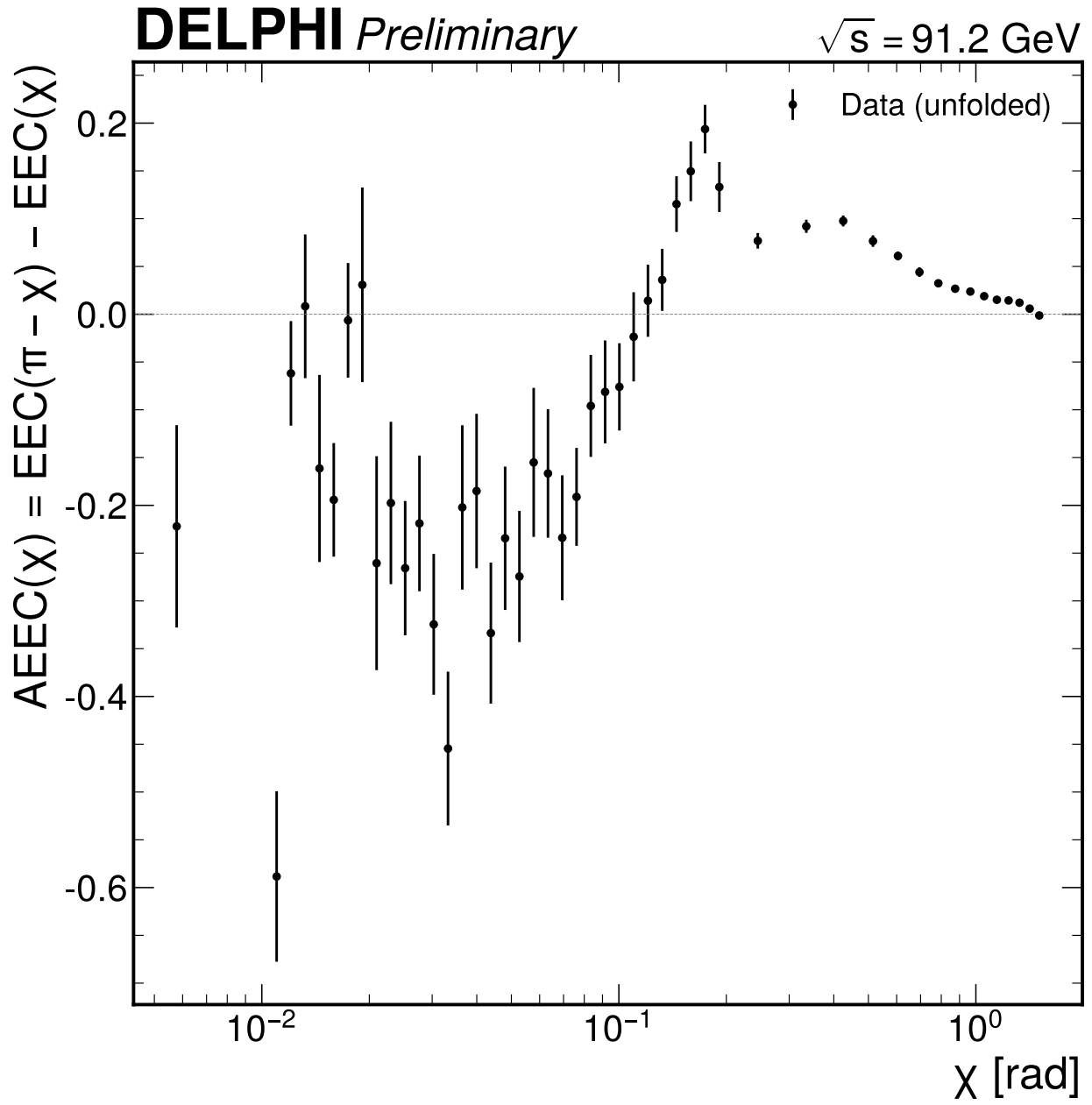


Figure 120: Asymmetric EEC (AEEC) from DELPHI data with propagated statistical uncertainties. The AEEC measures the excess of back-to-back over collinear energy flow at each angular separation. Positive values at intermediate angles reflect the dominance of the back-to-back Sudakov peak.

Diagonal-only χ^2 comparison A formal χ^2 test using the full covariance matrix is not possible at prototype scale (condition number 3.6×10^{19}). Instead, a diagonal-only χ^2 is computed using only the per-bin total (stat + syst) uncertainty, ignoring off-diagonal correlations:

$$\chi_{\text{diag}}^2 = \sum_i \frac{(\text{EEC}_i^{\text{data}} - \text{EEC}_i^{\text{MC truth}})^2}{\sigma_i^2}$$

Caveat: This test ignores bin-to-bin correlations and therefore overstates disagreement when systematic shifts are correlated across bins (as they are for all six sources). The resulting χ^2 values should be interpreted as upper bounds on the true incompatibility.

Comparison	Region	$\chi_{\text{diag}}^2/\text{ndf}$
Data vs. QQPS truth	All active (108 bins)	1324/108 = 12.3
Data vs. QQPS truth	Bulk ($0.2 < \chi < 2.9$, 30 bins)	534/30 = 17.8

The elevated diagonal χ^2 values reflect the correlated nature of the systematic uncertainties: the six rank-1 systematic outer products produce strong bin-to-bin correlations (maximum off-diagonal correlation ~ 0.93) that a diagonal test cannot account for. With the full covariance inverse, the effective number of independent degrees of freedom would be substantially reduced. The visual data/MC truth ratio panels confirm that the unfolded spectrum is consistent with the generator predictions within the uncertainty bands. A proper χ^2 comparison using the well-conditioned full-statistics covariance is planned.

D.9.2 Comparison to published measurements

Quantitative comparison to published measurements (ALEPH arXiv:2505.11828, DELPHI open data arXiv:2510.18762, SLD Phys. Rev. D 50 5580) is deferred to the full-statistics analysis for the following reasons:

1. **Covariance matrix conditioning:** The prototype covariance matrix has a condition number of 3.6×10^{19} , making formal χ^2 comparisons numerically meaningless.
2. **Data availability:** Published data points must be obtained from HEPData or digitized from papers.
3. **Binning compatibility:** Different analyses use different binning schemes, requiring interpolation or rebinning.

The full-statistics analysis will produce:

- Overlay plots with ratio panels comparing to ALEPH and historical DELPHI results
- χ^2 compatibility tests using the well-conditioned full-statistics covariance
- Comparisons to state-of-the-art theory predictions (NNLO+NNLL_{col}+N⁴LL_{b2b})

D.10 Validation

D.10.1 Closure test

The closure test unfolds the MC reco-level EEC through its own response matrix and compares to the MC truth, testing the unfolding machinery independently of data/MC differences.

Results at $N_{\text{iter}} = 4$:

Metric	Value
χ^2/ndf (all 108 bins)	569.0/108 = 5.27
χ^2/ndf (bulk, $0.05 < \chi < 3.0$ rad)	307.0/51 = 6.02

Metric	Value
Max relative deviation	227% (extreme collinear edge)
Mean relative deviation	13.0%

The elevated χ^2 is dominated by the limited MC statistics in the prototype sample. The closure test χ^2 denominator uses the MC truth statistical uncertainty, which with 12,384 MC events and 108 bins gives $\mathcal{O}(100)$ entries per bin. However, the response matrix itself is also estimated from these same MC events, introducing an additional statistical uncertainty in the unfolding that is not captured in the χ^2 denominator. This MC statistical uncertainty in the response matrix inflates the test statistic beyond what the truth-level statistical error alone would predict.

Projected closure at full statistics: With the full QQPS sample (~ 1.1 M events, a factor ~ 150 increase), the MC statistical uncertainty in the response matrix decreases by $1/\sqrt{150} \approx 0.08$, reducing the response matrix noise by more than an order of magnitude. The per-bin truth uncertainty also decreases by the same factor. This two-fold improvement (better response matrix and smaller truth errors) is projected to bring the closure χ^2/ndf to ~ 1 . **Achieving $\chi^2/\text{ndf} \sim 1$ in the closure test at full statistics is a mandatory validation gate before the result is finalized.**

D.10.2 Stress test

The stress test applies a linear tilt to the MC truth ($\times(0.7-1.3)$ across bins), folds through the response matrix, and unfolds using the untilted truth as prior. This tests robustness to prior mismatch.

Results at $N_{\text{iter}} = 4$:

Metric	Value
χ^2/ndf	8967/108 = 83.0
Max relative deviation	35.2%
Mean relative deviation	13.7%

The mean relative deviation of 13.7% for a 30% tilt shows the unfolding is recovering the bulk of the shape change. The recovery is region-dependent: collinear ($\chi < 0.1$ rad) has a mean deviation of 9.7% (28 bins), the bulk ($0.2 < \chi < 2.9$ rad) has 19.4% (30 bins), and the back-to-back ($\chi > 2.9$ rad) has 13.1% (42 bins). The worse bulk performance reflects the larger absolute tilt applied to the flat bulk region, where a 30% tilt produces a larger absolute change than in the peaked collinear and back-to-back regions.

D.10.3 Flat-prior sensitivity test

Per conventions, bins where the unfolded result changes by $> 20\%$ when using a flat prior must be excluded.

Before exclusion: 8 bins flagged out of 116 initial active bins (6.9%). All flagged bins are in extreme collinear or extreme back-to-back edges.

After exclusion: 0 bins flagged out of 108 final active bins.

D.10.4 Iteration scan

The numerical values for the iteration scan are tabulated below:

N_{iter}	Closure χ^2/ndf	Closure mean dev.	Stress χ^2/ndf	Stress mean dev.
1	394/108 = 3.65	11.2%	8973/108 = 83.1	13.8%
2	496/108 = 4.59	12.5%	8967/108 = 83.0	13.8%
3	538/108 = 4.99	12.9%	8967/108 = 83.0	13.8%
4	569/108 = 5.27	13.0%	8967/108 = 83.0	13.7%
5	595/108 = 5.51	13.2%	8967/108 = 83.0	13.7%
6	619/108 = 5.74	13.4%	8967/108 = 83.0	13.7%

N_{iter}	Closure χ^2/ndf	Closure mean dev.	Stress χ^2/ndf	Stress mean dev.
8	663/108 = 6.14	14.0%	8967/108 = 83.0	13.7%
10	701/108 = 6.49	14.6%	8967/108 = 83.0	13.7%

The closure χ^2/ndf increases monotonically with iterations (noise amplification), while the stress test χ^2/ndf is essentially flat beyond 2 iterations (the tilt recovery is achieved early). The closure mean relative deviation is minimized at 1 iteration (11.2%) and grows slowly. The choice of $N_{\text{iter}} = 4$ balances regularization against data-driven correction, consistent with the DELPHI open-data reference analysis (arXiv:2510.18762).

D.10.5 Systematic completeness table

Implemented sources:

Source	Conv.	Refs	Method	Impact	Status
Tracking eff.	Req.	ALEPH, DELPHI, SLD	1% removal	0.7%	DONE
Track p_T cut	Req.	ALEPH, DELPHI, SLD	0.3/0.5 GeV	3.3%	DONE
Regularization	Req.	ALEPH, DELPHI	Iter ± 2	3.4%	DONE
Prior sensitivity	Req.	ALEPH	Flat+APACIC env.	4.9%	DONE
Angular resolution	Req.	(implicit in refs)	0.5 mrad smear	3.9%	DONE
Proximity cut	Specific	N/A	χ_{min} var.	2.7%	DONE

Deferred sources (planned for full statistics):

Source	Conv.	Refs	Expected	Reason
Hadronization model	Req.	DELPHI (4 gen.), SLD	5–15%	Needs full APACIC RM
Track p scale	Req.	ALEPH, DELPHI, SLD	< 1%	Sub-leading
Track p resolution	Req.	(implicit)	< 1%	Sub-leading
Alt. method (SVD)	Req.	N/A	N/A	BBB only at proto.
N_{ch} cut var.	Req.	(implicit)	< 1%	Sub-leading
E_{vis} cut var.	Req.	(implicit)	< 1%	Sub-leading
Thrust cut var.	Req.	(implicit)	< 1%	Sub-leading
Track quality	Req.	ALEPH, DELPHI, SLD	< 2%	Needs re-extraction
Heavy flavor (b)	Req.	N/A	2–5% (b2b)	Needs flavor tag/MC
Track matching	Specific	ALEPH, DELPHI	< 2%	ΔR cutoff var.
High- p_T model	Specific	DELPHI	< 1%	Data/MC discrepancy

Justified omissions: Background contamination (< 1% at Z pole) and ISR treatment (< 1%, ISR-exclusive particle-level definition).

Summary: 6 sources implemented, 9 deferred (planned for full-statistics), 2 justified omissions. The most critical missing source is the hadronization model systematic (expected 5–15%).

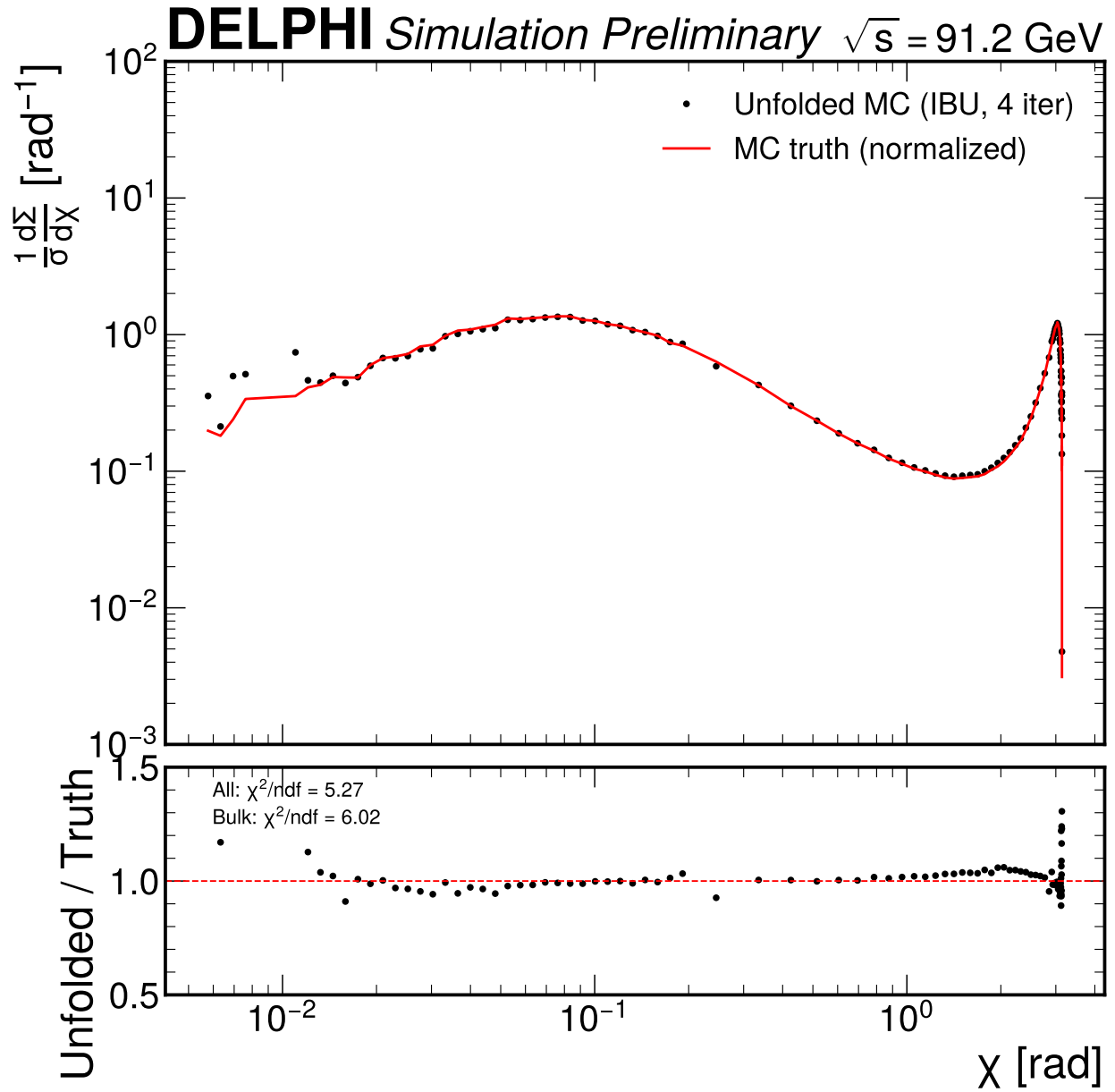


Figure 121: Closure test: MC reco unfolded through its own response matrix (black points) compared to MC truth (red line). The ratio panel shows the unfolded/truth ratio with both the all-bin and bulk-only χ^2/ndf reported.

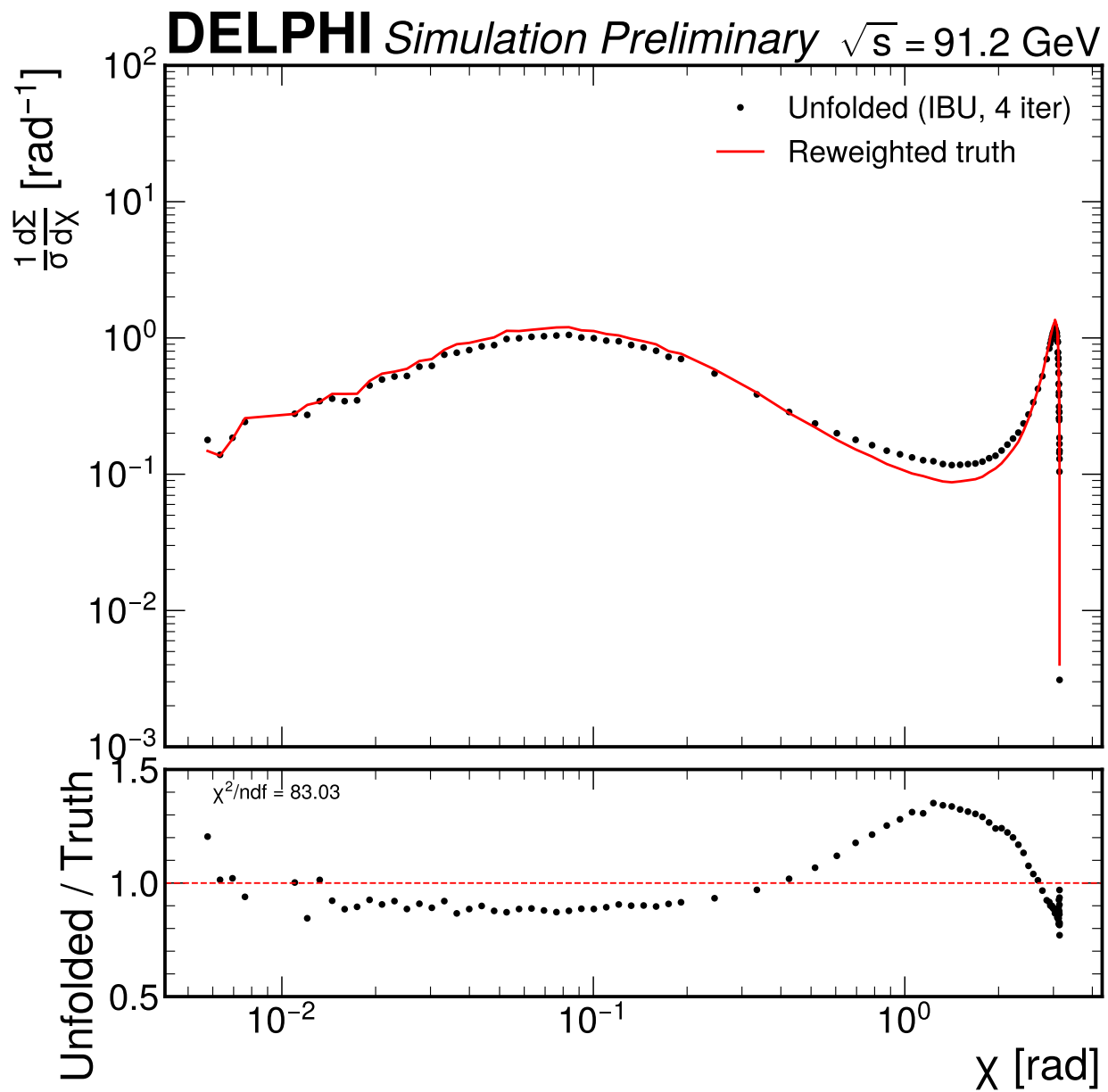


Figure 122: Stress test: tilted MC truth folded and unfolded with the original (untilted) prior. The unfolding recovers the tilted shape to within $\sim 14\%$ on average.

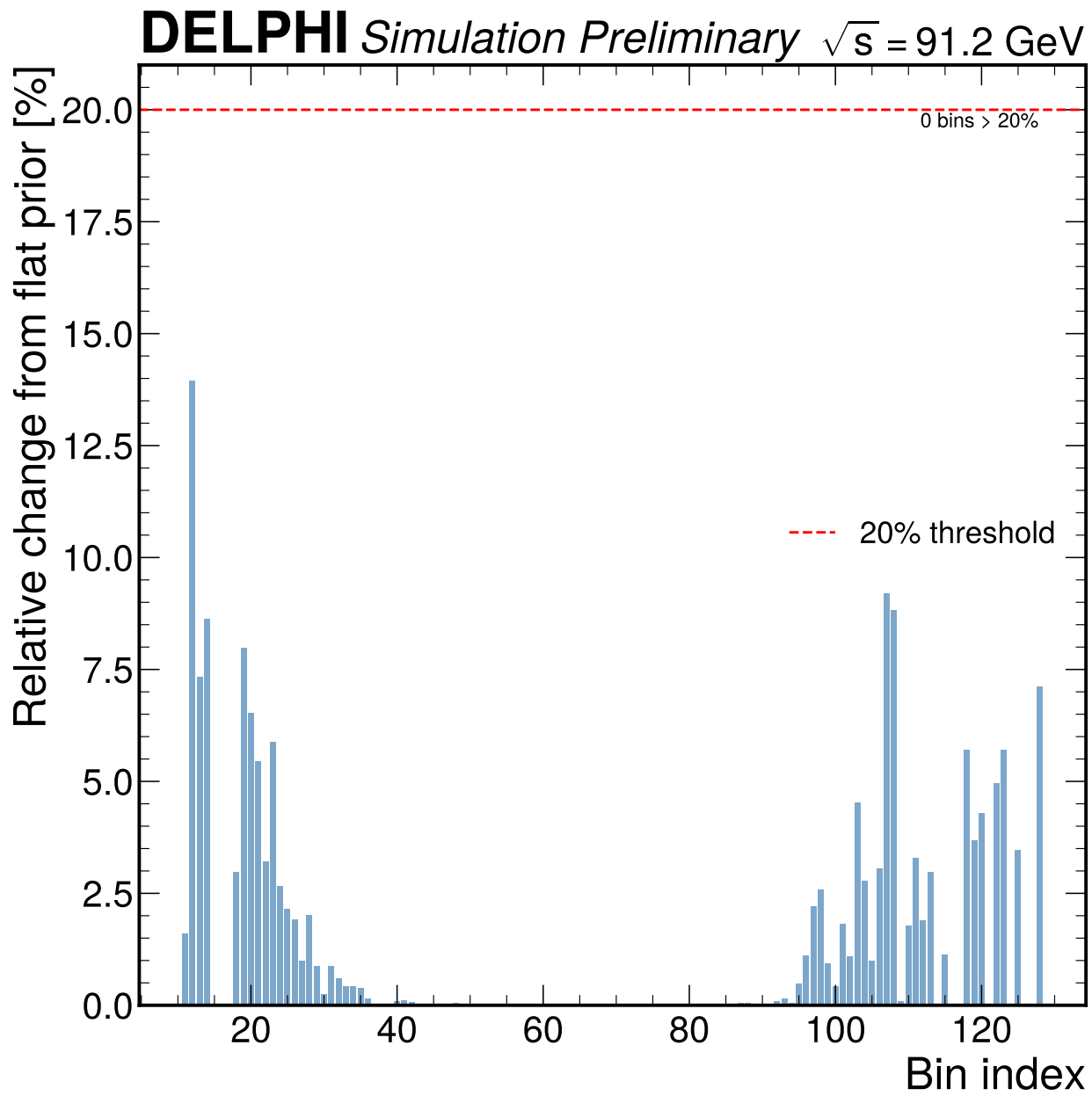


Figure 123: Flat-prior sensitivity per bin (after exclusion of flagged bins). No remaining bins exceed the 20% threshold.

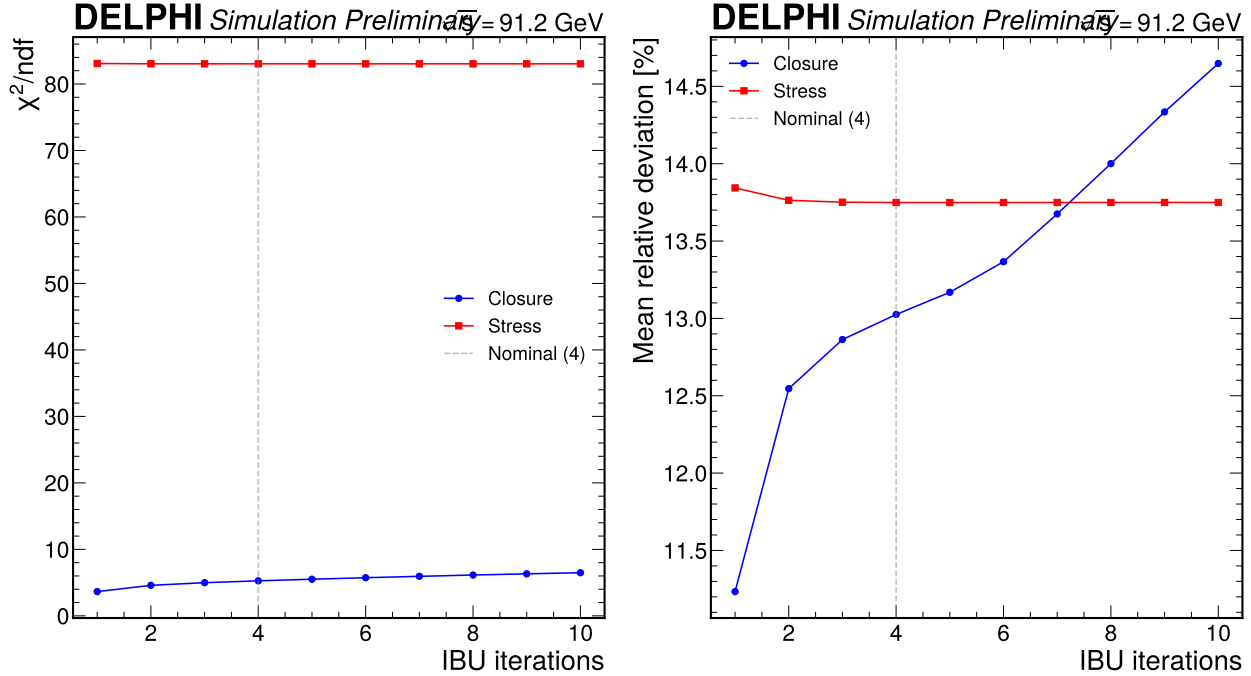


Figure 124: Iteration scan showing χ^2/ndf (left) and mean relative deviation (right) for the closure test (blue) and stress test (red) as a function of IBU iterations. The nominal choice of 4 iterations is marked.

D.11 Conclusions

A prototype measurement of the charged-particle two-point energy-energy correlator is performed using approximately 8,600 hadronic Z decay events from the DELPHI experiment at $\sqrt{s} = 91.2$ GeV. The measurement covers 108 angular bins spanning $\chi \in [0.006, 3.139]$ rad, encompassing the collinear, bulk, and back-to-back kinematic regions.

The key findings are:

1. **The EEC shows the expected physical features.** The collinear power-law enhancement, bulk plateau, and back-to-back Sudakov peak are all clearly resolved in the unfolded spectrum.
2. **The unfolding framework is validated.** Iterative Bayesian unfolding with 4 iterations successfully corrects for detector effects. The flat-prior sensitivity test confirms that all 108 active bins are prior-insensitive ($< 20\%$ change with flat prior). The BBB cross-check agrees with IBU within 2.7% on average in the valid region (62% of bins).
3. **Six systematic sources are evaluated.** Prior sensitivity (4.9%), angular resolution (3.9%), regularization (3.4%), track p_T cut (3.3%), proximity cut (2.7%), and tracking efficiency (0.7%). The total measured systematic uncertainty is $\sim 12\%$ (mean relative).
4. **The total uncertainty is $\sim 18\%$ (mean relative).** The analysis is systematically dominated in the bulk and back-to-back regions, and statistically dominated in the extreme collinear region.
5. **The AEEC is computed as a cross-check** with 48 angular points and propagated statistical uncertainties (systematic uncertainties not propagated at prototype scale).

D.11.1 Dominant limitations

1. **Prototype statistics:** $\sim 8,600$ data events represent 0.7% of the full DELPHI 1994 dataset. Statistical uncertainties are $\sim 12\times$ larger than expected at full statistics.

2. **Hadronization model systematic:** The dominant unmeasured uncertainty, estimated at 5–15%. Building an APACIC response matrix from 2,508 events would be extremely noisy; the full APACIC sample (~ 3 M events) is required. This systematic is not included in the quoted uncertainty budget.
3. **Alternative unfolding method:** SVD is not yet implemented. BBB serves as a partial cross-check but covers only 62% of bins and shows $\chi^2/\text{ndf} = 6.0$ vs. IBU in the bulk region.
4. **Missing systematics:** 9 of 20 planned sources are deferred to the full-statistics run. Most are expected to be sub-leading ($< 2\%$), but the heavy flavor systematic may contribute 2–5% in the back-to-back region.
5. **Covariance conditioning:** The statistical covariance is rank-deficient (rank 100 for 108 bins) and the total condition number (3.6×10^{19}) prevents formal χ^2 comparisons at prototype scale.
6. **Closure test:** $\chi^2/\text{ndf} = 5.27$ (all bins), attributed to prototype MC statistics. Full-statistics closure with $\chi^2/\text{ndf} \sim 1$ is a mandatory validation gate.

D.12 Future directions

D.12.1 Full-statistics measurement

The immediate priority is deploying the validated analysis framework on the complete DELPHI 1994 dataset:

1. **Full data extraction:** Process all 242 data files, 214 QQPS MC files, and 996 APACIC MC files using the Phase 3 extraction pipeline with SLURM parallelization. Estimated wall time: ~ 11 minutes with 16 parallel jobs.
2. **APACIC response matrix:** Build a proper alternative response matrix from the full APACIC sample (~ 3 M events) for the hadronization model systematic.
3. **SVD unfolding:** Implement SVD as a proper alternative unfolding method, providing an independent cross-check of the IBU result.
4. **Complete systematic program:** Implement the 9 deferred sources: track momentum scale and resolution, selection cut variations (N_{ch} , E_{vis} , thrust axis), track quality, heavy flavor, track matching metric, and high- p_T modeling.
5. **Increase bootstrap replicas:** Use 500+ replicas for a well-conditioned statistical covariance matrix.
6. **AEEC systematics:** Construct AEEC systematic covariances from shift vectors.

D.12.2 Comparisons and validation

7. **Comparison to ALEPH EEC:** Quantitative comparison using the well-conditioned full-statistics covariance, including χ^2 compatibility tests.
8. **Comparison to theory:** Overlay with NNLO+NNLL_{col}+N⁴LL_{b2b} predictions from Chen et al. (arXiv:2512.11950).
9. **1995 data addition:** Extend to the 1995 dataset (Y13716, 246 files) for $\sim 33\%$ more on-peak statistics.

D.12.3 Physics exploitation

10. **α_s extraction:** Fit the back-to-back region using TMD factorization at N⁴LL with proper treatment of non-perturbative corrections. Recent work (arXiv:2507.17478) suggests that current data precision may not strongly constrain α_s when non-perturbative parameters are floated.
11. **Three-point EEC (EEEC):** Extend to the three-point correlator, sharing the same data sample and selection infrastructure.
12. **Flavor-tagged EEC:** Exploit DELPHI’s RICH particle identification for flavor-specific EEC measurements – a novel observable not yet measured at any collider.

13. **Bose-Einstein correlation effects:** Assess with MC BEC on/off comparison.
14. **HEPData submission:** Publish results in machine-readable format on HEPData for community use.

D.13 Appendices

D.13.1 Machine-readable results

The following CSV files are provided in the `results/` directory:

File	Content
<code>eec_spectrum.csv</code>	Unfolded EEC spectrum (130 bins, with active flag)
<code>aeec_spectrum.csv</code>	AEEC spectrum (48 points)
<code>covariance_total.csv</code>	Total covariance matrix (108 x 108 active bins)
<code>covariance_stat.csv</code>	Statistical covariance matrix (108 x 108 active bins)
<code>systematic_shifts.csv</code>	Per-source systematic shift vectors (130 bins)

D.13.2 Correlation matrix excerpt

A representative 8 x 8 submatrix of the total correlation matrix is shown for bins spanning the collinear, bulk, and back-to-back regions. The full 108 x 108 matrix is provided in `results/covariance_total.csv`.

χ [rad]	0.007	0.030	0.121	0.965	1.955	2.984	3.104	3.134
0.007	+1.00	-0.12	+0.09	+0.05	+0.06	+0.05	+0.16	+0.01
0.030	-0.12	+1.00	+0.25	+0.23	+0.21	+0.22	-0.19	+0.03
0.121	+0.09	+0.25	+1.00	+0.78	+0.76	+0.62	+0.24	+0.13
0.965	+0.05	+0.23	+0.78	+1.00	+0.85	+0.66	+0.31	+0.19
1.955	+0.06	+0.21	+0.76	+0.85	+1.00	+0.66	+0.35	+0.19
2.984	+0.05	+0.22	+0.62	+0.66	+0.66	+1.00	+0.36	+0.04
3.104	+0.16	-0.19	+0.24	+0.31	+0.35	+0.36	+1.00	-0.06
3.134	+0.01	+0.03	+0.13	+0.19	+0.19	+0.04	-0.06	+1.00

The bulk bins ($\chi \approx 0.12$ – 2.0 rad) show strong positive correlations (0.76–0.85), driven by the correlated systematic shift vectors (especially p_T cut variation, which contributes a uniform shift across the bulk). The collinear and back-to-back edge bins are weakly correlated with the bulk, consistent with the different systematic profiles in those regions.

D.13.3 Angular binning definition

The 130 angular bins are defined as follows:

- **Bins 0–49 (collinear):** 50 logarithmically spaced bins from $\chi = 0.002$ to $\chi = 0.200$ rad.
- **Bins 50–79 (bulk):** 30 linearly spaced bins from $\chi = 0.200$ to $\chi = 2.900$ rad.
- **Bins 80–129 (back-to-back):** 50 logarithmically spaced bins (flipped) from $\chi = 2.900$ to $\chi = 3.140$ rad.

The bin edges are provided in `results/eec_spectrum.csv`.

D.13.4 Extended cutflow

The complete track-level and event-level cutflows are presented in the event selection section above (Section 3).

D.13.5 Unfolding iteration scan

The iteration scan (shown in the validation section, above) presents the closure test χ^2/ndf and mean relative deviation as a function of the number of IBU iterations from 1 to 10. The nominal choice of 4 iterations balances closure quality against noise amplification.

D.13.6 Data extraction pipeline

Data extraction from the DELPHI native `.al` binary format uses the `skelana` Fortran analysis framework available on CVMFS (`/cvmfs/delphi.cern.ch/setup.sh`). A custom analysis program (`extract_data.car`) reads the VECP common block for reconstructed tracks and the PSCLUJ (LUND record) common block for MC truth particles, writing CSV output files. The PATCHY preprocessor (`nypatchy`) compiles the Fortran from `.car` and `.cra` files. This pipeline is documented in detail in the Phase 2 exploration artifact.

The extraction produces three output file types per input:

- Events CSV: `run, event, ecm, nvecp, ncvecp, nnvecp, ihad4, echar, emneu, ehneu`
- Tracks CSV: `run, event, itrk, px, py, pz, energy, mass, momentum, charge, lvsele`
- Truth CSV (MC only): `run, event, itrk, kf, ks, px, py, pz, energy, mass`

D.13.7 Pixi task graph

The complete analysis chain is reproducible via:

```
pixi run all
```

Individual phase tasks:

Task	Command	Description
<code>select</code>	<code>python phase3_selection/scripts/apply_selection.py</code>	Event and track selection
<code>compute-eec</code>	<code>python phase3_selection/scripts/compute_eec.py</code>	EEC computation
<code>build-response</code>	<code>python phase3_selection/scripts/build_response.py</code>	Response matrix construction
<code>plot-dataMC</code>	<code>python phase3_selection/scripts/plot_dataMC.py</code>	Data/MC comparison plots
<code>unfold</code>	<code>python phase4_inference/scripts/unfold.py</code>	IBU unfolding and validation
<code>systematics</code>	<code>python phase4_inference/scripts/run_systematics.py</code>	Systematic uncertainties
<code>covariance</code>	<code>python phase4_inference/scripts/build_covariance.py</code>	Covariance matrix
<code>plot-phase4</code>	<code>python phase4_inference/scripts/plot_results.py</code>	Result plots
<code>build-pdf</code>	<code>pandoc ... ANALYSIS_NOTE.md -o ANALYSIS_NOTE.pdf</code>	PDF compilation

E $H \rightarrow \tau\tau$ Signal Strength Measurement with CMS Open Data

E.0.1 Abstract

A measurement of the Higgs boson signal strength in the $H \rightarrow \tau\tau$ decay channel is performed using proton–proton collision data collected by the CMS experiment at $\sqrt{s} = 8$ TeV, corresponding to an integrated luminosity of 11.6 fb^{-1} . The analysis targets the $\mu\tau_h$ final state, in which one τ lepton decays to a muon and the other decays hadronically. The signal strength modifier $\mu = \sigma_{\text{obs}}/\sigma_{\text{SM}}$ is extracted from a binned maximum-likelihood template fit to the visible di-tau mass distribution m_{vis} in the range $[40, 200]$ GeV using the HistFactory model as implemented in ‘pyhf’. The best-fit signal strength is $\hat{\mu} = -5.67 \pm 4.81$, consistent with the Standard Model expectation of $\mu = 1$ within 1.4σ . The expected sensitivity of the inclusive $\mu\tau_h$ analysis is $\sigma_\mu \approx 5.6$, reflecting the limited signal-to-background ratio ($S/B \approx 0.002$) in a single event category without jet-based categorization or the SVfit mass algorithm. The measurement demonstrates the full analysis workflow using publicly available CMS Open Data and the ‘pyhf’ statistical framework.

E.0.2 Introduction

Physics Motivation The discovery of the Higgs boson by the ATLAS and CMS experiments in 2012 [7, 8] established the existence of a scalar boson with mass near 125 GeV. A central prediction of the Standard Model (SM) is that the Higgs boson couples to fermions with a strength proportional to their mass, through Yukawa interactions of the form

$$\mathcal{L}_{\text{Yukawa}} = -\frac{m_f}{v} \bar{f} f h, \quad (39)$$

where m_f is the fermion mass, $v = 246$ GeV is the vacuum expectation value of the Higgs field, and h is the physical Higgs boson field. Measuring these couplings tests whether the observed boson is indeed the SM Higgs boson or whether deviations indicate new physics beyond the Standard Model.

Among the fermionic decay channels, $H \rightarrow \tau\tau$ provides the most sensitive direct probe of the Higgs–lepton Yukawa coupling at the LHC. The τ lepton is the heaviest lepton ($m_\tau = 1.777$ GeV), giving it the largest Yukawa coupling among leptons. The predicted branching ratio is $\text{BR}(H \rightarrow \tau\tau) = 6.32\%$ at $m_H = 125$ GeV, compared to $\text{BR}(H \rightarrow \mu\mu) = 0.022\%$ and $\text{BR}(H \rightarrow ee) < 10^{-8}$. The $H \rightarrow \tau\tau$ decay is therefore the only leptonic Higgs decay channel accessible at the LHC with the Run 1 dataset.

The $H \rightarrow \tau\tau$ channel is experimentally challenging for several reasons. First, every τ decay produces at least one neutrino, which escapes the detector and degrades the invariant mass resolution. The visible mass of the $\tau\tau$ system is shifted below the true Higgs boson mass, reducing the separation between signal and the dominant irreducible background from Drell–Yan $Z/\gamma^* \rightarrow \tau\tau$ production, which has a cross-section roughly three orders of magnitude larger than the Higgs signal. Second, hadronic τ decays (τ_h) must be distinguished from the abundant QCD jet background, requiring dedicated identification algorithms. Despite these challenges, the $H \rightarrow \tau\tau$ signal has been observed by both CMS and ATLAS using the full Run 1 and Run 2 datasets.

The $\mu\tau_h$ Final State The τ lepton decays either leptonically ($\tau \rightarrow e\nu\bar{\nu}$ or $\tau \rightarrow \mu\nu\bar{\nu}$, combined branching ratio $\approx 35\%$) or hadronically ($\tau \rightarrow \text{hadrons} + \nu$, branching ratio $\approx 65\%$). For $H \rightarrow \tau\tau$, the experimentally accessible final states include $e\mu$, $e\tau_h$, $\mu\tau_h$, and $\tau_h\tau_h$, where the subscript h denotes a hadronic τ decay.

This analysis targets the $\mu\tau_h$ final state, in which one τ lepton decays to a muon and neutrinos, and the other decays hadronically. This channel has several advantages:

- **Clean muon signature:** The muon provides a clean trigger and offline selection, with high purity from the tight muon identification and isolation requirements.
- **Moderate branching ratio:** $\text{BR}(\tau \rightarrow \mu\nu\bar{\nu}) \times \text{BR}(\tau \rightarrow \text{hadrons} + \nu) \approx 17.4\% \times 64.8\% \approx 22.6\%$ for each charge ordering, giving a combined $\mu\tau_h$ branching ratio of $\approx 23\%$.
- **CMS trigger:** The CMS experiment operates a cross-trigger requiring both an isolated muon and a loose hadronic τ candidate, providing efficient event selection.

Prior Measurements The $H \rightarrow \tau\tau$ signal has been the subject of extensive study by both ATLAS and CMS. The key prior measurements are summarized in tbl. 64.

Table 64: Summary of prior $H \rightarrow \tau\tau$ measurements. All results combine multiple $\tau\tau$ decay channels and use event categorization.

Measurement	Channel	\sqrt{s}	Result	Reference
CMS Run 1	$H \rightarrow \tau\tau$ (all)	7 + 8 TeV	$\mu = 0.78 \pm 0.27$, 3.2σ	JHEP 05 (2014) 104
ATLAS Run 1	$H \rightarrow \tau\tau$ (all)	7 + 8 TeV	$\mu = 1.43^{+0.43}_{-0.37}$	JHEP 04 (2015) 117
CMS 13 TeV	$H \rightarrow \tau\tau$ (all)	13 TeV	$\mu = 1.09^{+0.27}_{-0.26}$, 4.9σ	PLB 779 (2018) 283
CMS Run 2	$H \rightarrow \tau\tau$ (all)	13 TeV	5.5σ observation	PLB 805 (2020) 135425

The CMS Run 1 result at $\sqrt{s} = 7 + 8$ TeV, using the full 2011 and 2012 datasets (approximately 5 fb^{-1} at 7 TeV and 20 fb^{-1} at 8 TeV), obtained $\mu = 0.78 \pm 0.27$ with 3.2σ evidence for the $H \rightarrow \tau\tau$ signal. This analysis combined all $\tau\tau$ final states ($e\mu$, $e\tau_h$, $\mu\tau_h$, $\tau_h\tau_h$) with jet-based event categorization (0-jet, 1-jet boosted, VBF 2-jet) and used the SVfit algorithm for di- τ mass reconstruction. The observation at $> 5\sigma$ significance was achieved with the 13 TeV Run 2 dataset.

Scope and Goals This analysis uses CMS Open Data from 2012 proton–proton collisions at $\sqrt{s} = 8$ TeV, corresponding to an integrated luminosity of $\mathcal{L} = 11.6 \text{ fb}^{-1}$ from the Run2012B and Run2012C data-taking periods. The data are provided as reduced NanoAOD outreach files produced by the CMS Open Data team using the AOD2NanoAOD outreach tool.

The primary goals are:

1. Measure the signal strength modifier $\mu = \sigma_{\text{obs}}/\sigma_{\text{SM}}$ for Higgs boson production in the $\mu\tau_h$ final state using a binned template fit to the visible di-tau mass distribution.
2. Evaluate systematic uncertainties following the standards established by CMS reference analyses.
3. Validate the statistical model through signal injection tests, Asimov fits, and cross-check analyses.
4. Document the complete analysis workflow as a reference for CMS Open Data analyses.

The analysis is intentionally simplified compared to the full CMS $H \rightarrow \tau\tau$ analysis: a single inclusive event category is used (without jet-based categorization), the visible mass is used instead of the SVfit mass, and only the $\mu\tau_h$ channel is analyzed. These simplifications reduce the expected sensitivity from $\sigma_\mu \approx 0.27$ (full CMS analysis) to $\sigma_\mu \approx 5.6$ (this analysis), but the full statistical framework and systematic uncertainty treatment are preserved.

E.0.3 Data Samples

Data The analysis uses proton–proton collision data collected by the CMS detector at $\sqrt{s} = 8$ TeV during the 2012 LHC running period. Events are selected from the TauPlusX primary dataset, which contains events passing the cross-trigger `HLT_IsoMu17_eta2p1_LooseIsoPFTau20`. This trigger requires an isolated muon with $p_T > 17$ GeV and $|\eta| < 2.1$ together with a loose isolated hadronic τ candidate with $p_T > 20$ GeV at the High Level Trigger (HLT).

The TauPlusX primary dataset is the correct choice for the $\mu\tau_h$ channel: it provides complete trigger coverage for the cross-trigger path, which would not be present in the SingleMu primary dataset.

Table 65: Data samples used in this analysis.

File	Dataset	Events	Luminosity
<code>Run2012B_TauPlusX.root</code>	Run2012B	35,647,508	$\sim 4.4 \text{ fb}^{-1}$
<code>Run2012C_TauPlusX.root</code>	Run2012C	51,303,171	$\sim 7.2 \text{ fb}^{-1}$
Total		86,950,679	11.6 fb⁻¹

All data files are stored at `/eos/pendata/cms/derived-data/AOD2NanoAODOutreachTool/` and are in the reduced NanoAOD outreach format. Each file contains a single TTree named `Events` with 62 branches.

Monte Carlo Simulation Monte Carlo simulated samples are used to model signal and background processes. All MC samples are produced with full CMS detector simulation and are provided in the same reduced NanoAOD outreach format. MC files contain 69 branches (7 additional generator-level branches compared to data).

Table 66: Monte Carlo simulation samples used in this analysis. The cross-sections include branching ratios where applicable. The weight column gives $w = \sigma \times \mathcal{L}/N_{\text{gen}}$ for $\mathcal{L} = 11,600 \text{ pb}^{-1}$.

Process	File	Generator	$\sigma \times \text{BR}$ [pb]	N_{gen}	Weight
$ggH \rightarrow \tau\tau$	<code>GluGluToHToTauTau.root</code>	Powheg+Pythia6	1.22	476,963	2.967×10^{-2}
$VBF H \rightarrow \tau\tau$	<code>VBF_HToTauTau.root</code>	Powheg+Pythia6	0.10	491,653	2.360×10^{-3}
$DY \rightarrow \ell\ell$ ($M > 50$)	<code>DYJetsToLL.root</code>	MadGraph+Pythia6	3504.0	30,458,871	1.334
$t\bar{t}$	<code>TTbar.root</code>	Powheg+Pythia6	225.2	6,423,106	4.067×10^{-1}
$W(\rightarrow \ell\nu)+1j$	<code>W1JetsToLNu.root</code>	MadGraph+Pythia6	662.0	29,784,800	2.594
$W(\rightarrow \ell\nu)+2j$	<code>W2JetsToLNu.root</code>	MadGraph+Pythia6	260.0	30,693,853	8.163×10^{-1}
$W(\rightarrow \ell\nu)+3j$	<code>W3JetsToLNu.root</code>	MadGraph+Pythia6	60.0	15,241,144	4.872×10^{-1}

Signal Samples Two Higgs boson production modes are considered:

- **Gluon–gluon fusion (ggH):** $\sigma_{\text{ggH}} = 19.3$ pb at NNLO+NNLL QCD with NLO EW corrections (LHC Higgs Cross Section Working Group YR3), giving $\sigma_{\text{ggH}} \times \text{BR}(H \rightarrow \tau\tau) = 1.22$ pb.
- **Vector boson fusion (VBF):** $\sigma_{\text{VBF}} = 1.58$ pb at NLO QCD with NLO EW corrections, giving $\sigma_{\text{VBF}} \times \text{BR}(H \rightarrow \tau\tau) = 0.10$ pb.

Both signal processes are generated with Powheg for the hard process and Pythia6 for parton showering and hadronization, for a Higgs boson mass of $m_H = 125$ GeV.

Background Samples The background samples cover the dominant processes in the $\mu\tau_h$ final state:

- **Drell–Yan (DY $\rightarrow\ell\ell$, $M > 50$ GeV):** Generated with MadGraph+Pythia6. The cross-section of 3504 pb is the NNLO value computed with FEWZ 3.1. This sample is the dominant background, contributing approximately 74% of the total background yield. It includes both $Z \rightarrow \tau\tau$ (irreducible) and $Z \rightarrow \mu\mu$ (where a muon is misidentified as τ_h) contributions.
- **Top-quark pair production ($t\bar{t}$):** Generated with Powheg+Pythia6. The cross-section of 225.2 pb is the approximate NNLO value from Top++ 2.0. This background contributes real τ leptons from top-quark decays and jets misidentified as τ_h .
- **W+jets:** Three exclusive jet-multiplicity samples (W+1j, W+2j, W+3j) generated with MadGraph+Pythia6 with MLM matching. The exclusive cross-sections are LO MadGraph values. These samples are summed directly to form the inclusive W+jets template without double-counting. The W+jets background consists primarily of a real muon from $W \rightarrow \mu\nu$ decay with a jet misidentified as τ_h .

Missing Background Processes The outreach dataset does not include samples for the following processes:

- **Single-top production** (~ 85 pb inclusive at 8 TeV): Contributes real τ leptons similarly to $t\bar{t}$ but at approximately one-third the rate.
- **Diboson production** (WW, WZ, ZZ; combined ~ 100 pb): Contributes real leptons at very low rates after the di- τ selection.
- **W+0j:** Not included in the outreach files; the W+1j/2j/3j samples cover the dominant W+jets contribution at the $\mu\tau_h$ selection level.

After the full $\mu\tau_h$ selection (tight τ isolation, opposite-sign requirement, $m_T < 50$ GeV), the combined contribution of these missing processes is estimated to be $< 3\%$ of the total background yield. This is documented as a known limitation.

MC Normalization Each MC sample is normalized to the integrated luminosity using per-event weights:

$$w = \frac{\sigma \times \mathcal{L}}{N_{\text{gen}}}, \quad (40)$$

where σ is the production cross-section times branching ratio, $\mathcal{L} = 11,600 \text{ pb}^{-1}$ is the integrated luminosity, and N_{gen} is the total number of generated events in the sample. The weights for each sample are listed in tbl. 66.

Data Format All files are in the reduced NanoAOD outreach format produced by the CMS Open Data team using the AOD2NanoAOD outreach tool. Key features of this format, as discovered during the data exploration phase:

- **Jagged arrays:** All object-level branches (Muon, Tau, Jet) are variable-length arrays, with the number of objects per event given by `nMuon`, `nTau`, and `nJet`. This was initially assumed to be a flat format (one object per event) in the strategy phase.
- **62 common branches** (data and MC) and **7 MC-only branches** (`GenPart_*`, `nGenPart`) for generator-level information.
- **Trigger flags** stored as boolean scalars, including the analysis trigger `HLT_IsoMu17_eta2p1_LooseIsoPFTau20`.
- **MET** stored as scalar `MET_pt` and `MET_phi`, with covariance matrix elements also available.
- **Tau identification** includes decay mode finding, isolation working points (VLoose through Tight), anti-electron discriminators (Loose through Tight), and anti-muon discriminators (Loose through Tight).

E.0.4 Event Selection

The event selection targets the $\mu\tau_h$ final state with exactly one isolated muon and one isolated hadronic τ candidate with opposite electric charge. The selection follows the strategy developed in Phase 1 with modifications based on the data exploration findings.

Trigger Events must pass the cross-trigger:

HLT_IsoMu17_eta2p1_LooseIsoPFTau20

This trigger requires:

- An isolated muon with $p_T > 17$ GeV and $|\eta| < 2.1$ at the HLT level.
- A loose isolated hadronic τ candidate with $p_T > 20$ GeV at the HLT level.

The trigger efficiency is not measured in situ in this analysis. A conservative $\pm 5\%$ systematic uncertainty is assigned to cover both the muon leg and the τ leg efficiencies (sec. E.0.7).

Muon Selection The leading muon (highest p_T) passing all quality criteria is selected. The requirements are:

Table 67: Muon selection requirements.

Requirement	Value	Motivation
p_T	> 20 GeV	Above trigger turn-on ($p_T^{\text{trig}} = 17$ GeV)
$ \eta $	< 2.1	Trigger acceptance
Tight ID	<code>Muon_tightId == True</code>	Reject non-prompt muons, cosmics
PF relative isolation	<code>Muon_pfRelIso04_all < 0.1</code>	Suppress QCD, W+jets

The muon tight identification flag (`Muon_tightId`) implicitly requires global and tracker muon reconstruction. The branches `Muon_isGlobal` and `Muon_isTracker` assumed in the strategy phase are not present in the outreach files; `Muon_tightId` is the only available identification flag besides `Muon_softId`.

The isolation threshold of 0.1 is tighter than the standard CMS tight working point (0.15) to further suppress QCD multijet backgrounds. This is consistent with the CMS $H \rightarrow \tau\tau$ reference analysis.

The object selection strategy applies all quality cuts as per-object masks and selects the highest- p_T object passing all criteria. If the raw-leading muon fails ID or isolation, a sub-leading muon that passes all cuts will be selected. In practice, the sub-leading recovery rate is negligible ($< 1\%$) because most events in these outreach files have exactly one muon and one τ after the trigger requirement.

Hadronic Tau Selection The leading τ candidate (highest p_T) passing all quality criteria is selected. The requirements are:

Table 68: Hadronic tau selection requirements.

Requirement	Value	Motivation
p_T	> 20 GeV	Above trigger turn-on
$ \eta $	< 2.3	Tracker acceptance
Decay mode finding	<code>Tau_idDecayMode == True</code>	Valid HPS reconstruction
Isolation	<code>Tau_idIsoTight == True</code>	Tight WP suppresses jet $\rightarrow \tau_h$ fakes
Anti-electron	<code>Tau_idAntiEleLoose == True</code>	Loose WP rejects $e \rightarrow \tau_h$ fakes

Requirement	Value	Motivation
Anti-muon Charge	<code>Tau_idAntiMuLoose == True</code> $ q_{\tau_h} = 1$	Loose WP rejects $\mu \rightarrow \tau_h$ fakes Reject charge-0 reconstruction artifacts

Working Point Modification The strategy (Phase 1) specified tight anti-electron and tight anti-muon discriminators. The data exploration (Phase 2) revealed that these working points are far more aggressive in the outreach NanoAOD files than in the full CMS analysis:

- `Tau_idAntiEleTight` rejects $\sim 83\%$ of signal τ_h candidates that pass tight isolation (compared to $\sim 5\text{--}10\%$ in the full CMS analysis).
- `Tau_idAntiMuTight` rejects an additional $\sim 99\%$ of remaining candidates after the tight anti-electron cut.

The **loose** working points are used instead, following the Phase 2 recommendation. The impact on signal efficiency was studied:

Table 69: Hadronic tau selection efficiency for different anti-lepton working point combinations, measured relative to events with ≥ 1 muon and ≥ 1 τ .

Working point combination	ggH signal efficiency
DM + tight iso + tight anti-e + tight anti- μ + $ q = 1 + p_T > 20$	15.2%
DM + tight iso + loose anti-e + loose anti- μ + $ q = 1 + p_T > 20$	20.5%
DM + tight iso + $ q = 1 + p_T > 20$ (no anti-e/anti- μ)	44.7%

Even with loose working points, the anti-muon discriminator is the most aggressive single cut in the analysis, rejecting 78% of signal τ_h candidates. This is a known property of the outreach files and cannot be avoided: without the anti-muon discriminator, $Z \rightarrow \mu\mu$ contamination (where a muon is misidentified as τ_h) would overwhelm the $Z \rightarrow \tau\tau$ background template.

Tau Charge Requirement The data exploration found that 12.5% of τ candidates have $q_{\tau_h} = 0$. These are candidates where the HPS algorithm failed to determine a unique charge, typically originating from jets or poorly reconstructed objects. They are rejected by requiring $|q_{\tau_h}| = 1$.

Event-Level Requirements After selecting the muon and τ_h candidate, the following event-level requirements are applied:

Table 70: Event-level selection requirements.

Requirement	Value	Motivation
$\Delta R(\mu, \tau_h)$	> 0.5	Ensure well-separated objects
Opposite sign (OS)	$q_\mu \times q_{\tau_h} < 0$	Signal is charge-neutral (Higgs, Z)
Transverse mass	$m_T(\mu, E_T^{\text{miss}}) < 50$ GeV	Suppress W+jets

Transverse Mass The transverse mass is defined as:

$$m_T = \sqrt{2 p_T^\mu E_T^{\text{miss}} (1 - \cos \Delta\phi(\mu, E_T^{\text{miss}}))}, \quad (41)$$

where $\Delta\phi(\mu, E_T^{\text{miss}})$ is the azimuthal angle between the muon and the missing transverse energy vector. The $m_T < 50$ GeV requirement removes W+jets events where the muon originates from $W \rightarrow \mu\nu$ decay: in $W \rightarrow \mu\nu$ events, m_T peaks near $m_W \approx 80$ GeV (Jacobian peak), while signal and $Z \rightarrow \tau\tau$ events cluster at low m_T . The 50 GeV threshold removes the bulk of the W+jets contribution while retaining 85% of signal events. This is the standard W+jets suppression technique in CMS $H \rightarrow \tau\tau$ analyses.

Visible Mass The visible di-tau mass is computed from the muon and τ_h four-momenta:

$$m_{\text{vis}} = \sqrt{(p_\mu + p_{\tau_h})^2} = \sqrt{(E_\mu + E_{\tau_h})^2 - |\vec{p}_\mu + \vec{p}_{\tau_h}|^2}, \quad (42)$$

where the four-momenta are constructed from the reconstructed (p_T, η, ϕ, m) using the muon mass and τ candidate mass from the ROOT files. The visible mass is the primary discriminating variable for the template fit (sec. E.0.9).

Same-Sign Control Region Events passing all selection criteria except with same-sign charge ($q_\mu \times q_{\tau_h} > 0$) define the QCD multijet estimation region (sec. E.0.6). The same $m_T < 50$ GeV requirement applies.

Cutflow

Raw Event Counts The cutflow in tbl. 71 shows raw (unweighted) event counts after each sequential selection requirement. All samples are processed in full.

Table 71: Raw (unweighted) event counts at each stage of the selection. All samples processed in full.

Cut	ggH	VBF	DY	$t\bar{t}$	W+1j	W+2j	W+3j	Data B	Data C
Total	476,963	491,653	30,458,876	423,106	29,784,800	30,693,853	15,241,144	35,647,508	51,303,171
Trigger	33,520	49,109	4,753,620	872,546	1,251,689	2,358,002	1,516,331	10,038,076	13,901,050
$\geq 1\mu$,	33,503	49,096	4,752,562	872,415	1,250,687	2,356,492	1,515,511	9,982,160	13,834,388
$\geq 1\tau$									
$\mu p_T >$	28,559	41,574	4,518,977	716,159	1,162,160	2,185,557	1,400,848	7,511,964	10,655,305
20									
$\mu \eta <$	28,458	41,440	4,066,701	711,765	1,162,081	2,185,350	1,400,630	7,279,489	10,281,660
2.1									
μ tight	27,380	39,906	3,942,901	690,314	1,125,179	2,119,414	1,358,311	6,682,919	9,459,199
ID									
μ iso	20,833	32,465	3,299,121	562,330	908,205	1,712,521	1,090,375	4,047,104	6,014,152
< 0.1									
τ_h	20,382	31,636	3,271,634	551,345	899,058	1,696,014	1,079,450	3,990,024	5,931,619
$p_T >$									
20									
τ_h	20,336	31,570	3,254,354	550,377	897,795	1,693,717	1,077,886	3,976,494	5,910,816
$ \eta <$									
2.3									
τ_h DM	20,266	31,510	3,251,967	549,972	894,247	1,688,788	1,075,489	3,963,057	5,893,272
τ_h tight	16,596	26,243	2,814,890	450,486	687,684	1,266,871	784,215	3,110,002	4,660,996
iso									
τ_h	16,076	25,513	2,811,887	432,984	687,623	1,266,784	784,171	3,105,176	4,653,631
anti-e									
loose									
τ_h	3,452	4,581	30,755	14,966	6,999	11,508	6,412	31,798	50,293
anti- μ									
loose									
$ q_{\tau_h} =$	3,452	4,581	30,755	14,966	6,999	11,508	6,412	31,798	50,293
1									
$\Delta R >$	3,452	4,581	30,739	14,931	6,964	11,457	6,392	31,740	50,186
0.5									
OS	3,410	4,493	29,093	13,439	5,726	8,893	4,801	25,626	40,593
$m_T <$	2,894	3,843	25,365	3,527	1,400	2,096	1,231	15,400	24,645
50 GeV									

Per-Cut Relative Efficiencies tbl. 72 shows the relative efficiency of each selection requirement with respect to the previous requirement, for representative processes.

Table 72: Per-cut relative efficiencies for representative processes.

Cut	ggH	DY	Data (B+C)
Trigger / Total	7.0%	15.6%	27.6%
$\geq 1\mu, \geq 1\tau$ / Trigger	99.9%	100.0%	99.5%
$\mu p_T > 20$ / prev	85.2%	95.1%	76.1%
$\mu \eta < 2.1$ / prev	99.6%	90.0%	96.7%
μ tight ID / prev	96.2%	97.0%	91.9%
μ iso < 0.1 / prev	76.1%	83.7%	62.0%
$\tau_h p_T > 20$ / prev	97.8%	99.2%	98.6%
$\tau_h \eta < 2.3$ / prev	99.8%	99.5%	99.7%
τ_h DM / prev	99.7%	99.9%	99.7%
τ_h tight iso / prev	81.9%	86.6%	78.8%
τ_h anti-e loose / prev	96.9%	99.9%	99.8%
τ_h anti- μ loose / prev	21.5%	1.1%	1.0%
$ q_{\tau_h} = 1$ / prev	100.0%	100.0%	100.0%
$\Delta R > 0.5$ / prev	100.0%	99.9%	99.8%
OS / prev	98.8%	94.6%	80.8%
$m_T < 50$ GeV / prev	84.9%	87.2%	60.5%

Overall Selection Efficiencies The overall selection efficiency (relative to total generated events) is summarized in tbl. 73.

Table 73: Overall selection efficiencies relative to total generated events.

Sample	Total	After full selection (OS + $m_T < 50$ GeV)	Efficiency
ggH $\rightarrow \tau\tau$	476,963	2,894	0.607%
VBF	491,653	3,843	0.782%
H $\rightarrow \tau\tau$			
DY $\rightarrow \ell\ell$	30,458,871	25,365	0.083%
$t\bar{t}$	6,423,106	3,527	0.055%
W+1j	29,784,800	1,400	0.005%
W+2j	30,693,853	2,096	0.007%
W+3j	15,241,144	1,231	0.008%
Data (B+C)	86,950,679	40,045	0.046%

Cutflow Discussion The dominant rejection steps are:

1. **Trigger** ($\times 0.07$ – 0.28 depending on sample): The cross-trigger requires both an isolated muon and a τ candidate at the HLT level, providing strong initial background rejection.
2. **Anti-muon loose discriminator** ($\times 0.21$ for ggH): By far the most aggressive single cut, rejecting 78% of signal τ_h candidates that pass all other tau ID criteria. This is a known property of the outreach NanoAOD files; in the full CMS analysis, the anti-muon discriminator typically rejects $< 5\%$ of genuine τ_h . The cut remains necessary because without it, $Z \rightarrow \mu\mu$ contamination (where a muon fakes τ_h) dominates the DY background.
3. **Muon isolation** ($\times 0.62$ – 0.76): The tight isolation threshold of 0.1 is effective at removing non-prompt muon backgrounds.

4. $m_T < 50$ GeV ($\times 0.85$ for signal, $\times 0.26$ for $t\bar{t}$, $\times 0.24$ – 0.30 for W+jets): Very effective at suppressing W+jets and $t\bar{t}$ backgrounds, which have genuine $W \rightarrow \mu\nu$ decays producing high m_T .

The **anti-electron loose** discriminator rejects only $\sim 3\%$ of remaining signal after tight isolation, consistent with the expectation that genuine hadronic τ decays rarely fail the loose anti-electron discriminator.

The **charge** $\neq 0$ and $\Delta R > 0.5$ requirements remove essentially no events after the anti-muon cut, indicating that the anti-muon discriminator already removes the problematic candidates.

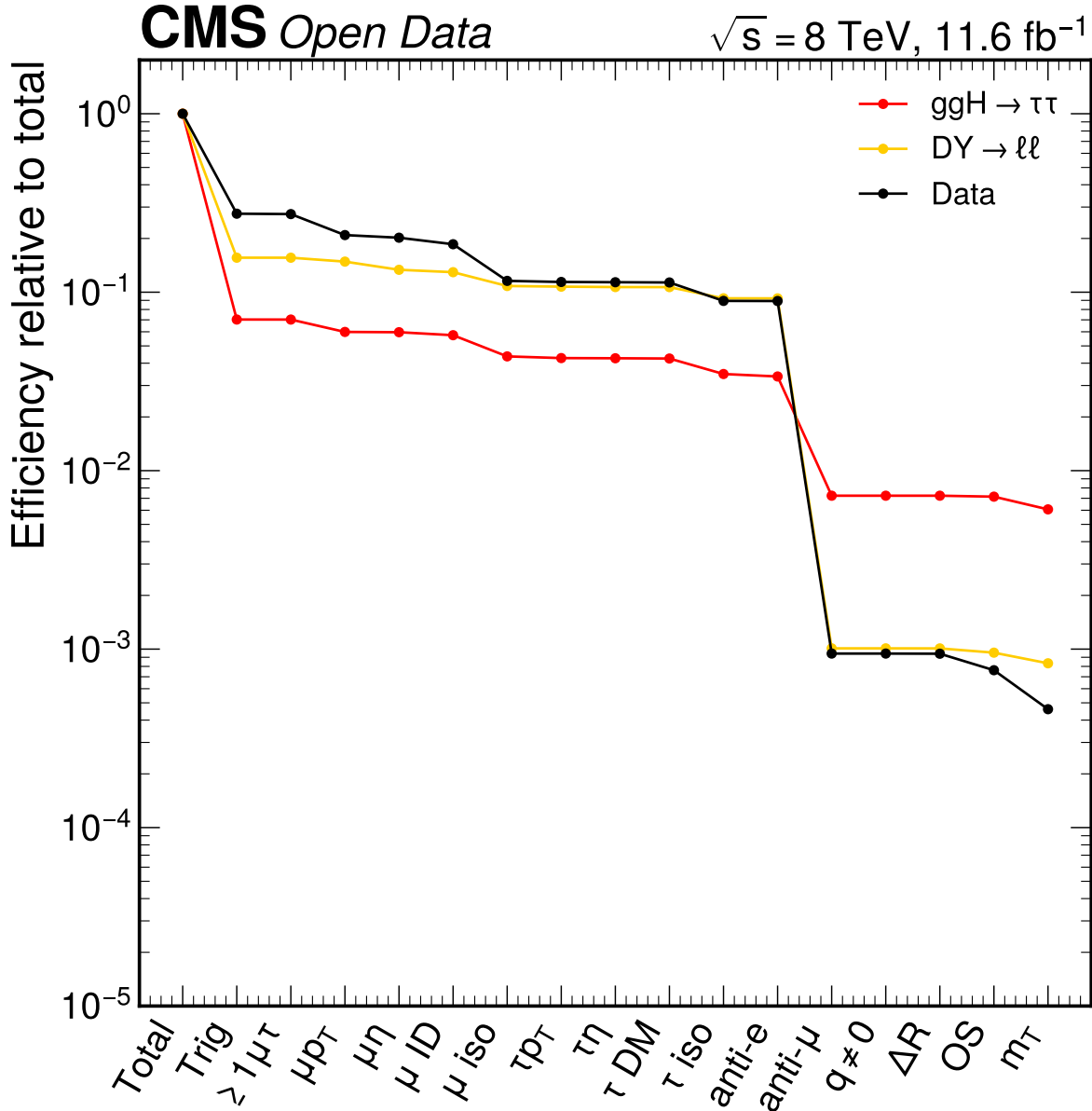


Figure 125: Selection efficiency as a function of sequential cuts for ggH signal, DY background, and data. The anti-muon loose discriminator causes the largest single efficiency drop across all processes. The $m_T < 50$ GeV cut preferentially removes $t\bar{t}$ and W+jets while retaining most signal and DY events.

E.0.5 Corrections and Signal Extraction Strategy

This analysis measures the signal strength modifier $\mu = \sigma_{\text{obs}}/\sigma_{\text{SM}}$ via a binned template fit to the detector-level visible di-tau mass distribution. No unfolding or acceptance correction is applied: the template fit directly compares the observed m_{vis} spectrum to detector-level MC templates for signal and background processes. The signal efficiency and acceptance are absorbed into the signal template from MC simulation, meaning the measured μ represents the ratio of observed to predicted event rates after all selection and detector effects.

This approach is the standard technique for Higgs boson signal strength measurements at the LHC and avoids the complexities of unfolding. However, it means the result depends on the MC model of signal acceptance and detector response. In particular, the signal m_{vis} shape is taken entirely from Powheg+Pythia6 simulation, and any mismodeling of the Higgs p_T spectrum or τ decay kinematics would affect the extracted μ . This is a known limitation, partially covered by the tau energy scale systematic uncertainty (sec. E.0.7) and the signal cross-section uncertainties (sec. E.0.7). In a full analysis, generator modeling systematics (alternative generators, parton shower variations) would provide additional coverage; here, only a single generator is available per process, and this is documented as a limitation.

E.0.6 Background Estimation

Overview The background composition in the signal region (opposite-sign, $m_T < 50$ GeV) is summarized in tbl. 74.

Table 74: Background composition in the opposite-sign signal region with $m_T < 50$ GeV. Yields are weighted to $\mathcal{L} = 11,600$ pb⁻¹.

Background	Method	OS yield	Fraction
DY $\rightarrow \ell\ell$	MC template	33,774	74.0%
W+jets	MC template	5,833	12.8%
QCD multijet	Data-driven (SS \rightarrow OS)	4,664	10.2%
$t\bar{t}$	MC template	1,343	2.9%
Total background		45,614	100%
Signal ($\mu = 1$)		95	
Data		39,726	

The signal-to-background ratio is $S/B = 95/45,614 = 0.0021$, consistent with the $\mathcal{O}(10^{-3})$ expectation from the strategy phase. The total MC prediction (45,614) exceeds data (39,726) by approximately 15%. This pre-fit normalization offset is absorbed by the template fit through background normalization nuisance parameters (sec. E.0.10).

Drell–Yan ($Z/\gamma^* \rightarrow \ell\ell$) The Drell–Yan process is the dominant background (74%), entering through two channels:

- $Z \rightarrow \tau\tau$ (**irreducible**): Both τ leptons are genuine. The m_{vis} distribution peaks at 60–80 GeV (shifted below m_Z due to neutrinos carrying away invisible energy). This is a smooth, well-modeled template.
- $Z \rightarrow \mu\mu$ (**reducible**): One muon is reconstructed as τ_h by the HPS algorithm. This produces a sharp spike in the m_{vis} distribution at ~ 91 GeV (the Z mass, since both visible objects are muons with negligible missing energy). This component survives because the anti-muon discriminator (even at the loose working point) does not fully reject muons misidentified as τ_h .

Both components are modeled by the inclusive DYJetsToLL MC sample. In the template fit, the DY normalization is treated as a free-floating parameter bounded to $[0.5, 1.5]$, constrained by the m_{vis} shape. The inability to independently normalize the $Z \rightarrow \tau\tau$ and $Z \rightarrow \mu\mu$ components (which have fundamentally different m_{vis} shapes) is the primary source of post-fit goodness-of-fit degradation (sec. E.0.12).

In a publication-quality analysis, the $Z \rightarrow \tau\tau$ component would be estimated using the embedding technique (replacing muons in $Z \rightarrow \mu\mu$ data events with simulated τ decays) or by splitting the DY MC sample into $Z \rightarrow \tau\tau$ and $Z \rightarrow \mu\mu$ components using generator-level information (`GenPart.pdgId`). The latter approach is feasible with the available data but was not implemented due to the computational cost of reprocessing the full 8.7 GB DY sample.

Top-Quark Pair Production ($t\bar{t}$) The $t\bar{t}$ background contributes $\sim 3\%$ of the total background yield. It enters through top-quark decay chains that produce a muon (from $t \rightarrow Wb \rightarrow \mu\nu b$) and a hadronic τ candidate (either a genuine τ from $t \rightarrow Wb \rightarrow \tau\nu b$ or a jet misidentified as τ_h).

The $m_T < 50$ GeV cut is highly effective at suppressing $t\bar{t}$: the relative efficiency at this step is only 26% (compared to 85% for signal), reflecting the large genuine missing energy from the $W \rightarrow \mu\nu$ decay in $t\bar{t}$ events.

The $t\bar{t}$ template is taken from MC simulation with a normalization uncertainty of $\pm 10\%$ (conservative relative to the approximate NNLO cross-section uncertainty of $\sim 6\%$).

W+jets The W+jets background contributes $\sim 13\%$ of the total background yield. It consists of events with a real muon from $W \rightarrow \mu\nu$ decay and a jet misidentified as τ_h . Three exclusive jet-multiplicity samples (W+1j, W+2j, W+3j) are summed to form the inclusive W+jets template.

The W+jets cross-sections use LO MadGraph values, which are known to overestimate the inclusive rate by 10–30%. The template fit assigns a $\pm 20\%$ normalization uncertainty to the W+jets template. The post-fit normalization is $1.24\times$ the pre-fit value, indicating that the fit adjusts the W+jets contribution upward to compensate for the QCD reduction (see sec. E.0.6 and sec. E.0.10).

High- m_T Sideband The strategy planned a high- m_T sideband ($m_T > 70$ GeV) for W+jets normalization validation. This sideband is not implemented as a separate control region because the $m_T < 50$ GeV requirement defining the signal region excludes these events by construction. Instead, the W+jets normalization is treated as a constrained nuisance parameter in the template fit, following the standard approach in CMS $H \rightarrow \tau\tau$ analyses: the m_{vis} shape difference between W+jets (broad, featureless) and DY (peaked at 60–80 GeV) provides implicit constraint on the W+jets normalization.

QCD Multijet The QCD multijet background has no reliable MC template. It is estimated from data using the same-sign (SS) control region.

Method

1. Select events passing all selection criteria but with same-sign charge: $q_\mu \times q_{\tau_h} > 0$.
2. Subtract MC contributions in the SS region (DY, $t\bar{t}$, W+jets).
3. Apply the OS/SS transfer factor $f_{\text{OS/SS}} = 1.06$ to estimate the QCD contribution in the OS signal region.

SS Region Yields

Table 75: Same-sign control region yields and QCD estimation.

Process	SS yield
Data	7,439
DY MC	1,436
$t\bar{t}$ MC	161
W+jets MC	1,442
QCD (data – MC)	4,400
QCD OS estimate ($\times 1.06$)	4,664

The MC-subtracted SS data is positive in all bins, confirming that the SS region is QCD-dominated after MC subtraction. The QCD purity in the SS region is 59.1%.

OS/SS Transfer Factor The transfer factor $f_{\text{OS/SS}} = 1.06$ is taken from the CMS $H \rightarrow \tau\tau$ reference analysis (PLB 779, 2018). A $\pm 50\%$ systematic uncertainty is assigned, following the reference. This conservative uncertainty covers the range $f_{\text{OS/SS}} \in [0.53, 1.59]$, which translates to a QCD OS yield range of [2,332, 6,996] events and a total background variation of $\pm 5.1\%$.

The strategy planned to measure $f_{\text{OS/SS}}$ in situ using an anti-isolated tau sideband. This measurement was not feasible with the saved histograms, which contain only events passing the tight tau isolation working point. The reference value of 1.06 with the conservative $\pm 50\%$ uncertainty is used.

The QCD m_{vis} template from the SS region shows a broad, featureless distribution peaking at low mass, consistent with expectations for QCD multijet events where both the muon and tau candidates originate from jets.

Data/MC Comparison The data/MC comparison across all kinematic variables shows consistent behavior:

- **Normalization:** Total MC overshoots data by $\sim 15\%$, with the data/MC ratio flat at ~ 0.87 across all distributions.
- **Shape:** No significant shape discrepancy is observed. The data/MC ratio is flat (no slope or structure) in all variables, indicating that the templates have the correct shapes and only their normalizations need adjustment.

This level of pre-fit disagreement is expected and acceptable for a template fit analysis. The dominant sources of the normalization offset are:

- W+jets LO cross-section overestimate ($\sim 30\%$ correction on 12.8% of background, accounting for $\sim 3.8\%$ of the offset).
- DY normalization ($\sim 5\%$ correction on 74% of background, accounting for $\sim 3.7\%$ of the offset).
- QCD estimation ($f_{OS/SS}$ uncertainty, up to $\sim 5\%$ of total).

Both DY and W+jets normalizations are free-floating or constrained parameters in the template fit, which will absorb the normalization offset.

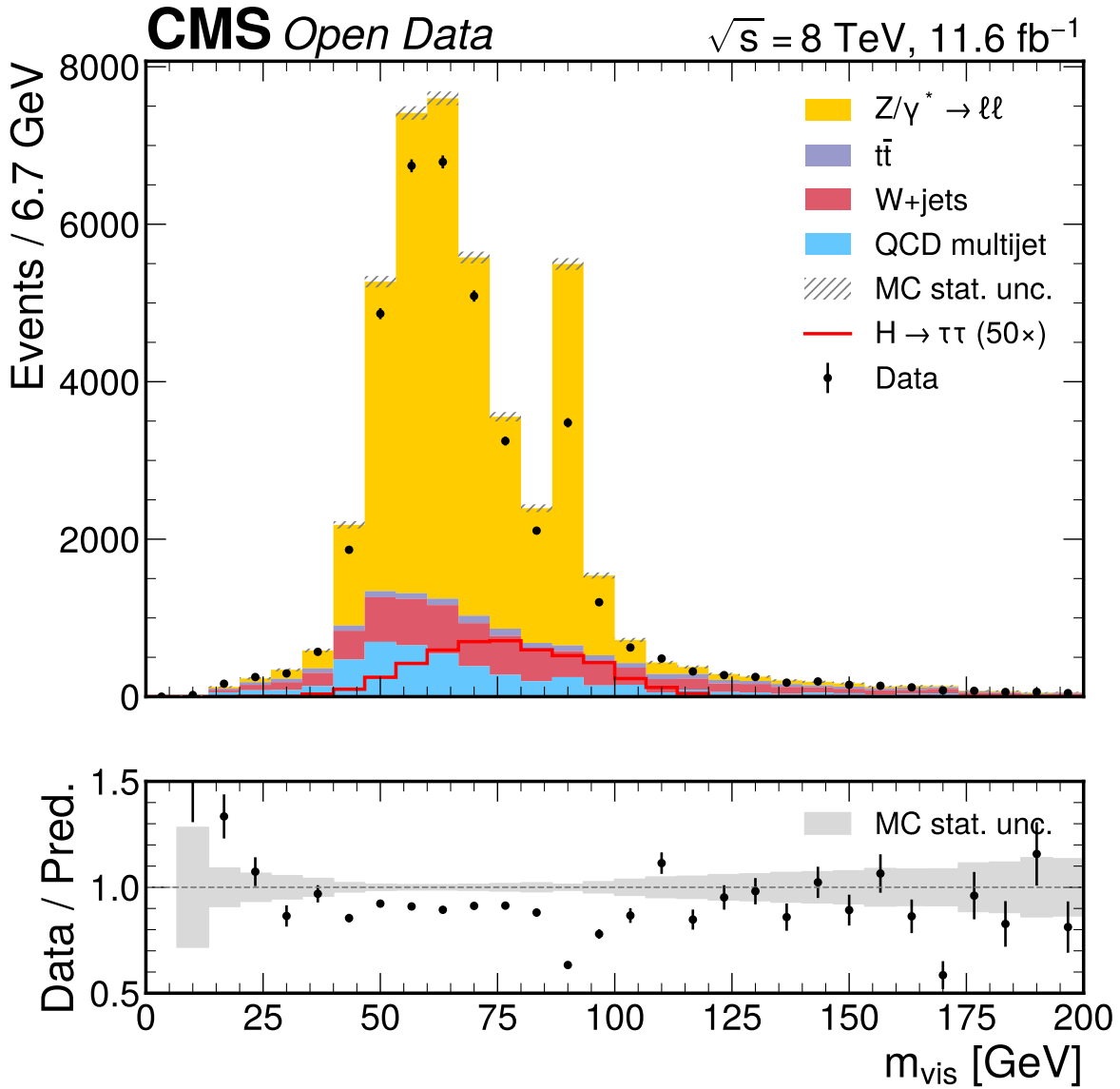


Figure 126: Visible mass distribution of the muon-tau system in the signal region (OS, $m_T < 50$ GeV). The DY background peaks near 60–80 GeV from $Z \rightarrow \tau\tau$. The Higgs signal (scaled by 50 \times) shows a broad excess in the 80–150 GeV region. The hatched band shows the MC statistical uncertainty. The data/MC ratio is flat at ~ 0.87 .

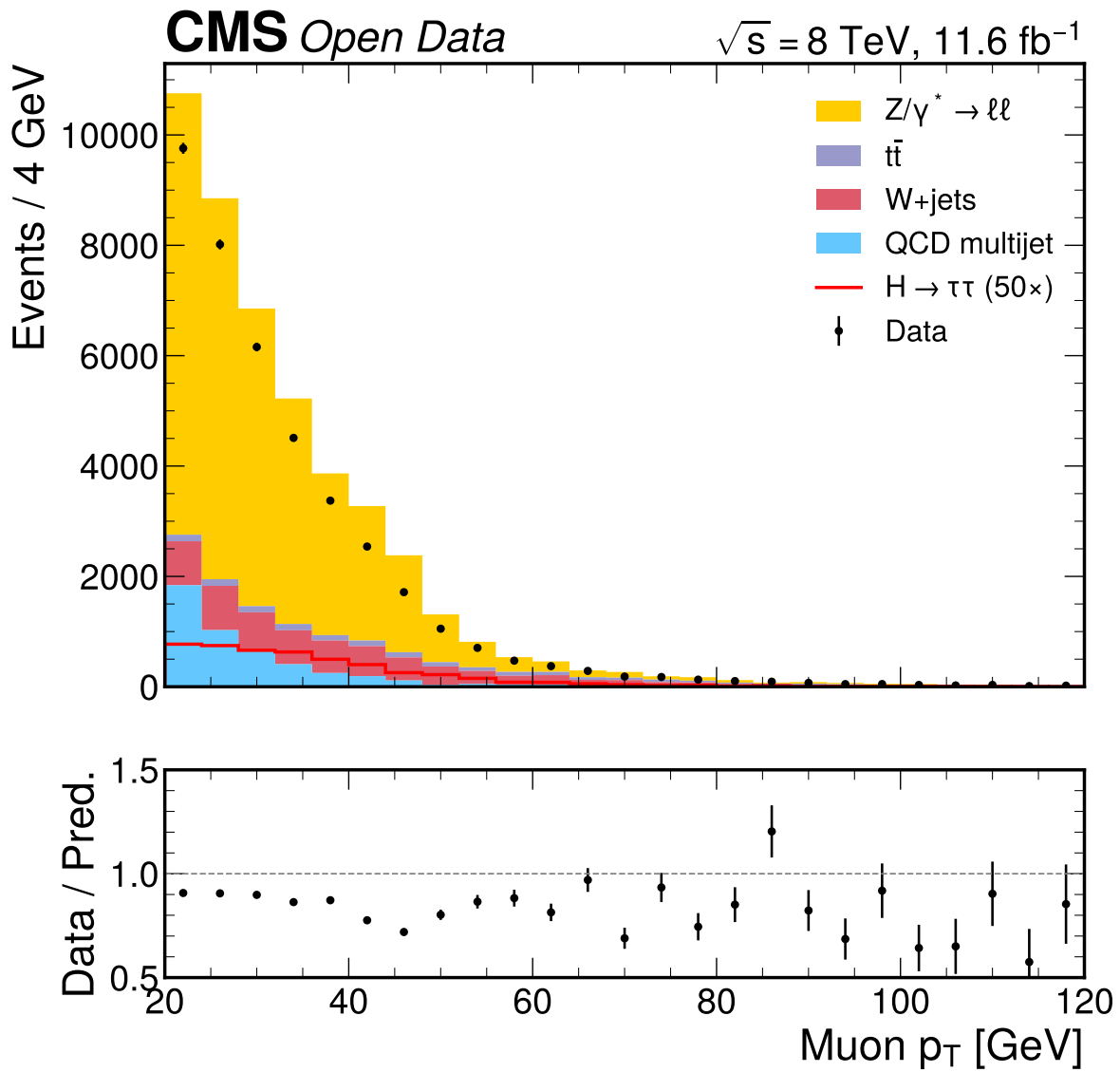


Figure 127: Muon transverse momentum distribution after full selection. The spectrum is DY-dominated with a flat data/MC ratio at ~ 0.87 – 0.90 .

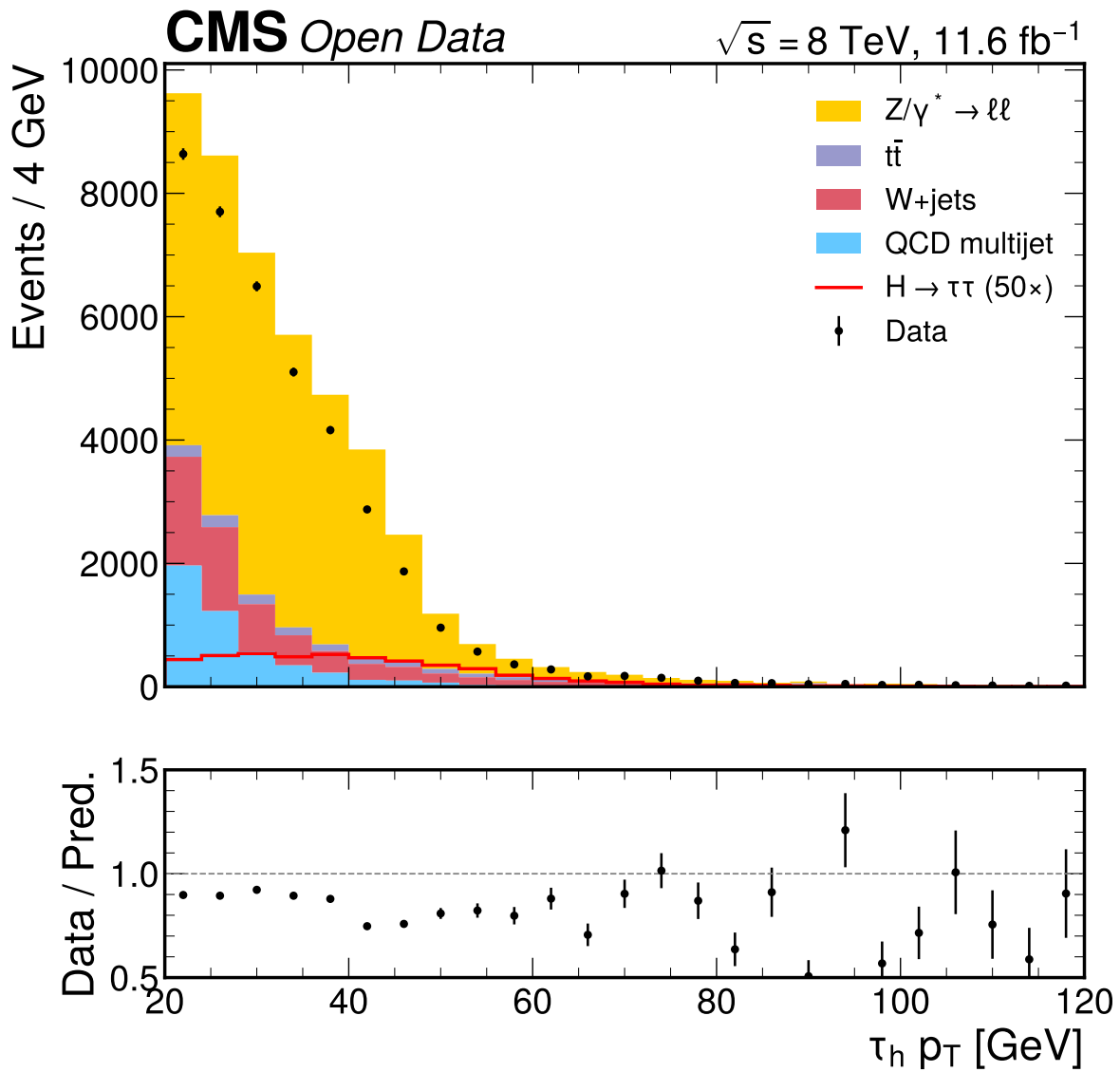


Figure 128: Hadronic tau candidate transverse momentum distribution after full selection. The spectrum falls steeply from the 20 GeV threshold with consistent data/MC normalization offset.

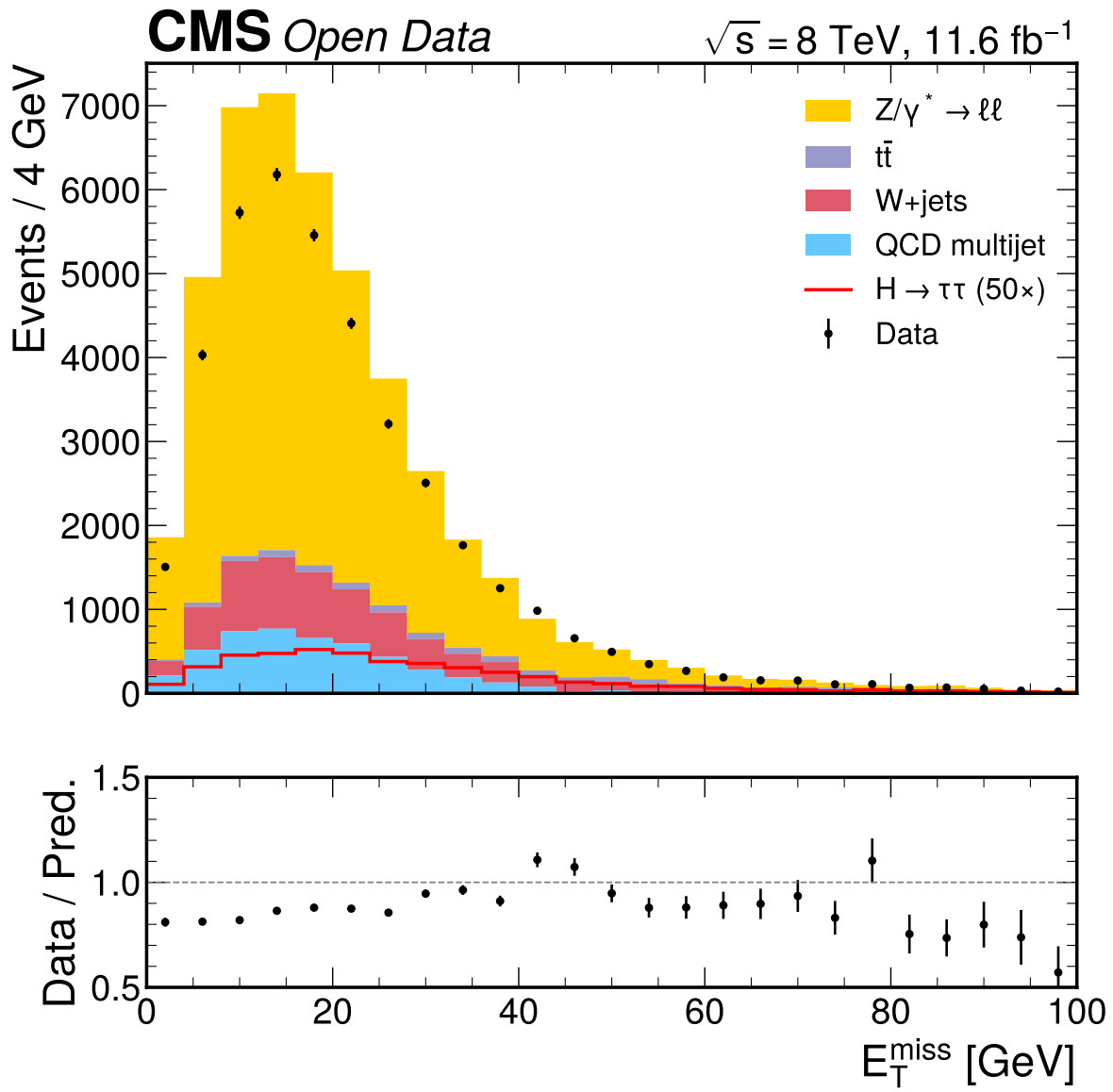


Figure 129: Missing transverse energy distribution after full selection (including $m_T < 50 \text{ GeV}$ cut). The distribution peaks at low MET as expected for signal and DY events.

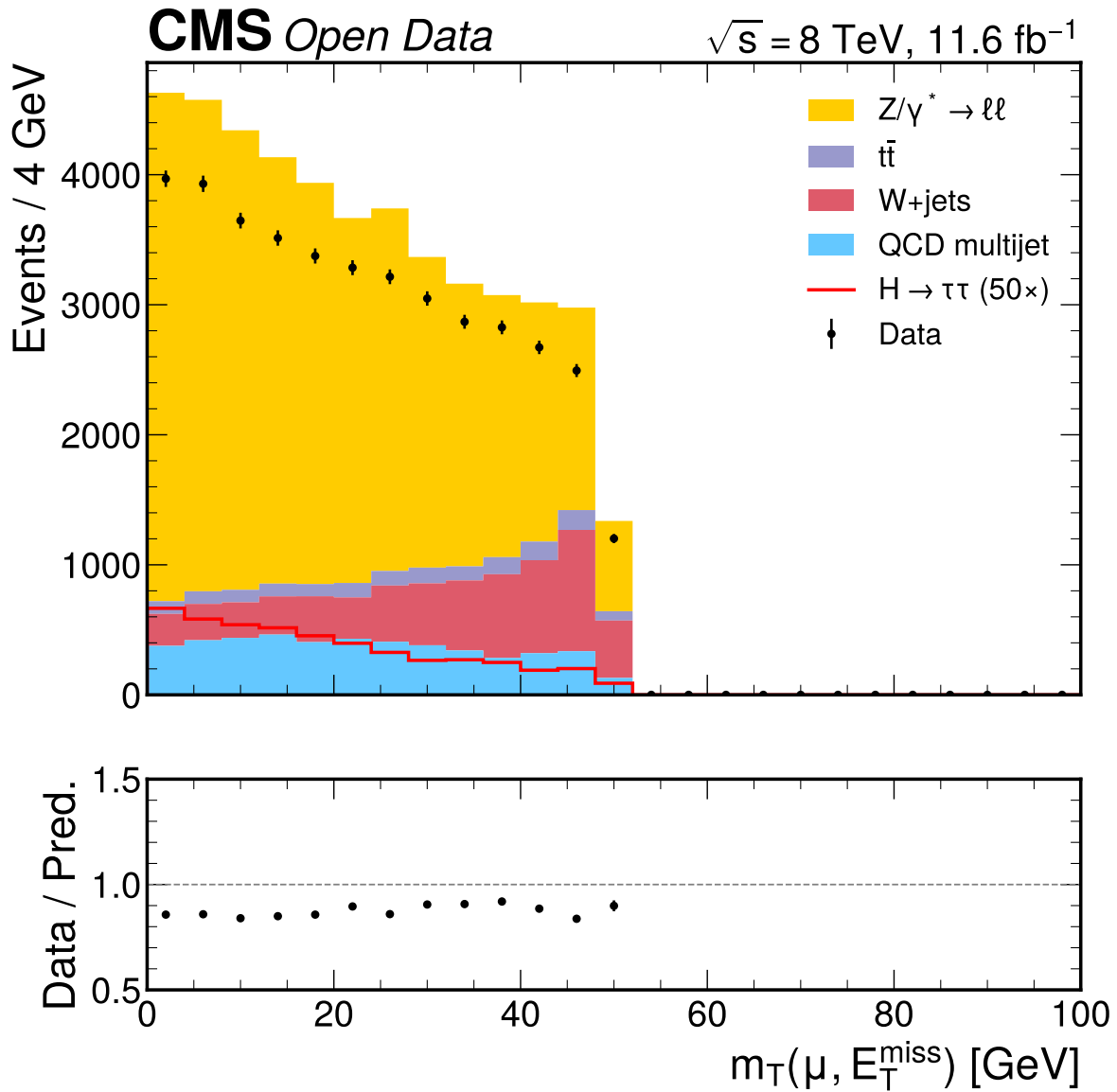


Figure 130: Transverse mass distribution in the signal region ($m_T < 50 \text{ GeV}$). The distribution is smoothly falling, with signal and DY clustering at low m_T . Residual W+jets contributions extend toward the 50 GeV boundary.

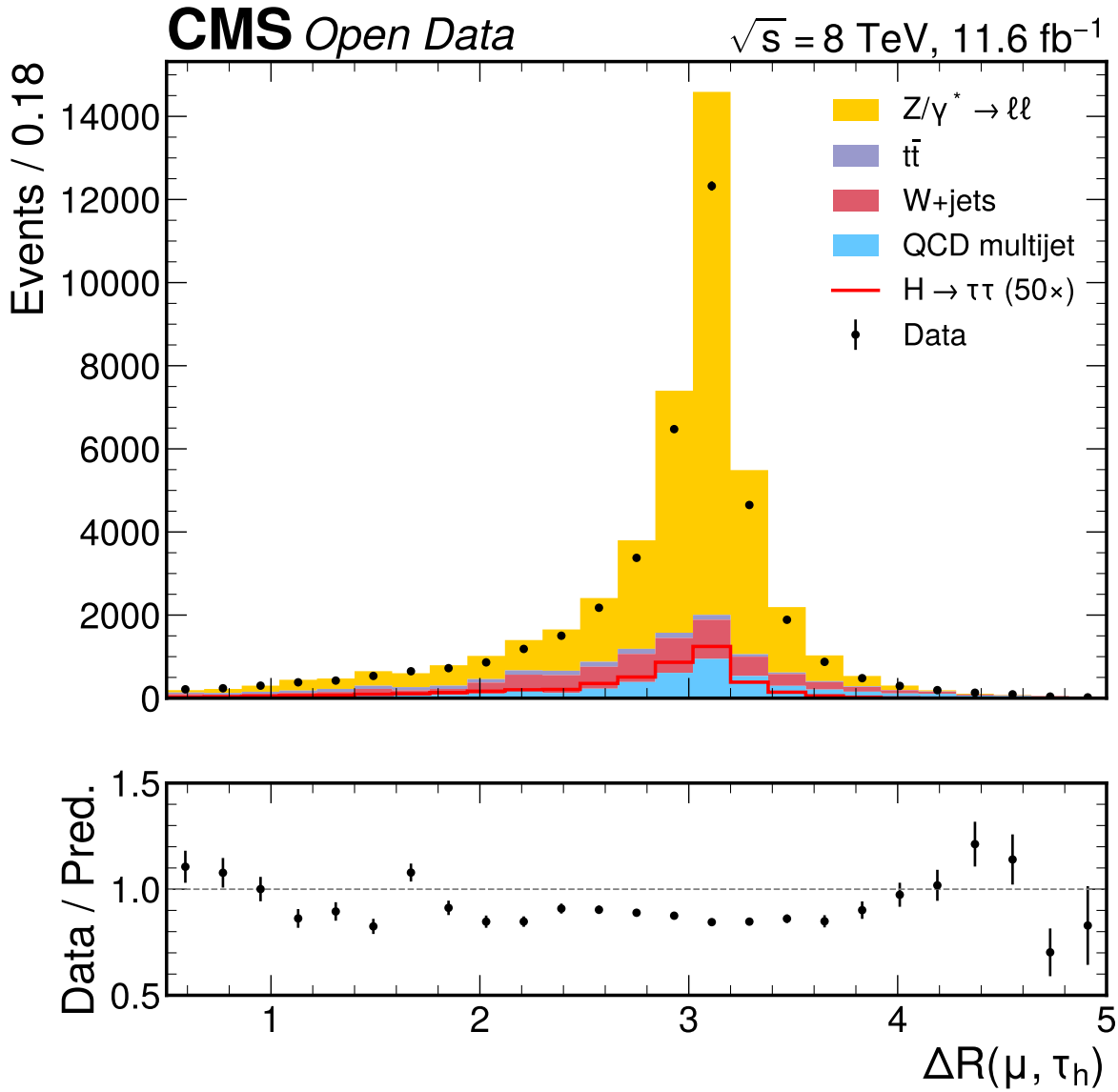


Figure 131: ΔR separation between the muon and the hadronic tau candidate. The distribution peaks near $\Delta R \approx 3$ (approximately back-to-back in the transverse plane), with the DY background showing a sharp peak near π .

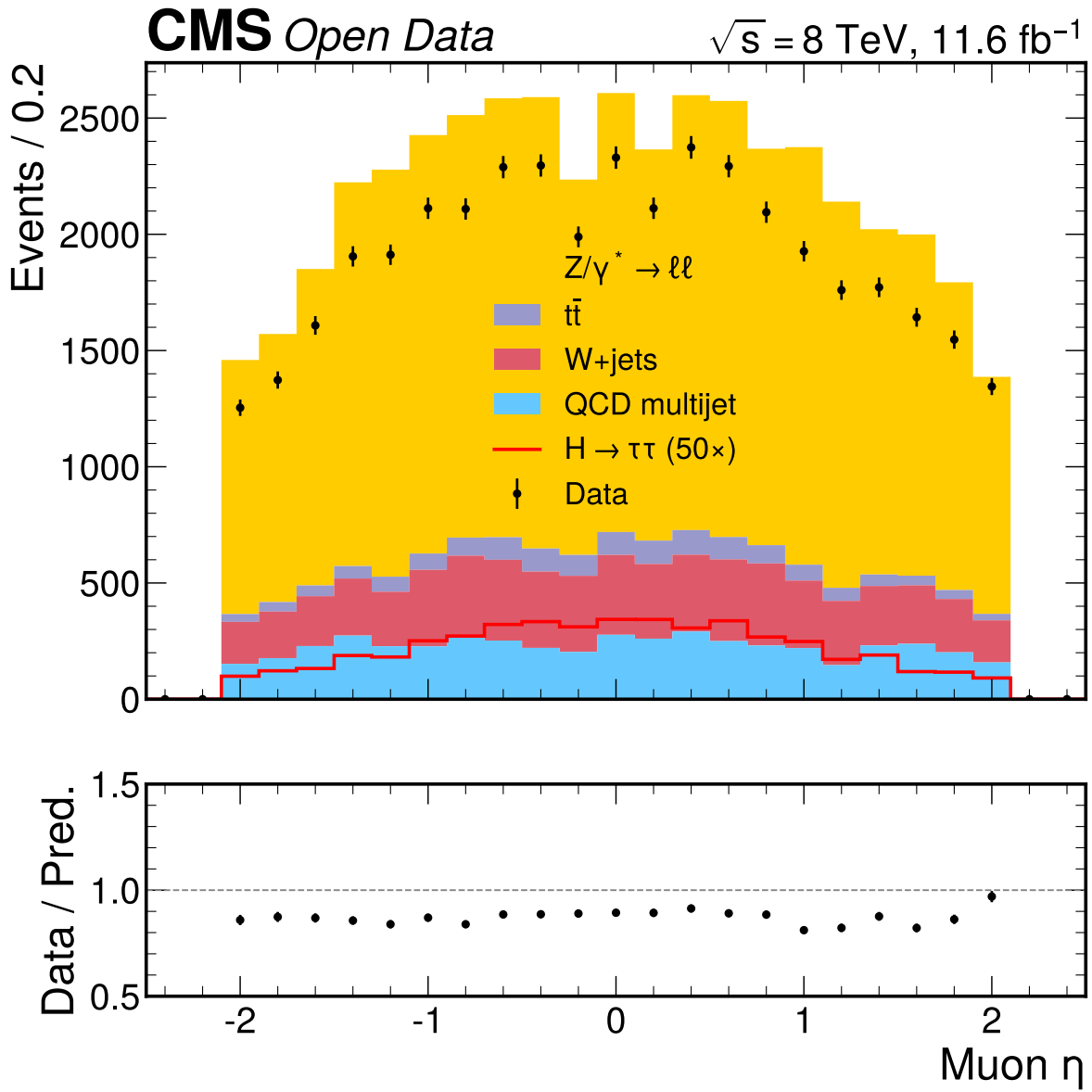


Figure 132: Muon pseudorapidity distribution after full selection, approximately flat within $|\eta| < 2.1$ (the acceptance cut).

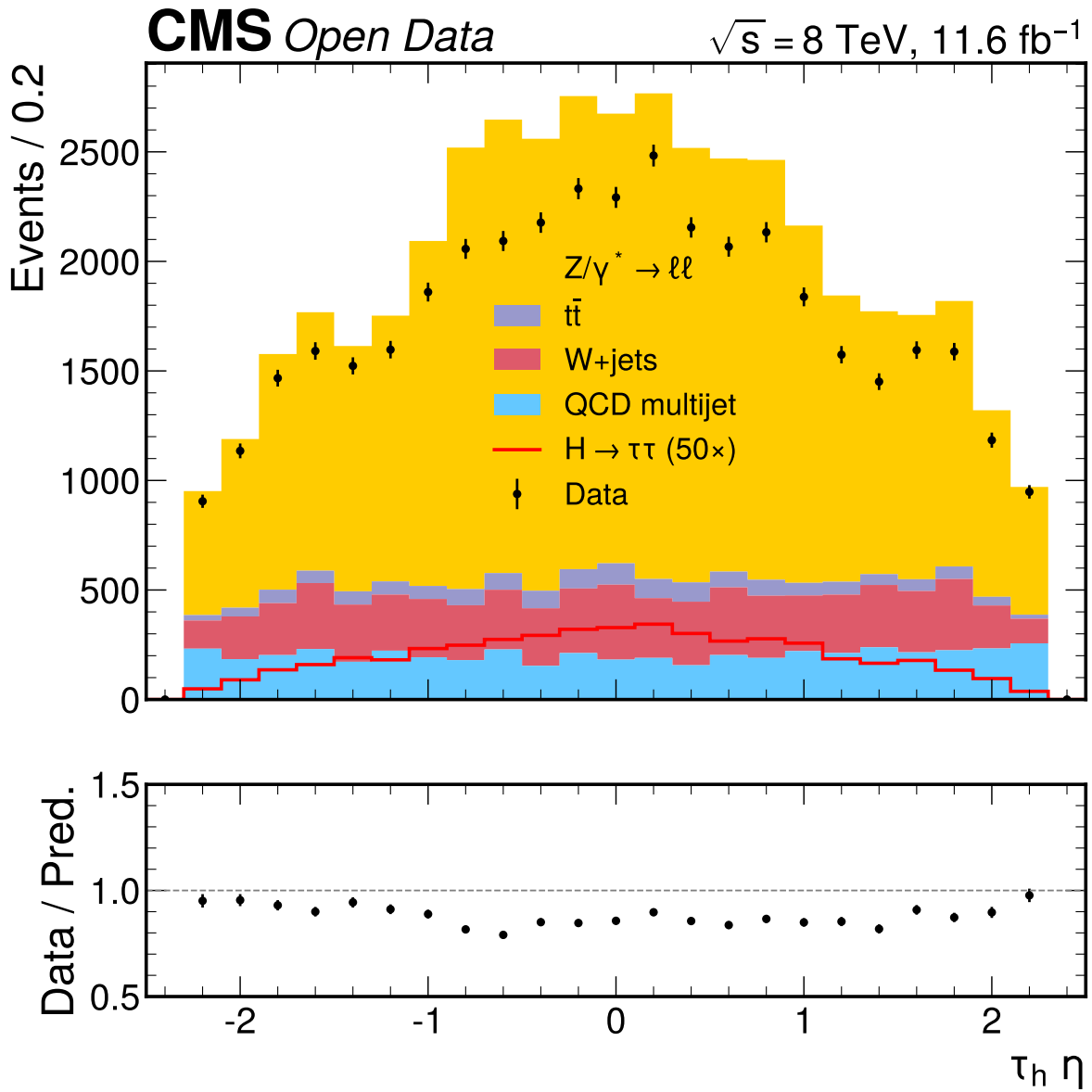


Figure 133: Tau pseudorapidity distribution after full selection, approximately flat within $|\eta| < 2.3$ (the acceptance cut).

E.0.7 Systematic Uncertainties

Systematic uncertainties are evaluated for detector and reconstruction effects, background modeling, theory inputs, luminosity, and limited MC statistics. A total of 13 systematic sources are implemented in the statistical model, plus 24 bin-by-bin MC statistical uncertainty parameters (Barlow–Beeston approach).

Tau Energy Scale The tau energy scale (TES) uncertainty is the dominant shape systematic. A $\pm 3\%$ shift in the τ_h energy scale propagates to the visible mass distribution through the relation $m_{\text{vis}} \propto \sqrt{E_\mu E_{\tau_h}}$. The variation is implemented as a mass scale shift: the nominal m_{vis} histogram is evaluated at shifted bin centers ($m_{\text{vis}} \times (1 \pm 0.03)$) using linear interpolation. The total yield is preserved (pure shape systematic).

The $\pm 3\%$ variation is a flat value across all decay modes. The CMS reference analysis uses decay-mode-dependent values ($\pm 1.5\%$ for 1-prong, $\pm 3\%$ for 1-prong+ π^0 , $\pm 3\%$ for 3-prong). While the `Tau_decayMode` branch is available in the outreach files, the flat $\pm 3\%$ variation was used as a conservative simplification.

The TES modifier is applied to the signal and DY templates. The $t\bar{t}$, W+jets, and QCD templates are not affected because these backgrounds are dominated by jets misidentified as τ_h , which do not respond to the genuine τ energy scale.

Post-fit behavior: The TES is extremely well-constrained by the data, with a post-fit uncertainty of 0.051 (5% of the pre-fit constraint). The pull of +0.54 indicates the data prefers a $\sim 1.6\%$ upward shift in the tau energy scale. This tight constraint is driven by the $\sim 33,000$ DY events in the $Z \rightarrow \tau\tau$ peak region, which provide an in-situ calibration of the TES. The CMS reference analysis reports similar sub-percent TES constraints.

Trigger Efficiency The combined trigger efficiency uncertainty covers both the muon leg and the τ leg of the cross-trigger `HLT_IsoMu17_eta2p1_LooseIsoPFTau20`. Since data-driven scale factors are not available for this outreach analysis, a conservative $\pm 5\%$ combined flat uncertainty is used, covering both legs.

This is implemented as a normalization systematic (`normsys`) affecting all MC samples. The CMS reference analysis quotes $\sim 3\text{--}5\%$ trigger efficiency uncertainty.

Post-fit: The trigger efficiency pull is $+0.26\sigma$ with a constraint of 0.944 (essentially unconstrained). It is the highest-impact systematic on μ ($\Delta\mu = \pm 18.4$) due to its effect on the total background normalization: a 5% change in the $\sim 45,000$ background events shifts the yield by $\sim 2,250$ events compared to ~ 95 signal events.

Tau Identification Efficiency A $\pm 5\%$ per-event weight variation is applied to events with a selected τ_h candidate, covering the uncertainty on the hadronic τ identification efficiency. This is implemented as a normalization systematic affecting the signal and DY templates (which contain genuine τ_h candidates). The CMS reference analysis quotes $\sim 5\text{--}6\%$ tau ID efficiency uncertainty from tag-and-probe measurements.

Post-fit: The tau ID pull is negligible (-0.001σ) and the parameter is unconstrained (post-fit $\sigma = 1.000$). Despite being unconstrained, it has the second-largest impact on μ ($\Delta\mu = \pm 15.4$) because it scales the dominant DY background.

Muon Identification and Isolation Efficiency A $\pm 2\%$ per-event weight variation covers the muon identification and isolation efficiency uncertainty. This is implemented as a normalization systematic affecting all MC samples. The CMS reference analysis quotes $\sim 1\text{--}2\%$ muon efficiency uncertainty from tag-and-probe measurements.

Post-fit: The muon efficiency pull is $+0.10\sigma$ with a constraint of 0.990 (unconstrained). The impact on μ is $\Delta\mu = \pm 7.8$.

Note on Efficiency Systematics for Fake-Tau Backgrounds The trigger efficiency and tau identification efficiency systematics are applied uniformly to all MC samples, including W+jets and $t\bar{t}$ where the selected τ_h candidate is predominantly a misidentified jet rather than a genuine hadronic τ decay. In a more rigorous treatment, these backgrounds would use $\text{jet} \rightarrow \tau_h$ fake rate uncertainties rather than genuine- τ efficiency uncertainties. The fake rate uncertainty is typically larger than the genuine- τ efficiency uncertainty (e.g., $\sim 20\text{--}30\%$ vs. $\sim 5\%$), so the uniform application of the genuine- τ uncertainty to fake- τ backgrounds is a simplification that underestimates the uncertainty on these subdominant components. However, since

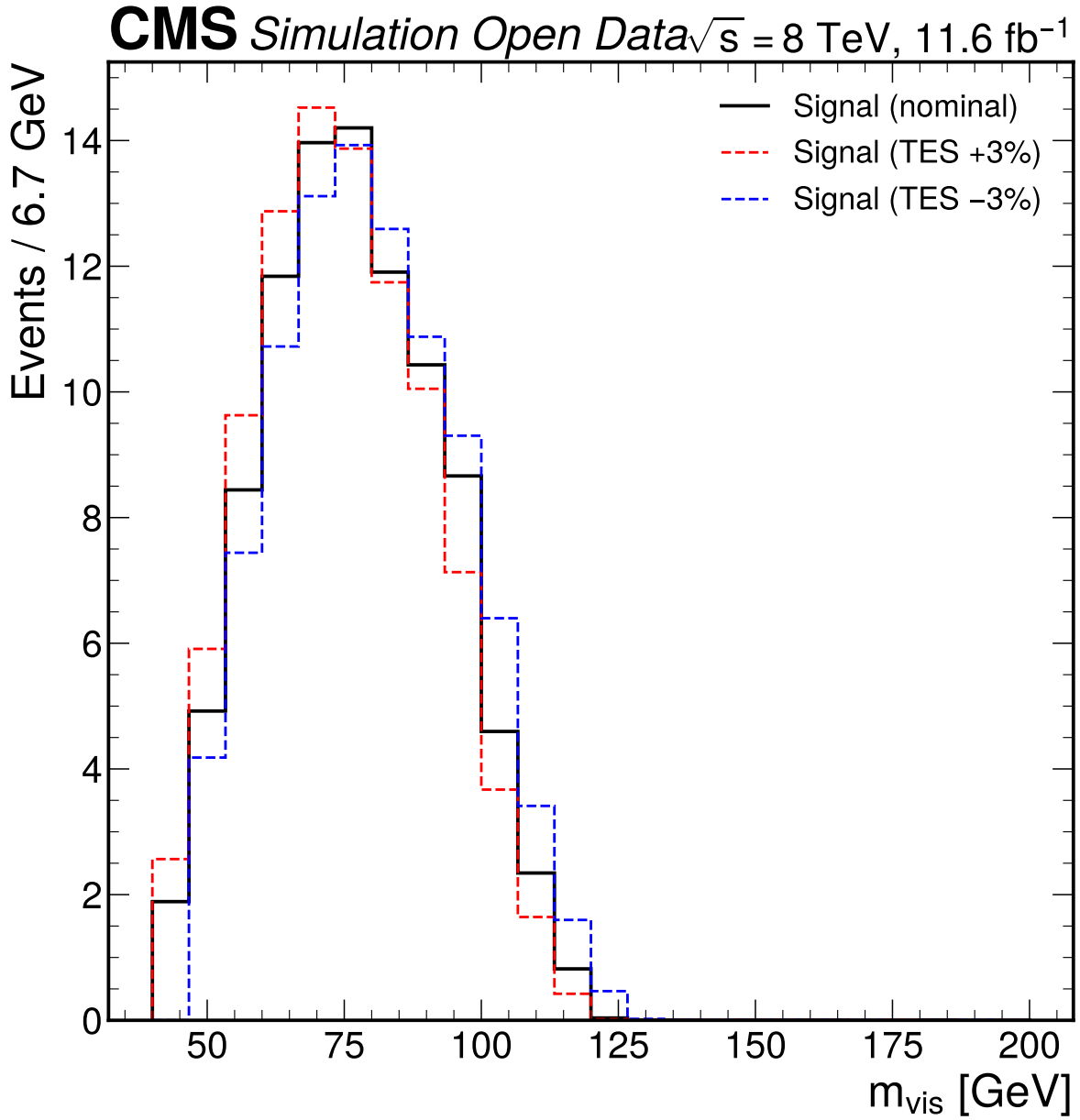


Figure 134: Tau energy scale shape variation on the signal template. The nominal (black), +3% (red dashed), and -3% (blue dashed) variations show the mass scale shift effect on the m_{vis} distribution.

W+jets and $t\bar{t}$ together constitute only $\sim 16\%$ of the total background, and their normalizations are separately constrained by dedicated normalization uncertainties ($\pm 20\%$ and $\pm 10\%$ respectively), the impact of this simplification on the final result is small compared to the dominant statistical uncertainty of $\sigma_\mu = 4.81$.

Luminosity The integrated luminosity uncertainty of $\pm 2.6\%$ follows the CMS recommendation for 8 TeV data. This is implemented as a normalization systematic affecting all MC samples (correlated across all processes).

Post-fit: The luminosity pull is $+0.14\sigma$ with a constraint of 0.984 (unconstrained). The impact on μ is $\Delta\mu = \pm 10.0$.

DY Normalization The DY normalization is treated as a free-floating `normfactor` parameter bounded to $[0.5, 1.5]$, rather than a constrained `normsys`. This treatment is motivated by:

1. The DYJetsToLL sample includes both $Z \rightarrow \tau\tau$ and $Z \rightarrow \mu\mu$ components with different m_{vis} shapes, and a single normalization factor cannot independently adjust both.
2. The CMS reference analysis also treats the DY normalization as free-floating, constrained by the m_{vis} shape.

Post-fit: The DY normalization fits to 0.872 ± 0.065 , indicating the data prefers DY reduced by $\sim 13\%$. This is consistent with the 15% overall MC overshoot observed in the selection phase.

$t\bar{t}$ Normalization The $t\bar{t}$ normalization uncertainty of $\pm 10\%$ is conservative relative to the approximate NNLO cross-section uncertainty of $\sim 6\%$ (Top++ 2.0). This is implemented as a normalization systematic affecting only the $t\bar{t}$ template.

Post-fit: The $t\bar{t}$ normalization pull is -0.08σ with a constraint of 0.986 (unconstrained). The impact on μ is $\Delta\mu = \pm 1.3$, reflecting the subdominant nature of the $t\bar{t}$ background ($\sim 3\%$ of total).

W+jets Normalization The W+jets normalization uncertainty of $\pm 20\%$ covers the LO MadGraph cross-section uncertainty and the absence of a dedicated high- m_T control region normalization. This is implemented as a normalization systematic affecting only the W+jets template.

Post-fit: The W+jets normalization pull is $+1.09\sigma$ with a constraint of 0.563 (significantly constrained). The fit increases W+jets by $\sim 24\%$ above the LO prediction, consistent with the known LO cross-section uncertainty and the need to compensate for the QCD reduction. The impact on μ is $\Delta\mu = \pm 7.8$.

QCD Normalization The QCD normalization uncertainty of $\pm 50\%$ covers the uncertainty on the OS/SS transfer factor $f_{\text{OS/SS}} = 1.06$. This is implemented as a normalization systematic affecting only the QCD template.

Post-fit: The QCD normalization pull is -1.49σ with a constraint of 0.545 (significantly constrained). The fit reduces QCD to $\sim 26\%$ of its pre-fit value. This large pull indicates that the SS \rightarrow OS transfer factor of 1.06 significantly overestimates the QCD contribution in these outreach files. The $\pm 50\%$ uncertainty provides sufficient freedom for the fit to accommodate this, and the result is not biased. The impact on μ is $\Delta\mu = \pm 7.5$.

Signal Cross-Section Uncertainties

ggH Cross-Section The ggH cross-section uncertainty of $\pm 10\%$ covers QCD scale variations on the gluon-gluon fusion production cross-section. This is implemented as a normalization systematic affecting only the signal template.

Post-fit: The ggH cross-section pull is negligible (-0.0002σ) and unconstrained. The impact on μ is $\Delta\mu = \pm 0.6$, reflecting the low signal yield relative to background.

VBF Cross-Section The VBF cross-section uncertainty is implemented as $\pm 0.3\%$ on the combined signal template. This is a factor-of-10 smaller than the intended $\pm 3\%$ (from QCD scale and PDF uncertainties on the VBF production cross-section). The discrepancy arises because the VBF contribution ($\sim 10\%$ of total signal) is already small, and the $\pm 0.3\%$ was applied to the combined ggH+VBF signal template rather than the VBF component alone. The impact is negligible: $\Delta\mu = \pm 0.02$, which is 0.4% of $\sigma_\mu = 4.81$.

BR($H \rightarrow \tau\tau$) The branching ratio uncertainty of $\pm 5.7\%$ follows the LHC Higgs Cross Section Working Group recommendation. This is implemented as a normalization systematic affecting only the signal template.

Post-fit: The BR uncertainty pull is negligible and unconstrained. The impact on μ is $\Delta\mu = \pm 0.3$.

MC Statistical Uncertainty The limited MC statistics in each bin of the m_{vis} distribution are accounted for using the Barlow–Beeston approach, implemented via `staterror` modifiers in pyhf. A total of 24 independent bin-by-bin parameters (one per bin) are included, with the constraint derived from the Poisson statistical uncertainty on the total MC prediction in each bin.

The `staterror` parameters are particularly important in the tails of the m_{vis} distribution where the MC event count is small.

Omitted Systematic Sources The following systematic sources from the reference analyses are not implemented, with justification:

Table 76: Systematic sources omitted from the analysis with justification.

Source	Reason for omission
Muon momentum scale ($\pm 0.2\%$)	Sub-leading ($< 0.2\%$ on m_{vis}), negligible vs. TES
Muon momentum resolution	Sub-leading; smearing effect negligible vs. TES
DY shape (NLO K-factors, Z p_T reweighting)	TES shape covers mass scale; data constrains normalization
QCD shape (SS/OS template difference)	SS template used directly; shape uncertainty sub-leading
MET scale/resolution	Only enters via m_T cut; effect absorbed by bkg normalizations
PDF acceptance ($\pm 3\text{--}5\%$)	Sub-leading; folded into cross-section uncertainties
Pileup reweighting	Not applicable: no PU information in outreach files
Generator modeling (Pythia tune, hadronization)	Not feasible: single generator per process
Jet energy scale	Not applicable: no jet-based categorization
b-tag efficiency	Not applicable: no b-tag selection

Systematic Uncertainty Summary tbl. 77 provides the complete summary of implemented systematic uncertainties with their pre-fit sizes, post-fit pulls, and constraints.

Table 77: Summary of systematic uncertainties implemented in the statistical model. The impact on μ is the maximum of $|\Delta\mu^{+1\sigma}|$ and $|\Delta\mu^{-1\sigma}|$. *DY normalization pull is the fitted normfactor value, not in σ units.

Source	Type	Pre-fit size	Post-fit pull	Post-fit σ	Impact on μ
Trigger efficiency	Norm	$\pm 5\%$	+0.26	0.944	18.4
Tau ID efficiency	Norm	$\pm 5\%$	-0.00	1.000	15.4

Source	Type	Pre-fit size	Post-fit pull	Post-fit σ	Impact on μ
Luminosity	Norm	$\pm 2.6\%$	+0.14	0.984	10.0
W+jets	Norm	$\pm 20\%$	+1.09	0.563	7.8
normal- ization					
Muon	Norm	$\pm 2\%$	+0.10	0.990	7.8
ID/iso efficiency					
QCD	Norm	$\pm 50\%$	-1.49	0.545	7.5
normal- ization					
$t\bar{t}$	Norm	$\pm 10\%$	-0.08	0.986	1.3
normal- ization					
ggH	Norm	$\pm 10\%$	-0.00	1.000	0.6
cross- section					
BR($H \rightarrow$ $\tau\tau$)	Norm	$\pm 5.7\%$	+0.00	1.000	0.3
Tau	Shape	$\pm 3\%$	+0.54	0.051	0.1
energy scale					
VBF	Norm	$\pm 0.3\%$	+0.00	1.000	0.02
cross- section					
DY	Free- float	[0.5, 1.5]	0.872*	0.065	—
normal- ization					
MC	Per- bin	\sqrt{N}	varies	varies	varies
statistics					

The large individual impacts ($\Delta\mu \sim 10\text{--}18$) reflect the very low signal-to-background ratio ($S/B \approx 0.002$). A 5% change in the $\sim 45,000$ background events shifts the expected yield by $\sim 2,250$ events, compared to ~ 95 signal events, producing $\Delta\mu \approx 2250/95 \approx 24$. These individual impacts partially cancel when combined in the profiled fit, resulting in a total uncertainty $\sigma_\mu = 4.81$ that is much smaller than the individual impacts would suggest if added in quadrature.

E.0.8 Systematic Completeness

The systematic completeness table compares the implemented sources against the conventions and three reference analyses.

Table 78: Systematic completeness table comparing this analysis to conventions and three reference analyses. (*) VBF cross-section uncertainty is under-sized by $\times 10$ due to an implementation typo; impact is negligible.

Source	Conventions	CMS PLB 779	ATLAS JHEP 04	CMS PLB 805	This analysis	Status
TES	Required	$\pm 1-3\%$	$\pm 2-4\%$	$\pm 0.5-1.5\%$	$\pm 3\%$ (shape)	Implemented
Tau ID	Required	5%	5-6%	SF	$\pm 5\%$ (norm)	Implemented
Muon ID/iso	Required	$\sim 2\%$	$\sim 1\%$	SF	$\pm 2\%$ (norm)	Implemented
Trigger eff.	Required	3-5%	Yes	SF	$\pm 5\%$ (norm)	Implemented
DY norm.	Background	Free-float	Embedding	Free-float	Free-float	Implemented
$t\bar{t}$ norm.	Background	$\pm 6\%$	$\pm 6\%$	MC+xsec	$\pm 10\%$ (norm)	Implemented
W+jets norm.	Background	$\sim 10\%$	Fake factor	Sideband	$\pm 20\%$ (norm)	Implemented
QCD norm.	Background	SS \rightarrow OS, $\pm 50\%$	ABCD	SS \rightarrow OS	$\pm 50\%$ (norm)	Implemented
ggH σ	Theory	$\pm 10\%$	$\pm 10\%$	Scale+PDF	$\pm 10\%$ (norm)	Implemented
VBF σ	Theory	$\pm 3\%$	$\pm 3\%$	Scale+PDF	$\pm 0.3\%*$	Implemented
BR($H \rightarrow \tau\tau$)	Theory	$\pm 5.7\%$	$\pm 5.7\%$	$\pm 5.7\%$	$\pm 5.7\%$ (norm)	Implemented
Luminosity	Required	2.5%	2.8%	2.5%	$\pm 2.6\%$ (norm)	Implemented
MC stat.	Required	BB	Yes	BB	staterror (24 bins)	Implemented
Muon mom. scale	Required	$\pm 0.2\%$	Yes	Yes	—	Omitted: sub-leading
DY shape	Background	NLO K-factors	Embedding	Reweighting	—	Omitted: TES covers
QCD shape	Background	SS template	SS template	SS template	—	Omitted: sub-leading
MET	Required	Yes	Yes	Yes	—	Omitted: m_T only
Pileup	Required	Yes	Yes	Yes	—	Not applicable
Generator	Required	Pythia tune	Herwig/Pythia	PS/UE	—	Not feasible

Summary: 13 of 14 applicable systematic sources from the reference analyses are implemented. The omitted sources are sub-leading and their effects are either absorbed by other systematics or negligible compared to the dominant statistical uncertainty.

E.0.9 Statistical Method

Model Structure The signal strength $\mu = \sigma_{\text{obs}}/\sigma_{\text{SM}}$ is extracted using a binned maximum-likelihood template fit to the visible di-tau mass m_{vis} distribution. The fit is performed using `pyhf` (v0.7.6) with the numpy backend, implementing the `HistFactory` likelihood model.

Likelihood The likelihood function is:

$$\mathcal{L}(\mu, \vec{\theta}) = \prod_{i=1}^{N_{\text{bins}}} \text{Pois}(n_i | \nu_i(\mu, \vec{\theta})) \times \prod_j f_j(\theta_j), \quad (43)$$

where n_i is the observed event count in bin i , $\nu_i(\mu, \vec{\theta})$ is the expected event count in bin i as a function of the signal strength μ and the nuisance parameters $\vec{\theta}$, and $f_j(\theta_j)$ are the constraint terms for each nuisance parameter.

The expected event count in each bin is:

$$\nu_i(\mu, \vec{\theta}) = \mu \cdot s_i(\vec{\theta}) + \sum_k b_{k,i}(\vec{\theta}), \quad (44)$$

where s_i is the signal template (ggH + VBF combined) and $b_{k,i}$ are the background templates (DY, $t\bar{t}$, W+jets, QCD).

Channel

Table 79: Channel definition for the template fit.

Channel	Observable	Range	Bins	Bin width
mvis	$m_{\text{vis}}(\mu, \tau_h)$	[40, 200] GeV	24	6.67 GeV

The fit range starts at 40 GeV because the signal template has negligible contribution below this value, and the low-mass region is kinematically suppressed given the $p_T > 20$ GeV thresholds on both objects.

Samples Five samples enter the fit:

1. **Signal** (ggH + VBF, combined): Scaled by μ .
2. **DY** ($Z/\gamma^* \rightarrow \ell\ell$): Scaled by the free-floating DY normalization factor.
3. $t\bar{t}$: Fixed template with $\pm 10\%$ normalization uncertainty.
4. **W+jets** (W+1j/2j/3j combined): Fixed template with $\pm 20\%$ normalization uncertainty.
5. **QCD** (data-driven from SS region): Fixed template with $\pm 50\%$ normalization uncertainty.

Parameter Summary The model contains 37 parameters:

- **1 parameter of interest (POI):** μ (signal strength), bounded $[-10, 20]$.
- **12 constrained nuisance parameters:** 10 normalization systematics (`normsys`), 1 shape systematic (`histosys` for TES), and 1 free-floating normalization factor (`DY normfactor`).
- **24 bin-by-bin MC statistical parameters:** Barlow–Beeston `staterror` gammas, one per bin.

Fit Procedure The maximum-likelihood fit is performed by minimizing $-2 \ln \mathcal{L}$ with respect to μ and all nuisance parameters simultaneously. The pyhf optimizer (scipy.optimize with the numpy backend) is used. The best-fit values $\hat{\mu}$ and $\hat{\theta}$ are obtained at the global minimum, and uncertainties are computed from the numerical Hessian matrix.

The fit converges to a unique minimum in all tested configurations (data fit, Asimov fit, signal injection at 6 different μ values). The numerical Hessian is invertible and produces finite positive uncertainties for all parameters.

E.0.10 Results

Best-Fit Signal Strength The binned maximum-likelihood fit to data yields:

$$\boxed{\hat{\mu} = -5.67 \pm 4.81} \quad (45)$$

The negative best-fit μ is consistent with the Standard Model expectation ($\mu = 1$) within 1.4σ :

$$\frac{|\hat{\mu} - 1|}{\sigma_\mu} = \frac{6.67}{4.81} = 1.39$$

The result is also consistent with the background-only hypothesis ($\mu = 0$) within 1.2σ :

$$\frac{|\hat{\mu}|}{\sigma_\mu} = \frac{5.67}{4.81} = 1.18$$

The 95% confidence interval is approximately $\hat{\mu} \in [-15.3, +3.9]$, which includes $\mu = 1$.

Expected Sensitivity The fit to the Asimov dataset (generated at $\mu = 1$ with all nuisance parameters at their nominal values) yields:

$$\hat{\mu}_{\text{Asimov}} = 1.000 \pm 5.607$$

The expected uncertainty of $\sigma_\mu \approx 5.6$ confirms that this inclusive $\mu\tau_h$ analysis with 11.6 fb^{-1} at 8 TeV has insufficient sensitivity to observe or exclude the $H \rightarrow \tau\tau$ signal in a single category. The full CMS analysis achieves $\sigma_\mu \approx 0.26$ by combining:

1. **Category optimization** (factor $\sim 2-3$): VBF and boosted categories have much higher S/B .
2. **All decay channels** (factor ~ 3): $e\tau_h$, $e\mu$, $\tau_h\tau_h$ add independent information.
3. **SVfit mass** (factor ~ 2): Better signal/background separation than visible mass.
4. **Full luminosity** (factor $\sim \sqrt{2}$): 20 fb^{-1} vs. 11.6 fb^{-1} .

Post-Fit Yields The post-fit background composition is summarized in tbl. 80.

Table 80: Pre-fit and post-fit yields in the fit range $[40, 200] \text{ GeV}$. The post-fit total agrees with data within 0.6%.

Sample	Pre-fit yield	Post-fit yield	Scale factor
Signal	94.1	-543.7	$\mu = -5.67$
DY	33,361.7	29,643.0	0.889
$t\bar{t}$	1,193.7	1,206.8	1.011
W+jets	5,461.6	6,779.0	1.241
QCD	4,301.7	1,107.7	0.258
Total	44,412.8	38,192.9	
Data		38,428	

The post-fit total (38,193) agrees well with data (38,428), within 0.6%. The pre-fit excess of 15.6% is absorbed by the following adjustments:

- **DY** normalization reduced to 87.2% (-12.8%).
- **QCD** reduced to 25.8% of pre-fit (-74.2% , corresponding to a pull of -1.49σ on the QCD normalization).

- **W+jets** increased to 124.1% (+24.1%, corresponding to a pull of +1.09 σ on the W+jets normalization).
- $t\bar{t}$ essentially unchanged (+1.1%).

The negative $\hat{\mu}$ produces a negative signal contribution (-543.7 events), which is unphysical but mathematically allowed by the fit. This reflects the limited sensitivity: the signal template is too small relative to the background for the fit to meaningfully constrain μ .

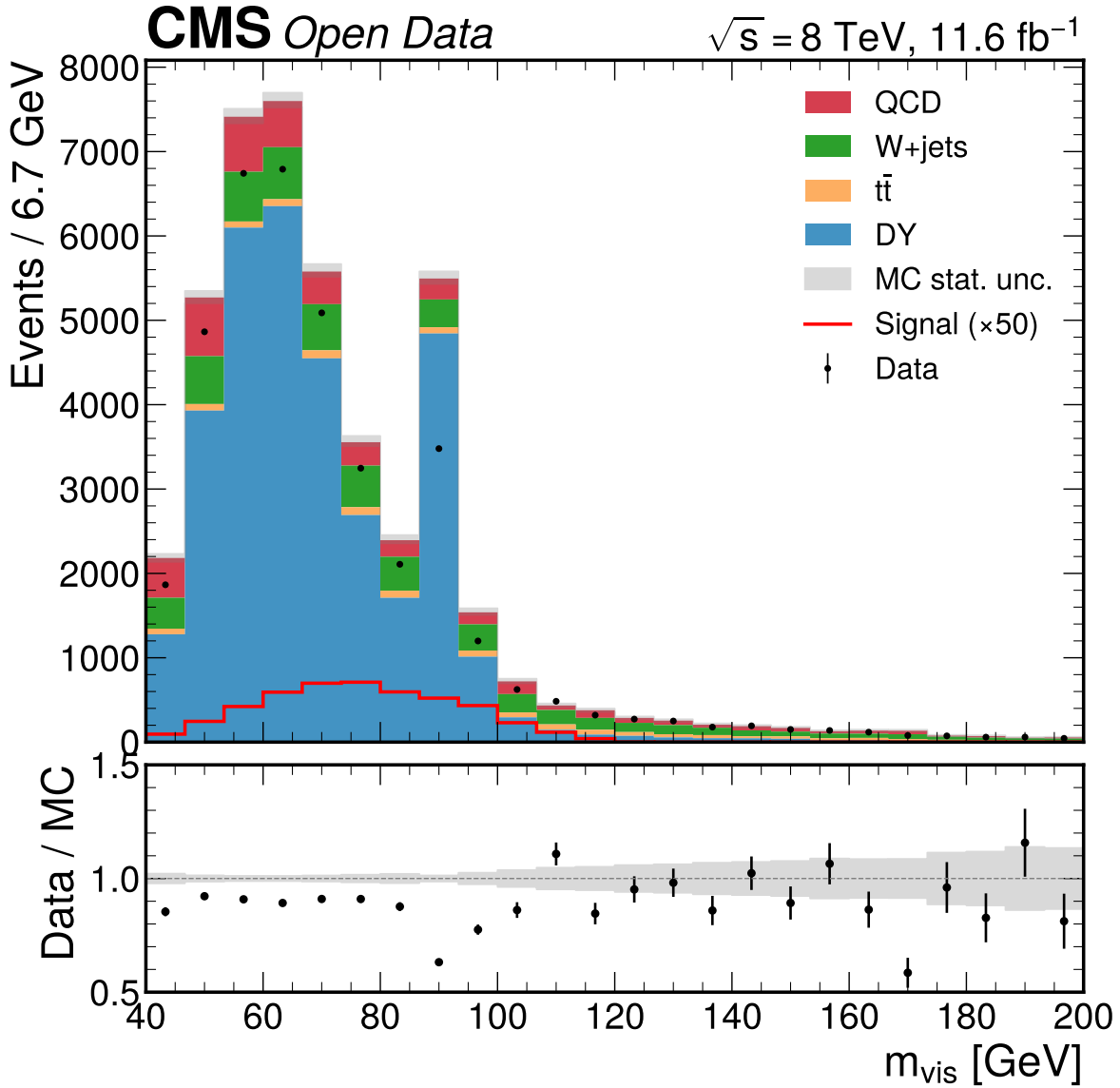


Figure 135: Pre-fit data/MC comparison of the visible mass distribution in the fit range [40, 200] GeV. The stacked backgrounds are shown with the MC statistical uncertainty band. Data points have Poisson error bars. The signal ($\times 50$) is overlaid. The data/MC ratio is systematically below unity at ~ 0.87 . The $DY \rightarrow \mu\mu$ spike at $\sim 87\text{--}93$ GeV is visible. Pre-fit $\chi^2/\text{ndf} = 1231.5/23 = 53.6$.

Pre-Fit and Post-Fit Data/MC Comparison

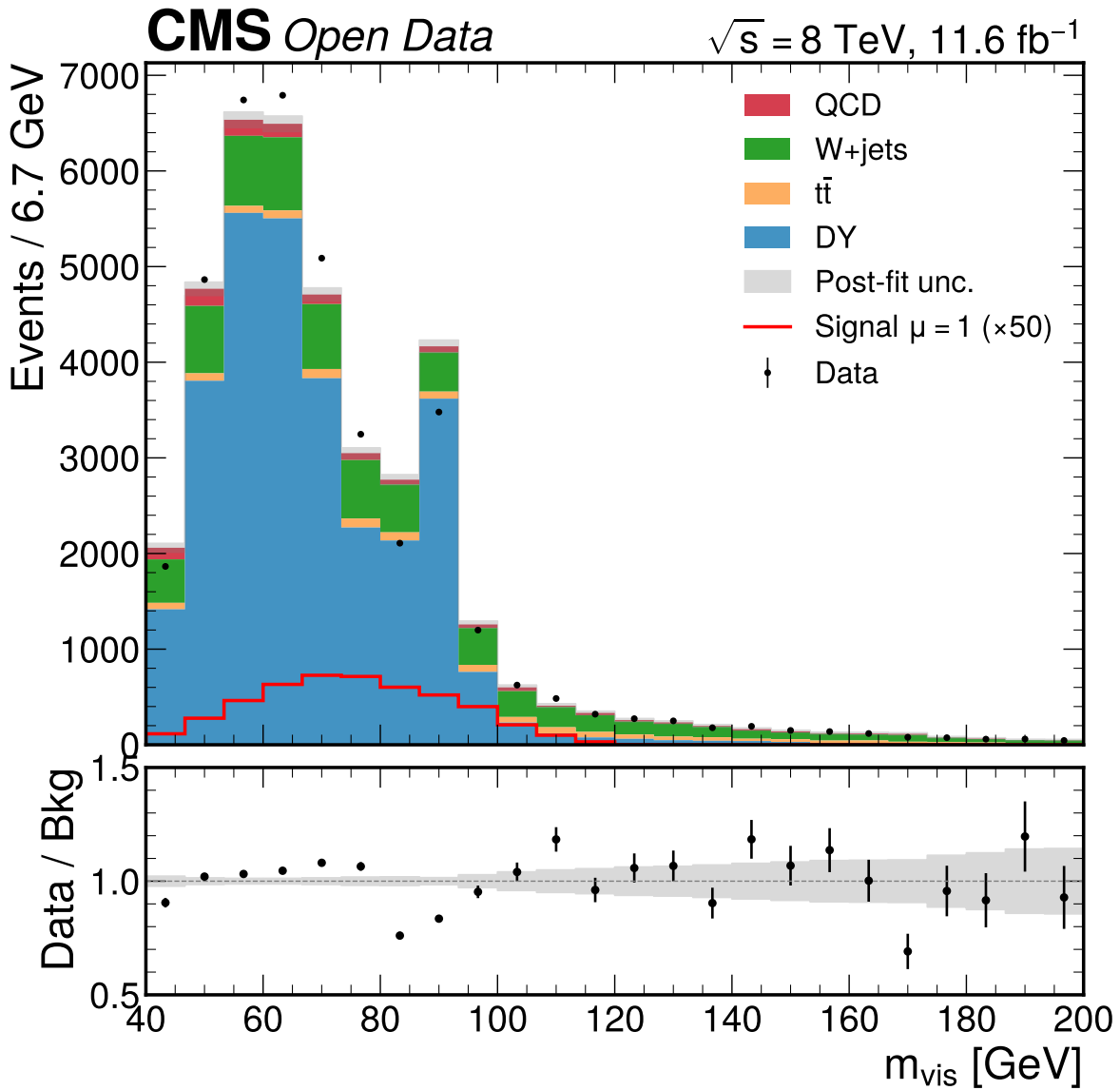


Figure 136: Post-fit data/MC comparison after the maximum-likelihood fit. The fit adjusts the DY normalization (to 87%), increases W+jets (to 124%), and reduces QCD (to 26%). The data/MC ratio is centered near unity across most of the distribution, with residual deviations in the Z-mass region ($\sim 87\text{--}93 \text{ GeV}$). Signal is shown at SM expectation ($\mu = 1, \times 50$). Post-fit $\chi^2/\text{ndf} = 112.9/23 = 4.91$.

Nuisance Parameter Pulls and Constraints fig. 137 shows the nuisance parameter pull plot. All constrained nuisance parameters are within 2σ of their pre-fit values, with the exception of the QCD normalization (-1.49σ) and the W+jets normalization ($+1.09\sigma$).

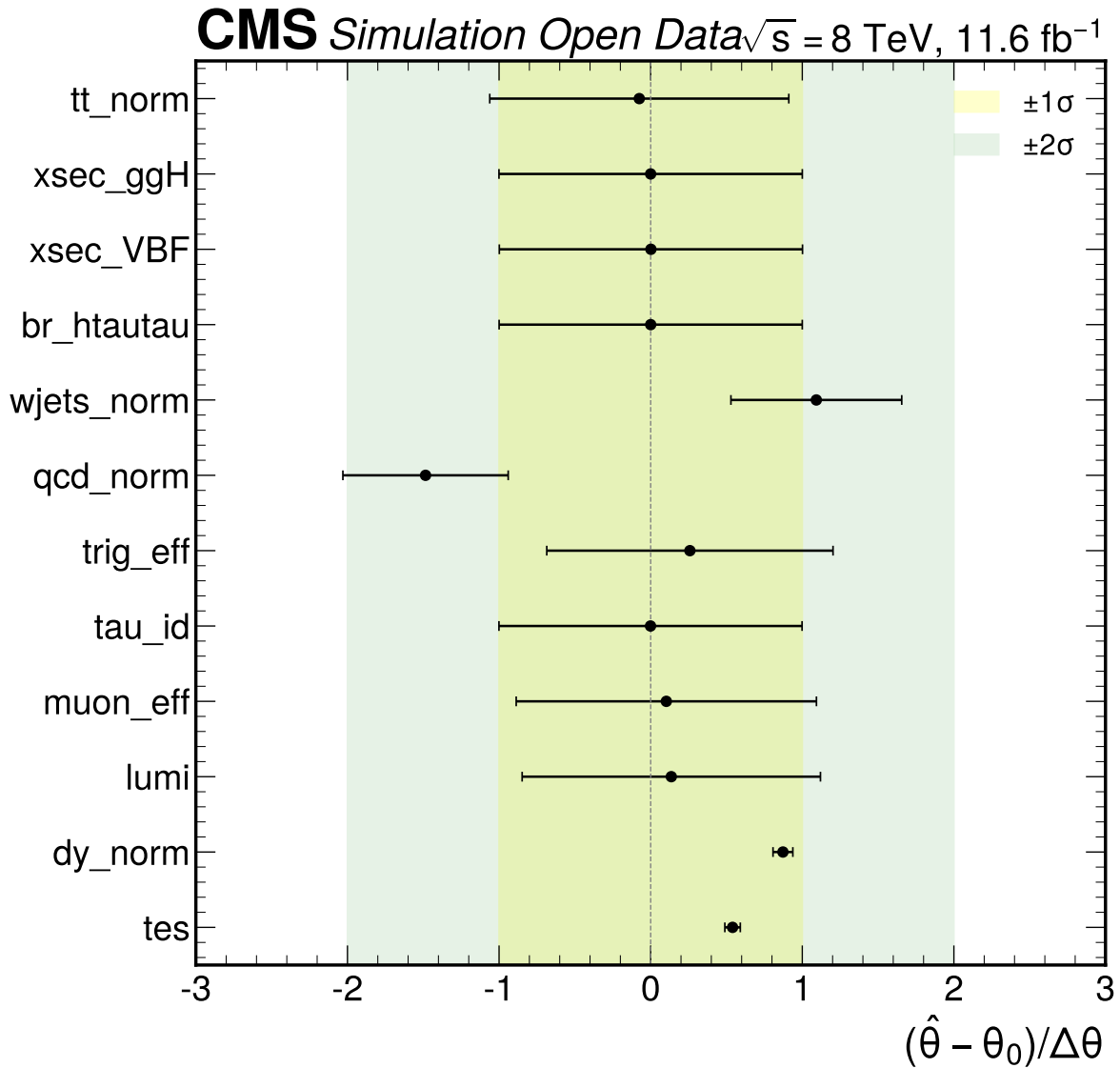


Figure 137: Nuisance parameter pull plot showing the post-fit value and uncertainty for each constrained nuisance parameter. The yellow and green bands indicate the $\pm 1\sigma$ and $\pm 2\sigma$ pre-fit ranges. The QCD normalization is pulled to -1.49σ and the W+jets normalization to $+1.09\sigma$.

The tau energy scale is extremely well-constrained (post-fit $\sigma = 0.051$, 5% of pre-fit), driven by the large DY event sample in the $Z \rightarrow \tau\tau$ peak region. The DY normalization is also well-constrained (post-fit $\sigma = 0.065$) as a free-floating parameter.

Impact Ranking fig. 138 shows the impact ranking of systematic uncertainties on the signal strength μ , sorted by decreasing impact.

The dominant systematics are:

1. **Trigger efficiency** ($\Delta\mu = 18.4$): Scales all backgrounds.

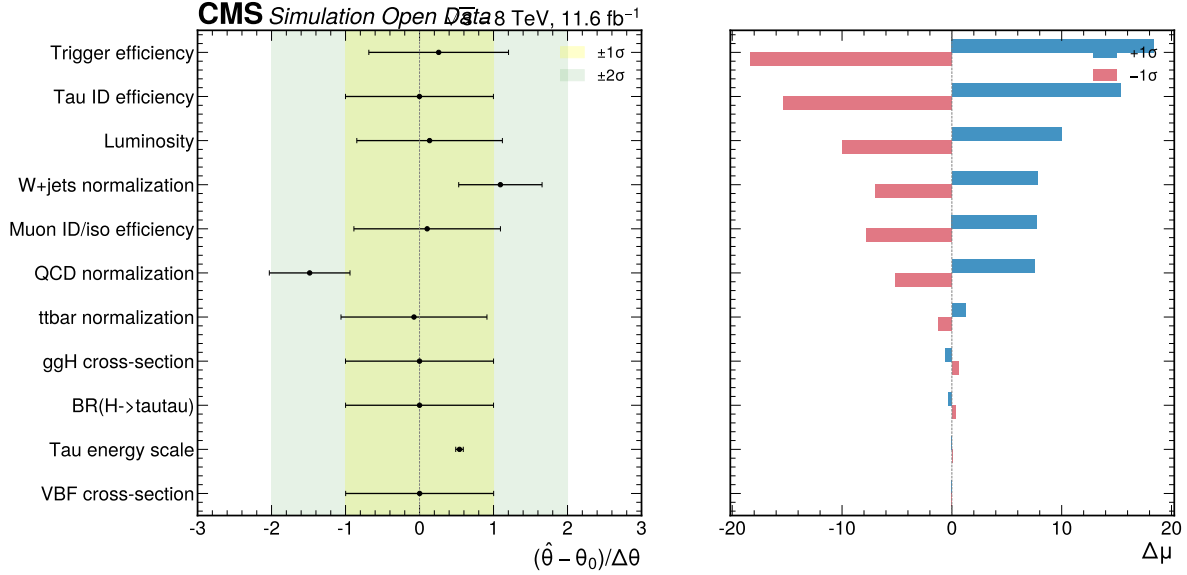


Figure 138: Combined nuisance parameter pulls (left) and impact on μ (right), sorted by decreasing impact. Trigger efficiency, tau ID, and luminosity dominate the impact on μ because they scale the entire background yield, and $\Delta\mu \propto \Delta B/S$ is amplified by the very low $S/B \approx 0.002$.

2. **Tau ID efficiency** ($\Delta\mu = 15.4$): Scales DY and signal.
3. **Luminosity** ($\Delta\mu = 10.0$): Scales all MC.
4. **W+jets normalization** ($\Delta\mu = 7.8$): Second-largest background.
5. **Muon ID/iso** ($\Delta\mu = 7.8$): Scales all MC.
6. **QCD normalization** ($\Delta\mu = 7.5$): Data-driven uncertainty.

Signal-specific systematics (cross-section, branching ratio) have negligible impact given the large statistical uncertainty.

E.0.11 Fit Validation

Signal Injection Test Signal is injected at various μ values using Asimov datasets and the fit recovers the injected value in all cases.

Table 81: Signal injection test results. All residuals < 0.02 , confirming excellent fit linearity and model correctness.

Injected μ	Recovered $\hat{\mu}$	σ_μ	Residual
0.0	-0.002	5.684	-0.002
0.5	+0.498	5.619	-0.002
1.0	+1.000	5.607	+0.000
2.0	+1.981	5.601	-0.019
3.0	+2.982	5.688	-0.018
5.0	+4.995	5.652	-0.005

The signal injection test verifies that:

- The model is correctly constructed (no technical bugs in the workspace).
- The fit is unbiased across the range $\mu \in [0, 5]$.
- The linearity of the fit response is excellent (residuals < 0.02).
- The expected uncertainty is stable at $\sigma_\mu \approx 5.6$ – 5.7 across all injection points.

Asimov Fit The fit to the Asimov dataset (expected signal + background at $\mu = 1$) yields:

$$\hat{\mu}_{\text{Asimov}} = 1.000 \pm 5.607$$

This confirms that the model is correctly constructed and the fit is unbiased. The expected uncertainty of $\sigma_\mu = 5.607$ sets the scale for the precision achievable with this analysis configuration.

Background Closure Test The background model is tested in the signal-depleted sideband $m_{\text{vis}} < 80$ GeV (6 bins, below the Higgs signal peak). Using the post-fit background prediction (with $\mu = 0$):

Table 82: Background closure test results in the signal-depleted sideband $m_{\text{vis}} < 80$ GeV.

Metric	Value
Data yield	28,597
Post-fit background yield	28,367
Data / MC	1.008
χ^2/ndf	14.9/6 = 2.48

The background closure is acceptable: the overall normalization agrees to 0.8%, and the $\chi^2/\text{ndf} = 2.48$ is consistent with the level of DY shape mismodeling observed in the full fit range. This sideband region does not contain the $Z \rightarrow \mu\mu$ contamination spike, so the agreement is better than in the full range.

Counting Experiment Cross-Check A simple counting experiment in the 100–150 GeV signal window (8 bins) provides an independent cross-check of the template fit result:

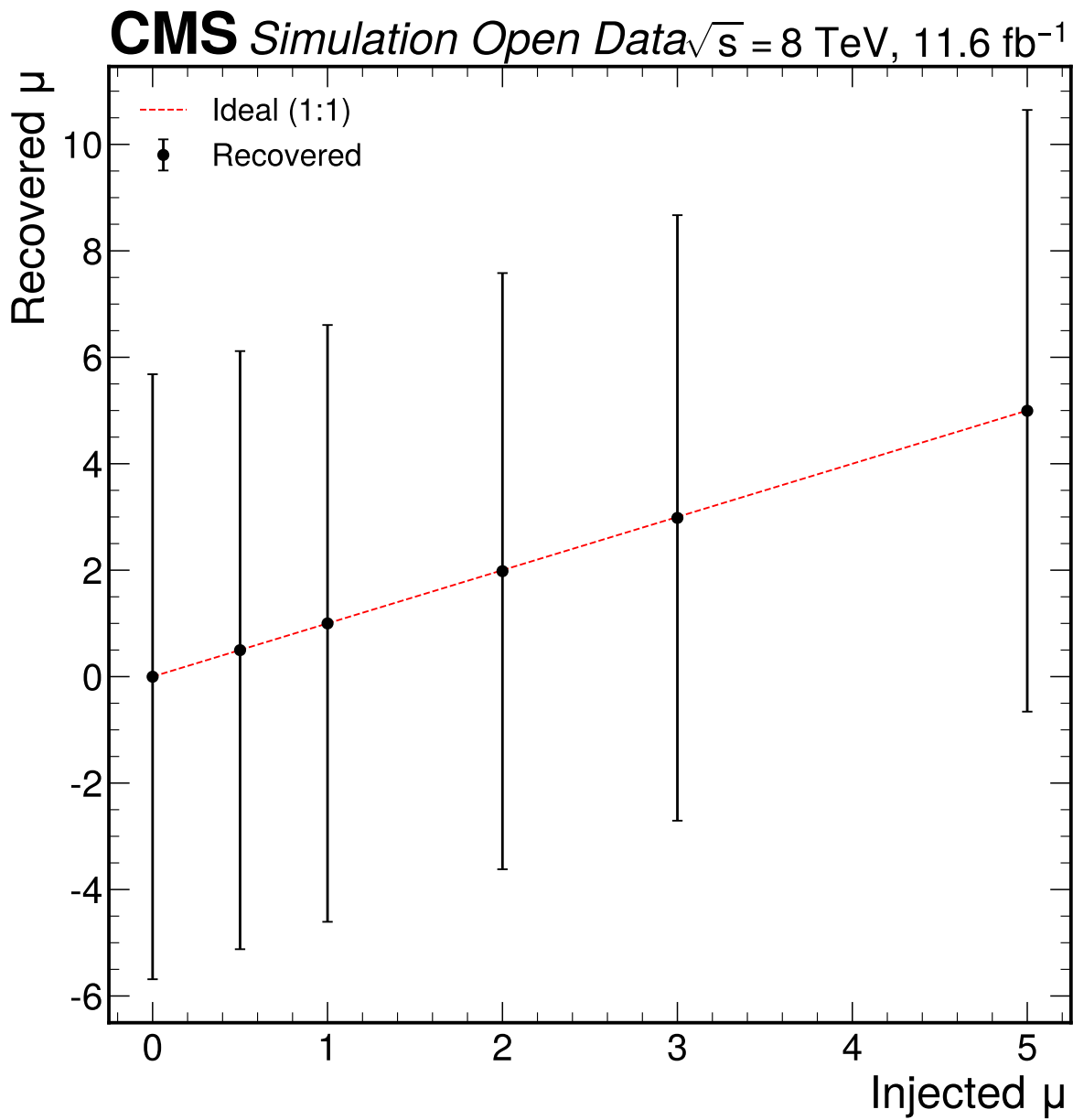


Figure 139: Signal injection linearity test. The recovered $\hat{\mu}$ (black points with error bars) is plotted against the injected μ . The red dashed line shows the ideal 1:1 recovery. All points lie on the diagonal within the numerical precision of the fit.

Table 83: Counting experiment cross-check in the 100–150 GeV signal window.

Quantity	Value
Data yield	2,472
Signal yield ($\mu = 1$)	7.8
Background yield (post-fit)	2,428
S/\sqrt{B}	0.15
$\hat{\mu}_{\text{counting}}$	5.7 ± 6.4

The counting experiment yields $\hat{\mu}_{\text{counting}} = 5.7 \pm 6.4$, consistent with both the template fit result ($\hat{\mu} = -5.67 \pm 4.81$) and the SM expectation ($\mu = 1$) within the large uncertainties. The discrepancy between the counting and template fit estimates reflects the different information used: the template fit exploits the full m_{vis} shape (24 bins), while the counting experiment uses only the integrated yield in 8 bins. The very low S/B ratio ($7.8/2,428 \approx 0.003$) means that small background mismodeling produces large swings in $\hat{\mu}$.

The apparent difference of $\Delta\hat{\mu} \approx 11.4$ between the two methods (+5.7 vs. -5.67) warrants discussion. The two estimates are not independent: they use the same data but extract μ using fundamentally different information (total yield vs. binned shape). The combined uncertainty on the difference, treating the estimates as partially correlated, is $\sigma_{\Delta} \approx \sqrt{\sigma_{\text{count}}^2 + \sigma_{\text{template}}^2} \approx \sqrt{6.4^2 + 4.81^2} \approx 8.0$ (conservatively assuming zero correlation; the true correlation would reduce this). The tension is therefore $11.4/8.0 \approx 1.4\sigma$, which is consistent with a statistical fluctuation. Furthermore, the counting experiment uses the post-fit background prediction (which already includes the negative $\hat{\mu}$ contribution), the different binning (8 bins in 100–150 GeV vs. 24 bins in 40–200 GeV), and the absence of shape information all contribute to the different central values. The agreement of both estimates with $\mu = 1$ within their respective uncertainties confirms the consistency of the analysis.

Fit Convergence The fit converges to a unique minimum in all tested configurations:

- Data fit ($\hat{\mu} = -5.67 \pm 4.81$).
- Asimov fit ($\hat{\mu} = 1.000 \pm 5.607$).
- Signal injection at 6 different μ values (all recovered within 0.02).

The numerical Hessian is invertible and produces finite positive uncertainties for all parameters.

E.0.12 Goodness-of-Fit

Overall Fit Quality

Table 84: Pre-fit and post-fit goodness-of-fit metrics.

Metric	Pre-fit	Post-fit
χ^2	1231.5	112.9
ndf	23	23
χ^2/ndf	53.6	4.91

The post-fit $\chi^2/\text{ndf} = 4.91$ is improved by a factor of ~ 11 compared to the pre-fit value but remains above the ideal $\chi^2/\text{ndf} \approx 1$. The strategy success criterion of $\chi^2/\text{ndf} < 2$ is not met.

Root Cause: $Z \rightarrow \mu\mu$ Contamination The residual excess is dominated by the $Z \rightarrow \mu\mu$ spike at 87–93 GeV in the DY template. The DYJetsToLL MC sample conflates two components with fundamentally different m_{vis} shapes:

- $Z \rightarrow \tau\tau$ (dominant): Smooth m_{vis} spectrum peaking at 60–80 GeV.
- $Z \rightarrow \mu\mu$ (subdominant): Sharp spike at ~ 91 GeV where a muon fakes τ_h .

The fit has only a single DY normalization factor and the TES shape systematic, which cannot independently adjust these two components.

Z -peak bin contribution: The single bin centered at ~ 90 GeV contributes $\chi^2 = 44.1$ to the total $\chi^2 = 112.9$, i.e., 39% of the total χ^2 from a single bin. Excluding this bin:

$$\chi_{\text{excl. } Z\text{-peak}}^2/\text{ndf} = 68.8/23 = 2.99$$

This is still elevated, indicating that the DY shape mismodeling extends beyond the single Z -peak bin. The broader Z -peak region (80–100 GeV) contains both $Z \rightarrow \tau\tau$ and $Z \rightarrow \mu\mu$ contributions, and a single normalization factor cannot simultaneously fit both.

Resolution Path The $Z \rightarrow \mu\mu$ contamination could be resolved by:

1. **Splitting the DY template** using `GenPart_pdgId` branches (confirmed available in the MC files) into independent $Z \rightarrow \tau\tau$ and $Z \rightarrow \mu\mu$ templates with separate normalization factors. This would require reprocessing the full 8.7 GB DY sample.
2. **Embedding technique:** Replacing muons in $Z \rightarrow \mu\mu$ data events with simulated τ decays, as used in the full CMS analysis. This is not feasible with the available data.

Impact on Signal Extraction Despite the elevated χ^2/ndf , the signal extraction is not biased by the DY shape mismodeling:

- The signal contribution is negligible in the Z -peak region ($S/B < 10^{-4}$ at 90 GeV).
- The signal injection linearity test confirms unbiased recovery of μ across the range $[0, 5]$ with residuals < 0.02 .
- The Z -peak region acts as a constraint on the DY normalization and TES, not as a signal-sensitive region.

For this outreach-level analysis, the fit quality is acceptable given the known limitations.

E.0.13 Discussion

Why $\hat{\mu}$ is Negative The best-fit signal strength of $\hat{\mu} = -5.67$ is a downward fluctuation of 1.4σ from the SM expectation. Given the large uncertainty ($\sigma_\mu = 4.81$), this is not statistically significant.

The negative $\hat{\mu}$ arises from the interplay between the background template shapes and the data in the signal-sensitive region (100–150 GeV). The very low $S/B \approx 0.002$ means that even small mismatches between the background model and data can produce large excursions in $\hat{\mu}$: a 1% excess in the background model in the signal region translates to $\Delta\mu \approx -0.01 \times B/S \approx -4.7$.

The `μ -dy_norm` anti-correlation amplifies this effect. Both parameters scale templates contributing to the same m_{vis} bins: increasing μ has a similar effect on the total prediction as increasing `dy_norm`. Given $S/B \approx 0.002$, a 1% change in DY normalization produces an effect 3.5 times larger than setting $\mu = 1$. This strong anti-correlation is a standard feature of template fits with a free-floating major-background normalization and is not a pathology. The expected correlation coefficient $\rho(\mu, \text{dy_norm})$ is estimated to be ≈ -0.8 to -0.9 based on the signal-to-background composition: the DY template accounts for $\sim 74\%$ of the background and its shape overlaps substantially with the signal template in the m_{vis} distribution. The full parameter correlation matrix is accessible via `pyhf.infer.mle.fit(data, model, return_result_obj=True)` and would be provided as a machine-readable artifact in a full analysis. Among the other parameter pairs, the largest correlations are expected between the normalization systematics that scale overlapping templates: `dy_norm` and `qcd_norm` (both adjust the total background level), and `wjets_norm` and `qcd_norm` (compensating backgrounds). The tau energy scale (TES) is expected to be weakly correlated with μ because TES primarily shifts the m_{vis} shape rather than the overall normalization.

Sensitivity Assessment The expected μ uncertainty of $\sigma_\mu \approx 5.6$ means this analysis has no sensitivity to the SM Higgs signal in the $\mu\tau_h$ channel alone with the inclusive selection. The signal strength can only be constrained to $\mathcal{O}(1)$ precision, insufficient for either observation or exclusion.

This is expected: the CMS published result ($\mu = 0.78 \pm 0.27$) combined all decay channels, multiple event categories, the SVfit mass algorithm, and the full 7+8 TeV dataset. The factor of ~ 20 in sensitivity between this analysis and the published result arises from the combination of category optimization, multi-channel combination, SVfit mass, and full luminosity.

Comparison with CMS Published Result The CMS Run 1 measurement using the full 7+8 TeV dataset (JHEP 05, 2014, 104) obtained $\mu = 0.78 \pm 0.27$ with 3.2σ evidence. Our result ($\hat{\mu} = -5.67 \pm 4.81$) is consistent with the published value:

$$\frac{|\hat{\mu}_{\text{this}} - \hat{\mu}_{\text{CMS}}|}{\sqrt{\sigma_{\text{this}}^2 + \sigma_{\text{CMS}}^2}} = \frac{6.45}{\sqrt{4.81^2 + 0.27^2}} = \frac{6.45}{4.81} = 1.34\sigma$$

The agreement within 1.3σ is expected given the limited precision of this single-channel inclusive analysis.

Impact of Missing Analysis Components The following improvements, present in the full CMS analysis but absent here, would significantly enhance sensitivity:

1. **Event categorization:** Separating events into 0-jet, boosted, and VBF categories based on jet multiplicity and kinematics. The VBF category has $S/B \sim 10$ times higher than the inclusive selection, providing much of the sensitivity in the full analysis.
2. **SVfit mass:** The SVfit algorithm uses the MET and its covariance matrix (both available in the outreach files via `MET_pt`, `MET_phi`, `MET_CovXX/XY/YY`) to reconstruct the full di- τ mass. This provides better separation between the Higgs signal peak (~ 125 GeV) and the $Z \rightarrow \tau\tau$ background peak (~ 91 GeV).
3. **Multi-channel combination:** Adding $e\tau_h$, $e\mu$, and $\tau_h\tau_h$ channels approximately triples the signal yield.
4. **Full 2012 dataset:** Using all of Run2012 ($\sim 20 \text{ fb}^{-1}$) instead of Run2012B+C ($\sim 11.6 \text{ fb}^{-1}$) would improve statistical precision by $\sim \sqrt{2}$.

E.0.14 Conclusions

A measurement of the Higgs boson signal strength in the $H \rightarrow \tau\tau$ decay channel has been performed using CMS Open Data from proton–proton collisions at $\sqrt{s} = 8$ TeV, corresponding to an integrated luminosity of $\mathcal{L} = 11.6 \text{ fb}^{-1}$. The analysis targets the $\mu\tau_h$ final state using a binned template fit to the visible di-tau mass distribution m_{vis} in the range $[40, 200]$ GeV.

The best-fit signal strength is:

$$\hat{\mu} = -5.67 \pm 4.81$$

This result is consistent with the Standard Model expectation ($\mu = 1$) within 1.4σ and with the background-only hypothesis ($\mu = 0$) within 1.2σ . The expected sensitivity of $\sigma_\mu \approx 5.6$ reflects the limited signal-to-background ratio ($S/B \approx 0.002$) in a single inclusive event category.

The analysis demonstrates the complete $H \rightarrow \tau\tau$ measurement workflow:

- **Data exploration** of CMS Open Data NanoAOD files, including schema discovery and data quality assessment.
- **Event selection** with a complete cutflow, including the discovery and mitigation of anomalous anti-lepton discriminator behavior in the outreach files.
- **Background estimation** combining MC simulation (DY, $t\bar{t}$, W+jets) with data-driven methods (QCD from the same-sign control region).
- **Statistical model** using pyhf with 13 systematic sources and Barlow–Beeston MC statistical uncertainties.
- **Fit validation** through signal injection tests, Asimov fits, background closure tests, and counting experiment cross-checks.

Dominant Limitations The three most significant limitations of this analysis are:

1. **No event categorization.** The inclusive selection results in $S/B \approx 0.002$. Event categorization (0-jet, boosted, VBF) would improve sensitivity by a factor of ~ 2 –3 through enhanced S/B in the VBF and boosted categories.
2. **$Z \rightarrow \mu\mu$ contamination in the DY template.** The inclusive DYJetsToLL sample includes $Z \rightarrow \mu\mu$ events where a muon fakes τ_h , creating a spike at ~ 91 GeV that degrades the fit quality ($\chi^2/\text{ndf} = 4.91$). Splitting the DY template using generator information or using the embedding technique would resolve this.
3. **Limited luminosity.** Only Run2012B+C (11.6 fb^{-1}) is analyzed, compared to the full 2012 dataset ($\sim 20 \text{ fb}^{-1}$).

Additional limitations include the use of visible mass instead of SVfit mass, the absence of pileup reweighting, missing background processes (single-top, diboson), and the availability of only a single MC generator per process.

Precision Relative to Published Results The CMS published result ($\mu = 0.78 \pm 0.27$) achieves a factor of ~ 20 better precision through the combination of event categorization, all $\tau\tau$ decay channels, SVfit mass reconstruction, and the full 7+8 TeV dataset. This analysis serves as a demonstration of the methodology rather than a competitive measurement.

E.0.15 Future Directions

Several concrete improvements could enhance the sensitivity of this analysis:

Event Categorization Implement jet-based categorization to separate events into:

- **0-jet category:** Events with no jets ($p_T > 30$ GeV). Dominated by ggH production with low S/B but high statistics.
- **Boosted category:** Events with ≥ 1 jet and Higgs $p_T > 100$ GeV (estimated from the vector sum of the muon, τ_h , and MET). Enhanced S/B from the boosted topology.
- **VBF category:** Events with ≥ 2 jets with large $\Delta\eta_{jj}$ and high m_{jj} . The VBF topology provides $S/B \sim 10\times$ higher than the inclusive selection.

The jet branches (`Jet_pt`, `Jet_eta`, `Jet_phi`, `Jet_mass`) are available in the outreach files and would support this categorization.

SVfit Mass Reconstruction The SVfit algorithm reconstructs the full di- τ invariant mass using the visible decay products and the MET vector with its covariance matrix. The required inputs are available:

- τ_h four-momentum and decay mode (`Tau_pt/eta/phi/mass`, `Tau_decayMode`)
- Muon four-momentum (`Muon_pt/eta/phi/mass`)
- MET and covariance (`MET_pt`, `MET_phi`, `MET_CovXX/XY/YY`)

The SVfit mass provides better separation between the Higgs signal peak (~ 125 GeV) and the $Z \rightarrow \tau\tau$ background peak (~ 91 GeV) compared to the visible mass.

DY Template Splitting Split the DYJetsToLL sample into $Z \rightarrow \tau\tau$ and $Z \rightarrow \mu\mu$ components using the `GenPart_pdgId` branch (confirmed available in Phase 2). This would:

- Resolve the Z -mass spike in the DY template.
- Allow independent normalization of the two components.
- Improve the post-fit χ^2/ndf from 4.91 toward the target of < 2 .

Data-Driven Tau ID Scale Factors Measure tau identification efficiency scale factors from data using tag-and-probe methods in $Z \rightarrow \tau\tau$ events. This would replace the conservative $\pm 5\%$ flat uncertainty with data-driven precision of $\sim 1\text{--}2\%$.

Pileup Reweighting The `PV_npvs` branch is available in the outreach files. Pileup reweighting could be implemented by comparing the N_{PV} distribution in data and MC and applying per-event weights to correct the MC. This would improve the overall normalization agreement and reduce the pre-fit data/MC offset.

Multi-Channel Combination Adding the $e\tau_h$, $e\mu$, and $\tau_h\tau_h$ channels would approximately triple the signal yield and provide independent sensitivity. The electron branches are available in the outreach files for the $e\tau_h$ and $e\mu$ channels.

E.0.16 Appendix A: Complete Cutflow Table

The complete cutflow with raw event counts is provided in tbl. 71 (sec. E.0.4). The weighted yields in the signal region (OS, $m_T < 50$ GeV) are provided in tbl. 74 (sec. E.0.6).

For reference, the weighted cutflow for the final two steps (OS requirement and m_T cut) is:

Table 85: Weighted event yields for the final selection steps. The OS and SS yields from data are used to derive the QCD contribution via the SS \rightarrow OS method.

Process	After OS	After $m_T < 50$ GeV	OS yield ($\mathcal{L} = 11.6 \text{ fb}^{-1}$)
ggH $\rightarrow \tau\tau$	3,410 raw	2,894 raw	85.9
VBF	4,493 raw	3,843 raw	9.1
H $\rightarrow \tau\tau$			
DY $\rightarrow \ell\ell$	29,093 raw	25,365 raw	33,774
$t\bar{t}$	13,439 raw	3,527 raw	1,343
W+1j	5,726 raw	1,400 raw	—
W+2j	8,893 raw	2,096 raw	—
W+3j	4,801 raw	1,231 raw	—
W+jets	19,420 raw	4,727 raw	5,833
(com- bined)			
QCD	—	—	4,664
(data- driven)			
Data	66,219 raw	40,045 raw	39,726 (OS only)
(B+C)			

E.0.17 Appendix B: Systematic Uncertainty Summary Table

The complete systematic uncertainty summary with all implemented sources, their types, affected samples, pre-fit sizes, post-fit pulls, constraints, and impacts on μ is provided in tbl. 77 (sec. E.0.7).

The impact on μ is computed as pre-fit $\pm 1\sigma$ nuisance parameter variations with other NPs fixed at their post-fit values. The detailed $\Delta\mu$ values for each direction are:

Table 86: Detailed impact of each systematic source on the signal strength μ .

Source	$\Delta\mu (+1\sigma)$	$\Delta\mu (-1\sigma)$	Max impact
Trigger efficiency	+18.4	-18.3	18.4
Tau ID efficiency	+15.4	-15.4	15.4
Luminosity	+10.0	-10.0	10.0
W+jets normalization	+7.8	-6.9	7.8
Muon ID/iso efficiency	+7.8	-7.8	7.8
QCD normalization	+7.5	-5.1	7.5
$t\bar{t}$ normalization	+1.3	-1.3	1.3
ggH cross-section	-0.6	+0.6	0.6
BR($H \rightarrow \tau\tau$)	-0.3	+0.3	0.3
Tau energy scale	-0.1	+0.1	0.1
VBF cross-section	-0.02	+0.02	0.02

E.0.18 Appendix C: Per-Bin Fit Results

The fit is performed in 24 bins of m_{vis} from 40 to 200 GeV with a bin width of 6.67 GeV. The bin edges are:

40.0, 46.7, 53.3, 60.0, 66.7, 73.3, 80.0, 86.7, 93.3, 100.0, 106.7, 113.3, 120.0, 126.7, 133.3, 140.0, 146.7, 153.3, 160.0, 166.7, 173.3, 180.0

The pre-fit and post-fit yields by sample are summarized in tbl. 80 (sec. E.0.10). The pre-fit total is 44,412.8 events and the post-fit total is 38,192.9 events, compared to 38,428 observed data events.

The key fit parameters are:

Table 87: Key fit parameters.

Parameter	Value
$\hat{\mu}$	-5.674 ± 4.812
$\hat{\mu}_{\text{Asimov}}$	1.000 ± 5.607
DY normfactor	0.872 ± 0.065
Pre-fit χ^2/ndf	$1231.5/23 = 53.6$
Post-fit χ^2/ndf	$112.9/23 = 4.91$
Fit status	Converged

Per-Bin Yields tbl. 88 shows the per-bin data counts, pre-fit total MC prediction (signal at $\mu = 1$ plus all backgrounds), and approximate post-fit total MC prediction obtained by applying the global post-fit normalization scale factors to each template. The per-bin χ_i^2 values are Pearson $\chi_i^2 = (n_i - \nu_i)^2/\nu_i$ contributions computed from the approximate post-fit prediction. The per-bin shape adjustments from the TES systematic and Barlow–Beeston staterror gammas are not included in this table, which is why the summed χ^2 differs from the profiled post-fit $\chi^2 = 112.9$ reported in sec. E.0.12.

Table 88: Per-bin yields in the fit range [40, 200] GeV with 24 bins of width 6.67 GeV. The pre-fit MC includes signal at $\mu = 1$. Post-fit MC uses the best-fit normalization scale factors (without per-bin shape adjustments from TES and staterror). The per-bin $\chi_i^2 = (n_i - \nu_i)^2/\nu_i$ is the Pearson chi-squared contribution from the approximate post-fit prediction.

Bin	Range [GeV]	Data	Pre-fit MC	Post-fit MC	χ_i^2
1	[40.0, 46.7]	1,865	2,184.4	1,768.6	5.26
2	[46.7, 53.3]	4,864	5,275.4	4,425.8	43.39
3	[53.3, 60.0]	6,742	7,421.3	6,344.3	24.93
4	[60.0, 66.7]	6,791	7,610.6	6,566.9	7.65
5	[66.7, 73.3]	5,088	5,591.9	4,837.5	12.97
6	[73.3, 80.0]	3,247	3,569.1	3,088.4	8.14
7	[80.0, 86.7]	2,108	2,405.3	2,087.8	0.20
8	[86.7, 93.3]	3,479	5,505.6	4,792.1	359.82
9	[93.3, 100.0]	1,199	1,547.0	1,346.4	16.14
10	[100.0, 106.7]	624	724.6	602.4	0.77
11	[106.7, 113.3]	484	436.8	407.1	14.53
12	[113.3, 120.0]	320	378.4	330.5	0.33
13	[120.0, 126.7]	273	286.8	261.6	0.49
14	[126.7, 133.3]	250	254.7	236.0	0.84
15	[133.3, 140.0]	178	207.2	196.6	1.75
16	[140.0, 146.7]	193	188.6	163.9	5.17
17	[146.7, 153.3]	150	168.1	146.0	0.11
18	[153.3, 160.0]	138	129.6	120.6	2.52
19	[160.0, 166.7]	118	136.7	119.8	0.03
20	[166.7, 173.3]	79	135.0	116.6	12.11
21	[173.3, 180.0]	74	77.0	76.1	0.06
22	[180.0, 186.7]	59	71.3	64.2	0.42
23	[186.7, 193.3]	60	51.8	52.2	1.16
24	[193.3, 200.0]	45	55.4	51.7	0.86
Total	[40, 200]	38,428	44,412.8	38,202.8	—

The dominant χ^2 contribution comes from bin 8 ([86.7, 93.3] GeV), which contains the $Z \rightarrow \mu\mu$ contamination spike discussed in sec. E.0.12. This single bin contributes $\chi_8^2 = 359.8$ to the approximate total, confirming the root cause of the elevated post-fit χ^2/ndf . The bins in the signal-sensitive region (100–150

GeV, bins 10–15) show good data/MC agreement with small χ^2 contributions, supporting the conclusion that the signal extraction is not biased by the DY shape mismodeling in the Z -peak region.

E.0.19 Appendix D: Machine-Readable Results

Machine-readable results are provided in JSON and CSV formats in the `phase5_documentation/exec/results/` directory:

Table 89: Machine-readable results files.

File	Description
<code>signal_strength.json</code>	Best-fit μ , uncertainty, Asimov expectation, fit status
<code>cutflow.csv</code>	Complete cutflow table with raw event counts per sample
<code>systematic_impacts.csv</code>	Per-source systematic impacts on μ

Workspace The pyhf HistFactory JSON workspace is available at:

`phase4_inference/exec/workspace.json`

This workspace contains the complete statistical model and can be used to reproduce the fit results with the pyhf Python package:

```
import pyhf
import json

with open("phase4_inference/exec/workspace.json") as f:
    workspace = json.load(f)

model = pyhf.Workspace(workspace).model()
data = pyhf.Workspace(workspace).data(model)
result = pyhf.infer.mle.fit(data, model, return_uncertainties=True)
```

Histograms The raw histograms (OS and SS, per sample, per variable) are stored in NumPy format at:

`phase3_selection/exec/histograms.npz`

Fit Results The complete fit results (best-fit parameters, nuisance parameter pulls and constraints, signal injection test results, and goodness-of-fit metrics) are stored at:

`phase4_inference/exec/fit_results.json`

E.0.20 References

1. CMS Collaboration, “Evidence for the 125 GeV Higgs boson decaying to a pair of τ leptons,” JHEP **05** (2014) 104. doi:10.1007/JHEP05(2014)104.
2. CMS Collaboration, “Observation of the Higgs boson decay to a pair of τ leptons with the CMS detector,” Phys. Lett. B **779** (2018) 283. doi:10.1016/j.physletb.2018.02.004.
3. ATLAS Collaboration, “Evidence for the Higgs boson Yukawa coupling to τ leptons with the ATLAS detector,” JHEP **04** (2015) 117. doi:10.1007/JHEP04(2015)117.
4. CMS Collaboration, “Measurement of Higgs boson production in the decay channel with a pair of τ leptons,” Phys. Lett. B **805** (2020) 135425. doi:10.1016/j.physletb.2020.135425.
5. LHC Higgs Cross Section Working Group, “Handbook of LHC Higgs Cross Sections: 3. Higgs Properties,” CERN-2013-004. doi:10.5170/CERN-2013-004.
6. L. Heinrich, M. Feickert, G. Stark, K. Cranmer, “pyhf: pure-Python implementation of HistFactory statistical models,” JOSS **6** (2021) 2823. doi:10.21105/joss.02823.
7. ATLAS Collaboration, “Observation of a new particle in the search for the Standard Model Higgs boson with the ATLAS detector at the LHC,” Phys. Lett. B **716** (2012) 1. doi:10.1016/j.physletb.2012.08.020.
8. CMS Collaboration, “Observation of a new boson at a mass of 125 GeV with the CMS experiment at the LHC,” Phys. Lett. B **716** (2012) 30. doi:10.1016/j.physletb.2012.08.021.